Shear wave splitting analysis of long-term data: Anisotropy studies in the Upper Rhine Graben area, Central Europe

Zur Erlangung des akademischen Grades einer

DOKTORIN DER NATURWISSENSCHAFTEN (Dr. rer. nat.)

von der KIT-Fakultät für Physik des
Karlsruher Instituts für Technologie (KIT)
genehmigte

DISSERTATION

von

M. Sc., Fröhlich, Yvonne

Tag der mündlichen Prüfung: 04. Juli 2025

1. Referent: Prof. Dr. Joachim R. R. Ritter
2. Korreferenten: Prof. Dr. Andreas Rietbrock

14.07.2022

What's next for science

- Theme of the AGU 2024 annual meeting, Washington, D.C., 08.12.-13.12. -

Abstract

As earthquake waves probe the Earth at all depths, seismology is a very powerful tool for providing insights into the structure and evolution of our planet. Elastic or seismic anisotropy, the dependence of the propagation velocity of seismic (elastic) waves on the propagation or polarization direction, is a widely used phenomenon to gain crucial insights into past and present geological and geodynamic processes within the Earth's interior. These processes cause deformations within the materials and rocks, which lead to a preferred orientation of structures and crystals, and by this to (bulk) anisotropy. Shear wave splitting (SWS; analogous to optical birefringence of light) is a unique indication for anisotropy. The two splitting parameters, the fast polarization direction of the anisotropic medium and the delay time the two split shear waves have accumulated after traveling through the anisotropic medium, are commonly used to quantify the anisotropy.
In addition to anisotropy related to large-scale processes such as absolute plate motion, subduction, continental rifting, and orogeny, anisotropy can vary on regional and local length scales. Especially for continental upper mantle anisotropy, small-scale complex 3-D anisotropy scenarios are suspected.

The Upper Rhine Graben (URG) area in Central Europe is characterized by a complex geological and geodynamic setting, and previous anisotropy studies propose indications for small-scale variations of anisotropy in the upper mantle. However, no 3-D anisotropy model is available for this area yet. According to this, the main goal of this doctoral thesis is to resolve the anisotropy in the upper mantle underneath the URG area in 3-D.
The Black Forest Observatory (BFO) is one of the most reliable operating and quietest recording stations worldwide and provides freely available seismological data of more than 25 yr. A quite surprising difference between the SWS measurements in the northeast and southwest is clearly indicating lateral variation: SWS with a characteristic variation of the fast polarization direction indicating a two-layer scenario in the northeast, but numerous *nulls* over a backazimuth range of 100° in the southwest (referred to as *null anomaly*).
To understand this striking observation, seismological data from five (semi-)permanent recording stations (10-25 yr) surrounding the BFO were analyzed uniformly. SWS of core-refracted phases PKS, SKS, and SKKS are manually measured with the widely used MATLAB package *SplitLab* (single-event analysis) with the plugin-in *StackSplit* (multi-event analysis).
The correct relative temporal alignment of the vertical (Z), North (N), and East (E) component traces is essential to achieve correct results (not only in terms of shear wave splitting). During the SWS analysis, an error source was found within *SplitLab*, leading to a wrong temporal alignment and, by this, to wrong shear wave splitting measurements. This bug was fixed and affected measurements were redone.

Complex anisotropy scenarios, i.e., vertical and lateral variations as well as a tilted symmetry axis, lead to backazimuthal variations of the splitting parameters. Many anisotropy studies suffer from poor directional or backazimuthal coverage due to the analysis of short-term data (2-3 yr) which leads to a small number of recorded earthquakes and, by this, a small number of shear wave splitting measurements. Additionally, often averaging over wide directional (backazimuthal) ranges is done. In case of less observations or / and averaging the splitting parameters, these variations are missed or ruled out, leading to oversimplified or wrong anisotropy models.
For the URG area, due to the analysis of long-term data, complicated splitting patterns could be observed. Due to missing differences between the observations on SKS and SKKS phases, there are no direct indications for a lowermost mantle contribution to the anisotropy, and based on a delay time longer than 0.5 s the anisotropy is

assumed to be located in the upper mantle, including both the lithosphere and asthenosphere. To explain the splitting observations, structural anisotropy models with two layers and a tilted symmetry axis are tested via the comparison of forward calculated synthetic splitting parameters with the observed ones. Subregions of the study area are outlined, based on similarities between the splitting patterns in the stereoplot representations and overlapping piercing points calculated at different depths in the upper mantle.
For the anisotropy in the upper mantle underneath the URG area a 3-D block model is proposed: (i) two layers in the Moldanubian Zone (south) but one layer in the Saxothuringian Zone (north), (ii) different fast polarization directions on the east and west sides of the URG in the Moldanubian Zone, and (iii) indications for a tilted symmetry axis close to the Lalaye-Lubine-Baden-Baden fault. For the *null anomaly* in the southwest of BFO, explanations besides the trivial solution of isotropy could be (i) orthogonal symmetry axes of the two layers canceling out the splitting effect, (ii) a vertical symmetry axis due to a C-type olivine fabric in case of high temperature and water content, (iii) vertical symmetry axis due to vertical mantle flow, and (iv) wave scattering due to heterogeneities. Possible is a link to the Kaiserstuhl Volcanic Complex due to a modification of the mantle during the Middle Miocene melting processes, including fluid-rock interaction. Magmatic processes may have produced structural modifications, including large intrusions resulting in a different olivine CPO or wave scattering. A tilted symmetry axis could be related to the terrane boundary being a remnant of the deformation during the Variscan subduction.

The anisotropy studies at BFO and in the URG area demonstrate that continental upper mantle anisotropy can be quite complex, which cannot be explained by large-scale processes such as *simple asthenospheric flow* or *vertical coherent deformation.* Analyzing long-term data allows us to observe both interstation and intrastation lateral variations. Especially such complicated splitting signals from the upper mantle can contaminate splitting signals originating from the LMM due to the integral nature of the measurements.
The variations of the observed splitting parameters and the modeled anisotropy occur on a significantly smaller length scale than expected from the size of the first Fresnel zone. However, *X*KS phases have a dominant period of 8-10 s. Thus, ray theory is only limitedly valid, and wave effects could become relevant. In a follow-up study, simulations with *AxiSEM3D* can be used to test the proposed or observation-based anisotropy model and considering arbitrary anisotropy and heterogeneities.

Contents

List of Figures

List of Tables

List of Abbreviations

a.s.l. absolute sea level

AASN AlpArray Seismic Network

AGU American Geophysical Union

AI artificial intelligence

APM absolute plate motion

BAZ backazimuth

BFO Black Forest Observatory

BGR Bundesanstalt für Geowissenschaften und Rohstoffe

BLZ Badenweiler-Lenzkirch Zone

CMB core-mantle boundary

CMT centroid Moment Tensor

CPO crystal preferred orientation

CPU central processing unit

DFG Deutsche Forschungsgemeinschaft

DOI digital object identifier

EV eigenvalue method

GEOFON Geoforschungsnetz

GMT The Generic Mapping Tools

GRF Gräfenberg Array

GRSN German Regional Seismic Network

H1 one layer with HTI

H2 two layers with HTI

HT Hunsrück-Taunus fault

HTI horizontal transverse isotropy

IASPEI International Association of Seismology and Physics of the Earth's Interior

ICB inner-core boundary

IRIS Incorporated Research Institutions for Seismology

KVC Kaiserstuhl Volcanic Complex

LAB lithosphere-asthenosphere boundary

LLBB Lalaye-Lubine-Baden-Baden fault

LLSVP large low shear wave velocity provinces (identical to LLVP)

LMM lowermost mantle

LPO lattice preferred orientation

LVZ low velocity zone

ML machine learning

Moho *Mohorovičić* discontinuity, crust-mantle boundary

MSAT MATLAB Seismic Anisotropy Toolkit

nCCC normalized cross-correlation coefficient

ORFEUS Observatories and Research Facilities for European Seismology

RC rotation-correlation method

RH Restivo and Helffrich

RMS root mean square

RMSE root mean square error

SAF simple asthenospheric flow

SC energy minimization

SEM spectral element method

SGT South German Triangle

SH horizontally polarized shear wave

SIMW simultaneous inversion of multiple waveforms

SNR signal-to-noise ratio

SPE Scientific Python Ecosystem

SPO shape preferred orientation

SV vertically polarized shear wave

SWS shear wave splitting

SWSM shear wave splitting measurement

T1 one layer with TTI

TI transverse isotropy

TIMO Deep Structure of the Central URG (Tiefenstruktur des mittleren ORGs)

TTI tilted transverse isotropy

ULVZ ultralow velocity zone

URG Upper Rhine Graben

VCD vertical coherent deformation

VTI vertical transverse isotropy

VVC Vogelsberg Volcanic Complex

WS Wolfe and Silver

1 Introduction

Knowledge about ongoing processes within the Earth's interior is essential to understand the present shape as well as the evolution through time of our planet. Seismology allows us to study recent and past geological and geodynamic processes on various length scales and at different depths. Due to their ability to probe the Earth at all depths, seismic waves are the most powerful tool to "look into" or probe the Earth's interior. Central is the concept of plate tectonics, i.e., lithospheric plates are moving over a more viscous asthenosphere. Even though it is known that mantle convection plays a key role, it is still part of ongoing research whether the main driving force is the slab pull (convergent plates, subduction zones) or the ridge push (divergent plates, mid-ocean ridges). Analyzing seismic data recorded at permanent single seismic stations as well as temporary networks or arrays[1], e.g., *USArray*, *ScanArray* (*Grund et al.*, 2017), and *AlpArray* (*Hetényi et al.*, 2018) installed worldwide can help to understand the shape of the Earth's surface (e.g., mountain belts, mid-ocean ridges, subduction zones, and continental rifts) as well as dynamic processes within the Earth's mantle (e.g., mantle convection and flow, mantle plumes and upwelling, ancient subducted slabs and downwelling) and the structure of the Earth's core (fluid [outer] core discovered 1906 by *Richard Oldham*, but solid inner core discovered 1936 by *Inge Lehmann*).

Understanding the elastic properties of rocks is crucial to describe the propagation of seismic (elastic) waves caused by earthquakes through the Earth to a receiver at the surface (Fig. **1.1**). Besides heterogeneity, which refers to the dependence on the location, a major property is anisotropy, the dependency of a quantity on the direction. Already *Hess* (1964) and *Forsyth* (1975) recognized that the Earth's mantle is anisotropic. The processes mentioned above cause deformation within rocks, favoring a preferred orientation of structures or minerals within the medium (*Savage*, 1999; *Long and Silver*, 2009). Such a preferred orientation leads to different propagation velocities of seismic waves coming from different directions or having different polarization directions, i.e., elastic or seismic anisotropy within the medium. Thus, seismic anisotropy can provide crucial insights into the understanding of past and present geological and geodynamic processes.

The major phenomenon studied to detect and quantify seismic anisotropy is shear wave splitting (SWS), which is the analogue to the optical birefringence of light. A shear (S) wave (transverse wave) entering an anisotropic region is "split" into two waves, which have orthogonal polarization directions and travel with different velocities. The fast polarization direction ϕ of the medium and the delay time δt accumulated after traveling through the anisotropic region can be used to quantify the anisotropy and are called splitting parameters. To study the Earth's mantle, the core-refracted phases PKS, SKS, SKKS (jointly referred to as *X*KS) are commonly used. SWS is an unambiguous indicator for anisotropy and allows, by this, for a clear discrimination from heterogeneity. A limitation is the integral nature along the travel path, similar to the measurement of travel time. For steeply inclining phases at the recording stations, this leads to a poor vertical resolution but a good lateral resolution.

With the highly and constantly increasing amount of seismic data (more stations and long recording times) as well as laboratory experiments to understand the behavior of minerals under different stress regimes and ambient conditions (pressure, temperature, water content), SWS measurements can be related to anisotropy scenarios and, by this, to past or present deformation processes.

[1] Definition of an array and the difference to a general network see *Rost and Thomas* (2002).

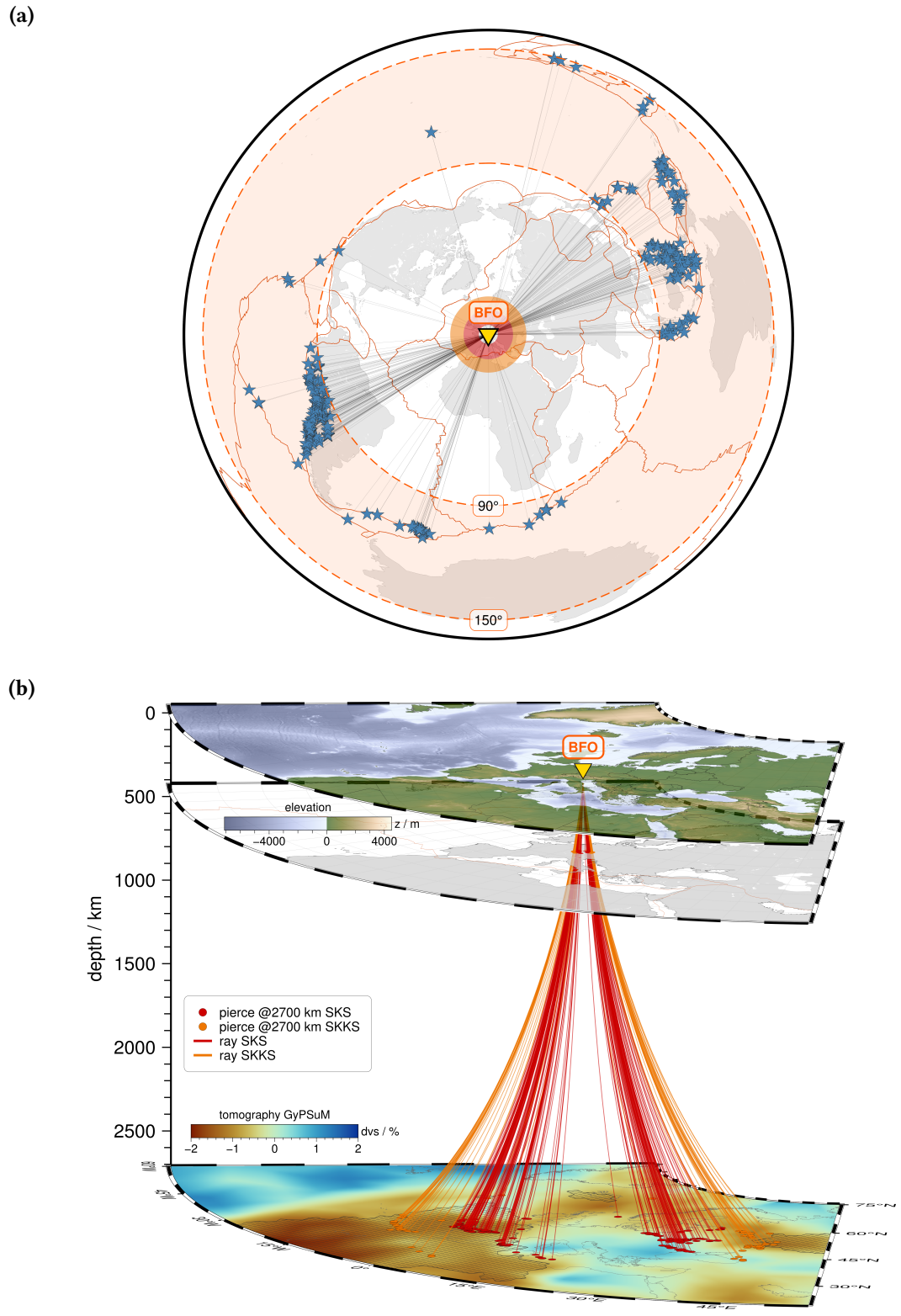

Figure 1.1: (a) Epicentral distance plot with projected ray paths (thin black lines) from the epicenters (blue stars) of the earthquakes to the recording station (yellow inverse triangle) BFO. The epicentral distance range 90°-150°, in which *X*KS phases can be observed at BFO, is highlighted in light orange. The orange and red rings around BFO refer to the area in which the piercing points in the lowermost mantle are located for SKS and SKKS phases, respectively. **(b)** Source-side 3-D plot with ray paths from the lowermost mantle (2700 km) to the BFO at the surface as red and orange lines for SKS or SKKS phases, respectively (see also Fig. C.3). Piercing points after *Ritter et al.* (2022) and *Fröhlich et al.* (2024b); in the lowermost mantle on top of the tomography ($d\upsilon_s$) *GyPSuM* (*Simmons et al.*, 2010). Please note, that the spherical shape of the Earth is not considered.

1.1 Motivation and research questions

A general issue in seismology is the directional or backazimuthal coverage, due to the possible or available source-receiver constellations (Fig. 1.1a) to probe a specific volume or region within the Earth. The earthquakes are primarily limited to the main source regions (Japan, Southeast Asia, the South Atlantic, and South America), located mainly at the plate boundaries. Thus, many studies suffer from a limited (under-representation) and uneven (over-representation) backazimuthal coverage. The first issue is significantly enhanced if short-term data (2-3 yr) are analyzed.

Seismic anisotropy does not only relate to large-scale processes as mentioned above, but can also vary on a small length scale (e.g., *Bastow et al.*, 2007). Especially for continental anisotropy, various studies report more complex anisotropy scenarios, i.e., vertical and lateral variations (e.g., *Aragon et al.*, 2017; *Qiang et al.*, 2022) as well as a tilted layer (symmetry axis) instead of a horizontal one (e.g., *Grund and Ritter*, 2020).
It has been recognized that the splitting parameters vary with the backazimuth (BAZ) for more complex anisotropy scenarios (*Savage*, 1999; *Long and Silver*, 2009). In case short-term data are analyzed, only in a few BAZ directions, and variations of the splitting parameters are very likely incompletely observed or even missed. In several studies, the splitting parameters are averaged over a wide or the complete backazimuthal range. In this case, any backazimuthal variation of the splitting parameters is removed, and valuable information is lost, excluding *a priori* more complex anisotropy scenarios. For complex anisotropy scenarios, the splitting parameters observed at the surface do not directly express the anisotropy in the subsurface, but they are apparent (or effective) splitting parameters (*Walker and Wookey*, 2012). According to this, a modeling procedure has to be carried out to find anisotropy models explaining the observations.
If no SWS is observed, this is called a *null* measurement or *null* (*Wüstefeld et al.*, 2008). The observation of SWS is referred to as *non-null* measurement or *split*. *Nulls* are commonly ignored in SWS analysis and anisotropy studies and excluded from the modeling and interpretation, although they may contain crucial information (*Wüstefeld and Bokelmann*, 2007), especially besides the trivial solution of isotropy.

The Upper Rhine Graben (URG) area is characterized by a quite complicated geological and geodynamic setting (*Grimmer et al.* 2017; Ch. 8). Several studies have already investigated the crust and upper mantle regarding anisotropy. However, most of these studies suffer from a small number of observations due to the analysis of short-term data, leading to a small earthquake catalog. Due to the poor directional or backazimuthal coverage, more complex anisotropy scenarios could not be resolved reliably, and there is still no 3-D model of the anisotropy in the upper mantle underneath the URG available.
The Black Forest Observatory (BFO) is one of the worldwide quietest and best operating recording stations (*Black Forest Observatory*, 1971). Already *Walker et al.* (2005a) mentioned an unexpected difference in their SWS observations between the northeast and the southwest. *Ritter et al.* (2018) presented a quite unexpected splitting pattern they observed at the BFO. While in the northeast splitting with strong backazimuthal variations is observed, in the southwest numerous *nulls* extending over a BAZ range of over 100° are observed. Such an observation cannot be explained by vertical variation (two or multiple layers) or a tilted symmetry axis, but is a strong indication for lateral variation.
To understand this striking and puzzling observation in more detail, a similar SWS analysis of long-term data (at least 10-15 yr) from recording stations surrounding the BFO is required. The permanent recording stations Stuttgart (*GEOFON Data Centre*, 1993) as well as Welschbruch (*RESIF*, 1995) and Échery (*GEOSCOPE*, 1982) have interstation distances of 60-80 km to the BFO and data of over 15 yr are freely available. Based on this, the URG area is excellently suitable to study complex anisotropy in a complicated geological and geodynamic setting.

In this doctoral thesis, the following research aspects are addressed with a focus on specific research questions:

Research aspects and questions

1. Backazimuthal variations of the splitting parameters

- *Are they useful for the modeling?*
- *Can long-term data help to observe characteristic patterns?*

2. *Null* observations

- *Do they contain useful information (besides the trivial solution of isotropy)?*
- *How can they be included in the modeling and interpretation?*

3. Seismic anisotropy in 3-D

- *Can intrastation (lateral) variations of anisotropy be observed?*
- *Can subregions of the study area be outlined based on interstation comparisons?*

1.2 Structure of this doctoral thesis

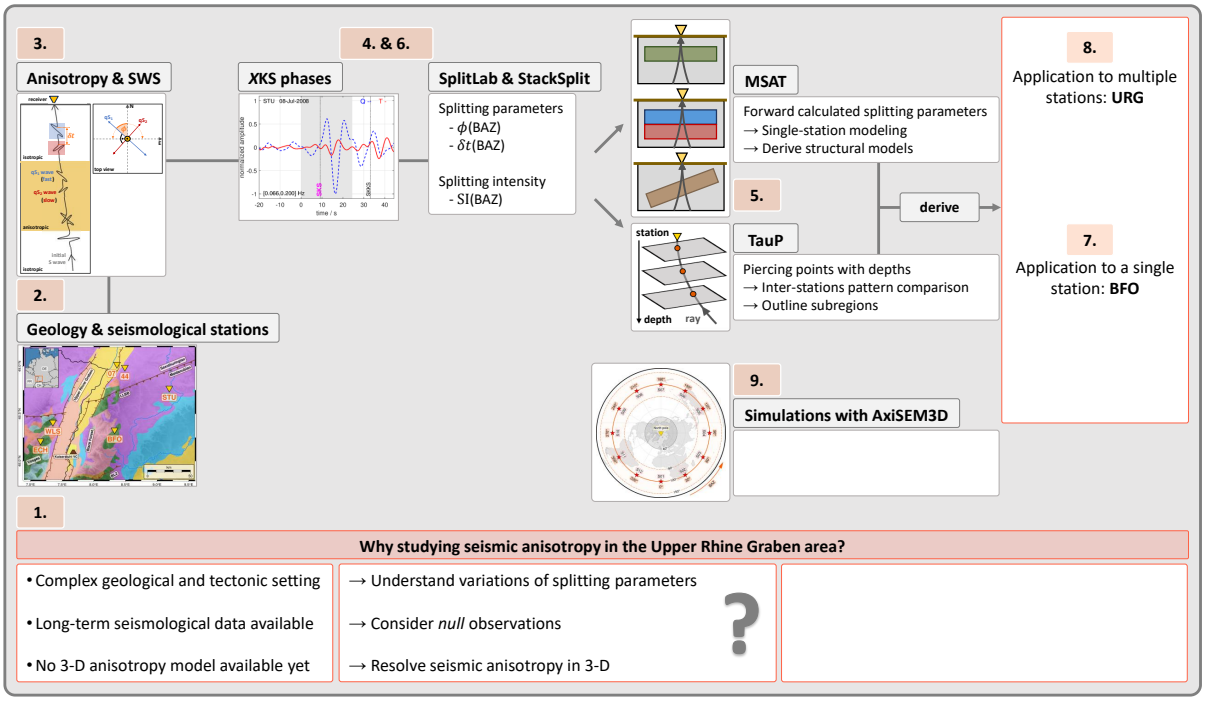

Figure 1.2: Workflow of this doctoral thesis: overview. The numbers 2. to 9. give the related chapters, for details see Sec. 1.2. The lower left box mentions aspects which make the URG area interesting for anisotropy studies, the lower middle box contains the research questions addressed in this doctoral thesis, and in the right box follow-up questions to the initial research questions will be added in Fig. 9.1 and discussed in Sec. 9.1. *Abbreviation*: BFO = Black Forest Observatory; URG = Upper Rhine Graben; SWS = shear wave splitting; *XKS* = core-refracted phases PKS, SKS, SKKS; BAZ = backazimuth; MSAT = *MATLAB Seismic Anisotropy Toolbox* (*Walker and Wookey*, 2012). The geology is shown in 2. (Fig. 2.1) after *Asch* (2005), the SWS sketch in 3. (Fig. 3.3) is after *Wüstefeld et al.* (2008, fig. 1), the seismograms in 4. are displayed via *SplitLab* (*Wüstefeld et al.*, 2008), the piercing point sketch is after *Fröhlich et al.* (2024b, fig. 9a).

In the following, a brief overview of the structure of this doctoral thesis is given.[2] The workflow is shown schematically in Fig. 1.2. In **Ch. 2**, the geological and geodynamic setting (Sec. 2.1) of the Upper Rhine Graben (URG) area is

[2] The presentation slides of the doctoral defense are available separately (reserved DOI `https://doi.org/10.5281/zenodo.15982580`).

presented, previous anisotropy studies in this area are summarized (Sec. 2.2), and the used seismological recording stations (Sec. 2.3) are introduced. **Ch. 3** covers the theoretical background on elastic or seismic anisotropy based on the elastic wave equation, including the *stress-strain* relation and symmetries (Sec. 3.1), wave propagation and wave types (Sec. 3.2), and shear wave splitting (Sec. 3.3) as well as anisotropy within the Earth's interior (Sec. 3.4) and existing databases (Sec. 3.5). **Ch. 4** explains how shear wave splitting can be measured using seismic data (Sec. 4.1) and quantified (Sec. 4.2) using the MATLAB program *SplitLab* (*Wüstefeld et al.*, 2008) with the plugin *StackSplit* (*Grund*, 2017) to determine the splitting parameters (Sec. 4.3). In **Ch. 5**, the concept used for modeling the SWS observations is explained. This covers depth constraints and testing for a potential lowermost mantle contribution to the anisotropy (Sec. 5.1) as well as defining structural anisotropy models with their related model parameters and the forward calculation of synthetic splitting parameters for these models as a function of the backazimuth (Sec. 5.2) using the *MATLAB Seismic Anisotropy Toolbox* (MSAT; *Walker and Wookey*, 2012). **Ch. 6** points out the importance of a correct (relative) temporal alignment of the seismogram components and addresses a related bug contained in the codes of *SplitLab*. These contents have been published as a research article *Fröhlich et al.* (2022a) in *Annals of Geophysics*. **Ch. 7** and **App. A** focus on one single seismological recording station, the Black Forest Observatory (BFO). These anisotropy studies have been published as a research article *Ritter et al.* (2022) in *Journal of Seismology*. In **Ch. 8** and **App. B**, multiple recording stations around the BFO are used to study the anisotropy beneath the URG area. These studies have been published as a research article *Fröhlich et al.* (2024b) in *Geophysical Journal International*. Finally, in **Ch. 9**, the findings are summarized and confronted with the initial research questions formulated in Sec. 1.1, and assumptions made during the analysis leading to limitations of the results and by this follow-up questions are mentioned (Sec. 9.1). In the outlook, it is evaluated whether upcoming machine learning techniques can ease measuring SWS (Sec. 9.2), and concepts for simulating synthetic seismograms with *AxiSEM3D* (*Leng et al.*, 2016; *Leng et al.*, 2019) are described to test and improve the proposed anisotropy models (Sec. 9.3). **App. C** contains visualizations to extend figures shown in the main part of this doctoral thesis. **App. D** gives an overview of the shear wave splitting measurement data (Sec. D.2) as well as the source codes, visualizations, and animations (Secs D.1, D.3, D.4, D.5) provided along with the research articles and this doctoral thesis and points out the *PyGMT* open-source project to which I contribute since June 2022 (Sec. D.6).

2 The Upper Rhine Graben Area

This chapter gives an overview of the study area of this doctoral thesis: the Upper Rhine Graben (URG) area. The geological and geodynamic setting is introduced (Sec. 2.1; see also the Secs 7.2, 8.2) following mainly the works by *Tait et al.* (1997) and *Matte* (2001) as well as *Grimmer et al.* (2017), *Schwarz and Henk* (2005), and *Ring and Bolhar* (2020). Past and recent anisotropy-related studies are summarized (Sec. 2.2), and the seismological recording stations used in this doctoral thesis are mentioned (Sec. 2.3).

2.1 Geological and geodynamic setting

The present-day shape of Europe originates from Laurentia (North America, Greenland, northwest Scotland), Baltica (Scandinavia and East European platform), and Gondwana (Africa and South America), as well as Avalonia (Ireland, North Germany, Poland) and Armorica (West Europe south of the British Isles) in the Paleozoic between 480 Myr and 250 Myr (*Tait et al.*, 1997, fig. 1).
During the Variscan Orogeny (Devonian and Permian), the supercontinent Pangaea was formed and the Variscides due to the collision of the continents Laurussia and Gondwana. However, there were terranes (microplates) between these two continents before they collided. The terranes Avalonia and Armorica are derived from paleomagnetism and palao-biostratigraphy as well as geology. Armorica has not been clearly defined and probably consists of several smaller terranes (Armorica Group or Armorica Terrane Assemblage). The northward or equatorward movement of Avalonia after its separation from Gondwana led to the opening of the Rheic Ocean. It is unclear how far Armorica moved away from Gondwana after it separated and how large the opening of the Galicia-Southern Brittany Ocean became. Laurussia was formed during the Caledonian Orogeny (Ordovician and Silurian) by the collision of Laurentia with Baltica and the collisions of Avalonia with Laurentia and Avalonia with Baltica. The Iapetus Ocean and the Tonquist Ocean (lateral branch of the Iapetus Ocean between Avalonia and Baltica) were subducted or closed, and the Caledonides unfolded. During the Variscan Orogeny, Avalonia plus Armorica collided with Gondwana, and the Rheic Ocean and the Galicia-Southern Brittany Ocean were subducted or closed in opposite directions. Accordingly, the Variscides in Europe are a collision zone of terranes detached from Gondwana (*Matte*, 2001, figs 4, 5).

The URG is part of the *European Cenozoic Rift System* located in western and Central Europe (*Grimmer et al.*, 2017, fig. 1). The continental rift is about 300 km long and, on average, 30-40 km wide, with a widening towards the ends. It extends with NNE orientation from Basel in the south via Freiburg, Strasbourg, Karlsruhe, Mannheim, and Darmstadt to Frankfurt am Main in the south (Figs 2.1, 8.1). The URG is divided into three segments, each being about 100 km long: the southern segment (Basel-Strasbourg, NNE orientation), the central segment (Strasbourg-Speyer, NE orientation), and the northern segment (Speyer-Frankfurt am Main, N to NNW orientation).
The URG is bordered by the Swiss Jura to the south and by the Rhenish Massif to the north (*Grimmer et al.*, 2017, fig. 1; Fig. 2.1). It crosses various tectono-stratigraphic units of the Variscan Internides *Moldanubian*, *Saxothuringian*, and *Rhenohercynian*, which are separated by the *Lalaye-Lubine-Baden-Baden* (LLBB) fault and the *Hunsrück-Taunus* (HT) fault, respectively. The LLBB fault is a southwards-dipping shear zone and has a sinistral NS displacement of >15 km within the URG (Fig. 2.1).

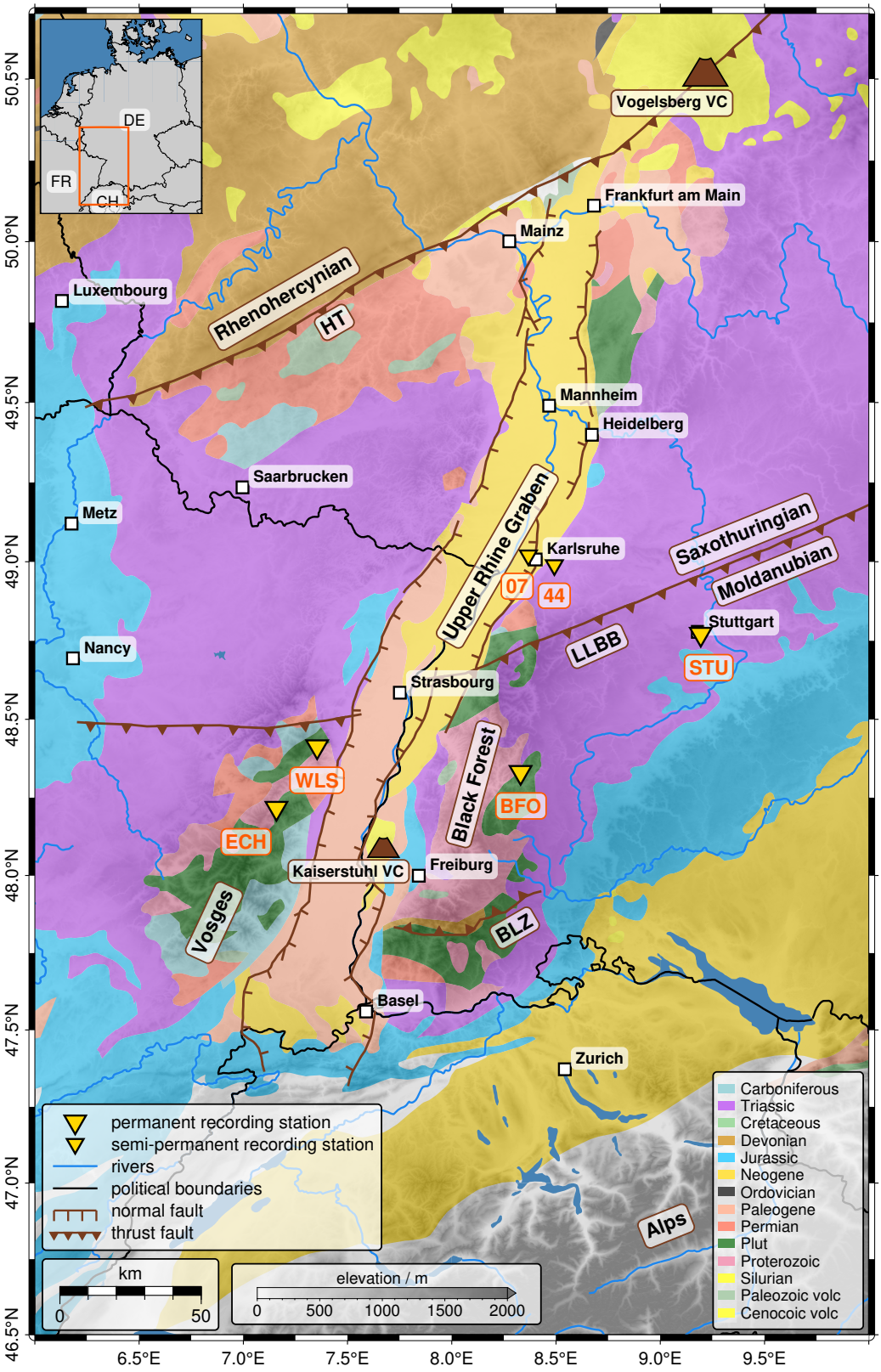

Figure 2.1: Geology (colored polygons, see the legend in the lower right corner) in the Upper Rhine Graben area (URG) area following *Asch* (2005); with the surface elevation shown in the Alps region (gray colormap). The seismological recording stations which are used in the studies of this doctoral thesis (Sec. 2.3) are marked as yellow inverse triangles. Besides the normal faults of the URG, the *Lalaye-Lubine-Baden-Baden* (LLBB) fault and the *Hunsrück-Taunus* (HT) fault are highlighted as thrust faults, and the *Volgelsberg Volcanic Complex* and *Kaiserstuhl Volcanic Complex* are marked. From south to north, the LLBB fault separates the *Moldanubian* and *Saxothurignian* zones and the HT separates the *Saxothurignian* and *Rhenohercynian* zones. The inset in the upper left corner shows the study area within Central Europe. For a topographic map, see Fig. 8.1.

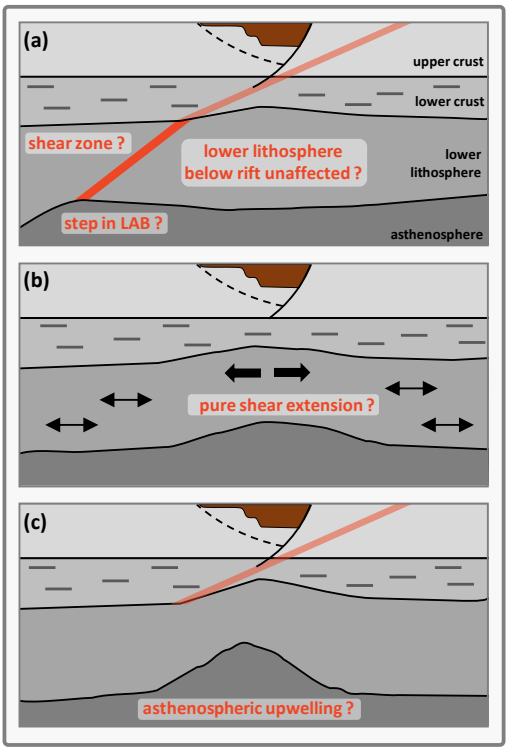

Figure 2.2: Continental rift mechanisms with focus on the Upper Rhine Graben (URG). **(a)** Rifting scenario with simple shear extension and a shear zone that cuts through the entire lithosphere, **(b)** scenario with pure shear extension and possible preferred mineral deformation and CPO (small arrows in the direction of deformation) in the lower lithosphere, and **(c)** scenario with a buoyantly upwelling asthenosphere. The sketches are not to scale. Modified after *Kirschner et al.* (2011, fig. 1), whereby the crustal structure is schematically redrawn from *Meier and Eisbacher* (1991) and represents the URG with a half graben and a possible crustal shear zone following *Eisbacher and Fielitz* (2010). *Abbreviation*: LAB = lithosphere-asthenosphere boundary.

The *Mittelgebirge* Black Forest and Odenwald in the east and the Vosges and Pfälzerwald in the west form the rift shoulders. Their height is about 1500 m a.s.l. in the south and <500 m a.s.l. in the north. The URG itself has a height of about 260 m a.s.l. in the south and about 90 m a.s.l. in the north (*Grimmer et al.*, 2017). The total extension is 5 km to 8 km. The URG is filled up to 3.5 km with sediments, with increasing thickness from west to east. The crust-mantle boundary (*Mohorovičić* discontinuity, Moho) is assumed to be relatively flat at a depth of 27 km to 30 km and the LAB at 60 km to 80 km depth.
The *Kaiserstuhl Volcanic Complex* located northwest of Freiburg within the URG (Fig. 8.1) was active during the Miocene (15-20 Myr). The Moho may have bulged up to 6 km to a depth of 24 km (*Fuchs et al.*, 1987).
The seismicity of the URG area is reflected in about 140 moderate (intensity ≥ V) and 36 very strong (intensity ≥ VII, magnitude $M_w = 4.5 - 7.0$; including Basel 1356) historical earthquakes (*Grimmer et al.*, 2017, fig. 11).

The geographic location and the (cross-sectional) asymmetry of the URG appear to be caused by lithospheric shear zones formed during the central stages of the Variscan orogeny between 330 Myr and 315 Myr
The development of the URG began ca. 47 Myr ago. The opening of the URG in the late Eocene was caused by N-S to NNE-SSW compression . This resulted in the reactivation of NNE- and ENE-trending pre-existing weakness zones as transtensional strike-slip. In the Oligocene, WNW-ESE to W-E extension caused subsidence and sedimentation throughout the trench. In the Miocene, the regional stress field was reorientated with the development of a sinistral transverse shift. Subsidence and sedimentation were limited to the northern segment. Uplift and erosion occurred in the central and southern segments (*Schwarz and Henk*, 2005, fig. 2).

There is a distinction between active and passive rifting (*Merle*, 2011, fig. 1). To explain the mechanical process of lithospheric extension, a rift model based on pure shear extension or simple shear extension is used (Fig. 2.2). Recent studies with travel time residuals of teleseismic P waves as well as with anomalies of teleseismic wave fronts, could not confirm an active upwelling of hot ($\Delta T > +100$°C) material from the asthenosphere into the lithosphere (*Kirschner et al.*, 2011). Initially, a low-velocity mantle anomaly (mantle cushion) was thought to be the origin of the URG (*Glahn and Granet*, 1992; *Glahn et al.*, 1993). Accordingly, no significant modification of the lower lithosphere and asthenosphere is expected, favoring a rift mechanism that does not modify the lower lithosphere. This is consistent with a passive rift mechanism such as shearing along a reactivated pre-existing

lithospheric shear zone, i.e., simple shear extension rather than pure shear extension. However, it remains unclear how deep the shear zone actually extends into the lithosphere and, in particular, if an offset in the LAB is present (*Kirschner et al.*, 2011). Overall, the deeper structure beneath the URG is still not well understood, and therefore its geodynamic evolution is not fully understood yet.

2.2 Previous anisotropy studies

Multiple studies were carried out addressing potential anisotropy in the crust and upper mantle beneath the URG area. Some of these studies are summarized in Tab. 2.1. The first studies by *Bamford* (1977), *Fuchs* (1983), and *Enderle et al.* (1996) used refraction profiles and analyzed travel times of Pn and partly Sn phases. Studies using shear wave splitting of core-refracted phase *X*KS phases from teleseismic earthquakes were conducted by *Vinnik et al.* (1994) and *Granet et al.* (1998). Observations from multiple stations were combined into one dataset. A variation of the splitting parameters with the BAZ is already proposed by *Walker et al.* (2005b), *Wagner* (2007), and *Walther et al.* (2014), and vertical as well as lateral variations of the anisotropy are considered in the discussions. However, no final anisotropy scenario or 3-D model for the URG could be proposed, as different anisotropy models can explain the observations equally well.
Most anisotropy studies share common issues, leading to limitations in understanding the anisotropy and the derived models. Due to the usage of short-term data, only a few observations are made in a few BAZ directions. Often only observations with shear wave splitting are considered in the interpretation, and *nulls* are rejected. Additionally, the splitting parameters, especially the fast polarization direction, are averaged over the whole BAZ range. Any indications and information in terms of complex anisotropy are lost, and *a priori* one layer with a horizontal symmetry axis is assumed. In particular, any indications of lateral variations are missed.
Ritter et al., 2018 presented a quite unexpected splitting pattern at the Black Forest Observatory (BFO). Splitting observations with a strong backazimuthal variation in the northeast but numerous *nulls* over a backazimuth range of 100° in the southwest are clear indications of lateral variation. Already *Walther et al.* (2014) mentioned *null* observations in the southwest of BFO.
Related to the *AlpArray* project or *AlpArray Seismic Network* (AASN, *AlpArray Seismic Network*, 2015) different anisotropy studies were conducted, e.g., *Petrescu et al.* (2020), *Link and Rümpker* (2021), *Link and Rümpker* (2023), and *Hein et al.* (2021). Partly an automatic analysis of the data was applied via *SplitRacer_auto* (*Link et al.*, 2022) based on the MATLAB toolbox *SplitRacer* (*Reiss and Rümpker*, 2017). As the AASN was a temporary network, it was installed only for 2-3 yr. This leads to the issues of less SWS measurements and a poor backazimuthal coverage. These studies focus on mantle flow related to subducted slabs, i.e., more large-scale processes, but their database does not allow them to resolve small-scale (lateral) variations in the anisotropy.

2.3 Seismological recording stations

Seismological data from six recording stations installed in Germany and France were analyzed (Figs 2.1 and 6.1): the permanent stations Black Forest Observatory (BFO, *Black Forest Observatory*, 1971), Welschbruch (WLS, *RESIF*, 1995), Stuttgart (STU, *GEOFON Data Centre*, 1993), and Échery (ECH, *GEOSCOPE*, 1982) as well as the semi-permanent stations Durlach (TMO44) and KIT-GPI (TMO07). For all stations, at least 10 yr data are freely available and were analyzed (start of recording until 2019/12/31). The BFO is one of the worldwide quietest and best operating seismological recording stations, and data of 25 yr could be analyzed. For details on the networks and analyzed recording periods, see Tab. 8.1. Ch. 7 focuses on the BFO in Sec. 7.2 (*Ritter et al.*, 2022). In Ch. 8, the other stations within the URG area surrounding the BFO are introduced in Sec. 8.3.1 (*Fröhlich et al.*, 2024b).

Table 2.1: Anisotropy studies in the Upper Rhine Graben area modified and translated from German to English based on *Fröhlich* (2020, tab. 2). *Notation*: *hd* hypocentral depth, Δ epicentral distance, $m_t extb$ body wave magnitude. *Abbreviations*: BFO = Black Forest Observatory, URG = Upper Rhine Graben, HTI = transverse isotropy with horizontal symmetry axis, TTI = transverse isotropy with tilted symmetry axis, BAZ = backazimuth, SWS = shear wave splitting, CPO = crystal preferred orientation, RC method = rotation-correlation method, SC method = energy minimization method, SGT = South German Triangle, GRSN = German Regional Seismic Network, GRF = Gräfenberg Array, TIMO = Deep Structure of the Central URG, *X*KS = core-refracted phases PKS, (PKKS,) SKS, SKKS.

Publication	Study area	Data	Method, phases	Results, anisotropy, petrology
Bamford (1977)	West Germany East France	refraction profile	travel time Pn	• anisotropy · depth: crust, uppermost mantle · qP: 10°-20°, 6-7 % qP: 8.05 ± (0.50-0.60) kms^{-1}
Fuchs (1983)	South Germany	refraction profile	travel time Pn	• anisotropy: anvil model (fig. 13) · 2 layers with horizontal a-axis, in between isotropic LVZ · depth: 25 km - 35 km - 46 km - 51 km · qP: upper 22.5° to 26.1°, lower 33° P: middle 8.10 kms^{-1} • petrology: orientated olivine crystals · 61.8 % to 100 % CPO orthorhombic with a and b-axes horizontal, c-axis vertical · 67.2 % to 100 % CPO orthorhombic with a and c-axes horizontal, b-axis vertical
Enderle et al. (1996)	South Germany	refraction profile	travel time, amplitude Pn, Sn	• anisotropy (fig. 17) · 1 layer with horizontal a-axis · depth: 30 km - 40 km, i.e., direct under the Moho · qP: 31° (x), 3-4 % to 11 % qP: 8.03 kms^{-1} to 8.63 kms^{-1} (x), 7.77 kms^{-1} to 7.77 kms^{-1} (y) · qS: 76° (x+45°) qS_1: 4.63 kms^{-1} to 4.79 kms^{-1} (x+45°), 4.57 kms^{-1} to 4.58 kms^{-1} (x) qS_2: 4.57 kms^{-1} to 4.59 kms^{-1} (x), 4.52 kms^{-1} to 4.41 kms^{-1} (y) • petrology: chemical inhomogeneity, orientated olivine crystals · olivine-poor harzburgite (57.3 % olivine) with 20 % CPO to olivine-rich peridotite (89.5 % olivine) with 40 % CPO

Tab. 2.1 continued.

Publication	Study area	Data	Method, phases	Results, anisotropy, petrology
Vinnik et al. (1994)	SGT	GRSN BFO, FUR, CLZ, WET, TNS, HAM (4, 5, 2, 6, 5, 4 *splits*)	SWS *X*KS Vinnik method	• building one dataset out of BFO, FUR, CLZ • variation of the splitting parameters with the BAZ • anisotropy · complicated 3-D structure · litho- (93 km) and asthenosphere (290 km) · 2 layers with HTI (transparent windows) • explanation · ϕ_2: $\nparallel$ strike Hercynian, Alpine mountain belt; pre-Hercynian orogeny · ϕ_1: mantle flow due to Alpine orogeny → more data required
Granet et al. (1998)	Rhine Graben Urach France Central Massive	permanent, broad,band i.a. ECH (16 *splits* and 72 earthquakes) mobile, long-period RG-N, RG-S semi-permanent, short-period RBG mobile, short-period	SWS *X*KS, S $m_b \geq 6.0$ $hd \geq 80$ km Vinnik method, RC method	• building one dataset out of ECH, RG-N, RG-N • variation of the splitting parameters with the BAZ • anisotropy · averaging over the whole BAZ range: geographic coherence · litho- and asthenosphere ($\geq$ 100-200 km) · unclear whether 2 layers with HTI or 1 layer with TTI • explanation · ϕ_2: $\parallel$ strike URG · ϕ_1: mantle flow → finally 2 layers with HTI

Tab. 2.1 continued.

Publication	Study area	Data	Method, phases	Results, anisotropy, petrology
Walker et al. (2005a)	URG Eifel	permanent broadband 18 stations, > 15 yr i.a. BFO, STU, ECH temporary short period 102 stations, 7 months	SWS *X*KS, S SC method	• variations of the splitting parameters with the BAZ • anisotropy · unclear whether 2 layers with HTI or 1 layer with TTI finally 1 layer with HTI and lateral variation
Wagner (2007)	middle URG	permanent stations TIMO project Eifel project 35 earthquakes	SWS *X*KS m_b > 5.6 Δ = [85,130]°	• variations of the splitting parameters with the BAZ • anisotropy · fast polarization direction: averaging separately for source regions Japan: E-W bis ENE-WSW, NE-SW (BFO) Indonesia: NE-SW South Atlantic: NNE-SSW (S) to ENE-WSW to NE-SW (N) South America: NE-SW (STU) to E-W (LUX) · delay time clearly faulty
Walther et al. (2014)	Germany	GRSN 34 stations, 22 yr i.a., BFO, STU GRF 3 stations, 34 yr	SWS *X*KS m_b > 5.5 Δ = [85,130]° SC method fully automatic routine (ADORE)	• variations of the splitting parameters with the BAZ • anisotropy · test 1 layer with HTI · test 2 layers with HTI → more complex model types required

3 Seismic Anisotropy

Anisotropy refers to the dependence of a quantity, feature, or process (e.g., magnetism, structure, radiation) on the *direction*. In contrast, heterogeneity describes the dependence on the *location*. In seismology, anisotropy refers to the dependence of the propagation velocity of elastic or seismic (earthquake) waves on the propagation or polarization direction, i.e., elastic or seismic anisotropy. The interest in seismic anisotropy arises from its connection to geological and geodynamic processes (Fig. 3.1). These processes cause deformation (e.g., simple shear, pure shear, and extension; *Creasy et al.*, 2020, fig. 1) within the Earth's interior and lead to a preferred orientation within materials or rocks at different depths.
This chapter covers theoretical aspects regarding seismic anisotropy based on the elastic wave equation, including the *stress-strain relation* and symmetries (Sec. 3.1), wave propagation and wave types (Sec. 3.2), and shear wave splitting (Sec. 3.3). These contents follow mainly the works *Babuška and Cara* (1991) and *Shearer* (2009) as well as *Savage* (1999), *Maupin and Park* (2007), *Long and Silver* (2009), and *Nowacki et al.* (2011). Seismic anisotropy occurs within the Earth at different depths, including the crust, the upper mantle, and the lowermost mantle, as well as the inner core (Sec. 3.4). Databases in terms of anisotropy and related aspects have been compiled (Sec. 3.5).

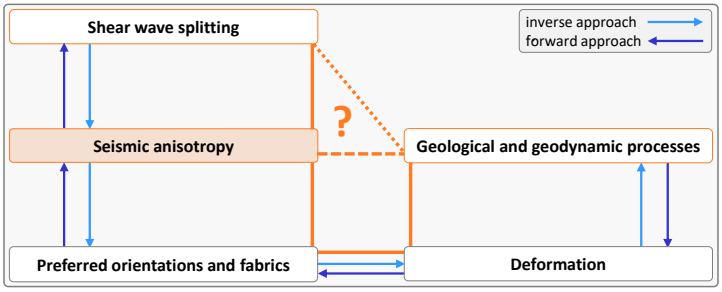

Figure 3.1: How can seismic anisotropy help to understand present and past geological and geodynamic processes within the Earth (orange dashed line and question mark)? Such processes cause deformation within materials and rocks, which can lead to a preferred orientation of structures and minerals, i.e., seismic anisotropy at different depths (Sec. 3.4). A commonly used phenomenon to study anisotropy is shear wave splitting (orange dotted line; Sec. 3.3).

3.1 *Stress-strain relation* and symmetries

In an ideal elastic medium (considering infinitesimal deformation) the *stress-strain relation* can be formulated in a linear and frequency-independent fashion as the generalized *Hooke's law* (Eq. 3.1; *Hudson*, 1980) using the index notation following the *Einstein summation convention*[3] (*Einstein*, 1916). The elasticity tensor $\mathbf{c}$ (rank 4, i.e., $3^4 = 81$ components) relates the stress tensor $\boldsymbol{\sigma}$ to the strain tensor $\boldsymbol{\varepsilon}$ (both rank 2, i.e., $3^2 = 9$ components). Considering the symmetries of $\boldsymbol{\sigma}$ and $\boldsymbol{\varepsilon}$ 36 and together with the three main invariants[4] of $\boldsymbol{\sigma}$ and $\boldsymbol{\varepsilon}$, 21 of the 81 components of $\mathbf{c}$ are independent. This represents *triclinic symmetry* or *full anisotropy*.

$$\begin{aligned} \sigma_{ij} &= c_{ijkl}\varepsilon_{kl} \\ c_{ijkl} &= c_{jikl} = c_{ijlk} = c_{klij} \end{aligned} \qquad \text{with } i, j, k, l = 1, 2, 3 \tag{3.1}$$

[3] Summation over double occurring indices.
[4] For a tensor $\mathbf{T}$ of rank 2 it is valid: $I_1 = \mathrm{spur}(\mathbf{T})$, $I_2 = \det(\mathbf{T})$, $I_3 = \frac{1}{2}\left[\mathrm{spur}(\mathbf{T})^2 - \mathrm{spur}(\mathbf{T}\cdot\mathbf{T})\right]$.

Making usage of the symmetries of the stress and strain tensors, leads to the *Voigt notation*, which allows to write the $3 \times 3 \times 3 \times 3$ tensor as 6×6 matrix, via the convention given below (Eq. 3.2) with $ij \rightarrow m$ and $kl \rightarrow n$.

$$\begin{gathered} 11 \rightarrow 1 \quad 22 \rightarrow 2 \quad 33 \rightarrow 3 \\ 23 \text{ or } 32 \rightarrow 4 \quad 13 \text{ or } 31 \rightarrow 5 \quad 12 \text{ or } 21 \rightarrow 6 \end{gathered} \tag{3.2}$$

Using the *Voigt* notation (*Voigt*, 1928) the *stress-strain relation* in Eq. 3.1 can be re-written as Eq. 3.3:

$$\begin{aligned} \sigma_m &= c_{mn}\varepsilon_n \\ c_{mn} &= c_{nm} \end{aligned} \qquad \text{with } m, n = 1, 2, \ldots, 6 \; . \tag{3.3}$$

Special symmetries of the anisotropy, based on symmetry planes or symmetry axes, allow for an additional reduction of the number of independent elasticity parameters (*Savage*, 1999). Seven different crystal systems are distinguished (*Crampin*, 1984b): *triclinic* (21 independent elasticity parameters), *monoclinic* (13), *orthorhombic* (9), *tetragonal* (7), *trigonal* (6), *hexagonal* (5), and *cubic* (3). In seismology, mainly the orthorhombic and hexagonal symmetries are relevant (*Savage*, 1999).
Single crystals, e.g., ice and olivine (Fig. 3.7), are characterized by orthorhombic symmetry. Three independent symmetry axes lead to nine independent elasticity parameters (Eq. 3.4; *Savage*, 1999; *Babuška and Cara*, 1991).

$$\boldsymbol{c} = \begin{pmatrix} c_{11} & c_{12} & c_{13} & 0 & 0 & 0 \\ c_{12} & c_{22} & c_{23} & 0 & 0 & 0 \\ c_{13} & c_{23} & c_{33} & 0 & 0 & 0 \\ 0 & 0 & 0 & c_{44} & 0 & 0 \\ 0 & 0 & 0 & 0 & c_{55} & 0 \\ 0 & 0 & 0 & 0 & 0 & c_{66} \end{pmatrix} \tag{3.4}$$

Hexagonal symmetry is characterized by one symmetry axis and five independent elasticity parameters (Eq. 3.5; *Savage*, 1999; *Babuška and Cara*, 1991). In the plane perpendicular to the symmetry axis the medium is isotropic. According to this, hexagonal symmetry is also called cylindrical symmetry or *transverse isotropy*. Based on the orientation of the symmetry axis, transverse isotropy with vertical (VTI), horizontal (HTI), or tilted (TTI) symmetry axis is present in the medium.

$$\boldsymbol{c} = \begin{pmatrix} c_{11} & c_{11} - 2c_{66} & c_{13} & 0 & 0 & 0 \\ c_{11} - 2c_{66} & c_{11} & c_{13} & 0 & 0 & 0 \\ c_{13} & c_{13} & c_{33} & 0 & 0 & 0 \\ 0 & 0 & 0 & c_{44} & 0 & 0 \\ 0 & 0 & 0 & 0 & c_{44} & 0 \\ 0 & 0 & 0 & 0 & 0 & c_{66} \end{pmatrix} \tag{3.5}$$

In case of transverse isotropy, the propagation velocities of the P (compression, longitudinal) wave v_P and the S (shear, transversal) wave v_S can be calculated via Eq. 3.6 using the five elasticity parameters (Eq. 3.5) and the density ϱ of the medium (*Maupin and Park*, 2007; *Babuška and Cara*, 1991). For a P wave, $\parallel$ and $\perp$ refer to a propagation or polarization direction parallel or orthogonal to the symmetry axis, respectively. For the two S waves, the meaning is more complicated. $\parallel$ corresponds to a propagation direction parallel (orthogonal) to the symmetry axis with a polarization direction orthogonal (parallel) to the symmetry axis. $\perp$ refers to a propagation direction orthogonal to the symmetry axis with a polarization direction orthogonal to the symmetry axis. If the propagation direction is parallel (orthogonal) to the symmetry axis, the two orthogonally polarized S waves will have the same (different) propagation velocities.

$$v_{P_\parallel} = \sqrt{\frac{c_{11}}{\varrho}} \qquad v_{P_\perp} = \sqrt{\frac{c_{33}}{\varrho}} \qquad v_{S_\parallel} = \sqrt{\frac{c_{44}}{\varrho}} \qquad v_{S_\perp} = \sqrt{\frac{c_{66}}{\varrho}} \tag{3.6}$$

For isotropy, only two independent elasticity parameters remain (Eq. 3.7; *Savage*, 1999). Mainly the first and second *Lamé parameters* λ and μ are used. In an equivalent way the elasticity modulus (*Young's modulus*) E and *Poisson's ration* ν or the compression modulus K and the modulus of rigidity G can be used. While μ refers to the ratio between the shear stress and shear strain, λ is difficult to understand from a physical perspective.

$$\boldsymbol{c} = \begin{pmatrix} \lambda+2\mu & \lambda & \lambda & 0 & 0 & 0 \\ \lambda & \lambda+2\mu & \lambda & 0 & 0 & 0 \\ \lambda & \lambda & \lambda+2\mu & 0 & 0 & 0 \\ 0 & 0 & 0 & \mu & 0 & 0 \\ 0 & 0 & 0 & 0 & \mu & 0 \\ 0 & 0 & 0 & 0 & 0 & \mu \end{pmatrix} \tag{3.7}$$

The *stress-strain relation* (Eq. 3.1) after inserting Eq. 3.7 is shown in Eq. 3.8 using the *Kronecker* delta δ_{ij}.

$$\sigma_{ij} = \lambda\varepsilon_{ii}\delta_{ij} + 2\mu\varepsilon_{ij} \quad \text{with } i,j,k,l = 1,2,3 \text{ and } \delta_{ij} = \begin{cases} 1 & \text{for } i = j \\ 0 & \text{otherwise} \end{cases} \tag{3.8}$$

The propagation velocities of the P and S waves v_p or v_s can be expressed via Eq. 3.9 (*Maupin and Park*, 2007).

$$v_\mathrm{P} = \sqrt{\frac{\lambda+2\mu}{\varrho}} \quad \text{and} \quad v_\mathrm{S} = \sqrt{\frac{\mu}{\varrho}} \tag{3.9}$$

3.2 Wave propagation and wave types

Starting with a three-dimensional (x_1, x_2, x_3) homogeneous medium (density ϱ) and assuming an infinitesimal stress, the strain tensor can be expressed as Eq. 3.10 using the displacement $\boldsymbol{u}$.

$$\varepsilon_{kl} = \frac{1}{2}\left(\frac{\partial u_k}{\partial x_l} + \frac{\partial u_l}{\partial x_k}\right) \quad \text{with } k,l = 1,2,3 \tag{3.10}$$

The *elastic wave equation* in three dimensions for a homogeneous medium is given as Eq. 3.11.

$$\varrho\frac{\partial u_i^2}{\partial t^2} = \frac{\partial \sigma_{ij}}{\partial x_j} \quad \text{with } i,j = 1,2,3 \tag{3.11}$$

Inserting the *stress-strain relation* for full anisotropy from Eq. 3.1 and assuming c_{ijkl} being spatial-independent:

$$\varrho\frac{\partial u_i^2}{\partial t^2} = \frac{\partial\left(c_{ijkl}\varepsilon_{kl}\right)}{\partial x_j} = c_{ijkl}\frac{\partial \varepsilon_{kl}}{\partial x_j} \quad \text{with } i,j,k,l = 1,2,3 \tag{3.12}$$

and further inserting the expression for small strain from Eq. 3.10:

$$\varrho\frac{\partial u_i^2}{\partial t^2} = \frac{1}{2}c_{ijlk}\frac{\partial}{\partial x_j}\left(\frac{\partial u_k}{\partial x_l} + \frac{\partial u_l}{\partial x_k}\right) \quad \text{with } i,j,k,l = 1,2,3\ . \tag{3.13}$$

Based on Eq. 3.13, the elasticity tensor can be used to represent anisotropy in the wave equation and allows, by this, to consider anisotropy in the simulation of seismograms or wavefields (Sec. 9.3).

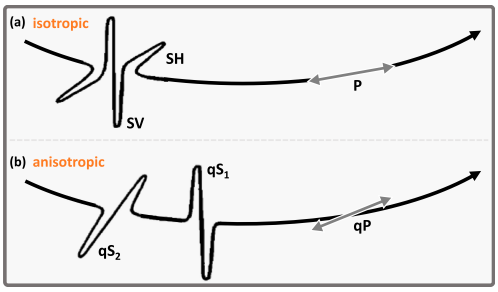

Figure 3.2: Wave types in an **(a)** isotropic medium with P (compression, longitudinal) wave and S (shear, transverse) waves with horizontal (SH) and vertical (SV) polarizations, and **(b)** anisotropic media with quasi P (qP) wave and quasi s_1 (qS_1, fast) and quasi s_2 (qS_2, slow) waves. For details on shear wave splitting, see the following Sec. 3.3 and Fig. 3.3. Slightly modified after *Savage* (1999, fig. 1).

For the isotropic case, Eq. 3.8 can be inserted into Eq. 3.11 with assuming λ and μ being spatially independent:

$$\varrho \frac{\partial u_i^2}{\partial t^2} = \frac{\partial \left(\lambda \varepsilon_{ii} \delta_{ij} + 2\mu \varepsilon_{ij}\right)}{\partial x_j} = \lambda \frac{\partial \varepsilon_{ii}}{\partial x_i} + 2\mu \frac{\partial \varepsilon_{ij}}{\partial x_j} \quad \text{with } i, j = 1, 2, 3 \tag{3.14}$$

and using again Eq. 3.10:

$$\varrho \frac{\partial u_i^2}{\partial t^2} = \lambda \frac{\partial \varepsilon_{ii}}{\partial x_i} + \mu \frac{\partial}{\partial x_j} \left(\frac{\partial u_i}{\partial x_j} + \frac{\partial u_j}{\partial x_i} \right) = (\lambda + \mu) \frac{\partial \varepsilon_{ii}}{\partial x_i} + \mu \nabla^2 u_i \tag{3.15}$$

$$\varrho \frac{\partial \boldsymbol{u}^2}{\partial t^2} = (\lambda + 2\mu) \nabla (\nabla \cdot \boldsymbol{u}) + \mu \nabla^2 \boldsymbol{u} \tag{3.16}$$

whereby Eqs 3.15 and 3.16 are only valid in cartesian coordinates (*Shearer*, 2009), and the isotropic P and S wave propagation velocities (see also Eq. 3.9) are directly visible in Eq. 3.16.

To solve the wave equation in Eq. 3.11 a *plane wave* can be assumed (Eq. 3.17), with the phase velocity c_{ph}, the unit vector $\boldsymbol{n}$ pointing in the direction normal to the wavefront, the vector $\boldsymbol{a}$ describing the amplitude and polarization, and the function f describing the particle motion.

$$\boldsymbol{u}(\boldsymbol{x}, t) = \boldsymbol{a} f \left(t - \frac{\boldsymbol{n} \cdot \boldsymbol{x}}{c_{\text{ph}}} \right) \tag{3.17}$$

This can be formulated as an eigenvalue problem (*Nowacki et al.*, 2011), known as *Christoffel equation* (Eq. 3.18) with the *Christoffel matrix* m_{il} (*Christoffel*, 1877).

$$\frac{1}{\varrho} c_{ijkl} n_j n_k a_l = m_{il} a_l = c_{\text{ph}}^2 a_i \tag{3.18}$$

Solving the determination equation (Eq. 3.19)

$$\det \left(m_{il} - c_{\text{ph}}^2 \delta_{il} \right) = 0 \tag{3.19}$$

gives the three eigenvalues $c_{\text{ph},1}^2$, $c_{\text{ph},2}^2$, and $c_{\text{ph},3}^2$ representing the phase velocities of the P and S waves as well as the eigenvectors a_1^2, a_2^2, and a_3^2 are the related polarization directions (*Nowacki et al.*, 2011).

In an anisotropic medium, the wave fronts are not spherical, even for a homogeneous medium. Thus, the wave vector is (locally) orthogonal to the wave front but not to the wave ray. In general, the phase velocity is orthogonal to the wave front in the direction of the wave vector, and the group velocity is parallel to the energy propagation in the direction of the wave ray. This means that the wave vector and the wave ray point in different directions, and the phase and group velocities are not parallel. There is one quasi P wave (qP wave) polarized parallel to the wave ray and two quasi S waves (qS waves) polarized orthogonal to each other and propagating with different velocities, which are called qS_1 (fast) and qS_2 (slow) waves (Fig. 3.2; *Savage*, 1999; *Maupin and Park*, 2007). The qP wave or the qS waves are not polarized parallel or orthogonal to the propagation direction, i.e., they are not pure or exact longitudinal or transverse waves, and the qS waves are not polarized orthogonal to the qP wave.

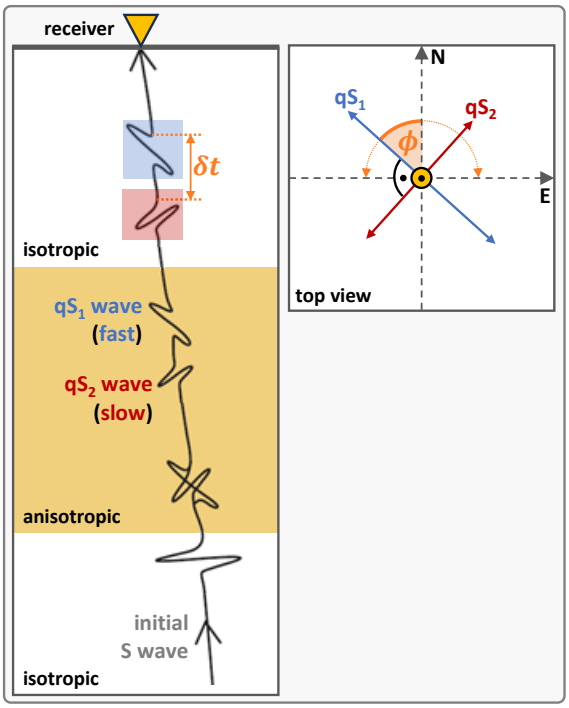

Figure 3.3: Principle of shear wave splitting (equivalent to the optical birefringence of light). **(left)** Travel path through a medium with an anisotropic region (yellow-orange part) between two isotropic regions (white parts) and **(right)** top view at the surface with the receiver (yellow) in the center.
The initial linearly polarized shear (S) wave enters the anisotropic region and is split into two waves, called *quasi* shear (qS) waves, which have orthogonal polarization directions and travel with different propagation velocities within the anisotropic region (qS_1 fast in blue and qS_2 slow in red). After leaving the anisotropic region, the qS waves have accumulated a time difference, which is preserved while traveling through the second isotropic region (top white part). To quantify the anisotropy, the two splitting parameters, the fast polarization direction ϕ (right; measured relatively to North; the value range used in this doctoral thesis is -90° to 90° as indicated by the dotted orange double arrow) of the fast qS wave and the delay time δt accumulated between the two qS waves after leaving the anisotropic medium (left), can be determined. There is a trade-off between the strength of the anisotropy and the length of the travel path within the anisotropic region, i.e., both a strong anisotropy and a long travel path within the anisotropic region can lead to a long delay time. The left part is modified after *Wüstefeld et al.* (2008, fig. 1).

Seismic anisotropy is reported as *intrinsic anisotropy* and *percent anisotropy* (*Savage*, 1999), whereby both quantities are multiplied by a factor of 100 to get values in percentage. The intrinsic anisotropy k_i of a material is the normalized difference between the maximum and minimum propagation velocities in an anisotropic medium v_{max} and v_{min} for a fixed wave type and polarization direction:

$$k_i = \frac{v_{max} - v_{min}}{(v_{max} + v_{min})/2} \cdot 100 \,. \tag{3.20}$$

The normalized difference between the propagation of the two qS waves within the anisotropic medium v_{qS_1} and v_{qS_2} for a given propagation direction is referred to as percent anisotropy k_s:

$$k_s = \frac{v_{qS_1} - v_{qS_2}}{(v_{qS_1} + v_{qS_2})/2} \cdot 100 \,. \tag{3.21}$$

Following *Savage* (1999), in this doctoral thesis anisotropy is reported as percent anisotropy (e.g., Fig. 3.4).

3.3 Shear wave splitting

Shear wave splitting (SWS) is the seismological (mechanical wave) equivalent to the phenomenon of optical (light, electro-magnetic wave) birefringence (*Savage*, 1999; *Long and Silver*, 2009). SWS is a unique identifier for anisotropy within a medium and thus allows for a clear distinction from heterogeneity. The principle of SWS is shown in Fig. 3.3. An S wave with linear polarization direction traveling in an isotropic medium enters an anisotropic medium and is split into two qS waves (assuming the same propagation directions and travel paths) with orthogonal polarization directions but different propagation velocities (qS_1 fast, qS_2 slow). The fast polarization direction ϕ of the anisotropic medium (i.e., the polarization direction of the fast qS wave) and the delay time δt accumulated between the two qS waves after traveling through the anisotropic medium are called *splitting parameters* and can be used to quantify the anisotropy. After leaving the anisotropic region, the two qS waves travel with the same velocity, and the accumulated delay time is preserved. In case the initial polarization direction is parallel or orthogonal to the fast or slow polarization directions of the medium, no SWS can occur.

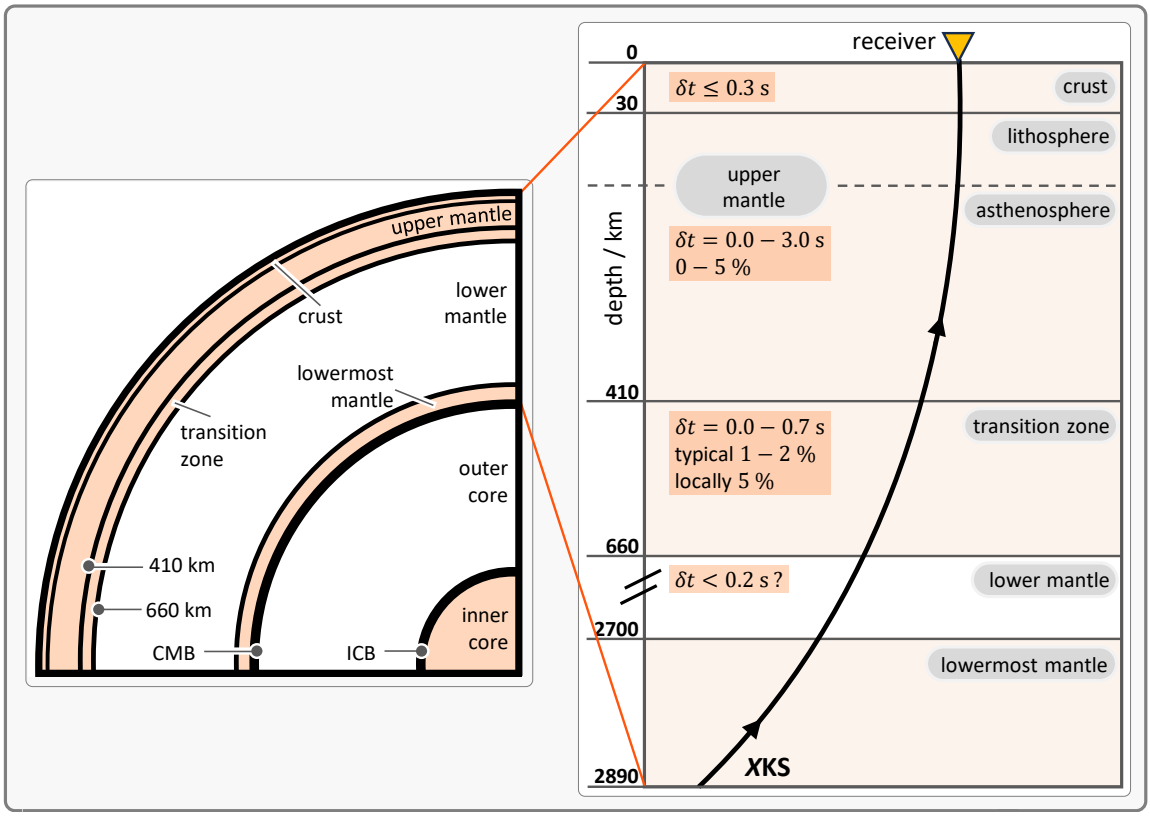

Figure 3.4: Anisotropy within the Earth: depth distribution. **(left)** Cross section through the Earth (1-D, radial, concentric shells) with anisotropic regions highlighted light orange. The different sources or structures causing the anisotropy in the crust, the upper mantle and transition zone, and the lowermost mantle are shown in Fig. 3.5. The lower mantle as well as the liquid outer core are (nearly) isotropic. **(right)** Depth range from the lowermost mantle (2900 km) to the surface (0 km) on the receiver (inverse yellow triangle) side, which is relevant for anisotropy studies using *XKS* phases as done in this doctoral thesis. Please note that the depth axis is not to scale. *Abbreviations*: CMB = core-mantle boundary, ICB = inner-core boundary. The right part is modified and the delay time and percentage anisotropy values are after *Savage* (1999, fig. 9).

The delay time can be calculated via Eq. 3.22 using the propagation velocities of the two qS waves $v_{\mathrm{qS}_1} > v_{\mathrm{qS}_2}$ and the length of the travel path L within the anisotropic medium (*Nowacki and Cottaar*, 2021).

$$\delta t = \frac{L}{v_{\mathrm{qS}_2}} - \frac{L}{v_{\mathrm{qS}_1}} = L\left(\frac{1}{v_{\mathrm{qS}_2}} - \frac{1}{v_{\mathrm{qS}_1}}\right) \tag{3.22}$$

The delay time contains (only) information on the term $(1/v_{\mathrm{qS}_2} - 1/v_{\mathrm{qS}_1})$. This points out an important trade-off between the length of the travel path within the anisotropic medium and the strength of the anisotropy, i.e., a short travel path through an anisotropic medium with strong anisotropy or a long travel path through a medium with weak anisotropy both lead to a long or the same delay time after leaving the anisotropic medium.
Knowing the polarization direction of the initial S wave significantly simplifies the determination of the splitting parameters. This is the case for the core-refracted phases PKS, PKKS, SKS, and SKKS, jointly referred to as *XKS* and in detail described in Sec. 4.1. Besides the determination of the splitting parameters, SWS can be quantified by calculating the so-called *splitting intensity* (*Chevrot*, 2000[8]) which is introduced in detail in Sec. 4.2.2.

3.4 Anisotropy within the Earth

In seismology, anisotropy refers to a (preferred) orientation of structures or crystals, i.e., so-called *bulk* anisotropy (*Long and Silver*, 2009; *Savage*, 1999). This means that the wavelength of the wave is significantly larger than the

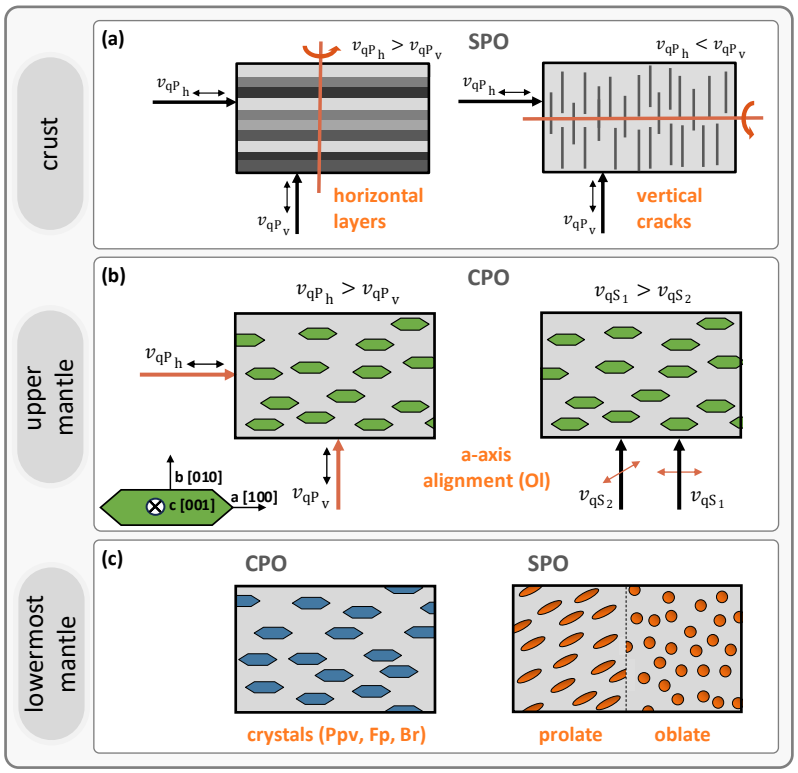

Figure 3.5: Anisotropy within the Earth: **(a)** crust, **(b)** upper mantle, and **(c)** lowermost mantle (LMM). *Notation*: "h" = horizontal, "v" = vertical. *Arrows*: The thick arrows point in the propagation directions, while the thin double-arrows show the polarization directions of the P and S waves.
In the crust, anisotropy is caused by SPO of (horizontal) layers (HTI) and (vertical) cracks (VTI). The orange line marks the symmetry axis. In the upper mantle, olivine (Ol) is the dominant mineral (single crystals schematically drawn in green; for details, see Fig. 3.7) showing CPO. The general assumption is an alignment of the a-axis (fast axis). In the LMM, besides the CPO of the minerals post-perovskite (pPv), bridgmanite (Br), and ferropericlase (Fp), SPO of lenses and pockets can cause anisotropy. (a) and (b) are modified after *Fröhlich* (2020, figs 2, 3) and (c) is modified after *Nowacki et al.* (2011, fig. 16).

characteristic length of the structure, and underlines the relationship between anisotropy and heterogeneity. Such a preferred orientation can be either a *shape preferred orientation* (SPO) or a *lattice* or *crystals preferred orientation* (LPO or CPO). In case of a random orientation, the medium is effectively isotropic.
Within the Earth, anisotropy occurs at different depths (*Long and Becker*, 2010, fig. 1), including the crust (Sec. 3.4.1), the upper mantle (Sec. 3.4.2), and the lowermost mantle (LMM, Sec. 3.4.3) as well as the solid inner core (*Long and Becker*, 2010, fig. 1). The anisotropy studies within this doctoral thesis focus on the Earth's mantle, especially the upper mantle. Details on the LMM can be found in *Nowacki et al.* (2011), *Nowacki and Cottaar* (2021) and *Wolf et al.* (2024c). Regarding the inner core, the reader is kindly referred to the works of *DeMets et al.* (2010), *Romanowicz and Wenk* (2017), *Frost et al.* (2021), and *Brett et al.* (2024).

3.4.1 Crust

In the crust (0-30 km depth), anisotropy is related to SPO of thin layers as well as (micro-)cracks and fractures (Fig. 3.5a). Both can introduce hexagonal symmetry into a medium. Horizontal layers with different or alternating elastic properties can lead to HTI, whereby the layers themselves can be isotropic. If horizontal layers are tilted at a later time, this may lead to TTI. Vertical cracks can cause VTI. The main mechanism leading to SPO of cracks is stress (*Crampin*, 1984a; *Crampin and Lovell*, 1991; *Crampin and Chastin*, 2003). They primarily align orthogonal to the minimum horizontal stress, with the fast axis direction parallel to the direction of the maximum horizontal stress. The fill of the cracks (fluids, melt, water) as well as the density of cracks determine the strength of the anisotropy. At a pressure larger than 200-300 MPa, e.g., deeper than 10-15 km, the cracks are closed (laboratory experiments). Thus, below this depth, anisotropy has to be explained in another way.
Typical delay times for crustal anisotropy analyzing *X*KS phases are smaller than 0.3 s (Fig. 3.4; *Silver and Chan*, 1988; *Savage*, 1999). Thus, crustal anisotropy is commonly ignored in mantle studies (Sec. 5.1). However, for some regions slightly longer delay times are reported (e.g., *Kong et al.*, 2016).

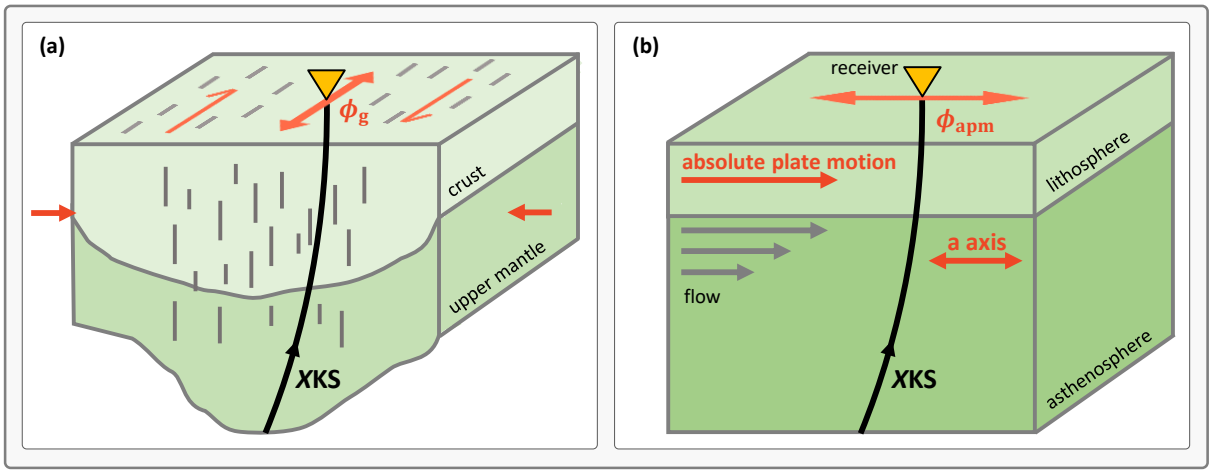

Figure 3.6: Anisotropy within the Earth: Large-scale processes within the upper mantle leading to LPO. **(a)** Lithosphere: *vertical coherent deformation* (VCD) in case of transpressional motion. The left and right orange arrows indicate the deformation. The fast polarization direction ϕ_g (orange double arrow) expected to be measured for steeply inclining *X*KS phases at the recording station (inverse yellow triangle) is parallel to the lineation direction. **(b)** Asthenosphere and partly lithosphere: *simple asthenospheric flow* (SAF). A lithosphere moving with the speed of the absolute plate motion (APM) leads to a shear zone in the asthenosphere (within a *hotspot reference frame*; *Gripp and Gordon*, 2002). The fast polarization direction ϕ_{apm} expected to be measured at the recording station is parallel to the direction of the APM. This can be coupled to a horizontal mantle flow, with the a-axis pointing in the direction of the flow. Note the influence of the ambient conditions on the fabric (*Long and Becker*, 2010; for details, see Tab. 3.1). Modified after *Silver* (1996, fig. 9) and *Yuan and Levin* (2014, fig. 1).

3.4.2 Upper mantle and transition zone

In the upper mantle (30-410 km depth), mainly CPO (Fig. 3.5b; *Savage*, 1999; *Long and Silver*, 2009) of intrinsic anisotropic minerals is responsible for anisotropy. The dominant mineral in the upper mantle is olivine (Ol) characterized by orthorhombic symmetry (Fig. 3.7).
The majority of the anisotropy is assumed to be located up to 250 km depth with a maximum around 150 km depth. The knowledge of the decrease with depth is based on surface wave studies, as they show decreasing anisotropy with increasing wavelength (*Yuan and Beghein*, 2014; *Zhu et al.*, 2015). The transition zone (410-660 km) is assumed to be weakly anisotropic (Fig. 3.4; *Vinnik et al.*, 1992).

For the lithosphere, recent crustal stress can be relevant (*Silver and Chan*, 1991), leading to SPO of melt-filled cracks in the uppermost mantle (*Savage*, 1999). Two main large scale approaches to explain CPO-induced anisotropy in the lithosphere and asthenosphere are proposed by *Silver*, 1996 (Fig. 3.6): (i) *vertical coherent deformation* (VCD) and (ii) *simple asthenospheric flow* (SAF). So-called *fossil anisotropy* is preserved over long geological times and can help to understand past geological and geodynamic processes. Below a *critical temperature*, for olivine ca. 900°C (*Savage*, 1999), the anisotropy within the medium is "*frozen in*" and cannot be changed anymore. A fourth approach is the recent mantle flow (*Long and Becker*, 2010), whereby a vertical mantle flow (i.e., a vertical a-axis or VTI) cannot be detected with *X*KS phases, due to their nearly vertical incidence in the upper mantle.
In general, the a-axis (of olivine) is considered to be oriented in the direction of the horizontal mantle flow. However, it has been shown that the CPO can differ from this assumption or scenario depending on the geodynamic setting (*Long and Becker*, 2010), which is referred to as *fabric types* (Tab. 3.1). To understand the behavior of minerals under different deformation regimes (e.g., simple shear, pure shear) and ambient conditions (water content, temperature), laboratory experiments are carried out (*Karato et al.*, 2008) and databases are compiled, e.g., for the upper mantle (*Jung et al.*, 2006) and for the LMM (*Creasy et al.*, 2020). While the A- or D-types dominate in the lithosphere, the C-, E- or A-types are expected in the asthenosphere (*Long and Becker*, 2010). The B-type is expected to be present in the cold corner of the subduction mantle wedge, whereby the horizontal mantle flow is not parallel but perpendicular to the a-axis (*Long and Becker*, 2010, fig. 3).

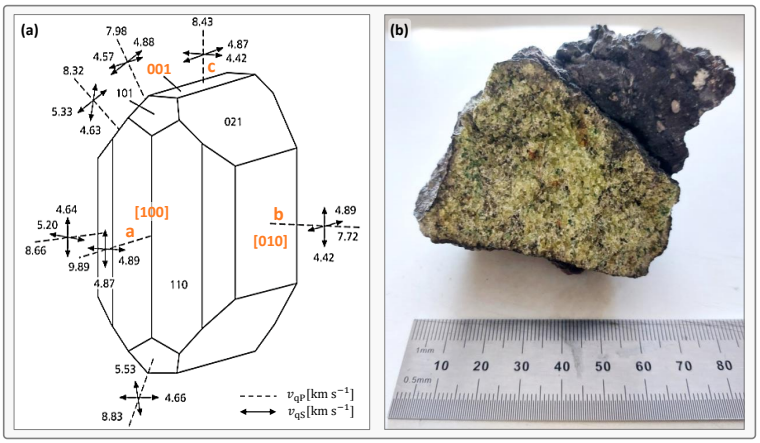

Figure 3.7: (a) Crystallographic axes of a single olivine crystal characterized by orthorhombic anisotropy, with being the a [100] axis the fast axis, the b [010] axis the slow axis, and the c [001] axis the intermediate axis. Slightly modified after *Babuška and Cara* (1991). **(b)** Peridotite (potentially originating from the upper mantle) collected in the Eifel volcanic field (Germany) during a master course excursion in summer 2018. The olivine crystals show their typical greenish color. Photo taken by Yvonne Fröhlich on 2025/02/25.

Two deformation mechanisms dominate in the upper mantle: (i) *dislocation creep* and (ii) *diffusion creep* (*Karato and Wu*, 1993; *Savage*, 1999). Dislocation creep occurs for large grain size or / and high stress leading to CPO and, by this, to anisotropy. In contrast, diffusion creep is present for small grain size or / and low stress, and no CPO is developed, and the medium remains isotropic.

Various studies relate anisotropy to subduction zones (*Long and Becker*, 2010, figs 2, 8; *Kenyon and Wada*, 2025) or slab deformation (*Cao et al.*, 2024), to past tectonic activity, e.g., for Fennoscandia proposing structures with tilted symmetry axes (*ScanArray*, *Grund and Ritter*, 2020, fig. 11), and current mantle flow around subducted slabs, e.g., for the Alps (*AlpArray*; *Petrescu et al.*, 2020; *Link and Rümpker*, 2021; *Link and Rümpker*, 2023; *Hein et al.*, 2021). For upper mantle anisotropy, delay times of *X*KS phases are longer than 0.5 s (Fig. 3.4; *Savage*, 1999) up to 2.5 s.

Table 3.1: Fabric types of olivine as a function of water, stress, and temperature named as A, E, C, and B (D-type corresponds to A-type under high stress). Data are from *Jung et al.* (2006) and *Long and Becker* (2010), colored (statistical distribution of the crystallographic axes: blue low, red high) pole figures (second column) are generated with a MATLAB re-implementation (*Thissen*, 2015) of the FORTRAN 90 code *D-Rex* (*Kaminski et al.*, 2004), schematic pole figures (third column) are from *Skemer and Hansen* (2016, tab. 4), and olivine crystal sketches (last column) are from *Bernard et al.* (2019, fig. 1). The pole figures are valid for simple shear deformation in horizontal direction; for details, see the mentioned publications.

Fabric type	Dominate slip system						Slip direction	Slip plane	Water content	Stress	Temperature	Hor. mantle flow vs. fast direction
	[100]	[010]	[001]	[100]	[010]	[001]						
A	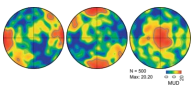			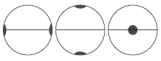			[100]	(010)	poor (dry)	modest	modest	∥ 
E	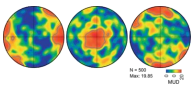			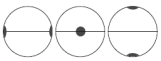			[100]	(001)	moderate	low	high	∥ 
C	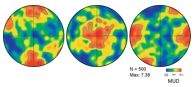			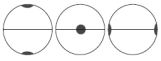			[001]	(100)	high	low	high	∥ 
B	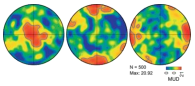			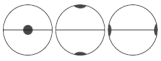			[001]	(010)	various	high	low	⊥ 

3.4.3 Lower and lowermost mantle

Initially, the lower mantle was called D layer of the Earth (*Bullen*, 1940). Based on new insights, the lower mantle was divided into upper and lower parts, called D' and D'' (D double prime), respectively (*Bullen*, 1949). The D'' layer or lowermost mantle (LMM) refers to the depth range 2650-2890/2900 km, i.e., it is a 200-250 km thick layer on

top of the core-mantle boundary (CMB). This layer is still not well understood but is known to be quite complex and heterogeneous (*McNamara*, 2019). Together with the CMB, the D'' region plays a key role in both mantle dynamics or convection (which is ultimately linked to plate tectonics) and outer core convection (leading to the Earth's magnetic field). Thus, the D''layer is an important subject of ongoing research (*Waszek*, 2024).

While the lower mantle is assumed to be nearly isotropic (*Panning and Romanowicz*, 2006), there are clear observations of anisotropy in the LMM (*Wookey and Kendall*, 2007, tab. 1; *Romanowicz and Wenk*, 2017, tab. 1; *Wolf et al.*, 2023) related to SPO as well as CPO (Fig. 3.5c; *Nowacki and Cottaar*, 2021). For CPO the minerals post-perovskite (pPv), bridgmanite (Br), and ferropericlase (Fp) are relevant (*Romanowicz and Wenk*, 2017, fig. 10). SPO has been proposed to occur as prolate and oblate (*Nowacki and Cottaar*, 2021). Processes related to down- and upwelling as well as horizontal and vertical mantle flow are assumed to cause anisotropy in the LMM (*Moore et al.*, 2004, fig. 18; *Long and Becker*, 2010, fig. 9). These lead to anisotropy at the edges (*Wolf et al.*, 2023; *Immoor et al.*, 2018, fig. 4) of the two large low shear wave provinces (LLSVPs; *Panton et al.*, 2025) underneath Africa (*Pisconti et al.*, 2022) and the Pacific (*Deng et al.*, 2017), related to ultra low velocity zones (ULVZ), e.g., underneath the Himalayas linked to a subducted slab (*Wolf et al.*, 2024d) and below the Central Pacific Ocean (*Wolf and Long*, 2023) , as well as related to plumes, e.g., Yellowstone (*Wolf et al.*, 2024b) and Iceland (*Wolf et al.*, 2019).

Various approaches have been and are applied to detect regions of LMM anisotropy (*Wolf et al.*, 2023; Fig. 3.10). Especially phase pairs (Fig. 5.1), e.g., SKS-SKKS (*Deng et al.*, 2017) or S-ScS (*Wolf and Long*, 2024a), are widely used. There are various challenges in terms of understanding LMM anisotropy (*Wolf et al.*, 2022), e.g., the limited directional or backazimuthal coverage due to the possible or available source-receiver constellations to sample specific target regions in the LMM (*Fröhlich et al.*, 2024a), the correction for as well as the implication on anisotropy in the upper mantle (*Wolf et al.*, 2024a), and the usage of non-*X*KS phases as ScS (*Wolf and Long*, 2024b).

3.5 Existing databases

Several databases related to seismic anisotropy, SWS, and elastic tensors were compiled and made freely available. Tab. 3.2 summarizes the databases that are used in this doctoral thesis. Besides these databases, quite recently *Wolf et al.* (2025)[5] published a quite promising database of SWSMs, which provides several details on the single measurements, including diagnostic plots.

Table 3.2: Databases on seismic anisotropy, SWS, and elastic tensors used in this doctoral thesis.

Database	Related publication	Content	Discussed in
shear wave splitting	*Wüstefeld et al.* (2009), *Barruol et al.* (2009)	splitting parameters of over 300 publications	Fig. 3.8
tomography EU_{60}	*Zhu et al.* (2015)	$\mathrm{d}v_\mathrm{p}$ and $\mathrm{d}v_\mathrm{s}$; fast polarization direction and strength	Fig. 3.9, Fig. 8.9a
deep anisotropy	*Wolf et al.* (2023)	regions of lowermost mantle anisotropy	Fig. 3.10
elastic tensors	*Jung et al.* (2006), *Creasy et al.* (2020)	elastic tensors for various minerals in the upper and lowermost mantle	Sec. 9.3, Tab. 9.2, Fig. 9.4

[5] *ADEPT* and *SWAT* are available at `https://adept.sese.asu.edu` or `https://swat.sese.asu.edu`, respectively; last accessed 2025/04/16.

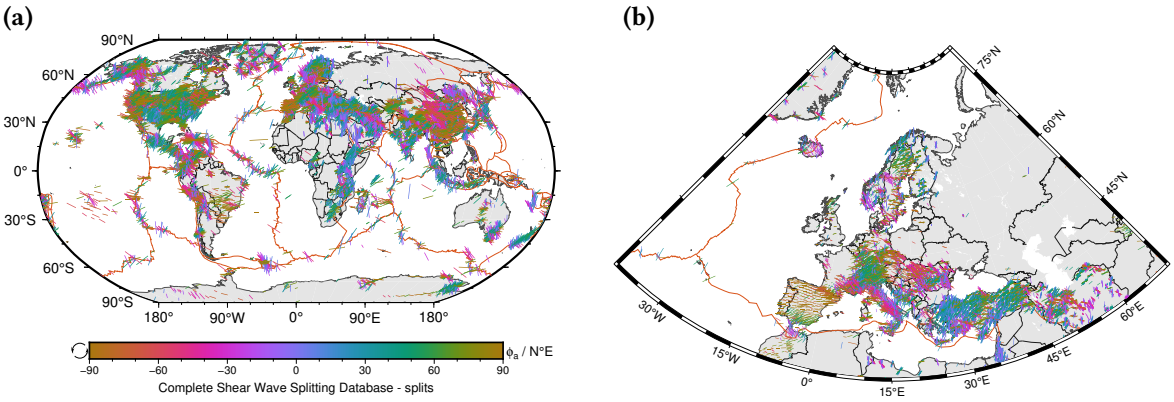

Figure 3.8: Shear wave splitting database containing shear wave splitting measurements of over 300 anisotropy studies (*Wüstefeld et al.*, 2009; *Barruol et al.*, 2009). **(a)** Global overview and **(b)** Europe. As for the majority of the studies, only the *splits* were reported to the database but not the *nulls* only the *splits* are displayed as color- and size-coded oriented bars for the (apparent) fast polarization direction and (apparent) delay time.

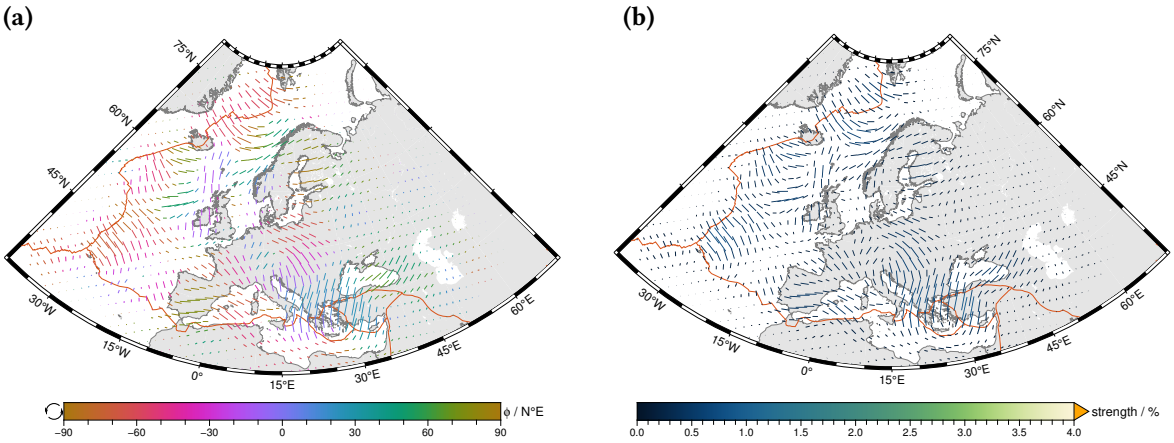

Figure 3.9: Tomography EU_{60} for Europe in 200 km depth (*Zhu et al.*, 2015). **(a)** Fast polarization direction and **(b)** strength.

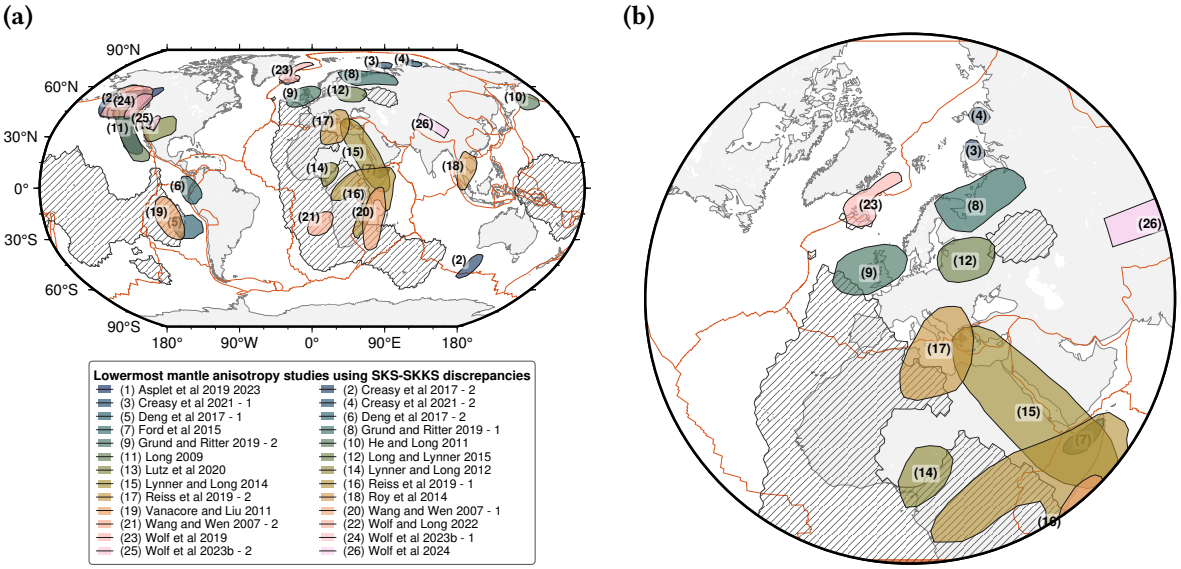

Figure 3.10: Deep anisotropy database with regions of anisotropy in the lowermost mantle proposed in several anisotropy studies (*Wolf et al.*, 2023). Here, the studies that used SWSMs on SKS-SKKS phase pairs are shown. **(a)** Global overview and **(b)** Central Europe centered around the URG area within 60° epicentral distance. Regions with reduced shear wave velocity (Iceland plume, Perm anomaly and the large low shear wave velocity provinces underneath Africa [Tuzo] and the Pacific [Jason]; hatched areas) digitized by *Wolf et al.* (2023).

4 Measuring of Shear Wave Splitting

The studies within the framework of this doctoral thesis focus on anisotropy in the Earth's mantle. Therefore, SWS of core-refracted shear waves (Sec. 4.1) is analyzed and modeled. To quantify SWS, the splitting parameters are determined and the splitting intensity is calculated (Sec. 4.2). The SWS analysis (Sec. 4.3) is carried out using the MATLAB program *SplitLab* (*Wüstefeld et al.*, 2008) with the plug-in *StackSplit* (*Grund*, 2017).

4.1 Seismic phases and earthquakes

Python codes using *PyGMT* (*Tian et al.*, 2025b) to reproduce several of the maps and visualizations presented in this doctoral thesis as well as the related scientific publications and conference contributions, whereby the codes for calculating (via *ObsPy*; *Krischer et al.*, 2015) and plotting (via *PyGMT*) the travel paths and travel time curves discussed in the following Secs 4.1 and 4.3.1 are contained in folder `003_taup`, is available at:

> ***Fröhlich Y.** (2025).* **Python Scripts and Jupyter Notebooks using PyGMT**. Development on GitHub at `https://github.com/yvonnefroehlich/gmt-pygmt-plotting`.

To study anisotropy in the Earth's mantle, the core-refracted phases PKS, PKKS, SKS, and SKKS[6], jointly referred to as *X*KS phases (Figs 4.2, B.9), are preferably used. On the source side, they travel either as P or as S wave down to the CMB, after an S-to-P conversion for the S wave, they travel as P wave ([first] "K", referring to "Kern", which is German for "core"; for the inner core "I" [P wave] or "J" [S wave] are used) through the liquid outer core. On the source side, a P-to-S conversion occurs at the CMB and an S wave travels up to the receiver. Compared to PKS and SKS, the travel paths of PKKS or SKKS have one downside reflection on the CMB (second "K"). *X*KS phases occur within limited epicentral distance ranges. The travel time curves of *X*KS phases as well as direct P and S phases and phase traveling through the inner core are shown in Fig. 4.2.
*X*KS phases have several advantages compared to other phases (e.g., S and ScS phases), as pointed out in Fig. 4.3, making them favorable for SWS analysis regarding anisotropy located in the Earth's mantle. Assumptions are a plane CMB and a laterally homogeneous Earth. Due to the S-to-P conversion on the source side, any observed splitting signal can be located along the ray path on the receiver side. Due to the P-to-S conversion on the receiver side, the S wave is a pure SV wave, and the initial polarization direction in the (isotropic) medium is known. Furthermore, the initial polarization direction is equivalent to the BAZ (neglecting the error in the earthquake location). For a pure SV wave, only a signal on the radial (R) or Q component occurs, but the transverse (T) component is zero in an isotropic medium. This results in a linearly horizontal particle motion. In contrast, an elliptical particle motion can be observed in the case of anisotropy, and a non-zero single is measured on the T component.

Mainly (only) SKS phases are analyzed. PKS and PKKS are quite rarely considered. PKS occurs only in a very limited epicentral distance range. For PKKS, only the branch "traveled the other way around" exists, which

[6] The nomenclature of the seismic phases follows the *IASPEI standard phase list*, available at `http://www.isc.ac.uk/standards/phases/`, last accessed 2025/05/05.

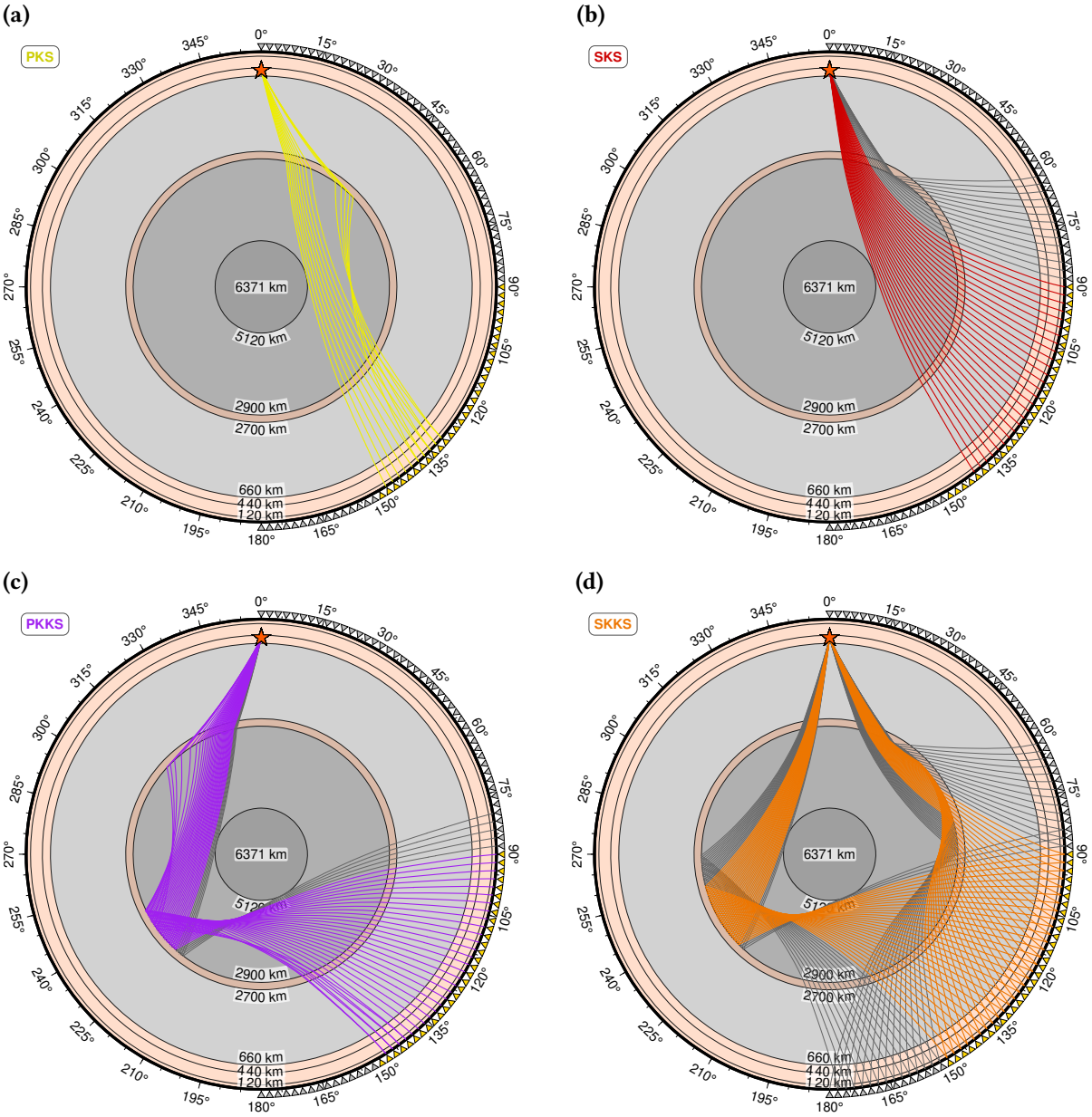

Figure 4.1: Travel paths of *X*KS phases calculated after the *iasp91* Earth model (*Kennett*, 1991) using *ObsPy* (*Beyreuther et al.*, 2010) based on the original *Java TauP* Toolkit (*Crotwell et al.*, 1999): **(a)** PKS, **(b)** SKS, **(c)** PKKS, and **(d)** SKKS. The hypocenter (red star) of the earthquake is in 500 km depth. Recording stations (inverse triangles) are placed in steps of 2° epicentral distance. For the epicentral distance range 90°-150°, the stations are colored in yellow, and the travel paths are plotted in color corresponding to the travel time curves in Fig. 4.1. Anisotropy located in the upper mantle, the transition zone, and the LMM (highlighted in light orange) can be studied by analyzing *X*KS phases. For combined plots at specific epicentral distances, see Fig. B.9. For the travel paths of P, S, PcP, and ScS phases as well as phases traveling through the inner core, see Fig. C.1 or Fig. C.2, respectively.

is difficult to observe in real data. In this doctoral thesis, PKS, SKS, and SKKS phases are analyzed within the epicentral distance range 90°-150°. Two specific phases analyzed in the same seismogram of one single earthquake, so-called *phase pairs* (e.g., SKS-SKKS), can provide crucial information on the location, especially the depth, of the anisotropy (Sec. 5.1).

Earthquakes are selected from the *Global Harvard Centroid Moment Tensor* (CMT) catalog (*Dziewonski and Anderson*, 1981; *Ekström et al.*, 2012) within the required epicentral distance range centered around the locations of the recording stations in the URG area (Figs 1.1a, 4.4, B.1). Only events with a moment magnitude $M_w \geq 6$ are used to ensure a clear signal amplitude to distinguish the phases from the noise contained in the data.

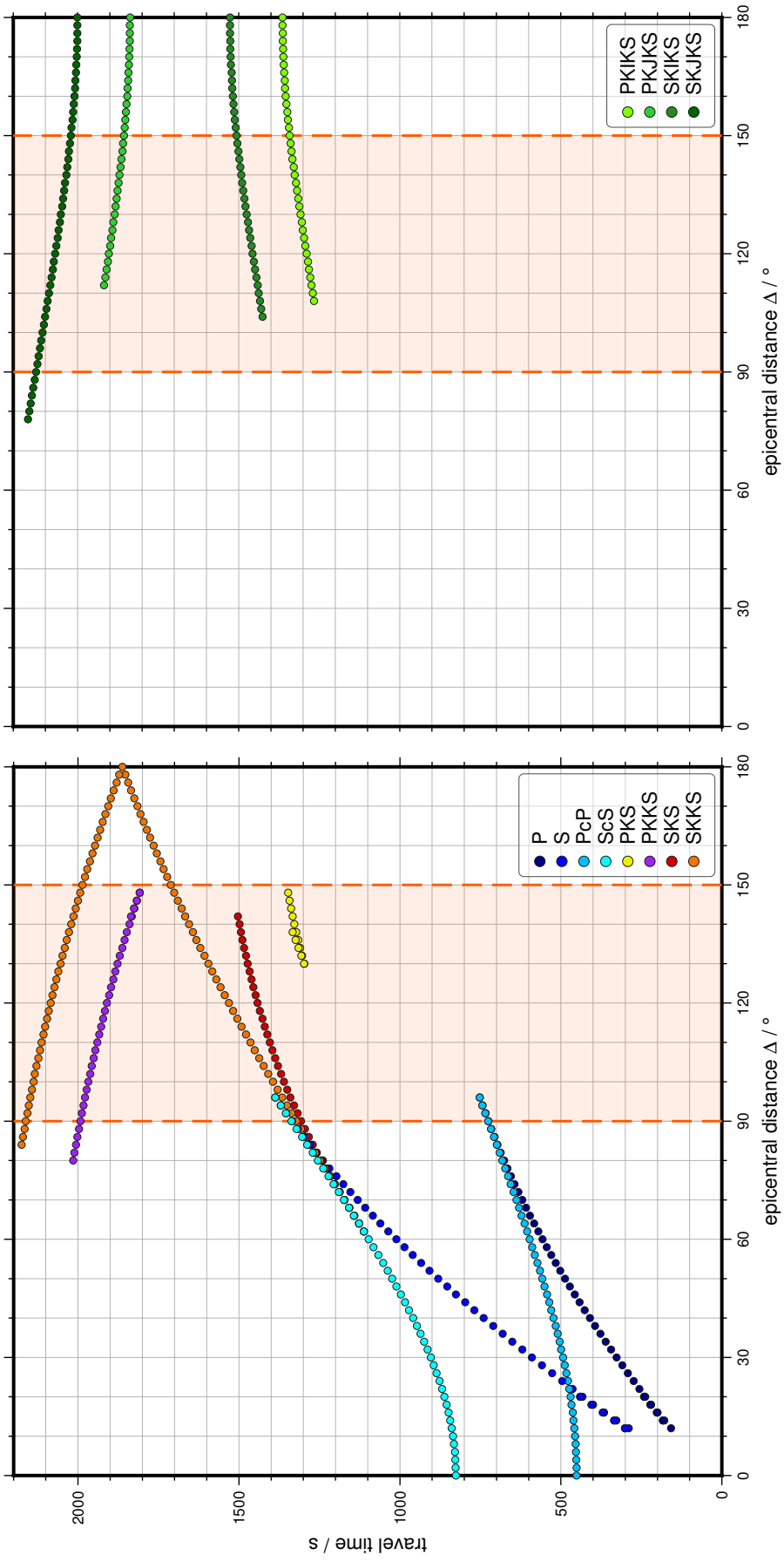

Figure 4.2: Travel time curves of several seismic phases within the epicentral distance range 0°-180° for an earthquake in 500 km depth calculated after the *iasp91* Earth model (*Kennett*, 1991) using *ObsPy* (*Beyreuther et al.*, 2010) based on the original *Java TauP* Toolkit (*Crotwell et al.*, 1999). The travel time curves are split over two plots to avoid over plotting, with the phases traveling through the inner core plotted in green hues in the right (bottom) plot. XKS phases are mainly observed within the epicentral distance range 90°-150° (highlighted in light orange). For epicentral distances 80°-96°, the travel times of SKS and SKKS are nearly identical, and interferences with the strong S and ScS phases occur. There can be also an interference with phases traveling through the inner core (the letter "I" refers to P and "J" to S waves). For the SKKS phase, there are two travel ways indicating the two different ("direct" and "indirect") travel paths. The PKS phase occurs only in a small epicentral distance range of 130°-150°. The PKKS phase has only an "indirect" branch. For the travel paths, see Fig. 4.1, Fig. C.1, and Fig. C.2.

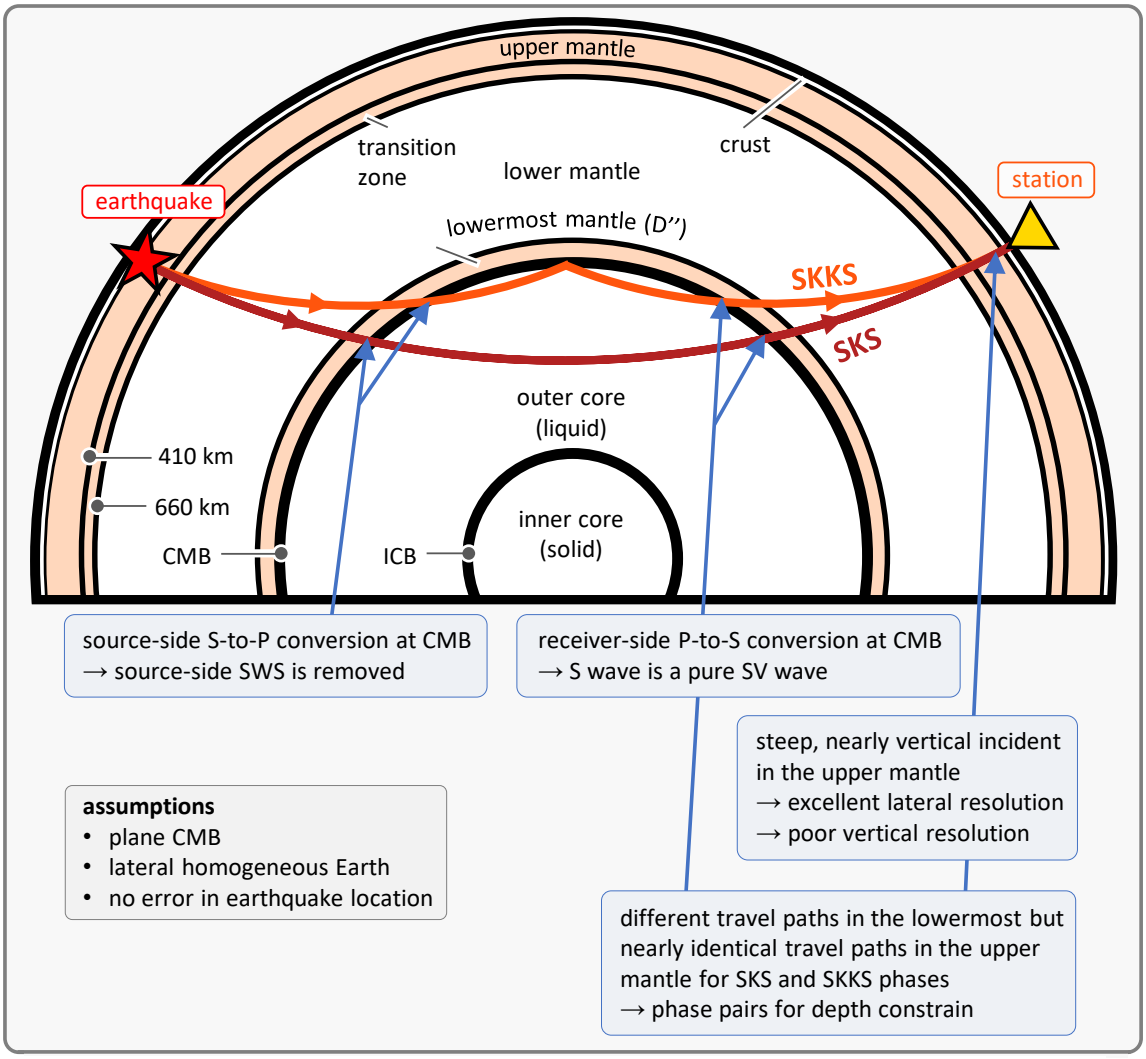

Figure 4.3: Advantages of *X*KS phases. Travel paths of SKS (red) and SKKS (orange) phases from the hypocenter (red star) in 500 km depth to the recording station (yellow inverse triangle) at the surface in 110° distance. The blue arrows point to different aspects along the travel paths of these core-refracted phases. The blue outlined boxes explain the related advantages used during the SWS analysis (Fig. B.2). The gray box lists assumptions. Anisotropic regions that are sampled by these phases are highlighted in light orange. For details on phase pairs, see Sec. 5.1 and Fig. 5.1. *Abbreviations*: CMB = core mantle boundary, ICB = inner core boundary, SWS = shear wave splitting, SV wave = vertically polarized shear wave.

4.2 Quantification of shear wave splitting

Shear wave splitting can be quantified based on determining the splitting parameters (Sec. 4.2.1) as well as calculating the splitting intensity (Sec. 4.2.2). As the typically measured delay times are significantly smaller than the dominant period of the used earthquake waves, no complete separation of the two waveforms of the qS waves can be reached within the seismogram in the time domain, and specific methods are needed to quantify the SWS. For the methods described in the following sections, the theoretical background is outlined with a focus on the application to real (noise-containing) data. Two observation types are differed: (i) no SWS is observed, referred to as *null* measurement, *null* or *null-split* and (ii) SWS is observed, referred to as *non-null* measurement or *split*.

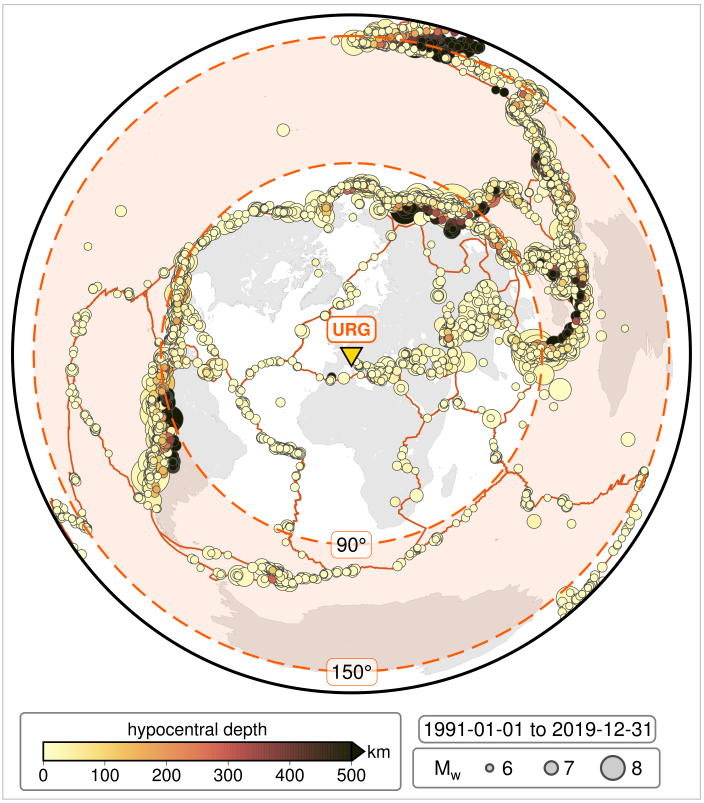

Figure 4.4: Global seismicity between 1991-01-01 and 2019-12-31 with moment magnitude $M_w \geq 6$. Each circle represents the epicenter of one earthquake, with color-coding for the hypocentral depth and size-coding for the moment magnitude. The epicentral-distance plot is centered around the URG area in Central Europe. The epicentral distance range 90°-150°, in which *XKS* phases can occur or can be observed at seismological recording stations in the URG area (Figs 2.1, 6.1, Sec. 2.3, Tab. 8.1), is highlighted in light orange. For the distribution of the hypocentral depth, see Fig. 4.8.

4.2.1 Determination of the splitting parameters

In the following, two different concepts to determine the splitting parameters are explained. Both the method after *Bowman and Ando* (1987; Sec. 4.2.1.1) as well as the method after *Silver and Chan* (1991; Sec. 4.2.1.2) were proposed for single waveforms. All methods share the underlying approach of removing or reverting the SWS effect from the waveforms (Fig. B.2). This inversion is implemented as a grid search. The specific features of the *XKS* phases (Fig. 4.3) allow for simplifications or special cases of these methods.

4.2.1.1 Method after Bowman and Ando

The *rotation-correlation* method proposed by *Bowman and Ando* (1987) is formulated in two variants, whereby variant 2 (referred to as RC method) is implemented in *SplitLab* and applied in this doctoral thesis.

***Rotation-correlation* method - variant 1**

The orientation of the first S wave motion is measured in the SN-WE hodogram and the seismograms of the horizontal (North and East) components are rotated by the estimated angle. The normalized cross-correlation coefficient (nCCC) is calculated between the two resulting seismograms of the fast and slow components within a time shift of ±2 s. The time shift, that leads to the maximum nCCC gives the time delay. The seismogram of the slow component is advanced by this time relative to the fast component. Finally, the back-rotation is performed, and the corrected particle motion can be drawn additionally into the SN-WE hodogram as a cross-check.

***Rotation-correlation* method - variant 2**

Instead of determining the orientation of the first S wave motion from the SN-WE hodogram, the seismograms of the horizontal components are iteratively rotated by 5° between 0° to 90°, whereby the nCCC is calculated after each rotation between the seismograms of the fast and slow components obtained in this way for a time shift of ±1 s. The minimum and maximum nCCCs are plotted as functions of the rotation angle. The rotation

angle that leads to the maximum of the maximum nCCCs gives the orientation of the first S wave movement. The determination of the time delay and the remaining steps follow variant 1.

4.2.1.2 Method after Silver and Chan

The second method applied in this doctoral thesis is the *eigenvalue* (EV) method. The concept as well as the mathematical derivations and notations follow *Silver and Chan* (1991). Using *X*KS phases allows for additional simplifications (Fig. 4.3), leading to the *energy-minimization* (SC) method. Both the general method and this special case are implemented in *SplitLab*.

***Eigenvalue* (EV) method**

SWS is understood as a geometric operation: the projection of the initial polarization direction in the isotropic medium $\widehat{\boldsymbol{p}}$ on the orthogonal polarization directions in the anisotropic medium $\widehat{\boldsymbol{f}}$ (fast) and $\widehat{\boldsymbol{s}}$ (slow) and the time shift of these two components by $+\delta t/2$ (earlier) or $-\delta t/2$ (later). The application of the splitting operator $\boldsymbol{\Gamma}$ (Eq. 4.1) with the splitting parameters β (angle between $\widehat{\boldsymbol{f}}$ and $\widehat{\boldsymbol{p}}$) and δt (accumulated time delay between fast and slow qS waves) to the initial S wave $\boldsymbol{u}(\omega)$ (Eq. 4.2) with the wavelet function w and the arrival time T_0 results in the split S wave $\boldsymbol{u}_\mathrm{s}(\omega)$ (Eq. 4.3). The dyadic products of the fast and slow polarization directions with themselves $\widehat{\boldsymbol{f}}\widehat{\boldsymbol{f}}$ or $\widehat{\boldsymbol{s}}\widehat{\boldsymbol{s}}$ represents the projection operators.

$$\boldsymbol{\Gamma} = \exp(\mathrm{i}\omega\delta t/2)\widehat{\boldsymbol{f}}\widehat{\boldsymbol{f}} + \exp(-\mathrm{i}\omega\delta t/2)\widehat{\boldsymbol{s}}\widehat{\boldsymbol{s}} \tag{4.1}$$

$$\boldsymbol{u}(\omega) = w(\omega)\exp(-\mathrm{i}\omega T_0)\widehat{\boldsymbol{p}} \tag{4.2}$$

$$\boldsymbol{u}_\mathrm{s}(\omega) = \boldsymbol{\Gamma}\boldsymbol{u}(\omega) = w(\omega)\exp(-\mathrm{i}\omega T_0)\boldsymbol{\Gamma}\cdot\widehat{\boldsymbol{p}} \tag{4.3}$$

The determination of the suitable splitting parameter pair $(\beta, \delta t)$ is based on reverting the geometric operation described above. This requires finding the inverse of the splitting operator $\boldsymbol{\Gamma}^{-1}$ (Eq. 4.4) so that the corrected S wave $\tilde{\boldsymbol{u}}_\mathrm{s}(\omega)$ is identical to the initial S wave.

$$\tilde{\boldsymbol{u}}_\mathrm{s}(\omega) = \boldsymbol{\Gamma}^{-1}\boldsymbol{u}_\mathrm{s}(\omega) = \boldsymbol{\Gamma}^{-1}\boldsymbol{\Gamma}\boldsymbol{u}(\omega) = \boldsymbol{u}(\omega) \tag{4.4}$$

To archive this, the 2-D covariance matrix is calculated in the time domain for two orthogonal components of the particle motion (which are assumed to lie in the known polarization plane of the initial S wave) with angles β or $\beta + \beta/2$ to $\widehat{\boldsymbol{p}}$ and a time difference δt between them. The eigenvalues λ_1 and λ_2 of the covariance matrix can be interpreted as a measure of linearity. In contrast to an anisotropic medium, in an isotropic medium only one of the two eigenvalues differs from zero. Thus, the inverse of the splitting operator (or the splitting parameter pair) has to be found, which leads to a singular covariance matrix for the corrected S wave. In this context, the four operations are equivalent: maximization of λ_1 or λ_1/λ_2 or minimization of λ_2 or $\lambda_1 \cdot \lambda_2$.

Introducing a splitting operator for each layer, Eq. 4.1 can be extended from one layer to two (multiple) layers with HTI, with the lower (first) layer (index 1: $(\beta_1, \delta t_1), \boldsymbol{\Gamma}_1$) and the upper (second) layer (index 2: $(\beta_2, \delta t_2), \boldsymbol{\Gamma}_2$). As there is no commutativity, the sequence of the layer can be determined (Figs 5.3, 5.8; *Silver and Savage*, 1994).

$$\boldsymbol{u}_\mathrm{s}(\omega) = \boldsymbol{\Gamma}_2\boldsymbol{\Gamma}_1\boldsymbol{u}(\omega) = w(\omega)\exp(-\mathrm{i}\omega T_0)\boldsymbol{\Gamma}_2\boldsymbol{\Gamma}_1\cdot\widehat{\boldsymbol{p}} \tag{4.5}$$

***Energy-minimization* (SC) method**

An important special case of the EV method described above can be formulated if the initial polarization direction, i.e., the polarization direction of the initial S wave, in the isotropic medium is known. This is the case for *X*KS phases (Fig. 4.3), as on the receiver side the S wave (after the P-to-S conversion at the CMB) is a pure SV wave. In

addition to the four operations mentioned above, the energy[7] on the corrected transverse (T) component $E_{\tilde{u}_{s,T}}$ can be minimized (Eq. 4.6). This operation is visually equivalent to linearizing the elliptical particle motion in the NS-EW or Q-T hodogram in the case of anisotropy.

$$E_{\tilde{u}_{s,T}} = \int_{-\infty}^{+\infty} \tilde{u}_{s,T}{}^2(t)\ \mathrm{d}t \tag{4.6}$$

In the time domain, the signals on the radial (R) and transverse (T) components of the split S wave $u_{s,R}(t)$ or $u_{s,T}(t)$ are given in Eqs 4.7 and 4.8, respectively.

$$u_{s,R}(t) = w(t + \delta t/2)(\cos(\beta))^2 - w(t - \delta t/2)(\sin(\beta))^2 \tag{4.7}$$

$$u_{s,T}(t) = -\frac{1}{2}\left(w(t + \delta t/2) - w(t - \delta t/2)\right)\sin(2\beta) \tag{4.8}$$

Following Eq. 4.8, in an isotropic medium the signal amplitude on the T component is zero, as expected; but for real data it is only close to zero due to the noise contained in the data. In an anisotropic medium with a much shorter delay time compared to the dominant period (*long-period approximation*) the waveform on the R component is only slightly broadened and distorted (Eq. 4.9) and the signal amplitude on the T component is directly proportional to the first temporal derivative of the signal amplitude on the R component (Eq. 4.10).

$$u_{s,R}(t) = w(t) \tag{4.9}$$

$$u_{s,T}(t) = -\frac{1}{2}\delta t\,\sin(2\beta)\dot{w}(t) = -\frac{1}{2}\delta t\,\sin(2\beta)\dot{u}_{s,R}(t) \tag{4.10}$$

4.2.2 Calculation of the splitting intensity

Besides the determination of the splitting parameters, the so-called *splitting intensity* (*Chevrot*, 2000)[8] can be calculated to quantify SWS. Here, the variation of the signal (or energy) on the T component with the initial polarization direction (for *X*KS phases the BAZ) is considered. Again, it is used that, in case of a significantly shorter delay time compared to the dominant period, the signal amplitude on the T component is directly proportional to the first temporal derivative of the signal amplitude on the R component, and the waveform on the R component is only slightly broadened and distorted (*Silver and Chan*, 1991). The splitting intensity SI is defined as the signal amplitude on the T component relative to the first temporal derivative of the signal amplitude on the R component. For real (i.e., noise-containing) data, the splitting intensity[9] should be defined as the projection of the signal amplitude on the T component $u_{s,T}(t)$ on the first temporal derivative of the signal amplitude on the R component $\dot{u}_{s,R}(t)$ (Eq. 4.11), and normalized by the square norm of $\dot{u}_{s,R}(t)$ (Eq. 4.12)

$$\mathrm{SI} = -2\frac{u_{s,T}(t)\cdot\dot{u}_{s,R}(t)}{\left\|\dot{u}_{s,R}(t)\right\|^2} \tag{4.11}$$

$$\left\|\dot{u}_{s,R}(t)\right\|^2 = \dot{u}_{s,R}(t)^{\mathrm{T}}\cdot\dot{u}_{s,R}(t) \tag{4.12}$$

In case of no SWS the splitting intensity is expected to be zero. Since for real data, there is still energy, i.e., a non-zero signal remains on the T-component (due to noise) *Deng et al.* (2017) propose an absolute upper limit

[7] Here, the term energy refers to the time-integrated squared amplitude, see the *Parseval's* formula.

[8] In this doctoral thesis and all related publications, the splitting intensity definition after *Chevrot* (2000) is used. There is a second definition by *Lin et al.* (2014) that differs by a factor of 0.5. The limits proposed by *Deng et al.* (2017) are based on the definition by *Chevrot* (2000).

[9] The splitting intensity has the unit seconds. However, due to no meaningful physical interpretation of the unit in this context, the SI is commonly reported unitless.

of $|\mathrm{SI}_{\mathrm{null}}| < 0.2$ for *nulls*. For one horizontal layer with HTI, Eq. 4.10 can be inserted in Eq. 4.11, where β is the angle between the fast polarization direction and the initial polarization direction (for *X*KS phases the BAZ).

$$\mathrm{SI} = -2\frac{\left[-\frac{1}{2}\delta t \sin(2\beta)\dot{u}_{\mathrm{s,R}}(t)\right] \cdot \dot{u}_{\mathrm{s,R}}(t)}{\left\|\dot{u}_{\mathrm{s,R}}(t)\right\|^2} = \delta t \sin(2\beta) \tag{4.13}$$

The *splitting function* describes the dependence of the SI on the initial polarization direction (for *X*KS phases the BAZ). The *splitting vector* contains the splitting intensities determined at different initial polarization directions for a limited or discrete dataset.

4.3 Shear wave splitting analysis with *SplitLab* and *StackSplit*

In this doctoral thesis, the MATLAB program *SplitLab* (*Wüstefeld et al.*, 2008) version 1.2.1 (*Porritt*, 2014) together with the plug-in *StackSplit* (*Grund*, 2017) versions v2.0 to dev (*Grund and Fröhlich*, 2021) are used for the SWS analysis. The determination of the splitting parameters (Fig. 4.5) is grouped into steps: a single-event analysis done with *SplitLab* (Sec. 4.3.1), followed by a (an optional) multi-event analysis using *StackSplit* (Sec. 4.3.2).

A *SplitLab* version updated for MATLAB R2020a to R2024b and new *StackSplit* versions[10] are available at:

> ***Fröhlich Y.*** *(2025).* **SplitLab (updated for higher MATLAB versions)**. *in preparation.* Uploaded to GitHub at `https://github.com/yvonnefroehlich/splitlab-stacksplit`, see folder `01_splitlab`.
>
> ***Fröhlich Y.*** *(2025).* **StackSplit (dev)**. *in preparation.* Development on GitHub at `https://github.com/yvonnefroehlich/splitlab-stacksplit`, see folder `02_stacksplit`.
>
> *Grund M. &* ***Fröhlich Y.*** *(2021).* **StackSplit (v3.0)**. *Zenodo.* `https://doi.org/10.5281/zenodo.5802051`.

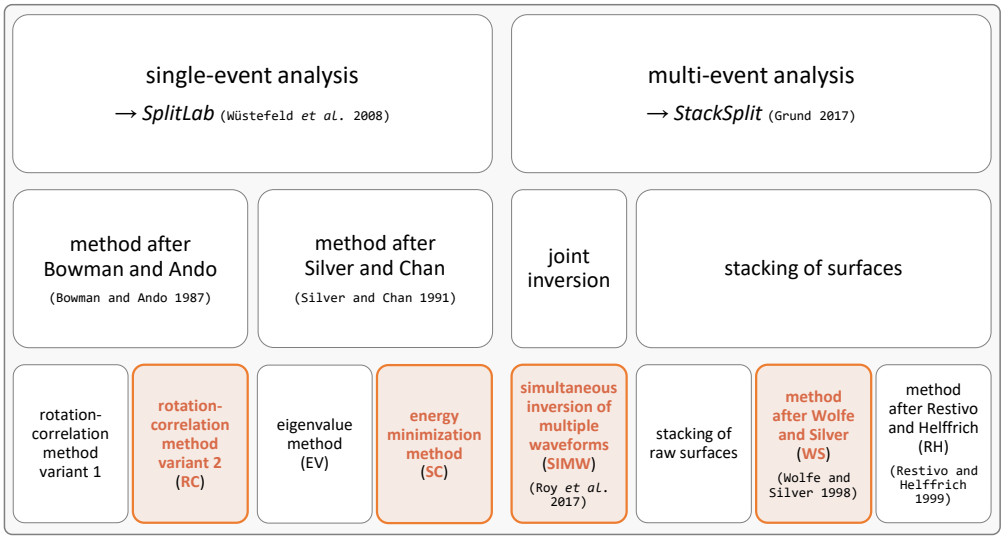

Figure 4.5: Overview of methods to quantify shear wave splitting (SWS) via determining the splitting parameters. The methods are grouped into two steps: a single-event analysis (left) followed by (an optional) a multi-event analysis (right). The methods, which are applied in this doctoral thesis are highlighted in orange: the *rotation-correlation* (RC, Sec. 4.2.1.1; *Bowman and Ando*, 1987) and *energy minimization* (SC, Sec. 4.2.1.2; *Silver and Chan*, 1991) methods as well as the *simultaneous inversion of multiple waveforms* (SIMW, Sec. 4.3.2.1; *Roy et al.*, 2017) and the method after Wolfe and Silver (WS, Sec. 4.3.2.2; *Wolfe and Silver*, 1998). Modified after *Fröhlich* (2020, fig. 7).

[10] Changelog at `https://github.com/yvonnefroehlich/splitlab-stacksplit/blob/main/02_stacksplit/changelog.md`.

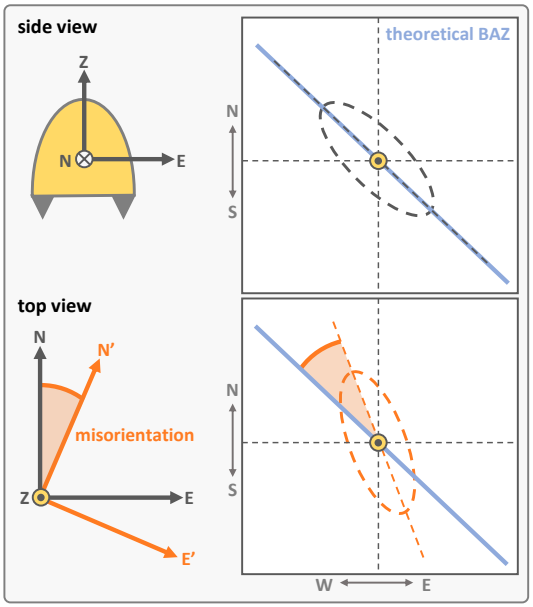

Figure 4.6: Sensor misorientation. Correct coordinate system Z, N, E (dark gray) and wrong coordinate system Z', N', E' (orange). Seismometer in side view (left top) and coordinate systems in top view (bottom right). Schematic horizontal (WE-SN) particle motion of a *X*KS phase in the case of a *split* (dashed ellipse): correct (top right) and wrong (bottom right) sensor installation, whereby the theoretical backazimuth (BAZ) is indicated by the blue line and the initial polarization direction by the dashed gray or orange line. For the correct installation, the initial polarization direction aligns with the theoretical BAZ. Besides a sensor misorientation, the selection of another (no-*X*KS) phase as well as 3-D Earth effects, e.g., wave scattering, can lead to a deviation of the initial polarization direction from the theoretical BAZ.

4.3.1 Single-event analysis with *SplitLab*

All SWSMs in the framework of this doctoral thesis are carried out manually. For details on the pre-processing as well as the actual SWS analysis, see Sec. 8.3.2.1. This section focuses on challenges and pitfalls. Examples for a *null* and a *non-null* measurement are shown in Fig. B.3.
Walsh et al. (2013) published a correction for the error calculation, which is considered in *SplitLab* via the implementation in *StackSplit*. A crucial aspect is the correct *relative* temporal alignment of seismic traces. Unfortunately, *SplitLab* contains an error source leading to a wrong alignment of the seismic traces and, by this, to wrong SWSMs (*Fröhlich et al.*, 2022a). This issue is discussed in detail in Ch. 6.

Applying the RC and SC methods simultaneously and independently (Fig. B.2) allows to define analytical criteria regarding observation types and quality categories based on the mathematical behavior of these two methods (Tab. 8.2, Fig. 8.4), in addition to the subjective evaluation of waveform and particle motion by the analyst. Different time windows (lengths, end and start times) are selected as well as different corner frequencies (band pass filter) are applied, to test the stability of the measurement.

For *X*KS phases, the initial polarization direction is known and equivalent to the BAZ (Fig. 4.3). Thus, a deviation of the initial polarization direction from the BAZ can be used as a cross-check regarding the selection of another or wrong phase, an unknown sensor misorientation (Fig. 4.6), or 3-D Earth effects or scattering.

The interference of *XKS* phases with other phases arriving (nearly) at the same time can lead to corrupted waveforms and wrong analysis results. S and ScS phases (in general no pure SV waves) are especially problematic within the epicentral distance range 80°-94° (Fig. 4.2).
So-called *depth phases* (indicated by a leading lower-case letter "p" or "s") are additional downside-reflections at the surface on the source side before traveling down into the Earth (Fig. 4.7a). Depending on the hypocentral depth, the additional travel path leads to a later arrival time compared to the main phase (Fig. 4.7b). For shallow earthquakes, depth phases arrive almost at the same time at the receiver as the main phase, which can lead to interference and a corrupted waveform. The distribution of the hypocentral depth shows that the majority of earthquakes occur in depths < 150 km (Fig. 4.8). Setting a lower limit of 20 km or 50 km for the hypocentral depth, as partly done in other studies, leads to the rejection of a great number of earthquakes from the SWS analysis. Thus, here no limit was set, and those seismograms were carefully analyzed.

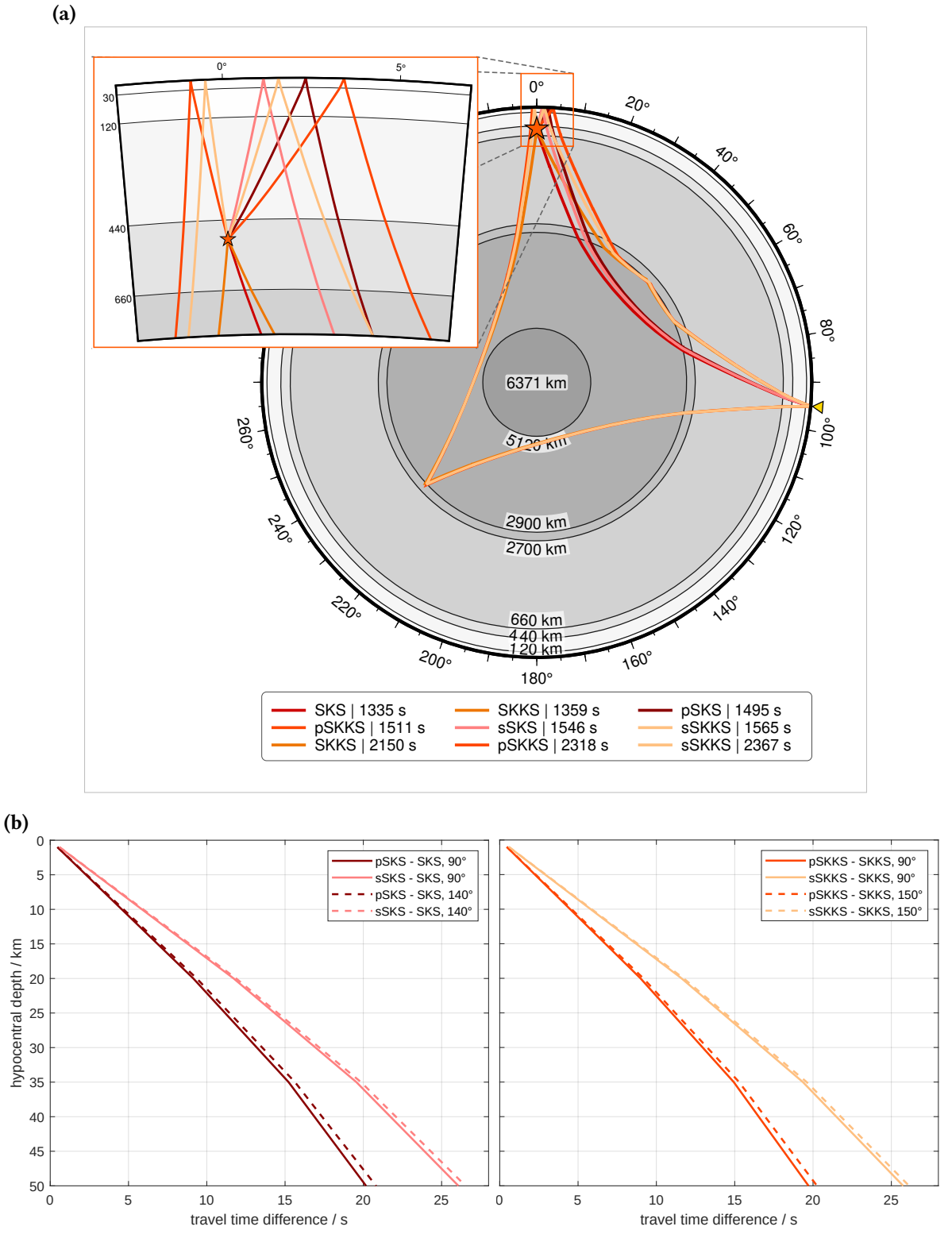

Figure 4.7: Depth phases (indicated by a leading lower-case letter "p" or "s") related to SKS and SKKS phases. **(a)** Travel paths for waves from an earthquake (red star) in 500 km depth and an epicentral distance of 95° to the recording station (inverse yellow triangle). Depth phases are due to an additional downside-reflection at the surface before traveling down into the Earth. **(b)** Travel time differences for SKS (left) at 90° (solid line) and 140° (dashed) epicentral distance as well as SKKS (right) at 90° (solid) and 150° (dashed) epicentral distance. For shallow earthquakes, main and depth phases arrive almost at the same time at the station, which can lead to interference and corrupted phases.

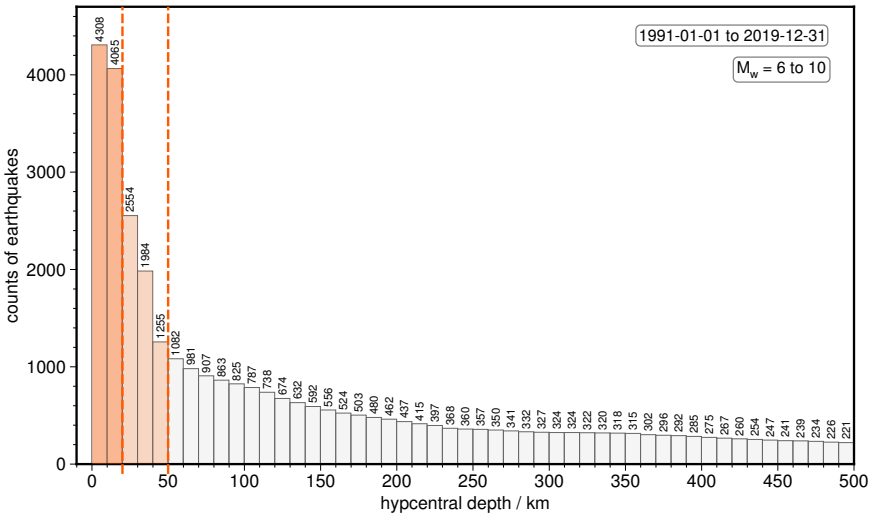

Figure 4.8: Global seismicity between 1991-01-01 and 2019-12-31 with moment magnitude $M_W \geq 6$ (see Fig. 4.4). The distribution of the hypocentral depth is shown as an inverse cumulative histogram with bins of 10 km. The dashed orange lines mark the hypocentral depths of 20 km and 50 km. Restricting the analysis to earthquakes deeper than 20 km or even 50 km leads to a significant reduction of the earthquake catalog.

Besides the signal of interest (here the *X*KS phases), real data contain noise that refers to all natural (e.g., ocean microseism[11]) and anthropogenic (e.g., cities, wind turbines, etc.) signals of no interest. The signal-to-noise ratio (SNR) calculated by *SplitLab* follows *Restivo and Helffrich* (1999) and is defined as the ratio between the maximum of the R component $\tilde{u}_{s,R}(t)$ and the 2-σ-envelope of the T component $2\sigma_{s,T}$ of the corrected S wave (Eq. 4.14).

$$\mathrm{SNR}_{method} = \frac{\max\left(\left|\tilde{u}_{s,R_{method}}(t)\right|\right)}{2\sigma_{s,T_{method}}} \quad \text{with} \quad method = \mathrm{SC, RC} \tag{4.14}$$

Noise contained in the data can affect a SWSM leading to wrong splitting parameters or a wrong observation type. Thus, a $\mathrm{SNR_{SC}} \geq 3$ is required (*Vecsey et al.*, 2008) and too noisy data is excluded from the analysis. Especially a *null* has to be decided actively and independently from a *split*. In case of a low SNR not observed SWS does not automatically imply a *null* measurement, as a weak splitting signal can be hidden in the noise.

4.3.2 Multi-event analysis with *StackSplit*

A general issue in seismology is the BAZ coverage due to the source or earthquake distribution (Figs 8.1, B.1) as well as (too) noisy data. Based on the results from the single-event analysis, a multi-event analysis can address both under- and over-representations. The *simultaneous inversion of multiple waveforms* (*Roy et al.*, 2017; Sec. 4.3.2.1) can help to gain more BAZ directions. Multiple observations from one BAZ direction allow for a comparison that can increase the confidence of the splitting parameter pair for this BAZ direction. However, for a later modeling, this over-representation of specific BAZ directions has to be equalized, which can be achieved by the stacking of surfaces (Sec. 4.3.2.2).

4.3.2.1 *Simultaneous inversion of multiple waveforms*

The *simultaneous inversion of multiple waveforms* (SIMW; *Roy et al.*, 2017) is a joint inversion of waveforms related to the single-event measurements. For each of the considered single-event measurements, the waveforms of the desired phase are cut out on the Q and T components as time windows of similar length. For *X*KS phases, time windows of 10-20 s are required, corresponding to the dominant period of 8-10 s. The time windows are tapered with a cosine window to avoid jumps between waveforms and normalized relative to the Q component to

[11] The ocean microseism occurs at 0.05–0.2 Hz, whereby primary (0.05-0.1 Hz, 14 s) and secondary (0.1-0.2 Hz, 7 s) ocean microseism are distinguished based on the different sources (*Juretzek and Hadziioannou*, 2016).

compensate for different moment magnitudes. Optionally, a frequency (bandpass) filter can be applied. Then the individual waveforms are appended in the time domain to one single time series for the Q and T components. This procedure differs from the classic approach of stacking, in which the individual waveforms are first aligned in time and then cumulatively summed (delay and sum or slant stack). Finally, the created time series are inverted entirely (all concentrated waveforms simultaneously) applying both the RC and SC (or EV) methods (as in the single-event analysis). The determined splitting parameter pair represents the best joint solution for all considered waveforms.
Often a SWSM with a narrower 95 % confidence interval and a better quality can be obtained. For a BAZ direction in which only SWSMs with poor quality were observed in the single-event analysis, a SWSM with sufficient quality may be obtained using the SIMW and by this an additional BAZ direction is added to the dataset. This method is especially helpful for studies using short-term recordings (2-3 yr). Examples for both a *null* and *split*, are shown in Fig. **B.5**. .

4.3.2.2 Stacking of surfaces

Besides the SIMW, the three common methods for the stacking of surfaces are implemented in *StackSplit*: (i) stacking of raw surfaces (*Wüstefeld*, 2007), (ii) method after Wolfe and Silver (WS method; *Wolfe and Silver*, 1998), and (iii) method after Restivo and Helffrich (RH method; *Restivo and Helffrich*, 1999).
The input is the surfaces of the evaluation parameter resulting from the single-event measurements that are interpreted as error surfaces. Depending on the method applied in the single-event analysis, this is the nCCC (maximum; RC method) or an eigenvalue (minimum or maximum; EV method) or the energy on the T component (minimum; SC method). The methods differ in the weighting and normalization of these surfaces. In the case of stacking raw surfaces, the considered surfaces are stacked without weighting and normalization. Using the WS method each surface is normalized either to its absolute minimum (for SC λ_2 or $\lambda_1 \cdot \lambda_2$ or $E_{\tilde{u}_{s,T}}$) or maximum (for RC nCCC, for SC λ_1 or λ_1/λ_2) before stacking them. The RH method applies first a weighting depending on the SNR of the considered surfaces and then a normalization to reduce the influence of overrepresented BAZ directions before stacking them. For more detail on the single methods, please refer to the mentioned scientific publications. In this doctoral thesis, the WS method is applied; an example is shown in Fig. **B.4**.

5 Modeling of Shear Wave Splitting

After detecting potential anisotropy by measuring SWS, the SWSMs with the determined splitting parameters need to be related to anisotropy scenarios in the subsurface that can explain the observations. Both the location, especially the depth of the anisotropy (Sec. 5.1) as well as the structure of the anisotropy (Sec. 5.2) have to be considered in the modeling. The forward calculation of synthetic splitting parameters is done using the *MATLAB Seismic Anisotropy Toolbox* (MSAT; *Walker and Wookey*, 2012).

The codes to create the visualization and perform the modeling routines for SWS observations are available at[12]:

> ***Fröhlich Y.** (2025).* **Visualization and Modeling of Shear Wave Splitting (v2.0)**. *in preparation. Zenodo.* `https://doi.org/10.5281/zenodo.13799086`. Development on GitHub at `https://github.com/yvonnefroehlich/sws-visualization-and-modeling`.
>
> ***Fröhlich Y.** & Grund M. (2022).* **Visualization and Modeling of Shear Wave Splitting (v1.0)**. *Zenodo.* `https://doi.org/10.5281/zenodo.7213157`.

5.1 Depth constraints

Due to the integral effect along the travel or ray path, the anisotropy related to a single SWSM cannot be located on the ray path. For *X*KS phases, only the receiver-side part between the CMB and the surface has to be considered (Fig. 4.3). The nearly vertical incidence (6°-12°) of *X*KS phases at the recording station leads to a vertical integral effect in the upper mantle, resulting in a good lateral but a poor vertical resolution in the upper mantle. The lower mantle is proposed to be weakly anisotropic or isotropic, but for the LMM various studies confirm anisotropy (Sec. 3.4.3). Concepts to constrain the depth of the anisotropy within in the Earth are the length of the delay time, phase pairs, and piercing points (see also Sec. 8.6.2).

A delay time δt larger than 0.3 s is a clear indication for a mantle contribution to the anisotropy (*Silver*, 1996; *Savage*, 1999), as the anisotropy cannot be located exclusively in the crust (Sec. 3.4.1).
Phase pairs, i.e., two specific phases, analyzed in the (identically filtered) seismogram of one single earthquake can provide crucial information on the location of the anisotropy. SKS-SKKS pairs (Fig. 4.3) can help to reveal a potential lowermost mantle contribution to the anisotropy by comparing the observation types, the splitting intensities, or the splitting parameters (Fig. 5.1). *Discrepant* pairs can be defined based on different observation types (i.e., *null* vs. *split*) or an absolute difference between the splitting intensities (of 0.4 following *Deng et al.*, 2017[8]). For the modeling, the SWSMs dataset should be (is) separated into two subsets, one for the discrepant pairs and one with the remaining SWSMs.
For a localization within the upper mantle, calculating the piercing points of the rays related to the SWSMs iteratively with depth can help to find and outline subregions within the study area based on overlapping (similar) splitting patterns observed at neighboring recording stations (Figs 8.8 and 8.9).

[12] Changelog at `https://github.com/yvonnefroehlich/sws-visualization-and-modeling/blob/add-changelog-v2.0/changelog.md` or `https://github.com/yvonnefroehlich/sws-visualization-and-modeling/blob/main/changelog.md`.

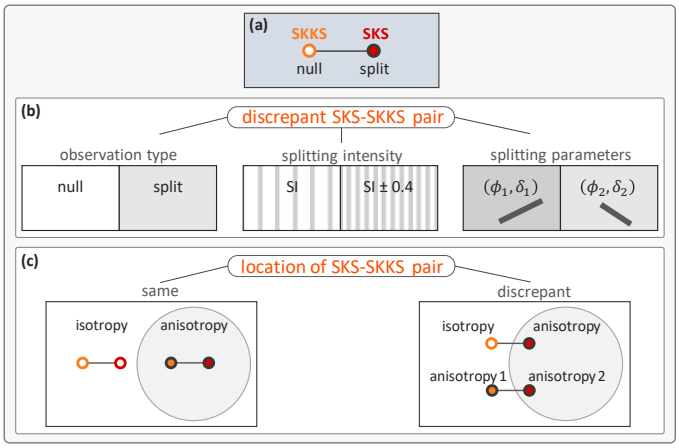

Figure 5.1: (a) Plotting convention for SKS-SKKS pairs; travel paths are shown in Fig. 4.3. **(b)** A *discrepant* pair can be defined by different observation types (*null* vs. *split*), an absolute difference (of 0.4, following *Deng et al.*, 2017) between the splitting intensities, or (if both phases split) a difference between the splitting parameters (the fast polarization direction is a cyclic quantity). Here, the first two criteria are used. For a *same* pair, the splitting parameters are compared and expected to be similar (cross-check). **(c)** Location of the pair. Even discrepant pairs are a clear indication for a LMM contribution to the anisotropy, same pairs do not exclude this, as both phases may travel through the same anisotropic structure in the LMM.

5.2 Structural anisotropy models

Seismic anisotropy can vary vertically, which can be represented by layers above each other (Fig. 5.3a). The orientation of the symmetry axis can be horizontal but also tilted (*Grund and Ritter*, 2020, fig. S4). One layer with transverse isotropy with a horizontal symmetry axis is called *simple anisotropy*. In contrast, every other anisotropy scenario is considered as *complex anisotropy*.
The measurement of SWS is done under the assumption of simple anisotropy (*Savage*, 1999). As this assumption is often not valid, the splitting parameters observed at the surface do not directly represent the anisotropy scenario in the subsurface and are *apparent* (or *effective*) splitting parameters. However, they still contain useful information because specific anisotropy scenarios are characterized by specific backazimuthal variations of the splitting parameters. These variations can be used to detect complex anisotropy and to distinguish different anisotropy scenarios. To be able to observe these backazimuthal variations, earthquakes from different BAZ directions and by this long-term recordings have to be analyzed.

In this doctoral thesis, besides one horizontal layer (H1), the model types two layers with horizontal symmetry axes (H2) and one layer with a tilted symmetry axis (T1) are considered (Fig. B.12). Within the layers, transverse isotropy is assumed. An overview of the characteristic backazimuthal variations of the splitting parameters is shown in Fig. 5.2 (*Fröhlich and Ritter*, 2024).
For H1 , the splitting parameters are constant with the BAZ, except the fast or slow polarization direction of the medium is parallel or orthogonal to the BAZ (*Savage*, 1999). For these four so-called *null directions*, no SWS occurs, and *nulls* are observed. This BAZ direction indirectly gives the fast or slow polarization direction of the layer and can be used as a cross-check for the fast polarization direction observed for the *splits* in the other BAZ directions.
For H2 , the equations after *Silver and Savage* (1994) are used (Sec. 4.2.1.2). The backazimuthal variations of the apparent splitting parameters are quite characteristic showing a $\pi/2$ periodicity. So-called *apparent null directions* occur together with characteristic $\pi/2$-jumps in the apparent fast polarization direction, and the apparent delay time scatters over the entire range up to the maximum of the grid search. In case the initial polarization direction is parallel or orthogonal to the fast polarization direction in the lower layer, SWS can only occur in the upper layer, and the splitting parameters represent the anisotropy in the upper layer. This is called *transparent windows* (*Vinnik et al.*, 1994) and can be used as a cross-check for the fast polarization direction.
For T1 , the Christoffel equation (Eq. 3.18; *Christoffel*, 1877) is solved under the assumption of an a-axis parallel to the down-dip direction. The apparent splitting parameters show smooth 2π variations with the BAZ, but note the v-shape formed by the orientation of the bars (apparent fast polarization direction) in the stereoplot representation. The four *nulls* are not equally spaced along the BAZ. They occur parallel to the down-dip direction and for the BAZ directions being orthogonal to the apparent fast polarization direction.

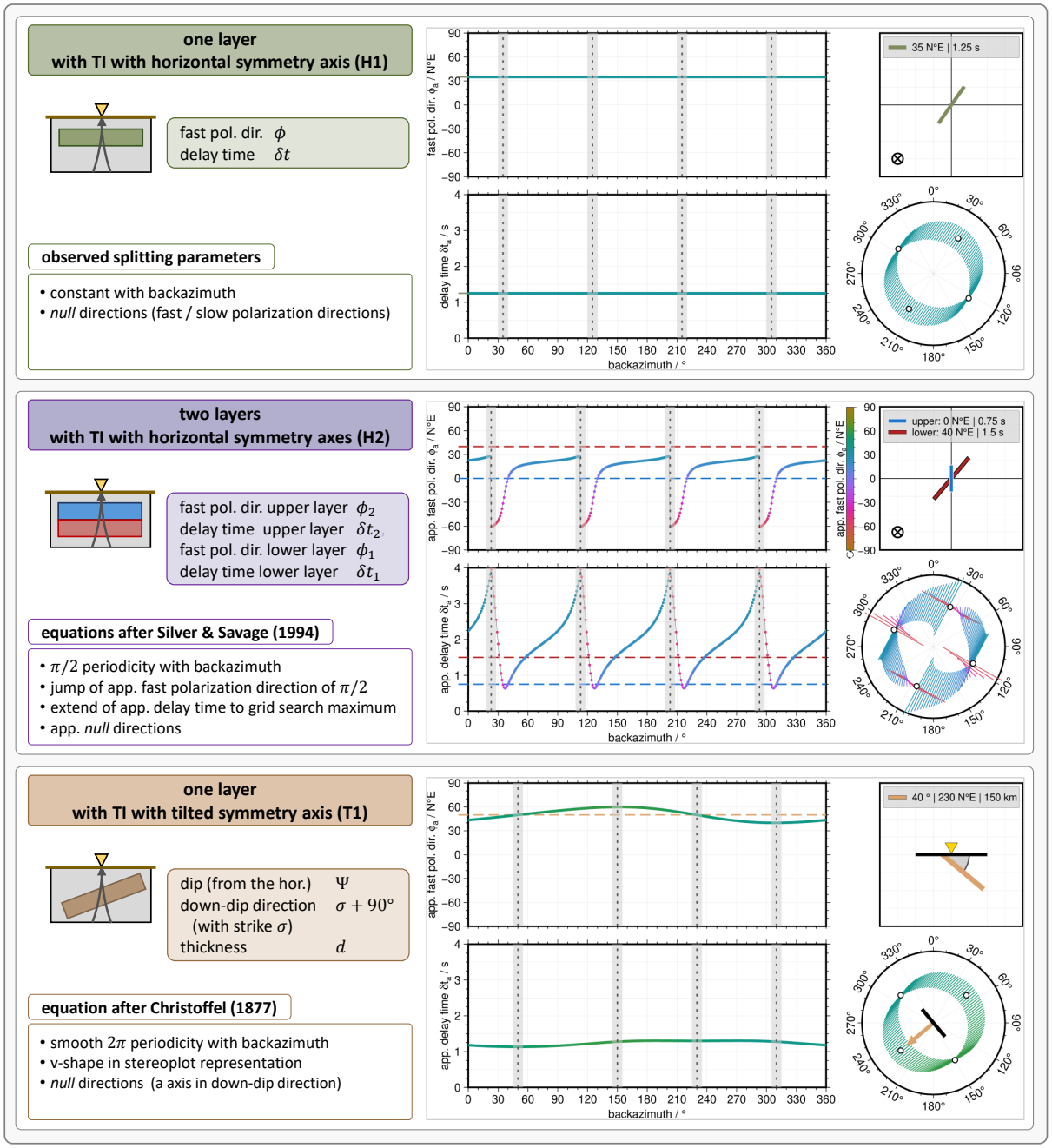

Figure 5.2: Model types and model parameters with the related backazimuthal variations of the splitting parameters (*Fröhlich and Ritter*, 2024) forward calculated via the *MATLAB Seismic Anisotropy Toolbox* (MSAT, *Walker and Wookey*, 2012) for a shear wave with a dominant period of 8 s (typical for *X*KS phases). Three model types with transverse isotropy (TI) are considered: **(top part)** one layer with horizontal symmetry axis (H1, green), **(middle part)** two layers with horizontal symmetry axes (H2, purple; *Silver and Savage*, 1994), and **(bottom part)** one layer with tilted symmetry axis (T1, brown; *Christoffel*, 1877).
The model types vary regarding the number of layers and the orientation of the layer or symmetry axis (sketches with recording stations as yellow inverse triangles and inclining rays in dark gray), as well as used model parameters (light-colored boxes). For H1 (*simple anisotropy*), the splitting parameters measured at the surface are identical to the model parameters and directly represent the anisotropy in the subsurface. For any other anisotropy scenario (*complex anisotropy*), the splitting parameters measured at the surface are *apparent* splitting parameters, which do not equal the model parameters in the subsurface, and a modeling procedure is needed to derive the anisotropy scenario. In the color-outlined white boxes the equations used in the forward calculation and characteristics of the backazimuthal variations are given (bottom left). Cartesian plots of the app. fast polarization direction (top middle) and the app. delay time (bottom middle) as a function of the BAZ, whereby (app.) *nulls* are expected within the BAZ directions of the gray areas, and some of the model parameters are indicated by the dashed lines. For the different behaviors of the RC and SC methods in case of a *null* measurement, see Fig. 8.4. Stereoplot (bottom right) with bars for *splits* and black-outlined white circles for (app.) *nulls*, whereby the azimuth (clockwise from north) gives the BAZ and the radial axis is the incidence angle (from the vertical) of the ray (here 10°, typical for *X*KS phases) at the station (center of the plot). The values of the model parameters are given in the gray boxes and visualized in the sketches (top right).

Furthermore, the anisotropy can vary laterally, which can be represented by blocks next to each other (Fig. 5.3b. Modeling lateral variation of the anisotropy at a single recording station (Ch. 7) can be achieved using only the SWSMs (or *splits*) from a (station-)specific BAZ range. To be able to outline subregions with different anisotropy regimes within the study area, several neighboring stations are needed (Ch. 8).

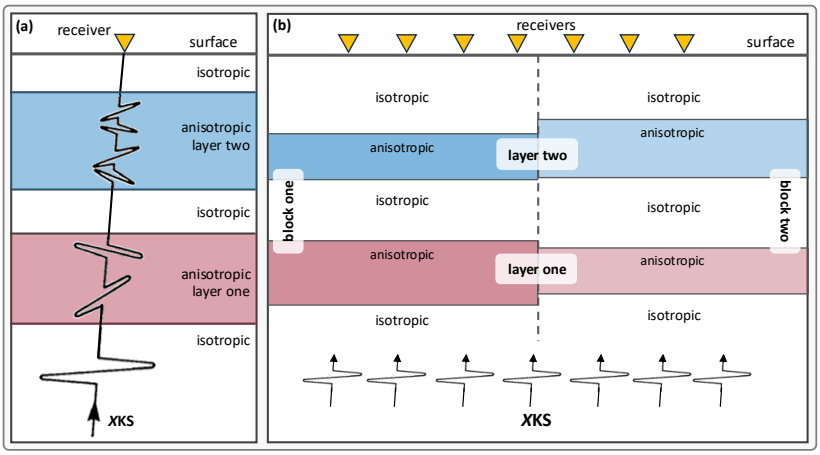

Figure 5.3: Representation of vertical and lateral variations within the anisotropy. **(a)** Vertical variation as horizontal layers on top of each other with different anisotropies. In each layer occurs SWS; in the upper (blue) layer the two qS waves caused by the SWS in the lower (red) layer are each split again. **(b)** Additionally, lateral variation as different blocks next to each other. The recording stations (yellow inverse triangles) record waves (rays) that have seen different anisotropic structures. (a) is modified after *Savage* (1999, fig. 10a).

The forward calculation of the synthetic splitting parameters as function of the BAZ is done using the *MATLAB Seismic Anisotropy Toolbox* (MSAT, *Walker and Wookey*, 2012). The inversion to find the most suitable anisotropy model is performed as a grid search with the value ranges and steps of the model parameters given in Tab. B.1. The best-fit model is selected by the minimum root mean square error (RMSE) between the observed and the synthetic splitting parameters calculated via the Eqs 8.1 - 8.3. The joint inversion uses both the fast polarization directions and the delay times. Following *Long and van der Hilst* (2005), the SC method is more stable compared to the RC method. Thus, the splitting parameters determined with the SC method are used in the modeling. For *Nulls*, the SC method shows a specific (unexpected) behavior (Fig. 8.4). The values for the apparent delay time are not nearly zero, but show strong scattering over the entire value range up to the maximum (here 4 s). Furthermore, the values of the apparent fast polarization direction can differ by 90° from the value expected for H1. According to this, *nulls* can not be directly included in the modeling, and only the *splits* are used.

In Tab. 5.1 specific anisotropy scenarios are listed, whereby the backazimuthal variations of the splitting parameters are discussed in Figs 5.4 to 5.11. The focus is on whether scenarios can be distinguished theoretically or mathematically and how realistically this can be achieved based on observations from real data containing noise and observational (backazimuthal) gaps.

Table 5.1: Forward calculation: specific anisotropy scenarios for the three different model types H1, H2, and T1. The backazimuthal variations of the splitting parameters (related to *X*KS phases) are directly discussed in Figs 5.4 to 5.11. For H2, complete variations of both the fast polarization directions (Fig. C.5, Fig. C.6) and the delay times (Fig. C.7, Fig. C.8) can be found in Sec. C.3. Additionally, animations will be provided, see Sec. D.5.

Model type	Anisotropy scenario	Figure(s)
H1	simple anisotropy	Fig. 5.4, Fig. 5.5
H1	thin layer or weak anisotropy	Fig. 5.5
H2	(nearly) identical fast polarization directions	Fig. 5.6
H2	(nearly) orthogonal fast polarization directions	Fig. 5.7
H2	flipped fast polarization directions	Fig. 5.8
T1	nearly horizontal layer	Fig. 5.10
T1	nearly vertical layer	Fig. 5.10
T1	opposite down-dip direction	Fig. 5.11

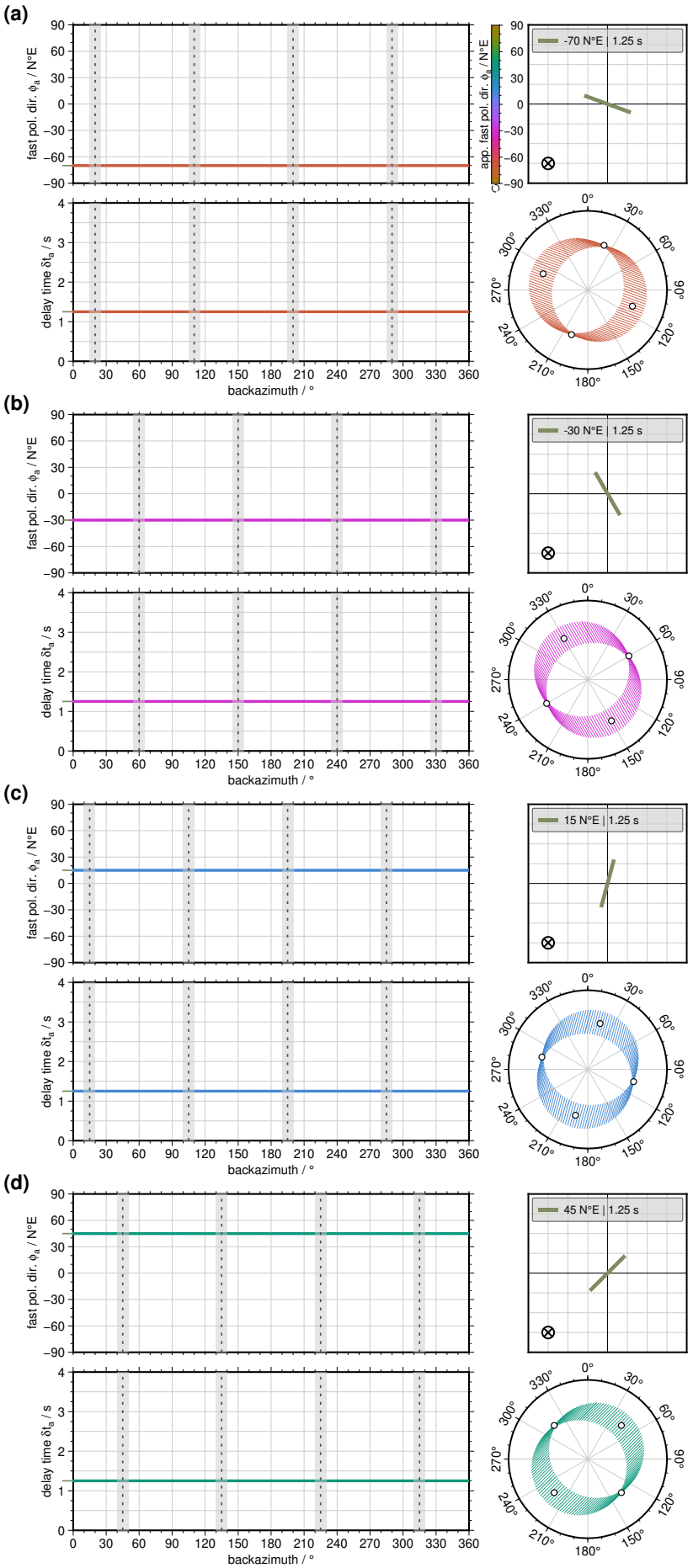

Figure 5.4: Forward calculation for model type H1: variation of the fast polarization direction.
Fixed delay time of 1.25 s. The fast polarization direction is **(a)** -70N°E, **(b)** -30N°E, **(c)** 15N°E, and **(d)** 45N°E. In case of simple anisotropy, the splitting parameters measured at the surface directly give the model parameters within the subsurface. The *nulls* occur within the BAZ directions for which the fast or slow directions of the medium are parallel or orthogonal to the polarization direction of the initial S wave, i.e. for *X*KS phases the BAZ. Visualizations as in Fig. 5.2.

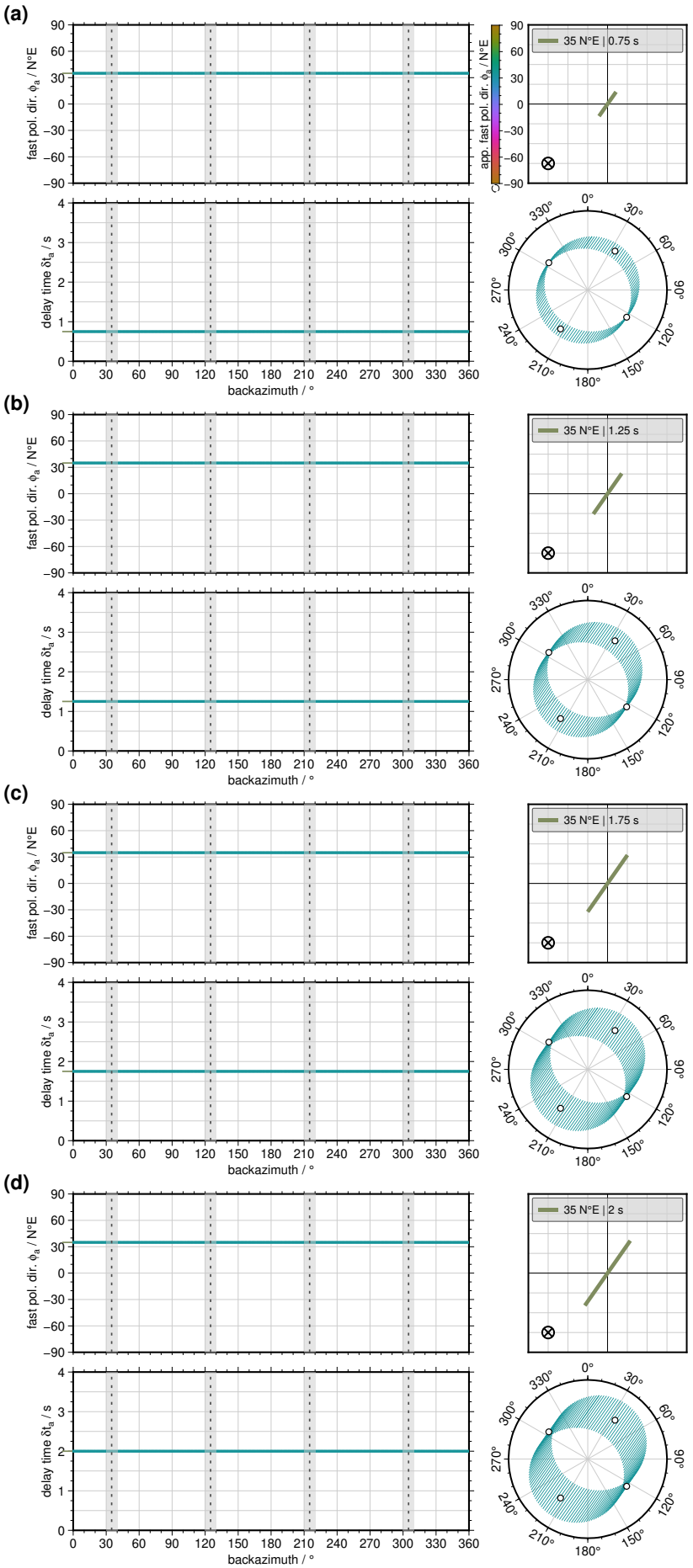

Figure 5.5: Forward calculation for model type H1: variation of the delay time.
Fixed fast polarization direction of 35N°E. The delay is **(a)** 0.75 s, **(b)** 1.25 s, **(c)** 1.75 s, and **(d)** 2 s.
In case of simple anisotropy, the splitting parameters measured at the surface directly give the model parameters within the subsurface. Both a thin (thick) layer or a weak (strong) anisotropy lead to a short (long) delay time (trade-off). Delay times shorter than 0.3 s are difficult to reliably measure or resolve using real data, i.e., a thin layer with weak anisotropy is likely to remain detected. Visualizations as in Fig. 5.2.

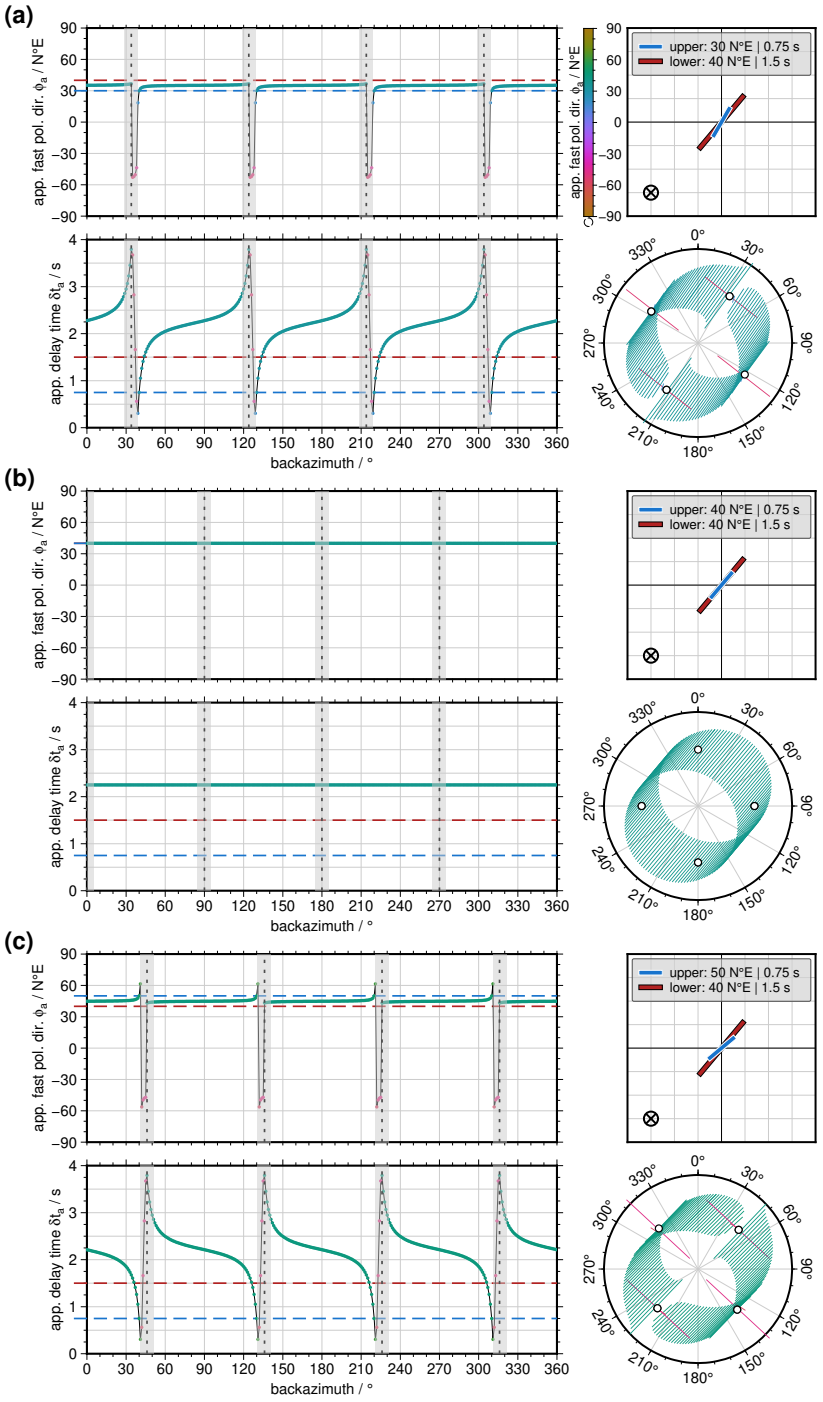

Figure 5.6: Forward calculation for model type H2: (nearly) identical fast polarization directions of the upper and lower layers.
Fixed delay times in the lower and upper layers of 1.5 s or 0.75 s and a fixed fast polarization direction in the lower layer of 40N°E. The fast polarization direction in the upper layer is **(a)** 30N°E, **(b)** 40N°E, and **(c)** 50N°E. In (a) and (c), the quite sharp $\pi/2$-jumps in the backazimuthal variation of the fast polarization direction can be easily missed due to backazimuthal gaps. In (b), the fast polarization directions within the two layers are identical. The two layers act or appear as one horizontal layer. The measured fast polarization direction corresponds to the fast polarization directions of the layers, and the delay time measured at the surface is the sum of the delay times of the two layers. Visualizations as in Fig. 5.2.

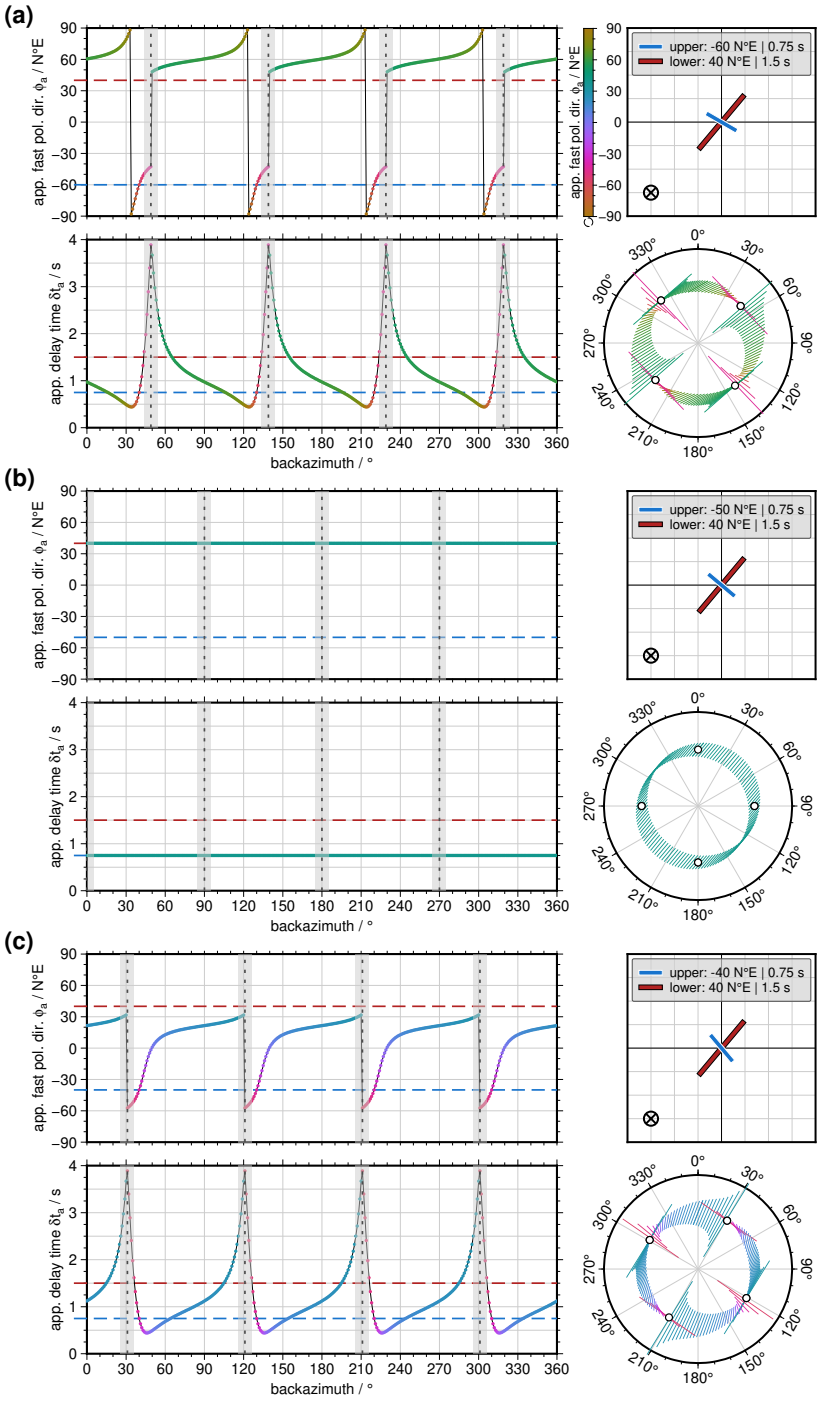

Figure 5.7: Forward calculation for model type H2: (nearly) orthogonal fast polarization directions.
Fixed fast polarization direction in the lower layer of 40N°E. **(a)** to **(c)** different delay times in the lower and upper layers of 1.5 s or 0.75 s, and **(d)** to **(f)** identical delay times in the two layers of 0.75 s. The fast polarization direction in the upper layer is **(a)** or **(d)** -60N°E, **(b)** or **(e)** -50N°E, and **(c)** or **(f)** -40N°E.
In (b) and (e), the fast polarization directions are orthogonal to each other, and no SWS occurs in the upper layer. In (b), the two layers appear as one layer with the fast polarization direction of the lower layer and the delay time being the difference between the delay times in the two layers. In (e), the splitting effect is canceled out and an apparent delay time of zero is measured at the surface. This leads to the observation of *nulls* over the whole (or wide) backazimuth range and the medium appears as apparent isotropic. Visualizations as in Fig. 5.2.

Fig. 5.7 continued.

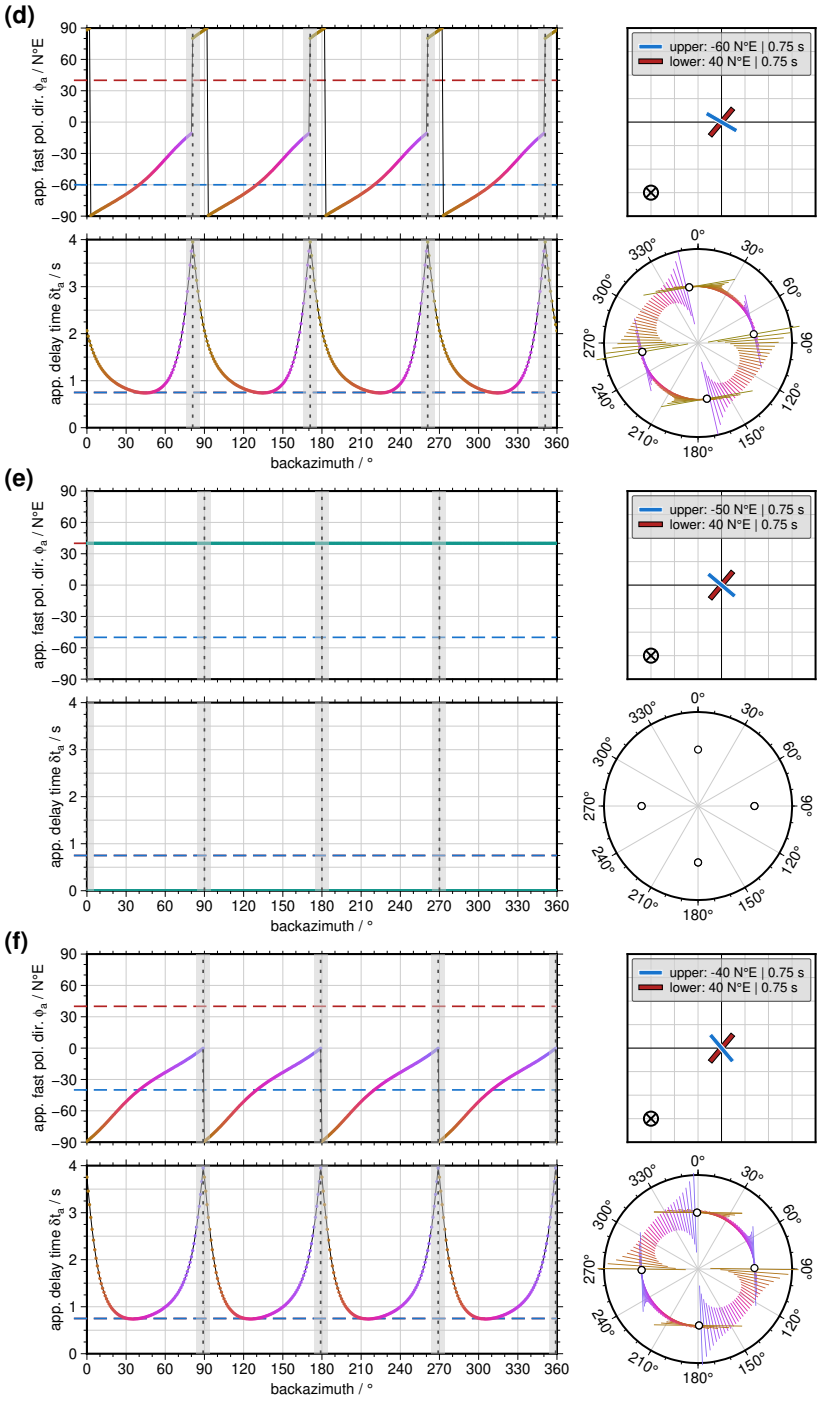

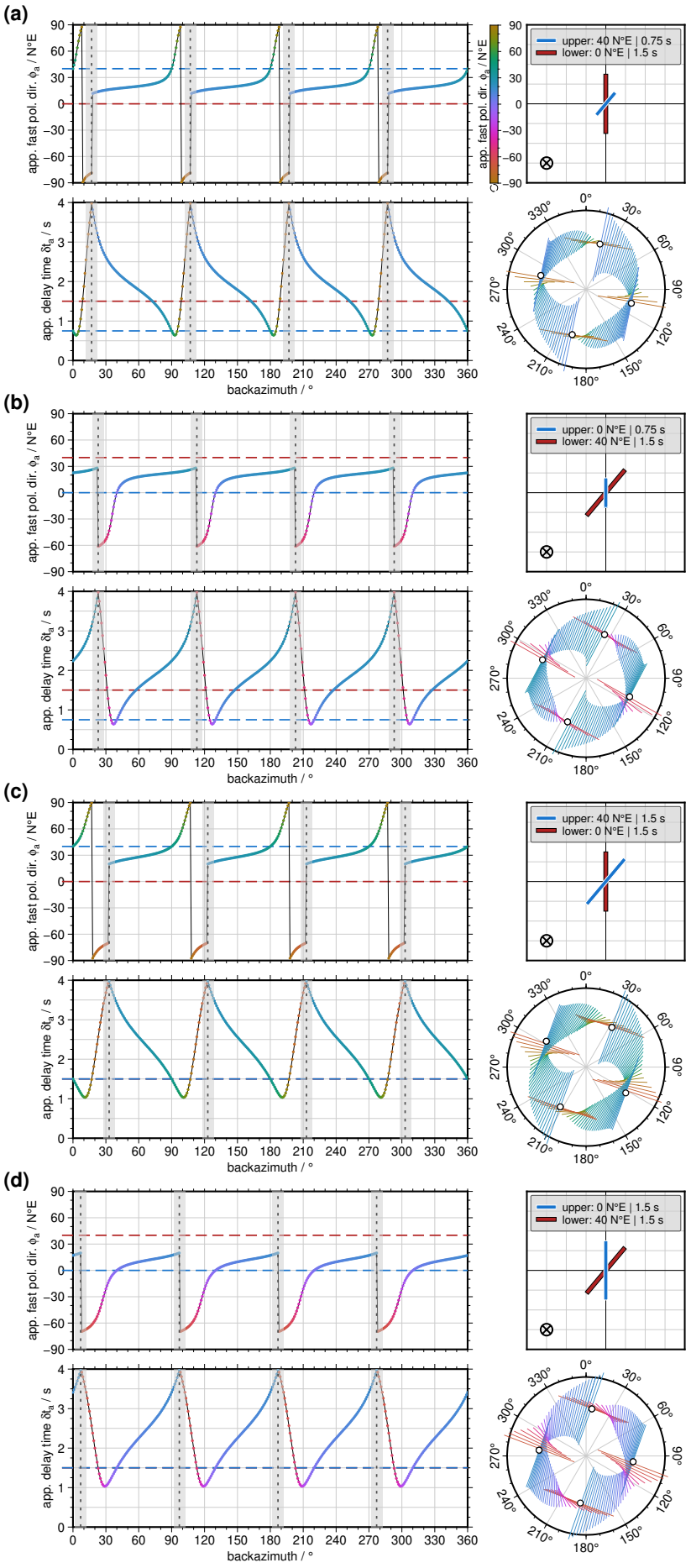

Figure 5.8: Forward calculation for model type H2: flipped fast polarization directions.
Fast polarization directions in the lower and upper layers of 40° or 0° and vice versa. **(a)** and **(b)** with different delay times in the lower and upper layers of 1.5 s or 0.75 s, as well as **(c)** and **(d)** with identical delay times in the two layers of 1.5 s.
In terms of the fast polarization direction, the order of the two layers can be resolved since the splitting operators are not commutative (*Silver and Savage*, 1994, fig. 2). Visualizations as in Fig. 5.2.

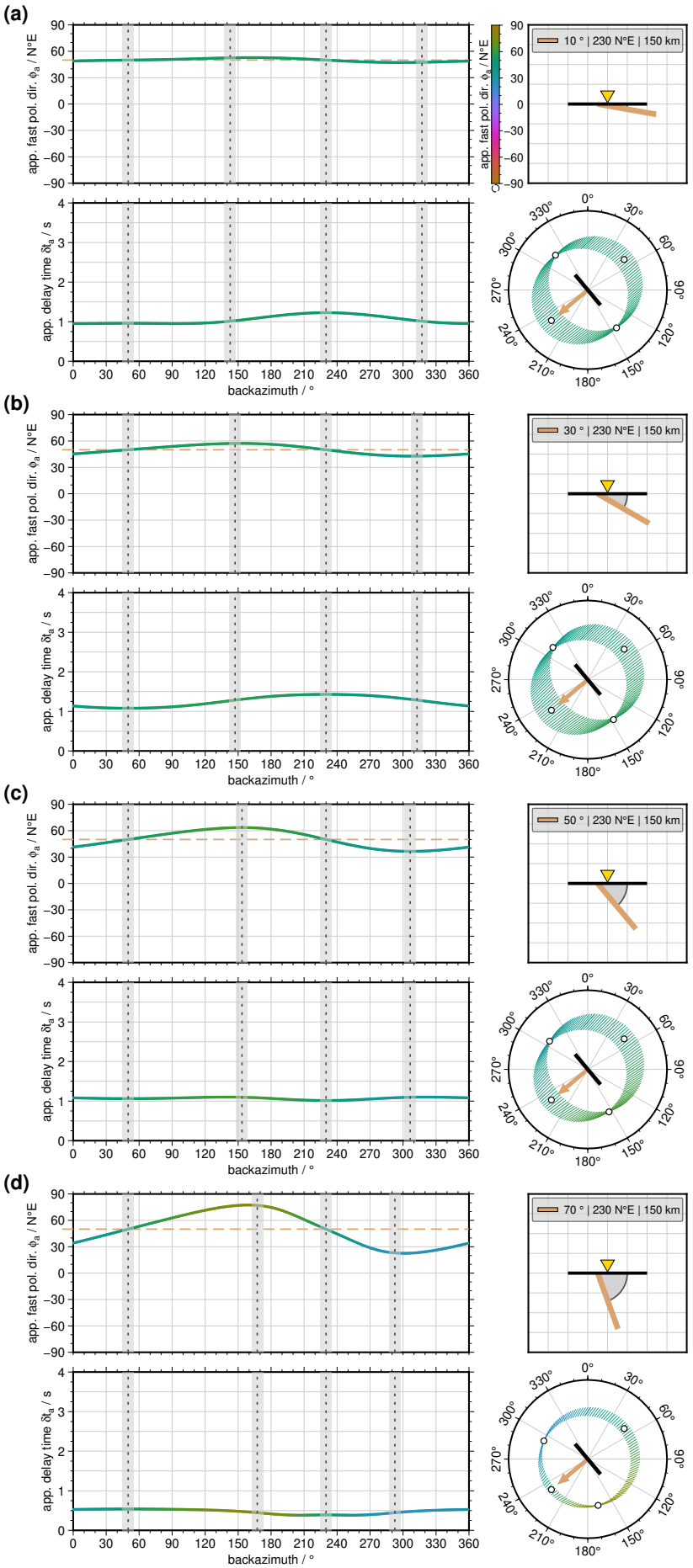

Figure 5.9: Forward calculation for model type T1: variation of the dip. Fixed down-dip direction of 230° and thickness of 150 km. The dip is **(a)** 10°, **(b)** 30°, **(c)** 50° and **(d)** 70°.
In (a), the layer is nearly horizontal and the weak backazimuthal variations of the apparent splitting parameters make it difficult to decide between a tilted layer with a small dip and a horizontal layer (model type H1). In (d), the layer is nearly vertical and the short delay time indicates that *XKS* phases experience only little of the anisotropy or splitting effect (in the upper mantle) due to their steep (nearly vertical) incidence at the recording station at the surface. Visualizations as in Fig. 5.2.

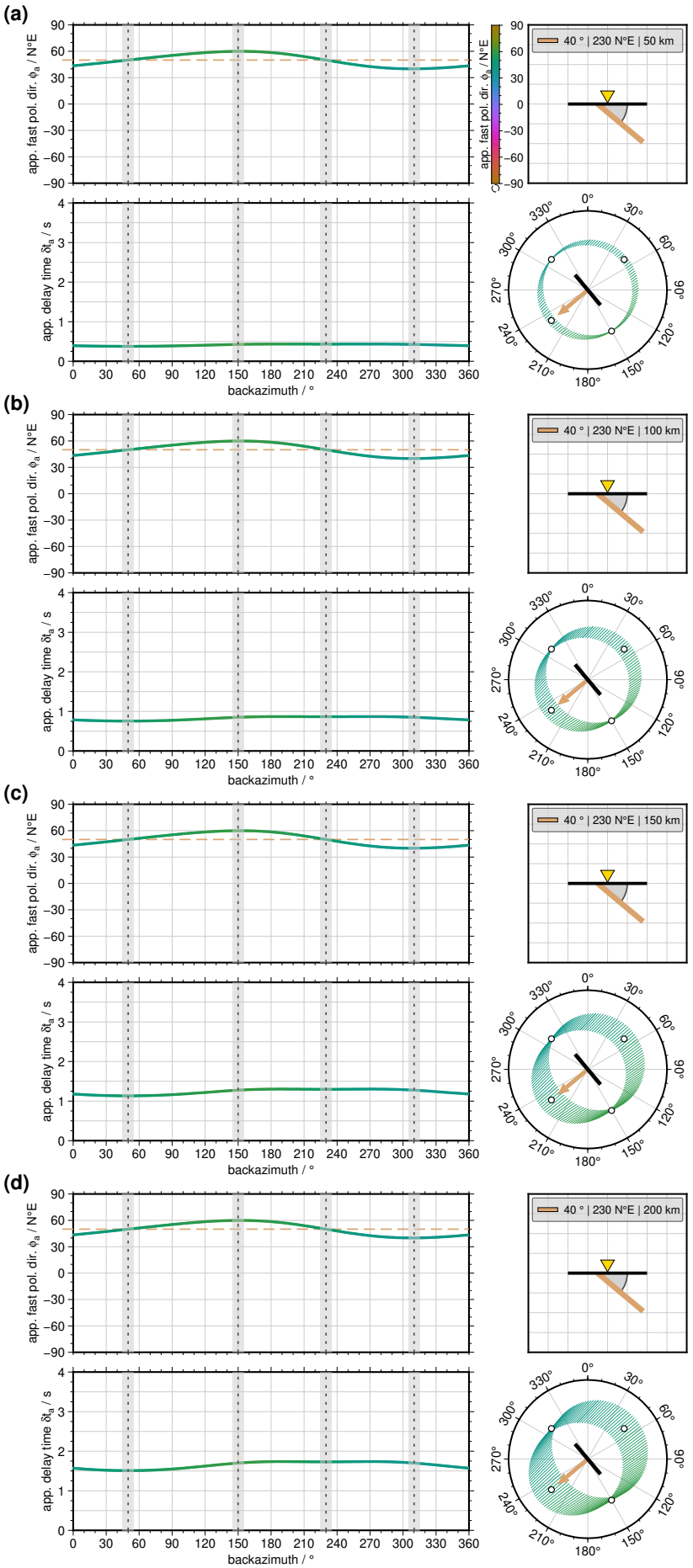

Figure 5.10: Forward calculation for model type T1: variation of the thickness.
Fixed dip of 40° and down-dip direction of 230°. The thickness is **(a)** 50 km, **(b)** 100 km, **(c)** 150 km, and **(d)** 200 km.
A thicker layer leads to a longer apparent delay time, but also a strong anisotropy could cause this (trad-off, see also Fig. 5.5). Due to the short apparent short delay time, a thin layer or a weak anisotropic layer is difficult to resolve based on real data. The apparent fast polarization direction is not affected by the layer thickness. Visualizations as in Fig. 5.2.

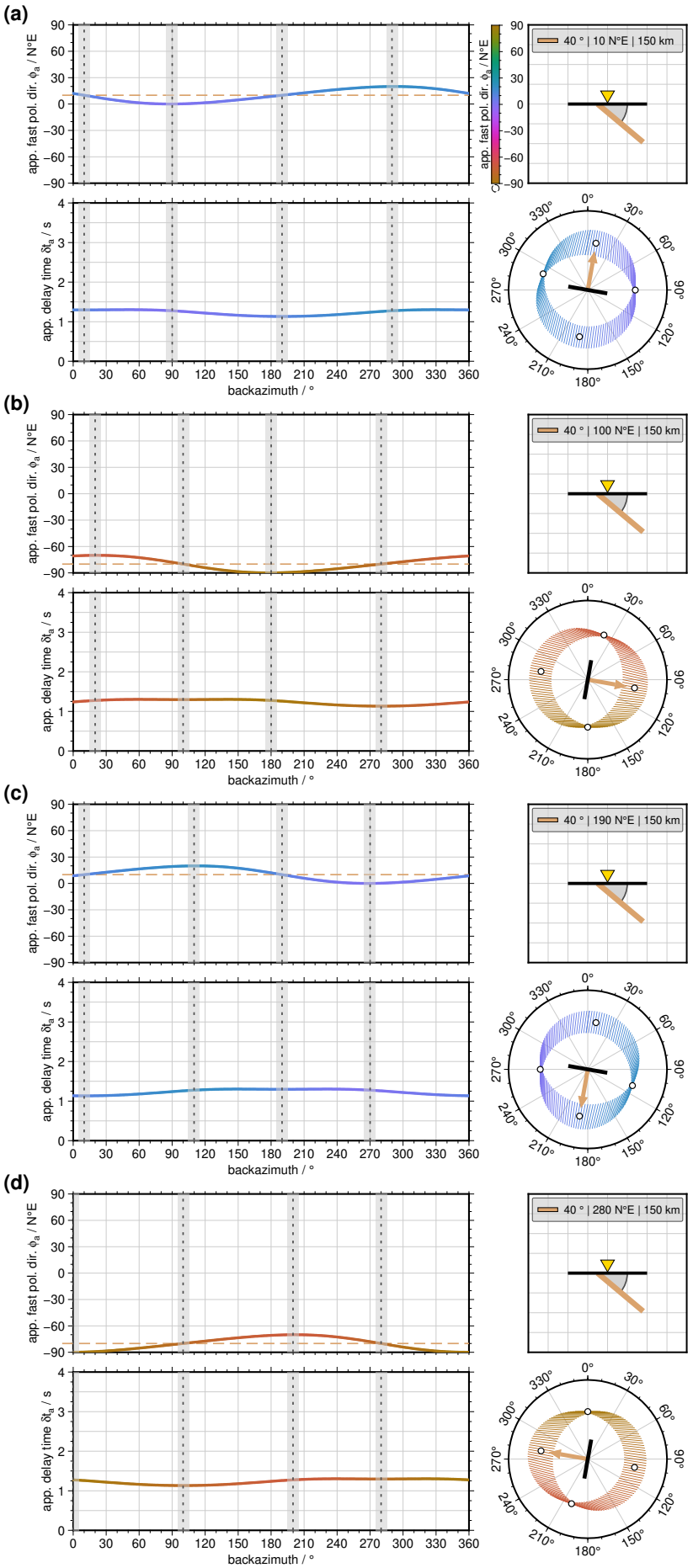

Figure 5.11: Forward calculation for model type T1: variation of the down-dip direction (strike + 90°).
Fixed dip of 40° and thickness of 150 km. The down-dip direction is **(a)** 10N°E, **(b)** 100N°E, **(c)** 190N°E, and **(d)** 280N°E.
(a) and (c) as well as (b) and (d) have opposite down-dip directions, i.e., differ by ±180°. For opposite down-dip directions, the curves of the apparent splitting parameters are flipped. However, for a shallow dip or a thin layer, the backazimuthal variations are quite small, making it difficult to distinguish opposite down-dip directions based on real data. Visualizations as in Fig. 5.2.

6 Temporal Alignment of Seismogram Components

The content presented in this chapter has been published in

> ***Fröhlich Y.****, Grund M. & Ritter J. R. R. (2022).* **On the effects of wrongly aligned seismogram components for shear wave splitting analysis**. *Annals of Geophysics*, 66(2). `https://doi.org/10.4401/ag-8781`.

The source code for the bug fix in *SplitLab* (*Wüstefeld et al.*, 2008) is available at[13]:

> ***Fröhlich Y.*** *(2024).* **Temporal Alignment of Seismic Traces in SplitLab (v2.0)**. *Zenodo*. `https://zenodo.org/records/13760807`. Maintenance on GitHub at `https://github.com/yvonnefroehlich/SplitLab-TemporalAlignment`.
>
> ***Fröhlich Y.*** *& Grund M. (2021).* **Temporal Alignment of Seismic Traces in SplitLab (v1.0)**. *Zenodo*. `https://doi.org/10.5281/zenodo.5805030`.

Additionally this bug fix is included in *StackSplit* (*Grund*, 2017) up on version v3.0[10] available at:

> ***Fröhlich Y.*** *(2025).* **StackSplit (dev)**. *in preparation*. Development on GitHub at `https://github.com/yvonnefroehlich/splitlab-stacksplit`, see folder `02_stacksplit`.
>
> *Grund M. &* ***Fröhlich Y.*** *(2021).* **StackSplit (v3.0)**. *Zenodo*. `https://doi.org/10.5281/zenodo.5802051`.

The SWSMs carried out within the frame work of the master these *Sanz Alonso* (2017) and *Fröhlich* (2020) were checked and if affected redone within *Ritter et al.* (2022; Ch. 7) or *Fröhlich et al.* (2024b; Ch. 8), respectively.

Abstract

Seismic anisotropy inside the Earth's interior, especially in the upper and lowermost mantle, is commonly studied by measuring shear wave splitting. This is mostly done by the determination of the splitting parameters fast polarization direction and delay time as well as the splitting intensity. The applied techniques highly rely on the correct temporal alignment of the single component traces (vertical, North, East referred to as Z, N, E components) of an earthquake relative to each other. Mixing wrongly aligned recording components would result in misleading and wrong data representations, including the particle motions in both the ZNE and the ray (LQT) coordinate systems and waveforms in the LQT coordinate system. The main pitfall in this context is that start and end times of the single traces in general differ due to data storage details. Unfortunately, the code of the widely used

[13] Including this bug fix directly in *SplitLab* was or is not possible as the source code is only arrival from websites (versions 1.0.5 at `https://splitting.gm.univ-montp2.fr/` and 1.2.1 at `https://robporritt.wordpress.com/software/`) and there is currently no active development at the official GitHub repository (beta version 1.9.0 at `https://github.com/IPGP/splitlab`), last accessed 2025/05/09.

MATLAB based shear wave splitting software package *SplitLab* contains an error which can cause a wrong relative temporal alignment of the input seismograms in some cases. This effect distorts under certain conditions splitting signals or simulates non-existing ones. We show examples and offer a remedy.

Keywords: *SplitLab* | *StackSplit* | Shear wave splitting | SKS | Seismic anisotropy

6.1 Introduction

Geodynamic or tectonic processes cause deformation inside the Earth's interior leading to a preferred orientation of crystals or structural elements within the rock masses and layered media and by this to elastic or seismic anisotropy (*Silver*, 1996). Therefore, studying seismic anisotropy can provide important information and constraints on recent asthenospheric mantle flow (*Long and Becker*, 2010) as well as past (fossil, frozen-in) and present deformation processes in the upper mantle (e.g., *Savage*, 1999; *Long and Silver*, 2009; *Margheriti et al.*, 2003; *Aragon et al.*, 2017; *Grund and Ritter*, 2020) and lowermost mantle (LMM, D'' layer) (e.g., *Nowacki et al.*, 2011; *Nowacki and Cottaar*, 2021; *Lynner and Long*, 2012; *Deng et al.*, 2017; *Grund and Ritter*, 2019).

Since shear (S) wave splitting (SWS; analogue to birefringence in optics) is an unambiguously phenomena of seismic anisotropy, it is commonly used to detect and to quantify anisotropy (e.g., *Savage*, 1999; *Long and Silver*, 2009; *Margheriti et al.*, 2021). To do so the splitting parameters the fast polarization direction ϕ and the delay time δt as well as the splitting intensity *SI* (*Chevrot*, 2000) are determined. ϕ and δt are mostly estimated using the *rotation-correlation* method (*Bowman and Ando*, 1987) and the *eigenvalue* or *energy-minimum* method (*Silver and Chan*, 1991). For investigating the Earth's mantle core-refracted phases, mainly SKS and SKKS, are favorable (*Savage*, 1999; *Long and Silver*, 2009).

The above-mentioned techniques for measuring SWS highly rely on a correct temporal alignment of the single traces, i.e. vertical, North, East or Z, N, E components, respectively, of an earthquake relative to each other. In case of a wrong relative temporal alignment the mixing of different components results in misleading particle motions in both the ZNE and the ray (LQT) coordinate systems as well as wrong waveforms in the LQT coordinate system. This is especially problematic for SKS phases since usually a change from the ZNE to LQT coordinate system is made to better detect these phases and their splitting behavior. Thus, a correct relative temporal alignment is absolutely essential to achieve correct shear wave splitting measurements. A correct alignment is in general important for all processing and analyzing steps relying on the mixing of seismic traces or components.

The main pitfall in this context is that requested (seismological) waveforms from data centers (e.g., IRIS, ORFEUS) have in general slightly different start and end times of the single traces for the specified time window of one earthquake. This is due to storage details of the data. Thus, the users have to make sure or (cross-)check that the traces are temporally aligned relative to each other in a correct way. This can be done based on a reference time, e.g. origin time, or by cutting the traces to their shared time window, i.e. the latest start time and the earliest end time, (Fig. **6.1**).

Unfortunately, especially the code of the widely used (229 citations as of beginning February 2022) MATLAB based software package *SplitLab* (*Wüstefeld et al.*, 2008) contains an error causing a wrong relative temporal alignment under some conditions in some applications and releases. Then fractions of a second are not included in the start time of the input seismograms, leading to a temporal misalignment of the traces. Subsequently, unrecognized wrong shear wave splitting measurements can follow regarding both observation types, i.e. SWS instead of a *null split* and vice versa, as well as corrupt measurements of splitting parameters and splitting intensity. Previous anisotropy studies based on SWS measurements carried out with *SplitLab* may be incorrect at least when the versions and options were used which are described in the following. The problem also affects the plugin *StackSplit* (*Grund*, 2017), which allows to carry out a multi-event analysis based on the single-event analysis results obtained with *SplitLab*.

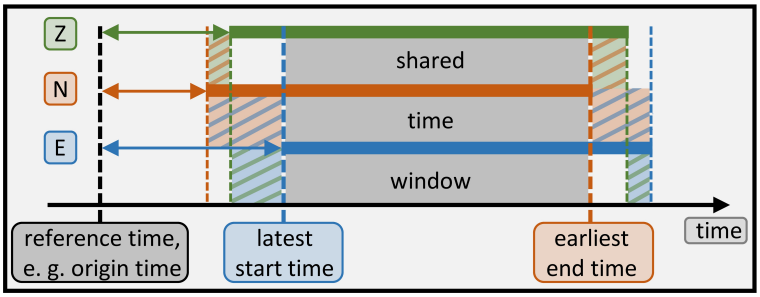

Figure 6.1: Schematic visualization of the Z, N, E components of a seismological recording with slightly different start and end times for the specified time window of one earthquake due to the storage details of the data. Arrows indicate the temporal offset to a reference time, here for instance the origin time. Colored areas represent the relative temporal difference between two traces or components. The gray area represents the shared time window according to the latest.

Here, we first outline this general issue and the error in *SplitLab* together with its impact on *StackSplit* based on real data examples. Furthermore, we provide recommendations, data for testing by other users and a modification or correction of the relevant *SplitLab* function which is also included in the new *StackSplit* version 3.0.

6.2 Description of the problem

The general effects of a wrong relative temporal alignment of the Z, N, E components of an earthquake are illustrated in Fig. 6.2.

In this example we used a deep earthquake underneath Bolivia (hypocentral depth 274 km) which occurred on 29 June 2001 at 18:35:51 (UTC). The waveforms were recorded at the broadband permanent seismological station Stuttgart (STU) in Southwest Germany which is part of the GEOFON (GE) network (*GEOFON Data Centre*, 1993) (backazimuth BAZ = 246.5°, epicentral distance Δ = 95.29°). During the pre-processing we removed both, trend and mean, and applied a third-order zero-phase Butterworth bandpass filter with corner frequencies of 0.02 Hz (lower corner) and 0.15 Hz (upper corner). The Z, N, E components were rotated into the LQT coordinate system using the theoretical backazimuth of the earthquake (BAZ = 246.5°) and the theoretical incidence angle of the SKS phase (inc = 9.2°) for better visibility of the phase.

In Fig. 6.2, in the upper (yellow) part the Z, N, E components are correctly aligned and in the lower (green) art they are wrongly aligned by less than one second, for the N and E components by 0.9 s (Fig. 6.2, white boxes with red or green font at the top or bottom of the hodogram of the wrongly aligned traces). For both cases the waveforms in the ZNE coordinate system, the horizontal (E-N) particle motion and the waveforms in the LQT coordinate system are displayed (from left to right). The hodogram in the W-E/N-S plane of the correctly aligned seismograms contains a linear particle motion. Furthermore, only on the Q component a SKS phase-related signal is visible. Thus, there are no clear indications for SWS in the correct waveforms. In contrast, the wrongly aligned components lead to an elliptical particle motion in the hodogram in the W-E/N-S plane. And additionally, a clear SKS phase-related signal on the transverse (T) component is visible (Fig. 6.2, orange circles with arrows). Both observations clearly indicate SWS.

6.3 Error of *SplitLab*

For the purpose of further analysis, we tried to reproduce our shear wave splitting observations made with *SplitLab* regarding particle motions and waveforms with the Python toolbox *ObsPy* (*Beyreuther et al.*, 2010; *Megies et al.*, 2011; *Krischer et al.*, 2015). In several cases, we recognized a slightly different temporal alignment of the Z, N, E components. We found that the *SplitLab* function `getFileAndEQseconds.m` does not always account for the milliseconds of the start time of the input seismograms when calculating the temporal offset to the origin time of the earthquake. For a sampling interval less than one second, there are three possible scenarios:

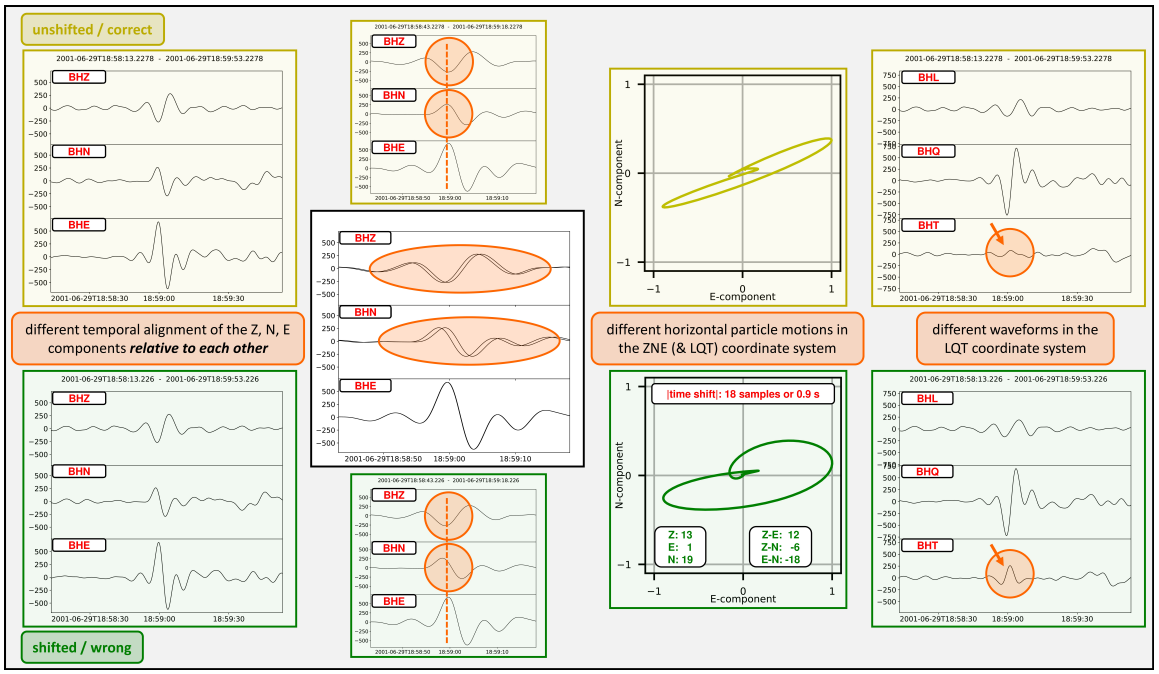

Figure 6.2: Effect of a different temporal alignment of the Z, N, E components relative to each other (left) on the particle motions in the ZNE (and LQT) coordinate system (middle) and the waveforms in the LQT coordinate system (right). As consequence there is an impact on the shear wave splitting measurement (the corresponding *SplitLab* diagnostic plots are shown in Fig. 6.4). The selected time window contains the SKS phase. Top in yellow unshifted / correct temporal alignment and bottom in green shifted / wrong temporal alignment. The sampling interval of the traces is 0.05 s. The N and the E components are shifted relative to each other by 18 samples or 0.9 s (white boxes with red or green font at the top or bottom of the hodogram of the wrongly aligned traces, for details on these values see text and Fig. 6.3). During the pre-processing, trend and mean were removed and a third-order zero-phase Butterworth bandpass filter with corner frequencies of 0.02 Hz (lower corner) and 0.15 Hz (upper corner) was applied. The shifted / wrong temporal alignment is caused by the problem that *SplitLab* does not always account for the milliseconds of the start time of the single traces.

(i) the start times of all traces have zero milliseconds,

(ii) the start times of all traces have the same (non-zero) milliseconds and,

(iii) the start times of the traces have different milliseconds.

For (i) there is no impact on the relative time between the traces. For (ii) “only” a common time shift occurs for all three traces, which does not affect the result of the SWS measurement, since this is a relative measurement. However, for (iii) the temporal alignment of the traces relative to each other is changed. As consequences the (E-N or Q-T) particle motions in both the ZNE and the LQT coordinate systems as well as the waveforms in the LQT coordinate system are corrupt leading to a potentially unrecognized wrong SWS measurement. Not taking into account the milliseconds in the start times, the maximum error in the temporal misalignment is one second minus the sampling interval. For a sampling rate of 0.05 s (often used for teleseismic recordings) this error can reach up to 0.95 s what is comparable to typical delay times of 0.4-1.5 s for continental anisotropy (*Silver*, 1996). In addition, a *split* may change to a *null split* or vice versa.

Also, the export option “Cut and save as SAC” of *SplitLab*, i.e. cutting the three traces (Z, N, E) of one earthquake to the shared time window (latest start time and earliest end time) and saving them afterwards as new files, is indirectly affected, since it uses the previous relative alignment of the single components.

6.3.1 Occurrence in the publicly available *StackSplit* versions

The crucial point regarding the above-described problem in *SplitLab* is the assignment of the earthquake catalogue with the seismogram data. *SplitLab* offers (depending on the version) several options regarding filename format and how the start time is extracted (Tab. 6.1). If the option "`Extract start time from SAC-header`" is used, one must be cautious, because only in *SplitLab* version 1.9.0 (*Wüstefeld et al.*, 2008) the milliseconds are accounted for. In the *SplitLab* versions 1.0.5 (*Wüstefeld et al.*, 2008), 1.2.1 (*Porritt*, 2014), and 1.3.0 (*Creasy*, 2020) the milliseconds are ignored. For the option "`Extract start time from filename`" with the filename format "`RDSEED`" the milliseconds are used in all versions. For the other filename formats only seconds are included, for "`YYYY_MM_DD_hhmm_stnn.sac.e`" even just minutes (Tab. 6.1). Thus, in case of non-zero milliseconds (or seconds) there are wrong start times. If the milliseconds (or seconds) differ for the single component traces, this leads to a wrong relative temporal alignment of the Z, N, E traces. Note, that even if the filename does not contain milliseconds, the start time needs not to begin automatically at zero milliseconds. A (re)naming of the traces has not necessarily to be done based on the start times. Therefore, the extraction of the start time from the SAC-header appears to be safer.

Table 6.1: Overview for which options of start time extraction and filename format the milliseconds (msec) are considered in the offset calculation by the publicly available *SplitLab* versions. Otherwise, only seconds (sec) or even just minutes (min) are included. If a filename format is not provided in the *SplitLab* version, "-" is set.

filename format	*SplitLab* version 1.0.5	*SplitLab* versions 1.2.1, 1.3.0	*SplitLab* version 1.9.0
extract start time from SAC-header			
all filename formats	sec	sec	msec
extract start time from filename			
`mseed2sac1`	-	sec	-
`mseed2sac2`	-	sec	-
`miniSEED`	-	-	sec
`RHUM-RUM`	-	-	sec
`RDSEED`	msec	msec	msec
`SEISAN`	sec	sec	sec
`YYYY.JJJ.hh.mm.ss.stn.sac.e`	sec	sec	sec
`YYYY.MM.DD.hh.mm.ss.stn.E.sac`	-	-	sec
`YYYY.MM.DD-hh.mm.ss.stn.sac.e`	sec	sec	sec
`YYYY_MM_DD_hhmm_stnn.sac.e`	min	min	min
`stn.YYMMDD.hhmmss.e`	sec	sec	sec

6.3.2 Impact on *StackSplit*

The *SplitLab* plugin *StackSplit* (*Grund*, 2017; at the moment compatible with *SplitLab* versions 1.0.5 and 1.2.1) allows to carry out a multi-event analysis based on the previous single-event analysis results obtained with *SplitLab*. The four implemented multi-event methods cover the simultaneous inversion of multiple waveforms (*Roy et al.*, 2017) and the stacking of error surfaces (stacking without weighting or normalization ("no weight") *Wolfe and Silver*, 1998; *Restivo and Helffrich*, 1999). These techniques are recommended to obtain more stable results for weak signals (low signal to noise ratio) and thus a wider and more even backazimuthal coverage, especially for studies based on short-term recording experiments. However, wrong single-event analysis results lead obviously also to wrong multi-event analysis results. Furthermore, *StackSplit* introduces the correct calculation of the degrees

of freedom for the error calculation using the modified equations of *Walsh et al.* (2013). This is only directly implemented in *SplitLab* version 1.9.0.

6.4 Real data examples

Here we show in details the effect of a wrong relative temporal alignment of the Z, N, E components on the corresponding SWS measurement using seismological data (SKS phase) of two teleseismic earthquakes recorded at two broadband permanent stations: In Fig. 6.3a one example is presented from the earthquake on 14. November 2011 at 19:44:29 (UTC) underneath Argentina recorded at the station Stuttgart (STU) in Southwest Germany which is part of the GEOFON (GE) network (*GEOFON Data Centre*, 1993). The other example in Fig. 6.3b is a recording from the earthquake on 8. August 2018 at 22:35:13 (UTC) underneath the Mariana Islands recorded at station the Échery (ECH) in East France which is part of the GEOSCOPE (G) network (*GEOSCOPE*, 1982). In Fig. 6.3 the waveforms (left) and the particle motions (right) both, in the ZNE (top) and the LQT (bottom) coordinate systems, are displayed.
In these examples the start times were extracted from the SAC-headers. We compare the data representation by the original *SplitLab* code ("cut by SplitLab data 01", wrong temporal alignment) with the representation by *ObsPy* ("original data", correct temporal alignment). Clear differences between the observations are visible regarding the shape of the waveforms on the Q and T components and the E-N or Q-T particle motions. The same comparison was conducted for the data representation by our self-modified *SplitLab* code ("cut by SplitLab data 02", corrected temporal alignment) and the representation by *ObsPy*. As result we were able to achieve identical observations with *SplitLab* and *ObsPy*. In addition to the visual comparison, a calculation of the temporal difference for the Z, N, E components was carried out. First, we determined the temporal difference for each component separately (Fig. 6.3, values in the lower left corners of the hodograms). Then, the temporal difference was estimated between these component-related differences across the components (6.3, values in the lower right corners of the hodograms). This value represents the error in the temporal alignment of two components relative to each other.
For SWS measurements using SKS phases the error in the relative temporal alignment of the N and the E components is most problematic. This is clearly visible from the two examples: in Fig. 6.3a a clear splitting observation turns out as *null split* and in Fig. 6.3a the vice versa case occurs. Beside a wrong observation type (*split* or *null split*) also false splitting parameters and splitting intensities are determined. Despite the relative temporal differences of all three components combinations (Z-E, Z-N, E-N) are below one second in all three examples, they lead to a completely different or opposite splitting observation. The *SplitLab* diagnostic plots of the SWS measurement for the wrong and correct(ed) relative temporal alignment for the three earthquakes used in Fig. 6.2, Fig. 6.3a, and Fig. 6.3b are shown in Fig. 6.4, Fig. 6.5, and Fig. 6.6, respectively.

6.5 Recommendations regarding a correct relative temporal alignment

To control whether seismograms are correctly displayed, for instance regarding waveform, amplitude or relative temporal alignment, by a specific analysis software, we recommend to use at least one other independent software for a cross-check, e.g. *ObsPy* (*Beyreuther et al.*, 2010; *Megies et al.*, 2011; *Krischer et al.*, 2015) or *Snuffler* (*Heimann et al.*, 2017). A first visual comparison should reveal larger differences or errors. However, small differences may remain unrecognized. Calculating the difference between the two different visualizations may help, because small amplitude difference will be better visualized. If it is possible, save the seismograms as new files in the same way they are displayed by the software. For an identical display regarding waveforms, amplitude, and relative

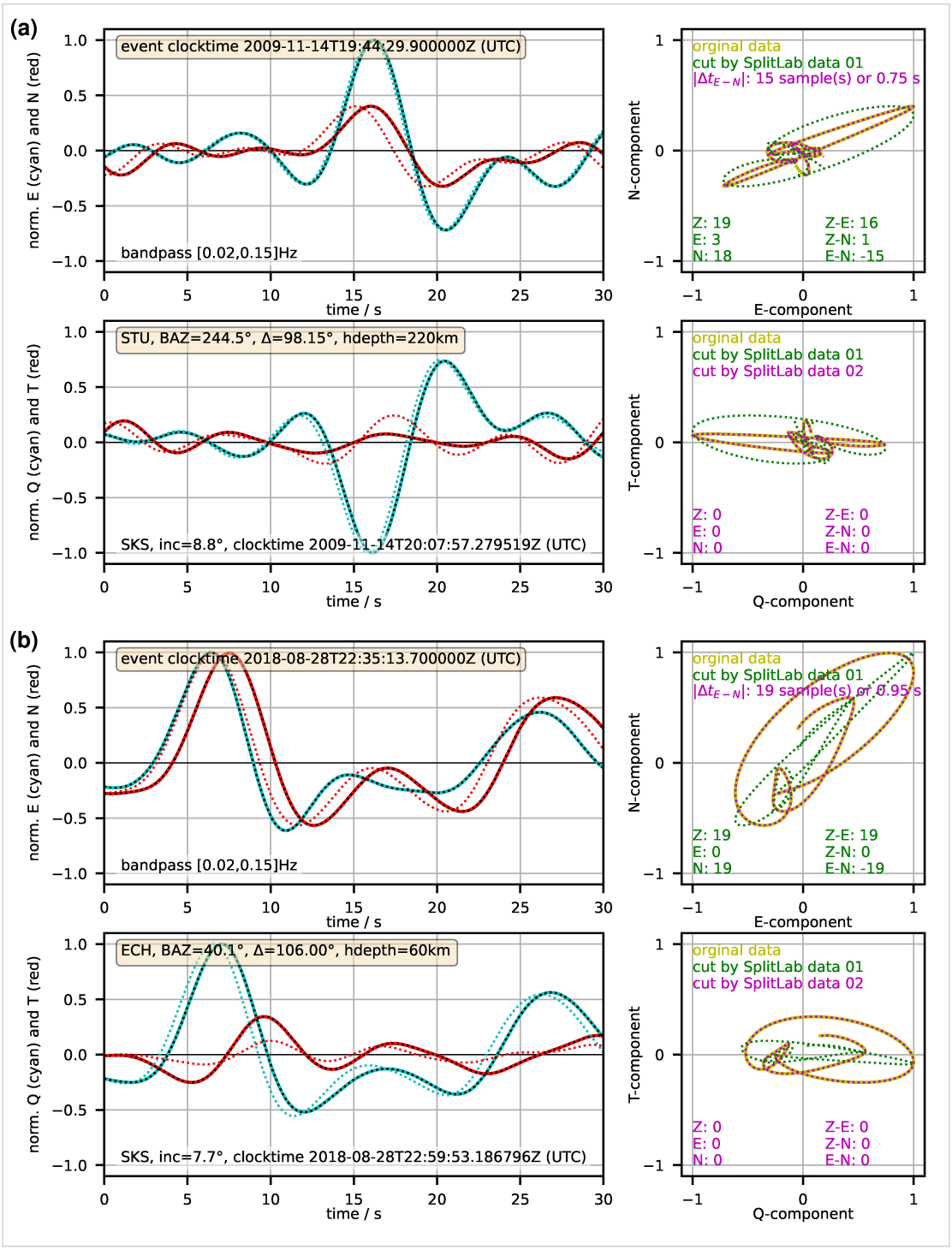

Figure 6.3: Two examples demonstrating how waveforms (left) and particle motions (right) in the ZNE (top) and the LQT (bottom) coordinate systems are affected by a wrong temporal alignment of the Z, N, E components (the corresponding *SplitLab* diagnostic plots are shown in Fig. 6.5 and Fig. 6.6). Both are misleading concerning the shear wave splitting measurement: **(a)** splitting observation turns out as *null split* and **(b)** vice versa. Seismograms (left): E or Q components in cyan and N or T components in red for the correct (solid lines) and the wrong (dotted lines) temporal alignment of the Z, N, E components. Black dotted lines after correction. Hodograms (right): solid yellow line correct ("original data") and dotted green line wrong ("cut by SplitLab data 01") temporal alignment, dotted purple line after correction ("cut by SplitLab data 02"). The numbers give temporal differences in samples (sampling interval 0.05 s): lower left corners difference between the wrong and the correct temporal alignment (right top panel green font) as well as between the corrected and the correct temporal alignment (right bottom panel purple font) and lower right corners difference between these differences for the Z, N, E components, respectively. Additionally, for the E and the N components the difference relative to each other is given in seconds (right top panel purple font).

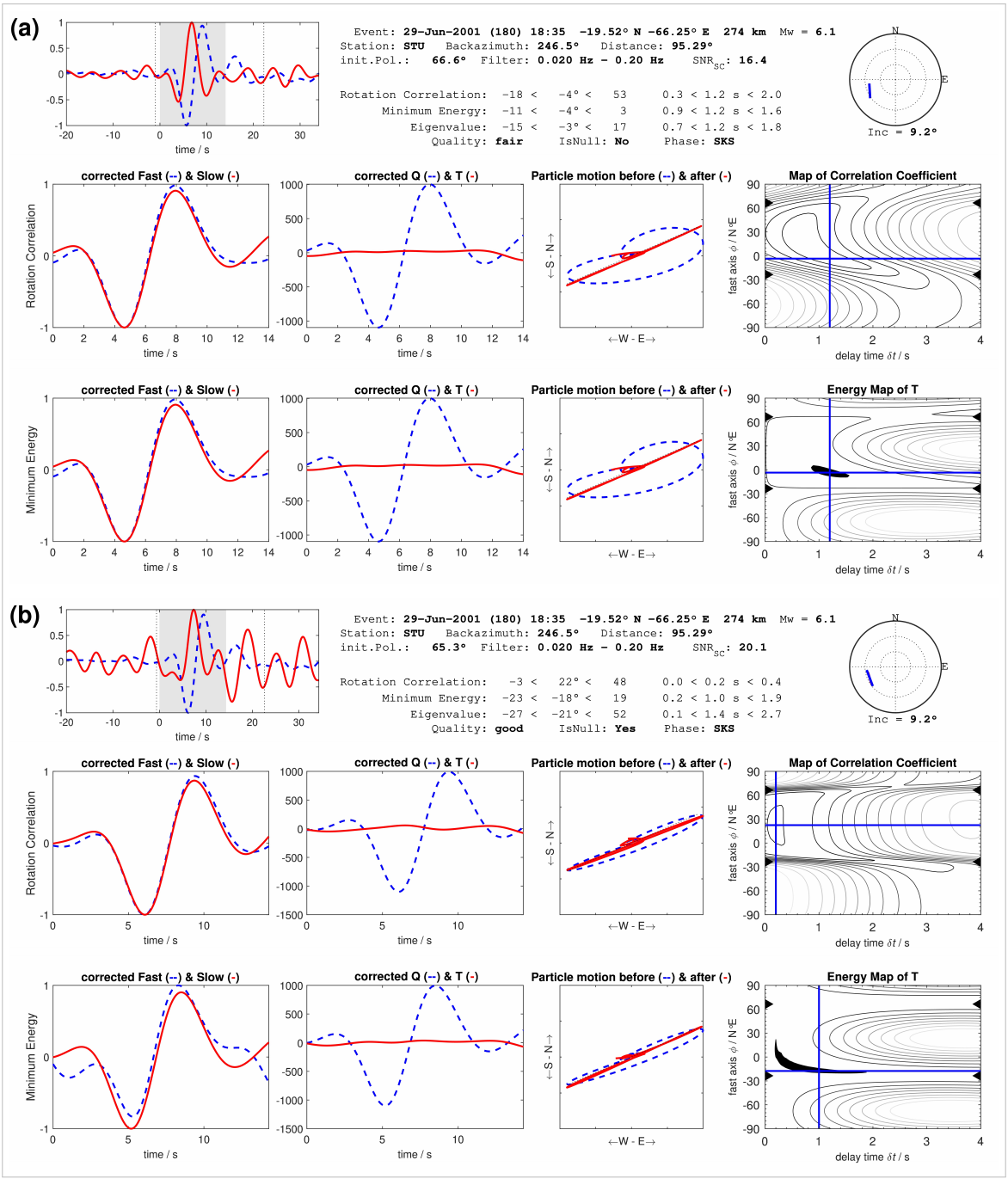

Figure 6.4: *SplitLab* diagnostic plot of the shear wave splitting measurement on the SKS phase of the earthquake underneath Bolivia on 29 June 2001 at 18:35:51 (UTC) recorded at the station Stuttgart (STU). **(a)** shifted / wrong relative temporal alignment (without consideration of the milliseconds) and **(b)** unshifted / correct relative temporal alignment (with consideration of the milliseconds).

temporal alignment, etc. a difference of zero is expected between the two representations. Of course, there is also the possibility for a cross-check with other software for shear wave splitting, e.g. in MATLAB *SplitRacer* (*Reiss and Rümpker*, 2017), in Python *SplitPy* (*Audet and Schaeffer*, 2019), or in Julia *SeisSplit* (*Nowacki*, 2019). Repeated processing as well as analysis with other software and comparison of the results across different software packages will help to obtain reliable (splitting) results. This should be done with several traces or events, not only for one example, to avoid verifications by chance.

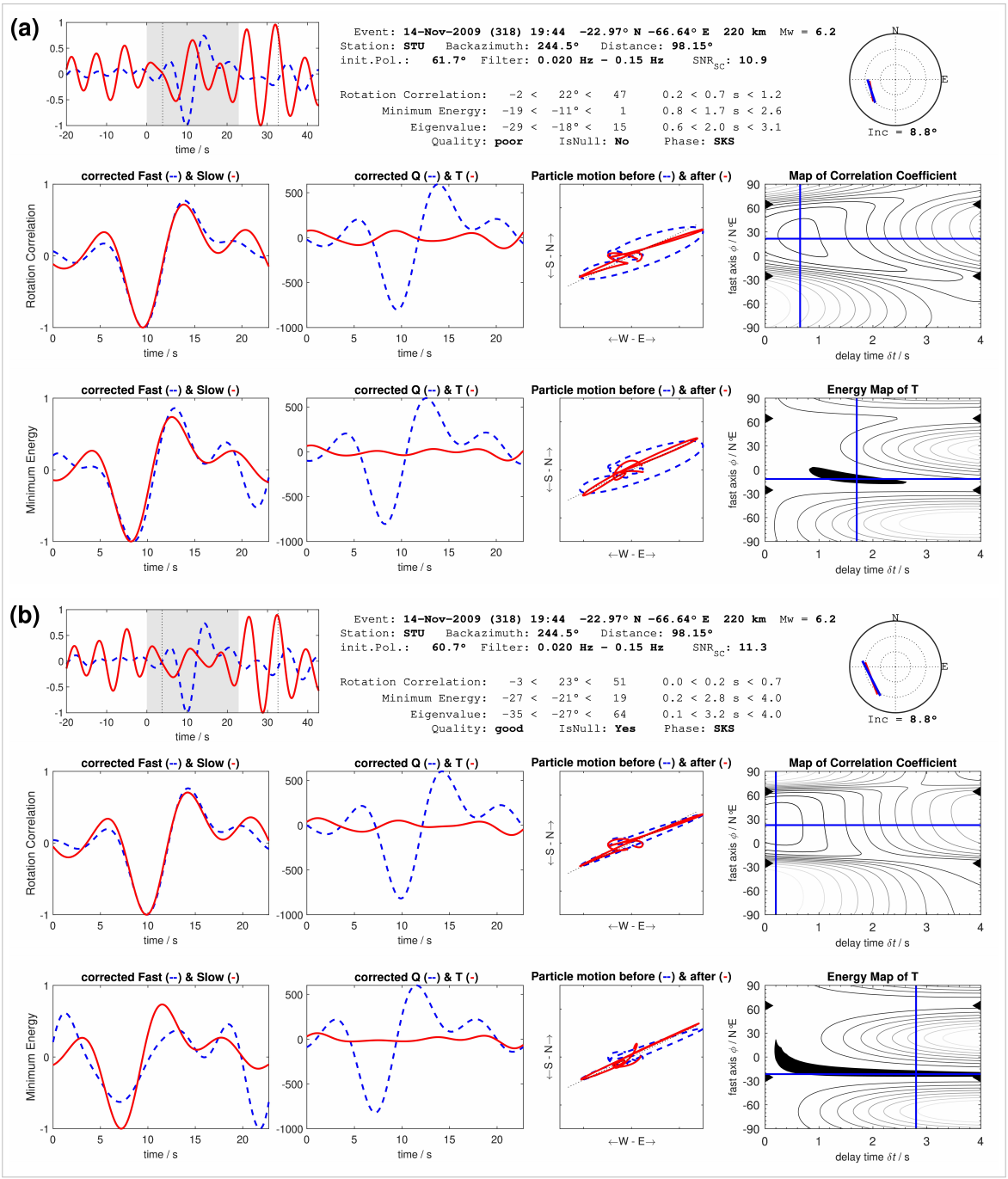

Figure 6.5: Analogous to Fig. 6.4 but for the earthquake underneath Argentina on 14 November 2009 at 19:44:29 (UTC) recorded at the station Stuttgart (STU).

6.5.1 Data to test by other users

We recommend to use shear wave splitting measurements with known (correct) results as reference to check *SplitLab* (or any other tool) before analyzing a new dataset. To facilitate such a test, we provide the waveforms used in the three examples of this study for testing by other users. The waveforms (Z, N, E components as SAC-files) of the three earthquakes shown in Fig. 6.2 or Fig. 6.4 as well as Fig. 6.3a or Fig. 6.5 and Fig. 6.3b or Fig. 6.6 are provided. For a general comparison of the user's result, e.g. regarding the shape of the E-N particle motion, the *SplitLab* diagnostic plots for both the wrong and the correct(ed) temporal alignment (without and with consideration of the milliseconds of the start times, respectively) can be used.

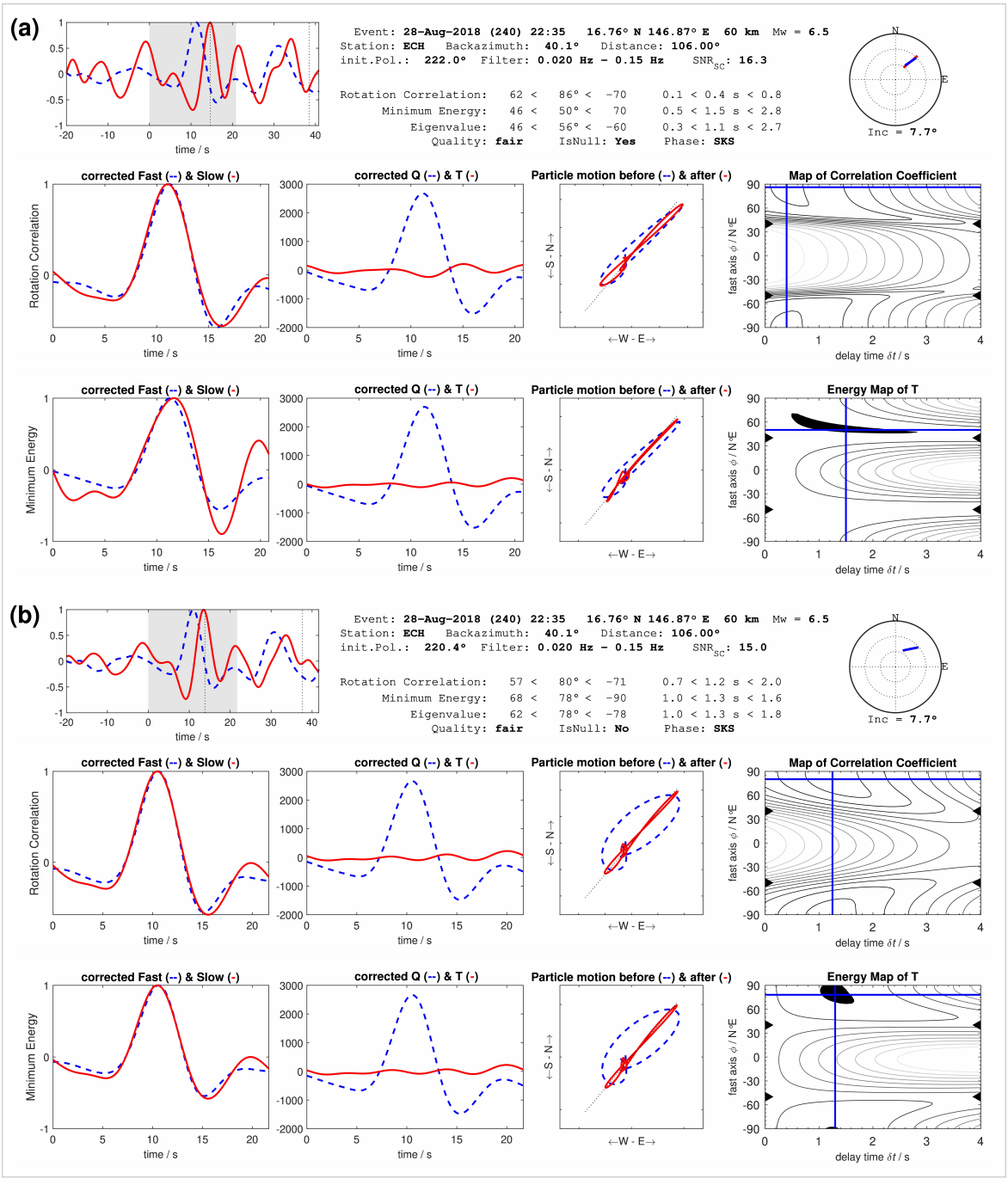

Figure 6.6: Analogous to Fig. 6.4 but for the earthquake underneath the Mariana Islands on 28 August 2018 at 22:35:13 (UTC) recorded at the station Échery (ECH).

6.5.2 Modified *SplitLab* function `getFileAndEQseconds.m` & new *StackSplit* version 3.0

Furthermore, we provide a corrected or modified *SplitLab* function `getFileAndEQseconds.m` for the publicly available *SplitLab* versions. Users can exchange the original function with the modified one in their personal *SplitLab* version. Additionally, the new *StackSplit* version 3.0 introduces this modified *SplitLab* function during the installation process (*SplitLab* versions 1.0.5 and 1.2.1). We are happy to receive feedback from users.

6.6 Conclusions

We recognize that the shear wave splitting software package *SplitLab* does not always account for the milliseconds (or seconds) in the start times of the input seismograms. Our real data examples show that the correct relative temporal alignment of the Z, N, E components is essential to achieve correct SWS measurements. A wrong relative temporal alignment results in misleading particle motions in both the ZNE and the LQT coordinate systems as well as wrong waveforms in the LQT coordinate system. Each processing and analyzing step which uses the mixing of traces or components will result in meaningless or wrong results. The different start and end times of the traces of one earthquake are the main pitfall for a wrong relative temporal alignment. Existing anisotropy studies based on a waveform analysis carried out in *SplitLab* may be at least partly incorrect, if a possible misalignment of the seismic traces was not checked and meaningless SWS measurements may have been conducted.
Beside general recommendations we provide the seismological data of our examples for testing by other users, a modified or corrected *SplitLab* function `getFileAndEQseconds.m` for the publicly available *SplitLab* versions and a new *StackSplit* version 3.0 which introduces this modified *SplitLab* function *SplitLab* versions 1.0.5 and 1.2.1). This should help to prevent other users to build modeling and interpretation on unrecognized wrong SWS measurements.

Data and sharing resources.
We used seismological data from two networks achieved by the German Research Centre for Geosciences (Deutsches GeoForschungsZentrum (GFZ) Potsdam): STU (GE, GEOFON Program GFZ Potsdam) (*GEOFON Data Centre*, 1993) and the Institut de Physique du Globe de Paris (IPGP) Data Centre: ECH (G, GEOCOP) (*GEOSCOPE*, 1982). The shear wave splitting measurements were carried out using the MATLAB based software package *SplitLab* (*Wüstefeld et al.*, 2008) version 1.2.1 (*Porritt*, 2014) modified for MATLAB R2020b. Fig. 6.1 and Fig. 6.2 were prepared with PowerPoint Home & Student 2016. The Python toolbox *ObsPy* (*Beyreuther et al.*, 2010; *Megies et al.*, 2011; *Krischer et al.*, 2015) version 1.2.2 (*The ObsPy Development Team*, 2020) was used to request and process the seismological data. The waveform and particle motion plots were generated with *ObsPy* and the Python toolbox *Matplotlib* (*Hunter*, 2007) version 3.4.3 (*Caswell et al.*, 2021). The seismological data of the examples as well as the modified *SplitLab* function `getFileAndEQseconds.m` for the publicly available *SplitLab* versions (`https://doi.org/10.5281/zenodo.5805030`) are available from YF's GitHub account (`https://github.com/yvonnefroehlich/SplitLab-TemporalAlignment`). The new *StackSplit* (*Grund*, 2017) version 3.0 (`https://doi.org/10.5281/zenodo.5802051`) which also introduces this modified *SplitLab* function is available from MG's GitHub account (`https://github.com/michaelgrund/stacksplit`).

Acknowledgments.
We thank two anonymous reviewers and Andreas Wüstefeld for useful comments which helped to improve the manuscript. YF is supported by a scholarship of the Graduate Funding from the German States (Landesgraduierten-förderung (LGF)).

7 Application to a Single Recording Station: The Black Forest Observatory

The content presented in this chapter has been published in

> *Ritter J. R. R.,* ***Fröhlich Y.****, Sanz Alonso Y. & Grund M. (2022).* **Short-scale laterally varying SK(K)S shear wave splitting at BFO, Germany – implications for the determination of anisotropic structures**. *Journal of Seismology*, 26:1137-1156. https://doi.org/10.1007/s10950-022-10112-w. Correction regarding the initially missing supplementary information https://doi.org/10.1007/s10950-023-10136-w.

The dataset of the related shear wave splitting measurements is available at (App. D.2):

> ***Fröhlich Y.****, Ritter J. R. R., Sanz Alonso Y. & Grund M. (2022).* **Longterm Shear Wave Splitting Measurements at the Black Forest Observatory**. *RADAR4KIT*. https://dx.doi.org/10.35097/684.

The supplementary information published along with this research article can be found in App. A.

My contributions include the control of the shear wave splitting measurements (SWSMs; see Ch. 6), performing the forward modeling, the generation of all figures (expect Fig. 7.1), help with writing the manuscript, and the preparation of the Supplementary information as well as the SWSMs dataset published on RADAR4KIT.

Abstract

The splitting of SK(K)S phases is an important observational constraint to study past and present geodynamic processes in the Earth based on seismic anisotropy. The uniqueness of the derived models is unclear in most cases, because the azimuthal data coverage is often limited due to recordings from only a few backazimuthal directions. Here, we analyze an exceptional dataset from the permanent broadband seismological recording station Black Forest Observatory (BFO) in SW Germany with a very good backazimuthal coverage. This dataset well represents the potential teleseismic ray paths, which can be observed at Central European stations. Our results indicate that averaging splitting parameters over a wide or the whole backazimuthal range can blur both vertical and lateral variations of anisotropy. Within the narrow backazimuthal interval of 30–100°, we observe a complete flip of the fast polarization direction. Such a splitting pattern can be caused by two layers with about NW–SE (lower layer) and NE-SW (upper layer) fast polarization directions for shear wave propagation. However, the possible model parameters have quite a large scatter and represent only the structure to the northeast of BFO. In contrast, within the wide backazimuthal range 155–335°, we prevailingly determine *null splits*, hence, no signs for anisotropy. This *null anomaly* cannot be explained satisfactorily yet and is partly different to published regional anisotropy models. Our findings demonstrate that there is significant small-scale lateral variation of upper mantle anisotropy below SW Germany. Furthermore, even low-noise long-term recording over 25 years cannot properly resolve these anisotropic structural variations.

Keywords: Shear wave splitting | Seismic anisotropy | Seismic modeling | Upper mantle

7.1 Introduction

Elastic or seismic anisotropy and its effects on seismic wave propagation in the upper mantle (lower lithosphere and asthenosphere) are caused by aligned melt-bearing structures, so-called shape preferred orientation (SPO) (*Kaminski*, 2006; *Long and Silver*, 2009) or preferred orientation of anisotropic minerals, so-called lattice or crystallographic preferred orientation (LPO, CPO) (*Mainprice and Silver*, 1993; *Long and Becker*, 2010). Such preferred orientations can be explained by the frozen-in stress field or flow field of the last tectonic deformation or by recent mantle flow (*Yuan and Romanowicz*, 2010; *Fouch and Rondenay*, 2006). In the crust, in addition, aligned cracks or sedimentary layering and structures may cause seismic anisotropy (*Crampin*, 1984a). Thus, measuring and interpreting seismic anisotropy is an important tool to image geodynamic processes and to bridge seismology, geodynamics, and tectonics (*Silver*, 1996; *Savage*, 1999; *Long and Silver*, 2009; *Long and Becker*, 2010).

If a shear (S) wave propagates through an anisotropic medium, it is split into two quasi shear (qS) waves (analogue to optics birefringence). One qS wave is polarized in the direction of the elastically fast axis and the other one perpendicularly in the direction of the elastically slow axis. Since the two qS waves travel with different wave velocities, they accumulate a delay time δt which is preserved after leaving the anisotropic medium. At the surface, it is possible to measure the apparent fast polarization direction and the apparent time delay (splitting parameters, see below). Particularly for studying anisotropy in the (upper and lowermost) mantle, teleseismic S waves with the core-refracted phases SKS, SKKS, and PKS are analyzed. These waves propagate through the liquid outer core as compressional (P) wave and then convert (back) to an S wave at the core mantle boundary (CMB), in particular to a radially polarized SV wave. If this SV wave propagates through an anisotropic medium, it is split and an additional signal on the transverse component (SH wave) should be found (except for the special cases with an initial polarization direction along the fast or slow axis of the anisotropic medium). In a polarization diagram of the radial (R or Q) and transverse (T) components (*Plesinger et al.*, 1986), shear wave splitting can be identified by an elliptical particle motion, whereas an unsplit S wave is linearly polarized along the Q component. Several methods are applied to extract the so-called splitting parameters the fast polarization direction ϕ (clockwise angle relative to north) and the delay time δt from the recordings (*Vecsey et al.*, 2008).

A major problem is non-uniqueness concerning the structural interpretation of the measured apparent splitting measurements (*Romanowicz and Yuan*, 2012). As SKS phases arrive steeply or near-vertically at the recording site, there is no good vertical resolution of anisotropic structures at depth. However, by analyzing recordings from neighboring sites, lateral variations may be resolved (e.g., *Bastow et al.*, 2007; *Walker et al.*, 2005a). A major drawback in many regions is the limited azimuthal observation: since the backazimuthal coverage (BAZ, clockwise angle from north) depends on the (rare) occurrence of strong earthquakes (moment magnitude M_w higher than ca. 6) with epicentral distances of $> 80°$, an equal source coverage is often not fulfilled. E.g. in Central Europe, there are typical observational gaps towards north, southeast, and northwest due to the distribution of the main earthquake zones (Fig. 7.1, inset in the lower right corner). Another problem is the limitation in recording time, especially for temporary networks for high-resolution regional studies. During typical measurement durations of 1–3 years often less than ten SK(K)S phases are recorded for splitting measurements and these observations cover only a very limited backazimuthal range or only specific backazimuth directions. As result, structural anisotropy models are often completely underdetermined even for simple model assumptions such as laterally homogeneous one- and two-layer scenarios with transverse isotropy. Thus, the discrimination between one- or two-layer models with horizontal or dipping symmetry axis remains often open within the modeling uncertainties. Averaging of the splitting parameters across a wide or the whole backazimuthal range is sometimes done to obtain stable values. Thereby, resulting models can provide erroneous fast polarization directions which may cause misleading geodynamic interpretations. Another problem is the assumption of laterally uniform structural anisotropy around

a recording station: backazimuthal variations of the splitting parameters may then be interpreted by affects due to anisotropy in one (possibly layered) laterally homogeneously anisotropic medium instead of lateral variations in anisotropy of the medium. This issue will be addressed here.
In the following, we carefully analyze 25 years of recordings at a low-noise site in Southwest Germany, the Black Forest Observatory, and discuss the backazimuthal variation of SK(K)S splitting observations. After a discussion of the observations, we present a preliminary structural anisotropy model and conclude with recommendations for similar future anisotropy studies.

7.2 Station BFO and geological setting

The Black Forest Observatory (BFO) is located in the northern Alpine foreland in the Black Forest Mountains which are bounded by the Upper Rhine Graben (URG) in the west and the South German Block in the east (Fig. 7.1). The URG is a part of the European Cenozoic Rift System and an approximately 300 km long NNE striking continental passive rift (*Kirschner et al.*, 2011), which extends from Basel in the south to Frankfurt am Main in the north. Its average width is 30–40 km and its total lithospheric extension is ca. 5–6 km. The graben structure is asymmetric, e.g., in the east, where there is the main boundary fault, the sedimentary infill is thicker compared to the west (*Grimmer et al.*, 2017 and references therein). The only major volcanic complex within the URG, the Kaiserstuhl, was active in Miocene time and is situated about 50 km SW of BFO. The South German Block (*Ring and Bolhar*, 2020) is characterized with smoothly SE dipping, mainly Mesozoic sedimentary rocks. In the central and southern Black Forest, these layers and the crystalline basement were strongly uplifted (up to 2.5 km) and eroded. The lithosphere around BFO consolidated mainly in late Paleozoic times (ca. 330–270 Myr) and it is about 60 km thick (*Seiberlich et al.*, 2013; *Meier et al.*, 2016). The former silver mine with the instruments of BFO is situated in the central gneiss complex of the Black Forest (*Black Forest Observatory*, 1971).
Due to its remote location, the stable environmental conditions inside the mine, and the excellent observers the recordings at BFO are of very high quality. Especially the noise level at BFO is among the lowest values worldwide in the Global Seismographic Network (*Berger et al.*, 2004). Nowadays, more than 25 years of seismic broadband waveforms from BFO are available at data centers (e.g., IRIS Washington or BGR Hannover). This allows us to study weak and rarely occurring seismic signals such as SK(K)S phases. Furthermore, in average these long-term recordings from BFO represent the potentially expected teleseismic ray paths to Central Europe, hence, the expected backazimuthal coverage at seismological stations there (Fig. 7.1, inset in the lower right corner).
The analyzed teleseismic S waves propagate steeply through the upper mantle. The piercing points at the 410 km discontinuity for the SKS, SKKS, and PKS phases recorded at BFO are shown in Fig. 7.1. This distribution includes three major sampled regions in the upper mantle: below the South German block (NE of BFO), below the northern rim of the Swiss Alps (south of BFO) and below the French Vosges Mountains, the URG and the Kaiserstuhl Volcanic Complex (SW of BFO).
There is known seismic anisotropy at different depth levels underneath the region around BFO. Most studies find a prevailing fast wave propagation direction for P and S waves in roughly NE-SW direction. *Lüschen et al.* (1990) analyzed seismic near-vertical reflection data from the Black Forest and they used synthetic anisotropic modeling to explain their observations. As a result, they inferred a laminated lower crust with horizontal anisotropic layers due to alignment of hornblende crystals, with E-W fast P wave direction, NW–SE and NE-SW fast SV wave direction, and fast ESE-WNW SH wave directions. *Eckhardt and Rabbel* (2011) studied teleseismic P-to-S conversions from the Moho and found transversely polarized S waves with a split time of 0.2 s in the crust below BFO. Their observations could be best explained by a ca. 30° fast polarization direction. Underneath the Moho anisotropy was inferred from seismic wide-angle refraction studies by *Fuchs* (1983) and *Enderle et al.* (1996) in SW Germany. Their model has a fast Pn propagation direction of 31° and based on petrological modeling, they suggest a fast shear wave propagation direction of 76°. A similar result of ca. 35° for the fast P wave polarization direction in the

lithospheric mantle was found by *Song et al.* (2004) by inverting travel times of Pn phases.
Vinnik et al. (1994) determined an effective ϕ of 40° and an effective δt of 1.0 s from SKS splitting measurements using BFO recordings that had been averaged over all backazimuths. Later a two-layer upper mantle model was proposed with fast polarization in 10–30° and 80–100° for the upper and lower layers, respectively, based on data from seismic stations around the URG (*Granet et al.*, 1998). *Walker et al.* (2005a) did a careful study of BFO recordings and observed a backazimuthal dependent SKS splitting. They suggest horizontal and dipping layer models for BFO and they also suggest a laterally varying anisotropy in comparison with two neighboring stations (STU Stuttgart to the NE and ECH Échery to the west of BFO). In their conclusions, they propose that there are different fast polarization directions on the eastern and western side of the southern URG with no splitting underneath the URG itself. However, they could not provide a more comprehensive model and propose two options for BFO: either one layer with transverse isotropy with dipping symmetry axis (ϕ = 40–50°, dip ≈ 30–50° or two different two-layer scenarios with transverse isotropy with horizontal symmetry axes (ϕ_1 = 70° ± 5°, δt_1 = (2.3 ± 0.7) s, ϕ_2 = 0° ± 15°, δt_2 = (1.1 ± 0.3) s or ϕ_1 = 90° ± 5°, δt_1 = (1.2 ± 0.4) s, ϕ_2 = 40° ± 5°, δt_2 = (1.4 ± 0.4) s). The results by *Walker et al.* (2005a) demonstrate the problem of non-uniqueness of the anisotropy models derived from SKS splitting observations.
Using 15 splitting measurements, *Walther et al.* (2014) determined a two-layer model with ϕ_1 = 170°, δt_1 = 0.6 s, ϕ_2 = 60°, δt_2 = 1.4 s for BFO that is explained with URG tectonics (upper layer) and an underlying Variscan-like strike direction (lower layer). Recent large-scale studies to determine mantle flow related to Alpine geodynamic processes also indicate a ϕ with NW–SE direction at and around BFO (*Petrescu et al.*, 2020; *Hein et al.*, 2021).
More large-scale models from regional tomography using surface waves also find a possible NE-SW trend for ϕ. For example, the tomography model EU_{60} by *Zhu et al.* (2015) contains relatively low anisotropy below the BFO area compared to surrounding regions with ca. a NE-SW trend in 50–220 km depth.

7.3 Methods and data analysis

We analyzed 25 years of continuously recorded data (July 1991 – October 2016) from BFO. Due to the excellent signal-to-noise conditions at BFO, seismograms could be selected from a total 1166 teleseismic earthquakes with $M_w \geq 6$ and epicentral distances between 90° and 130°. After a visual inspection of the waveforms, *poor* recordings were eliminated and unclear splitting measurements were rejected. This procedure left data from 318 events (Fig. 7.1, inset in the lower right corner) for the final analysis. Splitting parameters were determined using single-event and multi-event techniques and actually represent apparent splitting parameters derived from measurements. In the following, they are just called splitting parameters.
All single-event shear wave splitting measurements were made with the MATLAB based software package *SplitLab* (*Wüstefeld et al.*, 2008) using two different and independent approaches: the rotation-correlation method (hereinafter RC after *Bowman and Ando*, 1987) and the energy minimization method (SC after *Silver and Chan*, 1991). The multi-event analysis was done with the plugin *StackSplit* (*Grund*, 2017) using the methods after *Wolfe and Silver* (1998) and *Roy et al.* (2017). We checked the relative temporal alignment of the single traces (N, E, Z components) regarding an error source in *SplitLab*. For some input options provided by *SplitLab*, the milliseconds or seconds of the starting times of the single traces are ignored. This can lead to a wrong temporal alignment of the different T component traces of an earthquake and by this to wrong shear wave splitting measurements (*Fröhlich et al.*, 2022a). For the error estimation of all measurements, we applied the modified equations by *Walsh et al.* (2013) as implemented in *StackSplit* (*Grund*, 2017) to correctly calculate the required degrees of freedom.
Prior to the actual splitting measurements, all waveforms were filtered with a third-order zero-phase Butterworth bandpass with corner frequencies of 0.01 Hz and 0.2 Hz (in some cases, slightly adjusted to 0.1 Hz) to improve the signal-to-noise ratio (SNR) and the waveform clarity. Although BFO is a relatively low-noise site, the noise level of some SK(K)S phases is quite high (Fig. 7.2, upper two rows). *Non-null* measurements of such noisy records (left

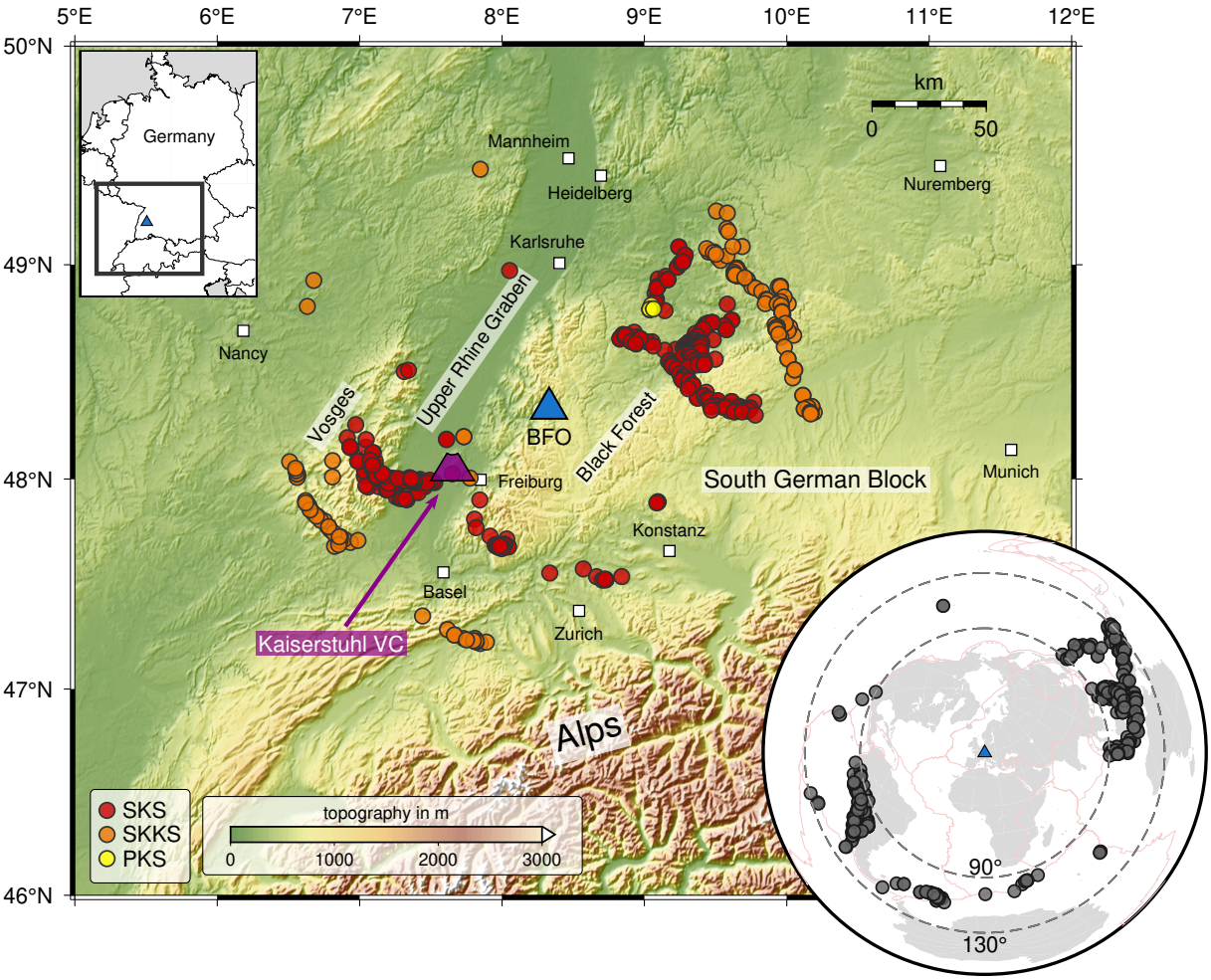

Figure 7.1: Location of the recording station Black Forest Observatory (BFO, blue triangle) in SW Germany and piercing points of SKS (red circles), SKKS (orange circles), and PKS (yellow circles) ray paths at 410 km depth calculated with the *TauP* Toolkit (*Crotwell et al.*, 1999) based on the *iasp91* Earth model (*Kennett and Engdahl*, 1991). The Kaiserstuhl Volcanic Complex (VC) is highlighted in purple. The global map in the lower right corner displays the epicenter distribution (gray circles) for this study. Please note only those events are included for which at least one splitting measurement was obtained rated as *good* or *fair* (single- or multi-event analysis) including *nulls*. For the ray path from the lowermost mantle to the surface as well as SKS-SKKS pairs, see the Supplementary information (Fig. A.4).

panels) were only accepted, if a clear elliptical particle motion is observed in the data and a clear linear particle motion is present after the correction for the splitting (middle panels). In addition, consistent results with the SC and RC methods need to be achieved for records with increased noise including a narrow 95 % confidence interval for both ϕ and δt (right panels). If possible, multi-event analysis techniques (*Wolfe and Silver*, 1998; *Roy et al.*, 2017) were applied to increase the SNR and to achieve stable splitting parameters. In this way, a reliable dataset could be determined (see Sec. 7.4). In the LQT coordinate system (*Plesinger et al.*, 1986), we manually windowed the visible SK(K)S waveform (approx. 20 s) to measure ϕ and δt. The waveform examples in Fig. 7.2 represent typical observations with and without shear wave splitting. The analyzed time window is shaded in gray and phase arrival times for the Earth model *iasp91* (*Kennett and Engdahl*, 1991) are highlighted (Fig. 7.2). The horizontal particle motion is also displayed to visualize a possible shear wave splitting. The simultaneous application of the two different single-event methods (RC and SC) allowed us to cross-check the reliability of the measurements and to rate them using strict quality criteria (e.g., *Wüstefeld and Bokelmann*, 2007). In Fig. 7.2, we display the results from the SC method as energy map for the transverse ground motion. As preferred values for ϕ and δt the minimum of the corrected T energy is selected and the 95 % confidence region of the splitting parameters is used as uncertainty range (gray area in energy maps in Fig. 7.2).

In the following, we report only results for which the SC and the RC methods agree within their error bounds (95 % confidence area) and the SNR is ≥ 7, as recommended, e.g., by *Restivo and Helffrich* (1999). Additionally, we defined a quality categorization for the splitting measurements: *good* means that RC and SC results differ less than 5° for ϕ and 0.2 s for δt as well as that the 95 % confidence region is < 40° for ϕ as well as the uncorrected particle motion is clearly elliptical. If the results are marked as *fair* the two methods RC and SC differ not more than 20° for ϕ and 1 s for δt. Measurements rated as *poor* do not fulfill the above listed criteria, mainly due to too low SNRs. Recordings which have a clear phase arrival on the Q component but no signal on the T component (except low amplitude noise) as well as a clear linear particle motion were classified as *null.* This classification means no splitting of the corresponding SK(K)S phase could be observed. In Fig. 7.3, we present four examples for *null* measurements. These observations cover four different BAZ directions (55.8°, 164.1°, 248.3°, 344.2°) and despite a very clear signal on the Q component (blue dashed), there is no signal on the T component (red solid). The horizontal hodograms in Fig. 7.3 do not indicate an elliptical ground motion that would be expected for a split SKS phase.

To stabilize the results of measurements rated as *poor*, we applied the simultaneous inversion of multiple waveforms (SIMW) method (*Roy et al.*, 2017) as implemented in *StackSplit* (*Grund*, 2017). In this routine, phases of different earthquakes from the same source region (here within a narrow backazimuthal range of 3° and an epicentral distance range of 3°) are concatenated in the time domain. Then, these new traces are simultaneously inverted with the SC method to determine the splitting parameters. These SIMW measurements are included in the *good*/*fair* dataset, if they provide a stable result.

In Fig. 7.1, only events are displayed for which we retained a *good*/*fair non-null* or *null* measurement (single- or multi-event). To smooth the dataset for the modeling, we binned the single-event measurements in 5° backazimuthal intervals using the stacking method after *Wolfe and Silver* (1998). The individual error surfaces of the single-event measurements are summed to generate a set of splitting parameters that represents an average for each defined BAZ bin.

7.4 Observations

In total, we achieved 51 *non-null* (two *good*, 49 *fair*) and 227 *null* measurements from single SK(K)S phases which we rank as reliable. In addition, using SIMW, we receive two *good* and 24 *fair non-null* measurements from combining mostly *poor* single measurements. In addition, the application of SIMW adds another 14 *null* measurements.

The single splitting results are displayed in Fig. 7.4 as stereoplots for five year-long periods and the complete observational period of 25 years. The direction of the bars gives the direction ϕ of the fast polarization axis relative to north which is also color-coded for better visibility. The length of the bars scales with the delay time δt. Details on the *good* and *fair* measured values are listed in the Supplementary information for the single splitting results. The separate results of the different 5-year-long periods indicate that such an observational period is too short to achieve a representative result even for a low-noise recording site such as BFO. This is mainly due to the limitation to specific source regions and the rare concurrency of strong enough earthquakes. For example, from 1992 to 1996, only four reliable splitting measurements are possible. As two measurements have ϕ values of 59° and 67° and two have ϕ values of -10° and 11°, these pairs are nearly perpendicular. Averaging these four values would result in a meaningless value, not representing the true polarization direction and this approach would lead to a wrong (one-layer) anisotropy model. Another clear observation from the 1992–1996 period is the tenfold occurrence of *nulls* compared to split waves, and the *nulls* also cover a wider backazimuthal range. This aspect also has a clear implication: leaving *nulls* out of modeling for anisotropic structure would be misleading, because the observational evidence for anisotropy is weak, although it is well known that *nulls* are predicted for many anisotropic models, see below.

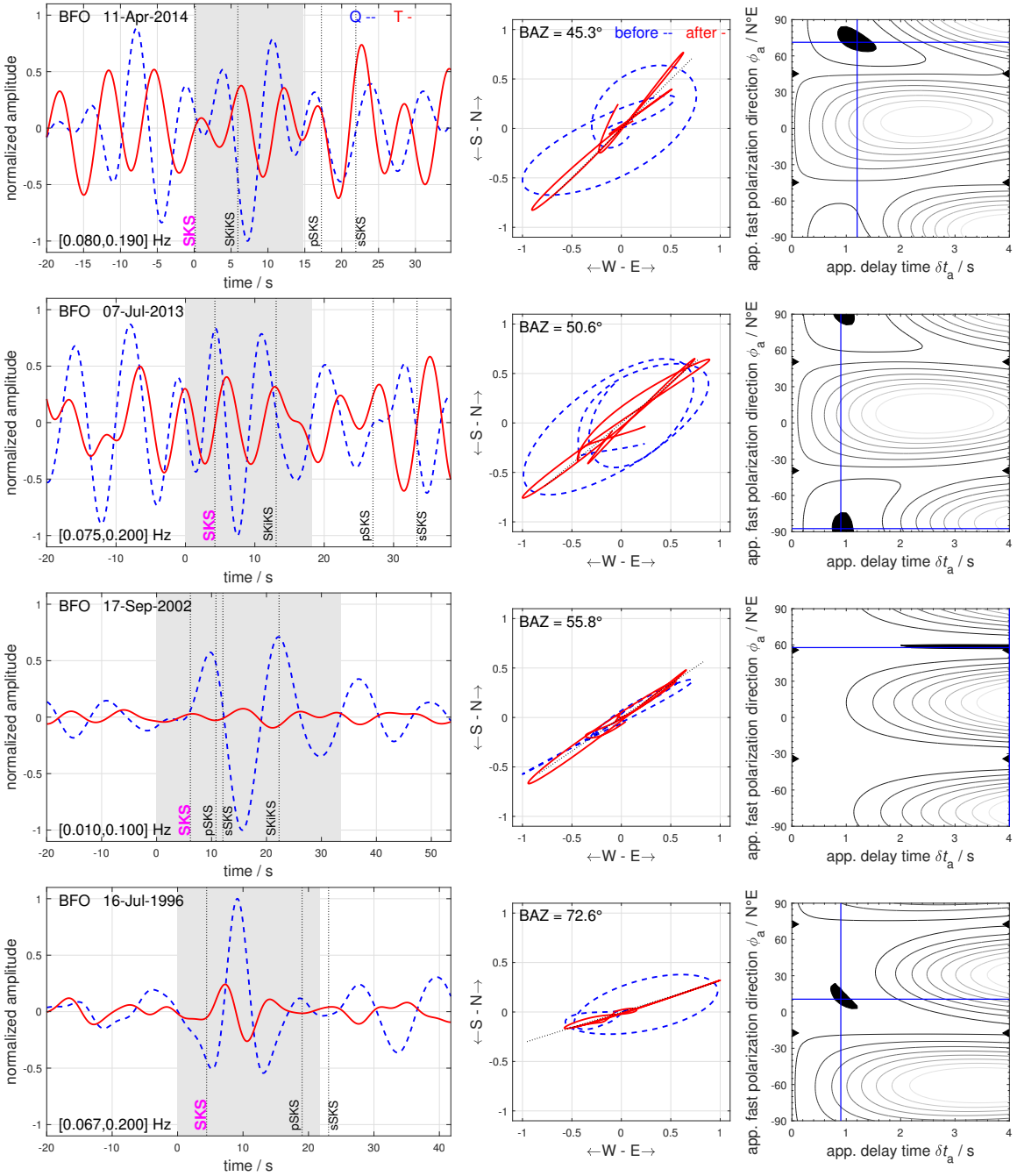

Figure 7.2: Waveform examples, particle motions, and apparent splitting results for SKS phases arriving from the NE back-azimuthal quadrant. The backazimuth (BAZ) increases from 45° (top) to 73° (bottom). Source regions and BAZ: Solomon Islands 45.3°, Papua New Guinea 50.6°, Papua New Guinea 55.8°, Minahassa Peninsula 72.6°. **left**: Waveforms with radial (Q) component (SV-polarization: blue dashed curve) and transverse (T) component (SH-polarization: red solid curve). Theoretical phase arrivals (vertical black dotted lines) are included and the time window in gray indicates the analyzed waveform segments. **center**: Particle motion diagrams of measured (blue dashed) and corrected (red solid) waveforms. **right**: energy maps for the T component displaying the inversion result using the SC method (*Silver and Chan*, 1991). The black area indicates the 95 % confidence interval for the estimated ϕ_a and δt_a values.

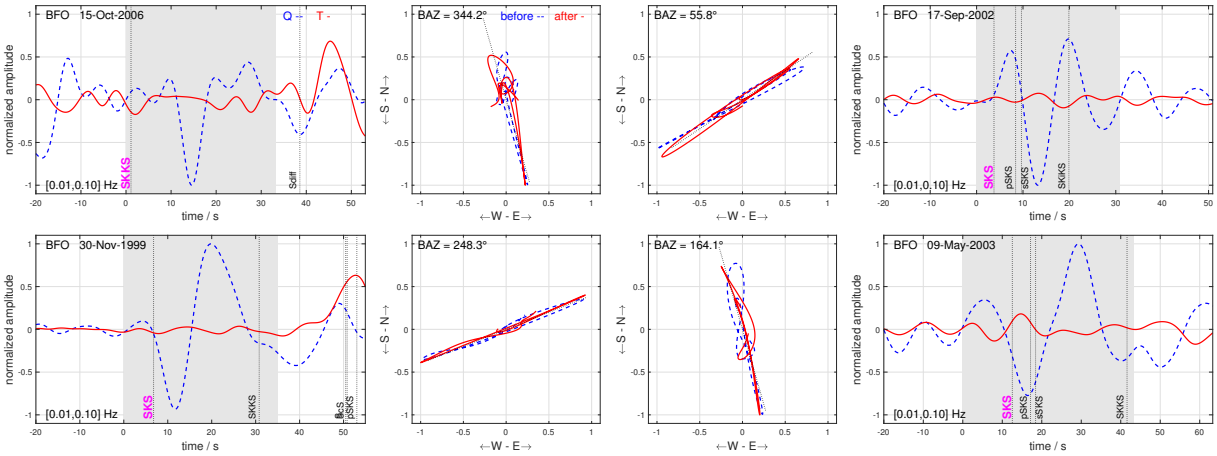

Figure 7.3: Examples for waveforms (dashed blue: Q component with SV-polarization; solid red: T component with SH-polarization) and particle motions (dashed blue: measured; solid red: corrected) of *null split* SKS or SKKS phases arriving from four different backazimuths (BAZ). Source regions and BAZ: Hawaii 344.2°, Papua New Guinea 55.8°, Northern Chile 248.3°, Prince Edwards Islands 164.1°. The particle motion diagrams display a linear polarization along the R or Q component (i.e., the BAZ direction) with measured (blue dashed) and minimally corrected (red solid) waveforms.

The other four observational periods (1997–2001, 2002–2006, 2007–2011, and 2012–2016) also cover only a limited backazimuthal range each. Especially, measurements from backazimuth ranges of 90–180° (SE quadrant) and 270–30° (NW quadrant and NNE range) are rare and this wide range of more than half the complete backazimuthal range is only poorly covered during the 5-year periods.

The 25 years (1992–2016) observational period provides a reasonable basis of SK(K)S splitting measurements including two distinct points of interest (Fig. 7.4): firstly, nearly three-quarters of the BAZ range are dominated by *nulls* (Fig. A.1) and secondly, in the NE range, there seems to be a short-scale flip of the fast polarization axis (Fig. A.2). The SK(K)S phases from events beneath the southernmost Indian Ridge (BAZ 155–180°), southernmost Atlantic Ocean incl. the South Sandwich subduction (BAZ 180–220°), South and Central America, and one in the NE Pacific (BAZ ≈ 340°) do not show a clear splitting. Six exceptions with particularly short δt do not seem to be representative due to the more than 20-fold occurrence of *nulls*. Possibly, these exceptions are due to unrecognized noise or wave scattering effects. The NE quadrant of the 1992–2016 dataset includes a clear rotation of the fast axis direction from around $\phi = 70°$ (green bars) over $\phi = 110°$ (reddish bars) to $\phi = 15°$ (bluish bars) and $\phi = 30°$ (bluish-green bars). In between, we observe a sector (BAZ 60–75°) with more than 50 *null* measurements. Another sector (BAZ ≈ 50°) also contains several *nulls*. The delay time of the split waves is mainly between 1 s and 2 s.

The reproducibility of the measured splitting parameters ϕ and δt is clear from Fig. 7.4. The fast axis directions and delay times (lengths of the bars) are clearly aligned for measurements from the same source region. This correlation is partly due to the rejection of measurements rated as *poor* which may blur the splitting parameter distribution with BAZ. Thus, only clear observations can be accepted to understand the anisotropic structure around a recording site. The determined values ϕ and δt do not differ between SKS and SKKS phases from the same source or source region (Fig. 7.4, time period 1992–2016; Fig. A.4 left). This means that the splitting is probably caused by an anisotropic structure in the upper mantle and that variations of anisotropy in the lowermost mantle (e.g., *Long*, 2009; *Long and Lynner*, 2015; *Deng et al.*, 2017; *Creasy et al.*, 2017; *Grund and Ritter*, 2019) do not seem to play a major role along the different ray paths of these two phases.

7.5 Modeling results and interpretation

To derive a structural anisotropy model for the region around BFO, we first restrict ourselves to the NE quadrant (here BAZ range 30–100°) and then continue with the incorporation of the *nulls* from the other quadrants.

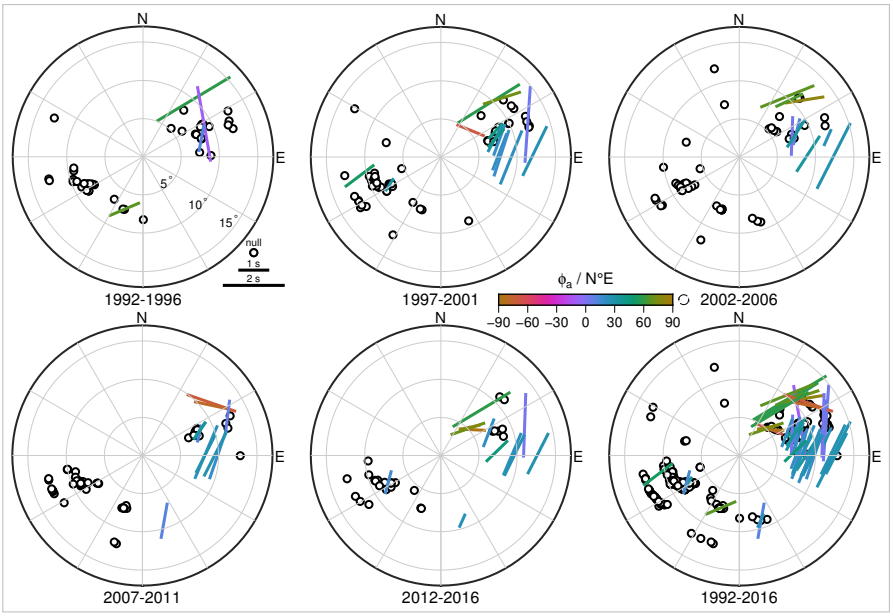

Figure 7.4: Stereoplot representation of all SKS and SKKS splitting measurements at BFO rated with *good* and *fair* with the single-event analysis for different observational periods. Backazimuth is measured clockwise from north; incidence angle is along the radial axis in 5° intervals. The apparent delay time δt_a scales with the length of each bar and the apparent fast polarization direction ϕ_a relative to north is along the direction of the bars and also color-coded. *Null* measurements are marked as white circles with black outline.

The forward modeling or calculation is done based on the equations by *Silver and Savage* (1994) as implemented in the *MATLAB Seismic Anisotropy Toolkit* (MSAT; *Walker and Wookey*, 2012) in a ray theory reference frame. Our azimuthally limited dataset does not allow to constrain complicated models including multiple (> 2) or dipping layers.

The modeling is done with *non-null* measurements of the SC method. *Long and van der Hilst* (2005) and *Vecsey et al.* (2008) showed that the SC method is the more stable technique compared to the RC method. This is consistent to the results of synthetic tests with high SNR data by *Wüstefeld and Bokelmann* (2007). They demonstrated that the splitting parameters are wrongly determined close to the *null* directions assuming one horizontal anisotropic layer. This effect is more severe for the RC method than for the SC method and causes a systematic pattern when the *non-null* results are plotted as function of backazimuth which can be used to determine *null* directions. A crucial point is that ϕ values have 45° slopes over backazimuth and a jump when the backazimuth coincides with the *null* direction. *Eakin et al.* (2019) proposed that for real data with a more realistic SNR of 5–10 also the SC method tends to show such a behavior. *Silver and Savage* (1994) showed that also for two-layer anisotropy, a jump in ϕ can appear for the SC method. Both this slope and a jump for ϕ can be found in our BFO shear wave splitting observations (Fig. A.3).

We limit the tested models to one-layer and two-layer cases with transverse isotropy and with apparent splitting parameters for the two-layer case. A trial-and-error procedure is applied: a systematic sampling of the model space is done with 5° steps for the fast polarization direction and 0.25 s for the delay time of an S wave with a period of 8 s. The predicted or synthetic ϕ and δt values are compared with the measured ones in the relevant backazimuth range. The goodness of fit is evaluated with the estimated root mean square error (RMSE) of the differences $\Delta\phi_i$ and $\Delta\delta t_i$ between the model curve and the individual measured data points $i = 1, ..., N$. At first, the RMSE is calculated separately for ϕ and δt:

$$\mathrm{RMSE}_\phi = \sqrt{\frac{1}{N}\sum_i^N (\Delta\phi_i)^2} \tag{7.1}$$

$$\mathrm{RMSE}_{\delta t} = \sqrt{\frac{1}{N}\sum_i^N (\Delta\delta t_i)^2} \tag{7.2}$$

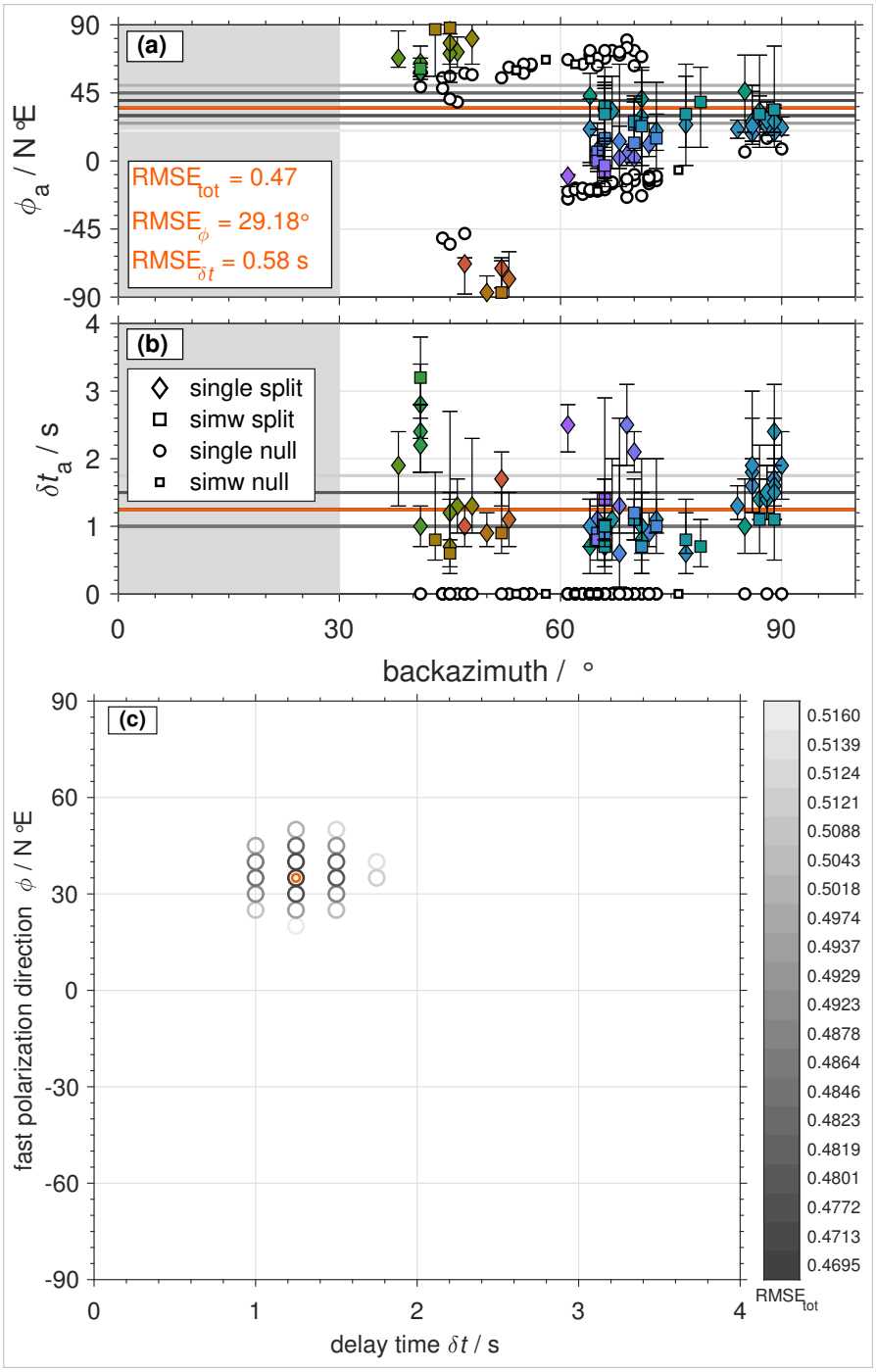

Figure 7.5: The 20 best-fit one-layer models for all *good* and *fair* measurements in the NE quadrant (30–100° BAZ). **a** Apparent fast polarization direction ϕ_a, **b** apparent delay time δt_a. The color-coding of the symbols of the measured data corresponds to the colormap for ϕ_a used in Fig. 7.4. The 20 best-fit model parameter combinations are shown in **c** with their corresponding RMSE (gray colormap). The best-fit model is highlighted in orange (minimum $\mathrm{RMSE_{tot}}$). Note that several of the curves with the forward calculated splitting parameters in a and b lie atop each other even if the anisotropy models are partly different in c. Note that the *nulls* are not included in the modeling, but shown in a and b as white circles for the sake of completeness with δt_a manually set to zero.

Then, these RMSE values are normalized (*Liddell et al.*, 2017) and summed to get a joint total value

$$\mathrm{RMSE_{tot}} = \frac{1}{90°}\mathrm{RMSE}_\phi + \frac{1}{4\ \mathrm{s}}\mathrm{RMSE}_{\delta t} \tag{7.3}$$

in the following just called RMSE. The models with the smallest $\mathrm{RMSE_{tot}}$ errors are assumed as the best-fit ones. Due to the limited resolution of our measurements and the sensitivity of the theoretical results on small changes of the input ϕ and δt values, we first examine the 20 best-fit models to estimate the stability of this approach. Only single splitting and SIMW results which have the quality *good* or *fair*, are used for the modeling. Besides fitting the *good* and *fair* splitting measurements (Figs 7.5, 7.6), also a reduced dataset with average values in 5° BAZ intervals is used (Figs 7.7, 7.8). This 5° smoothed dataset avoids the over-representation of data points within some BAZ ranges during the calculation of model parameters and RMSE.

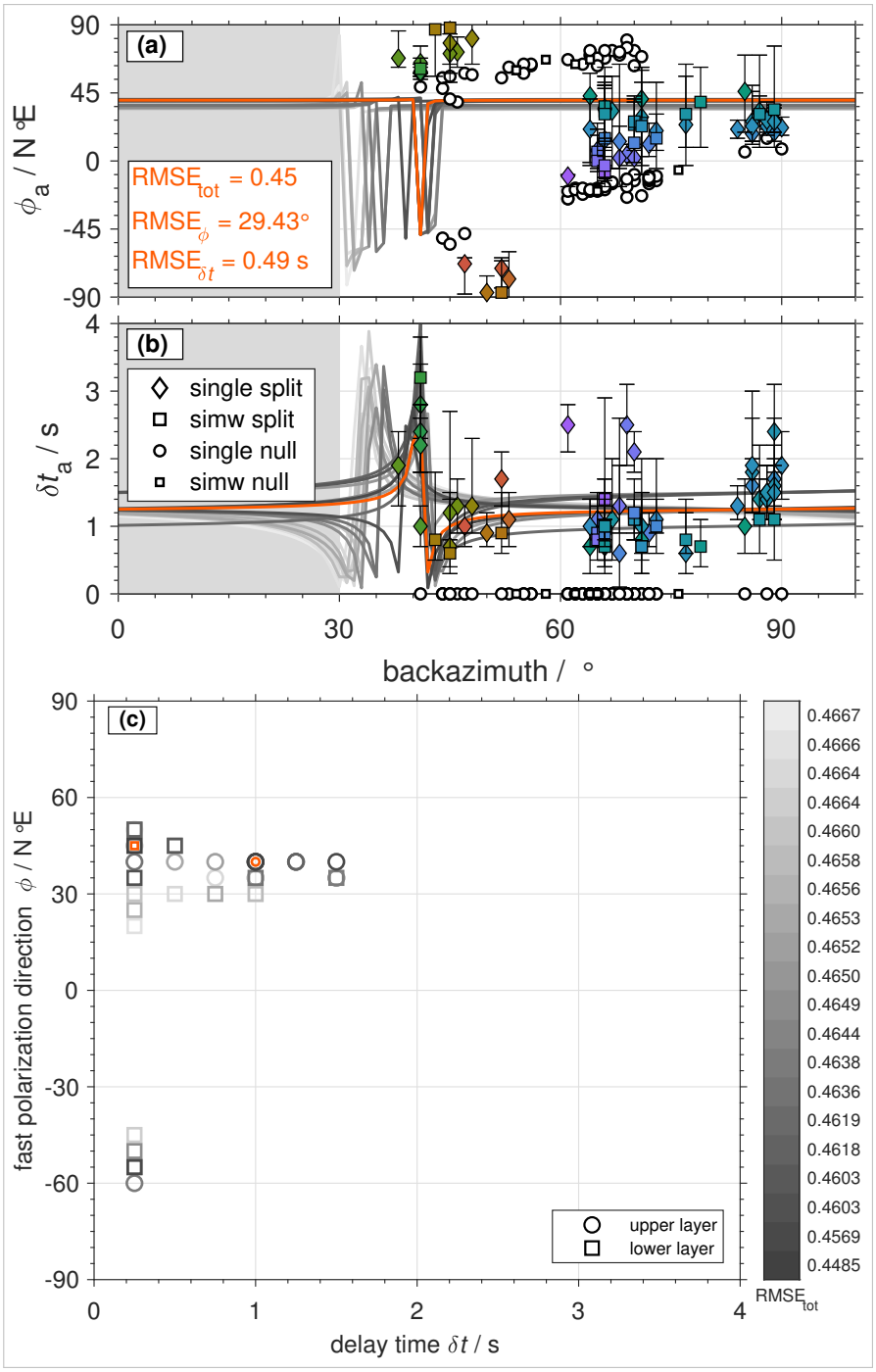

Figure 7.6: The 20 best-fit two-layer models for all *good* and *fair* measurements in the NE quadrant (30–100° BAZ). **(a)** Apparent fast polarization direction ϕ_a, **(b)** apparent delay time δt_a, and **(c)** model parameter combinations. Symbols and colors as in Fig. 7.5.

7.5.1 All measurements

For the NE quadrant (BAZ 30–100°) the one-layer modeling in Fig. 7.5 provides a stable result for a fast polarization axis of the medium in direction 35° and a time delay of 1.25 s. However, there are no observed *nulls* in the modeled fast polarization direction 35° as expected from theory, but *nulls* are observed in directions between 55° and 75°. The 20 best-fit models vary by ca. ± 20° in ϕ and ± 0.25 s in δt. The RMSE is about 0.5 with a minimum at 0.47. For the two-layer modeling with all *good* and *fair* splitting measurements (Fig. 7.6), we get similar RMSE values of ca. 0.46 for the 20 best-fit models. It is obvious that no theoretical curve for two-layer models fits very well the distributions of the measurements. The best model (orange curve with lowest RMSE) does reasonably well fit δt, but the fit to ϕ is poor. The upper layer (ϕ = 40° and δt = 1 s) has similar results as the one-layer model and the lower layer is not much different (ϕ = 45° and δt = 0.5 s). This is partly due to the uneven distribution of the

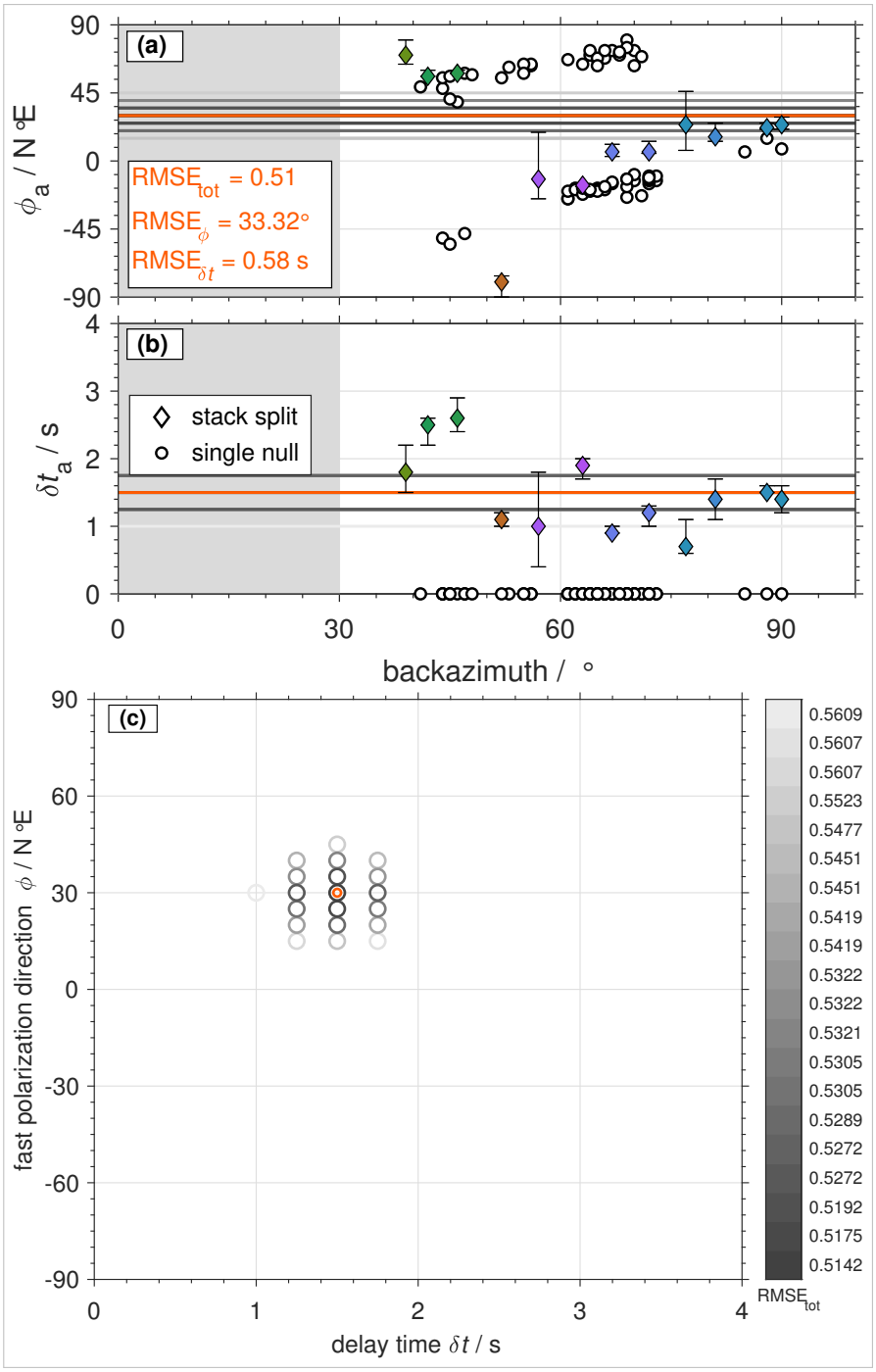

Figure 7.7: The 20 best-fit one-layer models for the 5° BAZ binned dataset in the NE quadrant (30–100° BAZ). **(a)** Apparent fast polarization direction ϕ_a, **(b)** apparent delay time δt_a, and **(c)** model parameter combinations. Symbols and colors as in Fig. 7.5. Note that the *nulls* are not binned.

measurements over backazimuth: modeling and RMSE determination are dominated by the data points between BAZ directions 60° and 90°.

7.5.2 5° bins

To avoid an over-representation of specific BAZ directions in the NE quadrant, we stacked the splitting parameters in 5° bins. This stacking results in a smooth representation of the ϕ and δt measurements (Figs 7.7 and 7.8) that should allow a better model fitting procedure.

The one-layer models are not appropriate to fit the measurements (Fig. 7.7), because they do not properly fit the BAZ variation of ϕ and δt. The lowest RMSE reaches 0.51 for the one-layer case. The minimum RMSE is 0.36 for

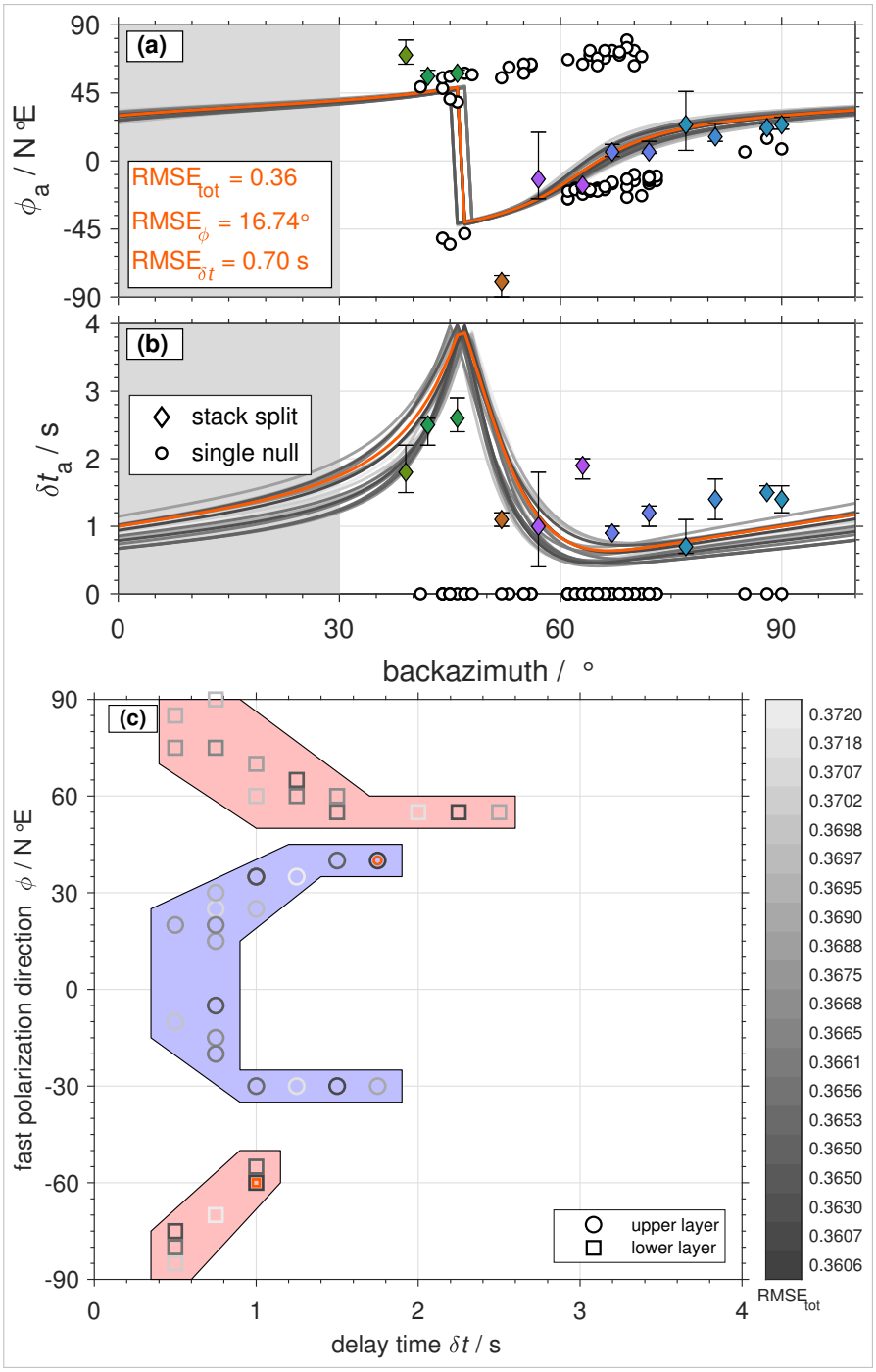

Figure 7.8: The 20 best-fit two-layer models for the 5° BAZ binned dataset in the NE quadrant (30–100° BAZ). **a** Apparent fast polarization direction ϕ_a, **b** apparent delay time δt_a, and **c** model parameter combinations. The light red and blue ranges outline the model parameter ranges covered by the 20 best-fit models for the lower and upper anisotropic layers respectively. Symbols and colors as in Fig. 7.5.

the two-layer modeling, so ca. 30 % lower than for the one-layer case. The two-layer modeling results provide a much better fit for both, ϕ and δt (Fig. 7.8a,b). The main BAZ variation of ϕ is well matched (Fig. 7.8a) and the extrema of the predicted δt values are also recovered (Fig. 7.8b). The observed *nulls* at ca. 60-75° BAZ (Fig. 7.4) are close to the predicted minimum of δt Fig. 7.8a and the *nulls* at ca. 45° BAZ are at the predicted maximum of δt (Fig. 7.8a) which coincides with the theoretical "*null*" direction for the two-layer case (*Silver and Savage*, 1994). Our observed jump in ϕ (SC method) of around $\pi/2$ appears to be larger than the synthetic error or jump for a one-layer anisotropy model proposed by *Eakin et al.* (2019; Fig. 7.7). It better coincides with the change in ϕ given in *Silver and Savage* (1994; Fig. 7.8a).

Surprisingly, the model parameter distribution of the 20 best-fit models in Fig. 7.8c has a quite large scatter with regard to the small changes in RMSE (bluish and reddish areas). The upper (second) layer has a fast polarization

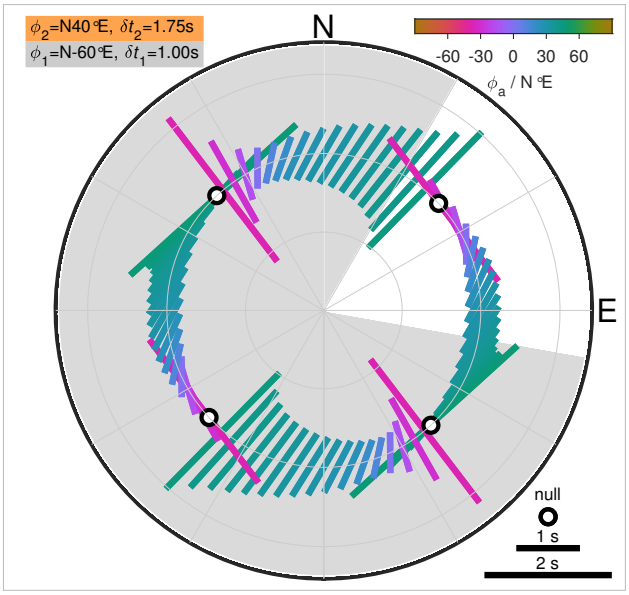

Figure 7.9: Forward calculated theoretical splitting parameters for the best-fit two-layer anisotropy model in the NE quadrant (lower layer: $\phi_1 = -60°$ and $\delta_1 = 1.0$ s, upper layer: $\phi_2 = 40°$ and $\delta t_2 = 1.75$ s; see Fig. 7.8). The dominant period is 8 s. The gray shaded area is not included in the model search (see text). The mainly *null* observations (see Fig. 7.4) do not fit to the prediction for the gray backazimuthal range, indicating a lateral variation of the anisotropy.

direction of ca. 30° for $\delta t_2 > 0.5$ s. The lower (first) layer has a fast polarization direction of ca. 50–60° for $\delta t_1 > 0.5$ s, but reasonable fits can also be achieved for a wide range of ϕ_1 around 90°. The synthetic effective splitting parameters for he best-fit model (upper layer: $\phi_2 = 40°$ and $\delta t_2 = 1.75$ s, lower layer: $\phi_1 = -60°$ and $\delta t_1 = 1.0$ s) are shown in Fig. 7.9. Compared to the measured data in Fig. 7.4, there is very good coincidence including the flip of the polarization direction and the position of the *nulls* in the NE quadrant.

7.5.3 *Null* measurements

The very wide backazimuthal range of *nulls* at BFO (Fig. 7.4) is still puzzling because (i) it covers 155–335° BAZ, so half of the incoming directional range, and (ii) it is completely contrary to the observed splitting pattern within 30–100° BAZ. Since *null* measurements are not always unique (*Wüstefeld and Bokelmann*, 2007), we carefully looked at the waveforms to confirm the missing signal on the T component for well-observed SK(K)S phases on the Q component. The following consideration may guide future studies to better understand this observation which we tentatively call the *null anomaly*:

(a) Compared to the NE quadrant the upper mantle structure underneath the other quadrants around BFO must be completely different, because the predicted splitting pattern in Fig. 7.9 would allow only three other distinct narrow backazimuthal ranges with *nulls*, so contrarily to our observations. An exception would be a model with two layers, which lie on top of each other and which have (nearly) identical delay times but orthogonal fast polarization directions. Such a constellation would cancel the splitting effects and *nulls* would be observed (*Liu and Gao*, 2013). Few available regional studies do not support such a setting for the Upper Rhine Graben region (*Granet et al.*, 1998; *Walker et al.*, 2005a; *Walther et al.*, 2014).

(b) Other simple anisotropy models with transverse isotropy in a horizontal plane also seem to be unrealistic, because one-, two- and even three-layer scenarios would predict wide ranges without *nulls*. These ranges are not observed. This holds also for one-layer models with a dipping symmetry axis.

(c) *null* measurements on nearly vertically propagating SKS phases can hint towards a fast axis direction in vertical direction, e.g., due to an upward mantle flow or a specific olivine CPO fabric type. Such a flow pattern may be related to the Miocene uplift of the Black Forest, the Vosges Mountains, and possibly the local mantle upwelling underneath the Kaiserstuhl Volcanic Complex (Fig. 7.1). One may also speculate that previously existing anisotropic fabrics in the lower lithosphere and asthenosphere were overprinted

by such vertically oriented processes. Beside the commonly assumed A-type CPO fabric, other olivine CPO fabric types, like the C-type may be present. It has been shown in experimental studies that the quite complex CPO of olivine depends on stress, water content, temperature, and pressure conditions (*Jung et al.*, 2006; *Skemer and Hansen*, 2016). The assumption of A-type olivine CPO, i.e., a horizontally orientated olivine a-axis in the direction of maximum shear, is (only) valid for dry olivine aggregates (*Long and Silver*, 2009; *Long and Becker*, 2010). The C-type, i.e., a vertically orientated olivine a-axis, occurs at moderate to high water content and high temperature. Such conditions could be related to mantle magmatism of the Kaiserstuhl Volcanic Complex. Since the propagation velocity difference between the olivine b-axis ([010]) and c-axis ([001]) is small, nearly vertically propagating SKS phases experience only a weak anisotropy effect and by this show only weak to no shear wave splitting. This may result in the observation of reduced or small delay times or numerous *nulls*. However, such reasoning should be supported by further high-resolution regional studies.

(d) The medium related to the *null anomaly* may be very weakly anisotropic and the related wave effects may be close to the limit of detection. However, even SKS phase observations with a high SNR of the Q component do not show a split phase on the T component recording with a relatively low-noise level (Fig. 7.3).

(e) The medium may be isotropic (or nearly isotropic). This seismic isotropy could either be a pristine structural characteristic which is most possibly not reasonable, because the surrounding regions, mostly also of Variscan origin, have well-resolved anisotropy (*Walker et al.*, 2005a; *Walther et al.*, 2014).

(f) Another option may be wave scattering effects due to strong heterogeneities that diffuses the, in general, already small wave amplitudes of the T component but leaving the R or Q component unaffected. The structure of the lithosphere and the asthenosphere underneath the southern Black Forest and the southern URG were possibly reworked during the rifting processes and the Kaiserstuhl magmatism (*Ziegler et al.*, 2004) that may have imprinted structural heterogeneities. However, the question is open why the R or Q component recordings remain unscattered.

(g) At the seismological station DBIC (Côte D'Ivoire), a similar splitting pattern can be observed as at BFO with *splits* only in a limited backazimuth range and for the rest mainly *nulls* (*Lynner and Long*, 2012). These authors explain this by lowermost mantle anisotropy for the observed *splits* and a nearly isotropic or apparently isotropic upper mantle for the *nulls*. An influence of anisotropy and splitting effects from the lowermost mantle cannot explain the *null anomaly* at BFO. Both phases, SKS and SKKS, are dominated by *nulls* within 155–355° BAZ and we do not observe clear discrepancies of the *split* or *null* signals between SKS and SKKS phases (Fig. A.4 right) as in *Long and Lynner* (2015).

Based on the currently available observations at BFO, the mystery about the *nulls* is not yet solved and similar studies need to be done analyzing long-term recordings from surrounding seismological stations. This is work under way in our research group.

7.6 Discussion and conclusions

We observe 77 *splits* of SK(K)S phases and 241 *null splits* at the high-quality recording seismological station BFO, SW Germany. This plenty of measurements was only possible because continuous recordings from 25 years were carefully and manually checked and the splitting analysis was assigned to strict quality measures. Our 77 plus 241 observations are much more than reported in other studies. A comparison of different time periods (Fig. 7.4) indicates that five or even 10 years of continuous recording may be too short to obtain representative splitting

observations in Central Europe, because SK(K)S phases from different backazimuths may not be available. Thus, very long observational records are required to gain a reasonable backazimuthal coverage which allows to resolve backazimuthal variations of SK(K)S splitting and by this both vertical and lateral variations in the anisotropy.
For three-fourths of the backazimuth range, we find that *null* measurements dominate at BFO. However, there is no structural anisotropy model which can explain this observation yet. It is necessary to conduct similar precise shear wave splitting measurements at surrounding seismological stations to better locate this *null anomaly* and possibly its depth extension. On the contrary, dense splitting observations in the NE quadrant of BFO contain a complete flip of the fast polarization axis at around 50° BAZ. This flip is currently explained best with a two-layer model with fast polarization directions of ϕ_2 = 40° (upper layer) and ϕ_1 = -60° (lower layer) (Figs 7.8, 7.9). The RMSEs for the 20 best-fit two-layer models are very similar but the large scatter of their determined model parameters may point to a considerable uncertainty (±10–20° for ϕ and ± 0.5 s for δt) even for the observationally well-covered NE backazimuthal range.
The observed backazimuthal variations of ϕ and δt at BFO do clearly not allow a backazimuthal averaging of the splitting parameters of all (*good* and *fair*) splitting measurements for the determination of a laterally homogeneous anisotropy model that was mainly done in the past. The averaging even across small backazimuthal gaps without observations may be misleading (Fig. 7.4), because short-scale changes of the splitting parameters (Fig. 7.9) can occur which might be due to both, vertical and lateral, variations of the anisotropy at depth. Such small-scale variations of the splitting parameters are also observed in other regions (e.g., *Bastow et al.*, 2007). Thus, small-scale laterally varying anisotropy may play a more important role in the study region than previously thought.
For temporary measurements, at least in Europe with limited backazimuth observations, we propose to include long-term recordings from permanent stations in the study region (see, e.g., *Grund and Ritter*, 2020). Then, subareas with similar splitting patterns should be outlined, e.g., based on ray paths or piercing points of the split phases. Only for those subareas with identical splitting pattern for crossing ray paths, a structural modeling should be conducted to resolve local lateral anisotropy instead of a station-wise modeling. Of course, a 3-D anisotropic wave propagation modeling (*Tesoniero et al.*, 2020) may be preferred for the rare cases with enough azimuth-dependent observations.

Acknowledgments.
We thank the scientific and technical staff at the Black Forest Observatory (BFO) for running the highly sensitive seismological instruments. Waveforms were requested from the EIDA center at the (Bundesanstalt für Geowissenschaften und Rohstoffe (BGR), Hannover). All geographic maps were prepared with *PyGMT*, the Python wrapper of the *Generic Mapping Tools* (*GMT*; *Wessel et al.*, 2019). A *Jupyter* Notebook using *PyGMT* v0.3.0 (*Uieda et al.*, 2021) and *GMT* 6.1.1 (*Wessel et al.*, 2020) to reproduce the map in Fig. 7.1 is available from MG's GitHub account (`https://github.com/michaelgrund/GMT-plotting`). *Jupyter* Notebooks using *PyGMT* v0.7.0 (*Uieda et al.*, 2022) and *GMT* 6.4.0 (*Wessel et al.*, 2022) to reproduce the maps in Fig. A.4 are available from YF's GitHub account (`https://github.com/yvonnefroehlich/gmt-pygmt-plotting`). All other figures were generated with MATLAB R2020b and R2022a. The shear wave splitting analysis was done using *SplitLab* (*Wüstefeld et al.*, 2008) version 1.2.1 by *Porritt* (2014) and *StackSplit* (*Grund*, 2017) version 2.0 (`https://github.com/michaelgrund/stacksplit`). A modified *SplitLab* code function is available from YF's GitHub account (`https://github.com/yvonnefroehlich/SplitLab-TemporalAlignment`). The forward calculation of the splitting parameters for the synthetic anisotropy models was done using the *MATLAB Seismic Anisotropy Toolkit* (MSAT; *Walker and Wookey*, 2012). MATLAB functions to generate the stereoplot representation as well as to perform the shear wave splitting modeling are available from YF's GitHub account (`https://github.com/yvonnefroehlich/sws-visualization-and-modeling`). These functions are extended from the ones used in *Grund and Ritter* (2020), available from MG's GitHub account (`https://github.com/michaelgrund/sws_tools`). Shear wave splitting measurements of *good* and *fair* qualities are available as CSV and PDF files in the Supplementary information as well as from *RADAR4KIT*

(https://doi.org/10.35097/684). The piercing points (Fig. 7.1, Fig. A.4) were calculated after the *iasp91* Earth model (*Kennett and Engdahl*, 1991) with the MATLAB Toolkit *MatTaup* by Qin Lin based on the original *TauP* Toolkit (*Crotwell et al.*, 1999). Color-coding was accomplished using the phase colormap from the *cmocean* colormaps (*Thyng et al.*, 2016) as well as the *grayC* colormap from the *Scientific colour maps* version 7.0.0 (*Crameri*, 2021). YF is supported by a scholarship of the Graduate Funding from the German States (Landesgraduiertenförderung, LGF). JR was partly supported by the Deutsche Forschungsgemeinschaft (DFG) by grant RI1133/13-1 within the framework of DFG Priority Programme "*Mountain Building Processes in Four Dimensions (MB-4D)*" (SPP 2017). We acknowledge support by the KITPublication Fund of the Karlsruhe Institute of Technology. We thank Caroline M. Eakin and Maureen D. Long for their very constructive and helpful reviews that helped to improve this manuscript.

Author contributions[14]

JR wrote the first version of the manuscript. YF controlled the shear wave splitting measurements (SWSMs), carried out the forward modeling, generated all figures (expect Fig. 7.1), helped with writing the manuscript, and prepared the Supplementary information as well as the SWSMs dataset published on RADAR4KIT. JSA initially carried out the SWSMs. MG created the map in Fig. 7.1 and helped with proofreading the manuscript.

Statements and declarations.

The authors declare no competing interests.

Funding.

Open Access funding enabled and organized by Projekt DEAL.

[14] Added for this doctoral thesis, but not included in the actual publication.

8 Application to Multiple Recording Stations: The Upper Rhine Graben Area

The content presented in this chapter has been published in

> ***Fröhlich Y.***, Grund M. & Ritter J. R. R. (2024).* **Lateral and vertical variations of seismic anisotropy in the lithosphere-asthenosphere system underneath Central Europe from long-term splitting measurements**. *Geophysical Journal International*, 239(1):112-135. https://doi.org/10.1093/gji/ggae245.

The dataset of the related shear wave splitting measurements is available at (App. **D.2**):

> ***Fröhlich Y.***, Grund M. & Ritter J. R. R. (2024).* **Longterm Shear Wave Splitting Measurements in the Upper Rhine Graben Area**. *RADAR4KIT*. https://dx.doi.org/10.35097/685.

The supplementary material published along with this research article can be found in App. **B**.

Abstract

Backazimuthal variations in the shear wave splitting of core-refracted shear waves (SKS, SKKS and PKS phases, jointly referred to as *X*KS) at the Black Forest Observatory (BFO, Southwest Germany) indicate small-scale lateral and partly vertical variations of the seismic anisotropy. However, existing anisotropy studies and models for the nearby Upper Rhine Graben (URG) area in the northern Alpine foreland are mostly based on short-term recordings and by this suffer from a limited backazimuthal coverage and averaging over a wide or the whole backazimuth range. To identify and delimit laterally confined anisotropy regimes in this region, we carry out *X*KS splitting measurements at six neighbouring (semi-)permanent broad-band seismological recording stations (interstation distance 10-80 km). We manually analyse long-term (partly > 20 yr) recordings to achieve a sufficient backazimuthal coverage to resolve complex anisotropy. The splitting parameters (fast polarization direction ϕ, delay time δt) are determined in a single- and multi-event analysis. We test structural anisotropy models with one layer with horizontal or tilted symmetry axis and with two layers with horizontal symmetry axes (transverse isotropy). To account for lateral variations around a single recording site, modelling is compared for the whole and for limited backazimuth ranges. Based on this, we provide a 3-D block model with spatial variation of anisotropic properties. Based on delay times > 0.3 s and missing discrepancies between SKS and SKKS phases, which do not support lower mantle anisotropy, the found anisotropy is placed in the lithosphere and asthenosphere. The spatial distribution as well as the lateral and backazimuthal variations of the splitting parameters confirm lateral and partly vertical variations in anisotropy. On the east side of the URG, we suggest two anisotropic layers in the Moldanubian Zone (south) and one anisotropic layer in the Saxothuringian Zone (north). In the Moldanubian Zone, a change of the fast polarization directions is observed between the east and the west side of the URG, indicating different textures. At the boundary between the two terranes, an inclined anisotropy is modelled

which may be related with deformation during Variscan subduction. Regarding the observation of numerous *null* measurements and inconsistent splitting parameters, especially (southwest of BFO) in the southern URG, different hypothesis are tested: scattering of the seismic wavefield due to small-scale lateral heterogeneities, a vertical a-axis due to a vertical mantle flow related to the Kaiserstuhl Volcanic Complex, as well as a different preferred orientation of the olivine crystals (not A-type, but C-type) due to specific ambient conditions (high temperature, water content).

Keywords: Europe | Numerical modelling | Body waves | Seismic anisotropy | Wave propagation | Dynamics of lithosphere and mantle

8.1 Introduction

To investigate the mantle, shear wave splitting measurements on core-refracted shear waves (mainly SKS, SKKS and PKS phases, jointly referred to as *X*KS) are well suited to map horizontal variations of seismic anisotropy. The interest in elastic or seismic anisotropy is based on its connection to geological and tectonic processes in the Earth's interior (*Silver and Chan*, 1991). Dynamic-driven rock deformations lead to a preferred orientation of structures or crystals in the medium. This includes sedimentary layering and parallel cracks in the crust as well as melt-filled structures, so-called shape preferred orientation (SPO), and mostly the alignment of intrinsically anisotropic minerals, so-called latticed or crystal preferred orientation (LPO, CPO), in the mantle (*Savage*, 1999; *Long and Silver*, 2009). The deformation can be explained by recent and ancient crustal stress, the last significant tectonic event (*Silver*, 1996) or a mantle flow pattern (*Long and Becker*, 2010). Therefore, studying anisotropy in the Earth's upper mantle (e.g., *Margheriti et al.*, 2003; *Aragon et al.*, 2017; *Grund and Ritter*, 2020) and lowermost mantle (e.g., *Lynner and Long*, 2012; *Deng et al.*, 2017; *Grund and Ritter*, 2019; *Reiss et al.*, 2019; *Asplet et al.*, 2020) provides crucial constraints on past (fossil, frozen-in) and present deformation processes (*Silver*, 1996) as well as the recent mantle flow (*Long and Becker*, 2010).

By propagating through an anisotropic medium, a linearly polarized shear wave (S wave) is split into two orthogonally polarized quasi shear waves (qS waves). These are polarized in the fast and the slow axis directions of the anisotropic medium, except the initial S wave is polarized in the direction of the fast or the slow axis (*Savage*, 1999; *Long and Silver*, 2009). According to the different propagation velocities in the anisotropic medium, the two qS waves develop a travel time difference, which is preserved after leaving the anisotropic medium. The related shear wave splitting (SWS, analogue to birefringence in optics) can be measured in seismograms by the determination of the two splitting parameters, fast polarization direction ϕ given relative to north and delay time δt accumulated between the two qS waves (*Bowman and Ando*, 1987; *Silver and Chan*, 1991) as well as the splitting intensity (*Chevrot*, 2000).

Often a simple homogeneous one-layer model with transverse isotropy with a horizontal symmetry axis is used to explain the splitting observations. In contrast to this *simple anisotropy*, lateral or vertical variation, a tilted symmetry axis, or a lower symmetry class of the anisotropy are called *complex anisotropy*. It causes splitting parameters which are characterized by a variation with the initial polarization direction (for *X*KS phases equivalent to the backazimuth direction). Thus, the measured splitting parameters are at first apparently measured splitting parameters and do not directly represent the anisotropy in the subsurface. Corresponding to this a separate modelling is required based on the backazimuthal variation of the apparent splitting parameters. By this a wide and dense observational backazimuthal coverage is needed to model complex anisotropy reliably and unambiguously. Seismic anisotropy studies in general suffer from a limited backazimuthal coverage. For instance, studies with teleseismic *X*KS phases are often limited due to large backazimuthal observational gaps and often consist of only a few SWS measurements due to limited source regions (mainly plate boundaries). Additionally, due to small signal amplitudes and low signal-to-noise ratios (SNR) only a limited number of the recorded seismograms

contain clear *X*KS signals. The situation is especially unfavourable, if only a time-limited dataset (1-3 yr) is available, for example from a temporary network. Averaging the (apparent) splitting parameters over a wide or the whole backazimuth (BAZ) range suppresses any existing backazimuthal variation of the (apparent) splitting parameters and assumes or even reinforces *a priori* a simple anisotropy constellation, which is mostly a vital oversimplification.

At the Black Forest Observatory (BFO, SW Germany; Fig. 8.1) SWS measurements reveal clear backazimuthal variations (Fig. B.6; *Walker et al.*, 2005a; *Ritter et al.*, 2022; *Link and Rümpker*, 2023). In the northeastern quadrant, the backazimuthal variations of the splitting parameters is currently explained by a structural anisotropy model with two layers with transverse isotropy with horizontal symmetry axes, extending into the lithospheric and asthenospheric mantle. In contrast the *X*KS phases from the west do not show (clear) shear wave splitting (*Ritter et al.*, 2022). Such completely different observations at a single recording site are a strong indication for small-scale lateral variation in the anisotropy. However, most of the existing seismic anisotropy studies using *X*KS phases and the derived anisotropy models for the upper mantle beneath the Upper Rhine Graben (URG) area are based on short-term recordings (e.g., *Vinnik et al.*, 1994; *Brechner et al.*, 1998; *Granet et al.*, 1998; *Walker et al.*, 2005a; *Walther et al.*, 2014). Thus, they suffer from a limited backazimuthal coverage and averaging over a wide or the whole BAZ range. Recent anisotropy models based on a dense temporal recording experiment (*AlpArray* network; *Hetényi et al.*, 2018) are characterized by a uniform fast polarization direction without (small-scale) lateral variations across the wider URG region (*Petrescu et al.*, 2020; *Hein et al.*, 2021). *Link and Rümpker* (2023) attribute the URG area to a common region anisotropic average with only slightly varying anisotropy. Overall, contrasting observations and models are not explained and there is no appropriate consideration of the regional complex anisotropy until now. Single splitting observations are not as uniform as published anisotropy models would predict. In addition, the missing splitting observations west of BFO are still puzzling. Here we present new investigations for a better understanding of the seismic anisotropy in the mantle beneath the Upper Rhine Graben area, especially regarding lateral variations.

In this paper, the lithosphere-asthenosphere system beneath the Upper Rhine Graben area is investigated (Sec. 8.2). We measure the SWS of *X*KS phases in long-term recordings (partly > 20 yr) from six nearby (interstation distance 10-80 km) (semi-)permanent broad-band seismological recording stations (Sec. 8.3). This exceptional dataset allows us to study complex anisotropy, including small-scale lateral variations around the recording sites (Sec. 8.4). Since vertical and lateral variations are taken into account (Sec. 8.5), we can derive a first suggestion of a 3-D block model of the seismic anisotropy underneath the Upper Rhine Graben area (Sec. 8.6). This approach may also be applicable for other regions where anisotropy may be more complex than currently thought.

8.2 Geodynamic setting

The Upper Rhine Graben (URG) is part of the European Cenozoic Rift System (*Schwarz and Henk*, 2005; *Grimmer et al.*, 2017). It developed in the aftermath of the Alpine collision in the south which caused a change in the (regional) stress field. The evolution of the URG in the northern Alpine foreland began 47 Myr ago due to a re-activation of the pre-existing Variscan shear zones (*Grimmer et al.*, 2017). The NNE striking continental graben between Basel in the south and Frankfurt am Main in the north is approximately 300 km long and in average 30-40 km wide (Fig. 8.1). The total crustal extension of the URG is 5-8 km and the overlaying rift sediments have a thickness of up to 3.5 km. The asymmetry of the URG is deduced from the thicker sediments in the east than in the west. Volcanic activity occurred in the Middle Miocene at the Kaiserstuhl Volcanic Complex (KVC) in the south near Freiburg and the Vogelsberg Volcanic Complex (VVC) north of Frankfurt (*Ring and Bolhar*, 2020). Apart from this, only a few very small volcanic centres are documented on the rift shoulders. The crust-mantle boundary (Mohorovičić discontinuity, Moho) is presumably nearly flat in 28 km depth (*Prodehl et al.*, 1992) and the lithosphere-asthenosphere boundary (LAB) is assumed in 60-80 km depth (*Seiberlich et al.*, 2013).

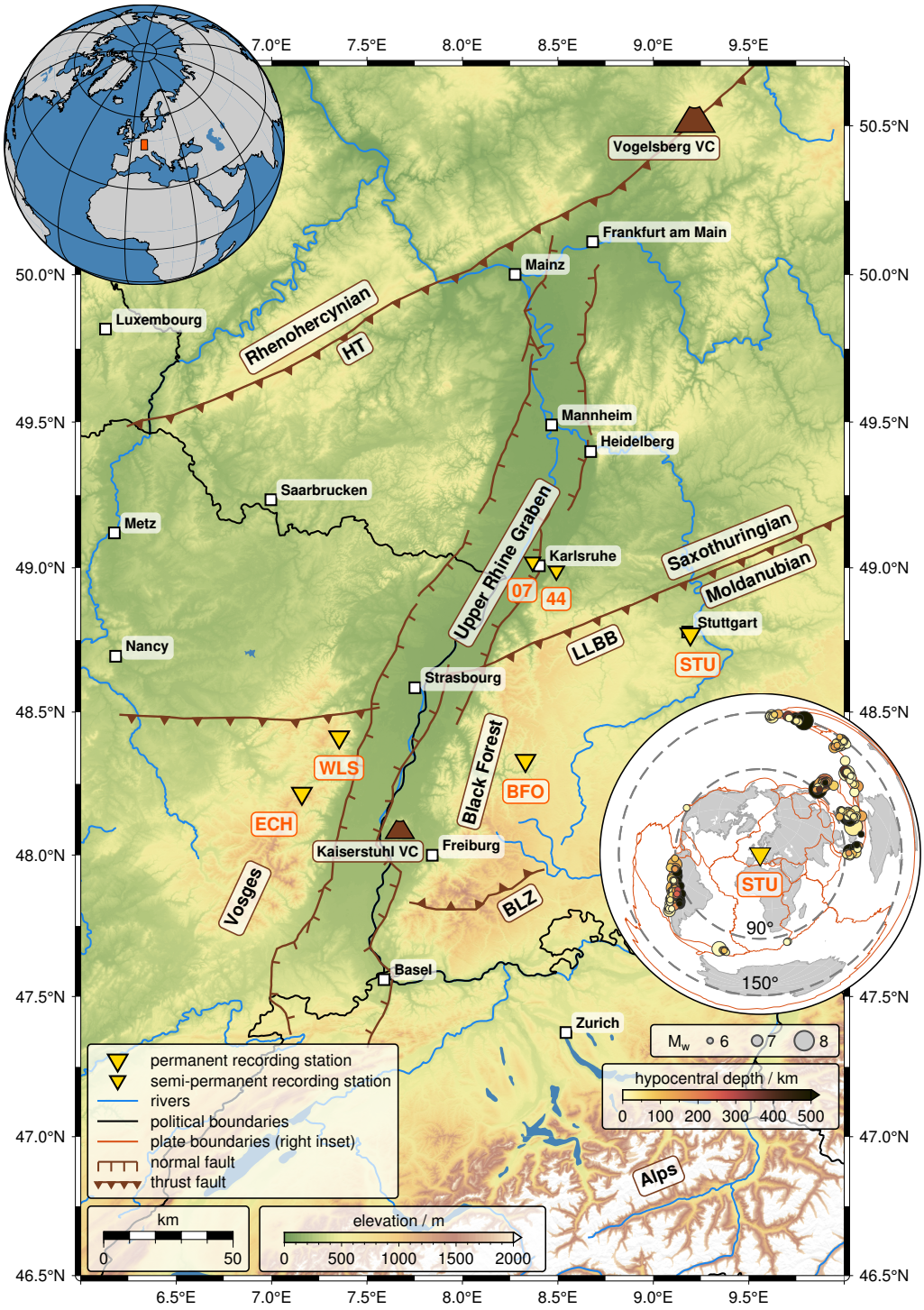

Figure 8.1: Map of the Upper Rhine Graben (URG) area with the used permanent (BFO, WLS, STU, ECH; large yellow inverse triangles) and semi-permanent (TMO44, TMO07; small yellow inverse triangles) broad-band seismological recording stations (Tab. 8.1). The normal faults of the URG, the Variscan tectono-stratigraphic units Rhenohercynian Zone, Moldanubian Zone and Saxothuringian Zone separated by the Hunsrück-Taunus (HT) fault and the Lalaye-Lubine-Baden-Baden (LLBB) fault, respectively, and the Badenweiler-Lenzkirch Zone (BLZ) or Todtnau thrust are displayed following *Grimmer et al.* (2017). The Miocene Kaiserstuhl Volcanic Complex (KVC) and the Vogelsberg Volcanic Complex (VVC) are plotted with brown symbols. Political boundaries between France, Germany, Switzerland (Fig. 8.9a, upper left inset) are drawn in black. The orange rectangle in the upper left inset indicates the study area within Central Europe. The middle right inset shows the epicentre distribution of the earthquakes which were usable for at least one shear wave splitting measurement at the station Stuttgart STU (for the remaining stations see Fig. B.1). The hypocentral depth is colour-coded and the moment magnitude M_w scales with size. The dashed circles centred around the station (yellow inverse triangle) limit the considered epicentral distance range $\Delta = 90° - 150°$. Plate boundaries are drawn in dark orange after *Bird* (2003) and land masses are shown in grey. Note the limited backazimuthal coverage (NE 30°–100° and SW 180°–270°) and gaps (NNE 0°–30°, SE 110°–170° and SSW 270°–360°) which are typical for *XKS* phases (PKS, SKS and SKKS; for the travel time curves and travel paths see Fig. B.9) in Central Europe.

The URG crosses three tectonostratigraphic units of the Variscan internides. These are from north to south the Rhenohercynian, Saxothuringian, and Moldanubian Zones or terranes, separated by the Hunsrück-Taunus (HT) fault and the Lalaye-Lubine-Baden-Baden (LLBB) fault, respectively (Fig. 8.1). These zones were formed and consolidated during the Caledonian Orogeny (Ordovician to Silurian, 500-450 Myr) and the Variscan Orogeny (Devonian to Triassic, 400-250 Myr; *Tait et al.*, 1997; *Matte*, 2001). The subductions and closures of the Iapetus Ocean and the Tonquist Sea caused the collision of the palaeo-continents Laurentia and Baltica/Avalonia to the large-continent Laurussia and the formation of the Caledonia Mountain Belt. During the following major tectonic episode, the Rheic Ocean and the Galicia-Southern-Brittany Ocean were subducted and closed and the collision of the large-continents Laurussia and Gondwana/Armorica formed the supercontinent Pangaea and the Variscan Mountain Belt In the collision area of the two terranes Avalonia and Armorica several lithospheric blocks and island arcs are attached to each other on a small lateral length-scale. It is proposed that rock fabrics in the different lithospheric blocks are still preserved, causing seismic anisotropy (*Babuška and Plomerová*, 2001; *Babuška et al.*, 2002). Since a passive rifting mechanism is preferred for the URG (*Wenzel and Brun*, 1991; *Kirschner et al.*, 2011), possibly no significant modification of the lower lithosphere and asthenosphere occurred (*Kirschner et al.*, 2011). However, the deeper structure beneath the URG is still poorly known. First anisotropy studies in South Germany and the URG area are based on data from seismic refraction profiles (*Bamford*, 1977; *Fuchs*, 1983; *Enderle et al.*, 1996) as well as tomographic inversions of regional traveltimes (*Song et al.*, 2004). The analysis of Pn and Sn phases reveals complex vertically varying anisotropy in the crust and uppermost mantle.

8.3 Data and methods

8.3.1 Seismological recording stations

We analyse seismological data from six (semi-)permanent broad-band recording stations in Southwest Germany and East France (Fig. 8.1 and Tab. 8.1). In the east these are the Black Forest Observatory (BFO, network code GR; *Black Forest Observatory*, 1971; *Federal Institute for Geosciences and Natural Resources*, 1976), station Stuttgart (STU, GE; *GEOFON Data Centre*, 1993) and station Durlach (TMO05/TMO44/A126A, KB/KB/Z3; `http://ws.gpi.kit.edu`; *AlpArray Seismic Network*, 2015; since this station was used in different projects it was renamed several times and it is part of different networks, hereafter for simplification it is just called TMO44). Inside the graben station KIT-GPI (TMO07, KB; `http://ws.gpi.kit.edu`; there are a few recording gaps due to usage of the instruments in other projects) is analysed and to the west in the French Vosges Mountains the stations Welschbruch (WLS, FR; *RESIF*, 1995) and Échery (ECH, G; *GEOSCOPE*, 1982). All stations provide recordings for at least 15 yr what allows us to achieve a sufficient backazimuthal coverage to resolve complex anisotropy.
The interstation distances vary between 10 km and 80 km. TMO44 and TMO07 are located in the Moldanubian Zone whereas the other four recording stations are installed at sites in the Saxothuringian Zone. BFO and STU are located on the east side of the URG, whereas WLS and ECH are situated on the west side of the URG (Fig. 8.1). The analysed teleseismic *XKS* phases propagate steeply through the upper mantle beneath the different geological and tectonic regions, including the French Vosges Mountains, the Upper Rhine Graben, the Kaiserstuhl Volcanic Complex and the German Black Forest Mountains as well as the South German Block and the northern edge of the Swiss Alps (Fig. 8.1).

[15] In the published research article erroneously 1 is given. The analysis and modeling and the provided dataset are correct.

Table 8.1: Information on the seismological recording stations (Fig. 8.1) and number of the shear wave splitting measurements (SWSMs) found in the single-event analysis with the *rotation-correlation* method (RC method; *Bowman and Ando*, 1987) and the *energy minimization* method (SC method; *Silver and Chan*, 1991). SWSMs are separated by two observation types (*nulls*, *splits*) and three quality categories (*good*, *fair*, *poor*) (Tab. 8.2). The SWSMs at BFO are expanded based on *Ritter et al.* (2022).

Station code	Network code	Data centre	Analysed time period	SWSMs *good, fair, poor*	SWSMs *nulls splits*
BFO	GR	BGR	1991/07 – 2019/12	91, 147, 234	2, 55, 313
WLS	FR	RESIF	1991/07 – 2019/12	6, 32, 30	0, 28, 113
STU	GE	GFZ	1994/05 – 2019/12	34, 36, 58	9^{15}, 52, 55
ECH	G	RESIF	1990/11 – 2019/12	38, 30, 56	1, 36, 64
TMO55	KB	KIT-GPI	2005/01 – 2006/05	6, 7, 17	1, 14, 35
TMO44	KB		2006/06 – 2015/12		
A126A	Z3		2016/01 – 2019/12		
TMO07	KB	KIT-GPI	2005/01 – 2019/12	3, 11, 28	0, 10, 22

8.3.2 Measurement of shear wave splitting

For the shear wave splitting measurements (SWSMs), we selected teleseismic earthquakes within the epicentral distance range $\Delta = 90^\circ - 150^\circ$ and a moment magnitude of $M_w \geq 6.0$ from the Global Harvard Centroid Moment Tensor (CMT) catalogue (*Dziewonski and Anderson*, 1981; *Ekström et al.*, 2012). For each recording station we requested the associated three-component ground velocity seismograms for the time period from the start of the recording until 2019 December 31 (Tab. 8.1) from the corresponding data centre.

Due to the S-to-P conversion at the core-mantle boundary (CMB) on the source side any source-side SWS contamination is removed and thus any observed SWS occurred definitely between the CMB and the surface on the receiver side. After traveling through the liquid outer core as P wave, the P-to-S conversion at the CMB on the receiver side causes a purely vertically polarized S wave (SV wave; signal on the Q component). Thus, the initial polarization direction is equivalent to the BAZ direction and it is a known quantity. This is a useful property to verify whether the selected waveform is actually the assumed type of phase or to detect a (before unknown) sensor misorientation. SWS generates a signal on the transverse (T) component (horizontally polarized S wave, SH wave) and leads to an elliptical (instead of a linear) particle motion in the WE-SN or Q-T hodogram (Fig. B.2). Together with the steep and nearly vertical incidence ($i < 15^\circ$, measured from the vertical) of *XKS* phases in the upper mantle, the integrating effect along the ray path is mainly in the vertical direction. According to this the lateral resolution of anisotropy is very good, but the vertical resolution is poor for single splitting observations at a recording station.

8.3.2.1 Splitting parameters

SWS is measured by the determination of the two splitting parameters: the fast polarization direction ϕ and the delay time δt. To determine the splitting parameters, we perform a grid-search using version 1.2.1 (*Porritt*, 2014) of the MATLAB package *SplitLab* (*Wüstefeld et al.*, 2008) together with the plugin *StackSplit* (*Grund*, 2017). In the single-event analysis we apply two independent methods simultaneously for comparison: the rotation-correlation method (hereafter RC method; *Bowman and Ando*, 1987) and the energy minimization method (SC method; *Silver and Chan*, 1991). In the multi-event analysis, the *simultaneous inversion of multiple waveforms* (SIMW; *Roy et al.*, 2017) and the energy (or error) surface stacking method (WS method; *Wolfe and Silver*, 1998) are applied. We apply an updated *SplitLab* code to ensure a correct relative temporal alignment of the single traces (N, E, Z components;

Fröhlich et al., 2022a). These SWSMs correct the SWSMs made in *Fröhlich* (2020). For the error estimation we use the modified equations by *Walsh et al.* (2013) to correctly calculate the required degrees of freedom as implemented in *StackSplit*.

The automatic pre-processing of the seismograms includes the subtraction of the mean and any linear trend in the waveform recordings. To remove frequencies not of interest (noise) and to increase the SNR, a third-order zero-phase Butterworth bandpass filter is applied with corner frequencies within 0.020-0.066 Hz (15-50 s, lower corner) and 0.15-0.20 Hz (5-0.66 s, upper corner) corresponding to the typical (5-30 s) and dominant (8-10 s) periods of *X*KS phases. To achieve SWSMs with similar frequency content mostly the corners at 0.020 Hz and 0.15 Hz are chosen and only in parts slightly adjusted to improve the clarity of the waveforms. The inversion itself is implemented as grid search for the (apparent) fast polarization direction and the (apparent) delay time over the value ranges $[-90, 90]^\circ$ and $[0, 4]$ s, respectively and applied inside manually selected time windows of around 20 s.

Each SWSM is manually classified regarding the two possible observation types *null* measurement (*null*, no SWS observable) and *non-null* measurement (*split*, SWS observable) (*Wüstefeld and Bokelmann*, 2007) as well as the three defined quality categories *good*, *fair*, *poor* (Tab. **8.2**). Thereby we considered a combination of subjective visual and objective analytical criteria (for examples of diagnostic plots provided by *SplitLab* after applying the RC method and the SC method see Fig. **B.3**). This includes: the form of the particle motion in the WE-SN hodogram before and after the correction, the SNR calculated after *Restivo and Helffrich* (1999) for the SC method and the visibility of the phase relative to the rest of the seismogram, the differences and the consistency between the measured (apparent) splitting parameters obtained with the RC method and the SC method, as well as the 95 per cent confidence intervals of the measured (apparent) splitting parameters. Only the SWSMs are kept with a SNR ≥ 3 (*Vecsey et al.*, 2008) (all recording stations) and a deviation of the initial polarization direction from the BAZ direction $< \pm 10^\circ$ for permanent recording stations STU and ECH and $< \pm 15^\circ$ for semi-permanent recording stations TMO44 and TMO07 (Fig. **B.12**). The SIMW (*Roy et al.*, 2017) with the SC method is applied to the *X*KS waveforms of *poor* SWSMs from the single-event analysis to gain additional BAZ directions (for examples of diagnostic plots provided by *StackSplit* after applying the SIMW see Fig. **B.4**). For SIMW stacking, the BAZ and the epicentral distance intervals are limited to 3° each.

An averaging procedure is used with 5° BAZ bins to reduce the dominance of the BAZ directions with many single-event analysis *non-null* measurements in the modelling. The WS method (*Wolfe and Silver*, 1998) with stacking of the energy surfaces is applied in each 5° BAZ bin only for the group with the most or the best *non-null* measurements (for an example of a diagnostic plot provided by *StackSplit* after applying the WS method see Fig. **B.5**). This binning preserves existing backazimuthal variations of the splitting parameters.

8.3.2.2 Splitting intensity

Another approach of measuring shear wave splitting is the determination of the splitting intensity SI introduced by *Chevrot* (2000). Strictly speaking the splitting intensity has the unit seconds. However, since a meaningful physical interpretation of the unit appears difficult it is mostly omitted (e.g., *Chevrot*, 2000; *Deng et al.*, 2017). Here we follow this. In case of no shear wave splitting the SI should be zero or close to zero depending on the noise in the data. So, the SI can support the classification of a SWSM as a *null* measurement. *Deng et al.* (2017) suggest an absolute upper limit of the SI allowed for a *null* measurement of $|\Delta SI| = 0.2$. Further they reported that a SI difference of $|\Delta SI| > 0.4$ between SKS and SKKS phases of the same source-receiver configuration (SKS-SKKS pair) can be a sign for a lowermost mantle contribution to the anisotropy.

We calculated the SI using modified functions of *SplitLab* (*Wüstefeld et al.*, 2008) version 1.9.0 for all of our SWSMs afterwards, mostly to test for anomalies and differences of the *null* measurements at BFO in the SW quadrant compared to the other recording stations.

Table 8.2: Manual classification of the shear wave splitting measurements (SWSMs) based on the criteria for the two observation types (*null*, *split*) and the three quality categories (*good*, *fair*, *poor*). Classification of *nulls* is following *Wüstefeld and Bokelmann* (2007). *Abbreviations*: RC = *rotation- correlation* method (RC method; *Bowman and Ando*, 1987), SC = *energy minimization* method (SC method; *Silver and Chan*, 1991), SNR = signal-to-noise ratio. For the principle of SWSMs on *X*KS phases see Fig. B.2.

Observation type, quality category	**SNR (SNR_{SC})**	$\lvert\Delta\phi\rvert/°$ ($\lvert\phi_{SC} - \phi_{RC}\rvert$)	$\lvert\Delta\delta t\rvert$/s ($\lvert\delta t_{SC} - \delta t_{RC}\rvert$)	**Confidence interval (95 per cent)**	**Particle motion (WE–SN / Q–T)**
null, *good*	> 10	[37,53]	maximum	no overlap	un
null, *fair*	> 7	[32,58]	large		changed
null, *poor*	≥ 3	as soon as one criterion is not fulfilled, and no shear wave splitting is recognizable			linear
split, *good*	> 10	≤ 5	≤ 0.2	small	from
split, *fair*	> 7	≤ 20	≤ 1.0		elliptic to
split, *poor*	≥ 3	as soon as one criterion is not fulfilled, but shear wave splitting is recognizable			linear

8.4 Observation of shear wave splitting

For each recording station, the numbers of SWSMs from the single-event analysis (RC method or SC method) are summarized in Tab. 8.1 separated by the observation types and the quality categories. In total we receive 700 *null* measurements (380 *good* or *fair*) and 682 *non-null* measurements (174 *good* or *fair*) from the single-event analysis. At the four permanent recording stations (BFO, ECH, STU and WLS) significantly more SWSMs could be determined than at the semi-permanent stations TMO07 und TMO44. The SWSMs at BFO are expanded by 40 (16 *good* or *fair*) *nulls* and 39 (10 *good* or *fair*) *splits* relative to *Ritter et al.* (2022) for the period 2016-2019 and the backazimuth range 130°-150°. The large number of SWSMs at BFO (456 *nulls*, 342 *splits*) is mainly a result of the excellent local site conditions in the former silver mine leading to a noise level among the lowest values worldwide (*Berger et al.*, 2004).

A helpful station-related visualization of the SWSMs is a stereoplot (Figs 8.2 and B.7). This kind of representation emphasizes the variations of the observation type as well as of the splitting parameters with BAZ and thus illustrates vertical or lateral variations or a tilted symmetry axis of the anisotropy. Furthermore, the observational concentrations and gaps in the backazimuthal coverage are directly visible.

Corresponding to the explanation in the Introduction (Sec. 8.1) at seismological recording stations in Central Europe, like ours, there are observational concentrations for teleseismic earthquakes in the northeast (BAZ range 30°-100°) and the southwest (180°-270°) and observational gaps in the north (0°-20°), the southeast (110°-170°) and the northwest (270°-360°). This is still the case for very long-term recordings (> 15 yr) which we use (Fig. 8.1, middle right inset; Fig. B.1). The WS method is applied at BFO, WLS, STU, ECH and TMO44 in the BAZ ranges with many observations.

At BFO the difference is obvious between the observations in the NE and the SW quadrant (Figs 8.2a, B.7 and B.8a). In the NE quadrant (BAZ range 30°-100°) there is a strong and characteristic backazimuthal variation of the splitting parameters, especially of the fast polarization direction. In contrast numerous *null* measurements (249) are observed within 180°-360° BAZ. The *splits* within 180°-360° BAZ are mainly of *poor* quality (277) and with inconsistent splitting parameters (Fig. 8.2a). The *nulls* extend over a BAZ range up to 180° which is unique at BFO and what is not observed at one of the other five recording stations. Actually, we identify several earthquakes where the SKS phase shows no splitting at BFO but clear splitting at STU and ECH (Figs 8.3 and B.25). At WLS the splitting parameters vary strongly with BAZ (Fig. 8.2b). Especially in the SW there are partly inconsistent splitting parameters within one BAZ direction. Compared to BFO (and the other recording stations) in the BAZ

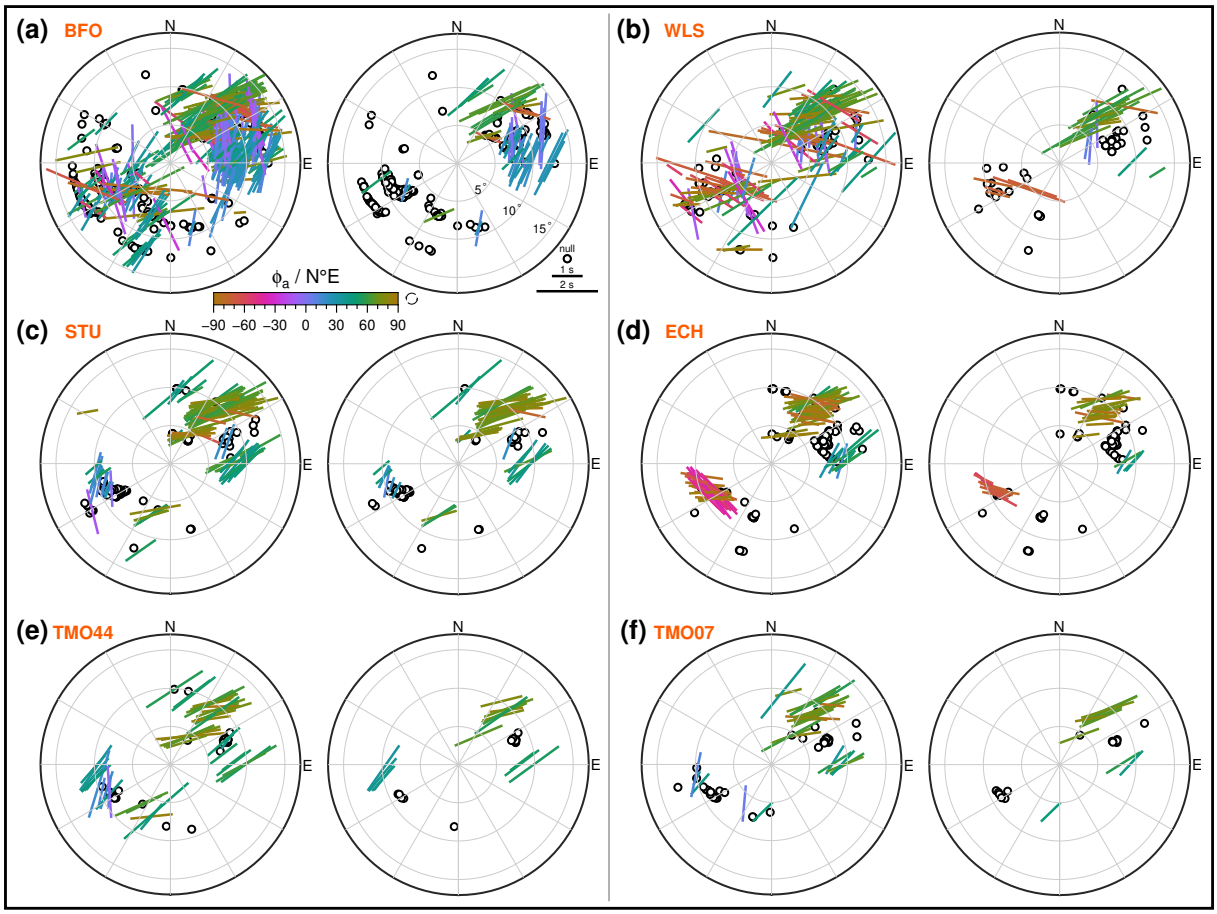

Figure 8.2: Shear wave splitting measurements (SWSMs) from the single-event analysis shown in stereoplots **(a)** BFO, **(b)** WLS, **(c)** STU, **(d)** ECH, **(e)** TMO44 and **(f)** TMO07. SWSMs at BFO are expanded based on *Ritter et al.* (2022). All SWSMs (left) and *good* and *fair* SWSMs (right). For each SWSM a bar or circle (for *nulls*) is drawn according to the backazimuth (angle axis, clockwise from north) and the incidence angle of the phase (radial axis, from the centre to the outside). For each *non-null* measurement, the bar points in the apparent fast polarization direction ϕ_a and it is colour-coded; its length is scaled relative to the apparent delay time δt_a (*energy minimization* method; *Silver and Chan*, 1991). Stereoplots for the *rotation-correlation* method (*Bowman and Ando*, 1987) (Fig. B.7) as well as for BFO (Fig. B.6), for separate and cumulative time periods (Fig. B.8), and for seismic phases (Fig. B.10) and epicentral distance ranges (Fig. B.11) can be found in the Supporting Information. For related Cartesian histograms see Figs B.23 and B.24.

range 60°-110° hardly any *good* or *fair non-null* measurements could be determined at WLS. At STU both, the fast polarization direction and the delay time vary with BAZ (Figs 8.2c and 8.4). The *nulls* are mainly located in the opposite BAZ ranges 60°-75° and 240°-250°. At ECH the splitting parameters are consistent within one BAZ direction. In the NE quadrant the *splits* are concentrated on two small BAZ intervals (35°-45° and 84°-89°; Fig. 8.2d). A strong variation of the fast polarization direction with the BAZ is visible. The delay time at ECH is smaller compared to the other recording stations. At ECH there is a concentration of *null* observations in the BAZ range 60°-90°.

The stereoplots for TMO44 (Fig. 8.2e) and TMO07 (Fig. 8.2f) appear to be similar what may be related to the small interstation distance of around 10 km. When considering only the measurements ranked *good* and *fair* the variation of the splitting parameters with the BAZ is weak(er) and the fast polarization direction is preferably around 50°-70°. The *null* measurements are mainly located in the opposite BAZ ranges 60°-70° and 235°-245°. The stereoplots for TMO44 and STU show some similarities (Fig. 8.2e, c). At TMO07 in the SW quadrant only a few *splits* are observed and one may draw a link to the numerous *null* observations at BFO in the SW quadrant (Fig. 8.2f, a). It has to be mentioned that a potentially existing backazimuthal variation of the splitting parameters can remain unrecognized due to a short(er) recording time and thus a reduced backazimuthal coverage with less

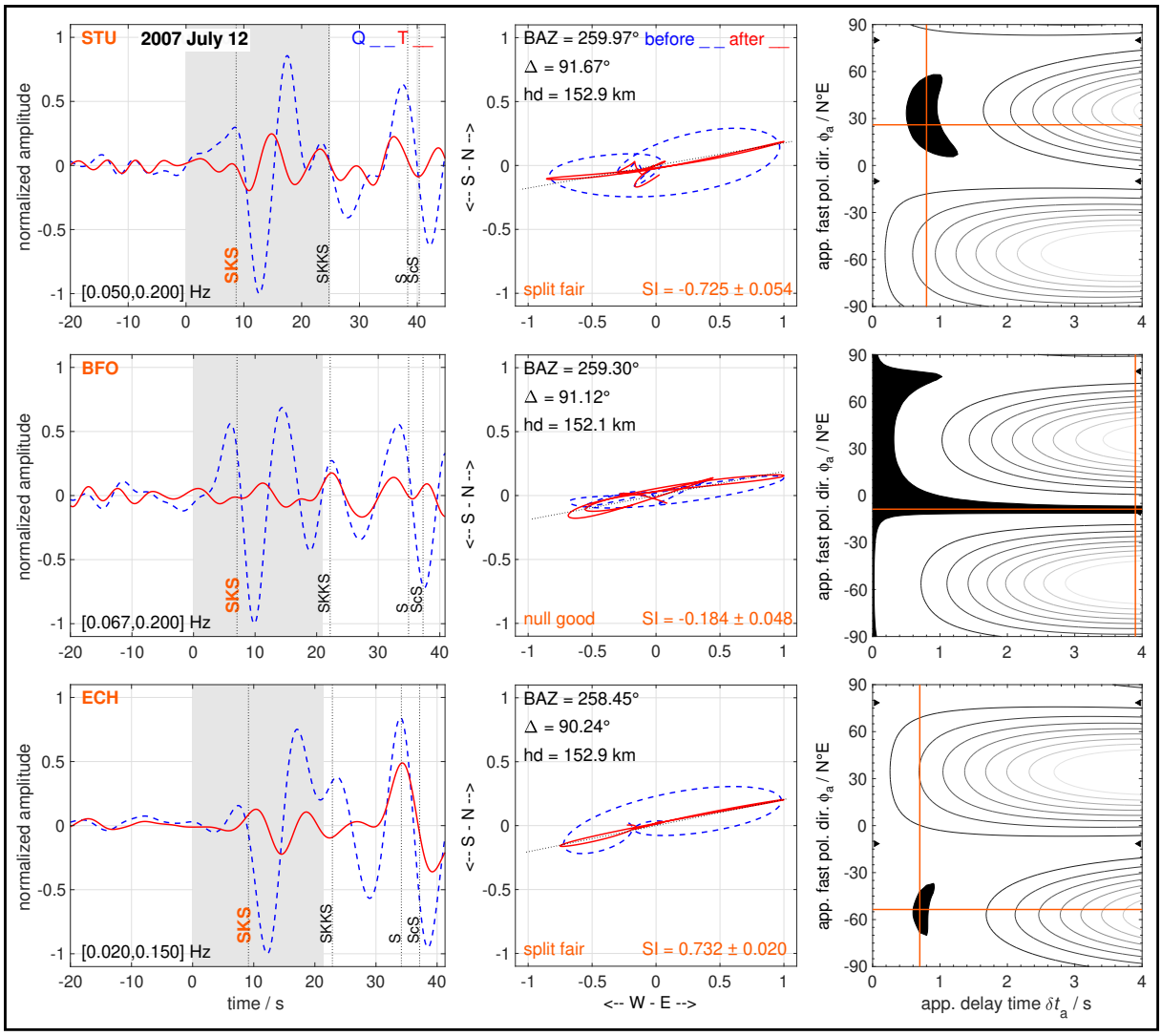

Figure 8.3: Observation of no shear wave splitting (*null*) at the BFO (middle row) but of shear wave splitting (*split*) at the recording stations STU (top row) and ECH (bottom row) for an earthquake beneath Northern Peru on 2007 July 12. The observation falls in the SW quadrant. **left-hand panel**: waveforms of the Q (dashed blue line) and T (solid red line) components, normalized to the absolute maximum and filtered with a bandpass (corner frequencies are given at the bottom). Black vertical lines mark the theoretical arrival times calculated with the *iasp91* Earth model (*Kennett and Engdahl*, 1991) with the *TauP* Toolkit (*Crotwell et al.*, 1999). The grey region indicates the selected time window around the SKS phase. **centre panel**: Horizontal (WE–SN) particle motion before (dashed blue line) and after (solid red line) the correction for the shear wave splitting. At the top backazimuth BAZ, epicentral distance Δ, and hypocentral depth *hd* and at the bottom observation type, quality category and splitting intensity *SI* with error are given. **right-hand panel**: result of the grid search (*energy minimization* method; *Silver and Chan*, 1991) for the apparent splitting parameters (ϕ_a, δt_a) with 95 per cent confidence interval (black area) and best solution (section point of the horizontal and vertical orange lines). For more examples see Fig. B.25.

SWSMs, here relevant especially for TMO07 in the SW.

At all recording stations the splitting intensity of the *null* measurements is significantly lower than the splitting intensity of the *non-null* measurements and a clear separation is possible between *nulls* and *splits* (Fig. B.21). We could not find significant discrepancies between the splitting intensities of SWSMs on SKS and SKKS phases. The splitting intensity does not show significant anomalies for the *null* measurements at BFO in the SW quadrant compared to the *null* measurements at BFO in the NE quadrant or to the *null* measurements at the other recording stations (Fig. B.22c, d).

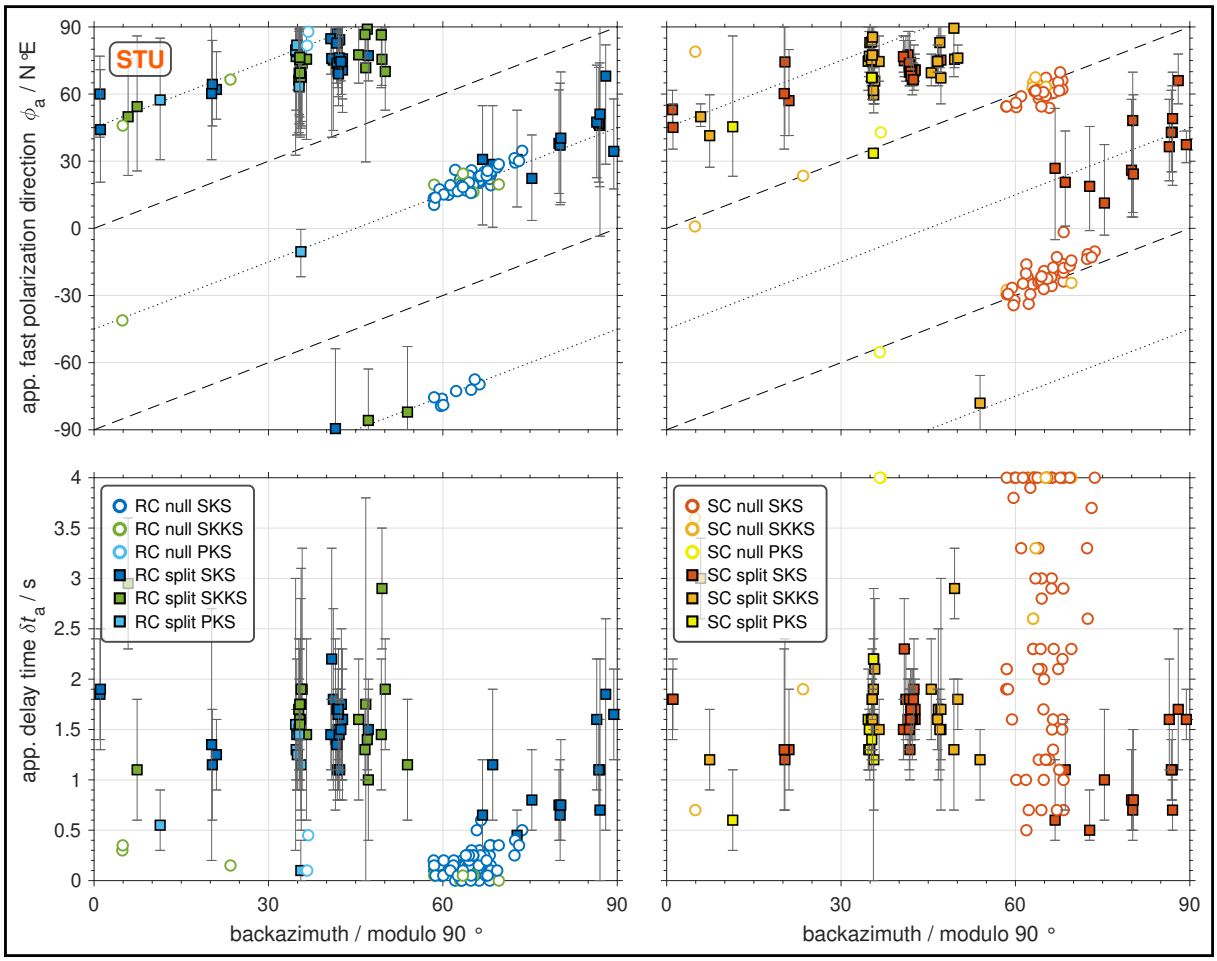

Figure 8.4: Apparent splitting parameters obtained in the single-event analysis at the recording station STU as function of the backazimuth in modulo 90° representation. Only the *good* and *fair* shear wave splitting measurements (SWSMs) are shown. For all SWSMs and the remaining stations see Figs B.14 and B.15. *Rotation-correlation* method (RC method; *Bowman and Ando*, 1987; **left**) *energy minimization* method (SC method; *Silver and Chan*, 1991; **right**). Apparent fast polarization direction ϕ_a (**top**), apparent delay time δt_a (**bottom**). *Nulls* are shown as white circles with coloured outline and *splits* as squares with coloured fill. SKS in dark blue (RC method) or dark orange (SC method), SKKS in green or light orange, and PKS in light blue or yellow. The 95 per cent confidence intervals of the apparent splitting parameters are given by the vertical error bars. The black dotted (RC method) and dashed (SC method) lines with a slope of 45° indicate the values of ϕ_a expected for *nulls* in case of simple anisotropy (model type H1). Note that for *nulls* δt_a tends to zero for the RC method but for the SC method it spreads over the whole range of the grid search up to the maximum, here 4 s (see Tab. 8.2).

8.5 Modelling of shear wave splitting

The observed intra- and interstation variations of *nulls* and *splits* as well as of the apparent splitting parameters are clear indications for complex anisotropy in the URG area, including vertical and small-scale lateral variations. In the simplest case, only no or a negligible backazimuthal variation of the splitting parameters suggests a transversely isotropic one-layer structure with horizontal symmetry axis. A test for such a simple scenario is the occurrence of *null* measurements for specific BAZ directions since the *nulls* should be limited to the four BAZ directions expected as the fast or slow polarization directions. Otherwise, complex anisotropy is likely present or at least cannot be ruled out.

The two-layer scenario should cause a systematic backazimuthal variation with a $\pi/2$-periodicity (in ϕ_a and δt_a) characterized by four discontinuous $\pi/2$-jumps of the apparent fast polarization direction (*Silver and Savage*, 1994) which can be identified in the modulo 90° representations with BAZ (*Liu and Gao*, 2013; *Krischer et al.*, 2015). Since the splitting operators do not commute, the order of the two layers can be inferred (*Silver and Savage*, 1994,

fig. 2). So-called transparent windows can serve as a verification for a two-layer model (*Vinnik et al.*, 1994). No shear wave splitting occurs in the lower layer for an S(V) wave with an initial polarization direction (for *X*KS phases equivalent to the BAZ direction) parallel or perpendicular to the fast polarization direction. Thus, only the SWS in the upper layer contributes to the splitting parameters measured at the surface, and these directly reflect the splitting parameters in the upper layer.

A one-layer model with a tilted symmetry axis exhibits (based on the varied model parameters, see below) a smooth and dip-dependent backazimuthal variation with a 2π-periodicity. It is also characterized by a v-shaped pattern of the fast polarization direction in the stereoplot representation for a larger dip of the layer (*Grund and Ritter*, 2020, fig. S5).

The backazimuthal variation of the splitting parameters is a crucial criterion to discern and describe complex anisotropy. Due to our analysis of long-term recordings, we were able to detect such variations. In case of large observational gaps in the backazimuthal coverage, complex anisotropy remains unrecognized and an anisotropy model cannot be derived reliably and unambiguously. Especially studies based on short-term recordings suffer from a poor backazimuthal coverage and the small number of SWSMs.

In order to explain our shear wave splitting observations and to constrain the seismic anisotropy at depth, we firstly develop a structural anisotropy model for each recording station. Corresponding to strong variations of splitting parameters with backazimuth we test beside the simple one-layer scenario (H1) more complex models including of two layers (H2) and a single layer with a tilted symmetry axis (T1) (Fig. **B.13**). Thereby a medium with transverse isotropy is assumed in which the fast axis (fast polarization direction) is parallel to the symmetry axis.

Synthetic anisotropy models are generated by systematic variation of the model parameters for each model type (Tab. **B.1**, upper part). The two model parameters used for H1 are equivalent to the splitting parameters (ϕ, δt). Analogous, for H2 the lower (index 1) and the upper (index 2) layers and their fast polarization directions and delay times are used as model parameters (ϕ_1, δt_1, ϕ_2, δt_2). For T1 the dip angle relative to the horizontal, the down-dip direction relative to north (strike direction plus 90°) and the layer thickness are varied (Ψ, $\sigma + 90°$, d). By this we assume that the symmetry axis dips in the down-dip direction of the layer. To forward calculate the apparent splitting parameters for the synthetic anisotropy models, we use the *MATLAB Seismic Anisotropy Toolkit* (MSAT; *Walker and Wookey*, 2012). A shear wave with a dominant period of 8 s and an incidence angle of 10° (typical values for *X*KS phases) is assumed which travels through one (two) anisotropic layer(s) composed of dry olivine (upper mantle) with a crystal alignment of 30 per cent (*Savage*, 1999; Tab. **B.1**, lower part). For H2, the equations from *Silver and Savage* (1994) are used, while for T1, the *Christoffel equation* (*Mainprice*, 2007) was solved using the MSAT. Subsequently we compare the measured and forward calculated apparent splitting parameters. Since the SC method is in general more robust than the RC method (*Long and van der Hilst*, 2005), the measured splitting parameters of the (*good* and *fair*) *non-null* measurements obtained with the SC method are selected together with the multi-event analysis results. To measure the misfit between each synthetic anisotropy model and the splitting observations, we calculate the root-mean-square error (RMSE) via Eqs **8.1**-**8.3**:

$$\mathrm{RMSE}_{\phi_\mathrm{a}} = \sqrt{\frac{1}{N}\sum_{n=1}^{N}\left(\Delta\phi_{\mathrm{a},n}\right)^2} \tag{8.1}$$

$$\mathrm{RMSE}_{\delta t_\mathrm{a}} = \sqrt{\frac{1}{N}\sum_{n=1}^{N}\left(\Delta\delta t_{\mathrm{a},n}\right)^2} \tag{8.2}$$

$$\mathrm{RMSE}_{\mathrm{tot}} = \frac{1}{90°}\mathrm{RMSE}_{\phi_\mathrm{a}} + \frac{1}{4\ \mathrm{s}}\mathrm{RMSE}_{\delta t_\mathrm{a}} \tag{8.3}$$

With the differences between the measured and the forward calculated apparent splitting parameters $\Delta\phi_{\mathrm{a},n}$ and $\delta t_{\mathrm{a},n}$ for each data point (included SWSM) $n = 1, \ldots, N$ the SWSM is calculated separately for ϕ and δt. To equally incorporate $\mathrm{RMSE}_{\phi_\mathrm{a}}$ and $\mathrm{RMSE}_{\delta t_\mathrm{a}}$ they are normalized with the maximum values of the grid search setting (90° for

ϕ and 4 s for δt) before they are summed up to achieve the total $RMSE_{tot}$ (unitless quantity), hereafter named as RMSE. The synthetic anisotropy model with the minimum SWSM is taken as the one which fits the observations best (joint fit of ϕ and δt).

This modelling procedure (especially the forward calculation) is based on ray theory and thus neglect S wave properties and wave propagation effects like finite frequency effects. Nevertheless, a first order of the underlying anisotropy can be derived (e.g., *Walker and Wookey*, 2012; *Aragon et al.*, 2017; *Grund and Ritter*, 2020). With this approach, the fit can be restricted to (station-)specific BAZ ranges and does not have to be carried out using the whole BAZ range (0°-360°). This allows us to test and account for intrastation (and therefore very small-scale) lateral variations, in addition to lateral interstation variations derived from the comparison of the station-related results. This approach is spatially more detailed as the applications by *Grund and Ritter* (2020) or *Link and Rümpker* (2023).

Null measurements cannot be included directly in the modelling procedure described above due to the mathematical behaviour of the SC method (*Silver and Savage*, 1994), especially the spread of the delay time across the whole range of the grid search up to the maximum, here 4 s (see Fig. 8.4). To indirectly include the *null* measurements, we compare the observed BAZ locations with the theoretically expected BAZ locations. This can be helpful to validate the modelling results, especially regarding one- and two-layer scenarios. BAZ intervals with mainly *null* measurements spreading over a significantly wider BAZ range than expected for a layer model are not covered by this modelling procedure. Therefore, this case is interpreted based on (*a priori*) geological and tectonic scenarios related to the study region.

8.6 Interpretation and discussion

8.6.1 Structural anisotropy models at the single recording sites

Here, we present our structural anisotropy models for the single recording stations at first. After considering the whole BAZ range (0°-360°) in the modelling, we focus on (stations-)specific BAZ ranges to account for backazimuthal variations of the splitting parameters. This allows us to investigate small-scale lateral variations in anisotropy and to outline subregions. The modelling results are visualized in Figs 8.5, 8.6 and 8.7, with focus on the 20 best-fitting synthetic anisotropy models and the 1000 best-fitting models are displayed as heatmaps, For the two-layer scenario, index 1 refers to the lower layer and index 2 to the upper layer. The comparison of our results with previous anisotropy studies is focused on BFO, STU and ECH, which were already used in previous anisotropy studies.

8.6.1.1 Fitting of the whole BAZ range

When considering the whole BAZ range, a horizontal symmetry axis seems to be more likely than a tilted one at the single recording sites (Fig. 8.5). At BFO, STU and ECH no-overlapping clusters for the model parameters in the single layers are visibly for the model type H2 (Fig. 8.5a-c). Two two-layer scenarios can account for the strong backazimuthal variations of the measured splitting parameters at these stations. The two-layer model at BFO refers only to the NE quadrant, and the numerous *null* measurements in the SW quadrant remain unexplained at this stage. The model parameter ranges of the 20 best-fitting two-layer models at BFO are ϕ_1 = 55° to -50°, δt_1 = 0.6 − 2.40 s for the lower layer and ϕ_2 = -30° to 45°, δt_2 = 0.60-1.60 s for the upper layer (Fig. 8.5b). Our best-fitting two-layer model at BFO is ϕ_1 = -80°, δt_1 = 0.60 s and ϕ_2 = 35°, δt_2 = 1.20 s. This is consistent with *Ritter et al.* (2022), reporting ϕ_1 = 55° to -55°, δt_1 = 0.50-2.50 s for the lower layer and ϕ_2 = -30° to 40°, δt_2 = 0.50-1.75 s for the upper layer as model parameter ranges of the 20 best-fitting two-layer models, and ϕ_1 = -60°, δt_1 = 1.0 s

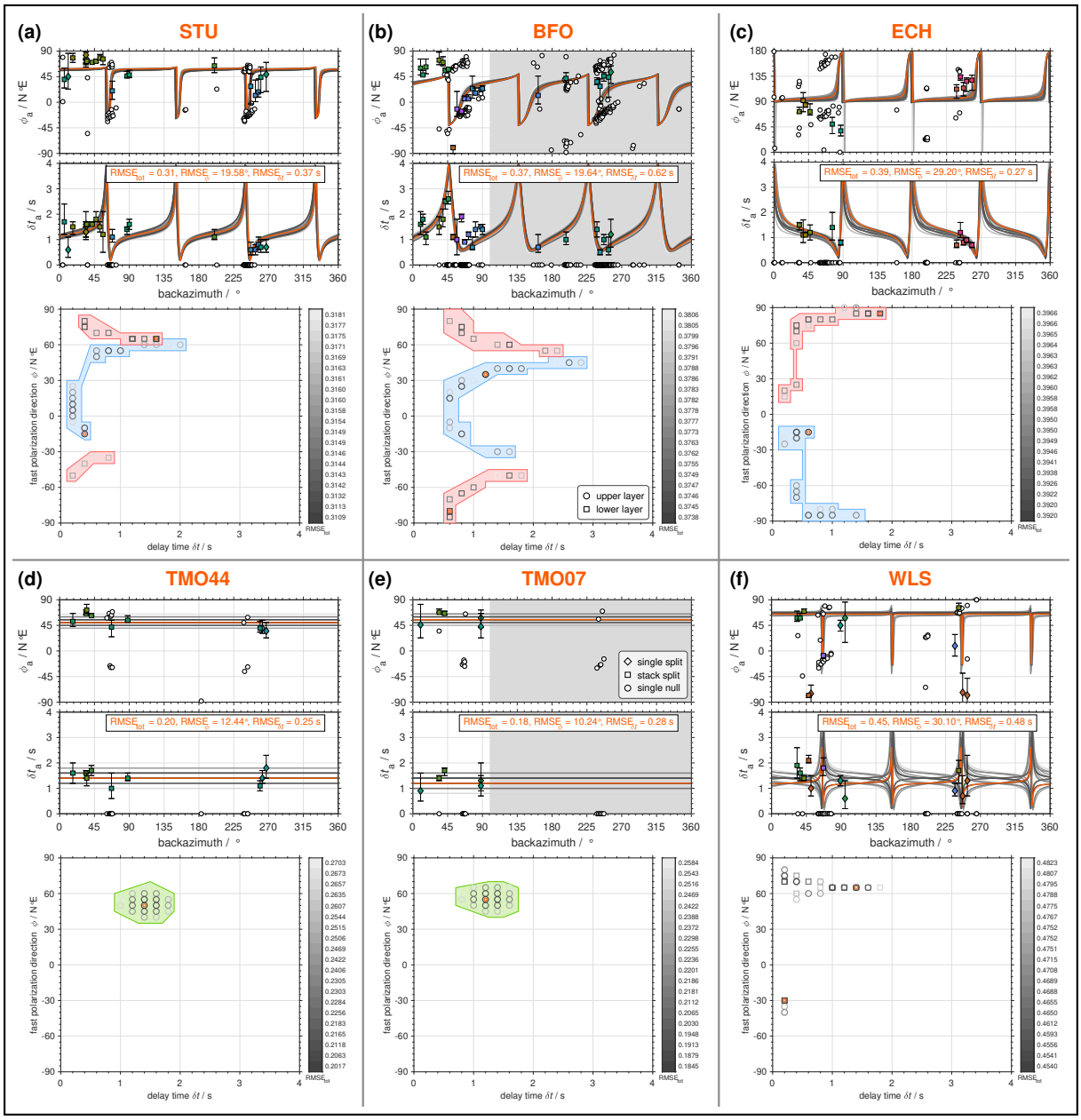

Figure 8.5: Modeling results for the preferred model type with a horizontal symmetry axis (H1 or H2) at **(a)** STU, **(b)** BFO, **(c)** ECH, **(d)** TMO44, **(e)** TMO07 and **(f)** WLS. Shown are the 20 best-fitting synthetic anisotropy models. The best-fitting model (minimum $\mathrm{RMSE_{tot}}$, horizontal text box with RMSE values in orange font) is highlighted in orange and the next 19 best-fitting models are drawn with a grey colourmap based on the $\mathrm{RMSE_{tot}}$. Only the backazimuth region in white is considered in the modeling, that is at BFO and TMO07 it is restricted to the NE quadrant (30°–110° backazimuth). Results at BFO are expanded based on *Ritter et al.* (2022). **top panel**: forward calculated apparent fast polarization direction ϕ_a and apparent delay time δt_a as well as observed *splits* from the single-event analysis (*energy minimization* method; *Silver and Chan*, 1991) as diamonds and from the multi-event analysis (stacking via the WS method; *Wolfe and Silver*, 1998) as squares. These symbols are color-coded based on ϕ_a using the same colourmap as in Fig. 8.2. The vertical error bars give the 95 per cent confidence intervals. Note that the *nulls* from the single-event analysis (white circles) are not included in the modelling, but shown for the sake of completeness with δt_a manual set to zero (different to Fig. 8.4). **bottom panel**: model parameter distribution with ranges for the two-layer models in red (lower layer, squares) and blue (upper layer, circles) as well as in green for the one-layer models (circles). Note the nearly identical $\mathrm{RMSE_{tot}}$ values for the different models, whereby the related splitting parameters in (a) are quite similar. Despite this non-uniqueness, clusters are visible with an exception at WLS. For the distribution of the model types within the 500 best-fitting models see Fig. B.19 (left-hand column).

and ϕ_2 = 40°, δt_2 = 1.75 s as best-fitting model (*Ritter et al.*, 2022, fig. 8). In the literature, two-layer models are suggested at BFO: ϕ_1 = 82°, δt_1 = 1.9 s and ϕ_2 = 10°, δt_2 = 1.1 s by *Vinnik et al.* (1994), ϕ_1 = 85° to 95°, δt_2 = 0.8-1.6 s and ϕ_2 = 35° to 45°, δ_2 = 1.1-1.8 s by *Walker et al.* (2005a), and ϕ_1 = 60°, δ_1 = 1.4 s and ϕ_2 = 170°, δt_2 = 0.6 s by *Walther et al.* (2014). However, *Vinnik et al.* (1994) combined their splitting observations at the recording stations BFO, CLZ and FUR to one dataset. Due to an unstable two-layer fit, *Walker et al.* (2005a) prefer a one-layer model (ϕ = 48° to 59° and δt = 0.9-1.3 s) and suggest lateral variations of the anisotropy around the southern URG. Similar to our observations at BFO *Walker et al.* (2005a) report an unexpected high number or dominance of *null* measurements in the SW quadrant. The issue that the systematic error proposed by *Wüstefeld and Bokelmann* (2007) for synthetic data and the RC method may be also present for real data and the SC method in case of low SWSM data (*Eakin et al.*, 2019), was already discussed in *Ritter et al.* (2022, fig. S3). Based on this strong backazimuthal variation of the splitting parameters observed at BFO in the NE quadrant, there is a clear indication of a two-layer anisotropy scenario in this direction.

At WLS the model parameters cannot be resolved well (Fig. **8.5**f). Two-layer anisotropy models are determined at STU (Fig. **8.5**a) and at ECH (Fig. **8.5**c). This is supported by the discontinuous $\pi/2$-jumps of the apparent fast polarization directions in the modulo 90° representations with BAZ (Figs **8.4**, **B.14** and **B.15**; *Liu and Gao*, 2013; *Krischer et al.*, 2015). However, for ECH the reduced number of SWSMs after applying the WS method has to be mentioned. We compare the modelling of two layers (H2) and a dipping layer (T1) at STU (Fig. **8.6**A) and ECH (Fig. **8.6**B). At STU the visual fit for H2 is better than for T1. Partly, there is a good fit of either the fast polarization direction or the delay time, but not jointly for both parameters together. This indicates that simple one and two-layer models cannot explain the deep, complex structure beneath the URG completely. However, these models allow for a first order understanding and interpretation of the anisotropy.

The fit of the fast polarization direction at ECH in the NE is poor for both H2 and T1, but it is acceptable for the delay time. At ECH the observed *nulls* fall a bit better in the expected BAZ directions for H2 than for T1. For STU a horizontal one-layer model is proposed in other studies (*Walker et al.*, 2005a; *Walther et al.*, 2014). However, this is conflicting with the observed backazimuthal variation of the splitting parameters based on our long-term SWSMs dataset. This demonstrates the need for long-term recordings to gain enough SWSMs to observe a sufficient backazimuthal variation of the splitting parameters. By using only short-term recordings (1-3 yr) such variations are very often simply missed and oversimplified, hence wrong anisotropy models are derived. At ECH both, a two-layer model (ϕ_1 = 10° to 30° and ϕ_2 = 80° to 100°, *Granet et al.*, 1998) and a one-layer model with a tilted symmetry axis (*Walker et al.*, 2005a) have been proposed. In both studies, the authors report nearly the same fit for the other model type, respectively. *Granet et al.* (1998) combined their splitting observations at the recording stations ECH, RG-N and RG-S to one dataset. Similar to BFO *Walker et al.* (2005a) discarded their two-layer model at ECH and suggest a one-layer anisotropy model (ϕ = 84° to 131° and δt = 0.4-0.8 s) and lateral variation of the anisotropy.

Our modelling at TMO44 (Fig. **8.5**d) and TMO07 (Fig. **8.5**e) suffers from a limited backazimuthal coverage. Since a weak and rather uncharacteristic backazimuthal variation of the splitting parameters is visible for both, only a single layer model (H1 or T1) can be supported by the existing dataset. At TMO44, a clear distinction between the model types H1 and T1 is not possible. The anisotropy model at TMO07 is primarily only valid in the NE quadrant, since nearly no SWS was observed in the SW quadrant. However, further SWSMs and a wider backazimuthal coverage possibly may reveal yet unrecognized more complex anisotropy in the future.

Our modelling results of the whole BAZ range demonstrate that a laterally uniform structural anisotropy model at one single recording station is not always appropriate to explain the observations. As lateral variations around a single recording site have to be taken into account, it is required to model limited (station-)specific BAZ ranges. The SWSMs obtained at neighbouring recording stations should not be handled isolated from each other, but set in a more holistic context to outline subregions of the study region with different anisotropy regions.

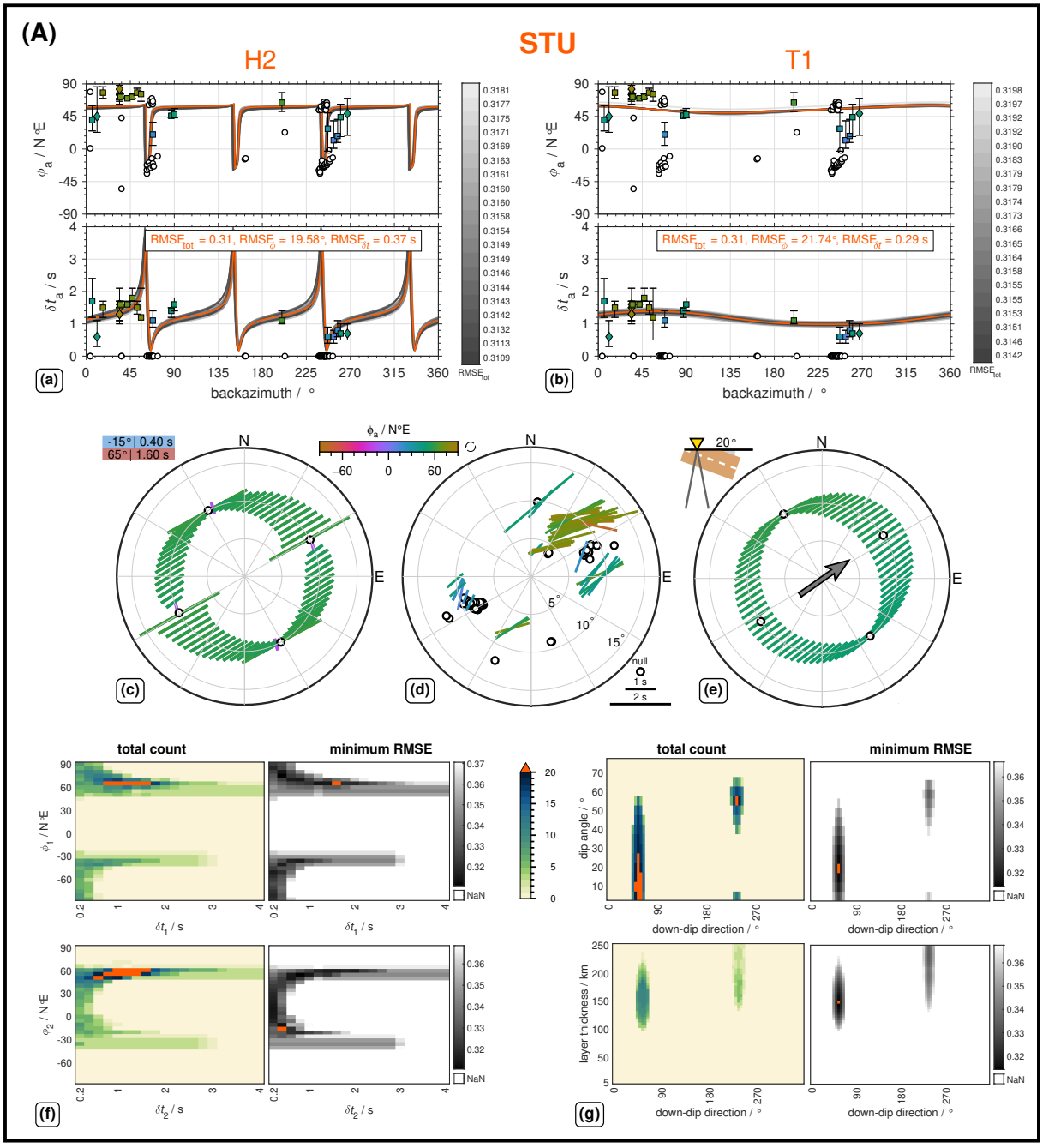

Figure 8.6: Modeling results for testing two-layer models with horizontal symmetry axes (H2, left) and one-layer models with tilted symmetry axis (T1, right) at the recording stations **(A)** STU and **(B)** ECH. Backazimuthal variations of the apparent splitting parameters for the 20 best-fitting synthetic anisotropy models for **(a)** H2 and **(b)** T1 (plotting conventions as in Fig. 8.5). Stereoplot representation (plotting conventions as in Fig. 8.2) of **(d)** the *good* and *fair* shear wave splitting measurements from the single-event analysis (*energy minimization* method; *Silver and Chan*, 1991) and the forward calculated apparent splitting parameters for the best-fitting model for **(c)** H2 and **(e)** T1 (for the eight best-fitting models see Fig. B.20a). The white circles indicate the expected backazimuth directions for the *nulls*. The sketches in the upper left corners give the corresponding model parameters. For H2, the modeled fast polarization directions $\phi_{1,2}$ and delay times $\delta t_{1,2}$ for the lower (index 1, blue rectangle) and upper (index 2, red rectangle) layers are displayed. For T1, the dip angle (relative to the horizontal, light grey sector) of the symmetry axis (parallel to the olivine a-axis, dashed white line) is given and the dark grey arrow shows the down-dip direction (strike direction σ + 90°) of the layer (brown rectangle). The two dark grey lines indicate rays arriving with an incidence angle (relative to the vertical) of around 10° at the recording station (yellow inverse triangle). Heatmaps for the 1000 best-fitting models showing the total count (left) and the minimum RMSE (right) for **(f)** H2 and **(g)** T1 (for the heatmaps of all model parameter combinations see Fig. B.16). For the distribution of the model types within the 500 best-fitting models see Fig. B.19 (left-hand column).

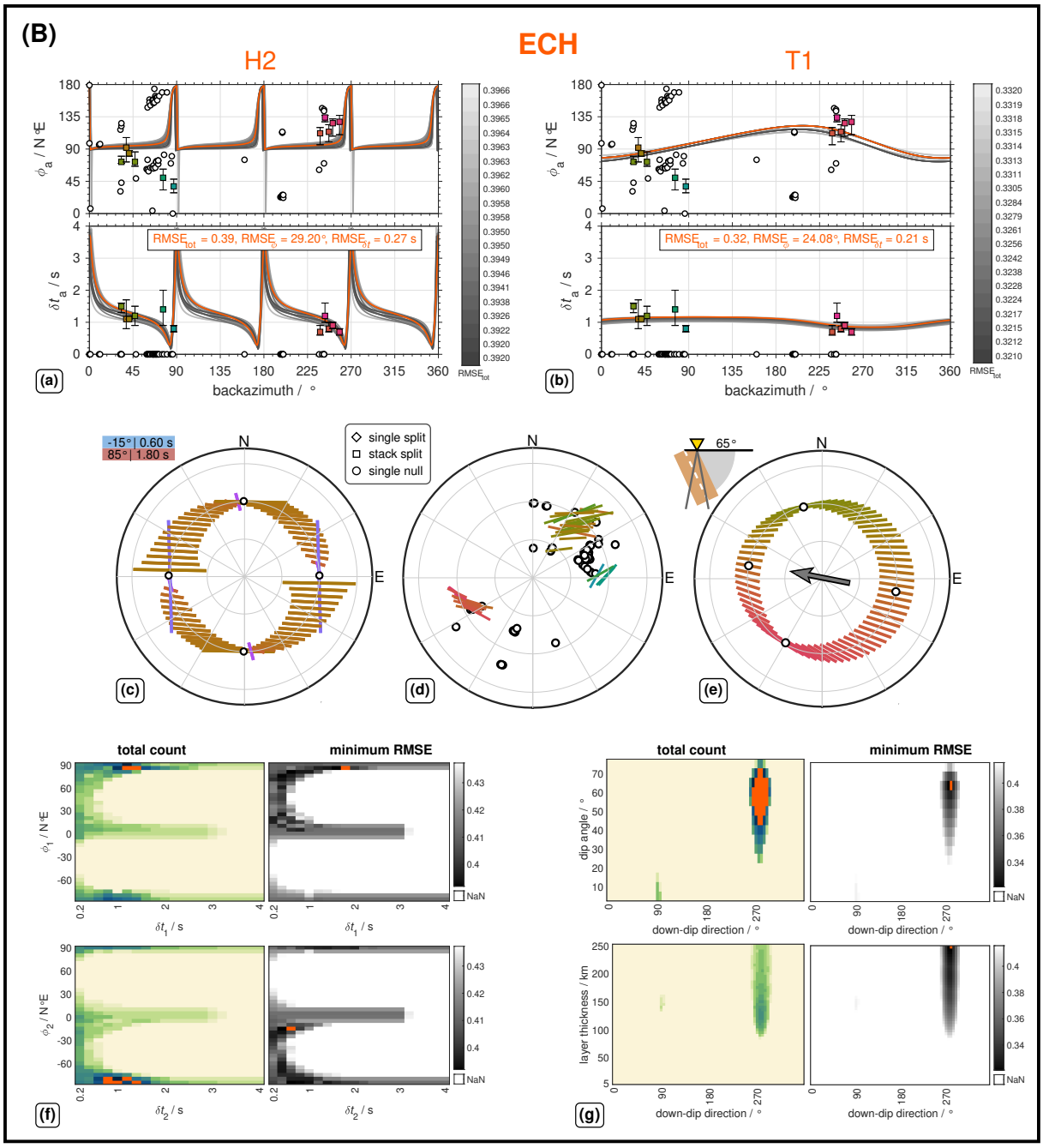

Fig. 8.6 continued.

8.6.1.2 Fitting of (station-)specific BAZ ranges

In this step, we test a fit of (station-)specific BAZ ranges to better account for lateral variations. A separation between the NE quadrant (30°-100°) and the SW quadrant (180°-270°) is made, because observations from both cannot be explained in one model. Less than four *splits* within one quadrant do not allow for a stable and reliable modelling and are discarded. The anisotropy models for BFO and TMO07 are already based on a modelling of the NE quadrant, since only the NE quadrants contain clear *non-null* measurements. A separate modelling of the NE quadrant at STU gives a similar result for H2 and T1 (Fig. 8.7A). In the SW quadrant, the backazimuthal data coverage is quite poor. At ECH the modelling of the NE quadrant results in a better visual fit for a dipping layer (T1), but the observed *nulls* do not fall in the expected BAZ directions (Fig. 8.7B). The *nulls* are better fitted for two layers (H2). The *non-null* measurements in the SW quadrant are concentrated in a small BAZ range 230°-250°.

This is visible in the similar fit of two layers (H2) and a dipping layer (T1). At TMO44 the number of splitting observations in the SW quadrant is too low for a backazimuth-dependent modelling.

8.6.2 Depth constraints

The modelled delay time indicates whether the anisotropy can be restricted to the crust or whether also a mantle contribution has to be considered (*Savage*, 1999; *Long and Silver*, 2009). In addition, SWSMs on phase pairs, here SKS and SKKS phases, can provide indications regarding a possible lowermost mantle contribution (*Deng et al.*, 2017).

Lüschen et al. (1990) analysed near-vertical reflections (ca. 10-40 Hz) in the Black Forest area and found shear wave splitting with maximum 0.3 s in the laminated lower crust. As model, about 10-30 per cent of aligned anisotropic hornblende crystals is proposed. Using teleseismic P-to-S conversions from the Moho, *Eckhardt and Rabbel* (2011) found transversely polarized S waves with a split time of 0.2 s in the crust below BFO. These studies suggest a minor crustal contribution to the SKS splitting, which may regionally add as noise on the splitting signal from the mantle.

Since the observed and modelled delay time (Figs **8.5**, **8.6** and **8.7**) is significantly longer than 0.3 s, the related anisotropy is mainly located in the mantle. Significant discrepancies between SWSMs of SKS and SKKS phases are not observed (Figs **B.10** and **B.22**a, b) and the splitting intensity for both phases is overall similar (Fig. **B.22**c, d). Thus, the anisotropy is most likely located in the upper mantle without a resolvable contribution from the lowermost mantle.

The delay time depends on both the thickness of the anisotropic layer and the strength of the anisotropy: a thin (thick) anisotropic layer with strong (weak) anisotropy would produce equivalent SWSMs. This trade off cannot be solved uniquely. However, a theoretical thickness and a theoretical minimum depth of the bottom of the anisotropic layer can be estimated from the modelled delay time, when assuming a realistic strength of the anisotropy as *a priori* information. The top of the anisotropic layer is assumed to be directly at the Moho. The calculation of the layer thickness is approximated with Eqs **8.4** and **8.5** (*Helffrich*, 1995).

$$L = \delta t \frac{v_{\text{fast}} v_{\text{slow}}}{v_{\text{fast}} - v_{\text{slow}}} \approx \delta t \frac{v_{\text{mean}} v_{\text{mean}}}{v_{\text{fast}} - v_{\text{slow}}} = \delta t \frac{v_{\text{mean}}}{k_{\text{s}}} \tag{8.4}$$

$$D = L \cos(i) \tag{8.5}$$

Here, L is the length of the travel path in the anisotropic layer, D is the thickness of the anisotropic layer, and i is the incidence angle (measured from the vertical) of the S wave. For a dry upper mantle, we assume an average (isotropic) shear wave propagation velocity of v_{s} = 4.3-4.4 kms^{-1} (*Legendre et al.*, 2012) and a percentage anisotropy (SWS in case of transverse isotropy) of k_{s} = 4.0 per cent (*Savage*, 1999). As incidence angle, we use $i = 10°$ to be consistent with the value for the model type T1 (tilted symmetry axis). As Moho depth we take 28 km in the URG area after *Prodehl et al.* (1992) and for the LAB a depth of 60-80 km (*Seiberlich et al.*, 2013). For the modelled delay times of $\delta t = (0.5, 1.0, 2.0)$ s we obtain thicknesses of $D = (53, 107, 214)$ km and minimum depths of $(81, 135, 242)$ km. Thus, for a delay time $\delta t \geq 1.0$ s lithospheric and asthenospheric anisotropy components must be assumed, because the minimum depth exceeds the lower limit for the LAB of 80 km. This is consistent with lithospheric anisotropy in the anvil model by *Fuchs* (1983) for a depth range of 25-51 km, its update by *Enderle et al.* (1996, fig. 17), and a deeper depth interval of 50-150 km with the strongest azimuthal anisotropy derived from surface waves (*Zhu et al.*, 2015, fig. 24).

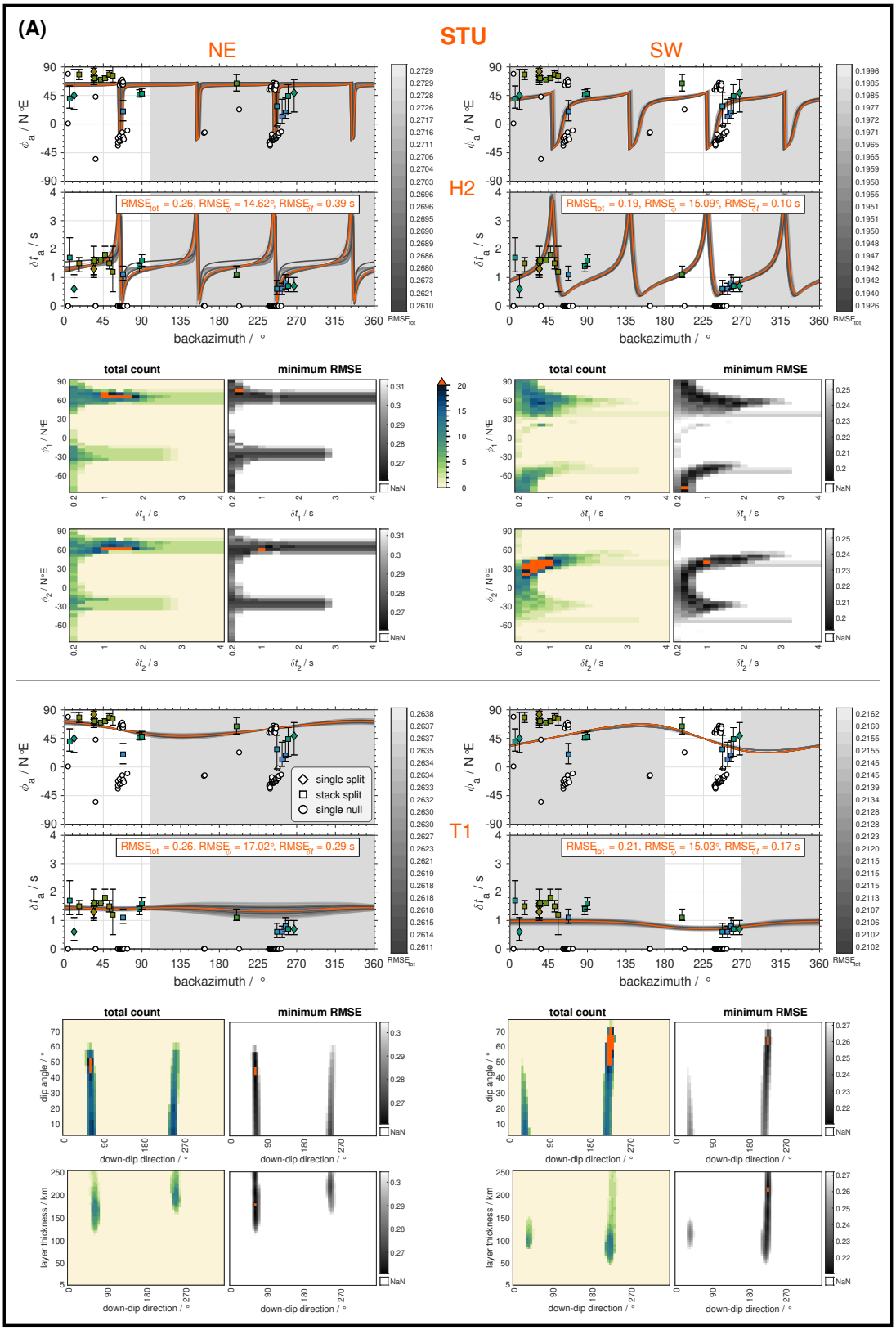

Figure 8.7: Modelling results (plotting conventions as in Figs 8.5 and 8.6) comparing the NE (left) and SW (right) quadrants at the recording stations **(A)** STU and **(B)** ECH for testing two-layer models with horizontal symmetry axes (H2, upper part) and one-layer models with tilted symmetry axis (T1, lower part). Backazimuthal variations of the apparent splitting parameters for the 20 best-fitting synthetic anisotropy models (top) and heatmaps for the 1000 best-fitting models (bottom). For the heatmaps of all model parameter combinations (Figs B.17 and B.18), the distribution of the model types within the 500 best-fitting models (Fig. B.19, middle and right columns), and the stereoplots for the eight best-fitting models (Fig. B.20b, c) see the Supporting Information.

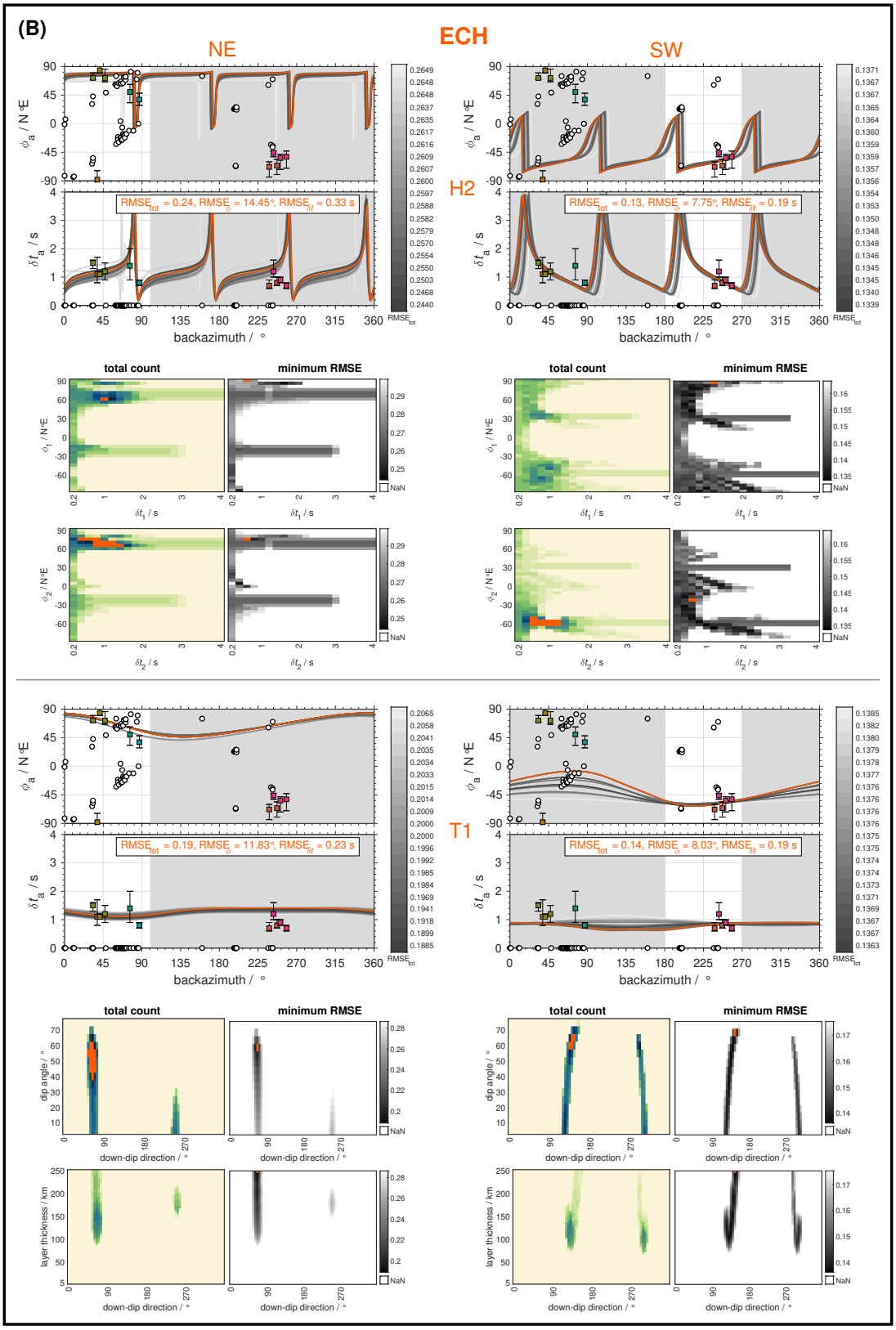

Fig. 8.7 continued.

8.6.3 Presence of vertical and lateral variations

Plotting the station-related SWSMs or stereoplots on top of a geographical map helps to identify similarities and differences in the splitting parameters across recording stations. Subareas of the study region can be delimited, which are related to (small-scale) lateral variations of the anisotropy. In Fig. 8.8, the stereoplots are arranged in geographical order, in which observation similarities are highlighted by sectors with the same colour.
To test which area or volume at depth is sampled by the waves or rays, we calculated piercing points and the corresponding first Fresnel zones in the upper mantle (depth range 0-450 km) and determined overlaps of observations. For a period of 8 s (dominant period of our analysed *X*KS phases) the ray theory is valid only limited and in principle the full waveform should be considered. The full wave sensitivity range is mostly associated with or restricted to the first Fresnel zone (*Alsina and Snieder*, 1995; *Favier and Chevrot*, 2003; *Tesoniero et al.*, 2020). Its extension increases with increasing period (decreasing frequency) and increasing depth (Eq. 8.6). The radius r_F of the first Fresnel zone at depth z is calculated via Eq. 8.6 (*Pearce and Mittleman*, 2002; *Margheriti et al.*, 2003; *Petrescu et al.*, 2020) with the respective incidence angle i of the *X*KS phase (within 5°-12°), a period T of 8 s (dominant period of *X*KS phases) and an average (isotropic) S wave propagation velocity v of 4.3 kms^{-1} (in the dry upper mantle; *Legendre et al.*, 2012).

$$r_F = \sqrt{\frac{T\, v\, z}{2\cos(i)}} \tag{8.6}$$

This yields a diameter of around 80-180 km for the first Fresnel zone in the upper mantle Fig. B.26). Such a wide sensitivity region blurs the ray path information and should not allow recovering splitting variations across small BAZ ranges of a few degrees.
Our observed variations of the SWSMs at and across the single recording stations (Fig. 8.8) cannot exclusively be explained by vertical variation of anisotropy or a tilted symmetry axis. Also, lateral variation of anisotropy is required. There are similar patterns at WLS and ECH which differ from the common pattern at TMO07, TMO44 and STU. Furthermore, there are differences in the shear wave splitting between the NE and SW quadrant at BFO. For the depth range of the upper mantle these variations occur on a smaller length scale than the extension of the first Fresnel zone, for example in 100-200 km depth the diameter of the first Fresnel zone is ca. 100-130 km. Thus, the first Fresnel zones overlap for the different *X*KS phases, and our observations cannot be explained entirely by wave theory. This is also reported from other studies (e.g., *Bastow et al.*, 2007; *Grund and Ritter*, 2020).
Regarding vertical and lateral variations of the anisotropy in the upper mantle beneath the URG area, we discuss the following observations (Fig. 8.8):

- BFO: NE quadrant vs. SW quadrant
  → characteristic two-layer splitting pattern vs. numerous *nulls* and inconsistent splitting parameters
- Moldanubian Zone: east side of the URG - west side of the URG
  → STU - BFO - ECH: change of the fast polarization directions
- east side of the URG: Moldanubian Zone - Saxothuringian Zone
  → STU, BFO, ECH - TMO44, TMO07: tendency from two layers (H2) to one layer (T1/H1)
- WLS, STU, TMO44, and TMO07: NE quadrant
  → interstation consistency of the splitting parameters

Between STU (or BFO in the NE quadrant) and ECH a significant change of the fast polarization direction is observed (Figs 8.5, 8.8 and 8.9b), especially in the upper layer. The delay times slightly differ. In case the fast polarization directions of the lower and the upper layers are (nearly) orthogonal somewhere between BFO and ECH, the splitting can be compensated. No splitting would be observed (at the surface), but *null* measurements

over a wide BAZ range, and the medium would appear apparently isotropic. Such a constellation may be the reason for the numerous *null* measurements at BFO in the SW quadrant (Fig. 8.8, light yellow sectors). It has to be mentioned that the *nulls* at BFO in the SW extend over a BAZ range of up to 180°. Beside the trivial solution of a real isotropic medium and a constellation for an apparent isotropic medium, other hypotheses for this *null anomaly* are already suggested by *Ritter et al.* (2022), which are tested in more detail in Sec. 8.6.4.

Overall, there are strong indications for lateral variations in anisotropy, especially of the fast polarization direction(s), in the Moldanubian Zone between the east side and the west side of the URG (Fig. 8.10). This is consistent with a lateral variation of the anisotropy between STU, BFO and ECH as suggested by *Walker et al.* (2005a). However, in contrast to *Walker et al.* (2005a) we also include vertical variations of the anisotropy (two-layer models) to explain the observed backazimuthal variation of the splitting parameters. *Walker et al.* (2005a) explain the *null* observations at BFO in the SW quadrant with weak to no anisotropy beneath the URG.

We find a lateral variation of the anisotropy on the east side of the URG from the Moldanubian Zone (BFO, STU) to the Saxothuringian Zone (TMO44, TM007), especially a tendency from two layers in the south to one layer in the north (Fig. 8.10b, c). However, due to the limited backazimuthal coverage a clear distinction is not possible between a horizontal and a tilted symmetry axis. Based on the currently available SWSMs, a horizontal symmetry axis (both H1) is preferred which may explain the observed weak backazimuthal variation of the splitting parameters.

The splitting patterns of the stereoplots in the NE quadrants (BAZ range 40°-90°) display more interstation consistency than in the SW quadrants (190°-260°, Fig. 8.8). Especially at WLS, STU, TMO44 and TMO07, the splitting patterns in the NE quadrants appear similar (Fig. 8.8, light green sectors). However, the splitting patterns in the SW quadrants differ clearly between these four recording stations. A common source of the observations in the NE quadrants would imply intrastation lateral variations between the NE and SW quadrants at one recording station. Here again the conflict regarding the wave sensitivity becomes visible. From a full wave perspective, such small-scale lateral variations are not expected or should not be visible in the data due to the large first Fresnel zones. One possible explanation may be that at WLS and STU in the NE quadrants the waves already experience anisotropy of the Saxothuringian Zone and at TMO44 in the SW quadrant anisotropy is recorded from the Moldanubian Zone. In this case, the anisotropy must be located deep enough that the piercing points overlap. Such an overlap occurs in 150-250 km depth (Fig. 8.9).

In Fig. 8.10a the stereoplots are plotted on top of a geographical map of the URG area. The schematic 3-D block model of the anisotropy in Fig. 8.10c summarizes our current knowledge of the upper mantle beneath the URG area.

8.6.4 Geodynamic implications

There are several possible geodynamic interpretations as consequence of the non-uniqueness of the structural anisotropy model regarding both, model parameters and partly the model type. Two anisotropic layers are often associated with fossil frozen-in anisotropy in the lithosphere above an anisotropic layer caused by current (horizontal) mantle flow in the asthenosphere (e.g., *Silver and Savage*, 1994; *Currie et al.*, 2004). One anisotropic layer with a tilted symmetry axis may be explained by palaeo-subduction (e.g., *Liddell et al.*, 2017; *Grund and Ritter*, 2020). The URG area was and is still affected by multiple geological and tectonic processes such as Variscan and Alpine Orogenesis including subduction, collision and mantle flow, or rifting of the URG. In the following, we consider possible causes for the observed shear wave splitting and the determined seismic anisotropy models, including approaches to explain the numerous *null*observations in the southern URG. We go through this from larger to smaller length scale (Tab. 8.3).

[16] The numbers of the related sections are adjusted by adding a leading "8." to match the numbering in this doctoral thesis.

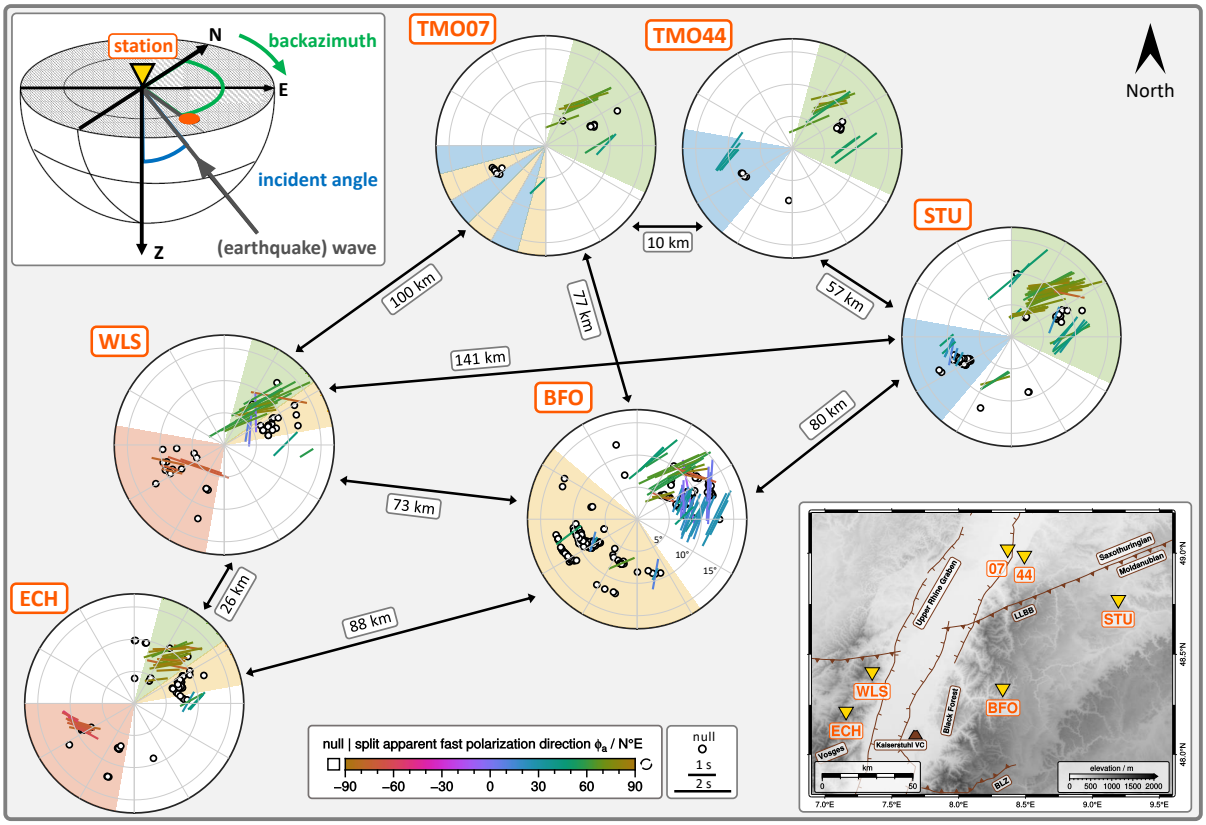

Figure 8.8: Roughly geographical arrangement of the *good* and *fair* shear wave splitting measurements from the single-event analysis visualized in stereoplots (plotting conventions as in Fig. 8.2) for each recording station. SWSMs at BFO are expanded based on *Ritter et al.* (2022). Similarities between the stereoplots are highlighted by coloured sectors (see Sec. 8.6.3). The values at the arrows give the interstation distances. The sketch in the upper left corner is modified after *Rost and Thomas* (2002, fig. 12). Note that dimensions are not to scale. For related Cartesian histograms see Figs B.23 and B.24.

8.6.4.1 Absolute plate motion and large-scale asthenospheric flow

The current absolute plate motion (APM) in the URG area has a direction of ca. 48-53 N°E and a speed of 23-26 mm yr^{-1} after recent plate motion models GSRM v2.1 (*Kreemer et al.*, 2014) and MORVEL (*DeMets et al.*, 2010). For a plate motion coupled to the horizontal simple asthenospheric mantle flow (*Silver*, 1996) abrupt small-scale variations of the fast polarization direction are unexpected. The APM direction cannot be seen directly in our data, but may be overprinted by the observed small-scale variations of the splitting parameters. In case of topography at the underside of the plate, complex flow patterns may be excited, e.g., edge-driven convection (*Long and Becker*, 2010). Presently, such a rugged topography at the lithosphere-asthenosphere is not known in the URG area (*Kirschner et al.*, 2011; *Seiberlich et al.*, 2013). In case of a fast APM and a low viscosity of the asthenosphere, significant anisotropy is induced by the movement of a lithospheric plate over a sublithospheric shearing zone (e.g., *Fouch et al.*, 2000; *Bokelmann and Silver*, 2002; *Mainprice et al.*, 2005). Possibly such a mechanism with minor side flows may cause the lateral variations in Fig. 8.8.

8.6.4.2 Vertical coherent deformation at Variscan mountain belts

In the concept of vertical coherent deformation (VCD), the fast polarization direction is expected to be parallel with the strike direction of a mountain belt (*Silver*, 1996). In our study region, the strike directions are 60-80 N°E for the Variscan Mountain Belt (*Meschede and Warr*, 2019). The fast polarization directions in the SW quadrants at WLS and ECH do not align with such a strike. For the NE quadrants the fast polarization directions are more consistent

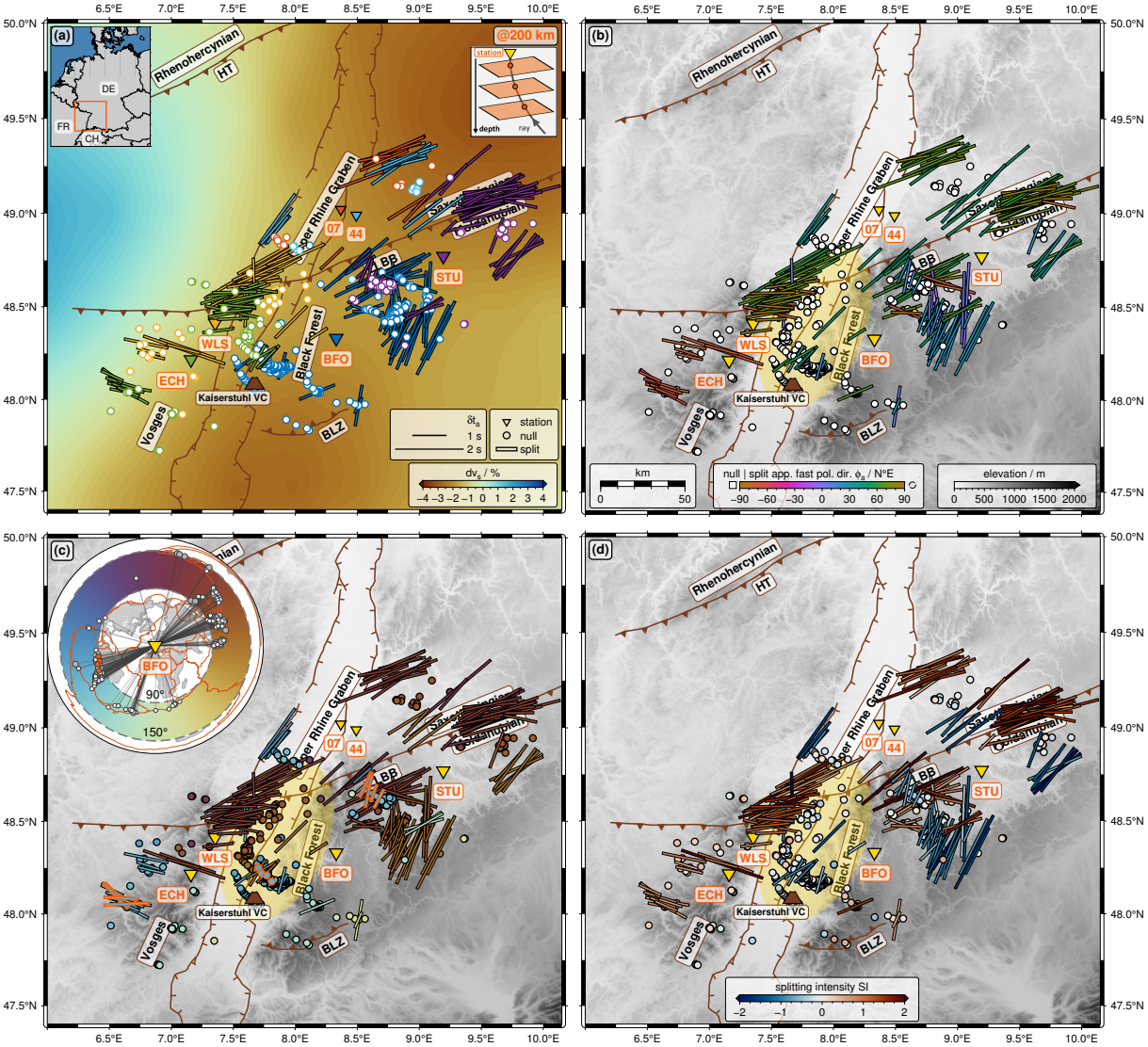

Figure 8.9: Maps of the central Upper Rhine Graben (URG) area (section of the map in Fig. 8.1) with piercing points in 200 km depth (upper mantle) calculated with the *iasp91* Earth model (*Kennett and Engdahl*, 1991). The *good* and *fair* shear wave splitting measurements (SWSMs) from the single-event analysis are included. SWSMs at BFO are expanded based on *Ritter et al.* (2022). *Nulls* are plotted as circles. *Splits* are displayed as orientated (apparent fast polarization direction ϕ_a clockwise from north), length-scaled (apparent delay time δt_a) bars (SC method; *Silver and Chan*, 1991). The colour-coding refers to the **(a)** recording station (respectively coloured inverse triangle), **(b)** apparent fast polarization direction ϕ_a, **(c)** backazimuth and **(d)** splitting intensity *SI*. Note the lateral concentration of *nulls* beneath the URG in 150–250 km depth (yellow ellipse in (b)–(d)) and the continuous rotation of ϕ along the west side of the URG. The tomography model EU_{60} (relative shear wave velocity anomaly dv_s) after *Zhu et al.* (2015) is used as background in (a). The inset in (a) in the upper right-hand corner shows the principle of the piercing points. The symbols with orange outline (main map) or fill (inset in the upper left-hand corner) in (c) refer to the SWSMs at STU, BFO and ECH show in Figs 8.3 and B.25. For the piercing points in the lowermost mantle see Fig. B.22.

across the stations WLS, STU, TM05 and TMO07 and they are close to the strike of the Variscan terranes. If the Variscan deformation represents not the last significant episode of VCD in the lithosphere, even a pre-Variscan (until now unknown) origin could be considered for anisotropic structures. Below a critical temperature, for olivine circa 900°C, the CPO is preserved, and the anisotropy remains unchanged (*Long and Becker*, 2010). Based on a (too) low temperature at the top of the mantle *Vinnik et al.* (1994) assess a recent origin for the anisotropy as unlikely in our study region. Following *Artemieva* (2019, fig. 9) the temperature in the upper mantle underneath the URG area exceeds 900°C in a depth below 40-50 km. This unusually high temperature is related to a thin lithosphere in the URG area (the LAB is located in 60-80 km depth; *Seiberlich et al.*, 2013) and would mean that old,

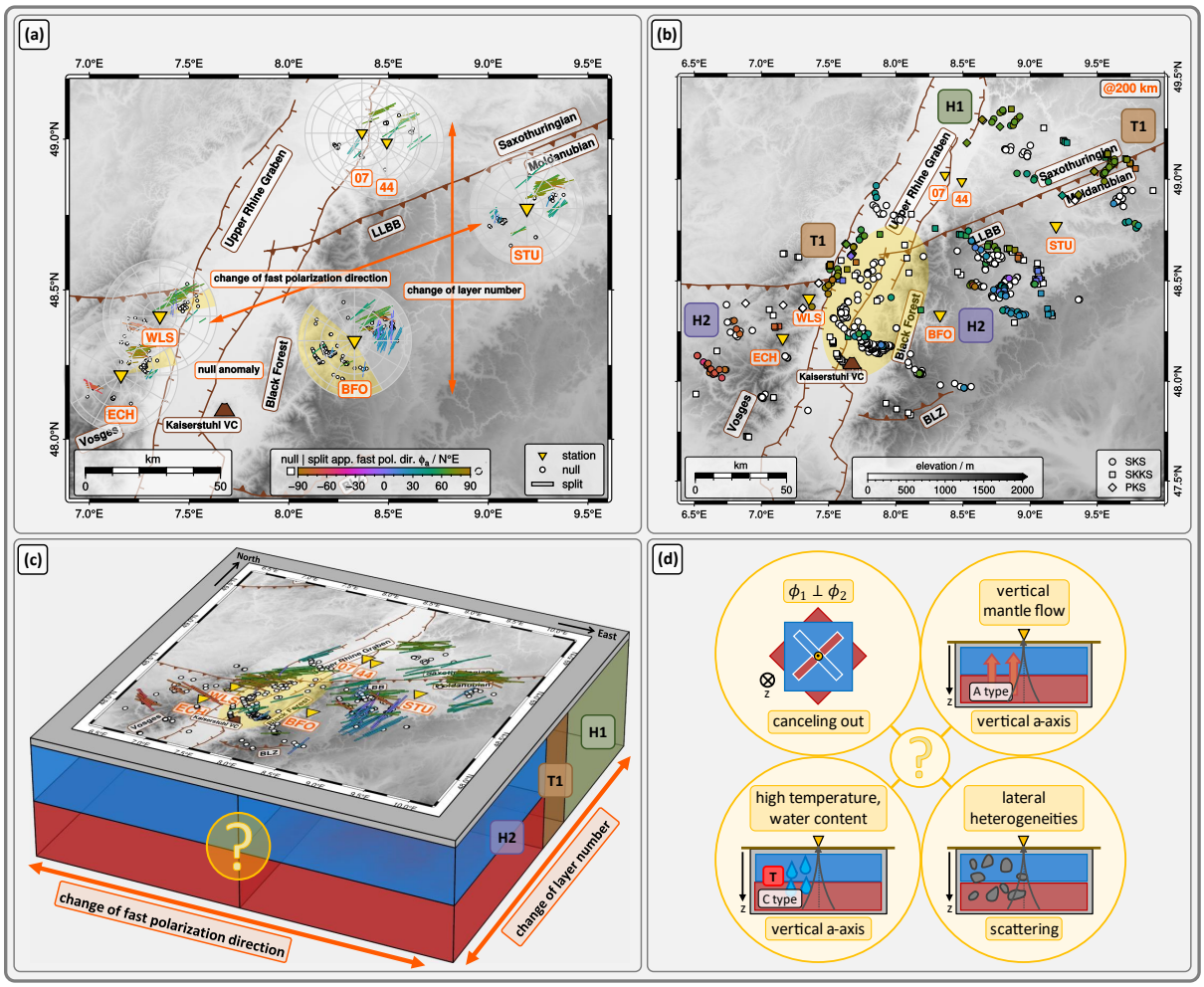

Figure 8.10: Seismic anisotropy in the upper mantle beneath the Upper Rhine Graben (URG) area (see also Tab. 8.3). **(a)** Map (section of the map in Fig. 8.1) with stereoplots of the *good* and *fair* shear wave splitting measurements (SWSMs) (plotting conventions as in Fig. 8.2) on top. SWSMs at BFO are expanded based on *Ritter et al.* (2022). **(b)** Map (section of the map in Fig. 8.9) with the piercing points in 200 km depth for the *good* and *fair* SWSMs on SKS (circles), SKKS (squares), and PKS (diamonds) phases. *Nulls* as symbols with white fill and *splits* as symbols filled with colour-coding for the fast polarization direction. The preferred model types based on the modelling results are given by the square labels: one horizontal layer (H1) in green, two horizontal layers (H2) in purple, and one dipping layer (T1) in brown. **(c)** First-order 3-D block model with map on the top showing the piercing points in 200 km depth (plotting conventions as in Fig. 8.9b). In a depth of 150-250 km the rays of the *nulls* cross the URG (Fig. 8.9b-d) highlighted by the yellow sectors in the stereoplots in (a) as well as the yellow ellipse in the maps in (b) and (c). The colours represent different anisotropic scenarios: two horizontal layers (H2) in red (lower layer) and blue (upper layer), one dipping layer (T1) in brown, and one horizontal layer (H1) in green. Note that dimensions are not to scale. **(d)** sketches of tested hypotheses (beside the trivial case of isotropy) to explain the numerous *nulls* and inconsistent splitting parameters of *splits* in the SW of BFO (see Sec. 8.6.4).

preserved anisotropy in the lower lithosphere should no longer be present. Only in the case of a lower temperature (< 900°C) the old deformation processes could still be present. The change of the fast polarization directions between the east side (STU) and the west side (ECH) of the URG is a hint towards different processes and/or different temperatures affecting lower lithospheric structures.

Between north and south, the Lalaye-Lubine-Baden-Baden (LLBB) fault separates the Moldanubian and Saxothuringian Variscan terranes, and it reaches as terrane boundary down to the LAB. *Babuška and Plomerová* (2001) proposed a change in the anisotropy at this terrane boundary. The interstation consistency of the splitting parameters within the NE quadrant at the stations WLS, STU, TMO44 and TMO07 (Fig. 8.8) may point to a common origin. These SWSMs have delay times of > 1 s and a fast polarization direction, being subparallel to the strike of the LLBB fault. An influence of the S-SSE dipping LLBB fault on the shear wave splitting may reveal itself in a tilted symmetry

Table 8.3: Overview of different hypotheses regarding the anisotropy in the upper mantle beneath the Upper Rhine Graben (URG) area and the *null anomaly* in the southwest of BFO which are tested in Sec. 8.6.4 (see also Fig. 8.10). The table is arranged by the decreasing length scale of the considered aspects (top to bottom) and shows in the middle column the different causes and structures related to anisotropy and in the right column at which recording stations the causes or structures may be supported by the observed splitting patterns. "Unclear" means that an aspect is not seen in the data, which is mainly because the observed variations of the splitting parameters occur on a smaller length scale. *Abbreviations*: APM = absolute plate motion; KVC = Kaiserstuhl Volcanic Complex; LLBB = Lalaye-Lubine-Baden-Baden.[16]

Scale	Causes and structures related to anisotropy	Observed
Huge	*8.6.4.1 Absolute plate motion, large-scale asthenospheric flow*	
	→ simple asthenospheric mantle flow	
	• APM in the URG area	unclear
Large	*8.6.4.2 Vertical coherent deformation at Variscan mountain belts*	
	→ critical temperature: anisotropy is overprinted or remains	
	• critical temperature: anisotropy is overprinted or remains	NE quadrants
	• LLBB fault: tilted symmetry axis	NE quadrants
Middle	*8.6.4.3 Recent regional mantle flow*	
	→ horizontal mantle flow	
	• Alpine Mountain Belts: strike	NE quadrants
	• Alpine and Adria slabs: barrier effect	unclear
Small	*8.6.4.4 Ambient mantle conditions*	
	→ olivine fabric types: variations in temperature, water, stress	
	• KVC: non-horizontal mantle flow, melt or fluids	*null anomaly*
	• URG: passive rifting, west vs. east sides	STU vs. ECH
	8.6.4.5 Lateral heterogeneities	
	→ wavefield scattering	
	• Variscan terrane	*null anomaly*
	• KVC: magmatism and intrusions	*null anomaly*

axis with a fast polarization direction subperpendicular to the strike of the LLBB fault. Such an anisotropy pattern is not clearly supported by the modelling at STU and ECH, but from the modelling of specific backazimuth ranges there is a slight indication of a tilted symmetry axis and thus the Variscan subduction related anisotropy cannot be excluded totally (Figs 8.7 and 8.10b, c).

8.6.4.3 Recent regional mantle flow

One expects the fast polarization direction to be orientated about parallel to the strike direction of a mountain belt in the asthenosphere and about orthogonal in the lithosphere for a collision zone with a mountain belt such as the Alps in the south of our study region (*Silver and Chan*, 1991; *Silver*, 1996).
Petrescu et al. (2020) suggest a present mantle flow pattern indicating a possible barrier effect of the Alpine and Adria slabs based on their anisotropy model. Compared to the large-scale trends proposed by *Petrescu et al.* (2020), *Link and Rümpker* (2021), *Link and Rümpker* (2023), and *Hein et al.* (2021) we find a splitting pattern with more lateral variations on a much smaller length scale in the analysis of long-term recordings. In Fig. 8.9a, the piercing points are plotted in 200 km depth together with the seismic tomography model EU_{60} (dv_s) by *Zhu et al.* (2015). This model has only very small velocity changes close to most of our piercing points. Towards the west, where we observe a more east-west trend of the fast polarization direction, the seismic velocity increases. However, there is no clear correlation between the shear wave velocity changes and the fast polarization directions. Overall, our model in Fig. 8.10c cannot be explained with a broad flow pattern related with the Alpine collision. Beneath the central URG, *Kirschner et al.* (2011) found no hint for a low-velocity mantle anomaly (mantle cushion) and therefore no evidence for an active flow of hot material from the asthenosphere into the lithosphere (upwelling)

based on teleseismic traveltimes (see also Fig. 8.9a). Instead, passive rifting, for example a simple shear mechanism, due to the reactivation of pre-existing shear zones is assumed as cause for the URG. According to this, a large-scale impact or change of the anisotropy through the evolution of the URG seems to be unlikely.

8.6.4.4 Small-scale mantle structures: ambient mantle conditions

Mostly A-type olivine CPO is assumed in our models. However, it has been shown that the CPO of olivine depends on ambient stress, water content, temperature, and pressure conditions (*Jung et al.*, 2006; *Skemer and Hansen*, 2016). The A-type, that is a horizontally orientated olivine a-axis in the direction of maximum shear, is primarily valid for dry olivine aggregates in the upper mantle (*Long and Silver*, 2009; *Long and Becker*, 2010). In contrast, the C-type, that is a vertically orientated olivine a-axis, occurs at moderate to high water content and high temperature. Since the seismic propagation velocities along the olivine b-axis ([010]) and c-axis ([001]) differ only slightly, *X*KS phases experience only a weak anisotropy effect due to their near vertical incidence in the upper mantle. This leads in turn to weak or no shear wave splitting and the observations of reduced or small delay times or numerous nulls.
The Kaiserstuhl Volcanic Complex (KVC) is a major volcanic complex located in the southern URG which was active in the Middle Miocene (Fig. 8.1). It is assumed that the width of the KVC is wider underneath the sediments of the URG than as it appears at the surface (*Braunger et al.*, 2018 and references therein). The KVC has a deeply rooted magmatic system with melt generation at the LAB and the carbonatitic melt evolution is thought to be related with fluids or melts interacting with the mantle lithosphere (*Braunger et al.*, 2018). A local vertical mantle flow as well as ambient mantle conditions like an increased water or volatile content and higher temperature could be related to the mantle magmatism of the KVC (Fig. 8.10d). The latter case can lead to a different olivine CPO, meaning C-type instead of A-type. For both, a vertical mantle flow and a C-type olivine CPO, a vertical symmetry axis would be present, reducing the splitting of *X*KS phases. Such a mechanism is known from other magmatic centres (*Walker et al.*, 2005b) and may be relevant for seismic stations with BAZ quadrants covering the KVC (Figs 8.8 and 8.10a). C-type olivine may explain the spatial restriction of the numerous *null* observations at BFO to the SW quadrant. At ECH in the BAZ range 60°-90°, many *null* measurements were found which overlap with the piercing point region of the *null* observations at BFO in the SW quadrant in 200 km depth (Fig. 8.9). Further north, at TMO07 mostly *nulls* are observed in the SW quadrant, but further west at TMO44 there are some *splits* of *poor* quality. This difference in splitting observations at an interstation distance of only 10 km between TMO44 (*split*) and TMO07 (*null*) (Fig. 8.8), partly for the same earthquake, may indicate the rim of the *null anomaly*. According to these piercing points (Figs 8.9 and 8.10b) the waves propagate beneath the KVC in a depth of 150-250 km (asthenosphere). Thus, the influence of modified mantle material related to the KVC, even deeper than the LAB, could explain the numerous *null* measurements beneath the URG, especially at BFO in the SW quadrant.

8.6.4.5 Small-scale mantle structures: lateral heterogeneities

A priori a laterally homogeneous medium or layer is assumed up to here. Small-scale lateral heterogeneities would cause wave scattering, which affects the signals on the R and T components. The latter is especially crucial because the concept of measuring SWS of *X*KS phases is based on an *X*KS-related signal on the T component, which often has a small amplitude. Therefore, scattering can cause erroneous SWSMs Several consequences may appear due to scattering: (i) a signal on the T component despite no SWS resulting in a (wrong) classification of the SWSM as *split*, (ii) damping of a very weak SWS-signal on the T component resulting in a (wrong) classification of the SWSM as *null* and (iii) a combined scattered and split signal on the T component due to a superposition or interference with the SWS signal resulting in a classification as *split* but with wrong splitting parameters or as

unmeasurable.
In our study region lateral heterogeneities could have been developed during the Variscan Orogeny when several small-scale lithospheric blocks and islands arcs collided (*Tait et al.*, 1997; *Matte*, 2001). The lithospheric blocks can potentially be responsible for the lateral variation between the observed splitting patterns. In addition, the heterogeneities can cause scattering of the seismological wavefield.
Later, magmatic intrusions related with the Miocene KVC modified the lithosphere-asthenosphere system. Generally, only a small portion of the mantle melt reaches actually the surface as lava in a volcanic complex. More voluminous intrusions are expected in the lithosphere (*White et al.*, 2006) and these lateral heterogeneities may cause scattering beneath the KVC. As consequence magmatic modification of the mantle may lead to the mainly *poorly* ranked *splits* with inconsistent splitting parameters at BFO in the SW quadrant which covers the KVC region.

8.7 Conclusions and outlook

To investigate the seismic anisotropy in the mantle beneath the URG area, we measure SWS of *X*KS phases using long-term data (15-25 yr) of six (semi-)permanent broad-band seismological recording stations. We determine the splitting parameters and calculated the splitting intensity afterwards. According to delay times > 0.3 s the prevailing part of the anisotropy must be located in the mantle. As there are no significant discrepancies between SKS and SKKS phases, lowermost mantle anisotropy should not play a significant role and the main part of the anisotropy must be located in the upper mantle (lithosphere and asthenosphere). The backazimuthal variations of the splitting parameters are modelled using single-station structural anisotropy models composed of two layers or one layer with transverse isotropy with horizontal symmetry axes, handling (stations)specific backazimuth ranges separately.
We find inter- as well as intrastation lateral and vertical variations of the anisotropy on the scale of at least interstation distances (Figs **8.8**, **8.9** and **8.10**): on the east side of the URG two anisotropic layers are suggested for the Moldanubian Zone (south; BFO, STU) and a single anisotropic layer in the Saxothuringian Zone (north; TMO44, TMO07). In the Moldanubian Zone a change of the fast polarization directions is found between the east (STU, BFO) and west (ECH) side of the URG. We summarize these findings in a schematic 3-D block model (Fig. **8.10**c) which also includes the *null anomaly* in the southwest at BFO (Fig. **8.10**d; *Ritter et al.*, 2022). In the south (Moldanubian Zone) the two anisotropic layers could be related with the lithosphere and asthenosphere, the latter being deformed by the present mantle flow. At the terrane boundary there is a zone with inclined anisotropy, possibly a remnant of the deformation during the Variscan subduction. Further north, in the Saxothuringian Zone, the modelled one-layer anisotropy could be due to mineral alignment which is about parallel in the lithosphere and asthenosphere.
The cause of the *null anomaly*, which partly coincides with the Kaiserstuhl Volcanic Complex, may be a modification of the mantle due to Middle Miocene melting processes including fluid-rock interaction. These magmatic processes may have produced structural modifications including large intrusions causing either a change in the olivine CPO or wave scattering.
Our 3-D block model has shorter length scales compared to other models. For example, the regionalized anisotropy model by *Link and Rümpker* (2023) averages over our study region, however, it also demonstrates the need for lateral variation in anisotropy.
Teleseismic SWS observations generally suffer from a limited backazimuthal coverage due to the uneven distribution of the global seismicity. Thus, only long-term recordings allow recognizing (characteristic) backazimuthal variations of the splitting parameters, which indicate complex anisotropy and related structures at depth. The small-scale lateral variations of the anisotropy in the URG area demonstrate that densely spaced recording stations and long-term observations are needed to recover anisotropic structures in the lithosphere-asthenosphere

system. Future numerical modelling should not only focus on separate station wise fitting, but the dataset of SWS measurements at several recording stations should be seen in a more holistic context. The dataset should be subdivided based on spatially similar splitting pattern across stations and piercing points sampling the same region. Doing so, subregions with different anisotropy pattern can be outlined (see also *Grund and Ritter*, 2020; *Link and Rümpker*, 2023). Beside *splits*, also *nulls* need to be included in the interpretation (*Wüstefeld and Bokelmann*, 2007). Furthermore, the inclusion of geological or tectonic constraints as *a priori* information should help to relate (not) observed splitting to present and past geodynamic processes and the determination of 3-D anisotropy models. Knowledge of the (continental) upper mantle anisotropy and its potentially very small-scale variations is essential to be able to correct SWS measurements when investigating lowermost mantle contributions to the anisotropy. Our 3-D block model in Fig. **8.10**c is still based on observations from a limited number of recording stations, especially SWS measurements from the south and northwest are still missing. Future work will focus on testing and improving this model based on synthetic seismograms simulated with *AxiSEM3D* (*Leng et al.*, 2016; *Leng et al.*, 2019), including scattering (*Leng et al.*, 2020) and arbitrary anisotropy (*Tesoniero et al.*, 2020).

Acknowledgments.
YF was supported by a scholarship of the Graduate Funding from the German States (Landesgraduiertenförderung). We used seismological data of the six recording stations from different networks achieved by (i) the Federal Institute for Geosciences and Natural Resources (Bundesanstalt für Geowissenschaften und Rohstoffe (BGR) Hannover): BFO (GR, German Regional Seismic Network (GRSN); *Black Forest Observatory*, 1971; *Federal Institute for Geosciences and Natural Resources*, 1976), (ii) the German Research Centre for Geosciences (Deutsches GeoForschungsZentrum (GFZ) Potsdam): STU (GE, GEOFON Program GFZ Potsdam; *GEOFON Data Centre*, 1993), (iii) the French Seismologic and Geodetic Network (RÉseau SIsmologique et géodésique Français (RESIF)): WLS (FR; *RESIF*, 1995), (iv) the IPGP (Institut de Physique du Globe de Paris (IPGP)) Data Centre: ECH (G, GEOCOP; *GEOSCOPE*, 1982), (v) the KArlsruhe BroadBand Array (Karlsruhe BreitBand Array (KABBA)) Data Centre: TMO05/TMO44 and TMO07 (KA, KABBA; `http://ws.gpi.kit.edu`) and (vi) the AlpArry Seismic Network (AASN): A126A (Z3, AASN, restricted; *AlpArray Seismic Network*, 2015).
Mrs F. Ritter is thanked for long-term support and assistance with running station TMO44. We thank Yasmin Sanz Alonso for providing her shear wave splitting measurements at the recording WLS (FR) (2011 October-2017 June). The Python toolbox *ObsPy* (*Beyreuther et al.*, 2010) 1.2.2 (*The ObsPy Development Team*, 2020) was used to request seismological data.
All maps were prepared with *PyGMT* v0.12.0 (*Tian et al.*, 2024) and the *Generic Mapping Tools* (*Wessel et al.*, 2019) 6.4.0 (*Wessel et al.*, 2022). The other figures were created with MATLAB R2023a/b as well as Microsoft PowerPoint Home and Student 2016 and combined using *PyGMT*.
The piercing points were calculated with the *iasp91* Earth model (*Kennett and Engdahl*, 1991) with *MatTaup* by Qin Li based on the original Java *TauP* Toolkit (*Crotwell et al.*, 1999).
Colour-coding was accomplished with the *cmocean* colormaps (*Thyng et al.*, 2016) as well the *Scientific Colour Maps* 8.0.1 (*Crameri*, 2023).

Author contributions.
YF analysed the data, prepared maps and figures and wrote text. MG and JR wrote text and supervised the analysis and interpretation.

Statements and declarations.
The authors declare no competing interests.

Data availability statement.
Shear wave splitting measurements of the single-event analysis of *good* and *fair* qualities are freely avail-

able for download as CSV and PDF files at *RADAR4KIT* as the dataset "*Longterm Shear Wave Splitting Measurements in the Upper Rhine Graben Area*" (`https://dx.doi.org/10.35097/685`). Additionally, the measurements are provided to the shear-wave splitting database(`https://ds.iris.edu/spud/swsmeasurement`, `https://ds.iris.edu/dms/products/sws-db/`). A corrected *SplitLab* code regarding the relative temporal alignment of the vertical, North, and East component traces (*Fröhlich et al.*, 2022a) is available at YF's GitHub account (`https://github.com/yvonnefroehlich/SplitLab-TemporalAlignment`). MATLAB functions to produce the stereoplot representation as well as to carry out the modelling are available at YF's GitHub account (`https://github.com/yvonnefroehlich/sws-visualization-and-modeling`). Python scripts or *Jupyter* notebooks using *PyGMT* to reproduce some of the geographical maps are available at YF's GitHub account (`https://github.com/yvonnefroehlich/gmt-pygmt-plotting`).

9 Summary and Outlook

In the following, the research questions formulated in Ch. 1.1 are confronted with the results from the SWS analysis and anisotropy studies in the previous chapters (Fig. 9.1) as well as unconsidered aspects and limitations resulting from the assumption made during different analysis steps are pointed out and follow-up research questions are formulated (Sec. 9.1). Potential research approaches to address these questions are discussed, including machine learning techniques to ease measuring SWS (Sec. 9.2) and simulations of synthetic seismograms with *AxiSEM3D* (*Leng et al.*, 2016; *Leng et al.*, 2019) to test and improve observation-based anisotropy models (Sec. 9.3).

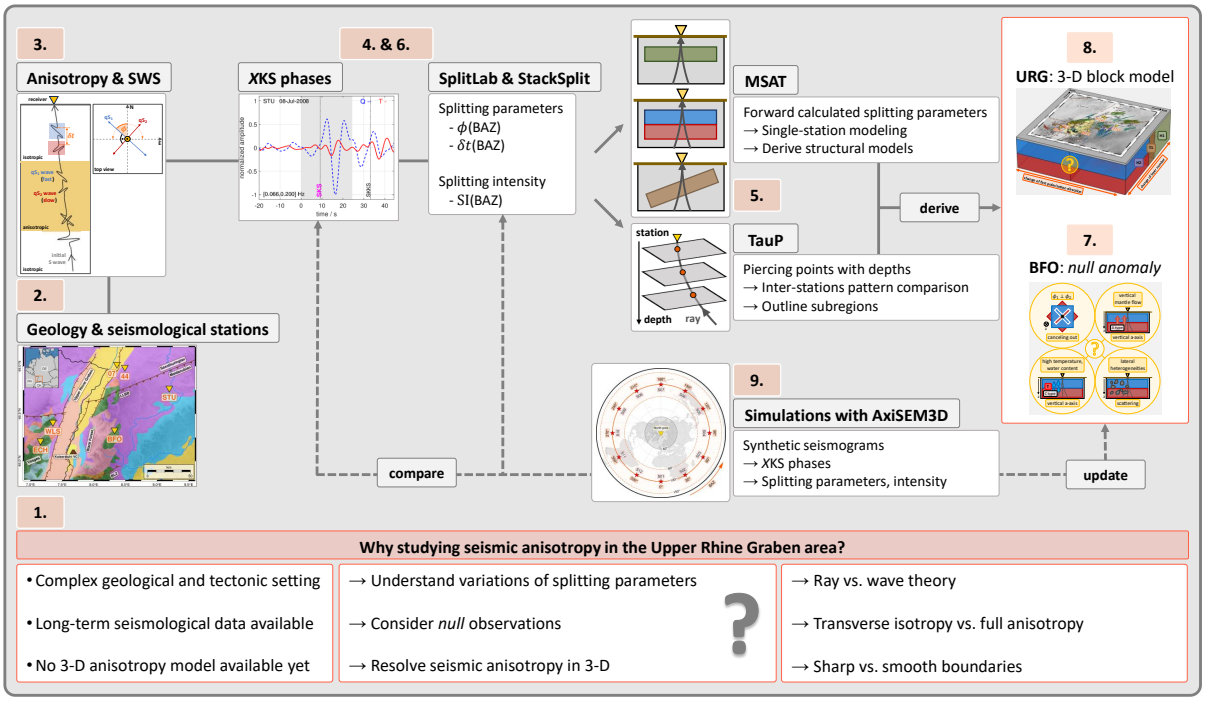

Figure 9.1: Workflow of this doctoral thesis: summary and outlook. Same as Fig. 1.2, but with results from the SWS analysis and anisotropy studies (upper right box) underneath the URG area (Fig. 8.10c; *Fröhlich et al.*, 2024b, fig. 10c) and at the BFO (Fig. 8.10d; *Fröhlich et al.*, 2024b, fig. 10d) as well as assumptions leading to limitations (bottom right box) and follow-up questions to the initial research questions (middle right box). The simulation of synthetic seismograms, e.g., with *AxiSEM3D* (*Leng et al.*, 2016; *Leng et al.*, 2019), can be used to test and improve proposed or observation-based anisotropy models (Sec. 9.3).

9.1 Findings, assumptions, and limitations

The main goal of this doctoral thesis was to understand complex seismic anisotropy and to resolve it in 3-D with a focus on the Upper Rhine Graben area in Central Europe. Therefore, shear wave splitting of *XKS* phases (PKS, SKS and SKKS) within the epicentral distance range 90°-150° was measured by the determination of the splitting parameters using both the RC (*Bowman and Ando*, 1987) and SC (*Silver and Chan*, 1991) methods as well as by the calculation of the splitting intensity (*Chevrot*, 2000). Long-term data (at least > 10-15 yr) from six (semi-)permanent seismological recording stations installed in Germany and France were analyzed manually

using *SplitLab* (*Wüstefeld et al.*, 2008; *Porritt*, 2014). During the manual shear wave splitting measurements, an error source regarding the correct relative temporal alignment of the component traces was found within *SplitLab* and corrected (Ch. 6). To improve (*simultaneous inversion of multiple waveforms*; *Roy et al.*, 2017) and equalize (stacking of surfaces; *Wolfe and Silver*, 1998) the backazimuthal coverage, the *SplitLab* plugin *StackSplit* (*Grund*, 2017; *Grund and Fröhlich* 2021) was used for a multi-event analysis based on the single-event analysis results.
The first study focused on one single recording station, the Black Forest Observatory, showing a quite striking and puzzling difference between the northeast and the southwest. While the backazimuthal variations of the splitting patterns show the characteristics for a two-layer scenario, in the southwest numerous *nulls* over a wide BAZ range up to 100° are observed (Ch. 7). Such an observation cannot be explained by vertical variation (two or multiple layers) or a tilted symmetry axis, but is a clear indication for lateral variation. In a second study, data from five additional recording stations in the URG area surrounding the BFO were analyzed in the same way (Ch. 8).
Synthetic splitting parameters as a function of the BAZ were forward calculated using the MSAT (*Walker and Wookey*, 2012) considering the three model types: one layer with a horizontal symmetry axis, two layers with horizontal symmetry axes, and one layer with a tilted symmetry axis. Understanding and accounting for the characteristic backazimuthal variations of the splitting parameters allow to detect and describe complex anisotropy. As the modeled delay times are significantly longer than 0.3 s the anisotropy must be located mainly in the mantle. SKS-SKKS phase pairs were analyzed to test for a lowermost mantle contribution to the anisotropy. As no clear discrepant pairs were found and the splitting parameters for same pairs (SKS and SKKS both split) are similar (Figs A.4, C.4), there is no direct indication for a LMM contribution, and the anisotropy is assumed to be located in the upper mantle within both the lithosphere and the asthenosphere.
For the URG area complicated splitting patterns are observed (Fig. 8.2). A 3-D block model (Fig. 8.10c) is proposed based on the station-wise forward modeling assuming a horizontal symmetry axis (Fig. 8.5, testing a tilted symmetry axis (Fig. 8.6), and considering only (station-)specific BAZ ranges (Fig. 8.7) as well as the interstation comparison of the splitting patterns (Fig. 8.8) and the calculation of piercing points with depth (Fig. 8.9):

(i) two layers in the Moldanubian Zone (south) but one layer in the Saxothuringian Zone (north),

(ii) different fast polarization directions on the east and west sides of the URG in the Moldanubian Zone, and

(iii) indications for a tilted symmetry axis close to the LLBB fault.

With explanations for the *null anomaly* in the southwest of BFO besides the trivial solution of isotropy (Fig. 8.10d):

(i) orthogonal symmetry axes of the two layers canceling out the splitting effect,

(ii) a vertical symmetry axis due to a C-type olivine fabric in the case of high temperature and water content,

(iii) a vertical symmetry axis due to vertical mantle flow, and

(iv) wave scattering due to heterogeneities.

In Tab. 8.3 the observations are related to geological and geodynamic processes with decreasing length scale. The observed variations occur on a much smaller length scale than for anisotropy related to the large-scale approaches SAF or VCD expected. This study demonstrates that continental upper mantle anisotropy can be quite complex, leading to complicated splitting patterns at single and across neighboring recording stations. Large-scale processes cannot explain the observed anisotropy. Furthermore, such splitting signals can contaminate splitting signals originating from the LMM due to the integral nature of the measurements.

In the following, the initial research questions (Sec. 1.1) are confronted with the results achieved and derived for the SWS analysis and anisotropy studies carried out and presented in the Chs 4 and 5 as well as Ch. 7 and 8.

1. Backazimuthal variations of the splitting parameters

- *Are they useful for the modeling?*
- *Can long-term data help to observe characteristic patterns?*

Only in case of simple anisotropy, the splitting parameters are constant with BAZ (except for the fast and slow polarization directions, *null* directions), otherwise apparent (or effective) splitting parameters are observed at the surface. Furthermore, complex anisotropy scenarios, described as two layers with a horizontal or tilted symmetry axis, show specific characteristics in the related backazimuthal variations of the apparent splitting parameters (Fig. 5.2). According to this (i) backazimuthal variations are a clear indication for complex anisotropy and allow to detect it, and (ii) the characteristics in the backazimuthal variations can be used to relate the apparent splitting pattern to an anisotropy scenario via a modeling procedure.
To clearly identify these characteristics within a splitting pattern, observations from different BAZ directions are needed. To achieve sufficient backazimuthal coverage, long-term data (10-15 yr) have to be analyzed to be able to gain enough (high-quality) SWSMs. This is consistent with *Evans et al.* (2006), who reported that roughly only 2 % of the analyzed data lead to reliable SWSMs.
However, there can still be ambiguities, as different anisotropy scenarios can lead to quite similar splitting patterns, i.e., different anisotropy models explain the observations equally well, leading to only slightly increasing RMSE values (Figs 8.5, 8.6, and 8.7). Partly it was recognized that there is a good fit for either the fast polarization direction or the delay time, but not for both. This can be an indication that the tested models are too simple or assumptions made (sharp boundaries) are actually not valid. While considering more complicated models, one should keep in mind that besides a mathematical fit, also the geophysical interpretation is important. For very complicated models, it gets less likely that these anisotropy scenarios can occur and are preserved over time (following the principle "Occam's razor").
Another difficulty can be the decision between vertical variation (two or multiple layers on top of each other) or a non-horizontal (tilted) symmetry axis and "real" lateral variation (two or multiple layers next to each other), as all scenarios lead to a backazimuthal variation of the splitting parameters. The latter would require dividing the SWSMs into subsets and modeling (stations-)specific BAZ ranges separately. This was done for BFO, and only the NE quadrat was used. To reliably resolve lateral variations, neighboring recording stations are needed to be able to find similarities or differences across the stations. This was done in a second study analyzing data from recording stations surrounding the BFO. The splitting patterns (Fig. 8.8) as well as the piercing points for different depths (Fig. 8.9) should be compared.

2. *Null* observations

- *Do they contain useful information (besides the trivial solution of isotropy)?*
- *How can they be included in the modeling and interpretation?*

The majority of anisotropy studies focuses on the waveforms with shear wave splitting. However, *nulls* do not exclusively indicate the trivial solution of isotropy, but contain relevant information. In case the initial polarization direction is orthogonal or parallel to the fast or slow polarization direction of the medium, no SWS can occur. According to this, for simple anisotropy, *X*KS phases should not show SWS for the BAZ directions being parallel or orthogonal to the fast or slow polarization directions, and for these four directions *nulls* should be observed. The fast polarization direction derived from the *splits* within the other BAZ directions should match the *null* directions. If this is not the case, it is likely that simple anisotropy cannot explain the observations well, and a more complex anisotropy scenario has to be considered. For H2, apparent *nulls* should be observed in the BAZ directions with the characteristic $\pi/2$ jumps of the apparent fast polarization direction and the scattering of the

apparent delay time (Fig. 8.4). For T1 the backazimuthal variation can be quite smooth and difficult to distinguish from H1 especially in the case of a small dip or / and only a few SWSMs.
According to this, *nulls* can be used as a cross-check for the modeling results derived from the synthetic forward calculation. In that way, *nulls* can be included within the modeling procedure, as *nulls* cannot directly be used in the comparison of forward calculated and observed splitting parameters. This is due to the behavior of the SC method for *nulls*, showing characteristic $\pi/2$ jumps in the apparent fast polarization direction and scattering of the apparent delay time over the entire value range up to the maximum considered in the grid search (Fig. 8.4). *Nulls* could verify specific scenarios or processes in combination with already existing knowledge regarding the geological and geodynamic setting of the study area. A different fabric type based on the ambient conditions can lead to a deviation from the assumption that the fast axis (a-axis) aligns with the direction of the (horizontal) mantle flow, and also simply some settings (e.g., vertical mantle flow or upwelling) may lead to anisotropy scenarios (e.g., VTI), which are not "visible" to specific (e.g., *X*KS) phases. Analyzing additional phases, e.g., S-ScS, can provide better constraints and maybe also be interesting for the *nulls* observed in the southwest at BFO.
Similar to the measurement of travel time,SWSMs are affected by the integral effect along the travel or ray path. Thus, constraints to locate observed splitting, especially in depth, are important. One approach is the analysis of phase pairs, e.g., SKS-SKKS. Discrepant pairs are mainly defined based on different observation types (i.e., one phase *split* and the other phase shows *null*), and indicate a LMM contribution to the anisotropy.
Overall, both observation types, *split* and *null*, are equally important. According to this, *nulls* should be included in the dataset of SWSMs. It is important to "actively" and "independently" observe *nulls* during the analysis. Data with too high noise or not clearly visible (*X*KS) phases could be excluded from the analysis to avoid contamination of the dataset by low-quality and unreliable SWSMs. *Wüstefeld and Bokelmann* (2007) reported that for *splits* in the directions close to a *null* measurement, the splitting parameters may differ from the correct values ("*near-null*" measurement).
Observing a *split* is a unique indicator for anisotropy, but an anisotropy scenario can be "invisible" for specific phases, and *nulls* are observed (Statement 9.1). In case of isotropy, *nulls* are observed, but *nulls* do not exclusively indicate isotropy (Statement 9.2). For example, VTI (e.g., due to upwelling) cannot be detected by the nearly vertical inclining *X*KS phases, and *nulls* are observed despite the present anisotropy.

$$split, \text{ i.e., shear wave splitting} \Rightarrow \text{anisotropy} \tag{9.1}$$

$$null, \text{ i.e., no shear wave splitting} \Leftarrow \text{isotropy} \tag{9.2}$$

3. Seismic anisotropy in 3-D

- *Can intrastation (lateral) variations of anisotropy be observed?*
- *Can subregions of the study area be outlined based on interstation comparisons?*

The studies within this doctoral thesis demonstrate that it is possible to detect complex anisotropy and that a first order of a 3-D anisotropy model can be derived based on SWS analysis. But, even for BFO (in the northeast), no unique anisotropy model could be derived, and only ranges for the model parameters could be given (Figs 7.8, 8.5). For very good BAZ coverage, it is possible to detect intrastation variation due to variations in the observation pattern, which cannot be explained by vertical variation or a tilted symmetry axis. It should be mentioned that quite different anisotropy scenarios have only slightly different RMSE values, including both different model parameters for one model type (Figs 8.5) as well as different model types (Figs 8.6, 8.7). Party, there is only a good fit for one of the two splitting parameters, which can indicate that the tested model types are too simple and more complex structures have to be considered. When selecting (station-)specific BAZ ranges for the modeling, it was partly difficult to decide whether the backazimuthal variation is due to vertical variation or a tilted symmetry axis or caused by real lateral variation. Important aspects for resolving anisotropy in 3-D are:

(i) Directional or backazimuthal coverage

To understand complex anisotropy, observations from different directions or earthquakes with different BAZs are needed. This requires the analysis of long-term data recorded at permanent stations. Otherwise, only a few SWSMs can be obtained in a few BAZ directions. Backazimuthal variations of the (apparent) splitting parameters are incompletely observed or missed, which leads to wrong interpretations and anisotropy models. In case of short-term data or / and a low SNR the *simultaneous inversion of multiple waveforms* can help to gain observations from additional BAZ directions. For the stations used in these studies, this method did not add significantly more BAZ directions, as there were not enough observations within small BAZ ranges outside the main source regions. This underlines that the SIMW is mainly useful for temporary recording stations to gain at least observations from the directions of the main source regions. The stacking of surfaces helped well to avoid an over-representation of backazimuth directions with many observations. The definition of analytical criteria for observation types and the quality categories besides the subjective evaluation of the waveform and the particle motion by the analyst helps to achieve a consistent and more reliable dataset.

(ii) Different seismic phases

Due to the integral nature of SWSMs one single splitting observation cannot be located along the ray path. For *X*KS phases, the possible location of the anisotropy is limited to the part between the CMB and the receiver (Fig. 4.3). The steep incidence of *X*KS phases in the upper mantle leads to a vertical integral effect, i.e., a good lateral resolution but a poor vertical resolution. Due to the different travel paths of SKS and SKKS phases in the LMM but nearly identical travel paths in the upper mantle, these phases can be used for testing for a LMM contribution to the anisotropy. In that way, discrepant phase pairs, e.g., SKS-SKKS, provide crucial depth constraints. Thus, it is recommended to analyze both (different) phases regarding SWS, and not only SKS. In case discrepant pairs are found, the dataset should be separated into two subsets and handled independently in the modeling and interpretation. Phases with different travel paths experience another anisotropy or SWS effect (for the same anisotropy scenario). The results from a simultaneous analysis can be used as a cross-check and can help to reduce the possible explanations or models for the observations, e.g., S and ScS phases. Regarding the *null anomaly* in the southwest of BFO it could be interesting to analyze S and ScS phases regarding SWS.

(iii) Neighboring recording stations

To resolve lateral variations, multiple recording stations are needed. For continental upper mantle anisotropy, various studies report lateral variations smaller than expected from the first Fresnel zone. Thus, the stations should have interstation distances not larger than 90 km. Calculating the piercing points with depth can help to outline subregions of the study area and to provide a depth constraint, especially in the upper mantle (Fig. 8.9). An interstation comparison of the splitting patterns shown in the stereoplots (Fig. 8.8) can help to outline subregions of the study area (see also aspect (iv)).

(iv) Modeling approach

As complex anisotropy scenarios show backazimuthal variations of the splitting parameters, the observed splitting parameters are apparent splitting parameters, and these values do not describe the anisotropy in the subsurface directly, but a modeling procedure is required, e.g., by a grid search via the comparison with forward calculated synthetic splitting parameters (see also research aspect 1). As similarities and differences in the splitting patterns across the recording stations can be an indication for lateral variation, modeling (station-)specific BAZ ranges should be tested. *Nulls* should be used as a cross-check of the modeling results as well as within the interpretation based on geological and geodynamic constraints or already existing knowledge to reduce the number of possible anisotropy scenarios or models that can explain the observations (see also research aspect 2).

Several assumptions were made during the analysis steps (Tab. 9.1), leading to limitations of the derived results and, by this, to follow-up questions. Possible research ideas to address these questions are machine learning techniques to measure SWS (Sec. 9.2) and simulations of synthetic seismograms to test anisotropy models (Sec. 9.3).

Table 9.1: Assumptions made regarding different analysis aspects or steps as well as the resulting unconsidered aspects.

Analysis aspect or step	Assumptions	Unconsidered aspects
*X*KS phases or S waves	rays	wave effects
anisotropy regimes anisotropy models	sharp boundaries simple layer models	smooth boundaries more complex models
measurement and forward calculation of splitting parameters	transverse isotropy A-type fabric	full anisotropy other fabrics
SWSMs	manual	time-consuming analyst-dependent

9.2 Machine learning techniques to measure shear wave splitting

In seismology, one central task is to find the onset time of the seismic phases within the seismogram ("picking"). Doing this manually is time-consuming and requires experience for reliable and consistent results. Considering the now-a-days available huge datasets, it becomes impossible to carry out the picking process by humans. Different approaches and tools have been developed to apply artificial intelligence (AI) and machine learning (ML) techniques to accomplish this analysis task, e.g., *SeisBench*[17] (*Woollam et al.*, 2022), *PhaseNet*[18] (*Zhu and Beroza*, 2018), and *Earthquake Transformer*[19] (*Mousavi et al.*, 2020).

Also, for the measurement of SWS finding and selecting the desired seismic phases, especially *X*KS phases, is a crucial analysis step. In this doctoral thesis, the measurement of SWS was done manually. To achieve consistent and reliable results, analytical criteria were defined for observation type and the quality category of the measurement. This reduces the analyst's influence and allows extending an existing dataset (continue with a station or add more stations) by another analyst. Applying different independent methods, testing different time windows and bandpass corner frequencies (stability of the measurement), as well as the classification of the measurement (*near-null* observation). However, such a manual analysis is quite time-consuming.

Most of the recently used tools, e.g., *SplitLab* (MATLAB; *Wüstefeld et al.*, 2008), *SplitRacer*[20] (MATLAB; *Reiss and Rümpker*, 2017), *SplitPy*[21] (Python; *Audet and Schaeffer*, 2019), *SeisSplit.jl*[22] (Julia; *Nowacki*, 2019), or *Sheaba*[23] (FORTRAN; *Wüstefeld et al.*, 2010), perform a grid search to determine the splitting parameters that correct best for the splitting effect. Besides these manual tools, semi-automatic tools, e.g., *SplitRacerAUTO*[24] (MATLAB; *Link et al.*, 2022) and *SWSPy*[25] (Python; *Hudson et al.*, 2023), can help to analyze huge datasets of several recording stations or networks (e.g., *USArray, AlpArray*), in case a manual analysis is too time-consuming or for another reason not possible. The recently published tools *CNN-SWS*[26] (*Zhang and Gao*, 2022) and *SWSNet*[27] (*Chakraborty et al.*, 2024), which apply AI and ML techniques in the context of *X*KS SWS, focus on the determination of the splitting parameters, rather than picking the *X*KS phases. In both works, the latter task is pointed out as a further or ongoing research aspect. According to this, a high-quality dataset of reliable SWSMs archived from long-term recordings at one recording station still requires a manual analysis of the seismic data, especially a careful selection of the desired phases. (Semi)-automatic approaches can significantly reduce the analysis time. An issue is that

[17] Available at `https://github.com/seisbench/seisbench`; last access 2025/04/15.
[18] Available at `https://github.com/AI4EPS/PhaseNet`; last access 2025/04/15.
[19] Available at `https://github.com/smousavi05/EQTransformer`; last access 2025/04/15.
[20] Available at `https://www.geophysik.uni-frankfurt.de/64002762/Software`; last accessed 2025/04/16
[21] Available at `https://github.com/paudetseis/SplitPy`; last accessed 2025/04/16.
[22] Available at `https://github.com/anowacki/SeisSplit.jl`; last accessed 2025/04/16.
[23] Available at `https://github.com/jwookey/sheba`; last accessed 2025/04/16.
[24] Available at `https://www.geophysik.uni-frankfurt.de/64002762/Software`; last accessed 2025/04/16.
[25] Available at `https://github.com/TomSHudson/swspy`; last accessed 2025/04/16.
[26] Available at `https://github.com/YW-Zhang94/CNN-SWS`; last accessed 2025/04/15.
[27] Available at `https://github.com/srivastavaresearchgroup/SWSNet`; last accessed 2025/04/15.

different (Fig. 4.2), especially depth (Fig. 4.7) phases can arrive almost at the same time at the recording station, which can lead to interference and corrupted waveforms, making it difficult or not possible to select or use these waveforms. When using an automatic approach, setting an upper limit for the hypocentral depth can help to exclude measurements on desired phases affected by depth phases.

9.3 Simulation of synthetic seismograms to test anisotropy models

In this doctoral thesis, the lateral variations of the measured splitting parameters and the modeled anisotropy occur on significantly smaller length scales than expected from the extent of the first Fresnel zone (Fig. B.26). This is clearly observed at the single recording station BFO by *Ritter et al.* (2022; Ch. 7, Fig. 7.9) as well as at neighboring recording stations in the URG area by *Fröhlich et al.* (2024b; Ch. 8, Fig. 8.8). However, for a period of 8-10 s (dominant period of *X*KS phases), ray theory is, strictly speaking, only valid in a limited way, and full wave effects have to be considered. There are other studies facing this issue or conflict (e.g., *Bastow et al.*, 2007; *Grund and Ritter*, 2020). Based on this, the observations cannot be explained entirely by wave theory, and *X*KS phases appear to be sensitive on a smaller length scale than the first Fresnel zone. Several studies were carried out on calculating sensitivity kernels to understand the sensitivity (e.g., *Alsina and Snieder*, 1995; *Favier and Chevrot*, 2003; *Chevrot et al.*, 2004; *Sieminski et al.*, 2008; *Wolf et al.*, 2021).

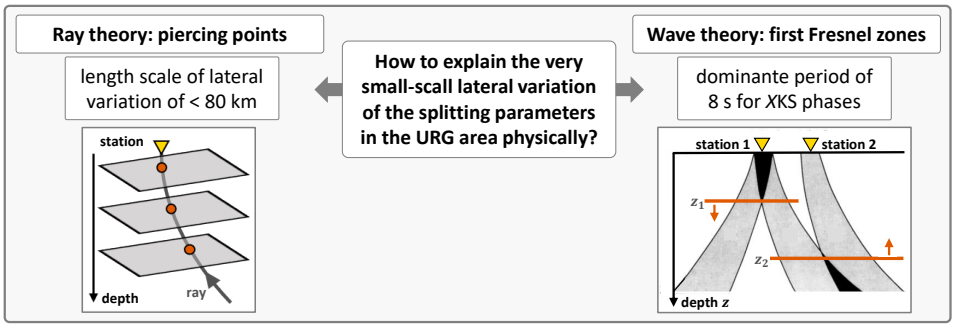

Figure 9.2: Conflict: **(left)** ray theory, i.e., piercing points vs. **(right)** wave theory, i.e., first Fresnel zones. Measuring and modeling SWS is mainly done by assuming the S waves as rays. The dominant period of *X*KS phases is 8-10 s, i.e., ray theory is, strikingly speaking, only valid in a limited way, and wave effects have to be considered. However, the inter- and intrastation variations of the observed splitting parameters occur on a significantly smaller length scale (Fig. 8.8) as expected from the size of the first Fresnel zone (Fig. B.26), i.e., the zones are overlapping (black areas). Thus, the observations cannot be explained entirely by way theory. Left part modified after *Fröhlich et al.* (2024b, fig. 9a) and right part modified after *Savage* (1999, fig. 8).

To test and improve proposed or observation-based anisotropy models, the simulation of wavefields and synthetic seismograms can be used. *AxiSEM3D* (*Axisymmetric Spectral Element Method - 3D*, written in C++; *Leng et al.*, 2016; *Leng et al.*, 2019), a new implementation of the old *AxiSEM* (written in FORTRAN; *Nissen-Meyer et al.*, 2014), is recently used for simulations in the context of anisotropy and SWS. *AxiSEM3D* is a solver for the elasto-dynamic wave equation (equation of motion) in homogeneous (Eq. 3.11) and heterogeneous media in three dimensions on local to global scales. Users can simulate seismograms and wavefields of displacement, acceleration, pressure, curl, stress tensor, and deformation. Additionally, *AxiSEM3D* offers the possibility to consider full or arbitrary seismic anisotropy (*Tesoniero et al.*, 2020) as well as to account for wave scattering (*Leng et al.*, 2020, fig. 10).
AxiSEM3D combines a dimension reduction leading to an axi-symmetric geometry (2.5-D, “Axi”; Fig. 9.3a; *Leng et al.*, 2016, fig. 1; *Leng et al.*, 2019, fig. 1) and a spectral element method (SEM). As the variations of seismic properties within the Earth are laterally significantly smaller than radially, i.e., the wavefield is less complex radially and less resource intensive to compute (*Fernando et al.*, 2024). Thus, the in-plane parts of the solution are found through spectral methods, but the azimuthal solution is derived via pseudo-spectral methods.

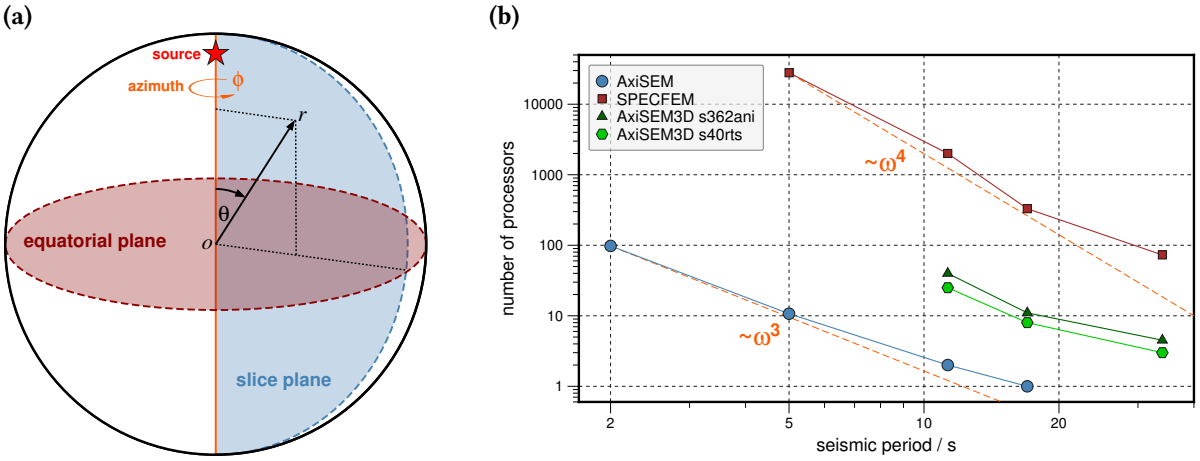

Figure 9.3: (a)Šketch of source (red star) centered coordinate system and positions of the equatorial (light red) and slice (light blue) planes. **(b)** Computational cost of global wavefield simulations in "real time" (i.e., seismogram length equals wall-clock simulation time) for the different solvers *SPECFEM*, *AxiSEM*, and *AxiSEM3D*. Each data point is based on actual runtime on *ARCHER* and gives as a result the number of processors needed to achieve this, assuming perfect scalability. The core numbers can be interpreted as the CPU hours required to produce 1 hour long waveform synthetics. The dashed orange lines show $O(\omega^3)$ and $O(\omega^4)$ with the frequency ω. (a) and (b) slightly modified after *Leng et al.* (2016, figs 1 and 16).

A major advantage of *AxiSEM3D* compared to other solvers, e.g., *SPECFEM* (*Komatitsch and Tromp*, 2002a; *Komatitsch and Tromp*, 2002b), is the required computational resources, mainly the shorter simulation time (Fig. 9.3b; *Leng et al.*, 2016, fig. 16; *Leng et al.*, 2019, fig. 9). It is proposed that it is possible to capture periods around 5 s (and maybe smaller) that are required to simulate *X*KS phases (and SWS in case of anisotropy). The so-called *wavefield scanning* or *wavefield learning* determines the minimum azimuthal resolution required to resolve all the features of the wavefield. It allows for a reduction of computational resources and can be described as the $N_r(s, z)$ field and visualized as a *complexity map*.

The 3-D block model proposed by *Fröhlich et al.* (2024b) can be tested and improved using simulations carried out with *AxiSEM3D* (Tab. 9.2). Synthetic seismograms and waveforms for traveling through this model can be generated and compared to the observed ones. Furthermore, the SWS can be measured by the determination of the splitting parameters and the calculation of the splitting intensity. The sequence of proposed simulations is structured in three runs: run A, run B, and run C (Tab. 9.3). The main simulations are covered by run C (Fig. 9.4).

Table 9.2: Working steps as well as software or data for simulations with *AxiSEM3D*. The overall goal is to generate synthetic seismograms containing *X*KS phases and measure the SWS of these phases by determining the splitting parameters as well as calculating the splitting intensity. In that way a proposed or observation-based anisotropy model can be tested and improved.

Aspect	Representation	Software / Data
background model	Earth model	isotropic *PREM* (*Dziewonski and Anderson*, 1981)
spatial grid	mesh	*SalvusMeshLite*[28]
seismic anisotropy	elastic tensors	data by *Jung et al.* (2006) and *Creasy et al.* (2020) NetCDF file via MSAT (*Walker and Wookey*, 2012)
receivers	recording stations	ASCII files with longitude, latitude, depth
source-receiver constellation	geographic maps	*PyGMT* (*Tian et al.*, 2025b)
synthetic seismograms	post-processing	*ObsPy* (*Beyreuther et al.*, 2010)
shear wave splitting	splitting parameters splitting intensity	*SplitLab* (*Wüstefeld et al.*, 2008)

Table 9.3: Source-receiver constellations for the different runs for simulations with *AxiSEM3D*. The simulations related to run A and run B are mainly for understanding purposes, while run C covers the actual simulations to test the proposed or observation-based anisotropy model for the URG area. *Notation*: Δ = epicentral distance.

Simulation	Earthquake	Recording station(s)	Figure
Run A	Virginia	networks (*USArray*, *AlpArray*, *ScanArray*)	Fig. C.9
Run B	North pole	global (theoretical, equally distributed)	Fig. C.10, Fig. C.11
Run C	along Δ = 120°	North pole (theoretical, one single)	Fig. 9.4

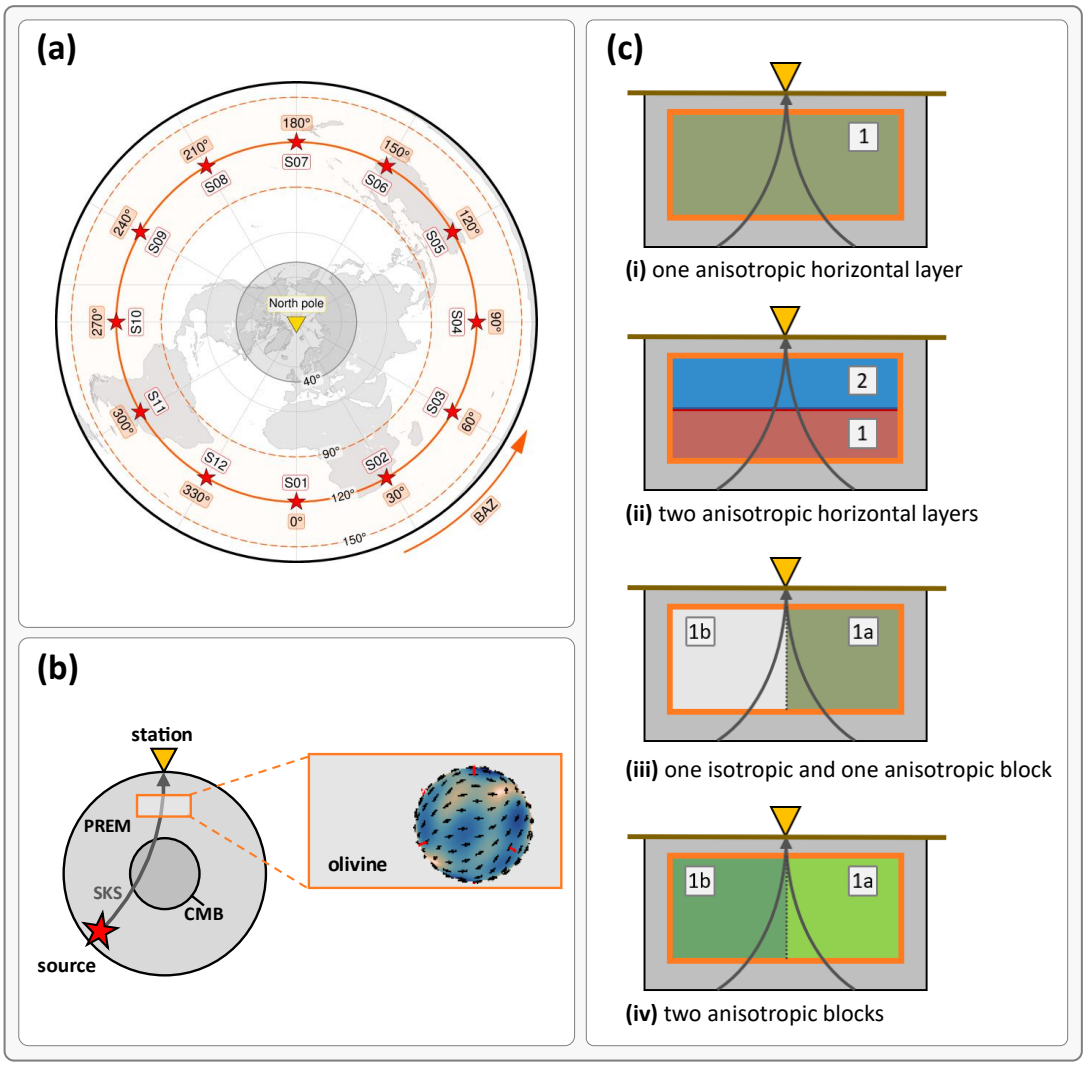

Figure 9.4: Simulations with *AxiSEM3D*: run C. **(a)** Source-receiver constellation with the receiver (inverse yellow triangle) at the North pole surrounded by receivers (red stars) at an epicentral distance of exemplary 120° (orange line) related to the range 90° to 150° (light orange ring) within *X*KS phases can be observed (Fig. 4.2). The gray circle of 40° around the station marks the area with different anisotropy scenarios in the upper mantle. **(b)** Seismic anisotropy is considered via the elastic tensor (Eq. 3.13). The mineral olivine (Fig. 3.7) is used to describe anisotropy in the upper mantle (Sec. 3.4.2) on the receiver side (orange-outlined box). Different orientations of the tensor represent different fabrics (Tab. 3.1). **(c)** Structural anisotropy models with layers and blocks (Fig. 5.3) corresponding to the ones used in the forward calculation of synthetic splitting parameters in Sec. 5.2 as a function of the BAZ (Fig. 5.2). For run A and run B, see Figs. C.9 or C.10, respectively.

[28] Available at `https://gitlab.com/swp_ethz/public/SalvusMeshLite`; last accessed 2025/05/08.

Funding

The presented research and YF received support:

- *2021/01 - 2021/12 and 2022/01 - 2022/12*: **Scholarship** of the Graduate Funding from the German States (Landesgradiertenförderung, LGF, `https://www.khys.kit.edu/english/graduate_funding.php`). Awarded by the Karlsruhe House of Young Scientists (KHYS).
- *2023/08 - 2024/03*: **Research Assistant** within the priority program (Schwerpunktsprogramm, SPP) 2404 "*Reconstructing the Deep Dynamics of Planet Earth over Geologic Time*" (*DeepDyn*, `https://www.geo.lmu.de/deepdyn/en/`) by the German research association (Deutsche Forschungsgemeinschaft, DFG) via grant RI1133/14-1 (`https://gepris.dfg.de/gepris/projekt/521545943?language=en`).
- *2022/08*: **Open Access publication** in Journal of Seismology. Publication feeds covered by the Karlsruhe Institute of Technology (KIT) library. Related to *Ritter et al.* (2022).
- *2024/07*: **Open Access publication** in Geophysical Journal International (GJI). Publications feeds covered by GJI via a special discount. Related to *Fröhlich et al.* (2024b).
- *2024/02*: **Online workshop** "*Visual Communication of Science Training*" by Jernej Zupanc. Offer of one free spot for a student or researcher within the SPP *DeepDyn* (first come, first served; the notes were shared with the members of *DeepDyn*).
- *2021/01 and 2022/01*: **Online participation** at the Global Young Scientist Summit. Awarded by the KHYS.
- *2024/06*: **In-person participation** at the 18th Symposium of Study of the Earth's Deep Interior, Great Barrington. Travel support by the German research association via the module "Standard Allowance for Gender Equality Measures" related to the SPP *DeepDyn*. Related to *Fröhlich et al.* (2024a).
- *2024/12*: **In-person participation** at the American Geophysical Union Annual Meeting, Washington, D.C.. Travel support by the National Science Foundation (NSF) via grant EAR-1948602 (`https://www.nsf.gov/awardsearch/showAward?AWD_ID=1948602`). Related to *Fröhlich et al.* (2024d), *Fröhlich and Ritter* (2024).

Software and data

Below I list software and data that were essential to carry out the analysis as well as to create the visualizations for this doctoral thesis as well as the related research articles and conference contributions. Besides these explicitly listed items, a **BIG** thanks go to all the people *asking*, *discussing*, and *answering* questions on platforms like *Stack Overflow* or any tool-specify forum as well as providing scripts related to publications on *GitHub*, especially regarding LaTeX, Python, MATLAB, *ObsPy*, *GMT* or *PyGMT*, *AxiSEM3D*, and so many more. You are all doing a great job there and help countless students, researchers, analysis, and developers at any knowledge level every day! I am hoping I can give something back to some of you through my answers on the *GMT* forum as well as my MATLAB codes and *PyGMT* maps on *GitHub*.

Software

- **Operating system**: Linux OpenSUSE 15.6, Windows 10-10.0.19045-SP0
- **MATLAB**: R2021a - R2024b
- **Python**: 3.7 - 3.12
- **Data processing and analysis**: *NumPy*, *pandas*
- **Creation of geographic maps**: *PyGMT* v0.7.0 - dev (*Tian et al.*, 2025b) with *GMT* (*Wessel et al.*, 2019) 6.3.0 - 6.5.0 (*Wessel et al.*, 2024)
- **Handling of seismological data**: *ObsPy* (*Beyreuther et al.*, 2010) v1.2.2 (*The ObsPy Development Team*, 2020)
- **Measuring of shear wave splitting**: *SplitLab* (*Wüstefeld et al.*, 2008) v.1.2.0 (*Porritt*, 2014), v1.9.0 with the plugin *StackSplit* (*Grund*, 2017) v2.0 - v3.0/dev (*Grund and Fröhlich*, 2021)
- **Forward calculation of SWS**: *MATLAB Seismic Anisotropy Toolbox* (MSAT; *Walker and Wookey*, 2012)
- **Visualization and modeling of SWS**: MATLAB functions and routines by *Fröhlich and Grund* (2022)
- **Calculation of piercing points as well as travel paths and travel time curves**: MATLAB toolkit *MatTaup* by Qin Lin and *ObsPy* (*Beyreuther et al.*, 2010) v1.2.2 (*The ObsPy Development Team*, 2020) based on the original *Java Taup* Toolkit (*Crotwell et al.*, 1999)
- **Simulation of synthetic seismograms**: *AxiSEM3D* (*Leng et al.*, 2016; *Leng et al.*, 2019)
- **Preparation of oral and poster presentations**: Microsoft *PowerPoint* Home and Student 2016
- **Creation of sketches**: Microsoft *PowerPoint* Home and Student 2016
- **Writing and typesetting of manuscripts and this doctoral thesis**: Microsoft *Word* Home and Student 2016, LaTeXvia *Overleaf* (the spelling is checked via a built-in AI-based tool)
- **Organization of literature and references**: *JabRef* v5.1

Data

- ***PREM* Earth model** by *Dziewonski and Anderson* (1981)
- ***iasp91* Earth model** by *Kennett and Engdahl* (1991)
- **Plate boundaries** by *Bird* (2003)
- **Digitized regions of reduced shear wave velocity** by *Wolf et al.* (2023)
- ***Scientific Colour Maps*** by *Crameri* (2023)
- ***cmocean* color maps** by *Thyng et al.* (2016)

Acknowledgments

Zuallererst möchte ich der **Landesgraduiertenförderung** für die uneingeschränkte und umfassende Unterstützung meines Promotionsvorhabens danken, sowohl finanziell als auch durch die immer freundliche und sehr hilfsbereite Betreuung der StipendiatInnen.

Ich danke **Prof. Dr. Joachim Ritter** für die Betreuung meiner Promotion. Hervorzuheben ist hier das umfangreiche Korrekturlesen von Manuskripten für Veröffentlichungen sowie dieser Dissertation.
Prof. Dr. Andreas Rietbrock danke ich für die Übernahme des Korreferats und das Interesse an meiner Arbeit.

Für das herzliche Willkommen im Herbst 2017, als ich für das Geophysik-Masterprogramm ans GPI nach Karlsruhe gekommen bin, möchte ich mich bei **Ellen Gottschämmer** und **Thomas Hertweck** bedanken.
Für die Unterstützung bei technischen Problemen danke ich **Michael Frietsch**, **Thomas Hertweck** und **Thomas Nadolney** sowie dem **Team vom SCC**. Für die Hilfe bei organisatorischen Aspekten geht ein Danke an **Kerstin Dick**, sowie für die umfassende Unterstützung der Promovierenden ein großer Dank an **Corinna Knodel-Rupp** und den Dekan der KIT-Fakultät für Physik **Prof. Dr. Guido Drexlin**!
Danke an die **Seismologie Arbeitsgruppe** für den Austausch und die Diskussionen während der Arbeitsgruppentreffen, insbesondere für die Rückmeldung zu Postern und Präsentationen bei der Vorbereitung auf Konferenzen.
Für die Unterstützung, Motivation und Aufmunterung sowie Gespräche über Forschung hinaus Danke an **Sarah Mader**, **Sarah Beraus**, **Janis Heuel**, **Mike Lindner**, **Laura Gaßner**, **Runa Ostermeier** und **Rune Helk**!
Ein großes Danke geht an **Jonathan Wolf**, **Runa Ostermeier**, **Alicia Rochnacher** und **Sarah Mader** für das Korrekturlesen verschiedener Kapitel dieser Dissertation!

Several international researchers visited GPI in person or gave online talks during my time as a master and doctoral student. I really enjoyed your talk in May 2020, **Prof. Maureen Long**.
A big thanks goes to **Jonathan Wolf** for visiting GPI for three days in April 2023 and introducing *AxiSEM3D*.

Thanks **Prof. Dr. Christine Thomas** for encouraging me to join the SEDI meeting in June 2024. I really enjoyed this week in Great Barrington. Thanks for introducing me to several international researchers. **Prof. Michael Bergmann**, you organized a great conference on such a beautiful campus, considering the smallest details!

A big thanks goes to the **GMT community** and the **GMT** and **PyGMT teams**! Especially thanks to **Prof. Dongdong Tian**, **Wei Ji Leong**, and **Max Jones** for the pleasant working environment on GitHub. I learned a lot by contributing to the *PyGMT* project, and I really hope I can continue contributing in the future!
Thank you so much to everyone for making it possible for me to participate at the AGU24 annual meeting in December 2024, especially to **Lily Shao** and **Prof. Garrett Apuzen-Ito** for handling all the organization in the background. I really enjoyed working and giving the pre-conference workshop together with you, **Wei Ji Leong**, **Max Jones**, **Jing-Hui Tong**, **Federico Esteban**, and **Prof. André Belem**. A big thanks to **Walter Smith**, **Prof. Anthony Watts**, **Prof. David Sandwell**, and **David Caress** for putting together a great memorial session for **Prof. Pål Wessel**. Giving a talk on *PyGMT* and meeting so many of you afterwards, during lunch, and in the poster session, including **Prof. Joaquim Luís** and **Prof. Xiaohua (Eric) Xu** as well as **Pål Wessel's family** was such an honor!

Seeing my anisotropy abstract being selected as a talk within the anisotropy and attenuation session was totally unexpected and super rewarding! Thanks to **Prof. Maureen Long**, **Frederik Link**, **Neala Creasy**, **Colton Lynner**, **Jonathan Wolf**, **Joseph Asplet**, and so many more for the interesting and nice discussions after the talks and during the poster session in the afternoon. **Prof. Edward Garnero**, your seismology talk "*What do the data say?*" was amazing!

Abschließend möchte ich mich bei meinen **Freunden** und meiner **Familie** für die immerwährende Unterstützung, Motivation und Aufmunterung in den letzten fünf Jahren bedanken.

Appendices

A Supplementary Information to *Ritter J. R. R., Fröhlich Y., Sanz Alonso Y. & Grund M. (2022) JSeismol*

This appendix is related to Ch. 7 and has been published as supplementary information to:

> *Ritter J. R. R.,* ***Fröhlich Y.****, Sanz Alonso Y. & Grund M. (2022).* **Short-scale laterally varying SK(K)S shear wave splitting at BFO, Germany – implications for the determination of anisotropic structures**. *Journal of Seismology*, 26:1137-1156. `https://doi.org/10.1007/s10950-022-10112-w`. Correction regarding the initially missing supplementary information `https://doi.org/10.1007/s10950-023-10136-w`.

A.1 Data information and availability

Our shear wave splitting measurements at the Black Forest Observatory (BFO) of the single-event analysis of *good* and *fair* qualities carried out in *SplitLab* (*Wüstefeld et al.*, 2008) are freely available for download as CSV and PDF files as part of this Supplementary Information (separately uploaded files) as well as from *RADAR4KIT* (`https://dx.doi.org/10.35097/684`).

MATLAB functions to generate the stereoplot representation (Fig. 7.4) as well as to perform the shear wave splitting modeling (Fig. 7.5 to Fig. 7.9) are freely available from YF's GitHub account (`https://github.com/yvonnefroehlich/sws-visualization-and-modeling`). These functions are extended and strongly modified from the ones used in *Grund and Ritter* (2020), available from MG's GitHub account (`https://github.com/michaelgrund/sws_tools`).

All geographic maps were prepared with *PyGMT*, the Python wrapper of the *Generic Mapping Tools* (*GMT*; *Wessel et al.*, 2019). A *Jupyter* Notebook using *PyGMT* v0.3.0 (*Uieda et al.*, 2021) and *GMT* 6.1.1 (*Wessel et al.*, 2020) to reproduce the map in Fig. 7.1 is available from MG's GitHub account (`https://github.com/michaelgrund/GMT-plotting`). *Jupyter* Notebooks using *PyGMT* v0.7.0 (*Uieda et al.*, 2022) and *GMT* 6.4.0 (*Wessel et al.*, 2022) to reproduce the maps in Fig. A.4 are available from YF's GitHub account (`https://github.com/yvonnefroehlich/gmt-pygmt-plotting`).
The piercing points (Fig. 7.1, Fig. A.4) were calculated after the *iasp91* Earth model (*Kennett and Engdahl*, 1991) with the MATLAB Toolkit *MatTaup* by Qin Lin based on the original *TauP* Toolkit (*Crotwell et al.*, 1999).
Color-coding of the fast polarization direction was accomplished using the *phase* colormap from the *cmocean* colormaps (*Thyng et al.*, 2016).

A.2 Additional figures

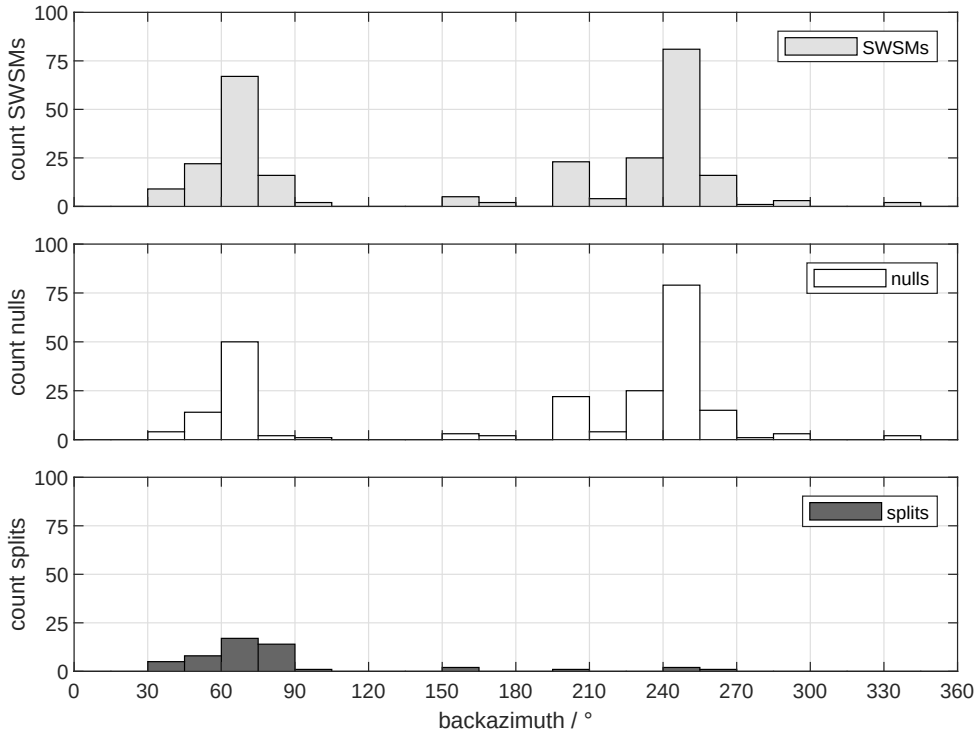

Figure A.1: Cartesian histograms showing the distribution of the number of the *good* and *fair* shear wave splitting measurements (SWSMs) of the single-event analysis (top, light gray) as well as the *nulls* (middle, white) and the *splits* (bottom, dark gray) separated in 15° backazimuth bins at the permanent broadband seismological recording station Black Forest Observatory (BFO).

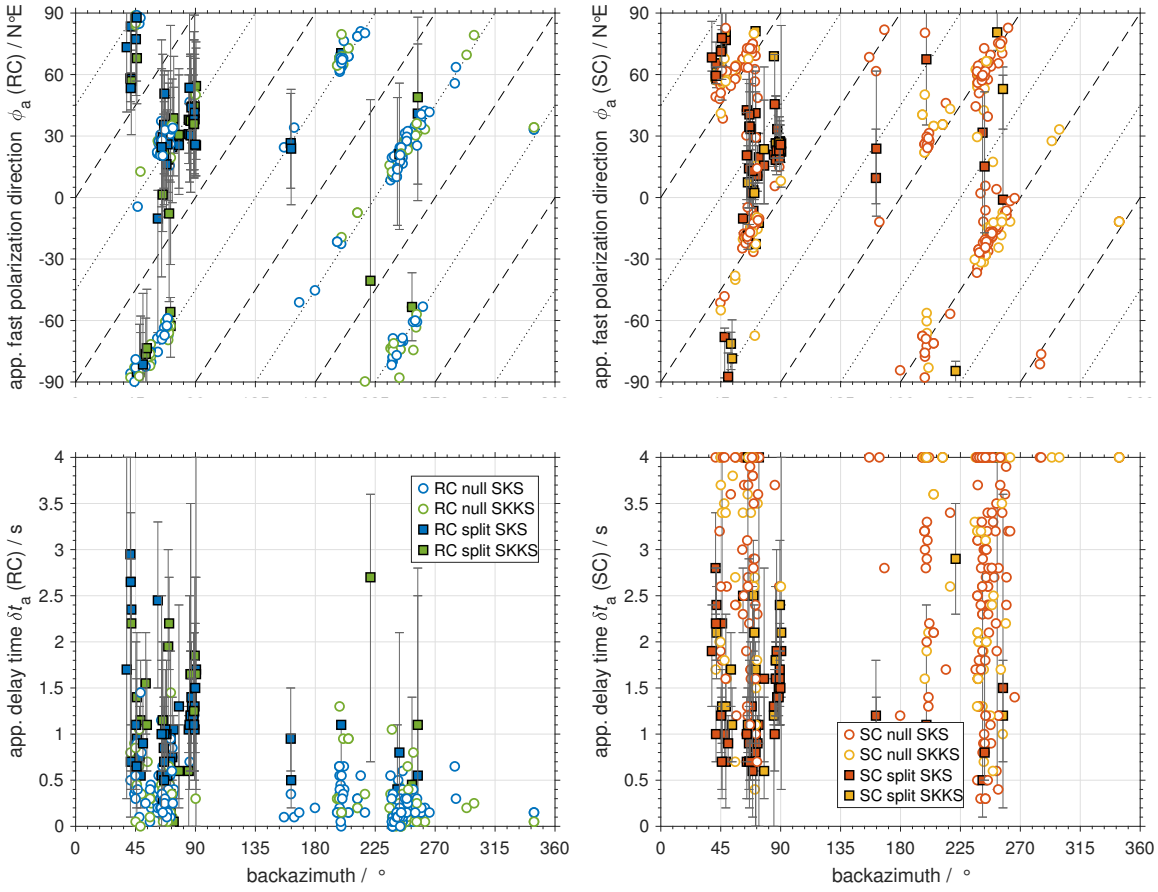

Figure A.2: Apparent splitting parameters of the *good* and *fair* shear wave splitting measurements of the single-event analysis at the permanent broadband seismological recording station Black Forest Observatory (BFO). **(left)** Rotation-correlation (RC) method (*Bowman and Ando*, 1987) and **(right)** energy minimization (SC) method (*Silver and Chan*, 1991). **(top)** Apparent fast polarization direction ϕ_a and **(bottom)** apparent delay time δt_a. *Nulls* are plotted as white circles with colored outline, *splits* as squares with colored fill. SKS phases are plotted in blue (RC) or red (SC), SKKS phases in green (RC) or orange (SC). For the *splits* the 95 % confidence intervals of the apparent splitting parameters are given by the vertical error bars. The black dotted (RC) or dashed (SC) lines with a slope of 45° indicate ϕ_a expected for *nulls* in case of simple anisotropy (one layer with transverse isotropy with horizontal symmetry axis). Note that for *nulls* δt_a tends to zero for the RC method, but for the SC method δt_a spreads over the whole range of the grid search up to the maximum, here 4 s. Note the $\pi/2$ jump in ϕ_a around 60°-65° backazimuth, indicating two-layer anisotropy (*Silver and Savage*, 1994).

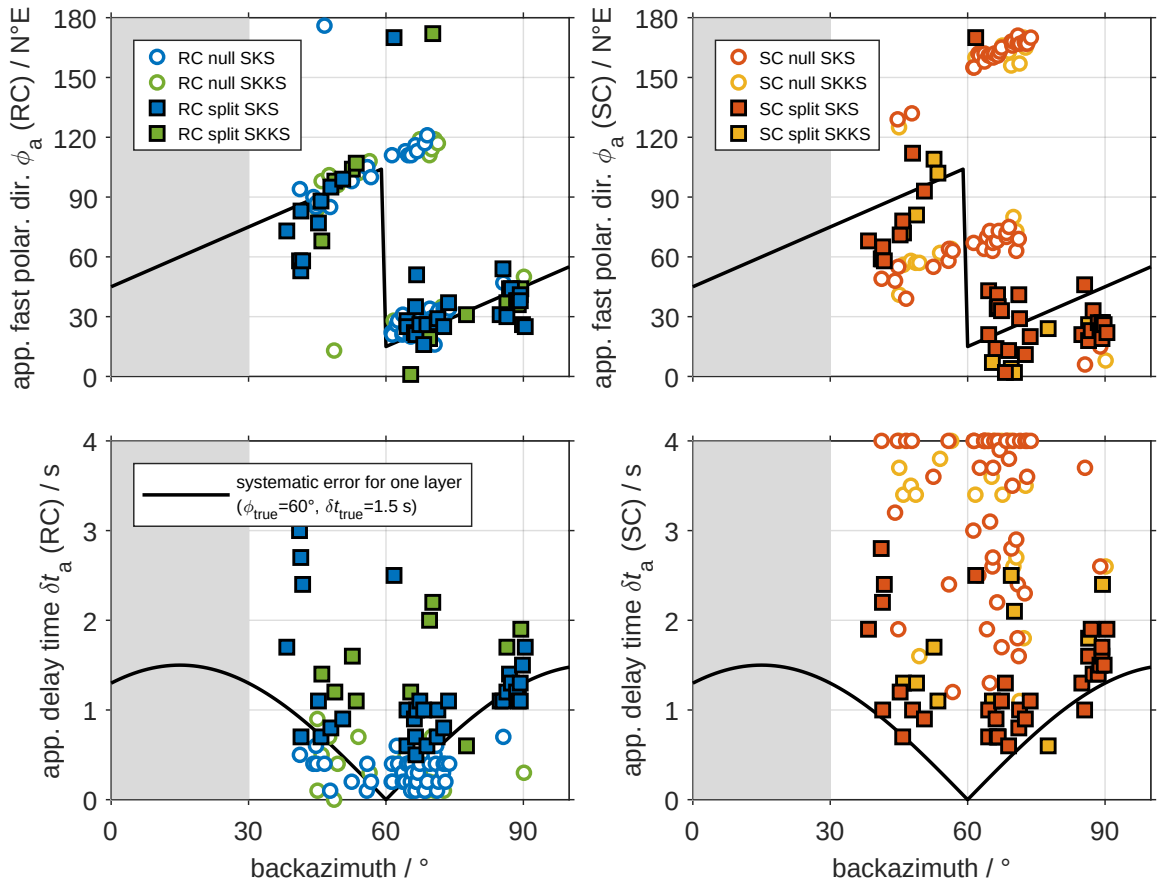

Figure A.3: Same as Fig. A.2, but only the shear wave splitting measurements in the backazimuth range 30°-100° corresponding the restriction of the modeling to the NE quadrant (see main text). The black lines indicate an expected systematic error in the measured splitting parameters for a transverse isotropic horizontal one-layer anisotropy scenario (simple anisotropy) following the equations (1) and (2) by *Eakin et al.* (2019). This error is strongest around the expected *null* directions. This behavior was firstly demonstrated by *Wüstefeld and Bokelmann* (2007) based on synthetic tests with high signal-to-noise ratio data (SNR around 15, calculation after *Restivo and Helffrich*, 1999) for the rotation-correlation method (*Bowman and Ando*, 1987). *Eakin et al.* (2019) propose, that for a lower, for real data more realistic SNR of 5 to 10 also the energy minimization method (*Silver and Chan*, 1991) tends to such a behavior. Note that the black lines were only roughly visually fitted. Here no modeling (systematic grid search based on minimizing the total root mean square error or extremizing any other metric) was conducted.

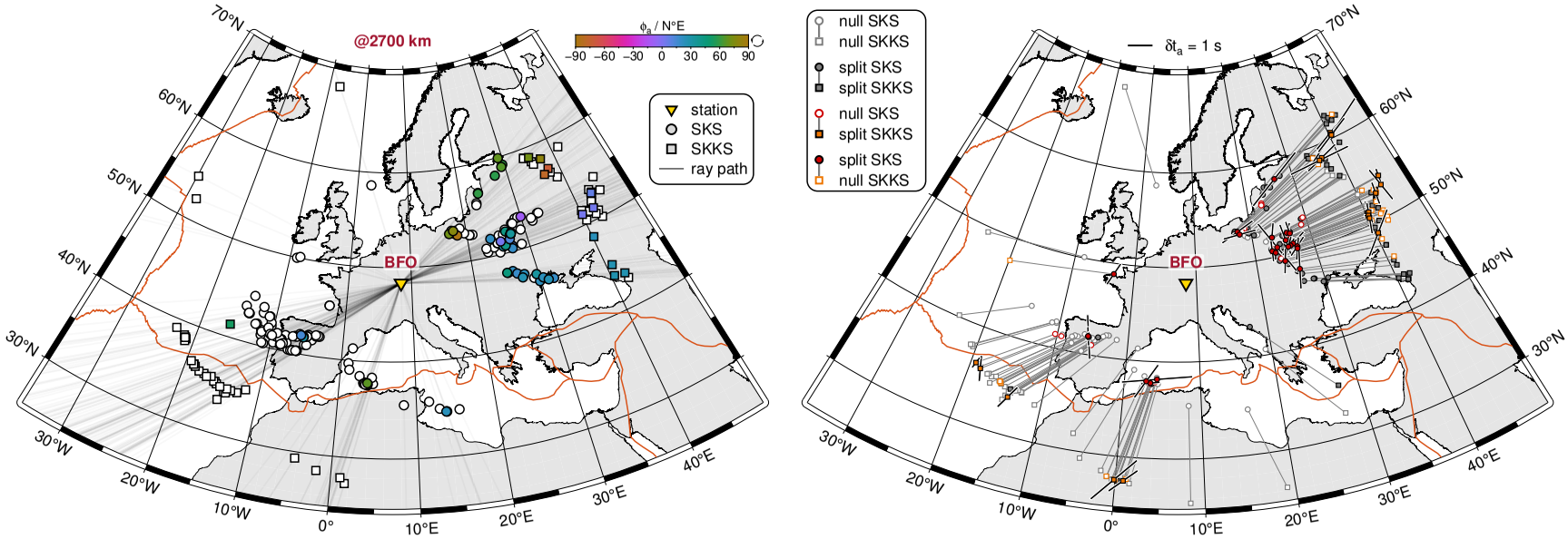

Figure A.4: Geographic maps of Europe and North Africa showing piercing points in 2700 km depth (lowermost mantle [LMM], D double-prime [D"] region) calculated after the *iasp91* Earth model (*Kennett and Engdahl*, 1991) with the *TauP* Toolkit (*Crotwell et al.*, 1999). Plate boundaries are in orange after *Bird* (2003). The piercing points are related to shear wave splitting measurements (SWSMs) on SKS (circles) and SKKS (squares) phases with the energy minimization method (*Silver and Chan*, 1991) at the permanent broadband seismological recording station Black Forest Observatory (BFO). **(left)** *Good* and *fair* SWSMs of the single-event analysis. For the *splits* the color-coding of the symbols refers to the apparent fast polarization direction ϕ_a relative to north. *Nulls* are plotted as black outlined white filled circles. The thin black lines indicate the (projected) ray paths. **(right)** sKS-SKKS pairs of all quality categories. Most pairs contain at least one *poor* SWSM. *Nulls* are plotted with colored outline, *splits* with colored fill. Non-discrepant pairs (*null-null*, *split-split*) in gray, discrepant pairs (*null-split*, *split-null*) in red (SKS) and orange (SKKS). Corresponding phases for the same event are connected by thin light gray lines. For the *split* phases of discrepant pairs, the (apparent) splitting parameters are represented by orientated (apparent fast polarization direction ϕ_a relative to north) length-scaled (apparent delay time δt_a) white outlined black bars.

B Supplementary Material to *Fröhlich Y., Grund M. & Ritter J. R. R. (2024) GJI*

This appendix is related to Ch. 8 and has been published as supplementary material to:

> ***Fröhlich Y.***, Grund M. & Ritter J. R. R. (2024).* **Lateral and vertical variations of seismic anisotropy in the lithosphere-asthenosphere system underneath Central Europe from long-term splitting measurements**. *Geophysical Journal International*, 239(1):112-135. `https://doi.org/10.1093/gji/ggae245`.

B.1 Data information and availability

Our shear wave splitting measurements (SWSMs) from the single-event analysis of *good* and *fair* qualities carried out in *SplitLab* (*Wüstefeld et al.*, 2008) are freely available for download as CSV and PDF files at *RADAR4KIT* as the dataset "Longterm Shear Wave Splitting Measurements in the Upper Rhine Graben Area" (`https://dx.doi.org/10.35097/685`); the PDF files are included in this Supplementary Material as separately uploaded files. These SWSMs were done on recordings at the stations Black Forest Observatory (BFO), Welschbruch (WLS), Stuttgart (STU), Échery (ECH), TMO044 (Durlach), and TMO07 (KIT-GPI). We report both the splitting parameters fast polarization direction and delay time (*Bowman and Ando*, 1987; *Silver and Chan*, 1991) as well as the splitting intensity (*Chevrot*, 2000). The SWSMs at BFO are partly also contained in the dataset "Longterm Shear Wave Splitting Measurements at the Black Forest Observatory" available from *RADAR4KIT* (`https://dx.doi.org/10.35097/684`) published along with *Ritter et al.* (2022). Here the SWSMs at BFO are extended for the period 2016-2019 and for the backazimuth range 130°-150°.

A corrected *SplitLab* code regarding the relative temporal alignment of the vertical, North, and East component traces (*Fröhlich et al.*, 2022a) is available at YF's GitHub account (`https://github.com/yvonnefroehlich/SplitLab-TemporalAlignment`).
The forward modelling was accomplished with the *MATLAB Seismic Anisotropy Toolkit* (MSAT) by *Walker and Wookey* (2012). MATLAB functions to generate the stereoplot representation as well as to perform the shear wave splitting modelling are freely available at YF's GitHub account (`https://github.com/yvonnefroehlich/sws-visualization-and-modeling`).

Geographic maps, Earth sections, and Cartesian histograms were prepared with *PyGMT* v0.12.0 (*Tian et al.*, 2024) and the *Generic Mapping Tools* (*Wessel et al.*, 2019) 6.4.0 (*Wessel et al.*, 2022). Python scripts or *Jupyter* notebooks to reproduce some of these maps are freely available at YF's GitHub account (`https://github.com/yvonnefroehlich/gmt-pygmt-plotting`).
Piercing points and travel paths were calculated with the *iasp91* Earth model (*Kennett and Engdahl*, 1991) with *MatTaup* by Qin Lin and *ObsPy* (*Beyreuther et al.*, 2010) 1.2.2 (*The ObsPy Development Team*, 2020) based on the original *Java TauP* Toolkit (*Crotwell et al.*, 1999).
Colour-coding was accomplished with the *cmocean* colormaps (*Thyng et al.*, 2016) as well as the *Scientific Colour Maps* version 8.0.1 (*Crameri*, 2023).

B.2 Earthquake and backazimuthal coverage

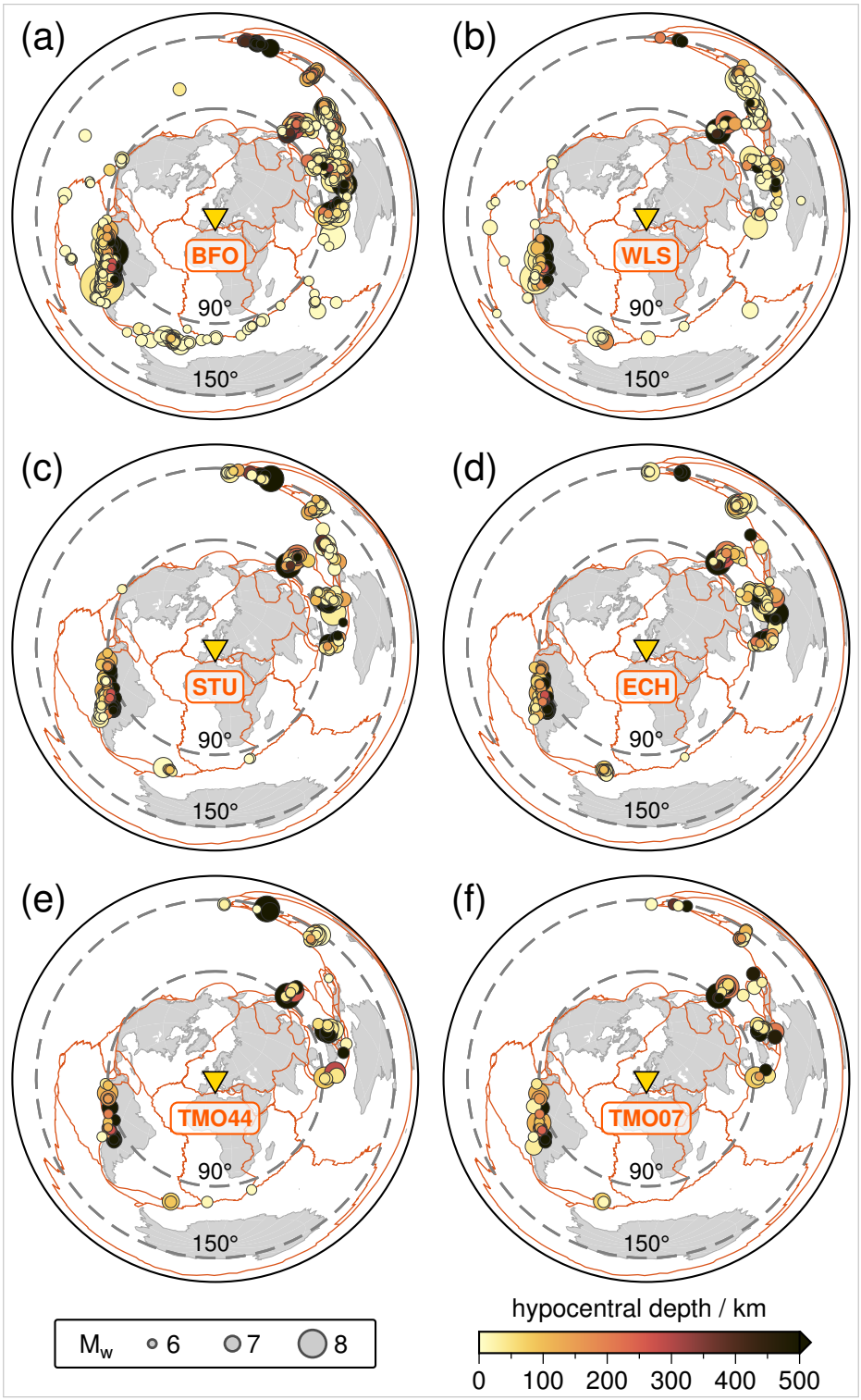

Figure B.1: Epicentre distribution of the earthquakes which were usable for at least one shear wave splitting measurement at the recording stations **(a)** BFO, **(b)** WLS, **(c)** STU, **(d)** ECH, **(e)** TMO44, and **(f)** TMO07. The hypocentral depth is colour-coded and the moment magnitude M_w scales with the size. The dashed circles centred around the station (yellow inverse triangle) limit the considered epicentral distance range Δ = 90°-150°. Plate boundaries are in dark orange after *Bird* (2003) and land masses are in grey. Note the limited backazimuthal coverage (NE 30°-100°, SW 180°-270°) with gaps (NNE 0°-30°, SE 110°-170°, SSW 270°-360°) which are typical for *X*KS phases (SKS, SKKS, and PKS; for the travel paths see Fig. B.9) in Central Europe.

B.3 Measurement of shear wave splitting

B.3.1 Principle (single-event analysis)

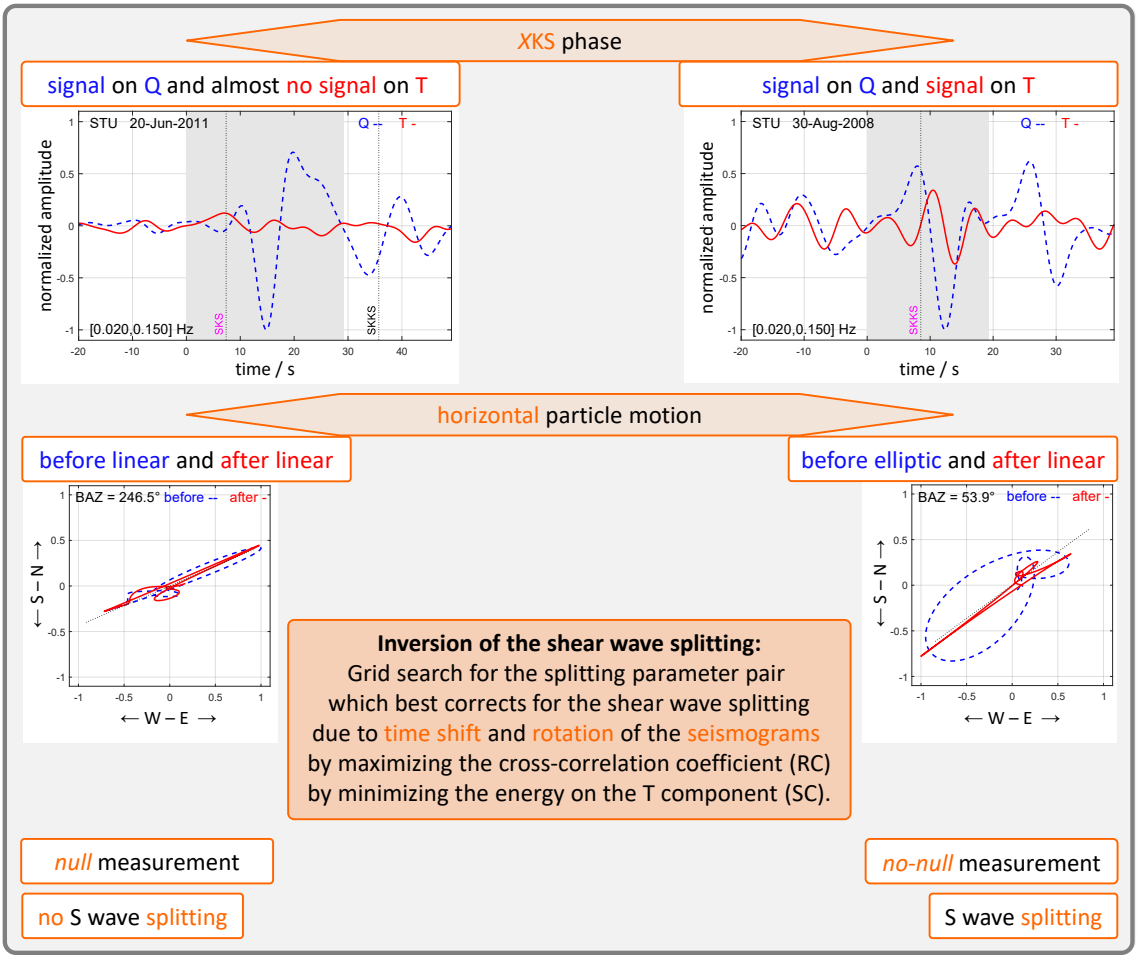

Figure B.2: Concept to measure shear wave splitting of *X*KS phases (SKS, SKKS, and PKS; for the travel paths see Fig. B.9) using the *cross-correlation* method (RC method; *Bowman and Ando*, 1987) or the *energy minimization* method (SC method; *Silver and Chan*, 1991). Waveform and particle motion plots are generated using *SplitLab* (*Wüstefeld et al.*, 2008).

B.3.2 Diagnostic plots of *SplitLab* and *StackSplit*

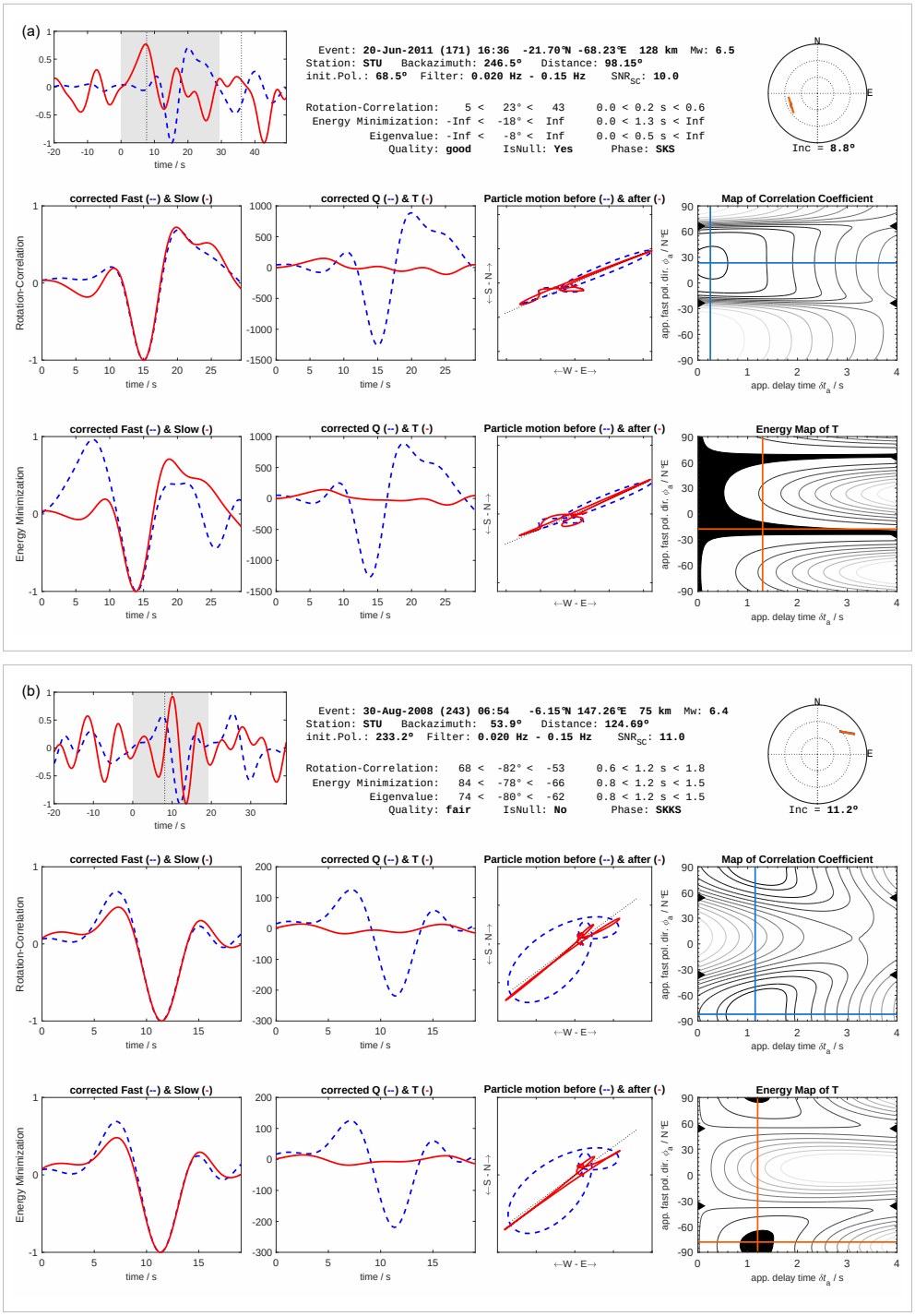

Figure B.3: Diagnostic plot provided by *SplitLab* (*Wüstefeld et al.*, 2008) for a shear wave splitting measurement (SWSM) after applying the *cross-correlation* method (RC method; *Bowman and Ando*, 1987, middle row) and the *energy minimization* method (SC method; *Silver and Chan*, 1991, lower row) in the single-event analysis. **(a)** *Null* measurement on a SKS phase and **(b)** *non-null* measurement on a SKKS phase exemplary at the recording station Stuttgart (STU). The hypocenter of the related earthquake (see the bars in the epicentral distance plot in the upper right corner) is below Chile-Bolivia and below Eastern New Guinea, respectively. The header of the diagnostic plot shows further information regarding the SWSM and the earthquake.

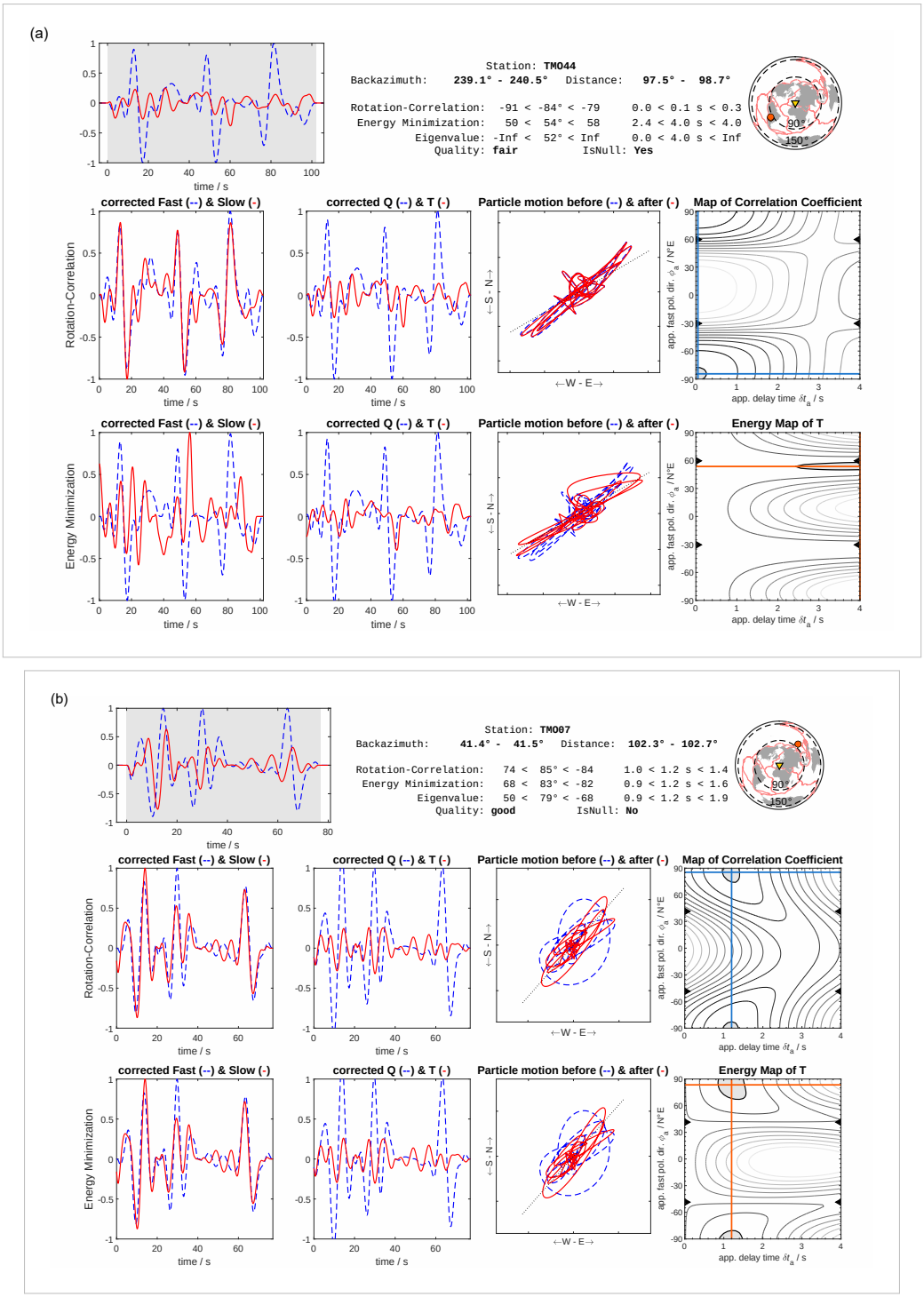

Figure B.4: Diagnostic plot provided by *StackSplit* (*Grund*, 2017) for a shear wave splitting measurement (SWSM) after applying the *simultaneous inversion of multiple waveforms* (SIMW; *Roy et al.*, 2017) in the multi-event analysis. **(a)** *Null* measurement exemplary at the recording station Durlach (TMO44) and **(b)** *non-null* measurement exemplary at the recording station KIT-GPI (TMO07). In both examples, the *X*KS waveforms from 3 single-event analysis results (*nulls* in (a), *splits* in (b)) were first concatenated in the time domain, and then jointly inverted. The hypocenters of the related earthquakes (orange dotes in the epicentral distance plot in the upper right corner) are below Argentina and below the Marian Islands, respectively. The header of the diagnostic plot shows further information regarding the SWSM and the earthquakes.

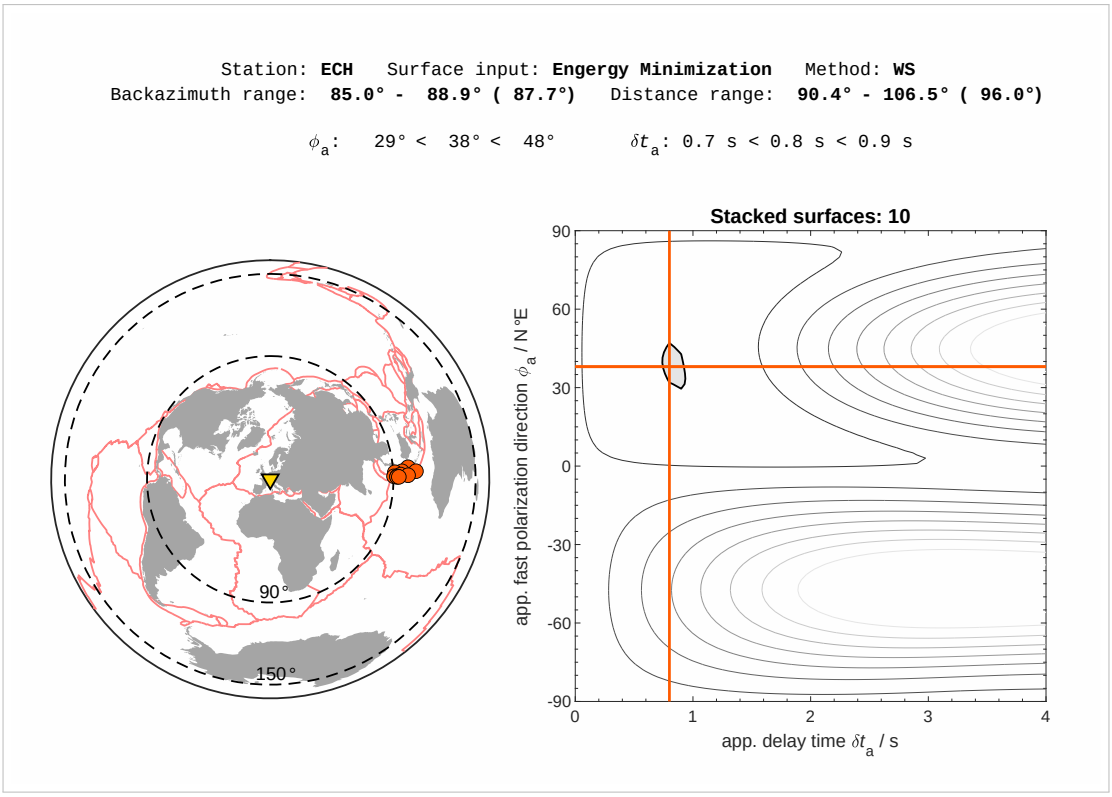

Figure B.5: Diagnostic plot provided by *StackSplit* (*Grund*, 2017) for a shear wave splitting measurement (SWSM) after applying the energy (or error) surface stacking method *Wolfe and Silver* (1998) based on the *energy minimization* method (SC method; *Silver and Chan*, 1991) in the multi-event analysis. *Non-null* measurement exemplary at the recording station Échery (ECH). 10 single-event analysis *splits* were stacked. The hypocenters of the related earthquakes (orange dotes in the epicentral distance plot) are below Sumatra and Indonesia. The header of the diagnostic plot shows further information regarding the SWSM and the earthquakes.

B.4 Observation of shear wave splitting

B.4.1 Overview

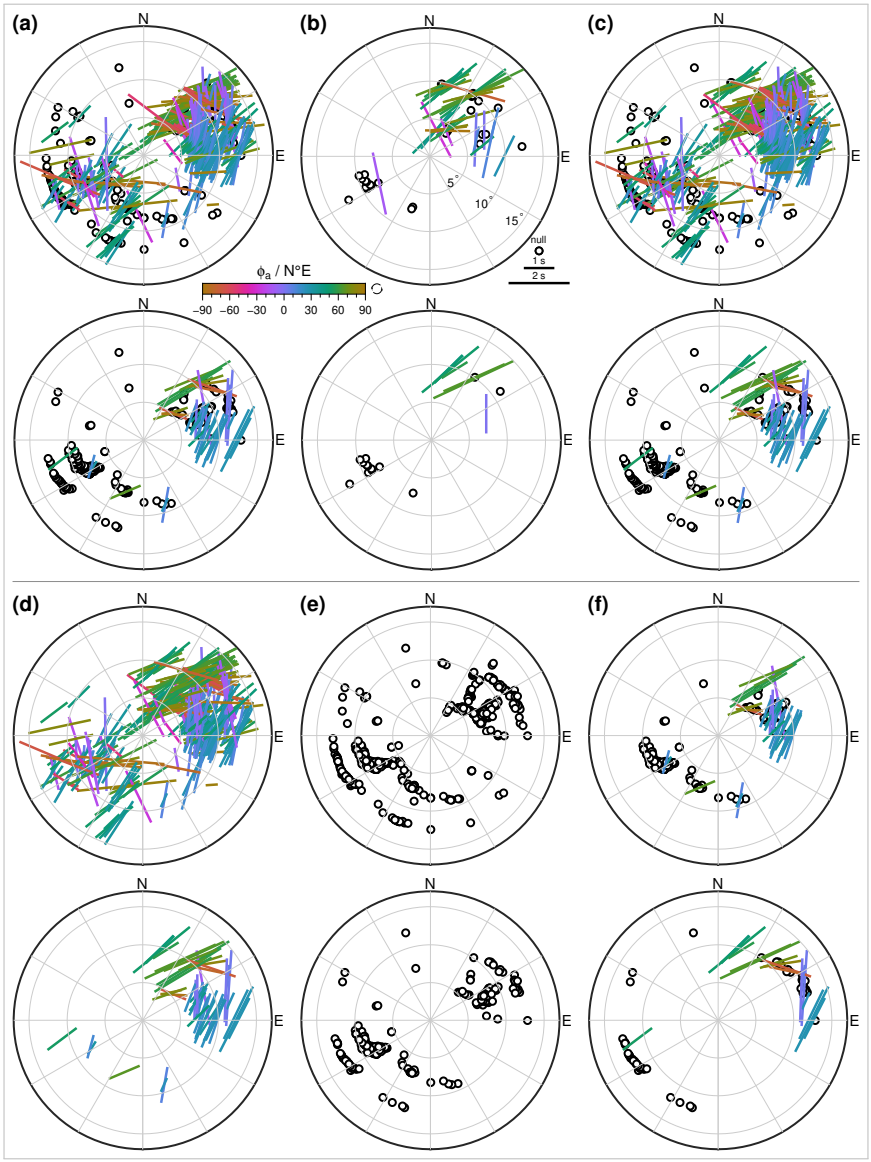

Figure B.6: Shear wave splitting measurements (SWSMs) from the single-event analysis at the recording station BFO visualised in stereoplots. **(a)** all (top), *good* and *fair* (bottom) SWSMs published in *Ritter et al.* (2022), **(b)** all (top), *good* and *fair* (bottom) SWSMs added in this study, **(c)** all (top), *good* and *fair* (bottom) SWSMs used in this study (combined dataset of (a) and (b)), **(d)** all (top), *good* and *fair* (bottom) *non-null* measurements, **(e)** all (top), *good* and *fair* (bottom) *null* measurements, and **(f)** *good* and *fair* SWSMs on SKS (top), on SKKS (bottom) phases. For *non-null* measurements, the apparent splitting parameters obtained with the *energy minimization* method (SC method; *Silver and Chan*, 1991) are given by the bars.

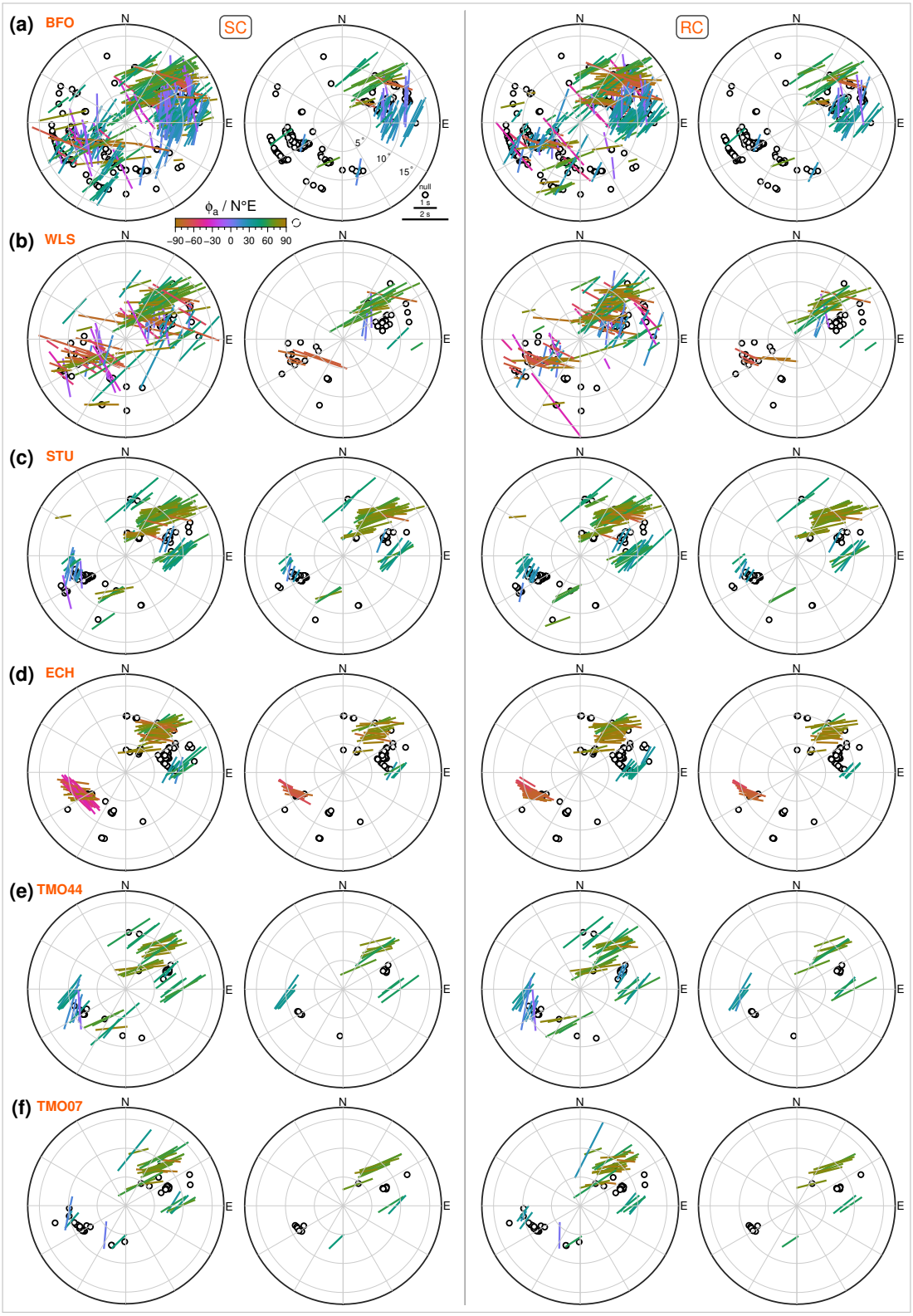

Figure B.7: Shear wave splitting measurements (SWSMs) from the single-event analysis at the recording stations **(a)** BFO, **(b)** WLS, **(c)** STU, **(d)** ECH, **(e)** TMO44, and **(f)** TMO07 visualised in stereoplots. SWSMs at BFO are expanded based on *Ritter et al.* (2022). *Energy minimization* method (SC method; *Silver and Chan*, 1991) in the first and second columns and *rotation-correlation* method (RC method; *Bowman and Ando*, 1987) in the third and fourth columns. Plotting conventions as in Fig. B.6.

B.4.2 Relevance of long-term data

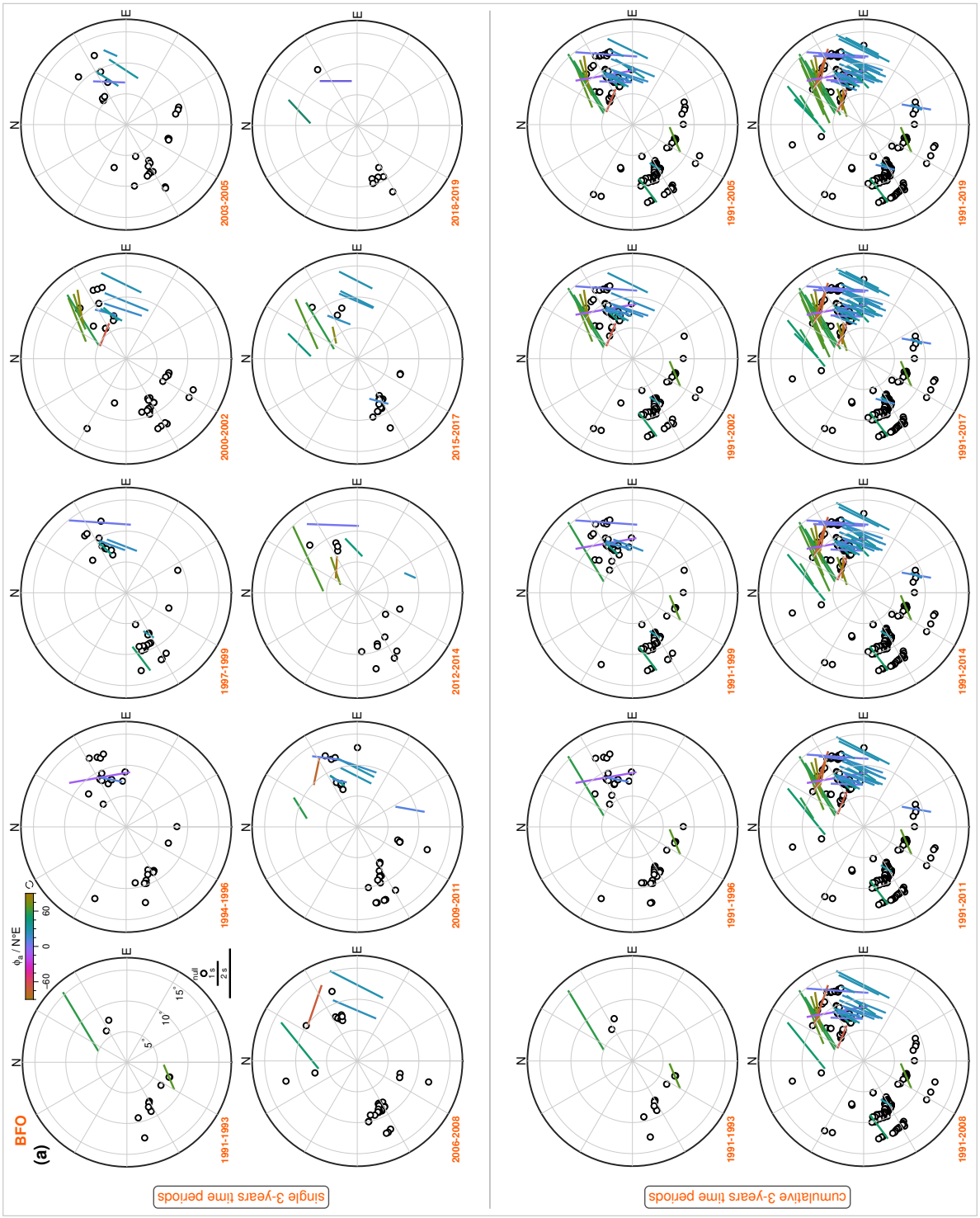

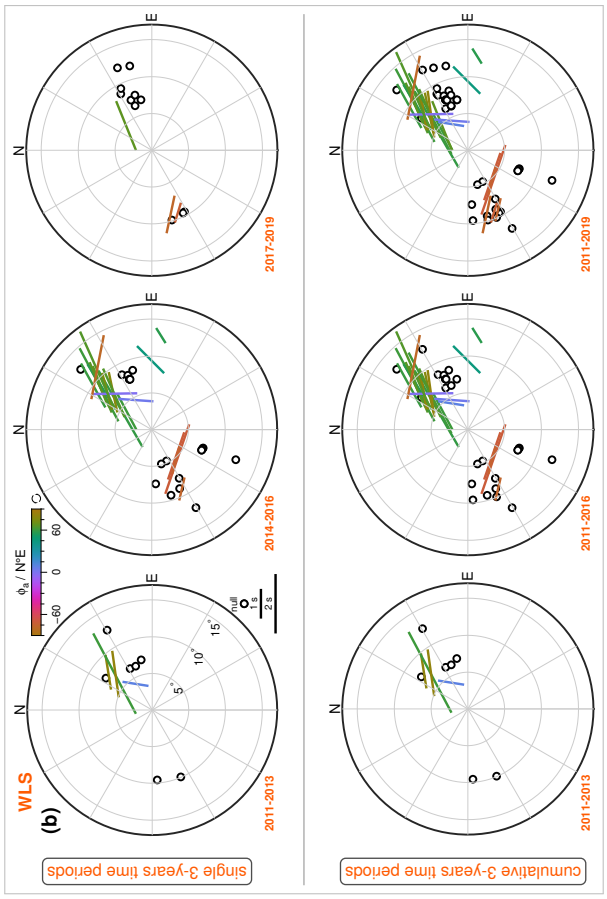
WLS
(b)
single 3-years time periods
cumulative 3-years time periods
2011-2013
2014-2016
2017-2019
2011-2013
2011-2016
2011-2019
N
E
5°
10°
15°
null
1 s
2 s
60
0
-60

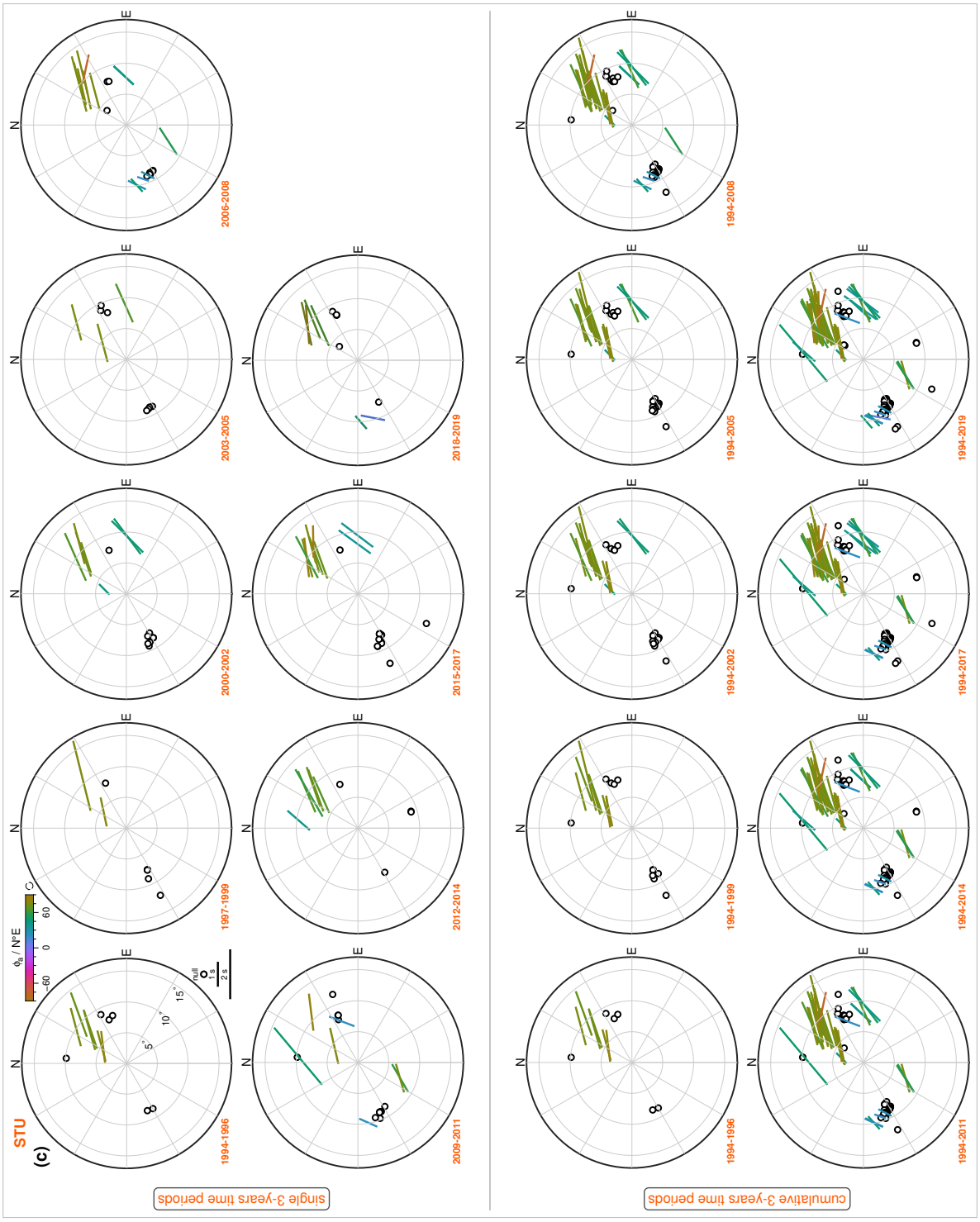
STU
(c)
single 3-years time periods
cumulative 3-years time periods
1994-1996
1994-1999
1994-2002
1994-2005
1994-2008
1994-2011
1994-2014
1994-2017
1994-2019
1997-1999
2000-2002
2003-2005
2006-2008
2009-2011
2012-2014
2015-2017
2018-2019
N
E
null
1.5
2.5
5°
10°
15°

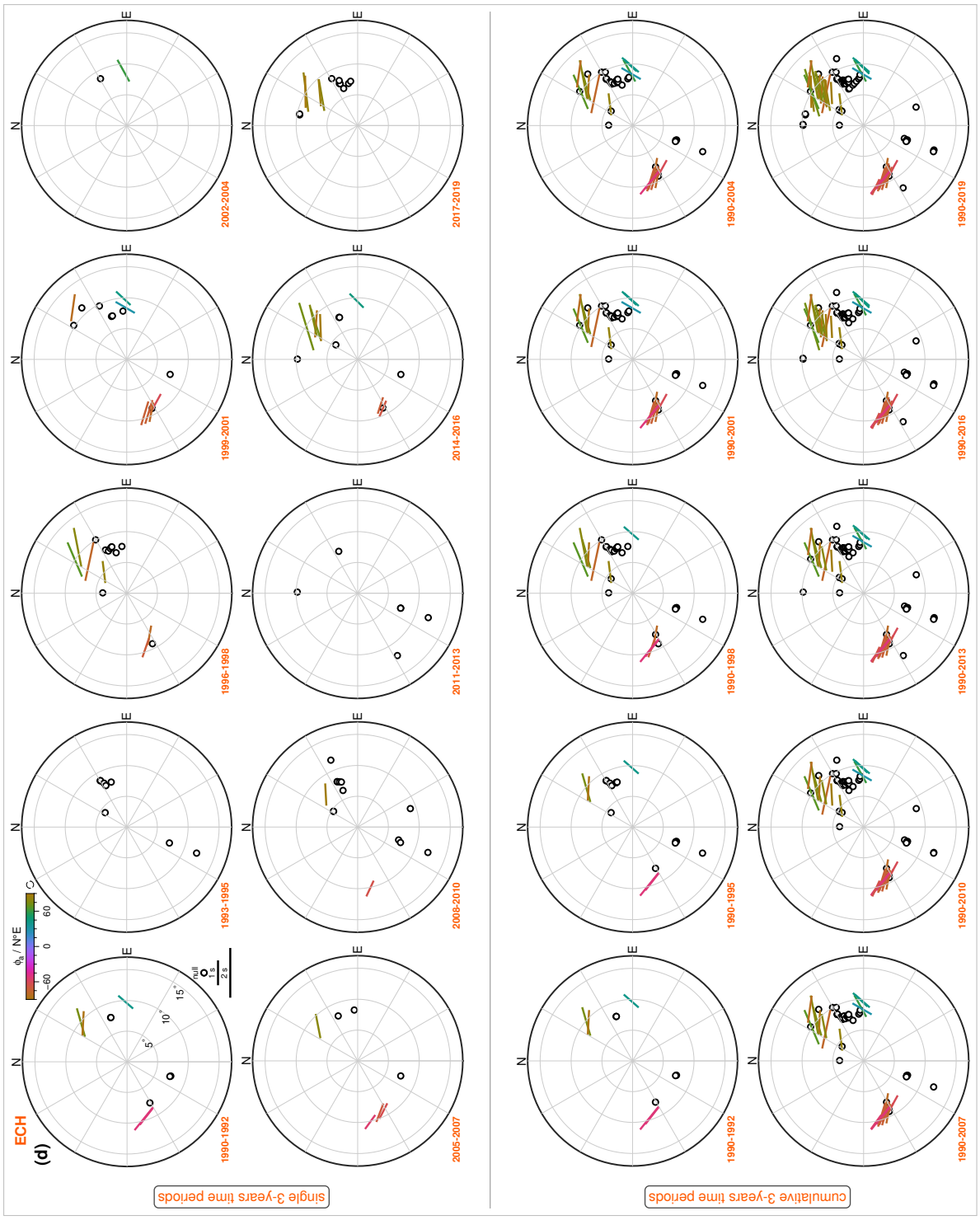
(d)
ECH
single 3-years time periods
cumulative 3-years time periods
1990-1992
1990-1995
1990-1998
1990-2001
1990-2004
1990-2007
1990-2010
1990-2013
1990-2016
1990-2019
1993-1995
1996-1998
1999-2001
2002-2004
2005-2007
2008-2010
2011-2013
2014-2016
2017-2019
N
E
5°
10°
15°
null
1 s
2 s
C
60
0
−60
Φs / N°E

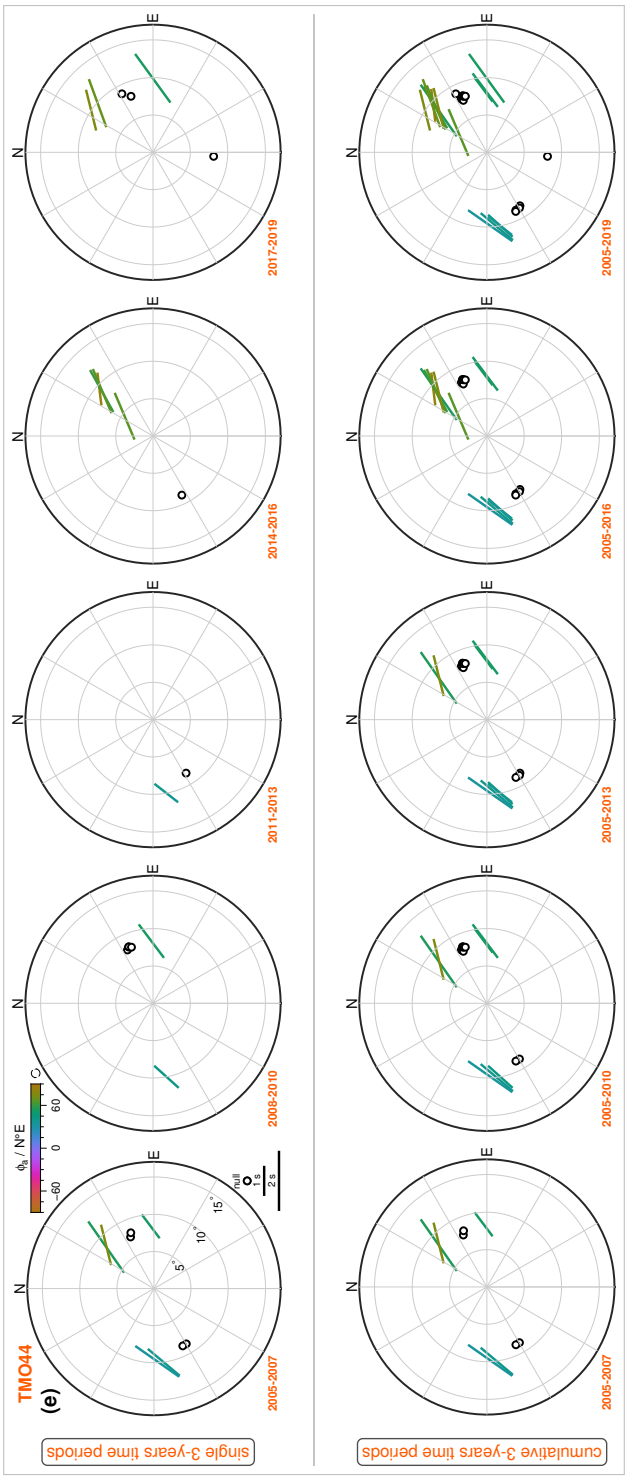
single 3-years time periods
cumulative 3-years time periods
TMO44
(e)
Φ_{fa} / N°E
δt
1 s
2 s
2005-2007
2008-2010
2011-2013
2014-2016
2017-2019
2005-2007
2005-2010
2005-2013
2005-2016
2005-2019
N
E

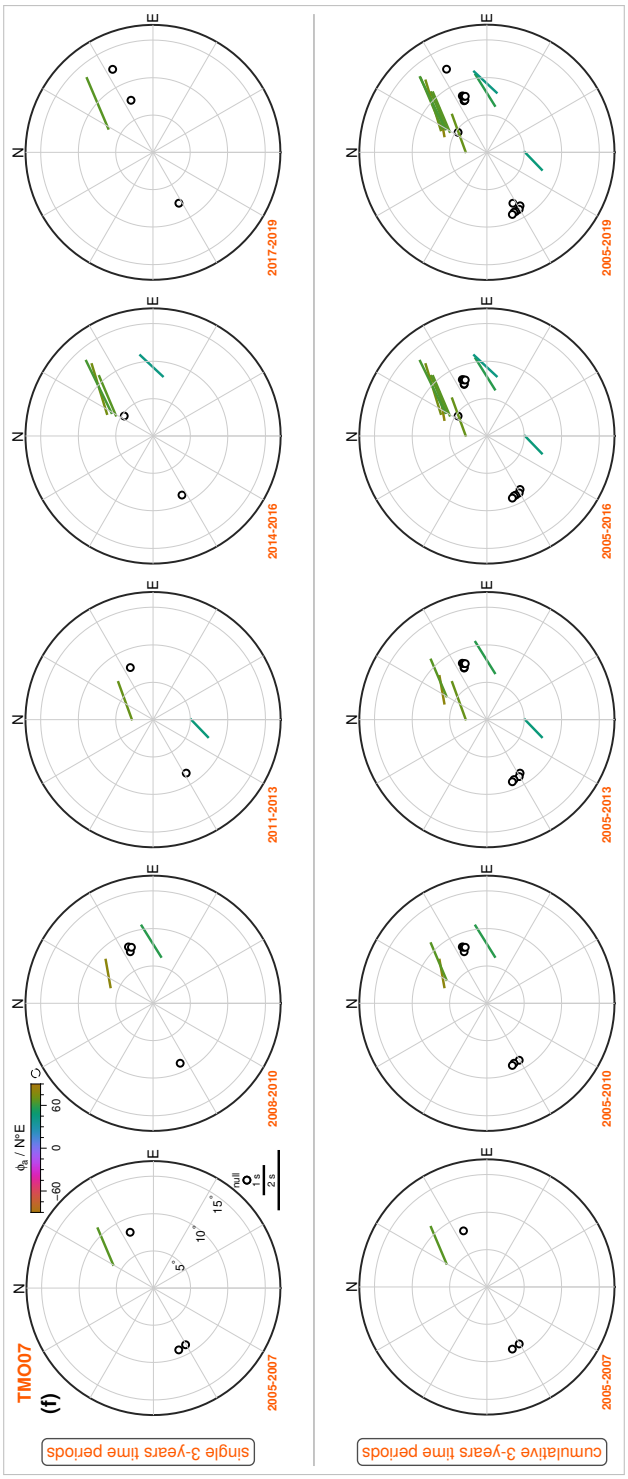

Figure B.8: *Good* and *fair* shear wave splitting measurements (SWSMs) from the single-event analysis at the recording stations **(a)** BFO, **(b)** WLS, **(c)** STU, **(d)** ECH, **(e)** TMO44, and **(f)** TMO07 visualised in stereoplots. **Top**: single 3-years time periods. **Bottom**: cumulative 3-years time periods. Displayed are the splitting parameters obtained with the *energy minimization* method (SC method; *Silver and Chan*, 1991). Plotting conventions as in Fig. B.6. The time dependence of the splitting pattern is clearly related with the (random) occurrence of appropriate earthquakes (epicentral distance, backazimuth, radiation pattern) during recording periods of 3 years. The cumulative pattern cannot be achieved during 3-6 years of recording.

B.4.3 Seismic phases and epicentral distance

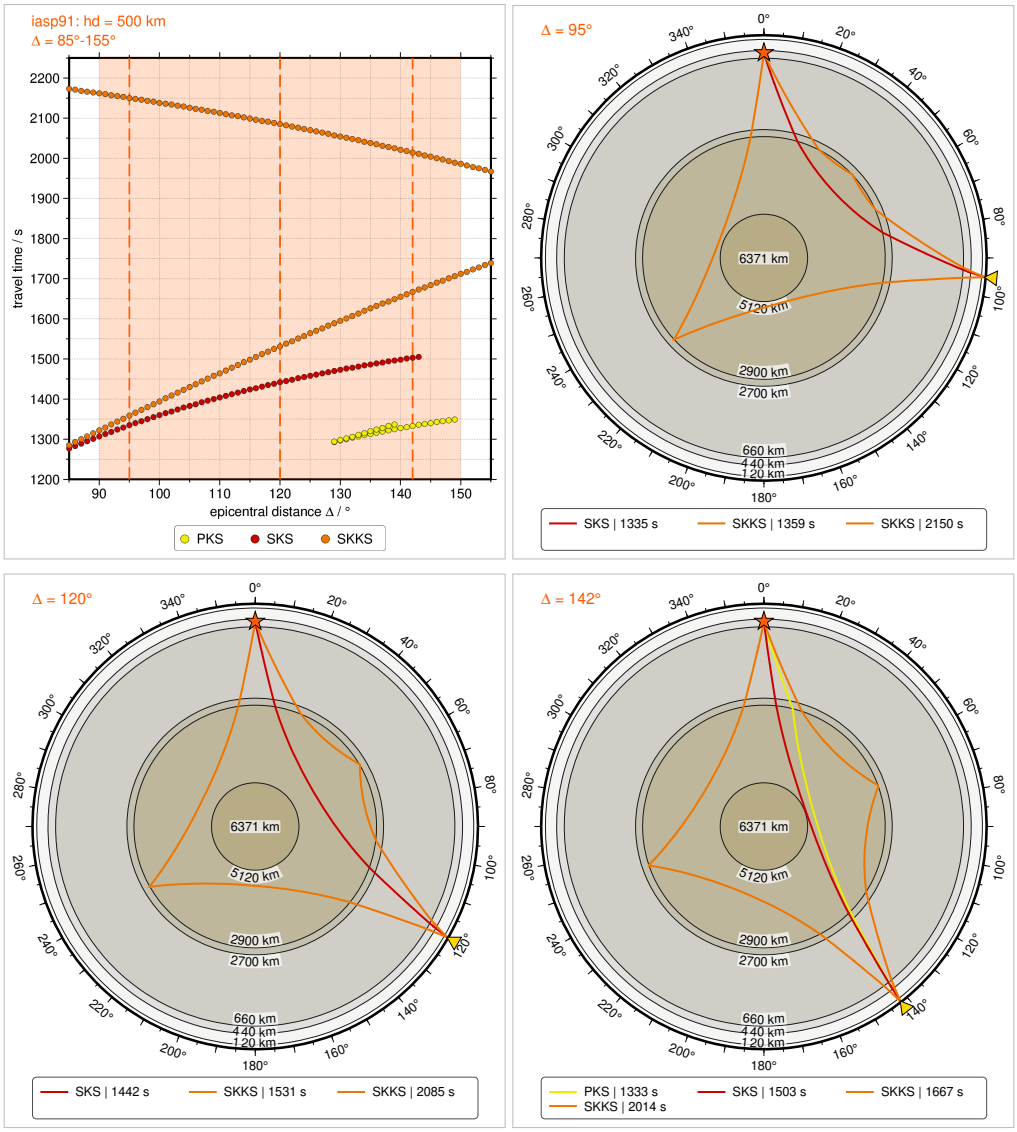

Figure B.9: Travel time curves and travel paths of the SKS (red), SKKS (orange), and PKS (yellow) phases through the Earth's mantle and outer liquid core calculated with the *iasp91* Earth model (*Kennett and Engdahl*, 1991). The light orange area marks the considered epicentral distance range of 90°-150° (left top); the dashed orange lines mark the epicentral distances 95° (top right), 120° (bottom left), and 142° (bottom right) for which the travel paths are displayed The red star represents the source or earthquake in 500 km depth and the yellow inverse triangle the receiver or seismometer at the surface. Additionally, the travel times are given in the legends. Note the different ray paths of the different phases in the mantle on the receiver side. SKS and SKKS phases have nearly the same ray paths in the upper mantle but their ray paths differ in the lowermost mantle (LMM). Thus, differences in the shear wave splitting between these two phases may indicate a potential LMM contribution to the anisotropy (see also Fig. B.22).

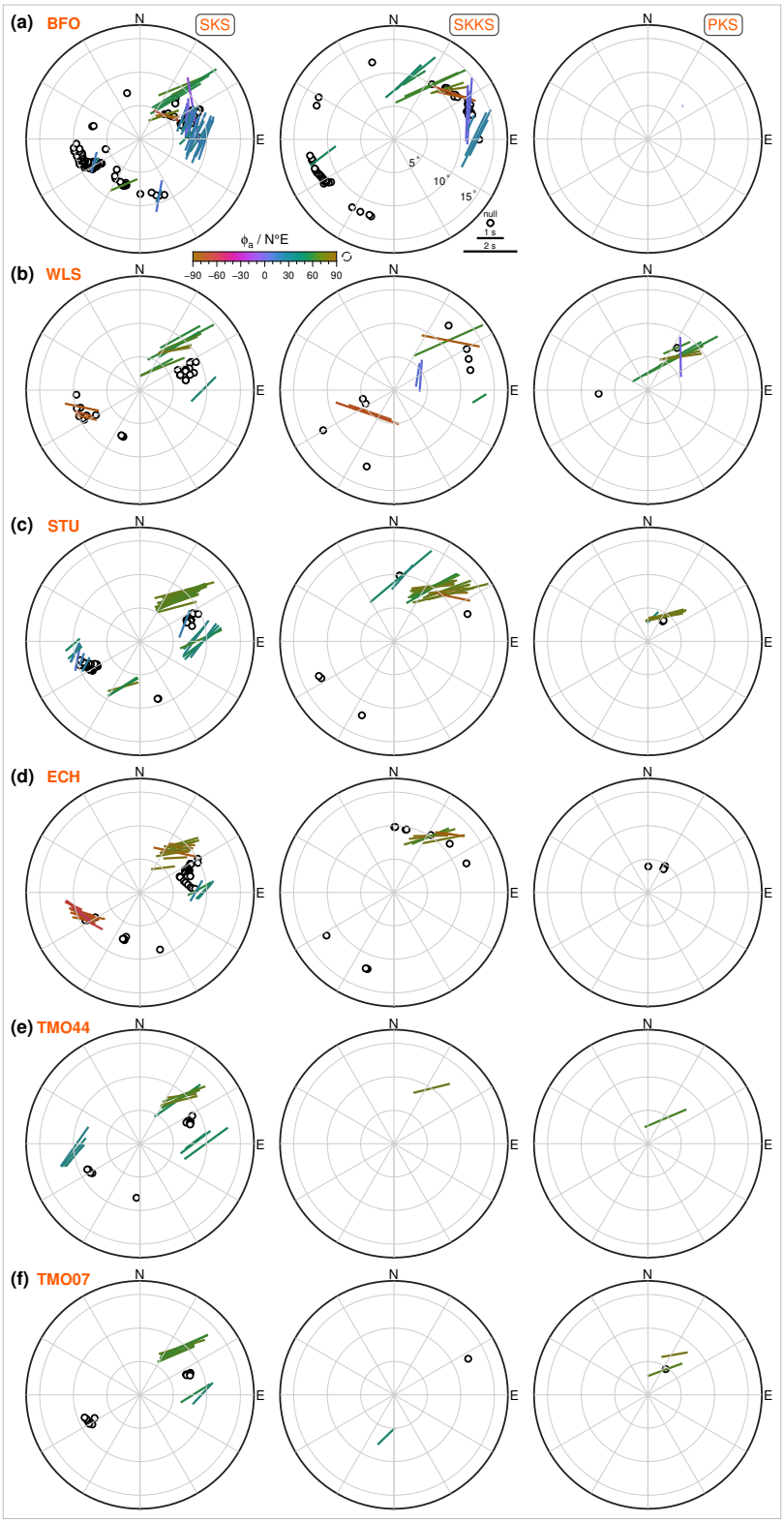

Figure B.10: *Good* and *fair* shear wave splitting measurements (SWSMs) from the single-event analysis at the recording stations **(a)** BFO, **(b)** WLS, **(c)** STU, **(d)** ECH, **(e)** TMO44, and **(f)** TMO07 visualised in stereoplots separate for the SKS (left), SKKS (middle), and PKS (right) phases. Displayed are the splitting parameters obtained with the *energy minimization* method (SC method; *Silver and Chan*, 1991). Plotting conventions as in Fig. B.6. At BFO, all SWSMs on PKS phases where classified as *poor*. Different seismic phases are useful to achieve a wide range of splitting measurements. In addition, they can be used to constrain the anisotropic region in the Earth's interior. Here, the SWSMs are similar for the SKS and SKKS phases at the single recording stations, which is especially visible at BFO. This observation points to a common source of the anisotropy and hence a source in the upper mantle (not in the lowermost mantle) where the ray paths are similar (Fig. B.9).

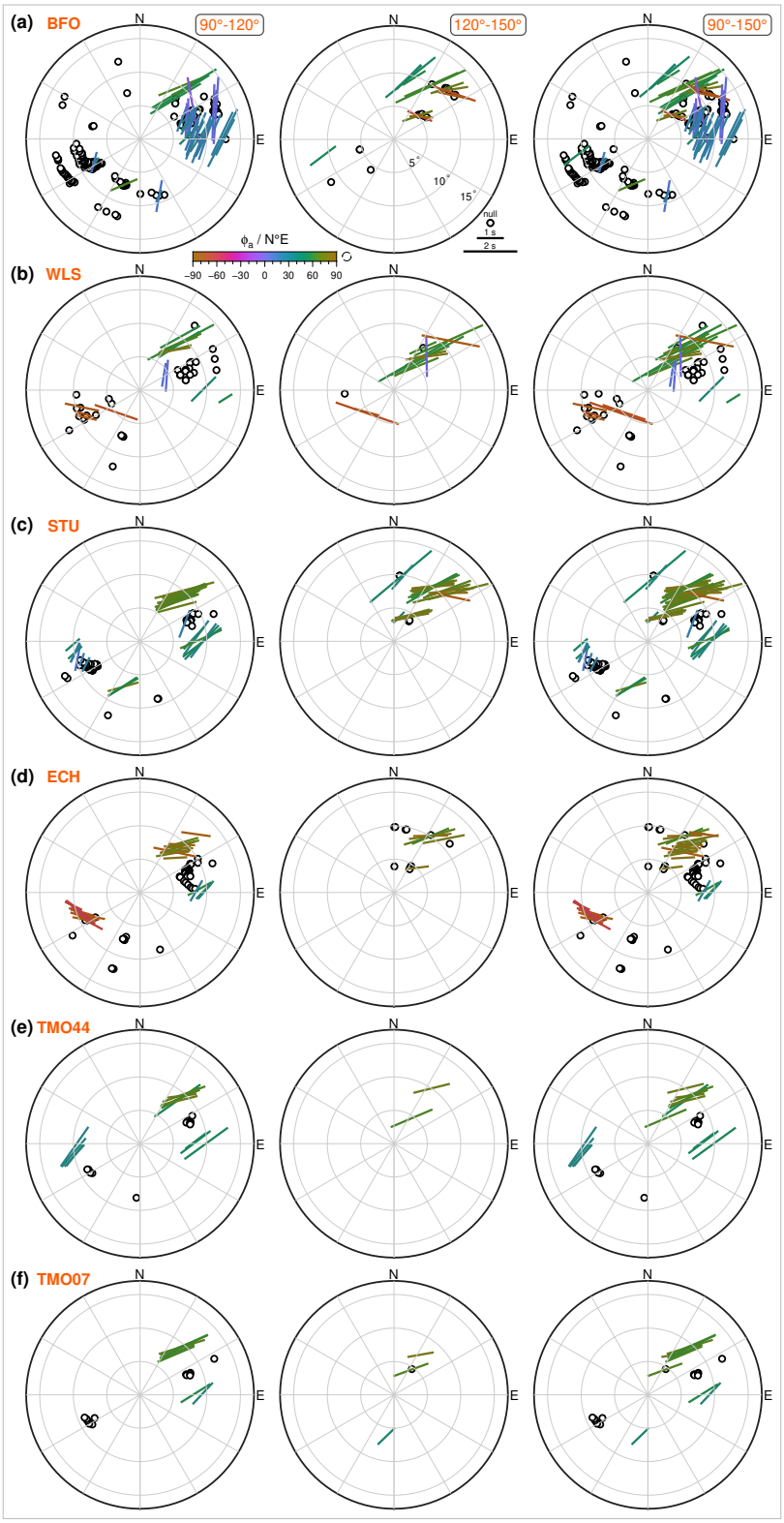

Figure B.11: *Good* and *fair* shear wave splitting measurements (SWSMs) from the single-event analysis at the recording stations **(a)** BFO, **(b)** WLS, **(c)** STU, **(d)** ECH, **(e)** TMO44, and **(f)** TMO07 visualised in stereoplots separately for the epicentral distance ranges 90°-120° (left), 120°-150° (middle), and 90°-150° (right). Displayed are the splitting parameters obtained with the *energy minimization* method (SC method; *Silver and Chan*, 1991). Plotting conventions as in Fig. B.6. Often only the epicentral distance range 90°-120° is studied. In this study the epicentral distance range 120°-150° is included to test whether this allows for additional SWSMs. For Central Europe, additional SWSMs (*nulls* and *splits*) are mainly possible in the NE quadrant, i.e., at backazimuths between 0°-60°. At BFO, the combined stereoplot shows a complete flip of the fast polarization direction in the NE quadrant which is not observed which in the epicentral distance range 90°-120°.

B.4.4 Deviation between initial polarization and theoretical backazimuth directions

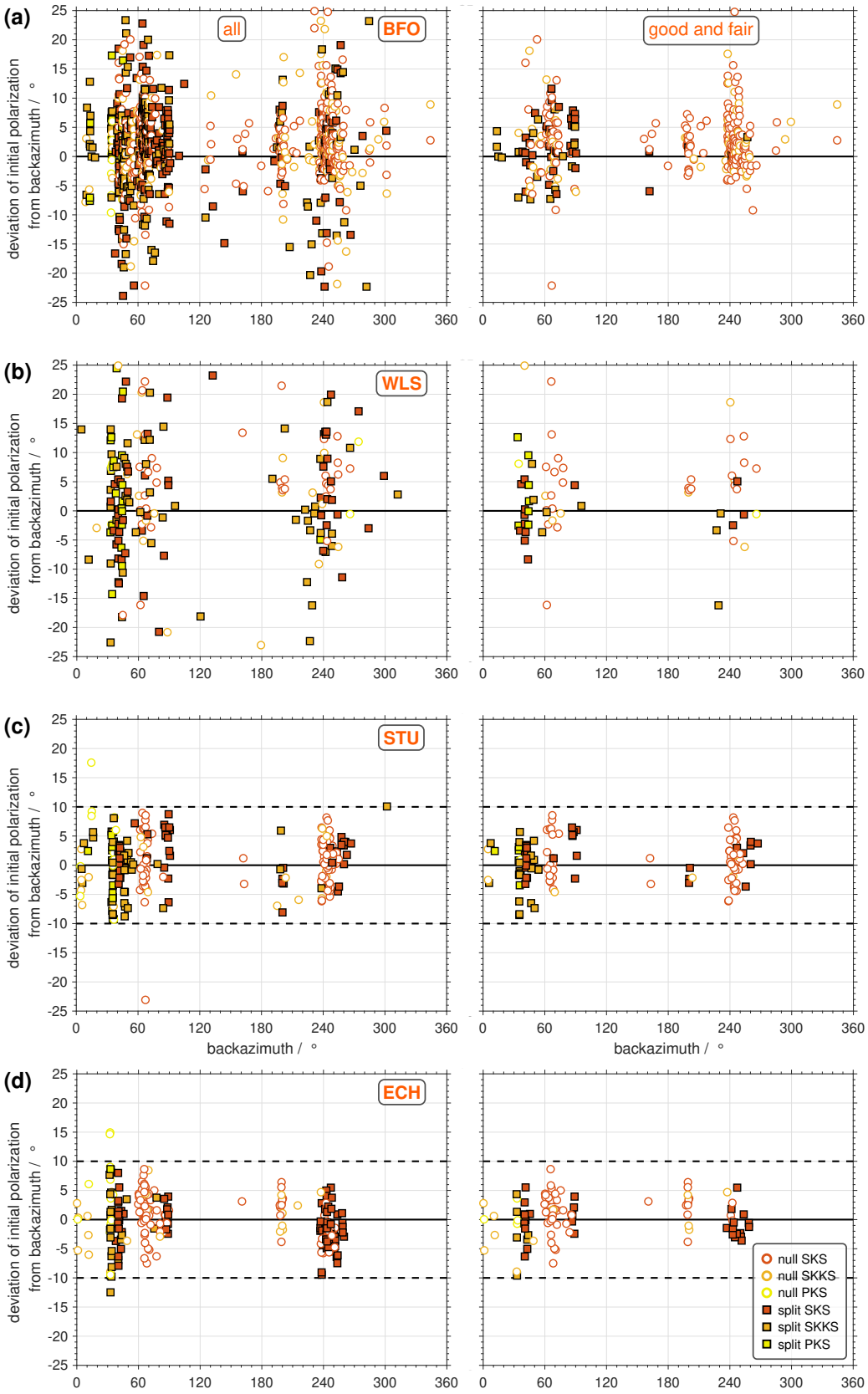

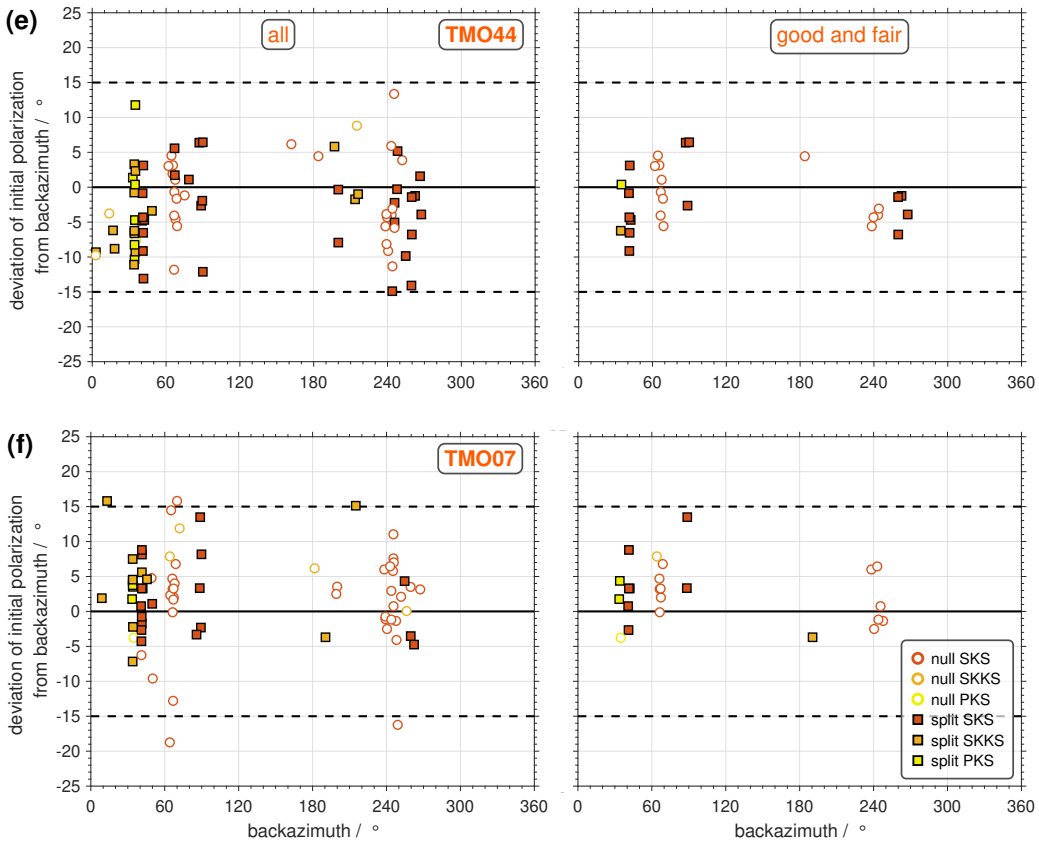

Figure B.12: Deviation of the initial polarization direction of the *X*KS phases (SKS, SKKS, and PKS) from the theoretical backazimuth direction for the shear wave splitting measurements (SWSMs) from the single-event analysis at the recording stations **(a)** BFO, **(b)** WLS, **(c)** STU, **(d)** ECH, **(e)** TMO44, and **(f)** TMO07. SWSMs at BFO are expanded based on *Ritter et al.* (2022). All SWSMs (left), only *good* and *fair* SWSMs (right). *Nulls* are displayed as white circles with coloured outline and *splits* as squares with coloured fill. SKS in red, SKKS in orange, and PKS in yellow. The black dashed horizontal lines indicate the allowed (station-specific) limits for the deviation: none for BFO and WLS, ±10° for STU and ECH, and ±15° for TMO44 and TMO07. A systematic deviation may indicate a (before unknown) sensor misorientation or 3-D heterogeneities in the Earth which can deviate the wavefront. Both was not observed at the recording stations used in this study.

B.5 Modelling of shear wave splitting

B.5.1 Model types and model parameters

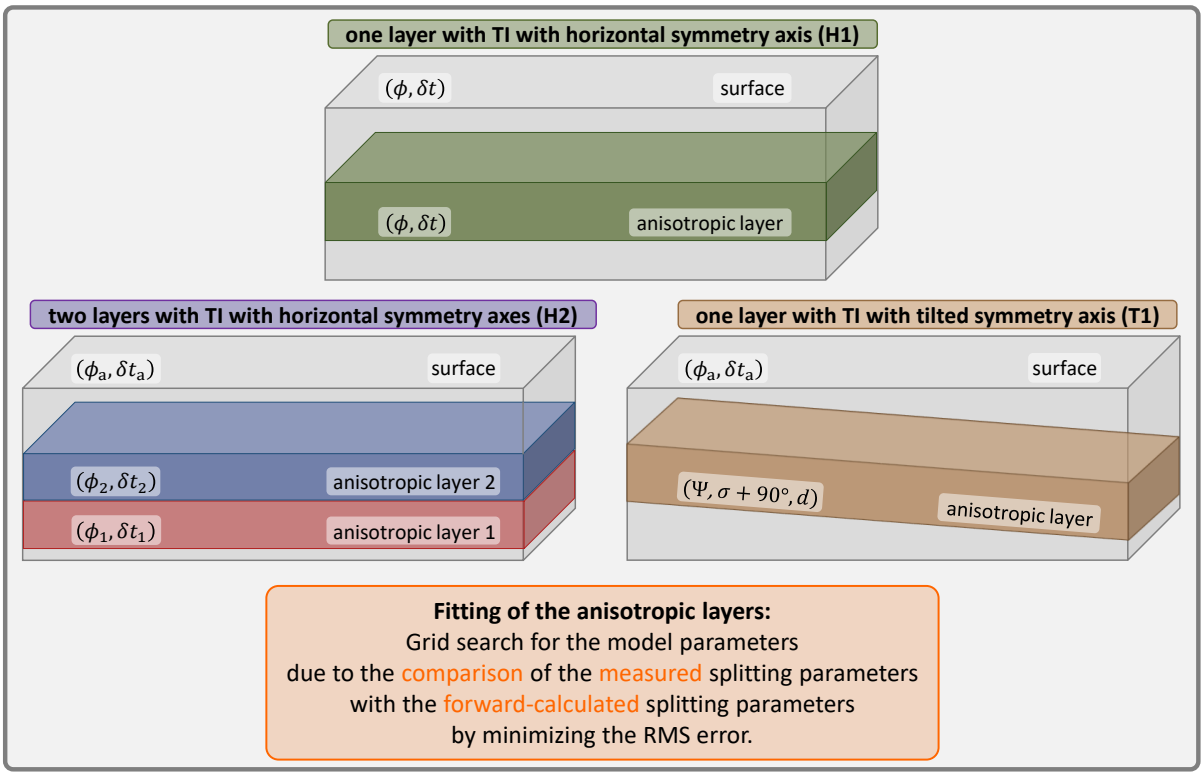

Figure B.13: Tested model types: one layer with transverse isotropy with horizontal symmetry axis (H1, top), two layers with transverse isotropy with horizontal symmetry axes (H2, bottom left), and one layer with transverse isotropy with tilted symmetry axis (T1, bottom right). In each layer the varied model parameters to generate the synthetic anisotropy models are given (Tab. B.1). On the surface the apparent fast polarization direction ϕ_a and the apparent delay time δt_a are measured. In case of simple anisotropy (model type H1) the apparent splitting parameters are equal to ϕ and δt. Abbreviations: TI = transverse isotropy, RMS = root mean square.

Table B.1: Systematic variation of the model parameters for the model types H1, H2, and T1 (Fig. B.13) to generate the synthetic anisotropy models (upper part). Lower layer in the lower line (index 1) and upper layer in the upper line (index 2). The forward calculation of the splitting parameters was done using the *MATLAB Seismic Anisotropy Toolkit* (MSAT) by *Walker and Wookey* (2012). For H2, the equations from *Silver and Savage* (1994) were used. For T1, the *Christoffel equation* (*Mainprice*, 2007) was solved. To avoid a layer thickness of zero the start values of delay time and layer thickness are set to the used step width, respectively. To avoid a horizontal layer the start value of the dip angle is set to the used step width and to avoid a (sub)vertical layer the dip angle is limited to 75°. The fast polarization direction and the down-dip direction (strike direction plus 90°) are cyclic quantities. Assumptions regarding the anisotropic medium and the S wave are given in the lower part. Abbreviations: HTI = transverse isotropy with horizontal symmetry axis, TTI = transverse isotropy with tilted symmetry axis. In total 573120 models where tested: 720 for H1, 518400 for H2, and 54000 for T1.

model type **model parameter**	**H1** **(one layer with HTI)**	**H2** **(two layers with HTI)**	**T1** **(one layer with TTI)**
number	2 (ϕ, δt)	4 (ϕ_1, δt_1, ϕ_2, δt_2)	3 (Ψ, $\sigma + 90°$, d)
fast polarization direction ϕ [relative to north]	[−85 : 5 : 90]	[−85 : 5 : 90] [−85 : 5 : 90]	-
delay time δt / s	[0.2 : 0.2 : 4]	[0.2 : 0.2 : 4] [0.2 : 0.2 : 4]	-
dip angle Ψ / ° [relative to the horizontal]	-	- -	[5 : 5 : 75]
down-dip direction (strike σ + 90 °) [relative to north]	-	- -	[0 : 5 : 355]
layer thickness d / km	-	- -	[5 : 5 : 250]
dominant period T_{dom} / s [SKS phase]	8	8	8
incidence angle i / ° [100 km depth]	-	-	10
fraction aligned [pure olivine, dry, A-type CPO]	-	-	0.3

B.5.2 Modulo 90° backazimuth representation

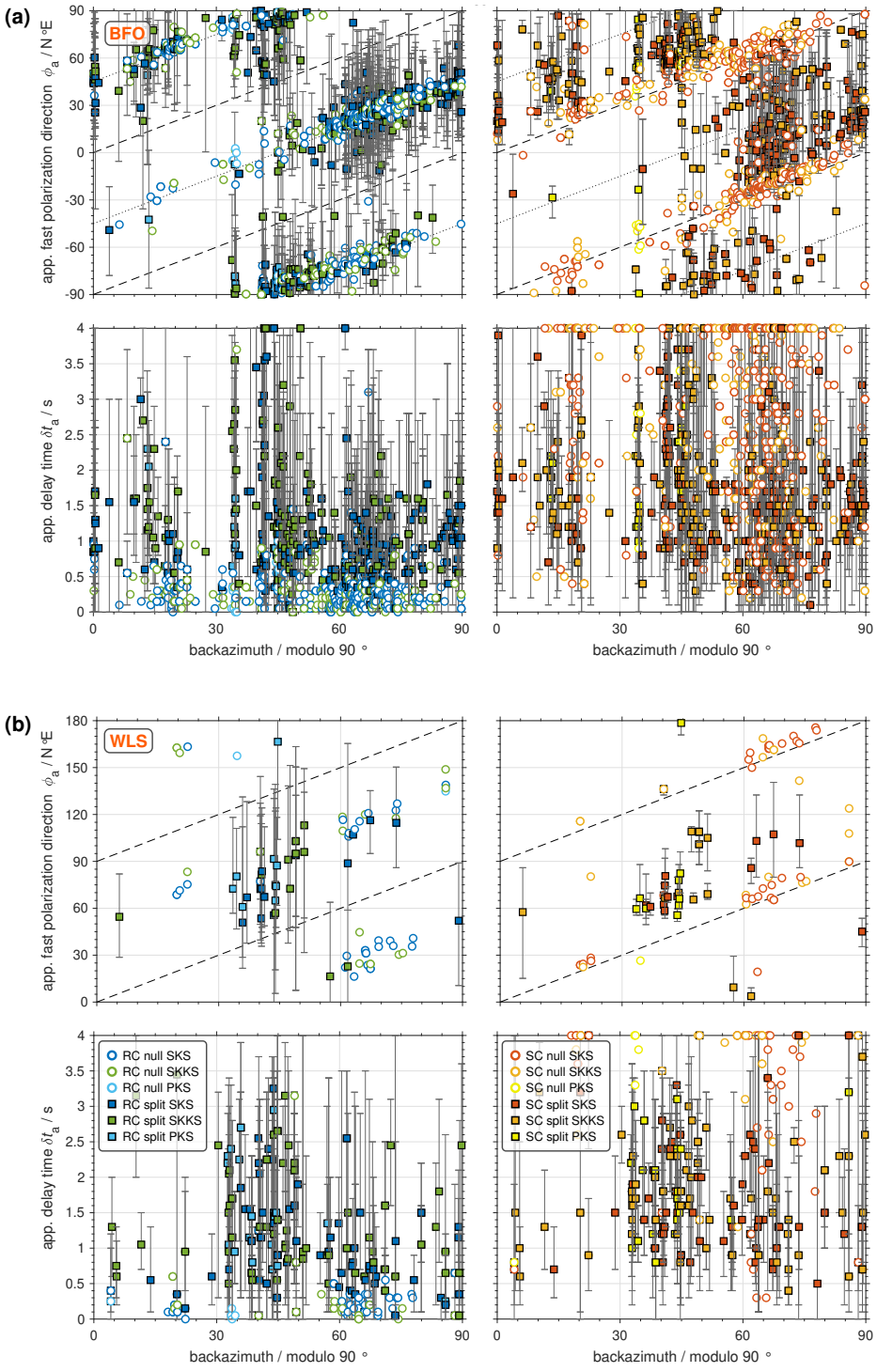

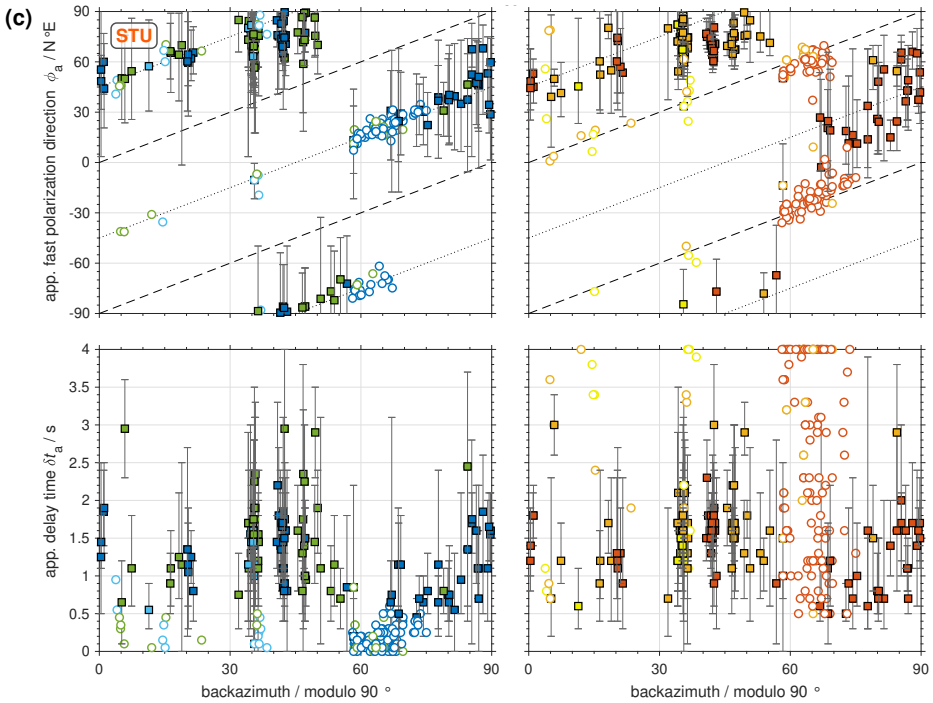
(c)
STU
app. fast polarization direction ϕ_a / N°E
app. delay time δt_a / s
backazimuth / modulo 90 °
backazimuth / modulo 90 °

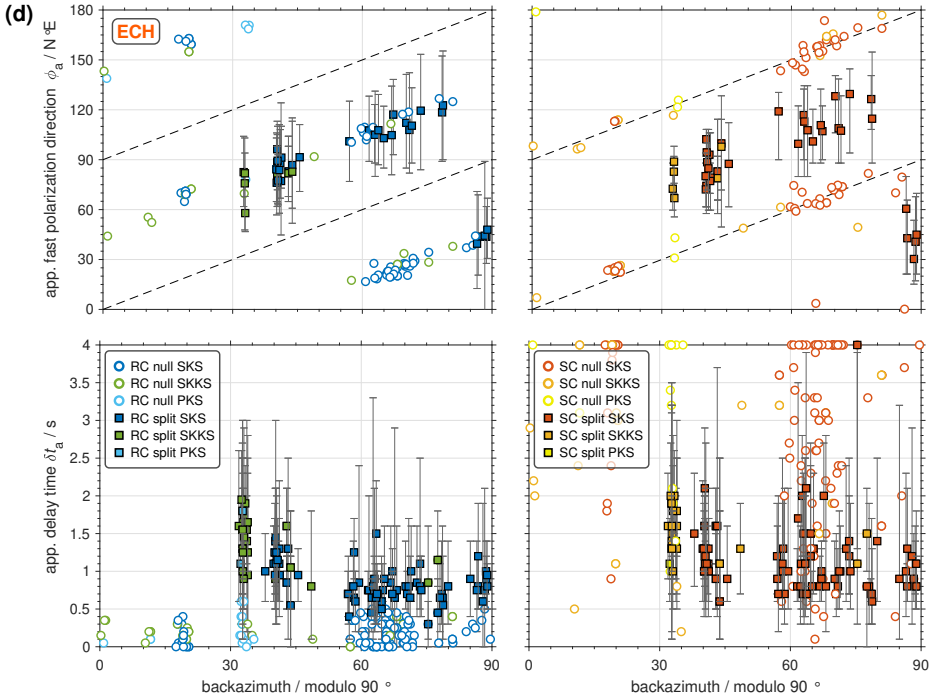
(d)
ECH
app. fast polarization direction ϕ_a / N°E
app. delay time δt_a / s
RC null SKS
RC null SKKS
RC null PKS
RC split SKS
RC split SKKS
RC split PKS
SC null SKS
SC null SKKS
SC null PKS
SC split SKS
SC split SKKS
SC split PKS
backazimuth / modulo 90 °
backazimuth / modulo 90 °

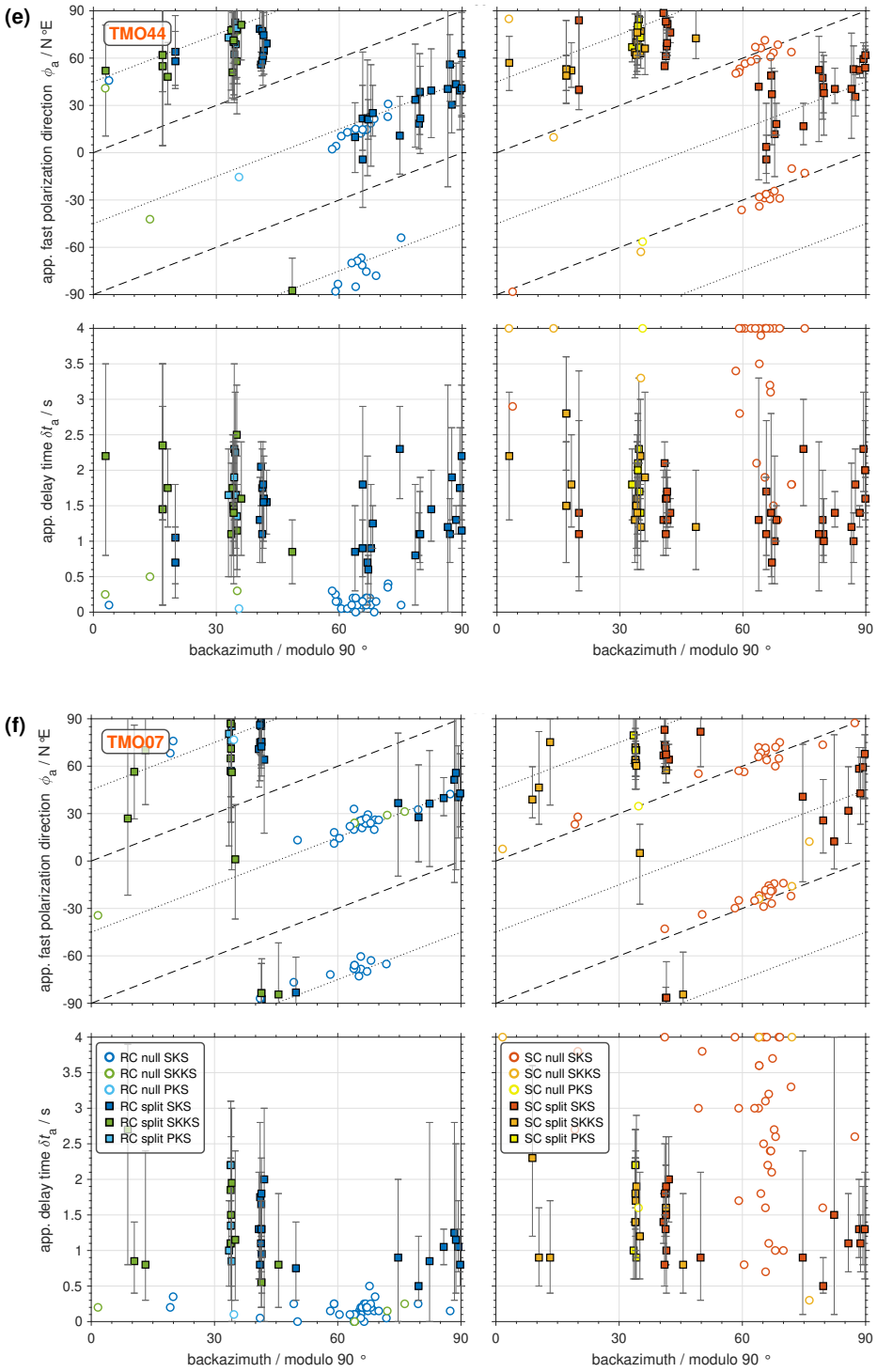

Figure B.14: Apparent splitting parameters obtained in the single-event analysis as function of the backazimuth in modulo 90° representation. Shear wave splitting measurements (SWSMs) of all qualities are displayed at the recording stations **(a)** BFO, **(b)** WLS, **(c)** STU, **(d)** ECH, **(e)** TMO44, and **(f)** TMO07. SWSMs at BFO are expanded based on *Ritter et al.* (2022). *Rotation-correlation* method (RC method; *Bowman and Ando*, 1987; left), *energy minimization* method (SC method; *Silver and Chan*, 1991; right). Apparent fast polarization direction ϕ_a (top), apparent delay time δt_a (bottom). *Nulls* are displayed as white circles with coloured outline and *splits* as squares with coloured fill. SKS in dark blue (RC method) or dark orange (SC method), SKKS in green or light orange, and PKS in light blue or yellow. The 95 per cent confidence intervals of the apparent splitting parameters are given by the vertical error bars. The black dotted (RC method) and dashed (SC method) lines with a slope of 45° indicate the values of ϕ_a expected for *nulls* in case of simple anisotropy (model type H1). Note that for *nulls* δt_a tends to zero for the RC method but for the SC method it spreads over the whole range of the grid search up to the maximum, here 4 s.

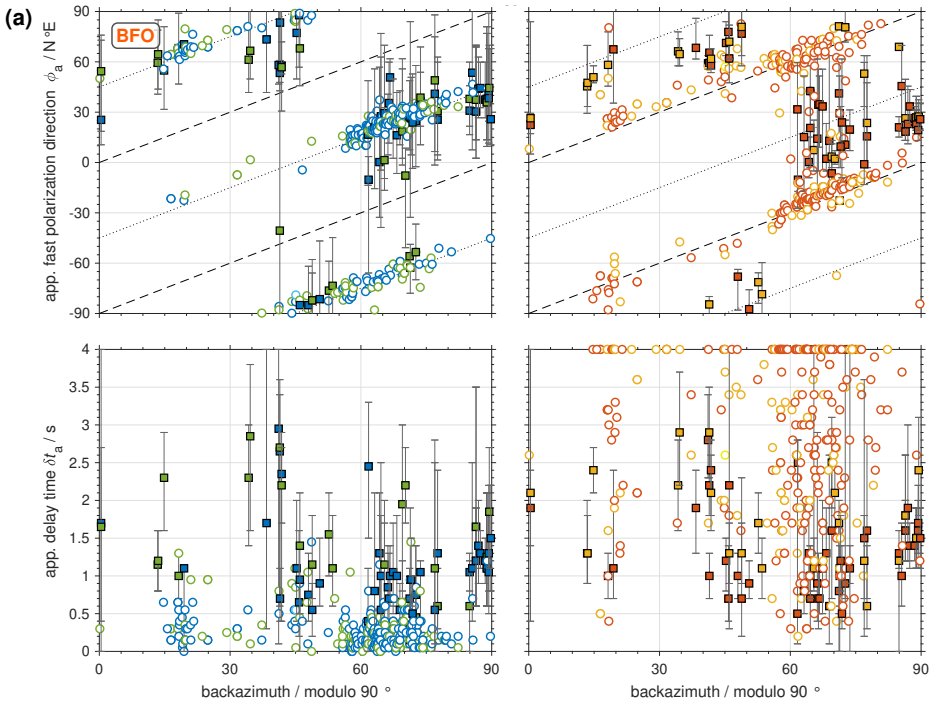
(a)
BFO
app. fast polarization direction ϕ_a / N°E
app. delay time δt_a / s
backazimuth / modulo 90 °
backazimuth / modulo 90 °

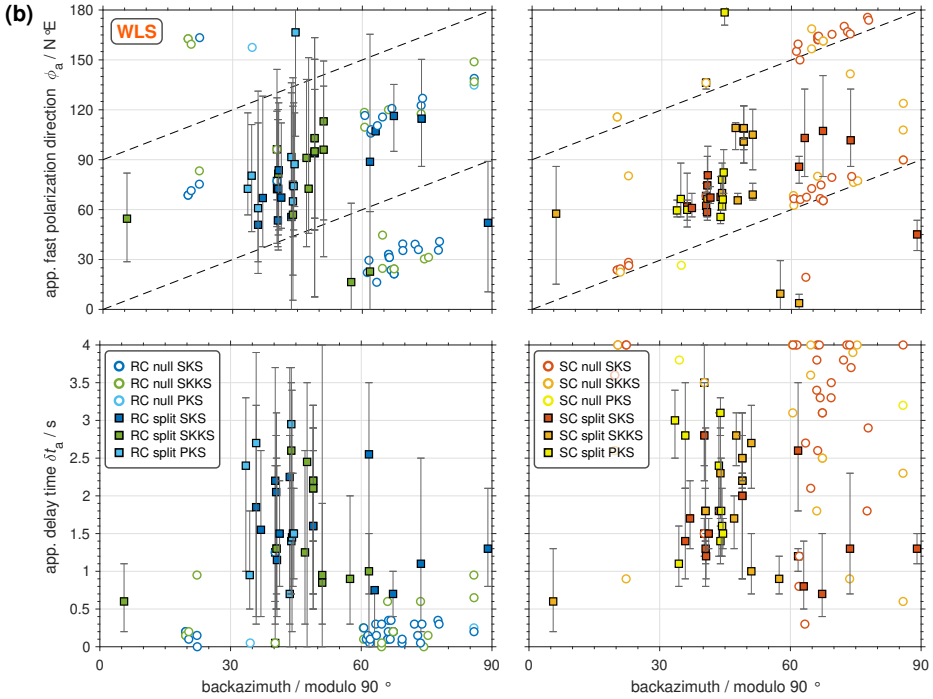
(b)
WLS
app. fast polarization direction ϕ_a / N°E
app. delay time δt_a / s
RC null SKS
RC null SKKS
RC null PKS
RC split SKS
RC split SKKS
RC split PKS
SC null SKS
SC null SKKS
SC null PKS
SC split SKS
SC split SKKS
SC split PKS
backazimuth / modulo 90 °
backazimuth / modulo 90 °

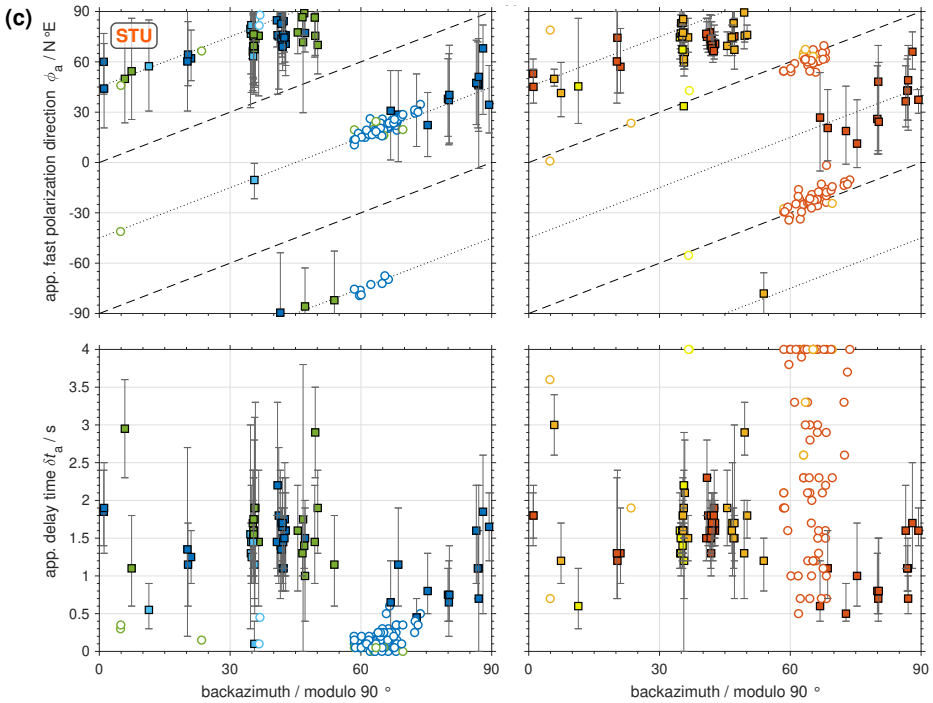
(c)
STU
app. fast polarization direction ϕ_a / N°E
app. delay time δt_a / s
backazimuth / modulo 90 °
backazimuth / modulo 90 °

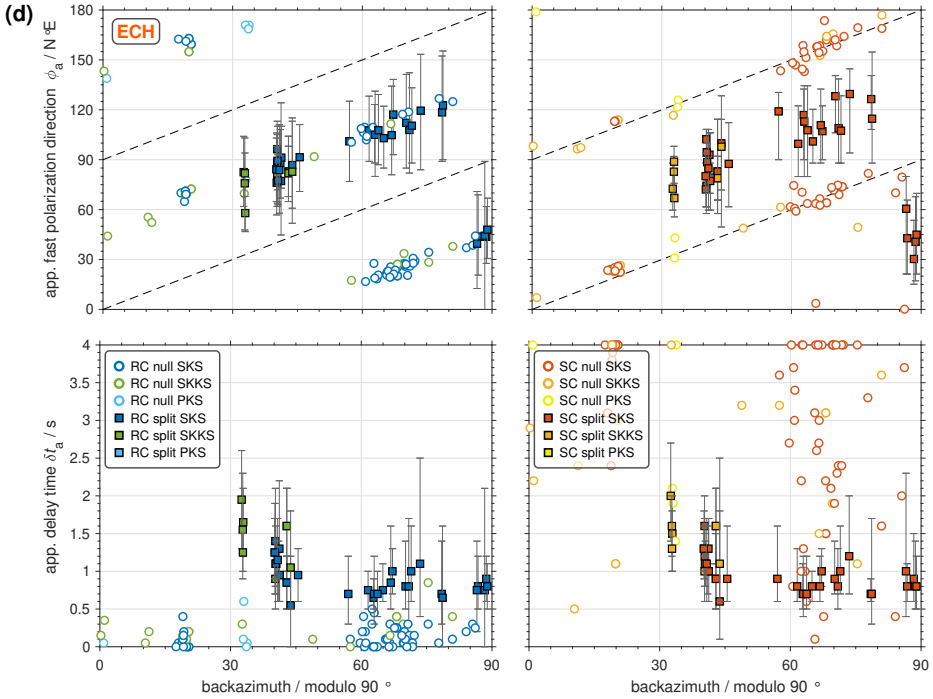
(d)
ECH
app. fast polarization direction ϕ_a / N°E
app. delay time δt_a / s
RC null SKS
RC null SKKS
RC null PKS
RC split SKS
RC split SKKS
RC split PKS
SC null SKS
SC null SKKS
SC null PKS
SC split SKS
SC split SKKS
SC split PKS
backazimuth / modulo 90 °
backazimuth / modulo 90 °

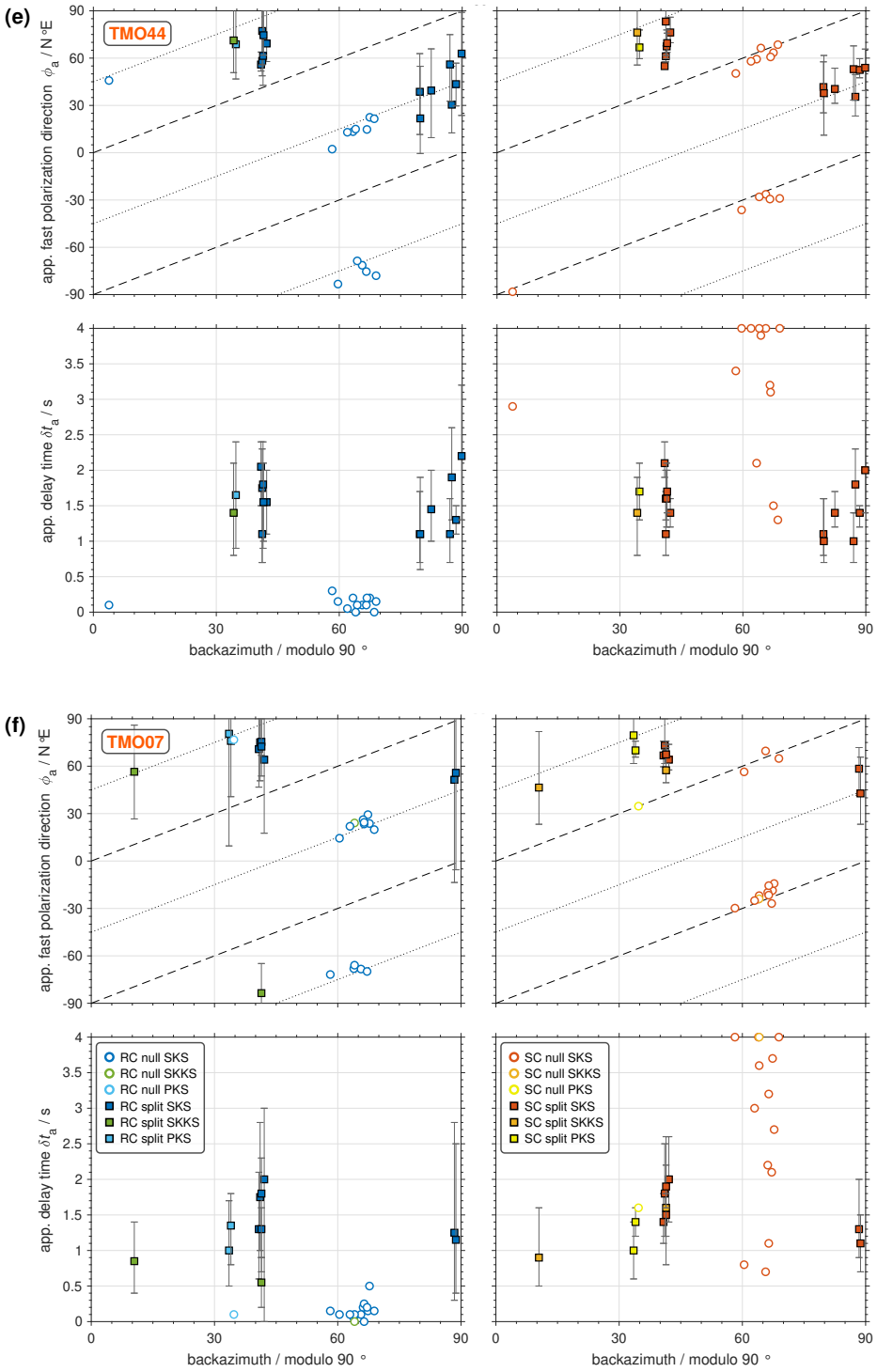

Figure B.15: Same as Fig. B.14, but only for the *good* and *fair* shear wave splitting measurements (SWSMs). SWSMs at BFO are expanded based on *Ritter et al.* (2022).

B.5.3 Modelling results

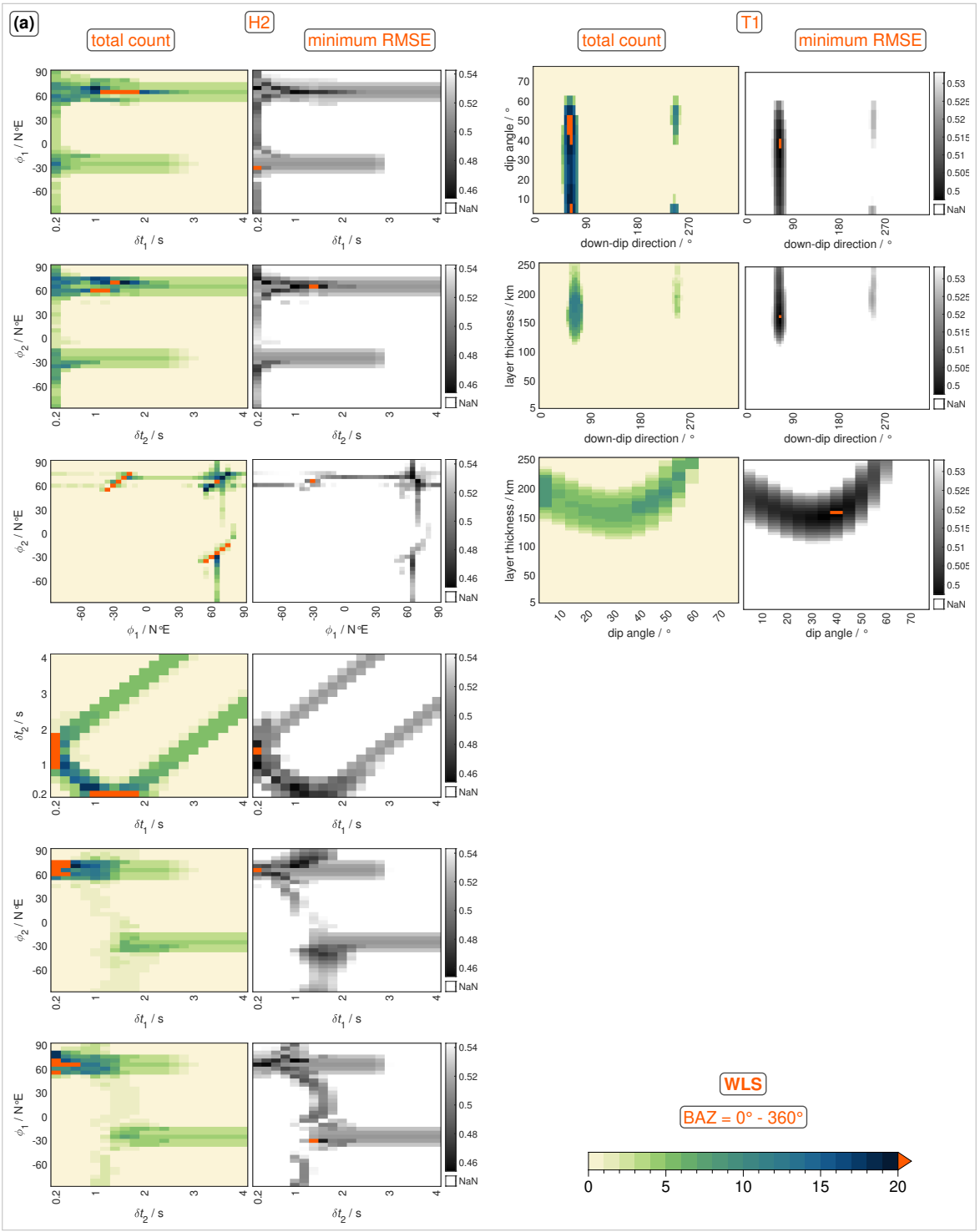

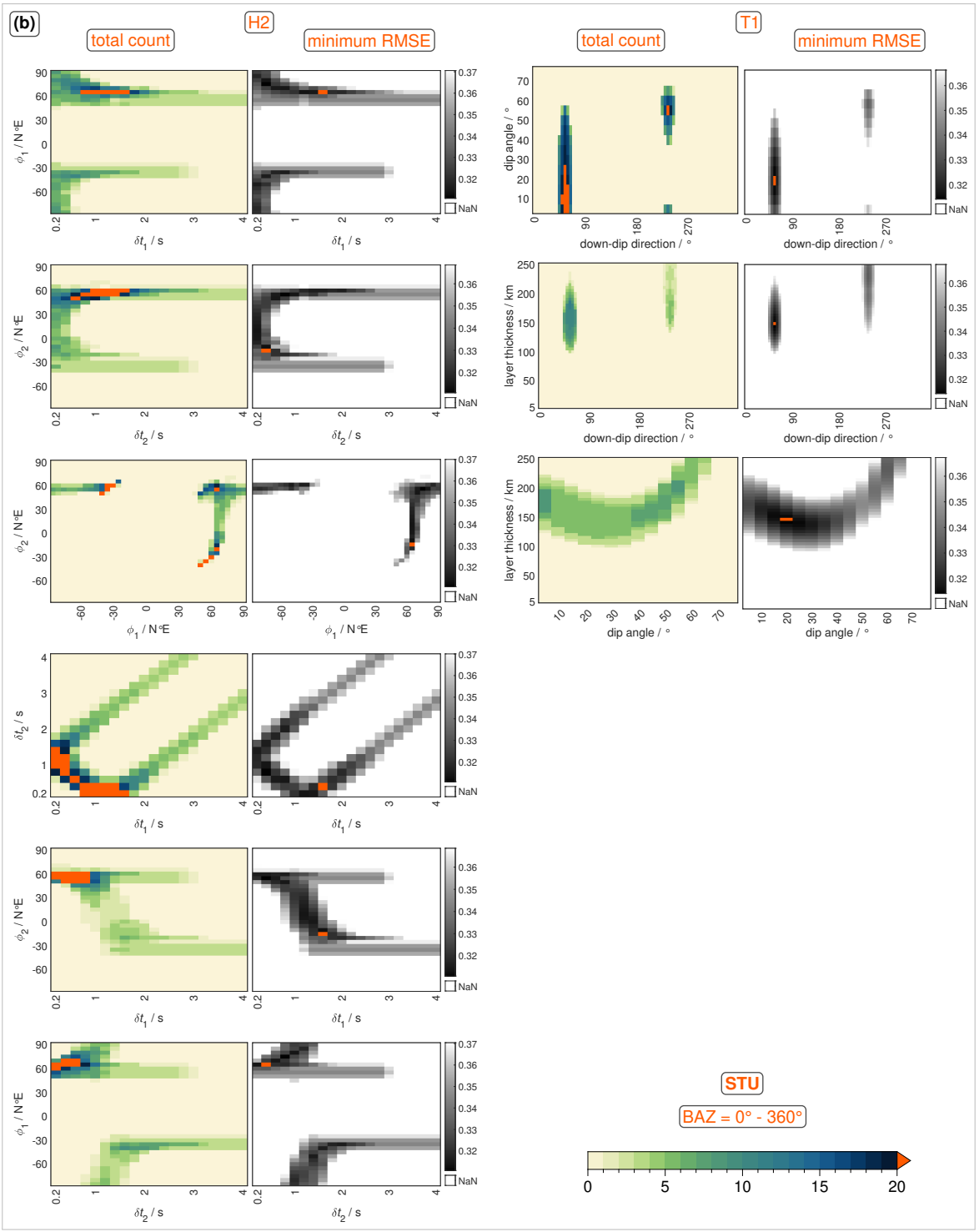
(b)
H2
total count
minimum RMSE
T1
total count
minimum RMSE
ϕ_1 / N°E
ϕ_2 / N°E
δt_1 / s
δt_2 / s
dip angle / °
down-dip direction / °
layer thickness / km
NaN
STU
BAZ = 0° - 360°
0
5
10
15
20

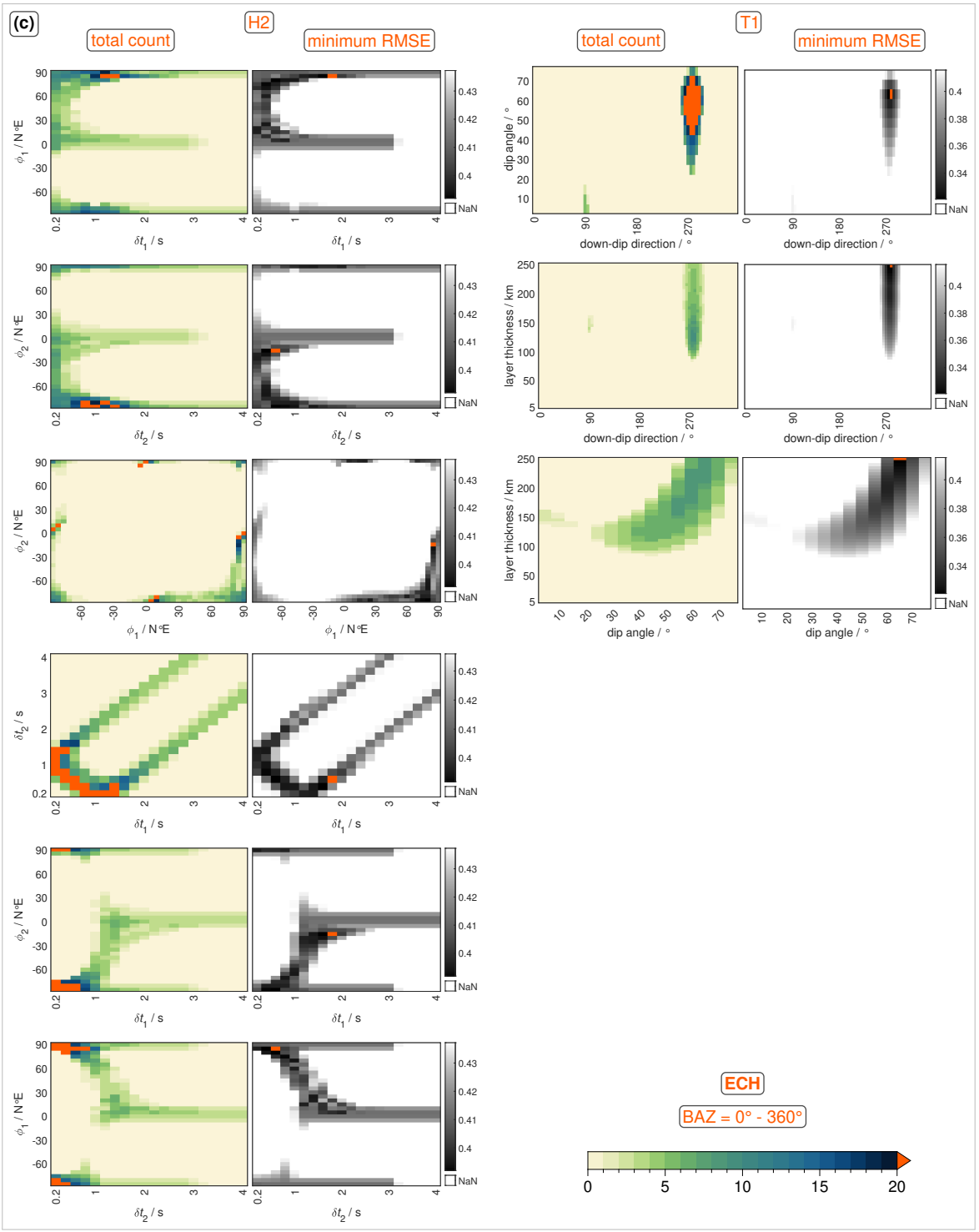
(c)
H2
total count
minimum RMSE
T1
total count
minimum RMSE
ϕ_1 / N°E
ϕ_2 / N°E
δt_1 / s
δt_2 / s
dip angle / °
down-dip direction / °
layer thickness / km
NaN
ECH
BAZ = 0° - 360°
0
5
10
15
20

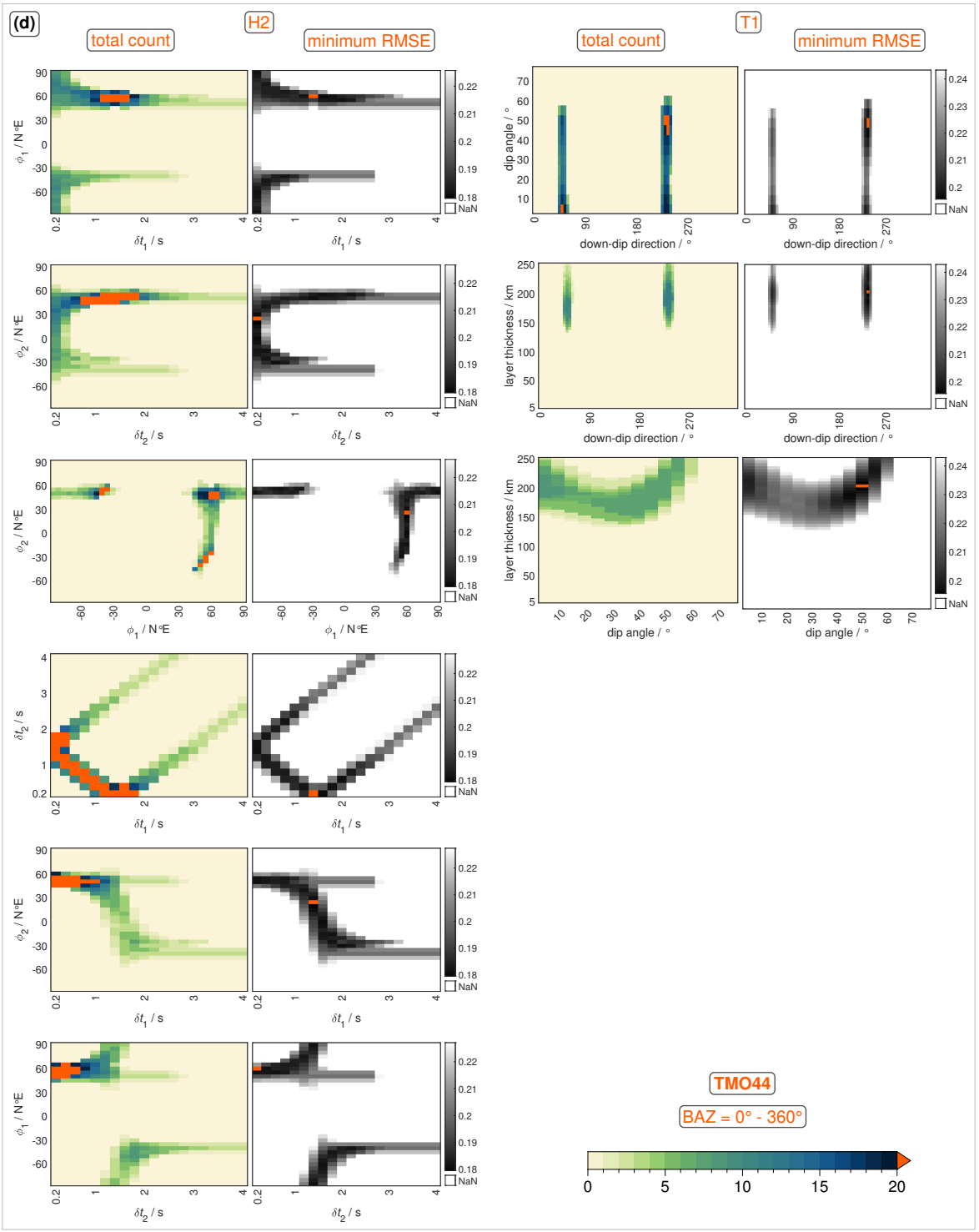

Figure B.16: Heat maps of the 1000 best-fitting synthetic anisotropy models for two horizontal layers (H2) and one dipping layer (T1) at the recording stations **(a)** WLS, **(b)** STU, **(c)** ECH, and **(d)** TMO44. The modelling is based on the *splits* observed in the backazimuth (BAZ) range 0°-360°. For BFO and TMO07, only the BAZ range 0°-100° was modelled. Displayed are the total count (left, common colourmap) and the minimum RMSE (right, individual colourmaps). For the model types and model parameters see Fig. B.13 and Tab. B.1, respectively.

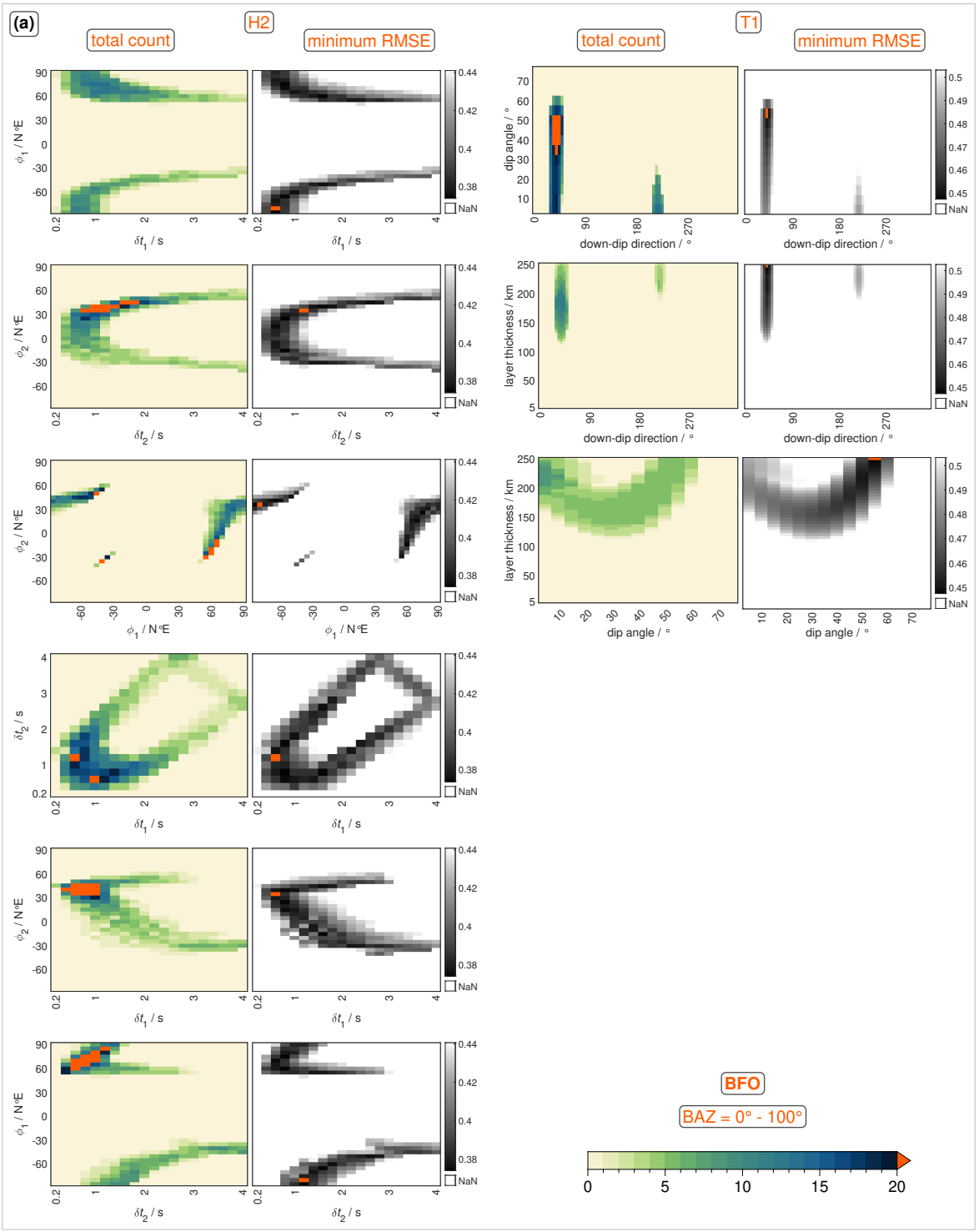
(a)
H2
total count
minimum RMSE
T1
total count
minimum RMSE
BFO
BAZ = 0° - 100°
0
5
10
15
20
NaN
down-dip direction / °
dip angle / °
layer thickness / km

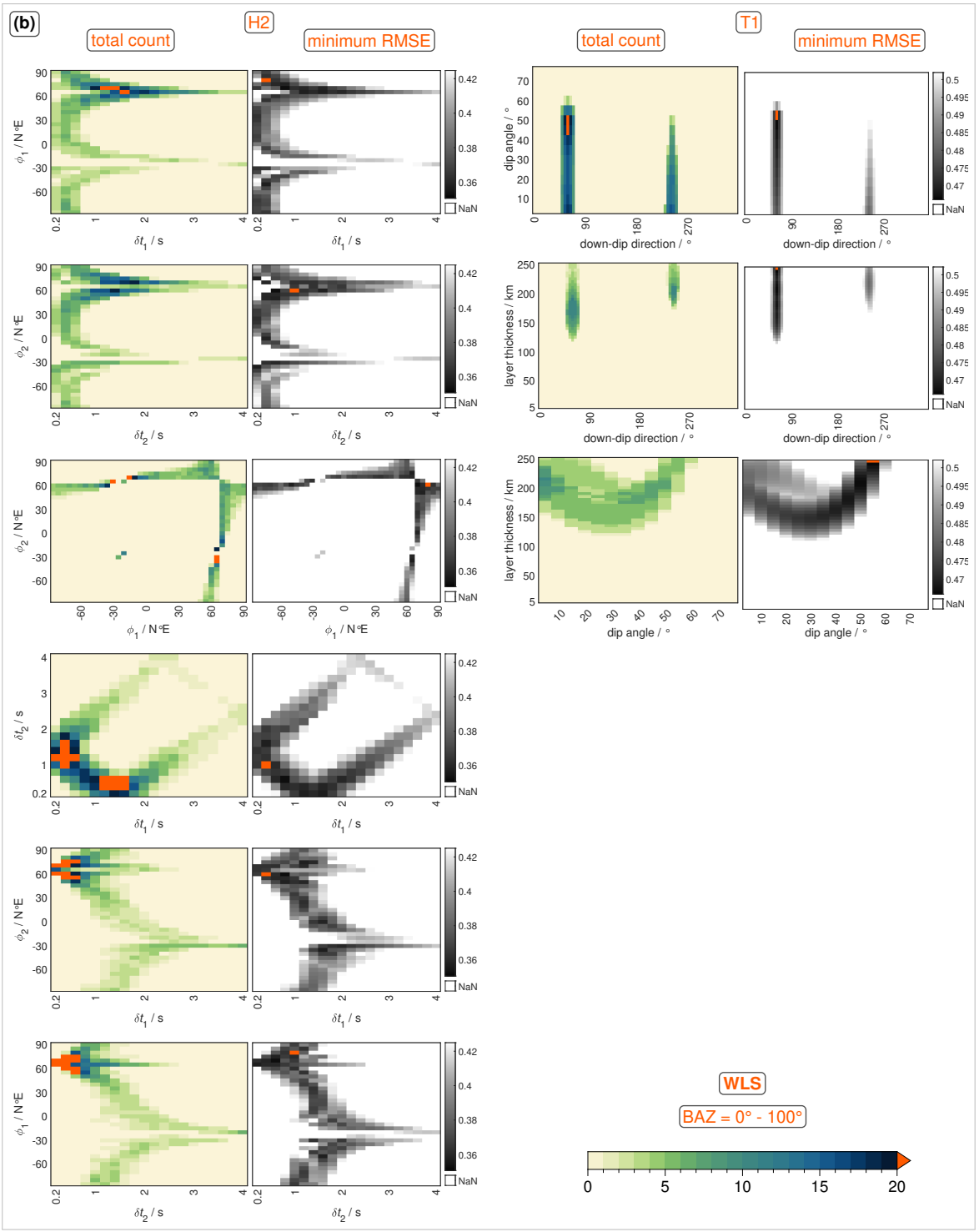
(b)
H2
total count
minimum RMSE
T1
total count
minimum RMSE
ϕ_1 / N°E
ϕ_2 / N°E
δt_1 / s
δt_2 / s
dip angle / °
down-dip direction / °
layer thickness / km
NaN
WLS
BAZ = 0° - 100°
0
5
10
15
20

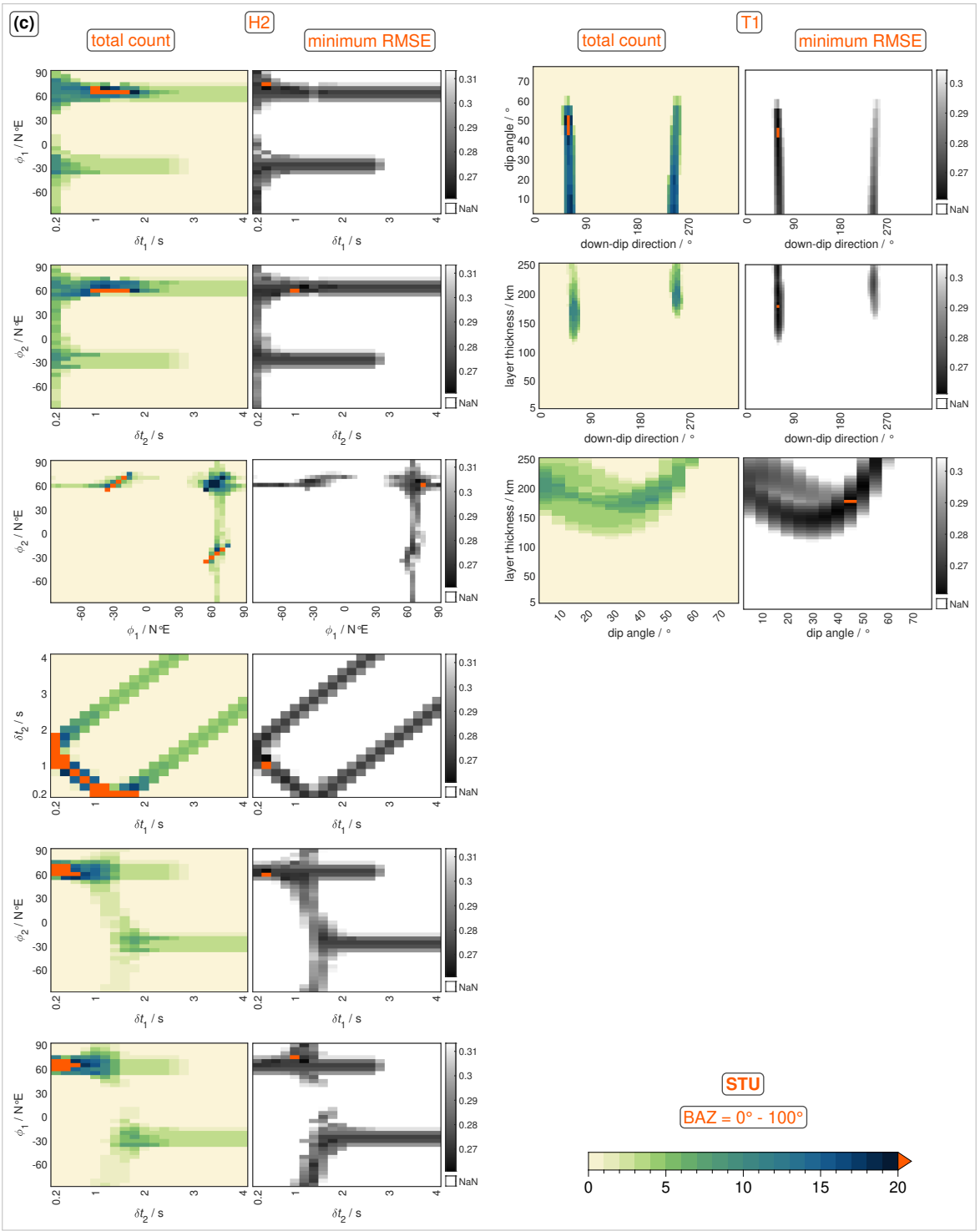
(c)
H2
total count
minimum RMSE
T1
total count
minimum RMSE
ϕ_1 / N°E
ϕ_2 / N°E
δt_1 / s
δt_2 / s
dip angle / °
layer thickness / km
down-dip direction / °
NaN
STU
BAZ = 0° - 100°
0
5
10
15
20

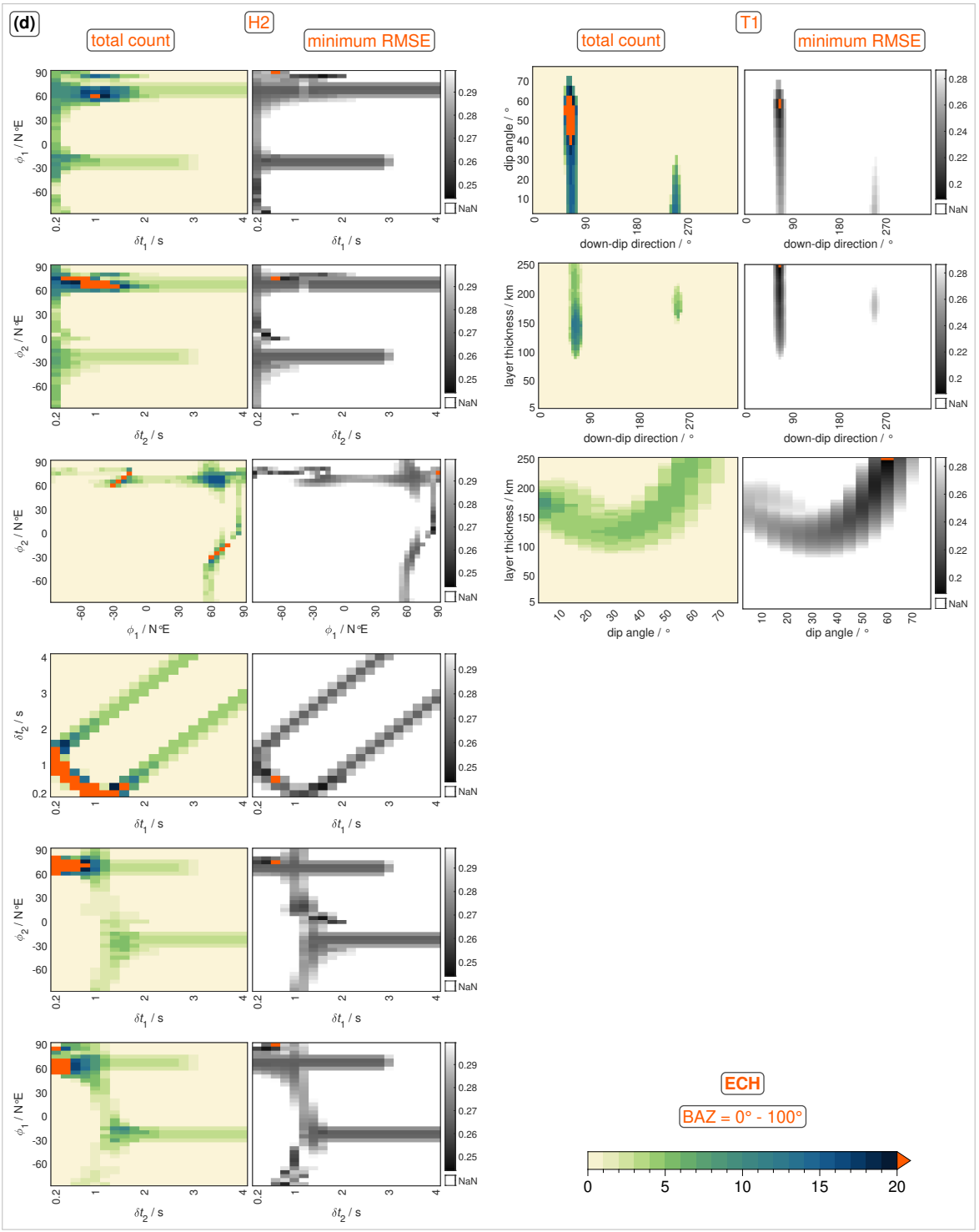
(d)
H2
total count
minimum RMSE
T1
total count
minimum RMSE
ϕ_1 / N°E
ϕ_2 / N°E
δt_1 / s
δt_2 / s
dip angle / °
down-dip direction / °
layer thickness / km
NaN
ECH
BAZ = 0° - 100°
0
5
10
15
20

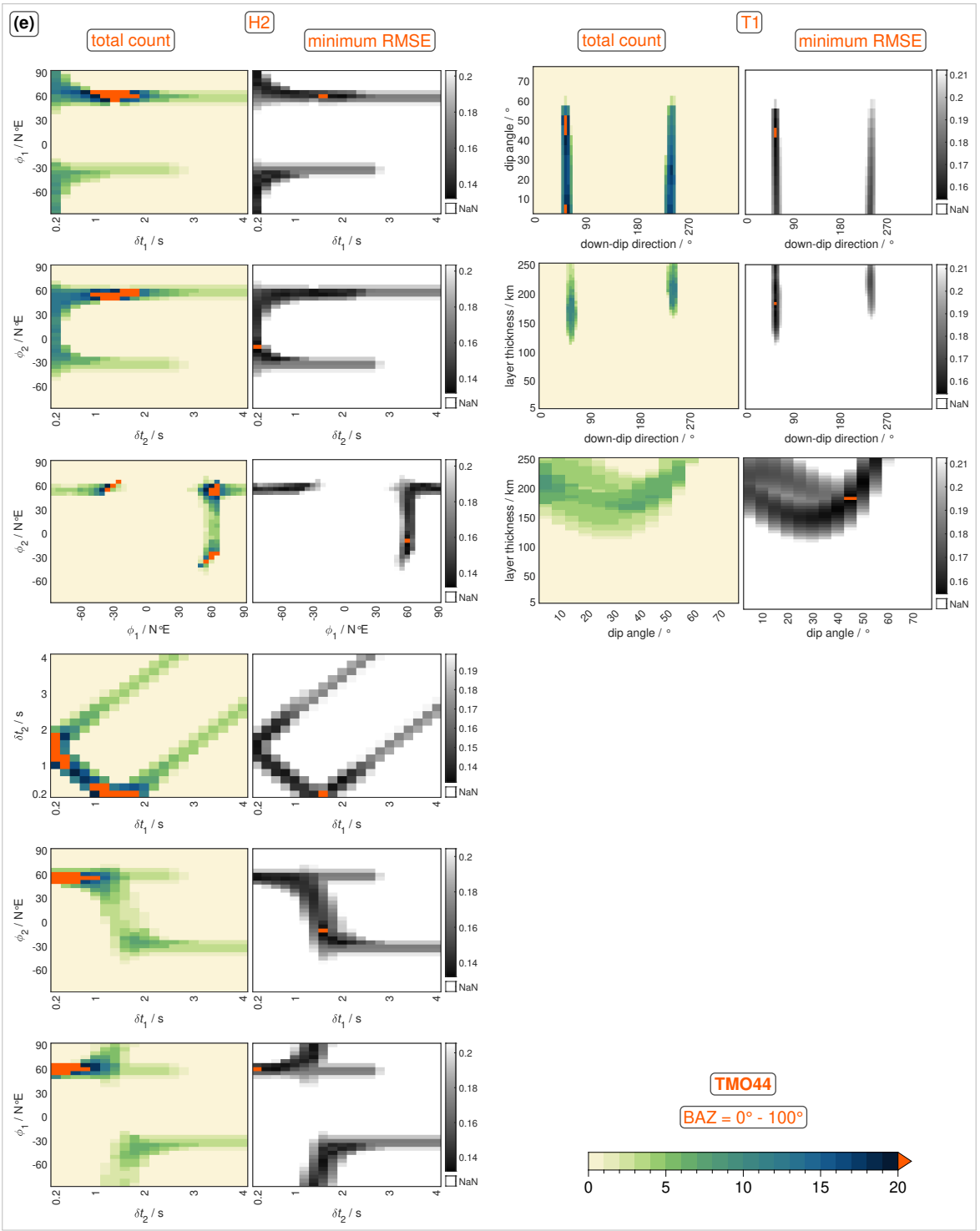
(e)
H2
total count
minimum RMSE
T1
total count
minimum RMSE
ϕ_1 / N°E
ϕ_2 / N°E
δt_1 / s
δt_2 / s
dip angle / °
down-dip direction / °
layer thickness / km
NaN
TMO44
BAZ = 0° - 100°
0
5
10
15
20

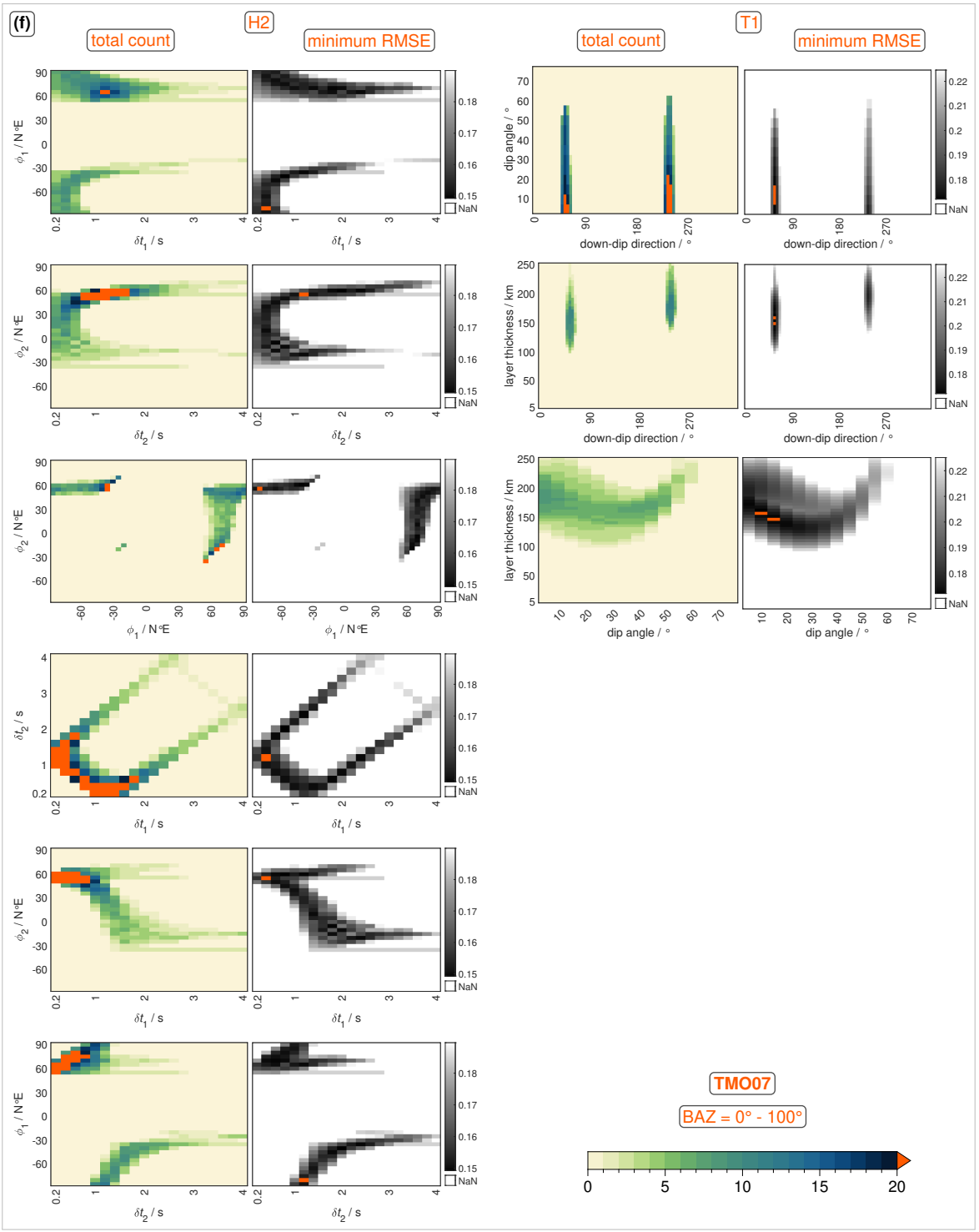

Figure B.17: Same as Fig. B.16, but for a modelling based on the *splits* observed in the backazimuth (BAZ) range 0°-100° at the recording stations **(a)** BFO, **(b)** WLS, **(c)** STU, **(d)** ECH, **(e)** TMO44, and **(f)** TMO07.

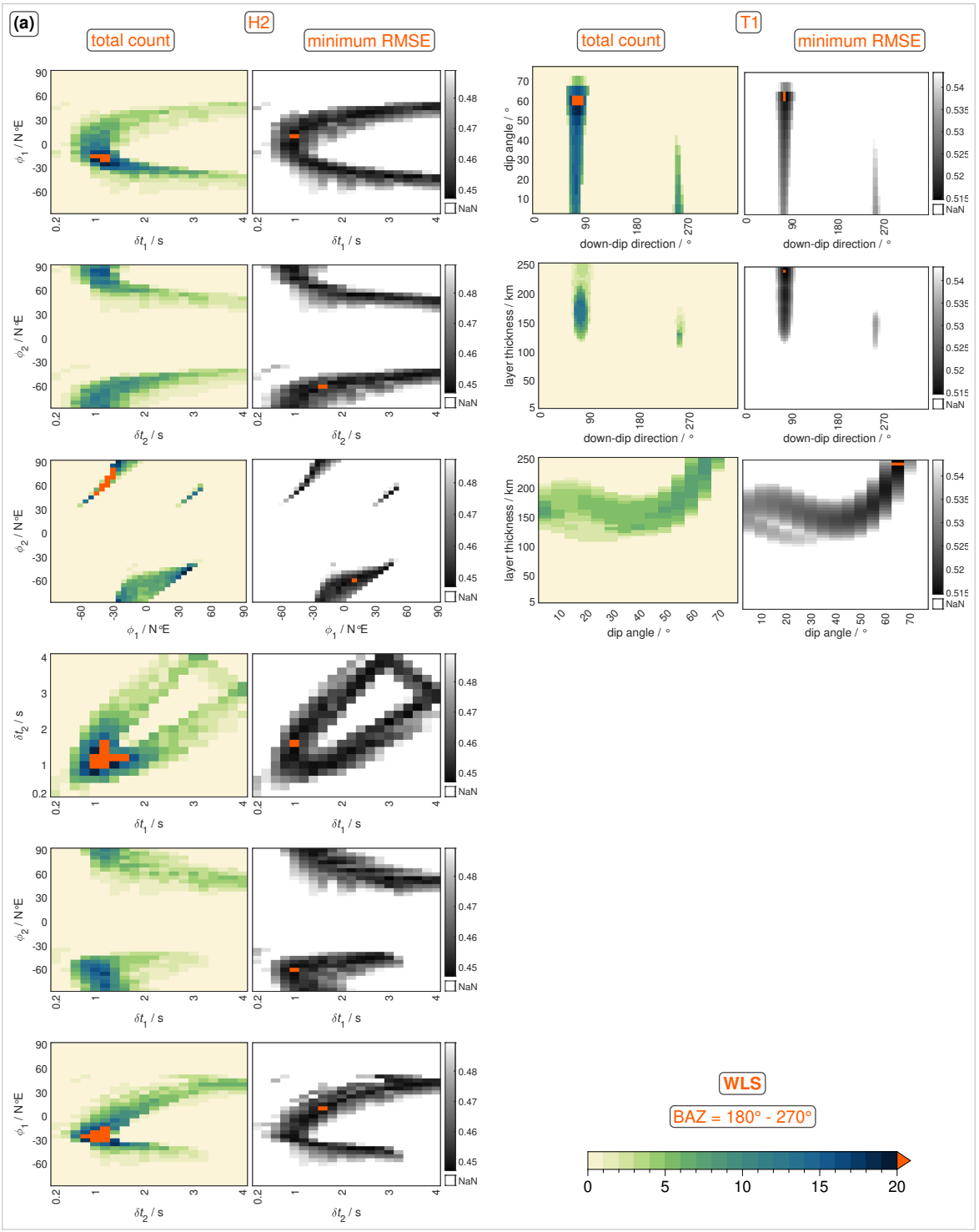
(a)
H2
total count
minimum RMSE
T1
total count
minimum RMSE
ϕ_1 / N°E
ϕ_2 / N°E
δt_1 / s
δt_2 / s
dip angle / °
down-dip direction / °
layer thickness / km
NaN
WLS
BAZ = 180° - 270°
0
5
10
15
20

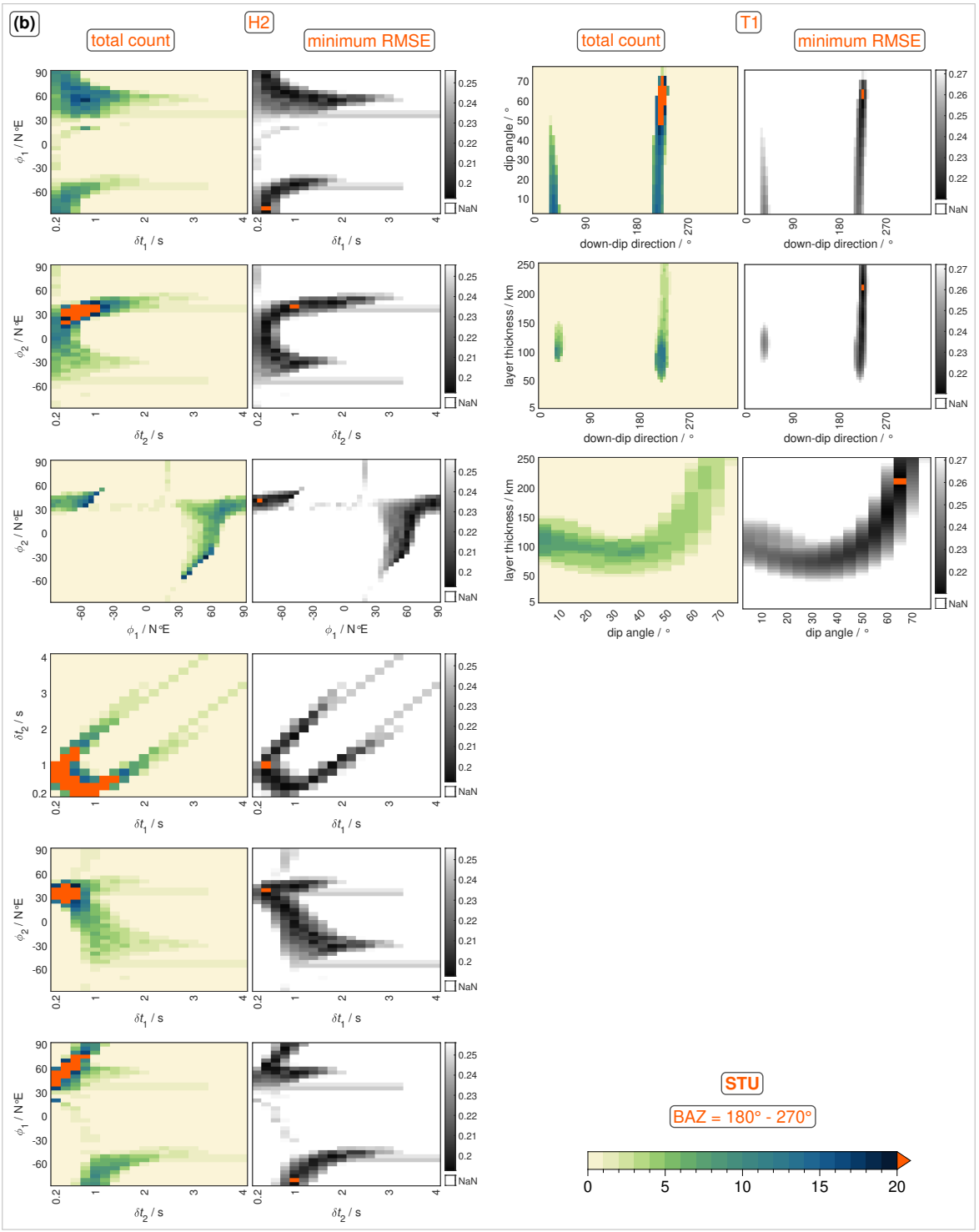
(b)
H2
total count
minimum RMSE
T1
total count
minimum RMSE
ϕ_1 / N°E
ϕ_2 / N°E
δt_1 / s
δt_2 / s
dip angle / °
down-dip direction / °
layer thickness / km
NaN
STU
BAZ = 180° - 270°
0
5
10
15
20

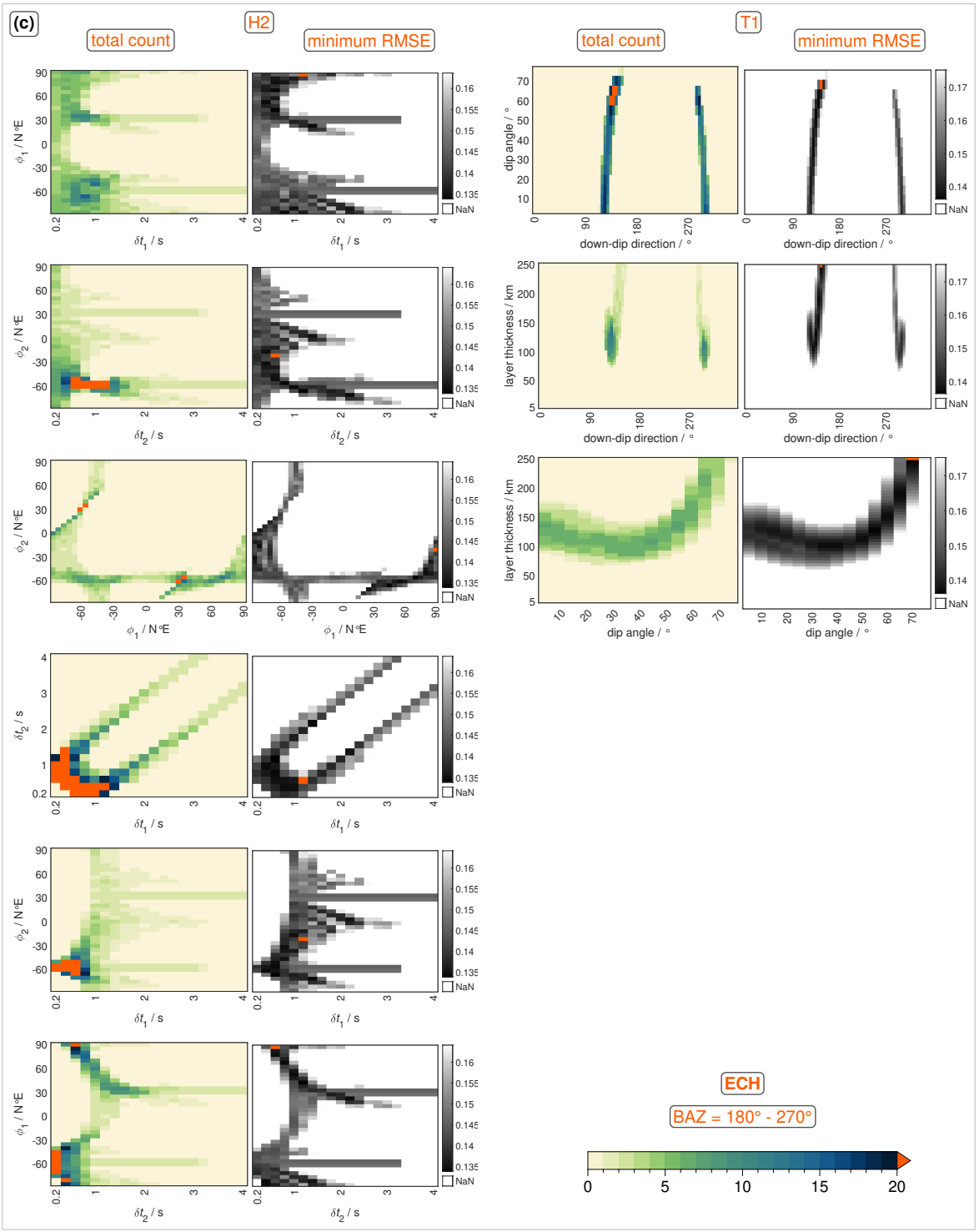
(c)
H2
total count
minimum RMSE
T1
total count
minimum RMSE
ϕ_1 / N°E
ϕ_2 / N°E
δt_1 / s
δt_2 / s
dip angle / °
down-dip direction / °
layer thickness / km
NaN
ECH
BAZ = 180° - 270°
0
5
10
15
20

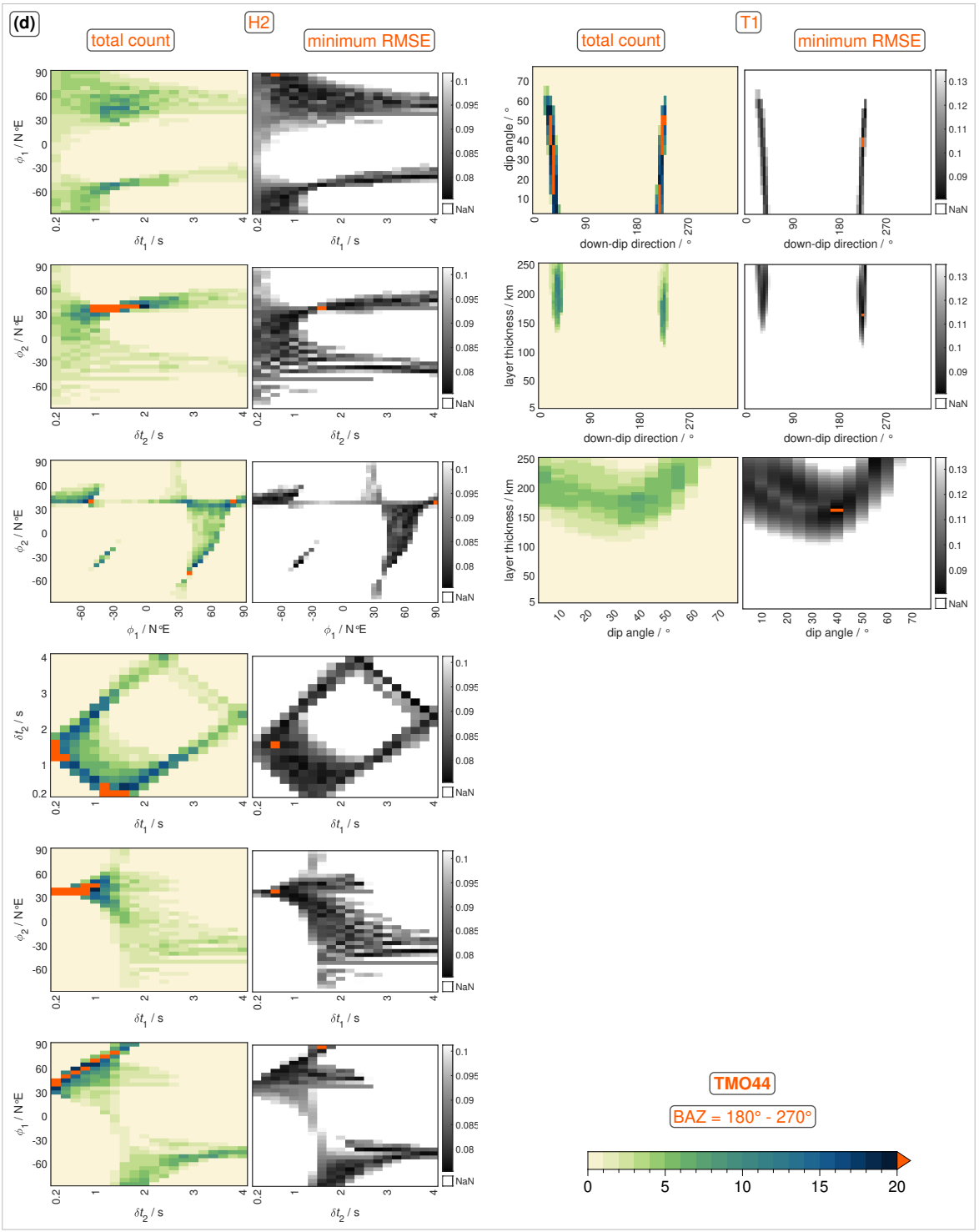

Figure B.18: Same as Fig. B.16, but for a modelling based on the *splits* observed in the backazimuth (BAZ) range 180°-270° at the recording stations **(a)** WLS, **(b)** STU, **(c)** ECH, and **(d)** TMO44. For BFO and TMO07, only the BAZ range 0°-100° was modelled.

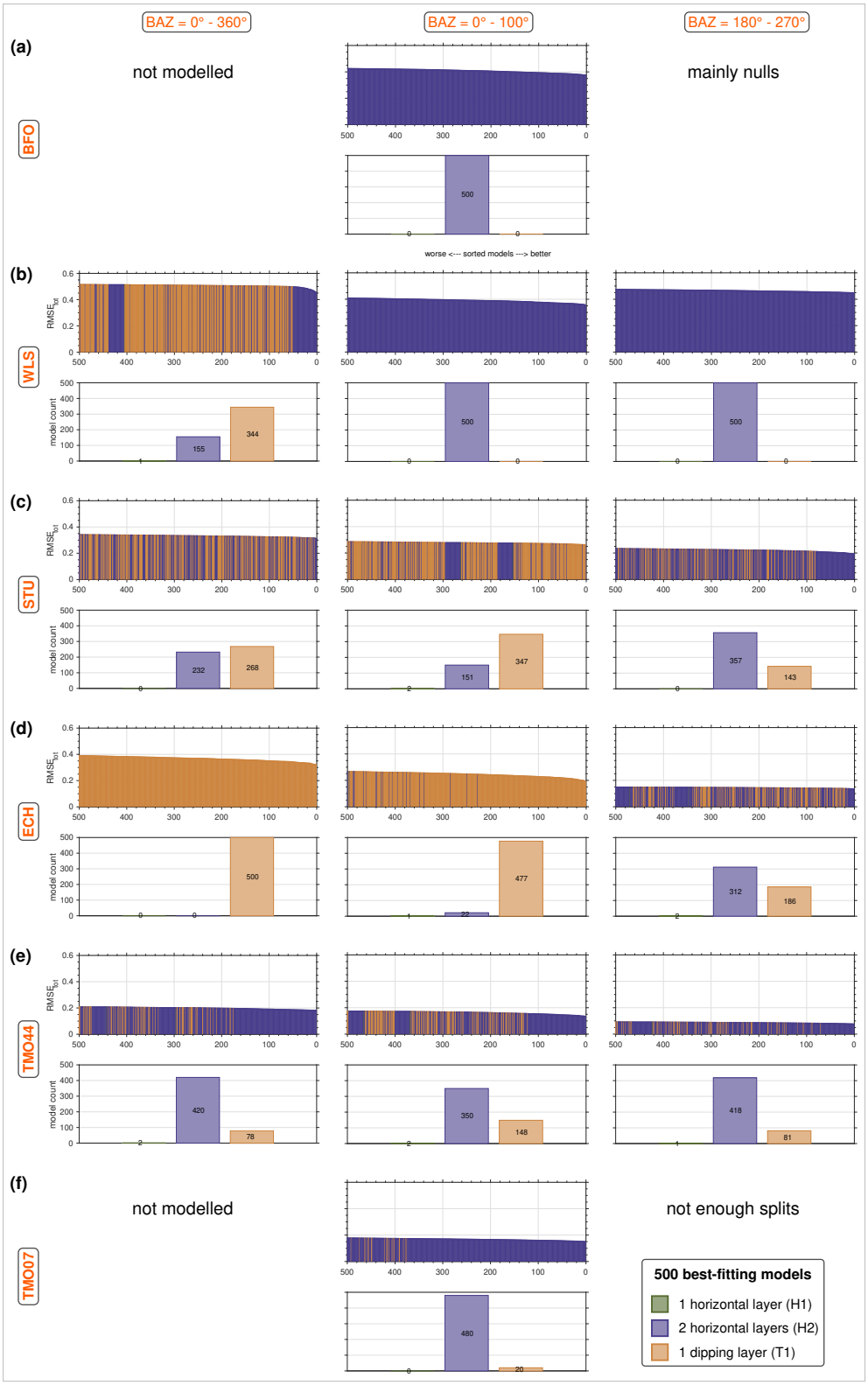

Figure B.19: Distribution of the model types one horizontal layer (H1, dark green), two horizontal layers (H2, purple), and one dipping layer (**T1**, light brown) within the 500 best-fitting synthetic anisotropy models at the recording stations **(a)** BFO, **(b)** WLS, **(c)** STU, **(d)** ECH, **(e)** TMO44, and **(f)** TMO07. The modelling is based on the *splits* observed in the backazimuth (BAZ) ranges 0°-360° (left column), 0°-100° (middle column), and 180°-270° (right column). For BFO and TMO07, only the BAZ range 0°-100° was modelled. For the model types see Fig. B.13.

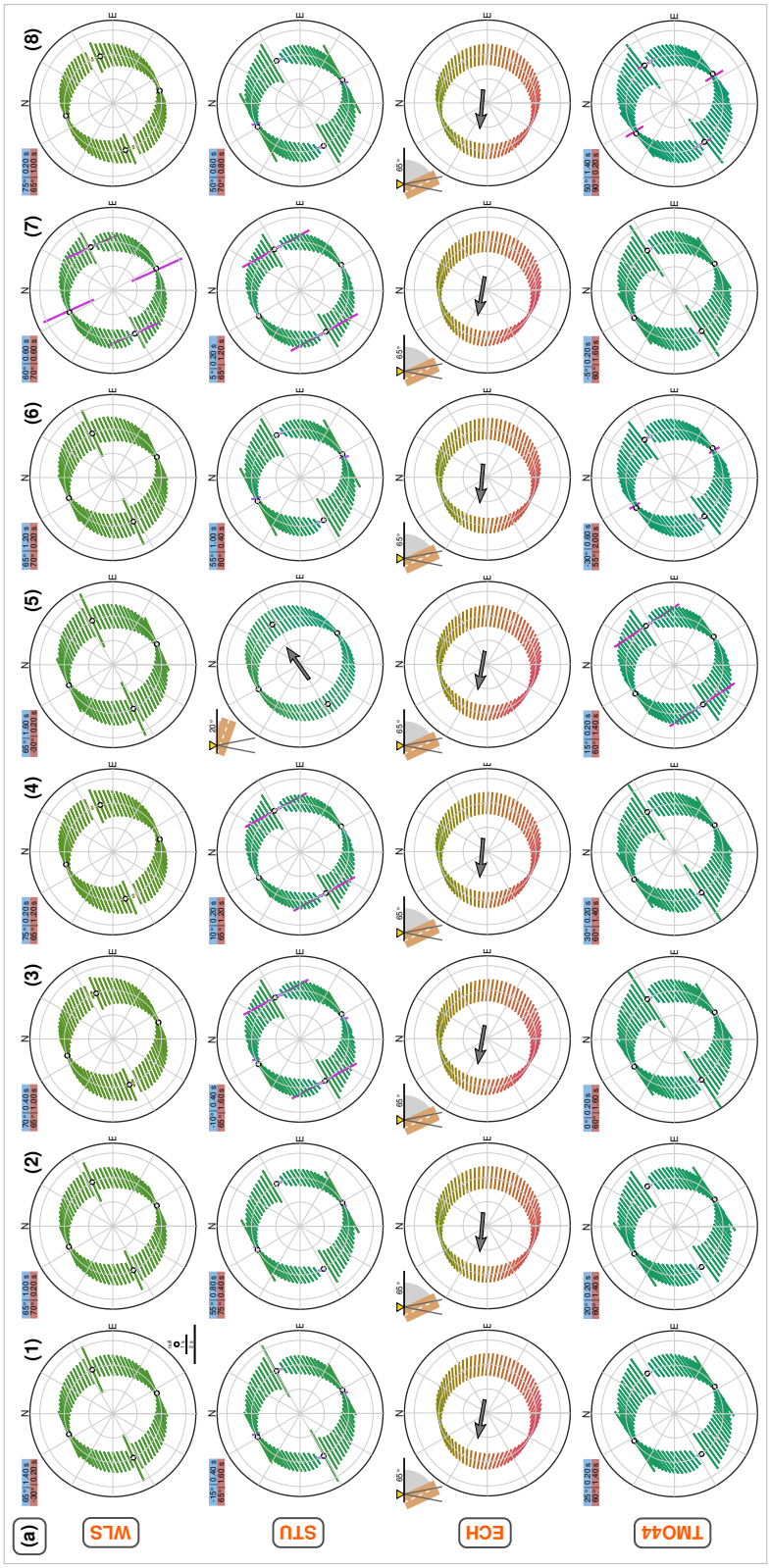
(a)
WLS
STU
ECH
TMO44
(1)
(2)
(3)
(4)
(5)
(6)
(7)
(8)
N
E

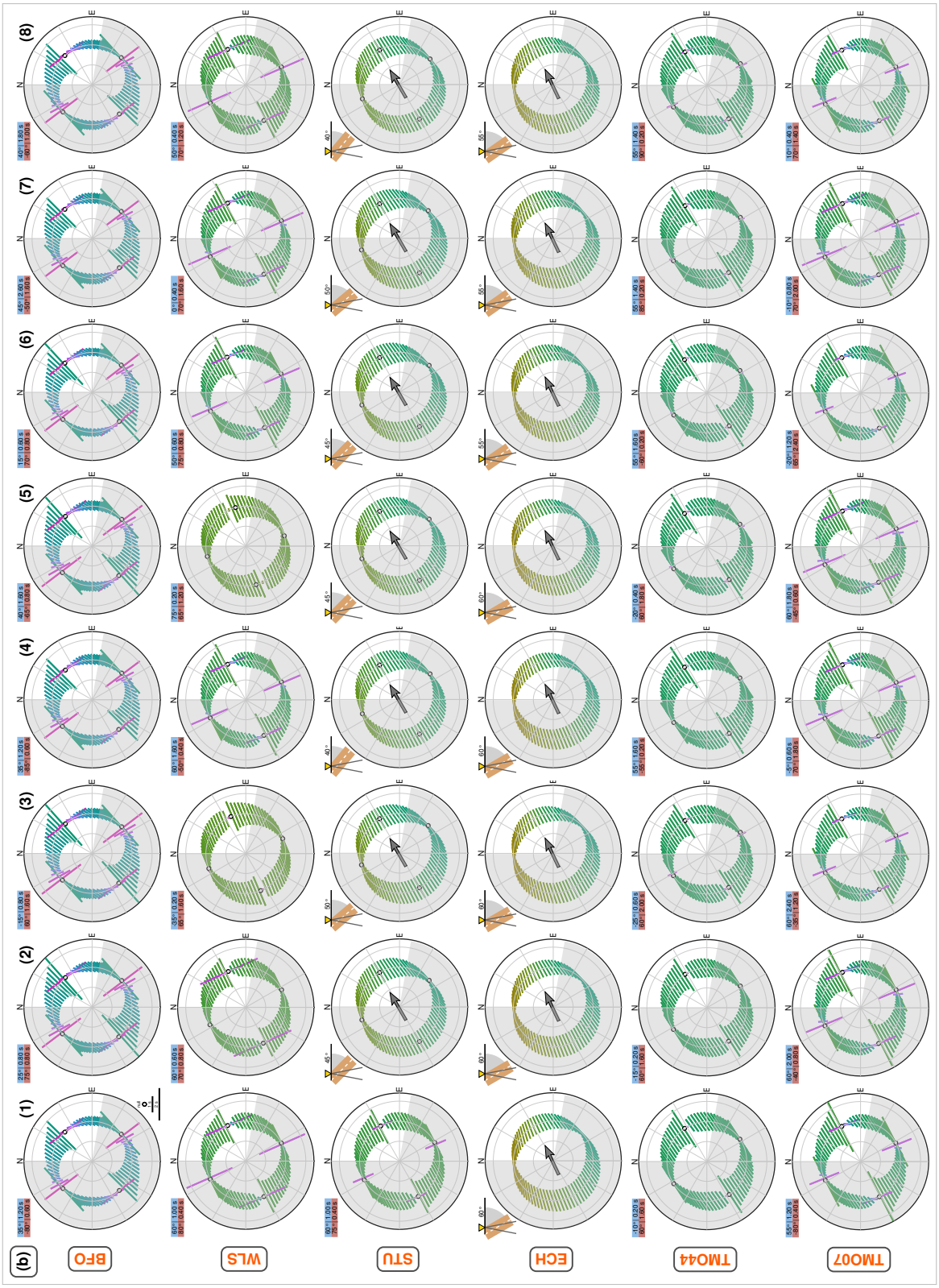
(a)
BFO
WLS
STU
ECH
TMO44
TMO07
(1)
(2)
(3)
(4)
(5)
(6)
(7)
(8)
N
E

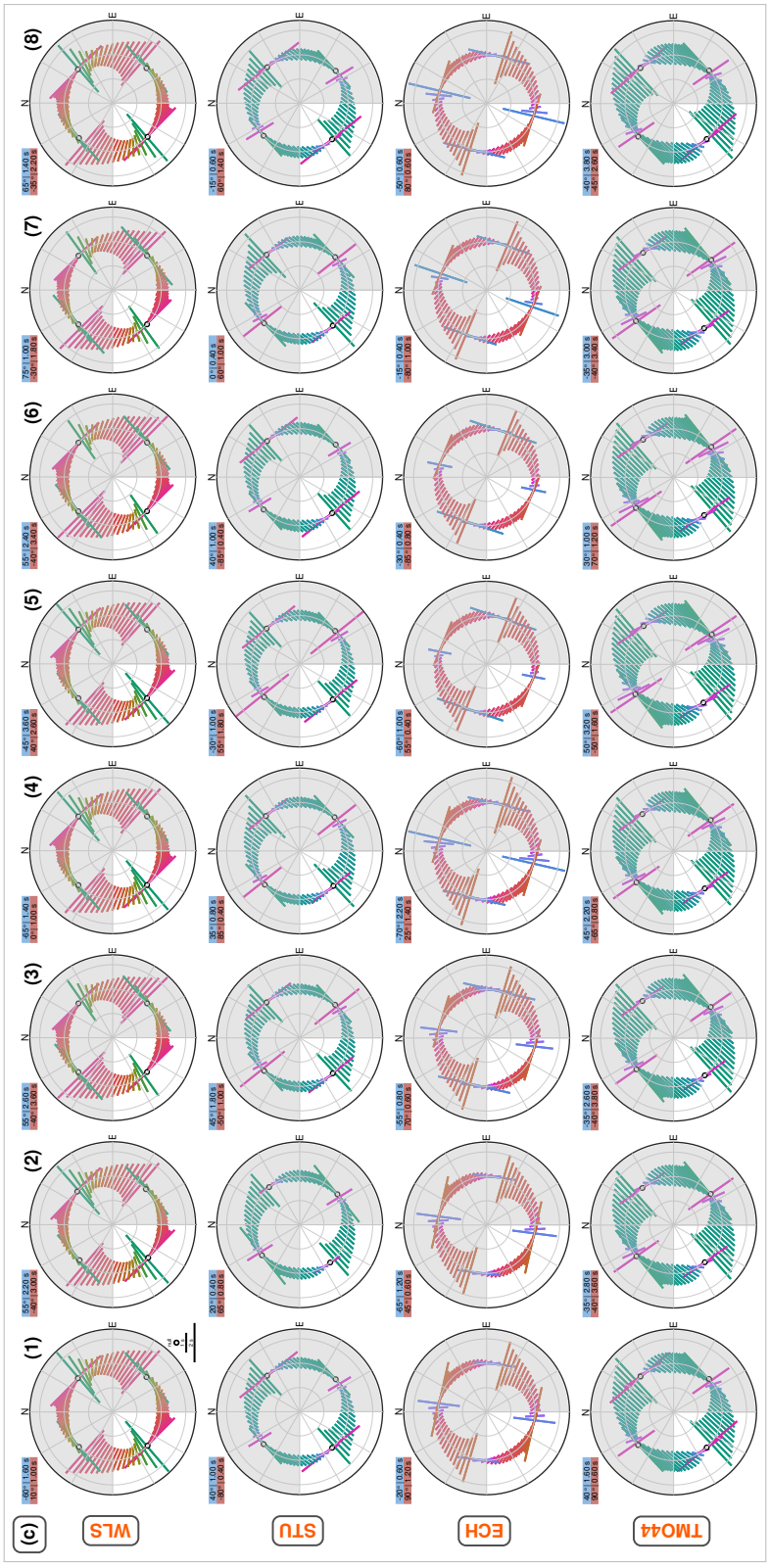

Figure B.20: Stereoplots for the apparent splitting parameters of the eight best-fitting synthetic anisotropy models (*energy minimization* method, SCmethod; *Silver and Chan*, 1991). The modelling is based on the *splits* observed in the backazimuth (BAZ) ranges (white sectors) **(a)** 0°-360°, **(b)** 0°-100°, and **(c)** 180°-270°. For BFO and TMO07, only the BAZ range 0°-100° was modelled. Plotting convention and colourmap for the fast polarization direction as in Fig. B.6. For the model sketches in the upper left corners, see the model types and model parameters explained in Fig. B.13 and Tab. B.1, respectively. Note the quite similar observations at the surface (stereoplots) for different model scenarios in the subsurface (sketches).

B.6 Lowermost mantle contribution

B.6.1 Splitting intensity

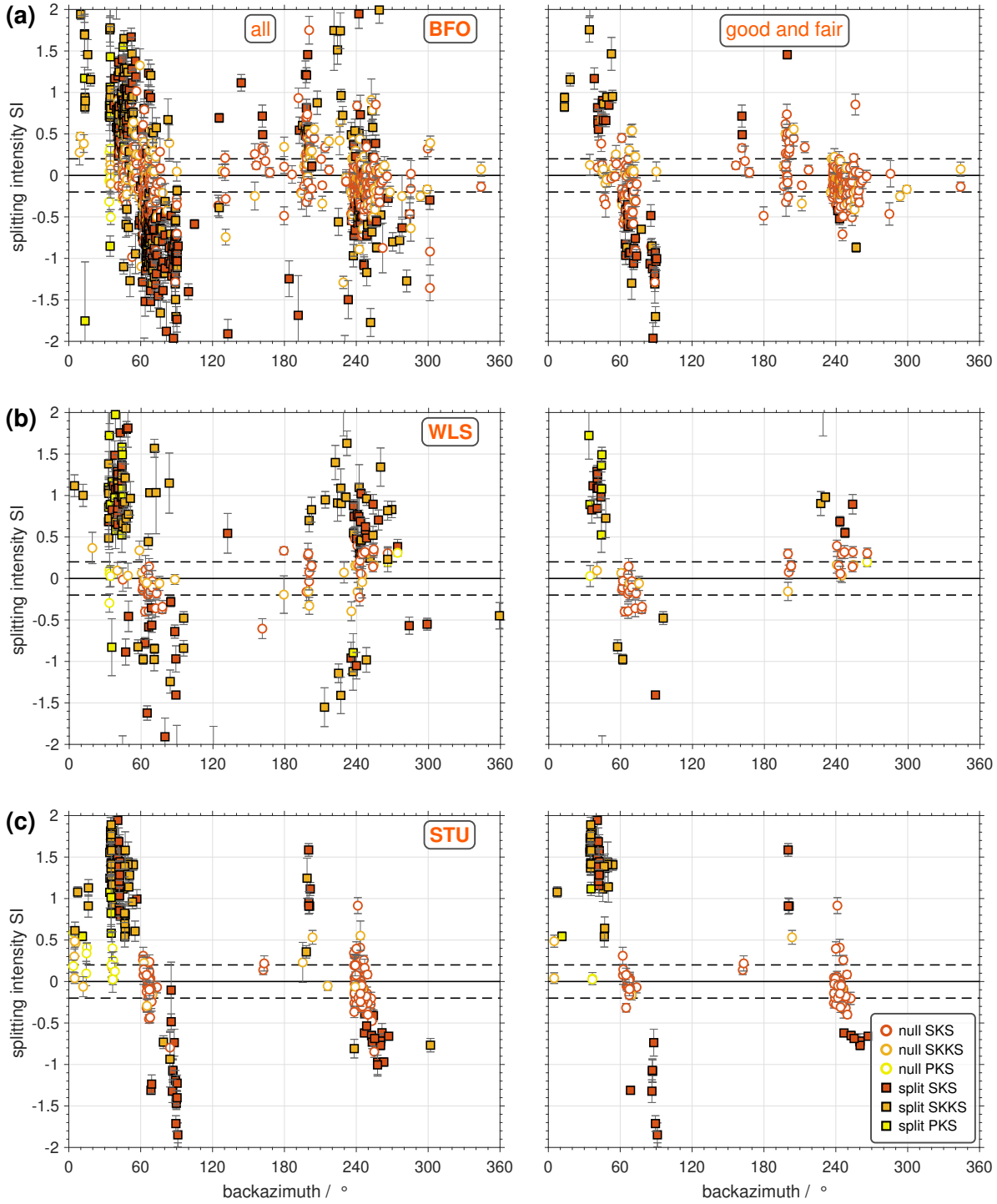

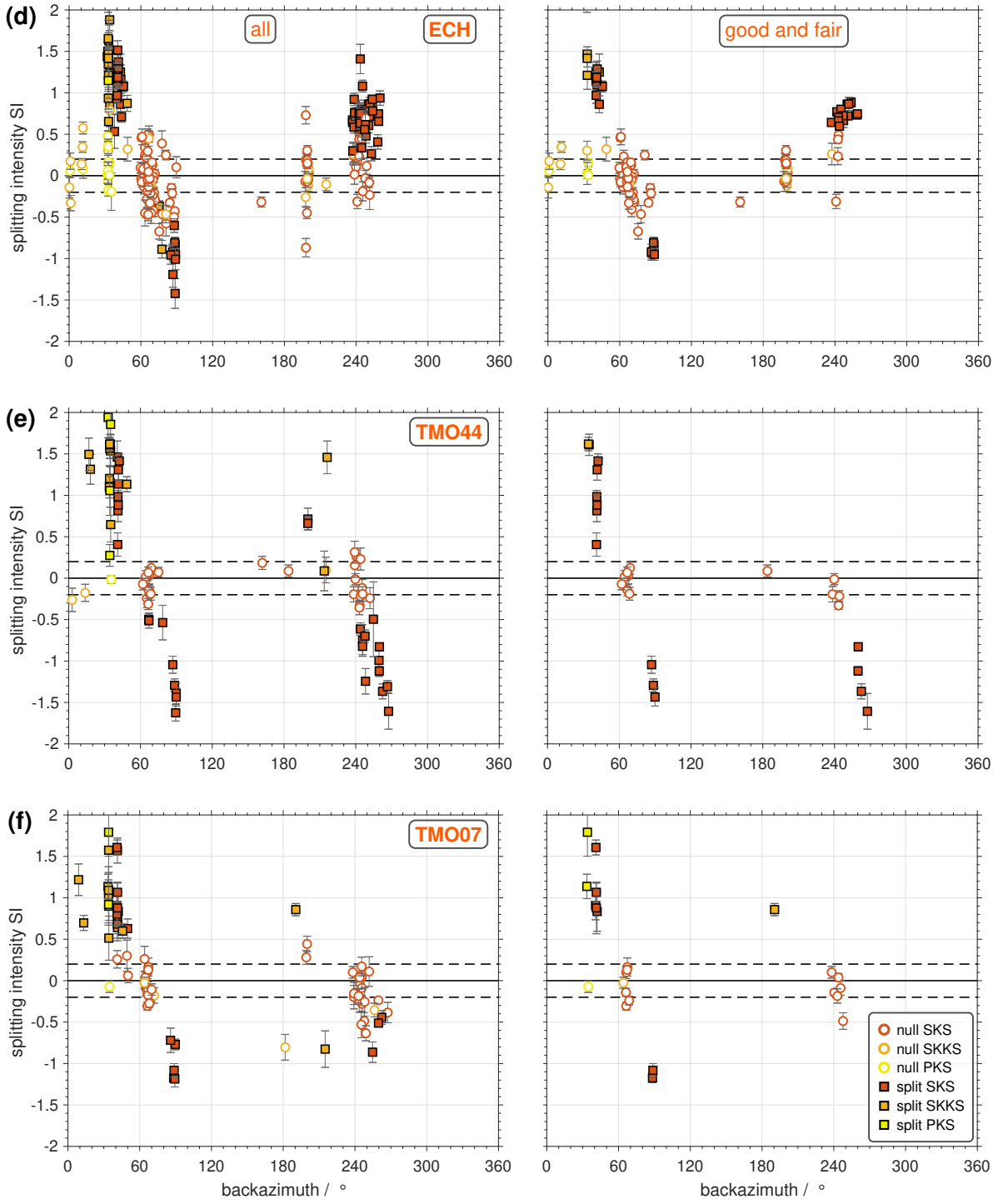

Figure B.21: Splitting intensity *SI* (*Chevrot*, 2000) for the shear wave splitting measurements (SWSMs) from the single-event analysis at the recording stations **(a)** BFO, **(b)** WLS, **(c)** STU, **(d)** ECH, **(e)** TMO44, and **(f)** TMO07. SWSMs at BFO are expanded based on *Ritter et al.* (2022). All SWSMs (left), *good* and *fair* SWSMs (right). *Nulls* are displayed as white circles and *splits* as squares. SKS in red, SKKS in orange, and PKS in yellow. The two dashed horizontal lines indicate the absolute upper limit of the splitting intensity of $|SI| = 0.2$ allowed for a *null* measurement suggested as by *Deng et al.* (2017).

B.6.2 Piercing points in the lowermost mantle

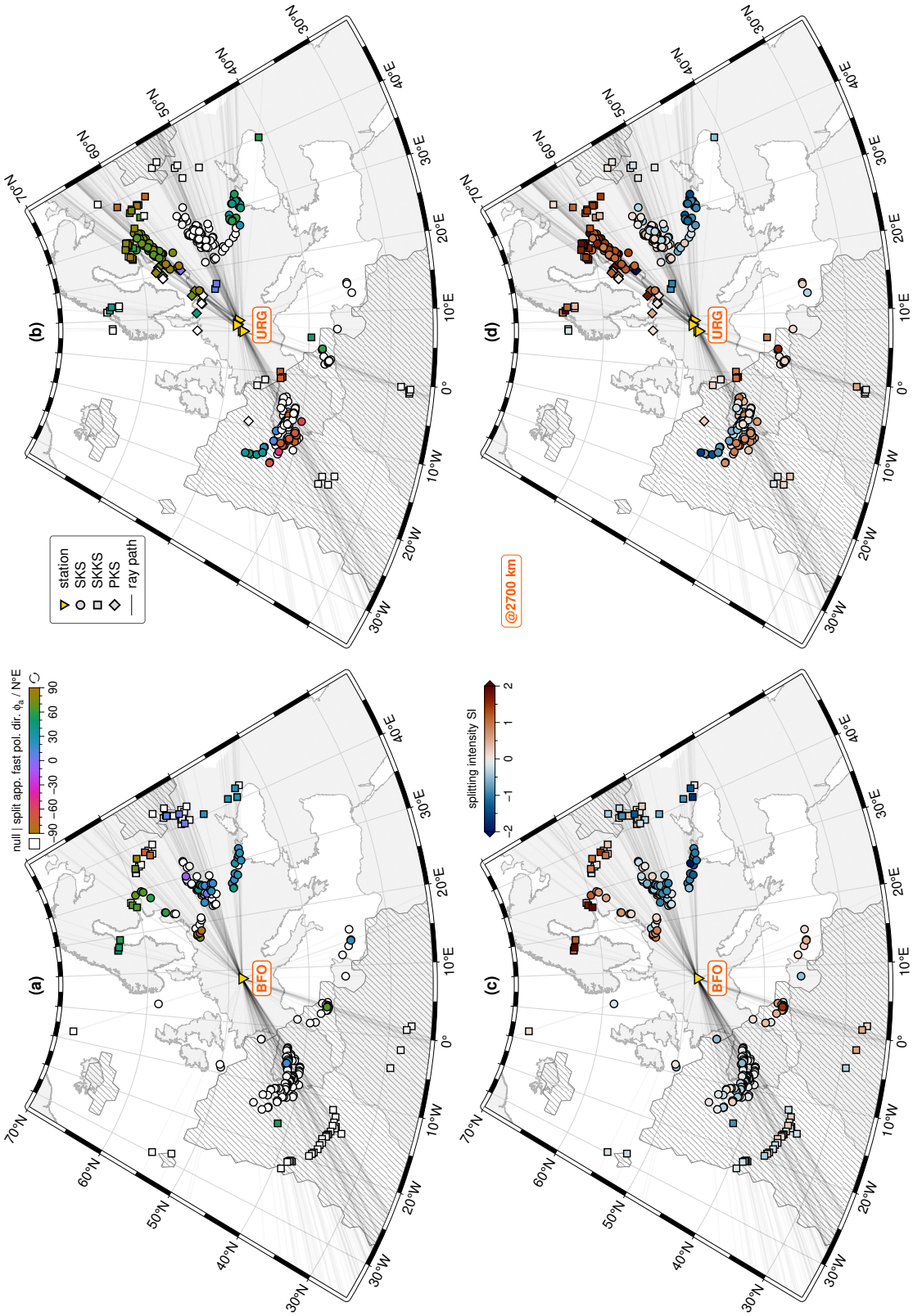

Figure B.22: Maps of Europe and North Africa with piercing points in 2700 km depth (lowermost mantle (LMM)) calculated with the *iasp91* Earth model (*Kennett and Engdahl*, 1991). They relate to the *good* and *fair* shear wave splitting measurements (*nulls* and *splits*) on SKS (circles), SKKS (squares), and PKS (diamonds) phases from the single-event analysis at **(a)** and **(c)** the BFO as well as **(b)** and **(d)** the remaining recording stations in the URG area WLS, STU, ECH, TMO44, and TMO07 (yellow inverse triangles). SWSMs at BFO are expanded based on *Ritter et al.* (2022). The colour-coding of the symbols refers to **(a)** and **(b)** the apparent fast polarization direction ϕ_a (*Silver and Chan*, 1991) of the *splits* as well as **(c)** and **(d)** the splitting intensity *SI* (*Chevrot*, 2000) of *nulls* and *splits*. Grey lines display the projected ray paths with the ray coverage density given by the darkness (for the ray paths through the Earth's interior see Fig. B.9). Land masses are in grey. The large low-shear-velocity province underneath Africa, the Iceland Plume, and the Perm anomaly are highlighted as hatched areas (using data digitised by *Wolf et al.*, 2023). Note the consistency between SWSMs on SKS and SKKS phases at the single recording stations (same observation type and similar fast polarization directions for *splits*; see also Fig. B.10) as well as the low absolute *SI* for the SWSMs on SKS and SKKS phases in the "Southwest" at BFO compared to the other stations. As no SKS-SKKS phase discrepancies were observed, there is no direct indication for a LMM contribution to the anisotropy.

B.7 Lateral variation

B.7.1 *Nulls* and *splits* distributions

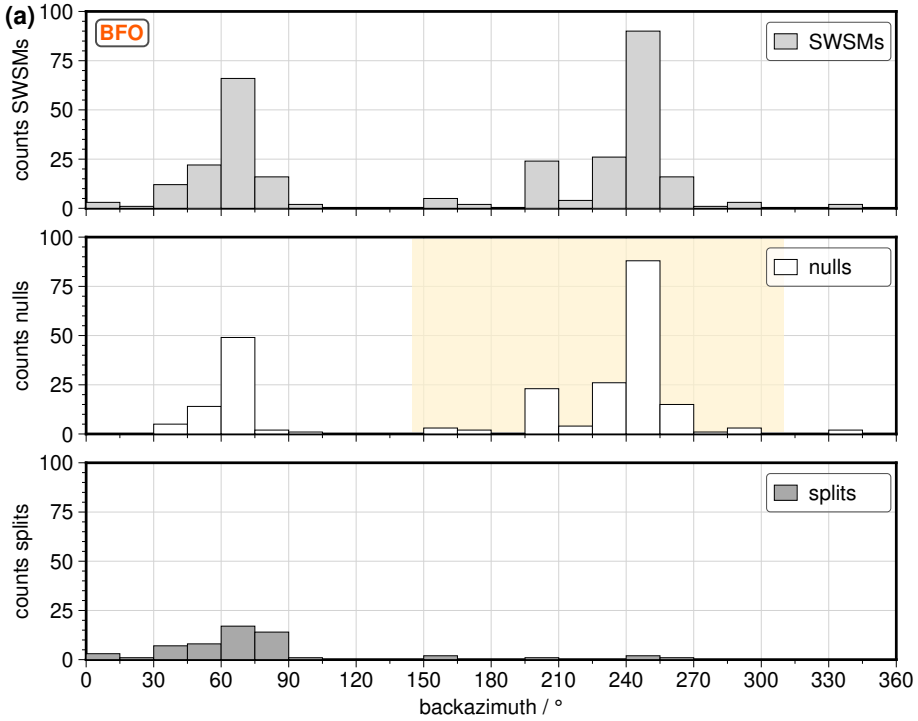

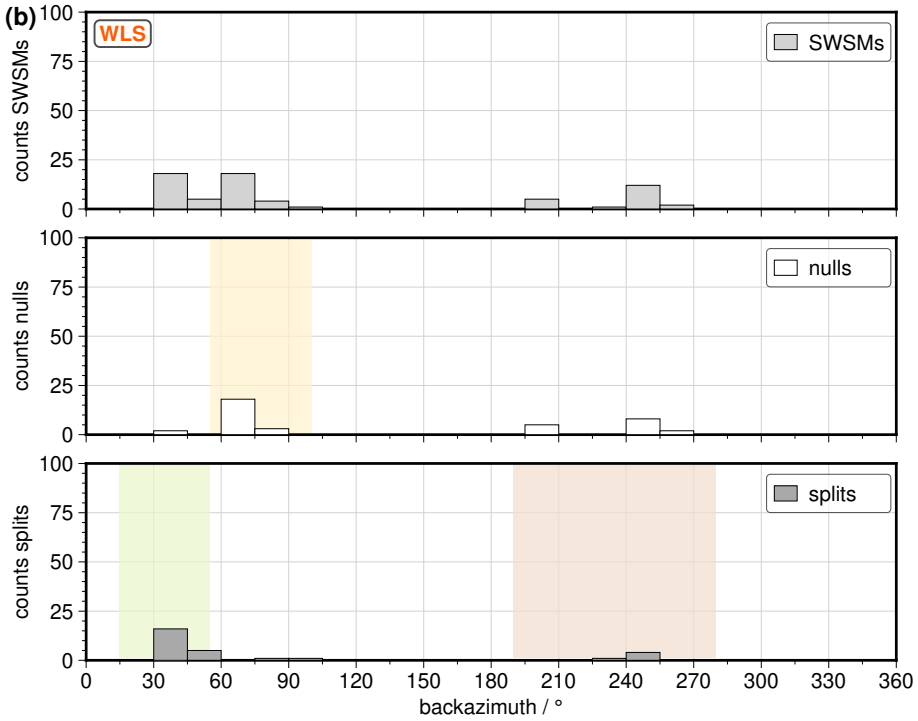

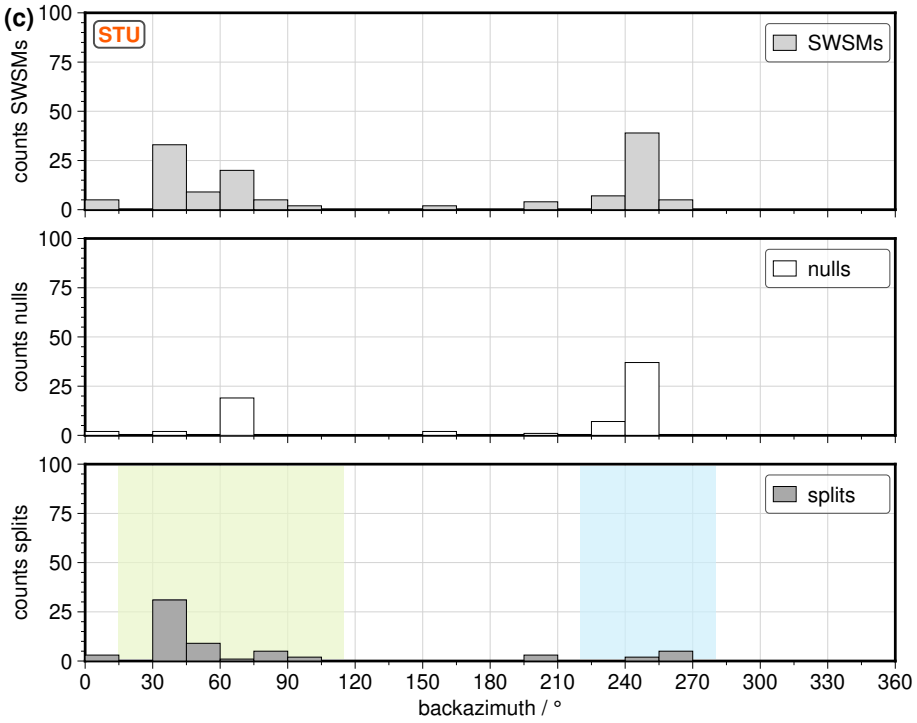
(c)
STU
SWSMs
nulls
splits
counts SWSMs
counts nulls
counts splits
0
25
50
75
100
0
30
60
90
120
150
180
210
240
270
300
330
360
backazimuth / °

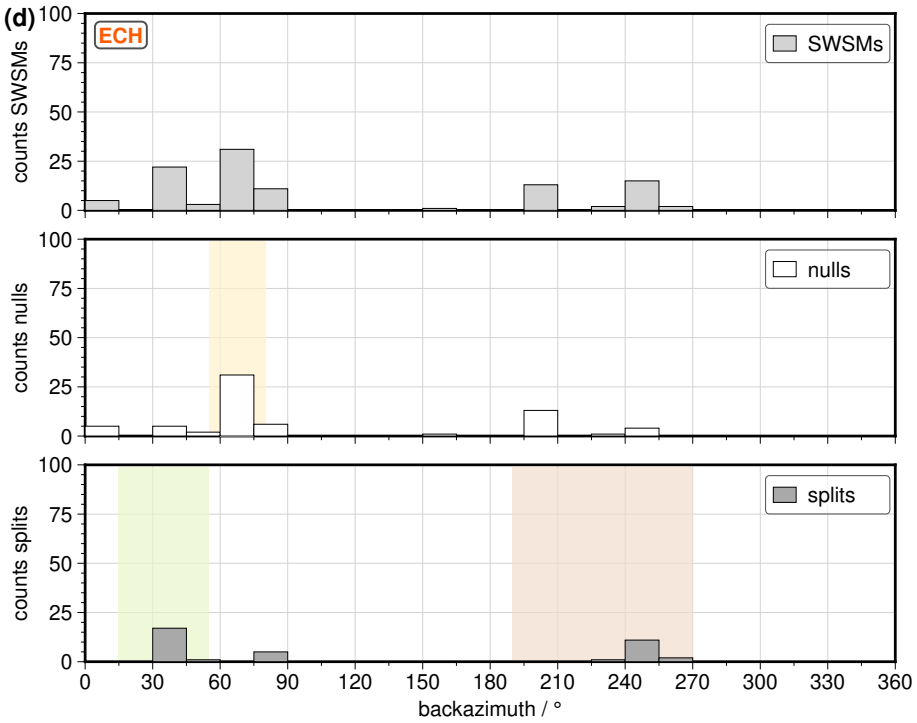
(d)
ECH
SWSMs
nulls
splits
counts SWSMs
counts nulls
counts splits
0
25
50
75
100
0
30
60
90
120
150
180
210
240
270
300
330
360
backazimuth / °

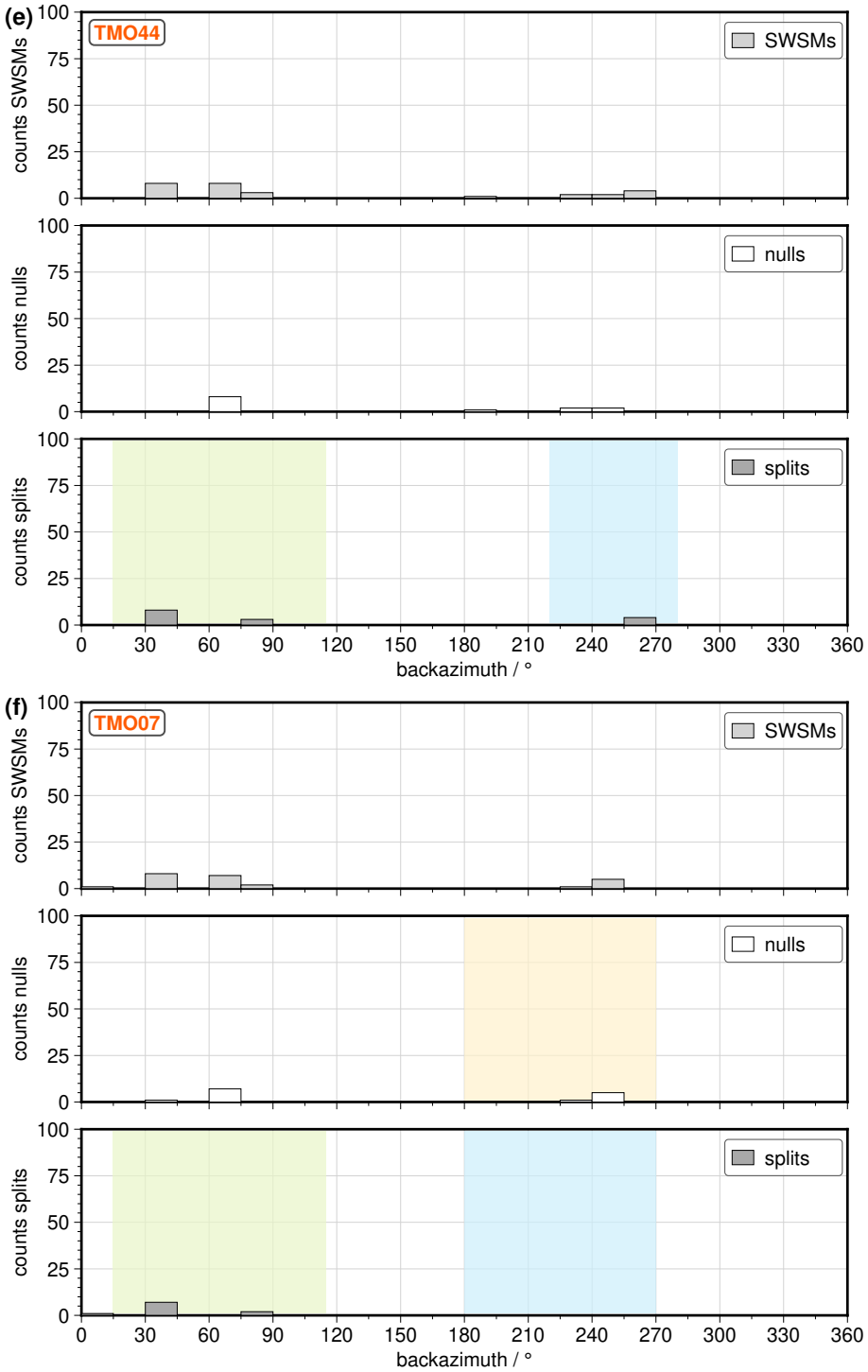

Figure B.23: Cartesian histograms showing the distribution of the number of the *good* and *fair* shear wave splitting measurements (SWSMs) from the single-event analysis (top, light grey) as well as the *nulls* (middle, white) and the *splits* (bottom, dark grey) separated in 15° backazimuth (BAZ) bins at the recording stations **(a)** BFO, **(b)** WLS, **(c)** STU, **(d)** ECH, **(e)** TMO44, and **(f)** TMO07. SWSMs at BFO are expanded based on *Ritter et al.* (2022). The coloured BAZ ranges correspond to the sectors highlighted in Fig. 8.8

B.7.2 Variation of the fast polarization direction

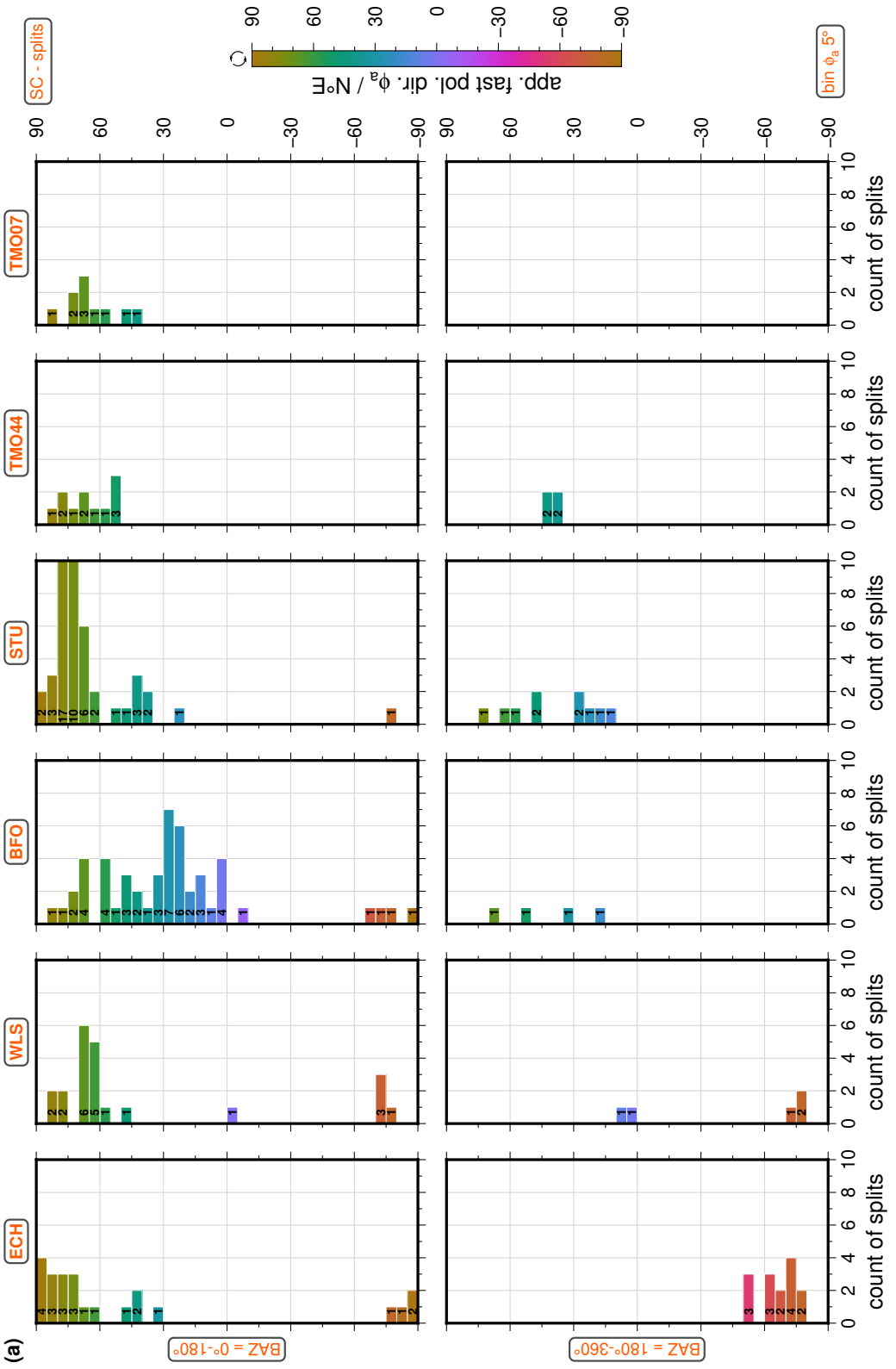

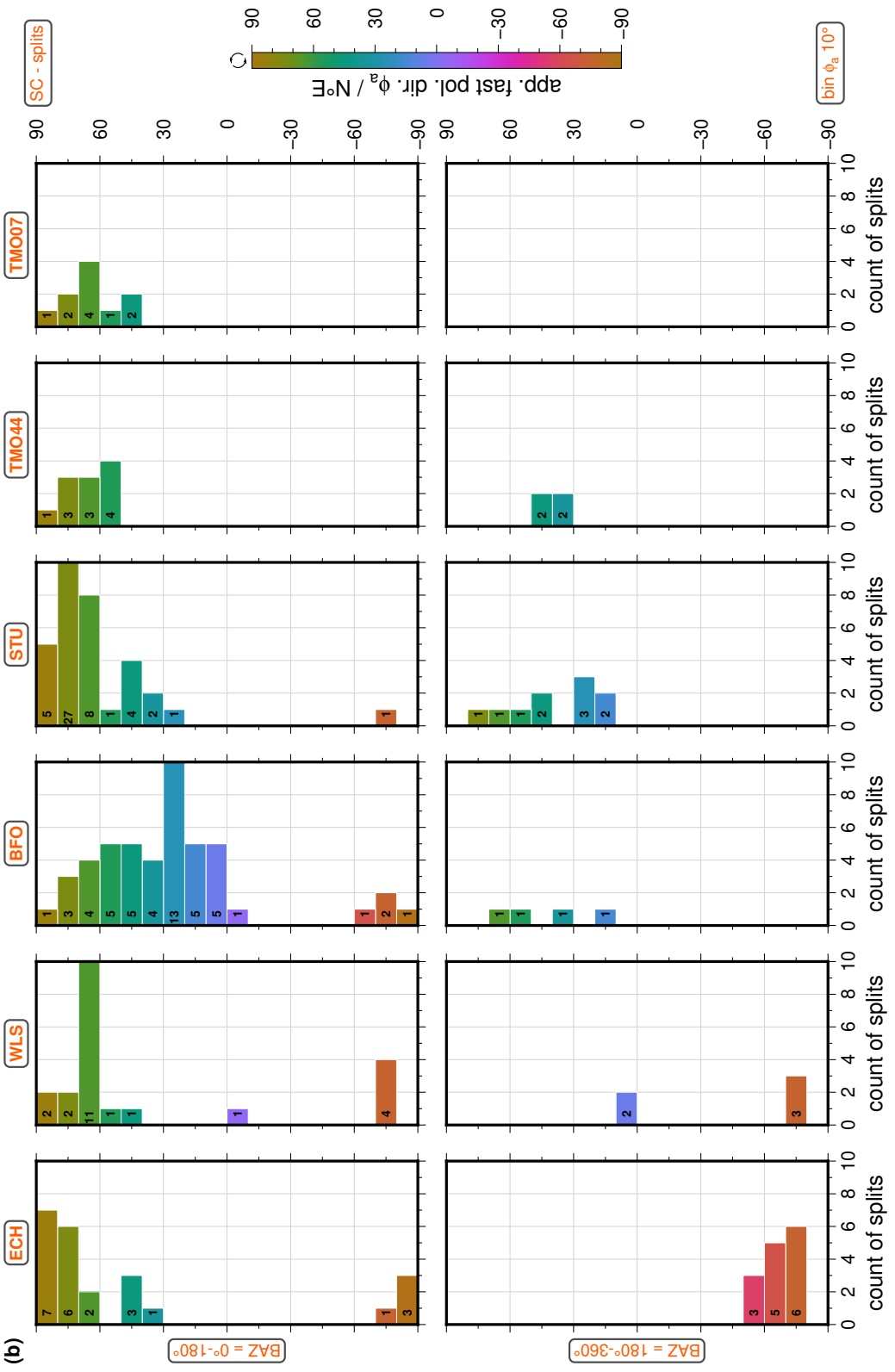
(b)
BAZ = 0°-180°
BAZ = 180°-360°
ECH
WLS
BFO
STU
TMO44
TMO07
SC - splits
bin ϕ_a 10°
count of splits
app. fast pol. dir. ϕ_a / N°E

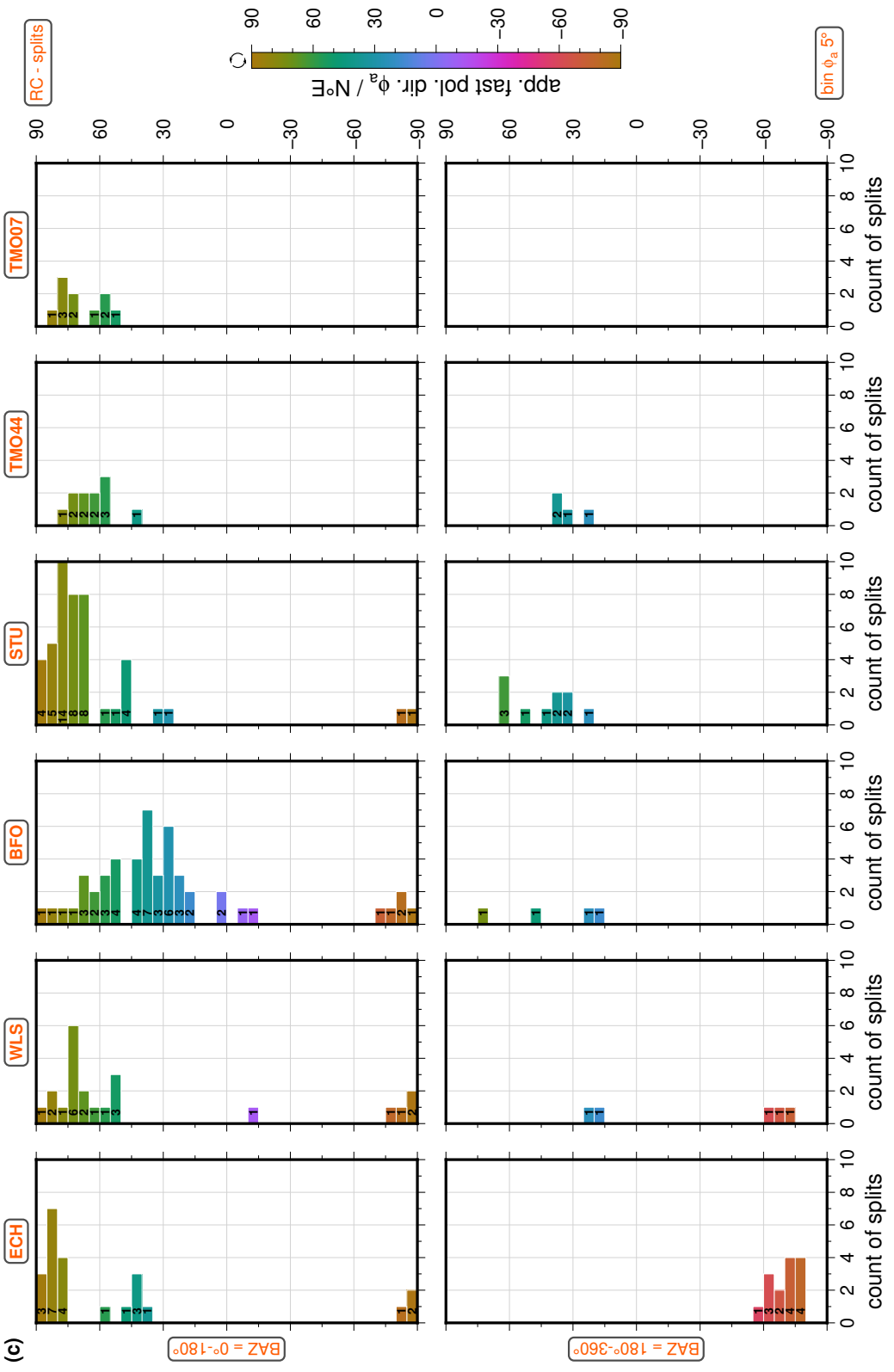
(c)
BAZ = 0°-180°
BAZ = 180°-360°
ECH
WLS
BFO
STU
TMO44
TMO07
RC - splits
bin ϕ_a 5°
count of splits
app. fast pol. dir. ϕ_a / N°E

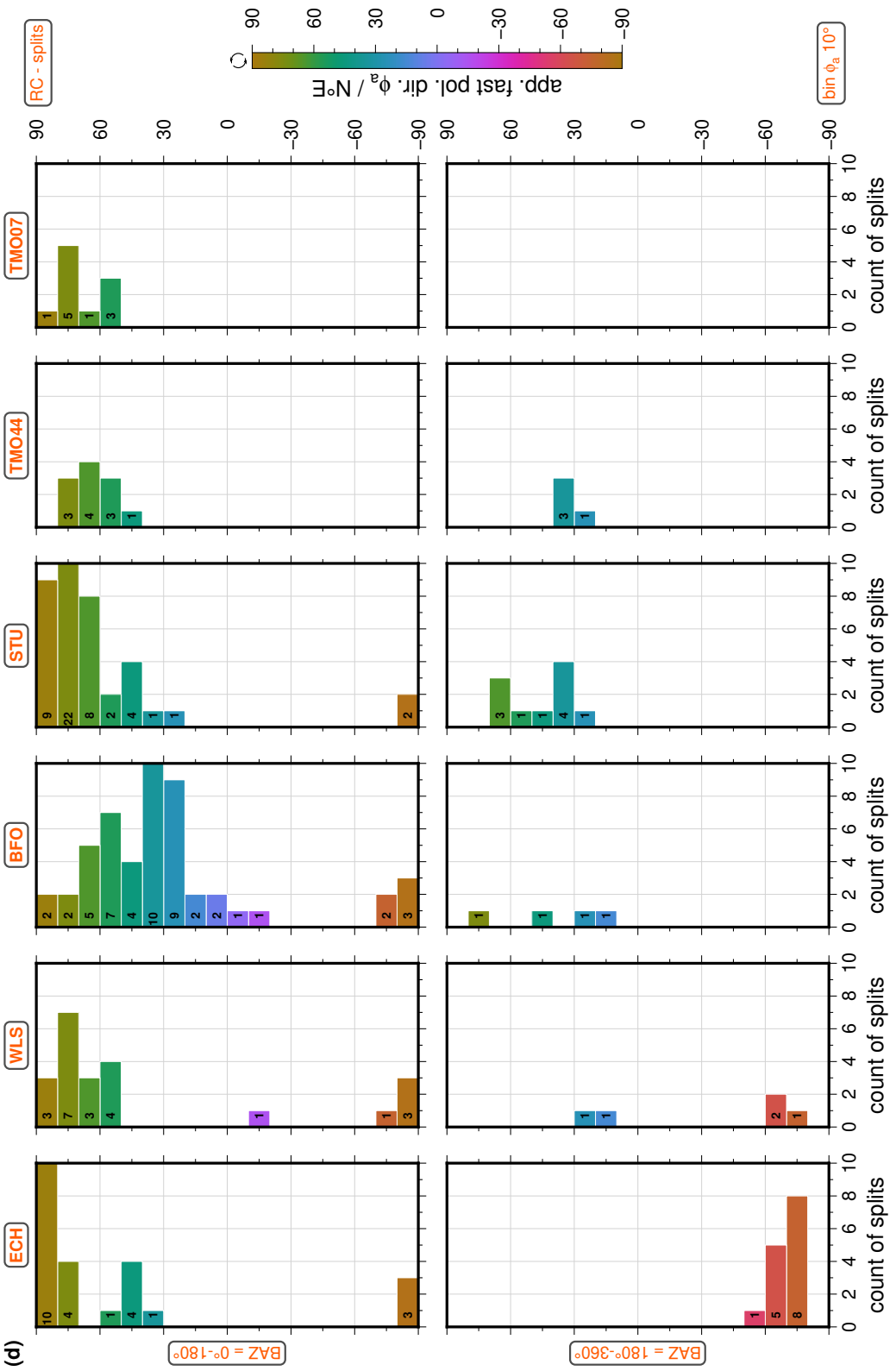

Figure B.24: Cartesian histograms of the fast polarization direction ϕ_a of the *good* and *fair splits* from the single-event analysis at the recording stations ECH, WLS, BFO, STU, TMO44, and TMO07 (left to right) for the backazimuth (BAZ) ranges 0°-180° (top) and 180°-360° (bottom). SWSMs at BFO are expanded based on *Ritter et al.* (2022). **(a)** *Energy minimization* method (SC method; *Silver and Chan*, 1991) with ϕ_a bins of 5°, **(b)** SC method with ϕ_a bins of 10°, **(c)** *rotation-correlation* method (RC method; *Bowman and Ando*, 1987) with ϕ_a bins of 5°, and **(d)** RC method with ϕ_a bins of 10°. The total count of *splits* is given by the numbers written at the bottom of the bars. Note that partly the bars are cut to fit into the histogram.

B.7.3 *Null anomaly* at neighbouring recording stations

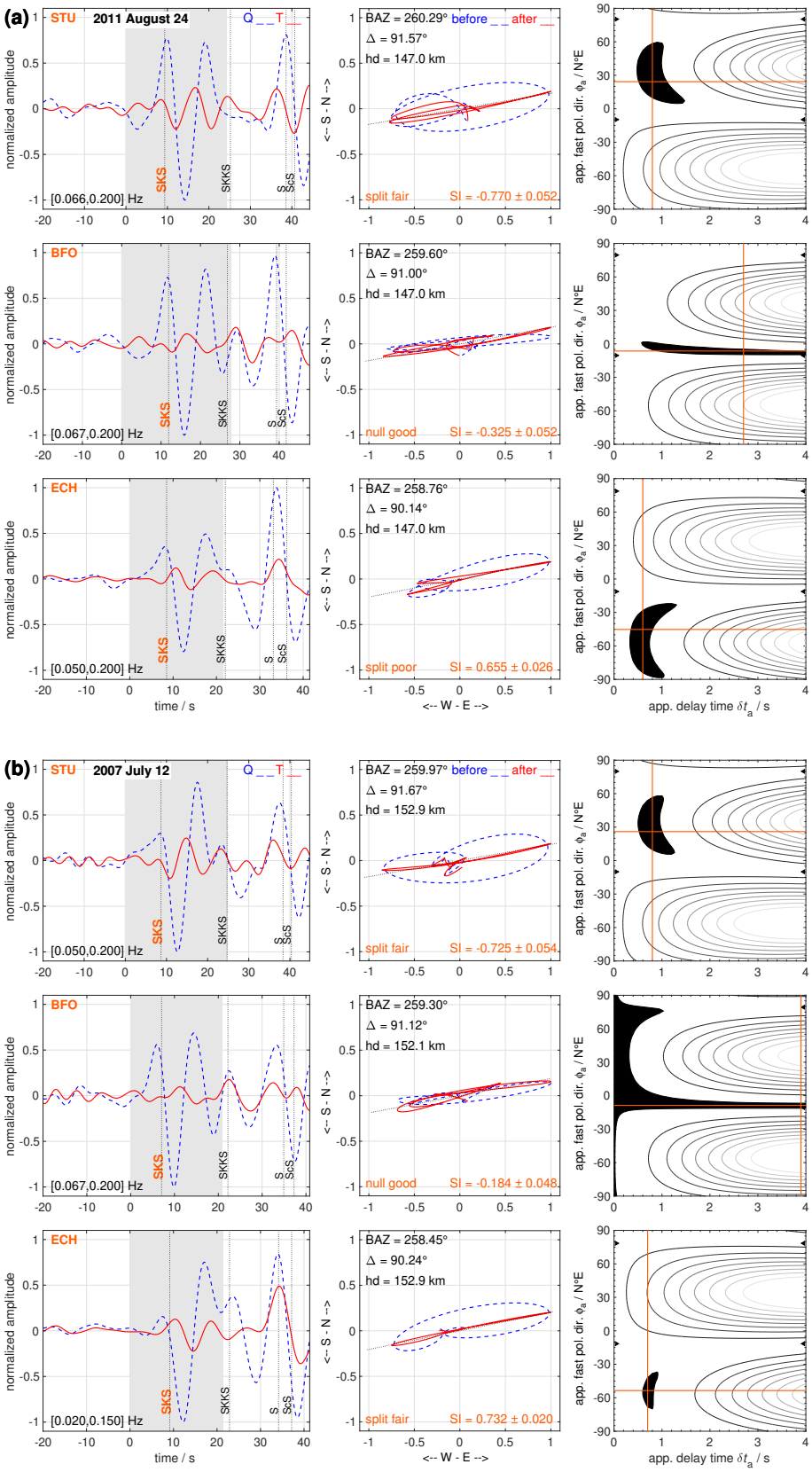

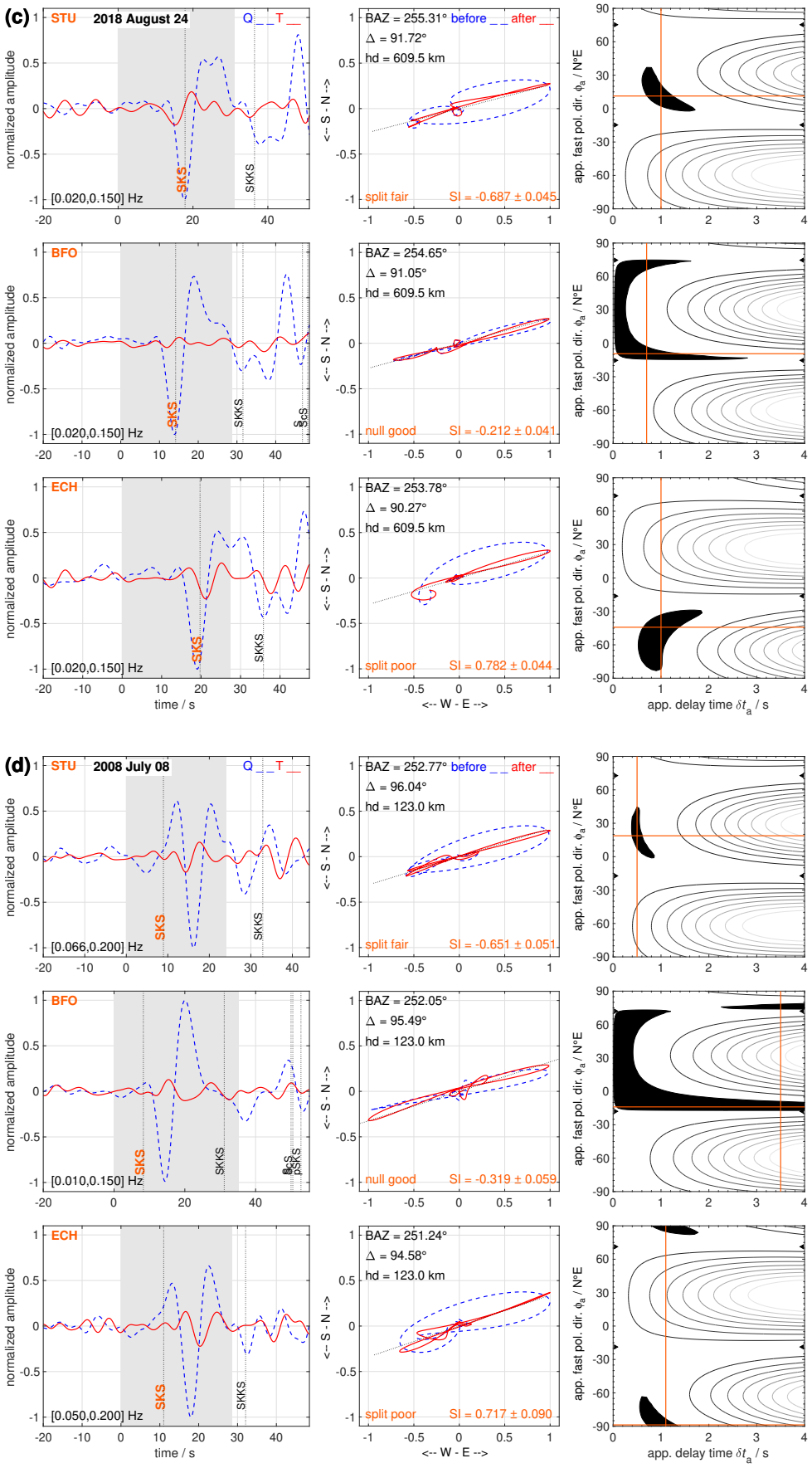
(c)
STU
2018 August 24
Q
T
normalized amplitude
[0.020,0.150] Hz
SKS
SKKS
BAZ = 255.31° before after
Δ = 91.72°
hd = 609.5 km
split fair
SI = -0.687 ± 0.045
<-- S - N -->
app. fast pol. dir. φa / N°E
BFO
BAZ = 254.65°
Δ = 91.05°
hd = 609.5 km
null good
SI = -0.212 ± 0.041
ECH
BAZ = 253.78°
Δ = 90.27°
hd = 609.5 km
split poor
SI = 0.782 ± 0.044
time / s
<-- W - E -->
app. delay time δta / s
(d)
2008 July 08
[0.066,0.200] Hz
BAZ = 252.77° before after
Δ = 96.04°
hd = 123.0 km
split fair
SI = -0.651 ± 0.051
[0.010,0.150] Hz
BAZ = 252.05°
Δ = 95.49°
hd = 123.0 km
null good
SI = -0.319 ± 0.059
[0.050,0.200] Hz
BAZ = 251.24°
Δ = 94.58°
hd = 123.0 km
split poor
SI = 0.717 ± 0.090

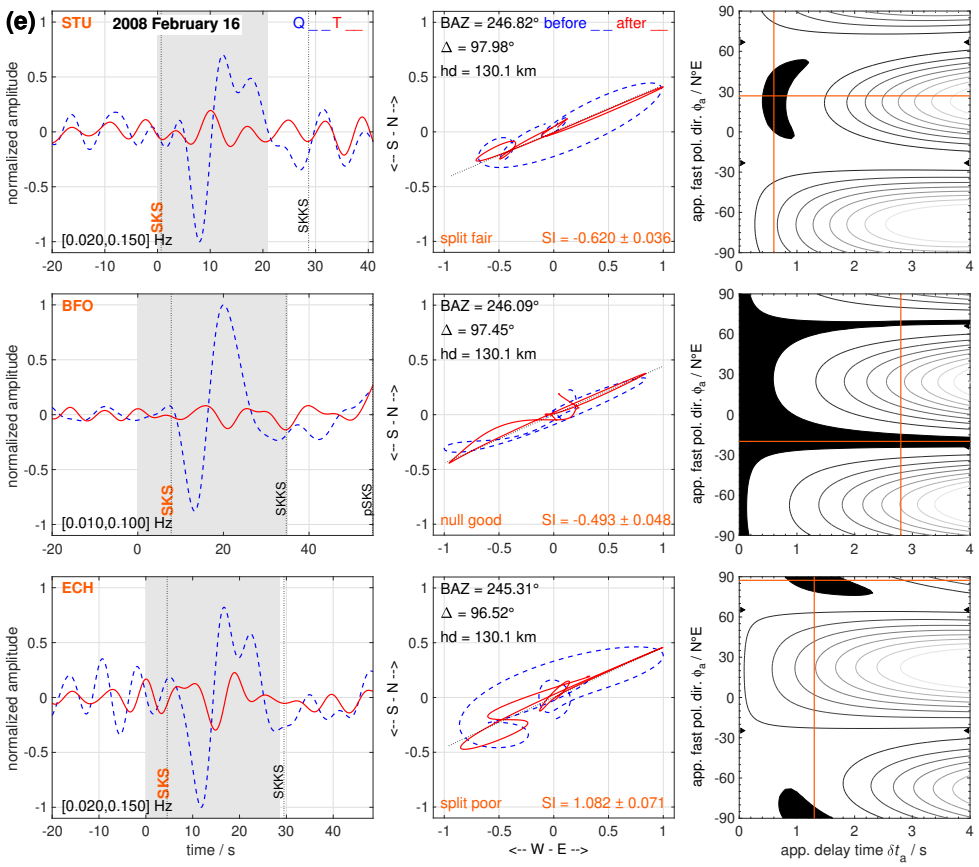

Figure B.25: Observation of no shear wave splitting (*null*) at BFO (middle row) but of shear wave splitting (*split*) at the recording stations STU (top row) and ECH (bottom row) for the same earthquake. Earthquakes occurred underneath **(a)** Peru-Brazil Border Region on 2011 August 24, **(b)** Northern Peru (also in main text) on 2007 July 12, **(c)** Peru-Brazil Border Region on 2018 August 24, **(d)** Southern Peru on 2008 July 08, and **(e)** Chile-Bolivia Border Region on 2008 February 16. **left**: Waveforms of the Q (dashed blue line) and T (solid red line) components, normalised to the absolute maximum and filtered with a bandpass (corner frequencies are given at the bottom). Black vertical lines mark the theoretical arrival times calculated with the *iasp91* Earth model (*Kennett and Engdahl*, 1991) with the *TauP* Toolkit (*Crotwell et al.*, 1999). The grey region indicates the selected time window around the SKS phase. **centre**: Horizontal particle motion before (dashed blue line) and after (solid red line) the correction for the shear wave splitting. At the top backazimuth BAZ, epicentral distance Δ, and hypocentral depth *hd* and at the bottom observation type, quality category, and splitting intensity *SI* with error are given. **right**: Result of the grid search (*energy minimization* method; *Silver and Chan*, 1991) for the apparent splitting parameters (ϕ_a, δt_a) with 95 per cent confidence interval (black area) and best solution (section point of the horizontal and vertical orange lines).

B.7.4 First Fresnel zone

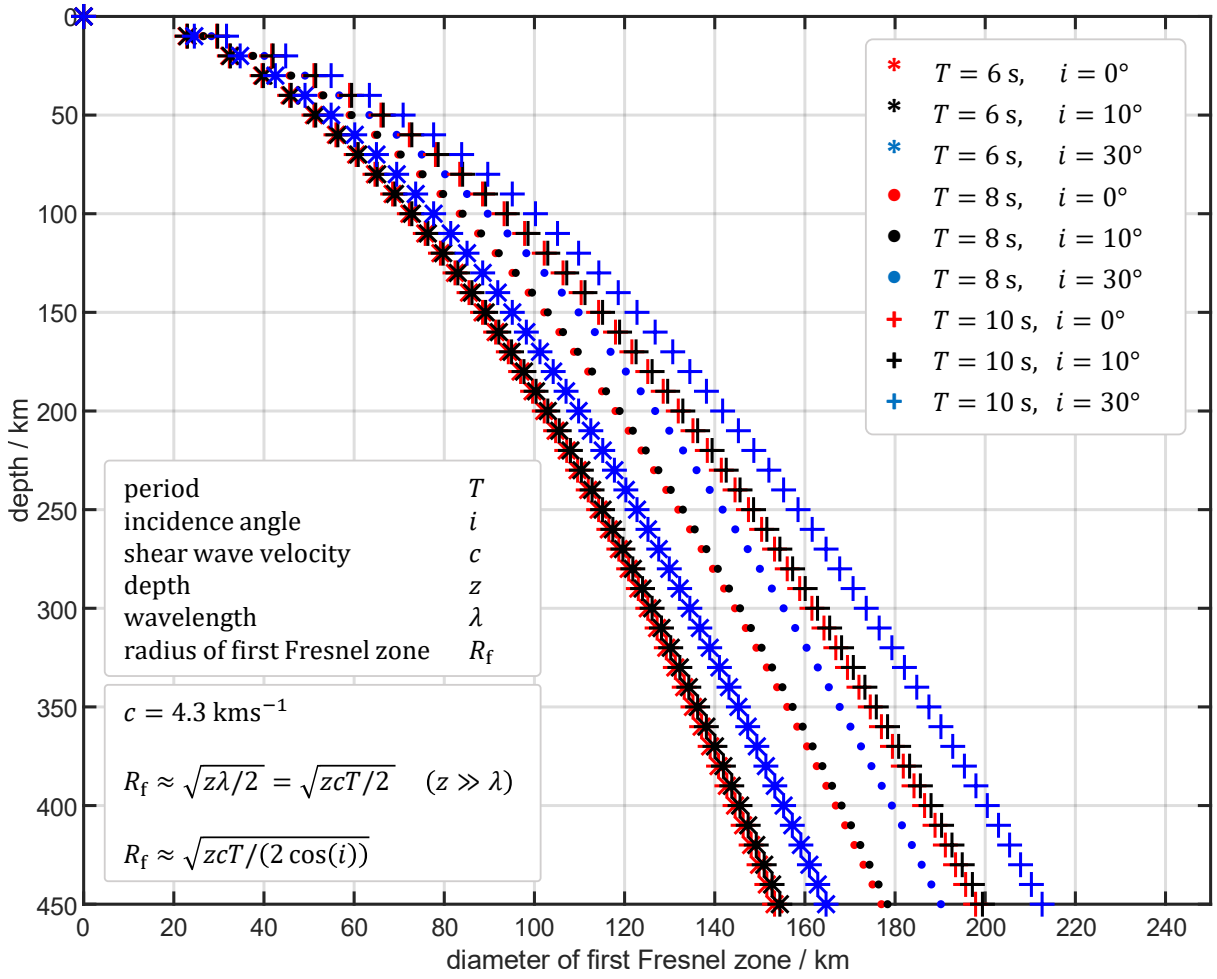

Figure B.26: Diameter of the first Fresnel zone as function of depth for different periods $T = (6, 8, 10)$ s (shape-coded) and different incidence angles (measured from the vertical) $i = (0, 10, 30)°$ (colour-coded). The equations to calculate the radius of the first Fresnel zone are taken from *Pearce and Mittleman* (2002) and *Margheriti et al.* (2003) and the S wave propagation velocity in the dry upper mantle is following *Legendre et al.* (2012).

C Additional Visualizations

C.1 Travel paths

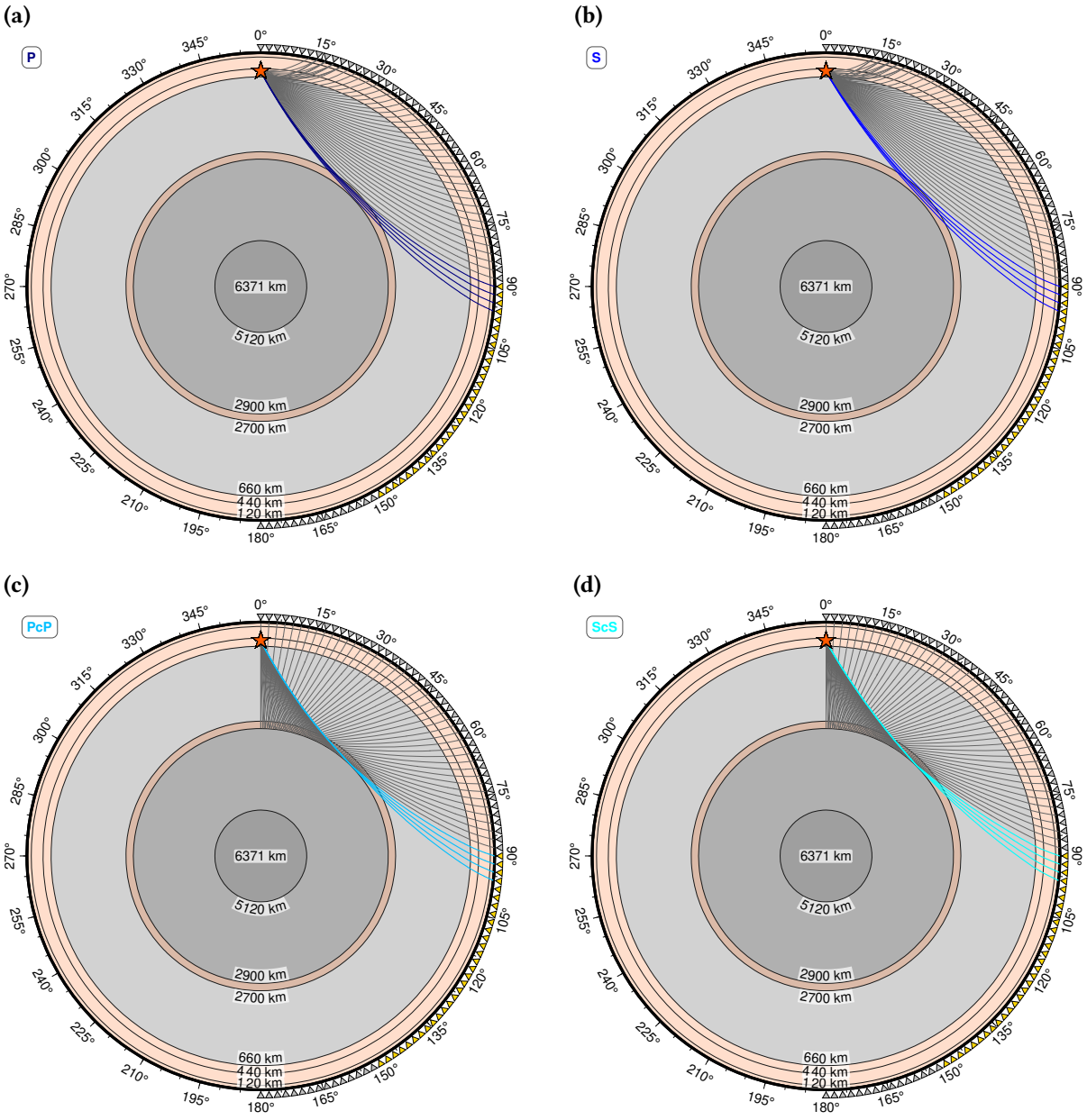

Figure C.1: Travel paths of **(a)** P, **(b)** S, **(c)** PcP, and **(d)** ScS phases. Plotting conventions as in Fig. 4.1. The corresponding travel time curves are shown in Fig. 4.2.

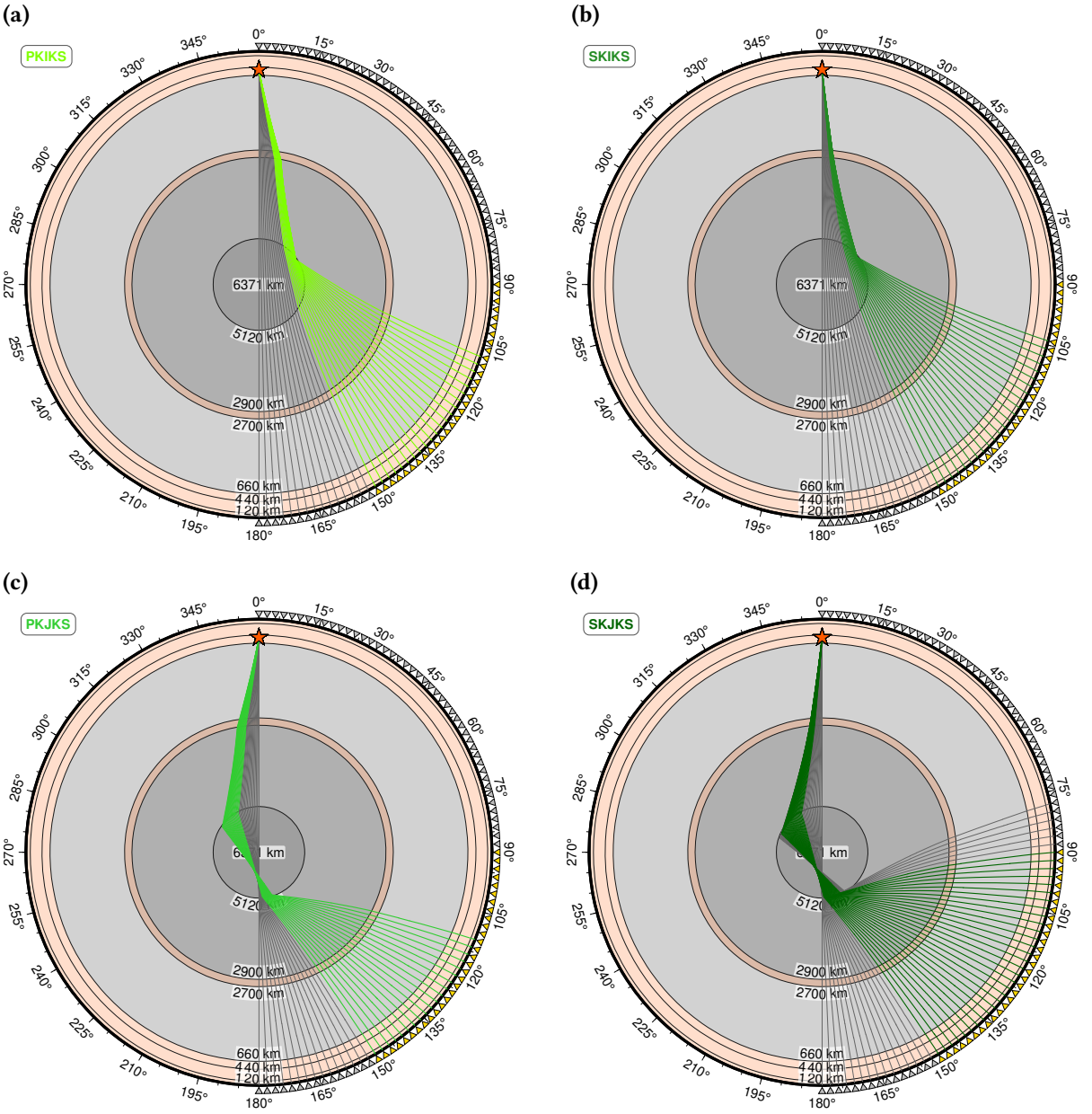

Figure C.2: Travel paths of phases traveling through the inner core: **(a)** PKIKS, **(b)** SKIKS, **(c)** PKJKS, **(d)** SKJKS phases. Plotting conventions as in Fig. 4.1. The corresponding travel time curves are shown in Fig. 4.2.

C.2 Shear wave splitting measurements at BFO

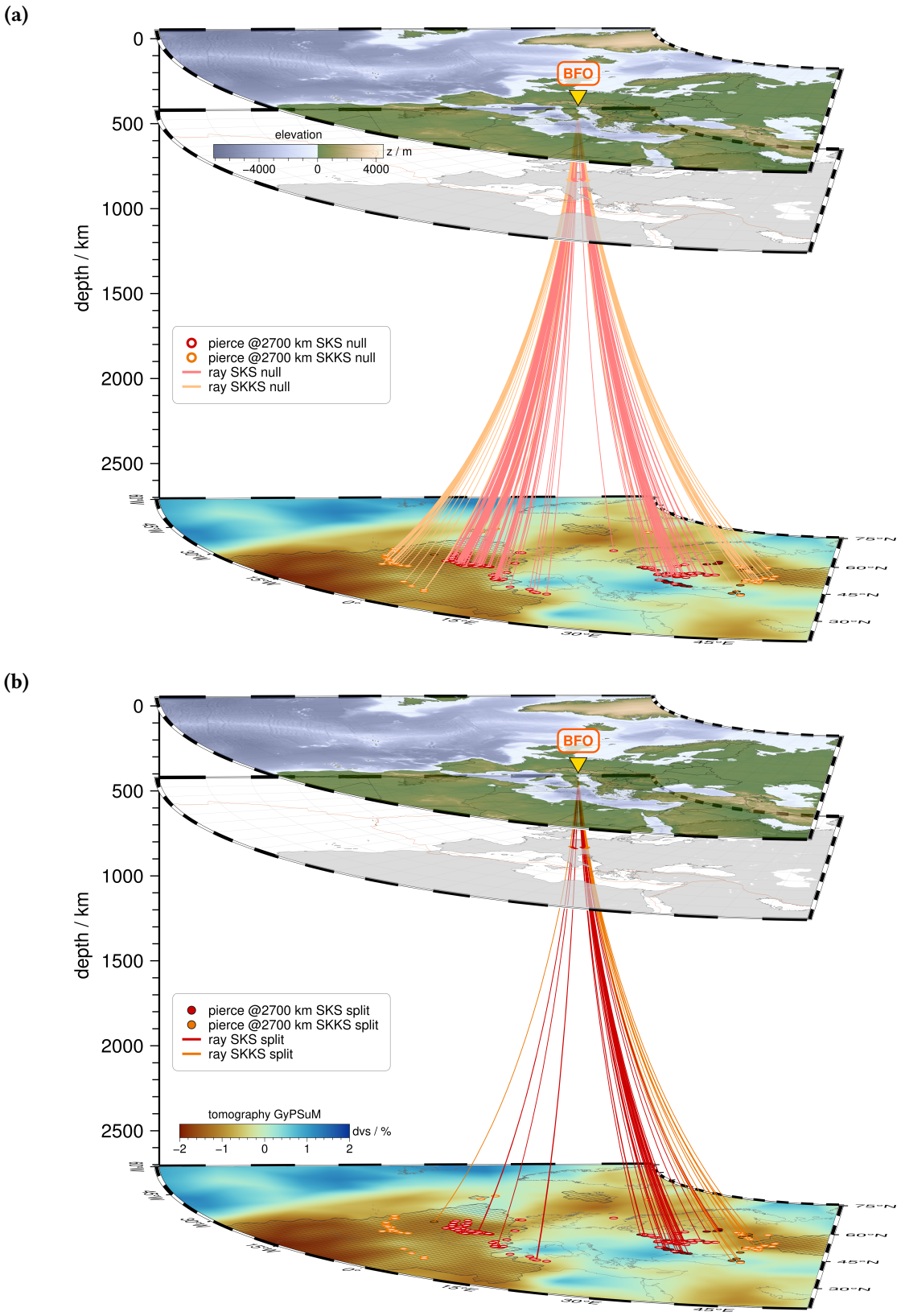

Figure C.3: Same as Fig. 1.1b, but rays separately for **(a)** *nulls* and **(b)** *splits*.

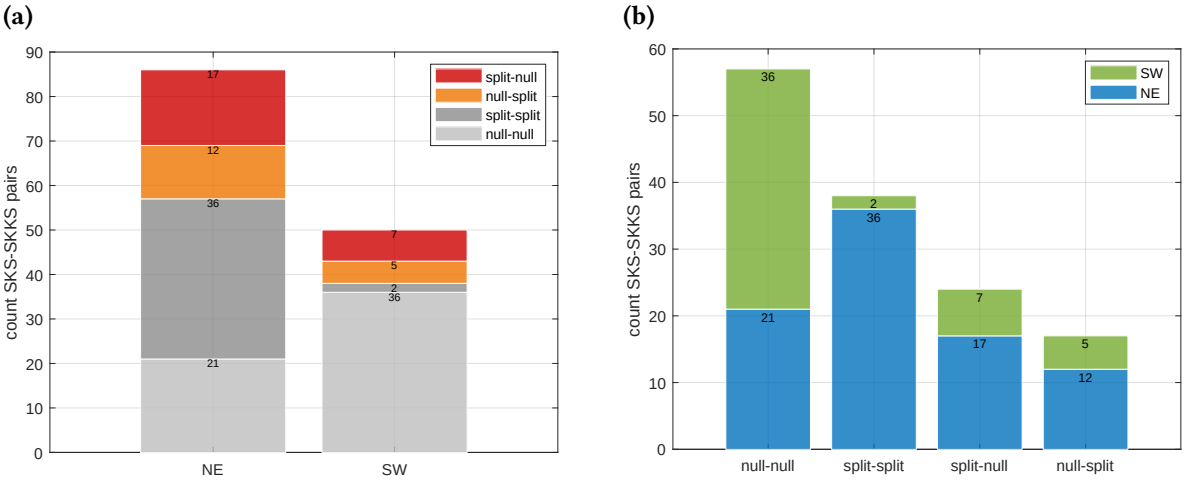

Figure C.4: Distributions of the SKS-SKKS pairs at the recording station BFO. Occurrence of the pair types *null-null* and *split-split* (same) as well as *split-null* and *null-split* (discrepant) within the northeast (NE) and southwest (SW) quadrants sorted by **(a)** the quadrants and **(b)** the pair types.

C.3 Forward calculated splitting parameters

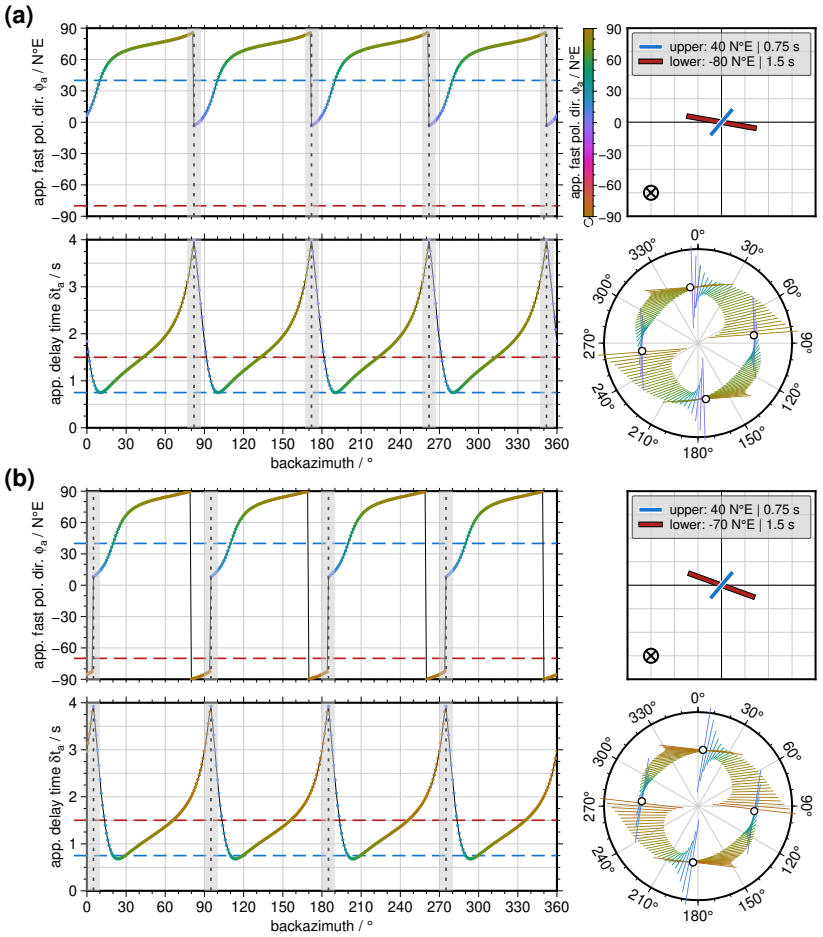

Figure C.5: Forward calculation for model type H2: variation of the fast polarization direction in the lower layer.
Fixed delay times in the lower and upper layers of 1.5 s or 0.75 s and fixed fast polarization direction in the upper layer of 40N°E. The fast polarization direction in the lower layer varies in steps of 10° from **(a)** -80N°E to **(r)** 90N°E.
Visualizations as in Fig. 5.2; for a related animation, see Sec. D.5.

Fig. C.5 continued.

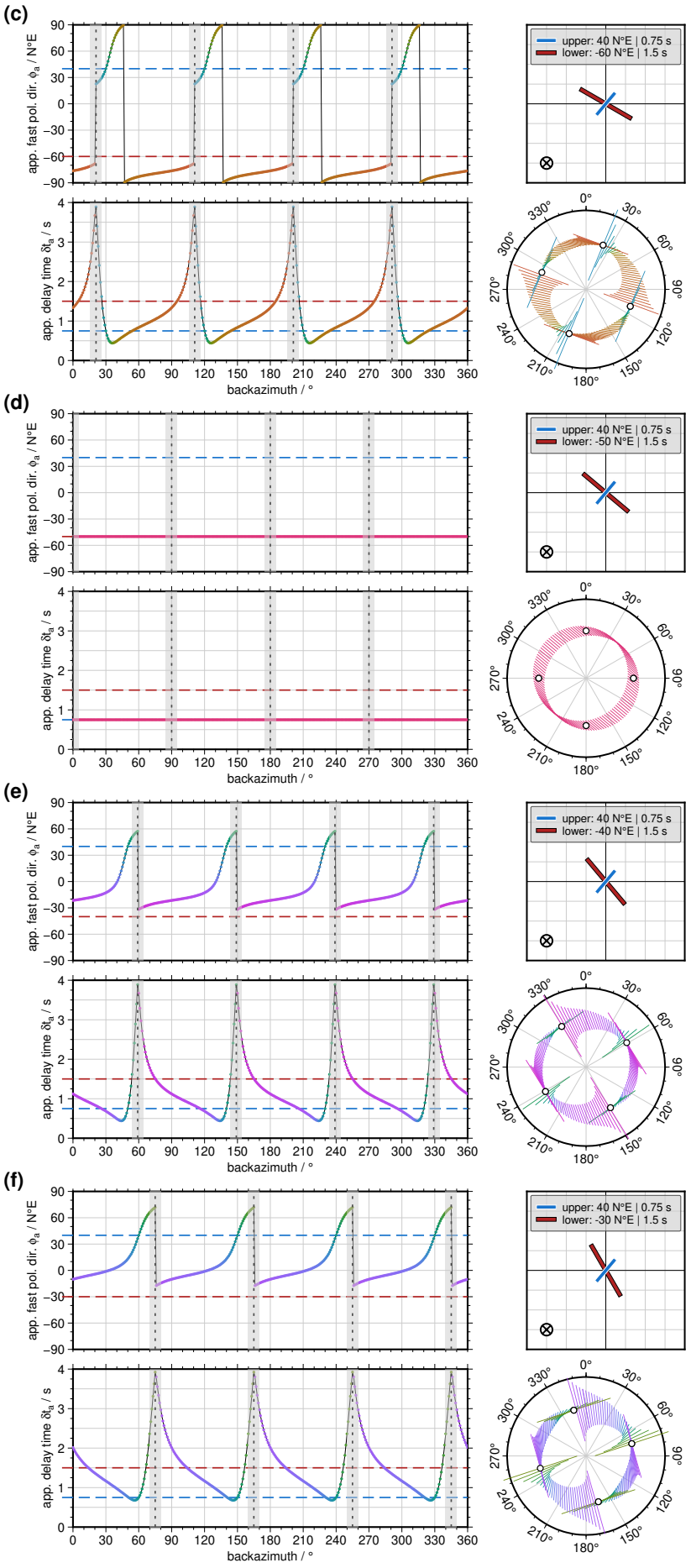

Fig. C.5 continued.

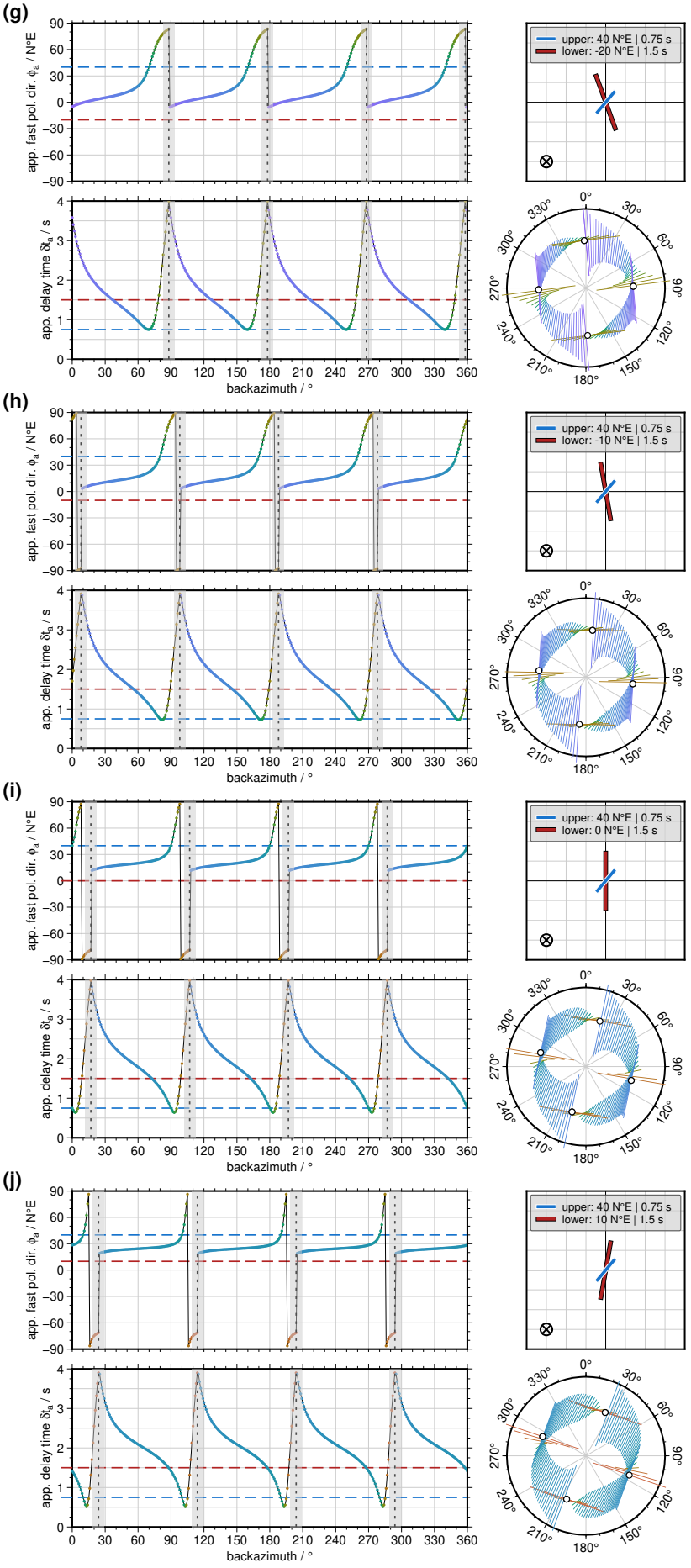

Fig. C.5 continued.

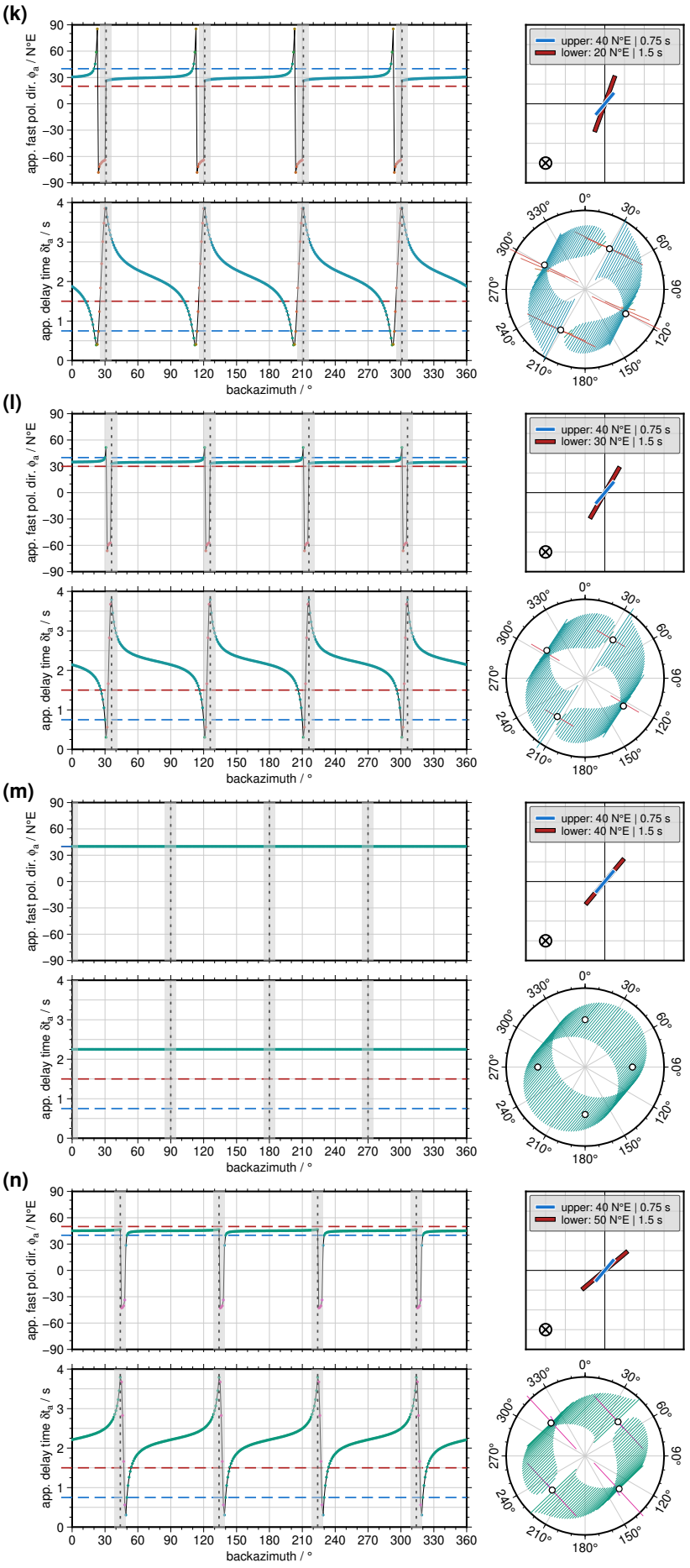

Fig. C.5 continued.

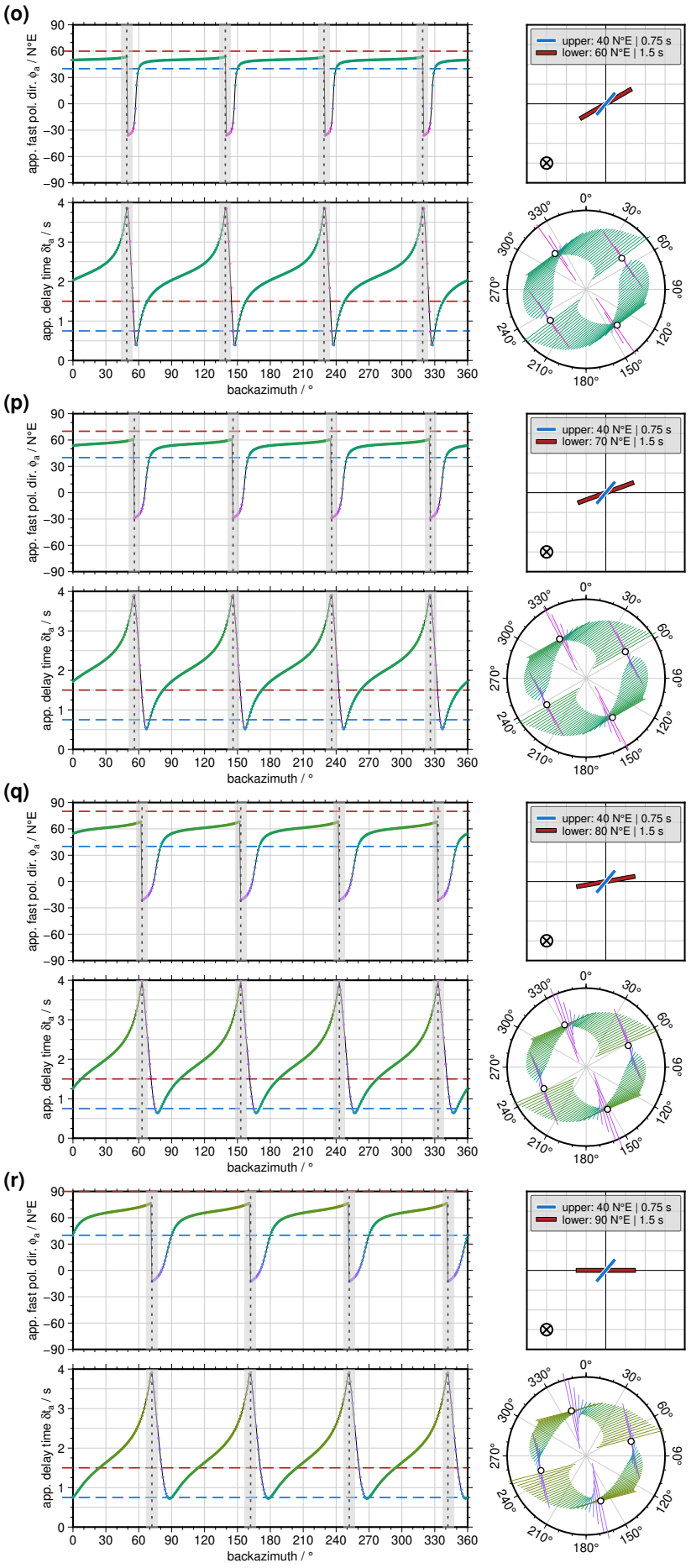

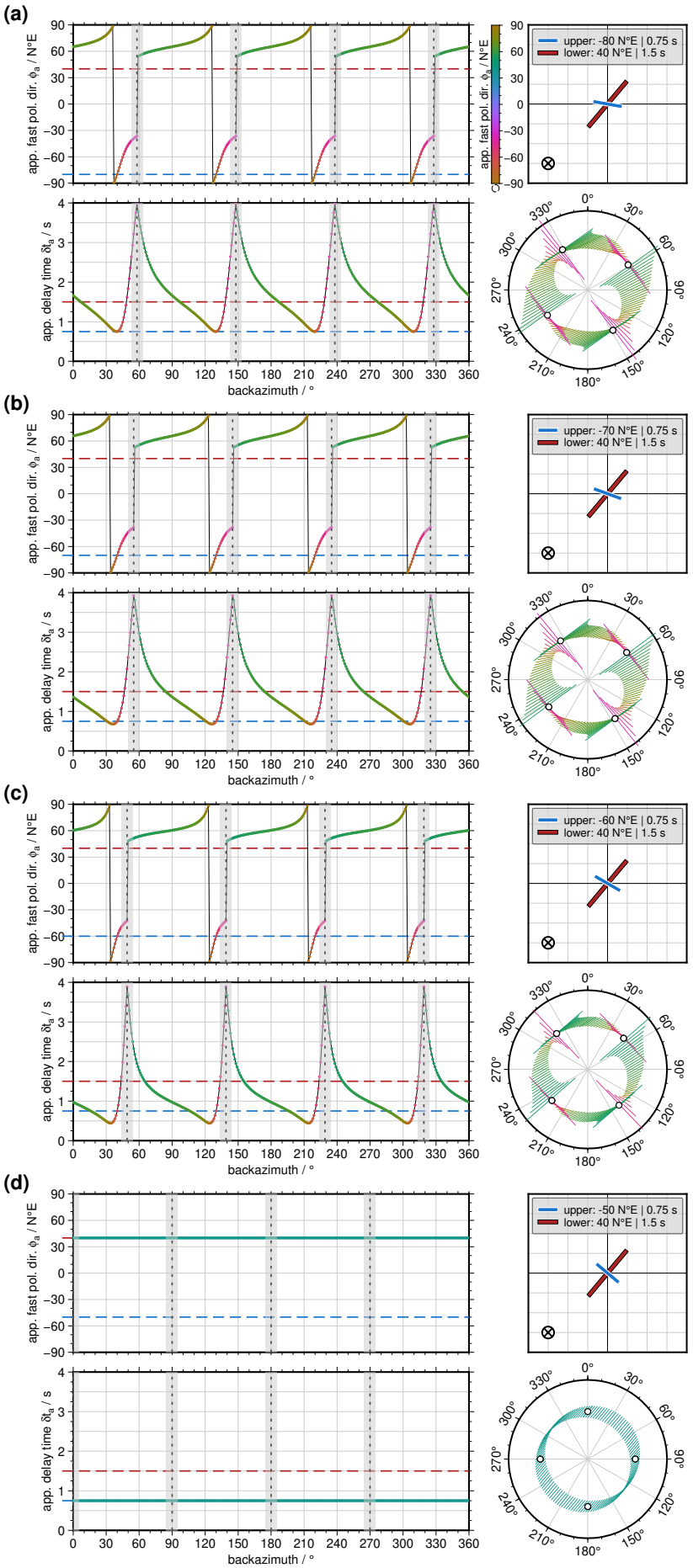

Figure C.6: Forward calculation for model type H2: variation of the fast polarization direction in the upper layer.
Fixed delay times in the lower and upper layers of 1.5 s or 0.75 s and fixed fast polarization direction in the lower layer of 40N°E. The fast polarization direction in the upper layer varies in steps of 10° from **(a)** -80N°E to **(r)** 90N°E.
Visualizations as in Fig. 5.2; for a related animation, see Sec. D.5.

Fig. C.6 continued.

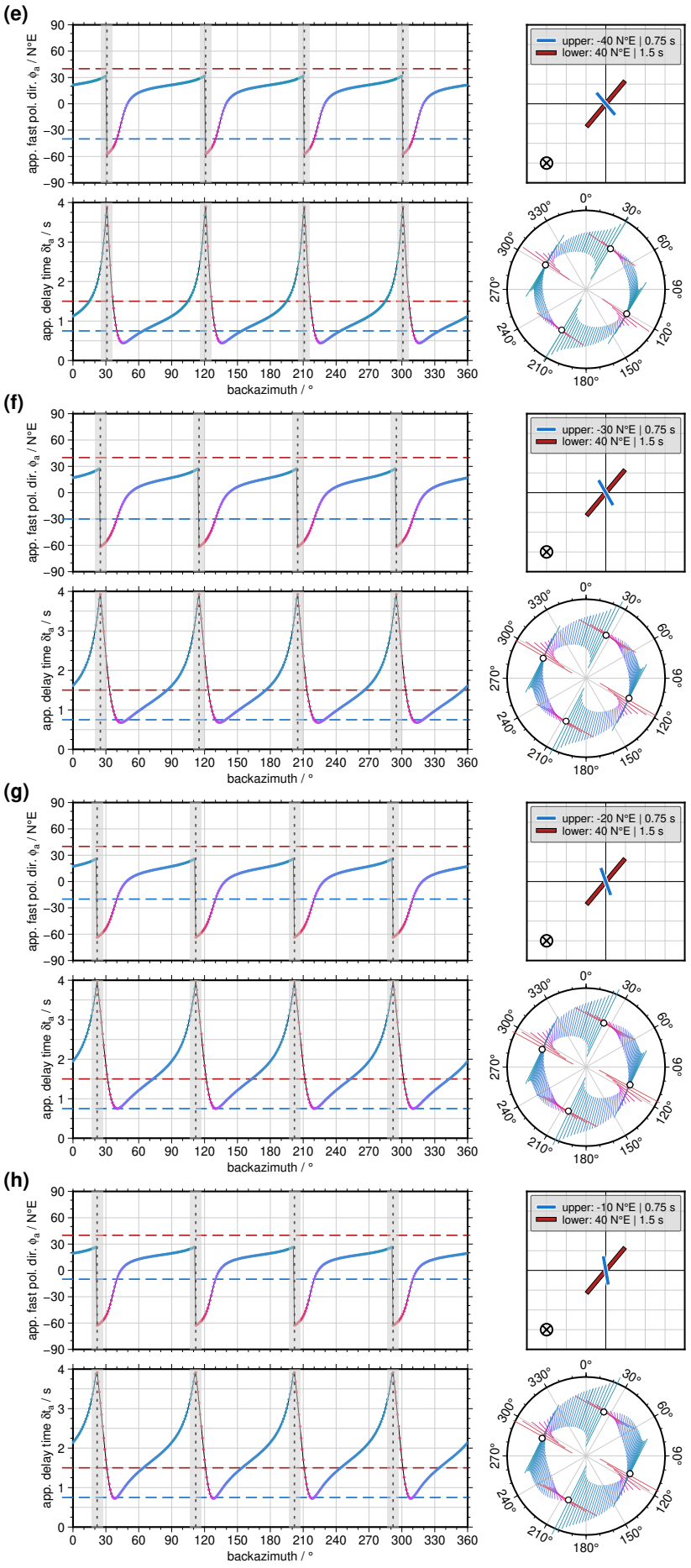

Fig. C.6 continued.

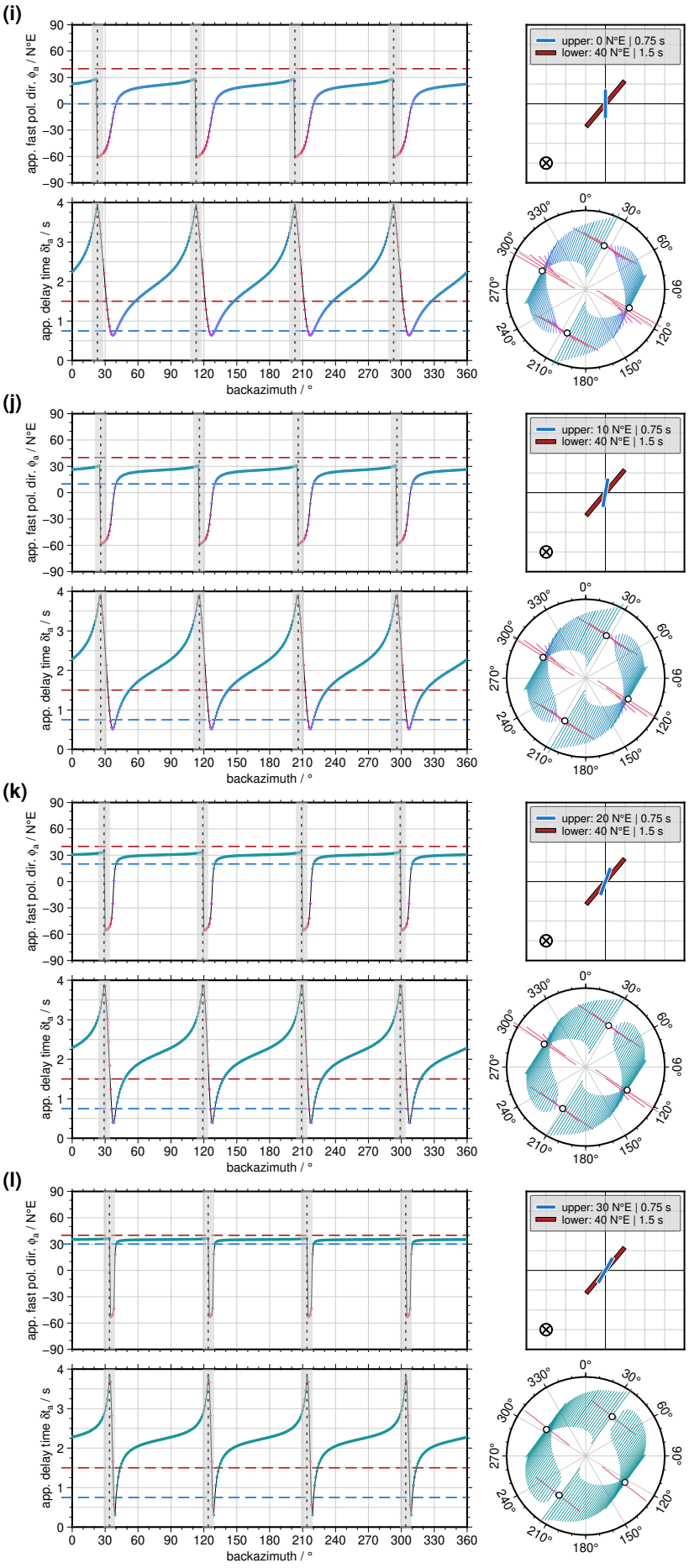

Fig. C.6 continued.

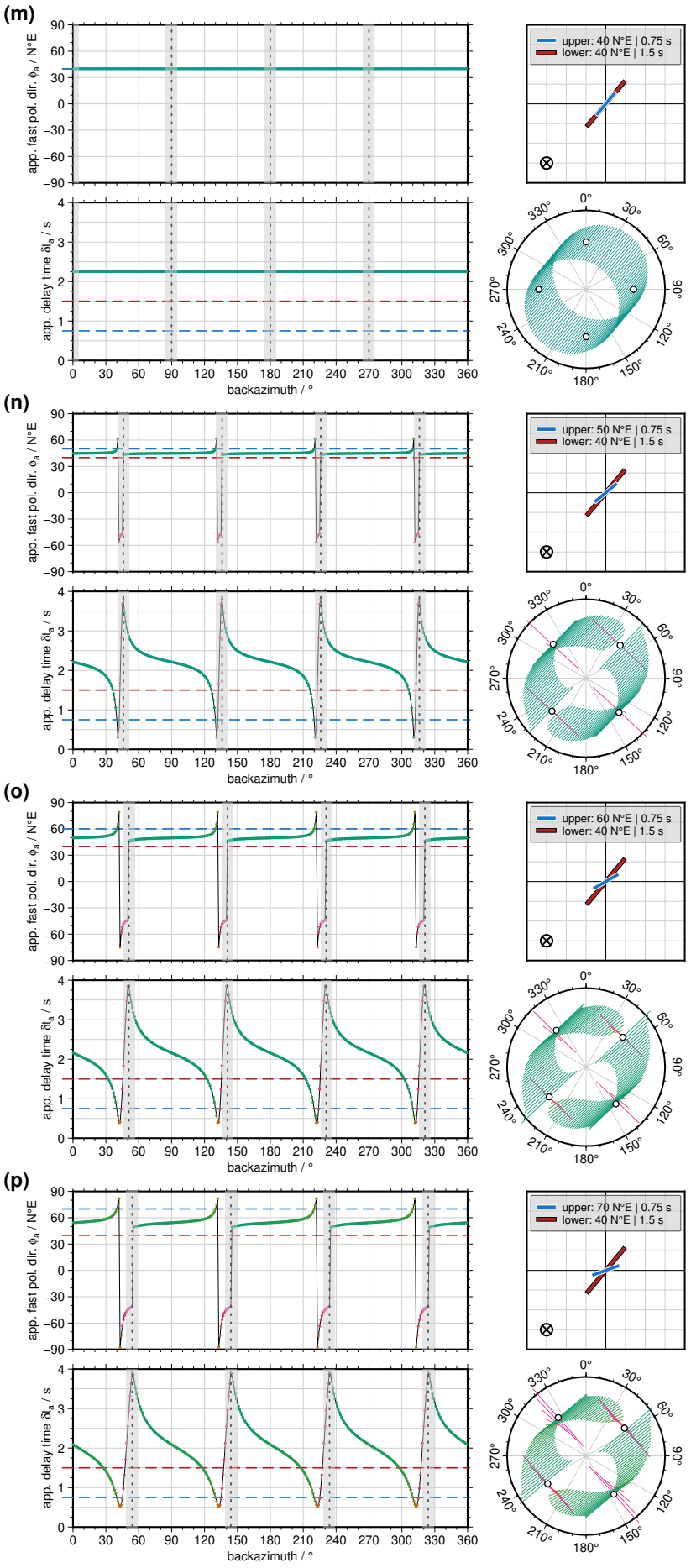

Fig. C.6 continued.

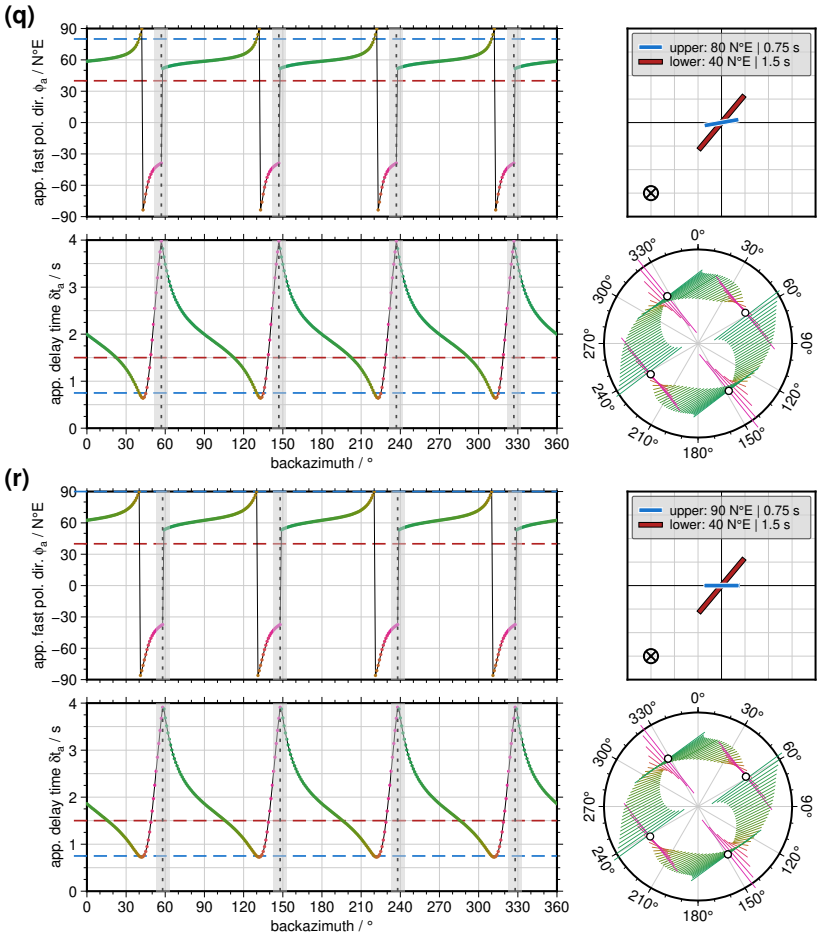

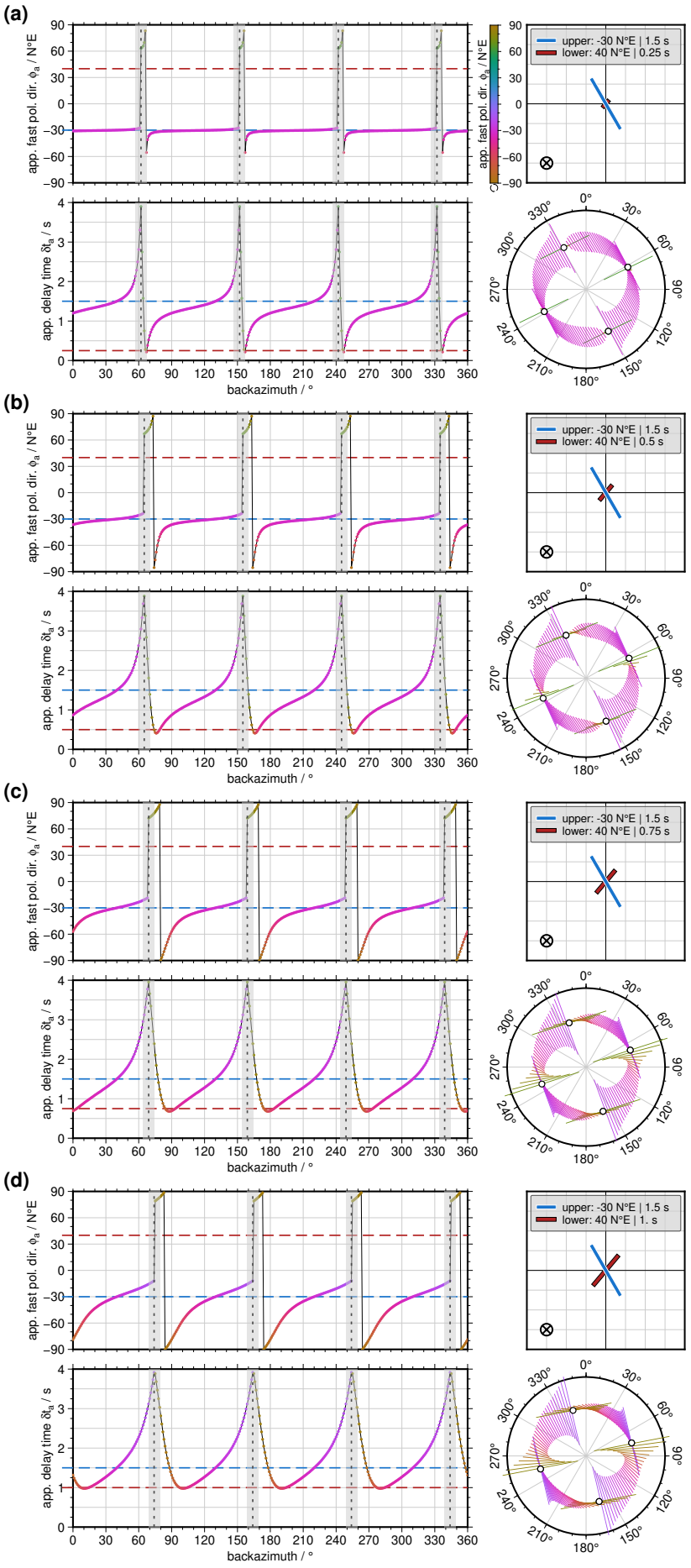

Figure C.7: Forward calculation for model type H2: variation of the delay time in the lower layer.
Fixed polarization directions in the lower and upper layers of 40N°E or -30N°E and a fixed delay time in the upper layer of 1.5 s. The delay time in the lower layer varies in steps of 0.25 s from **(a)** 0.25 s to **(p)** 4 s.
Visualizations as in Fig. 5.2; for a related animation, see Sec. D.5.

Fig. C.7 continued.

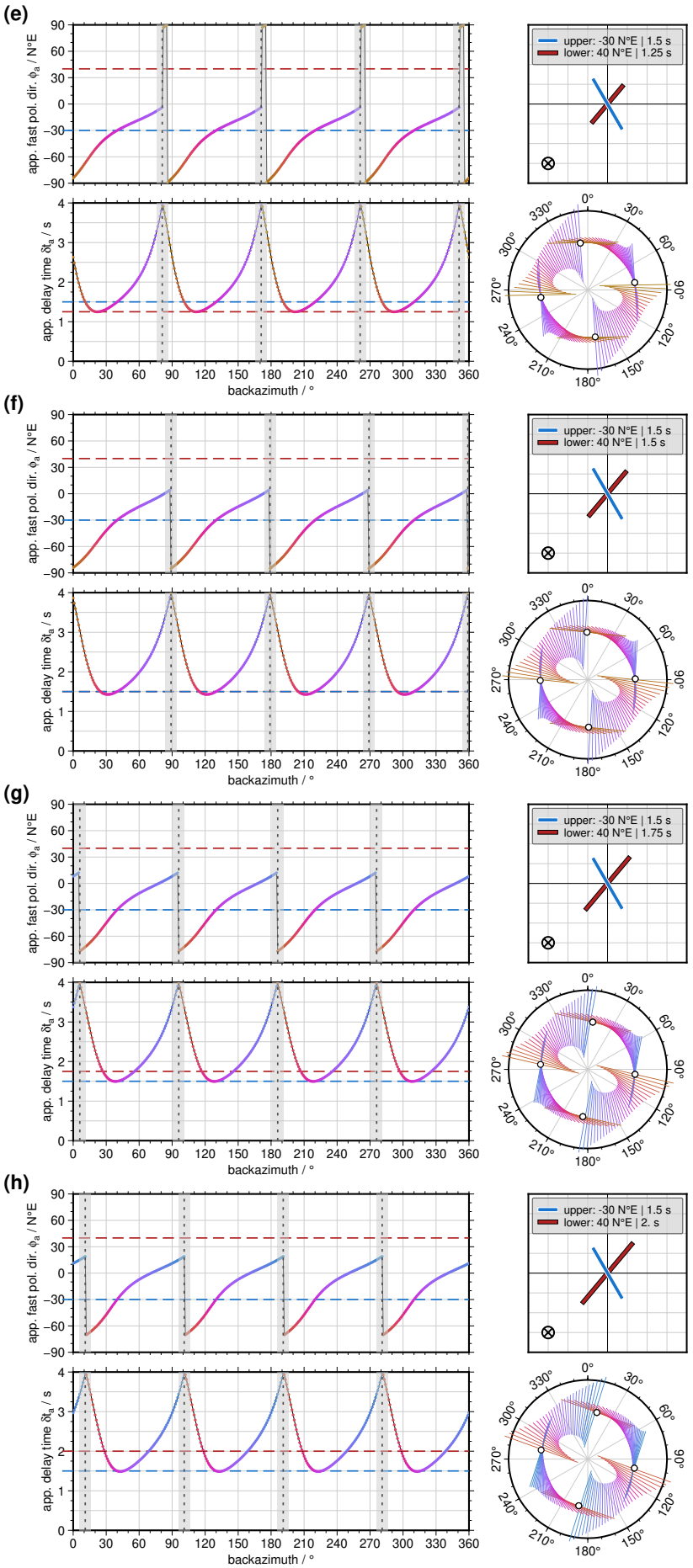

Fig. C.7 continued.

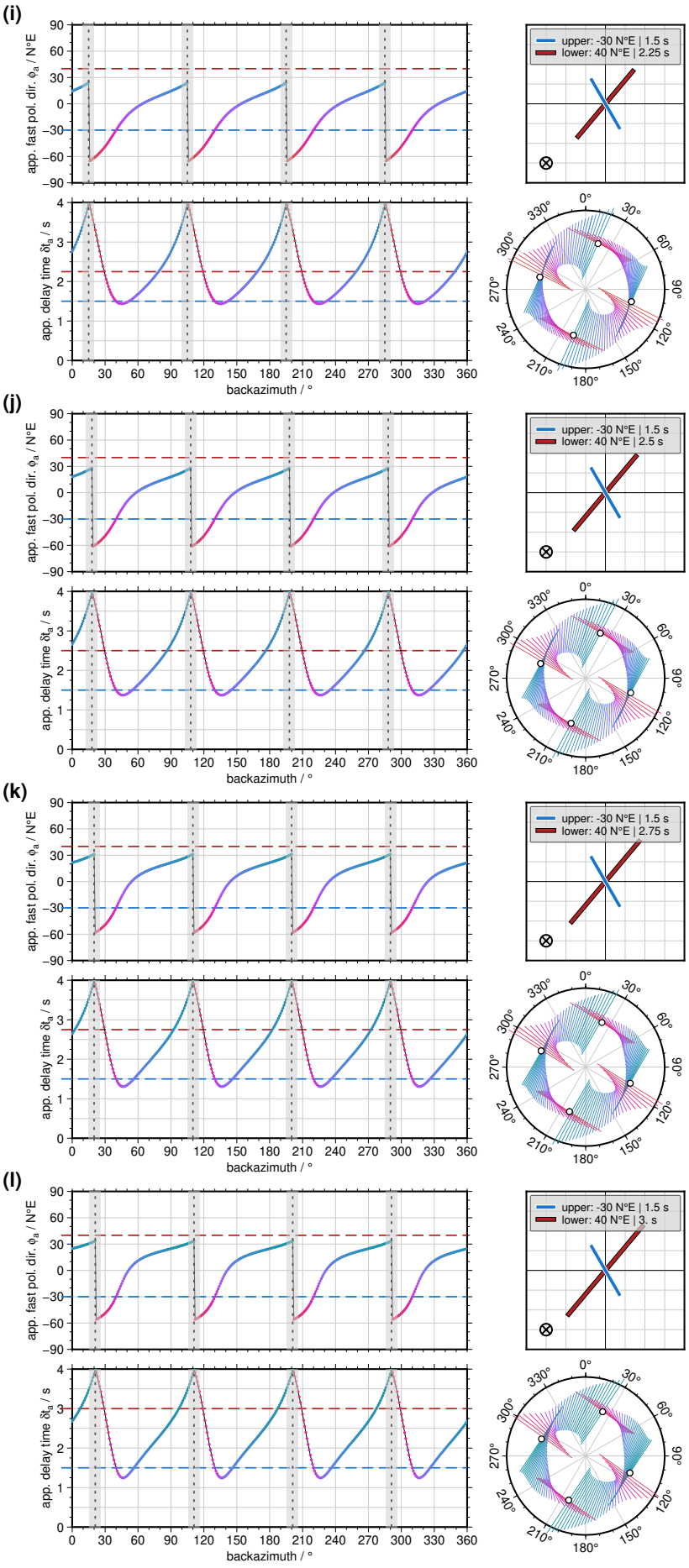

Fig. C.7 continued.

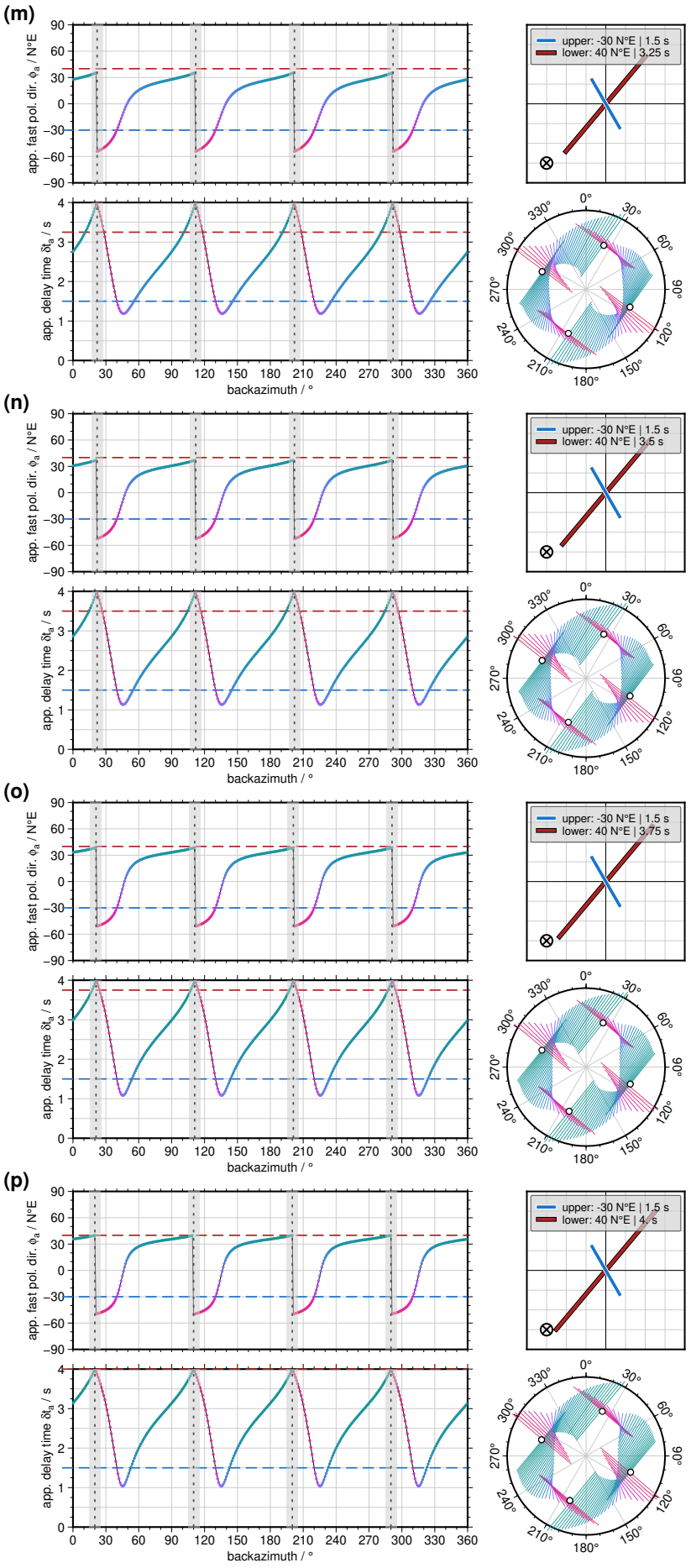

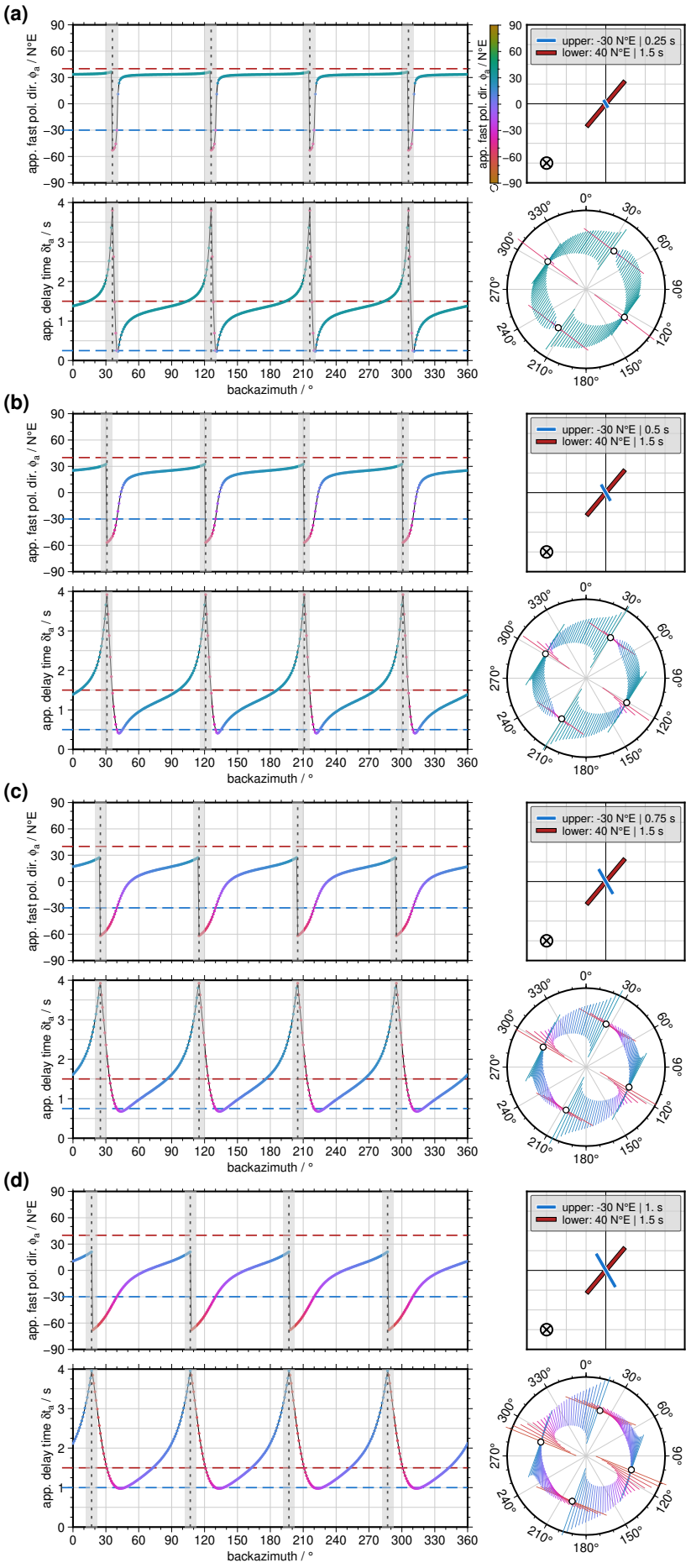

Figure C.8: Forward calculation for model type H2: variation of the delay time in the upper layer.
Fixed polarization directions in the lower and upper layers of 40N°E or -30N°E and a fixed delay time in the lower layer of 1.5 s. The delay time in the upper layer varies in steps of 0.25 s from **(a)** 0.25 s to **(p)** 4 s.
Visualizations as in Fig. 5.2; for a related animation, see Sec. D.5.

Fig. C.8 continued.

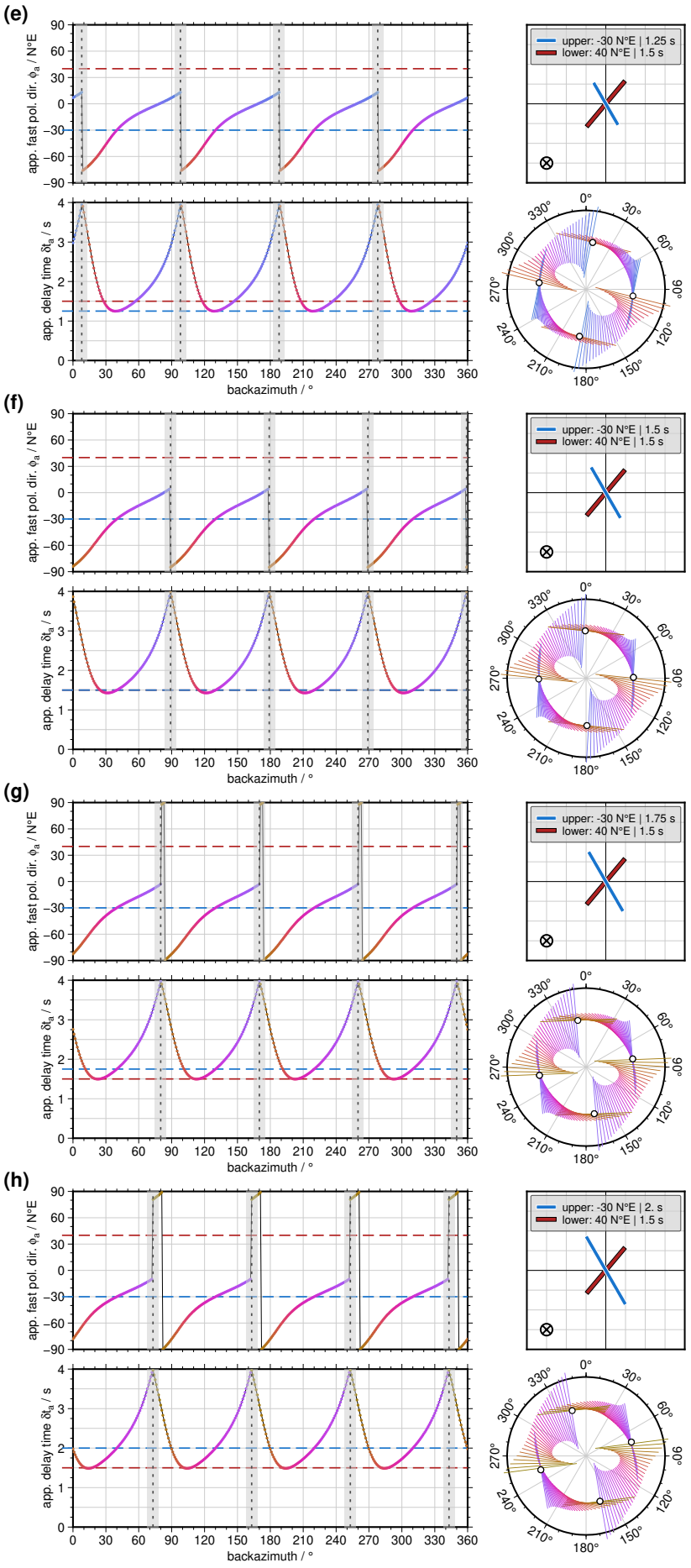

Fig. C.8 continued.

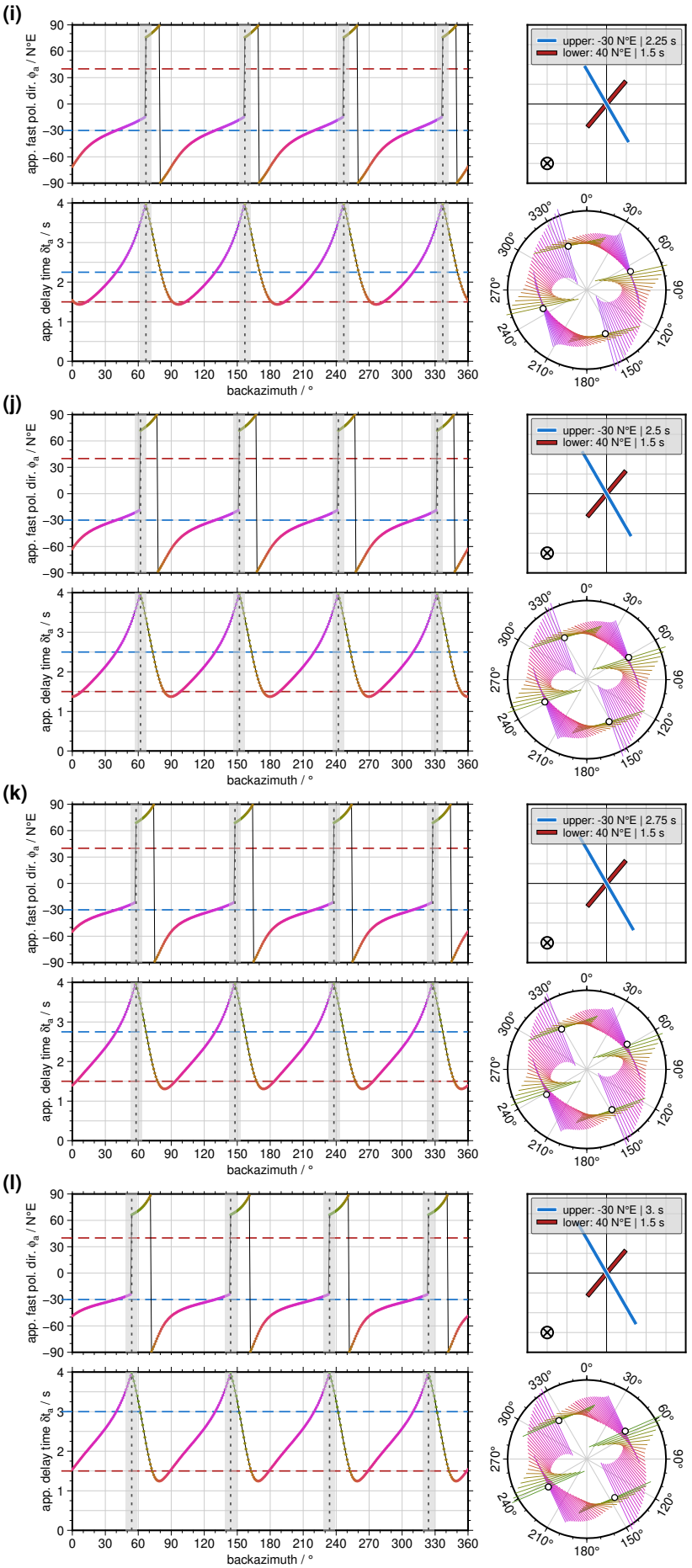

Fig. C.8 continued.

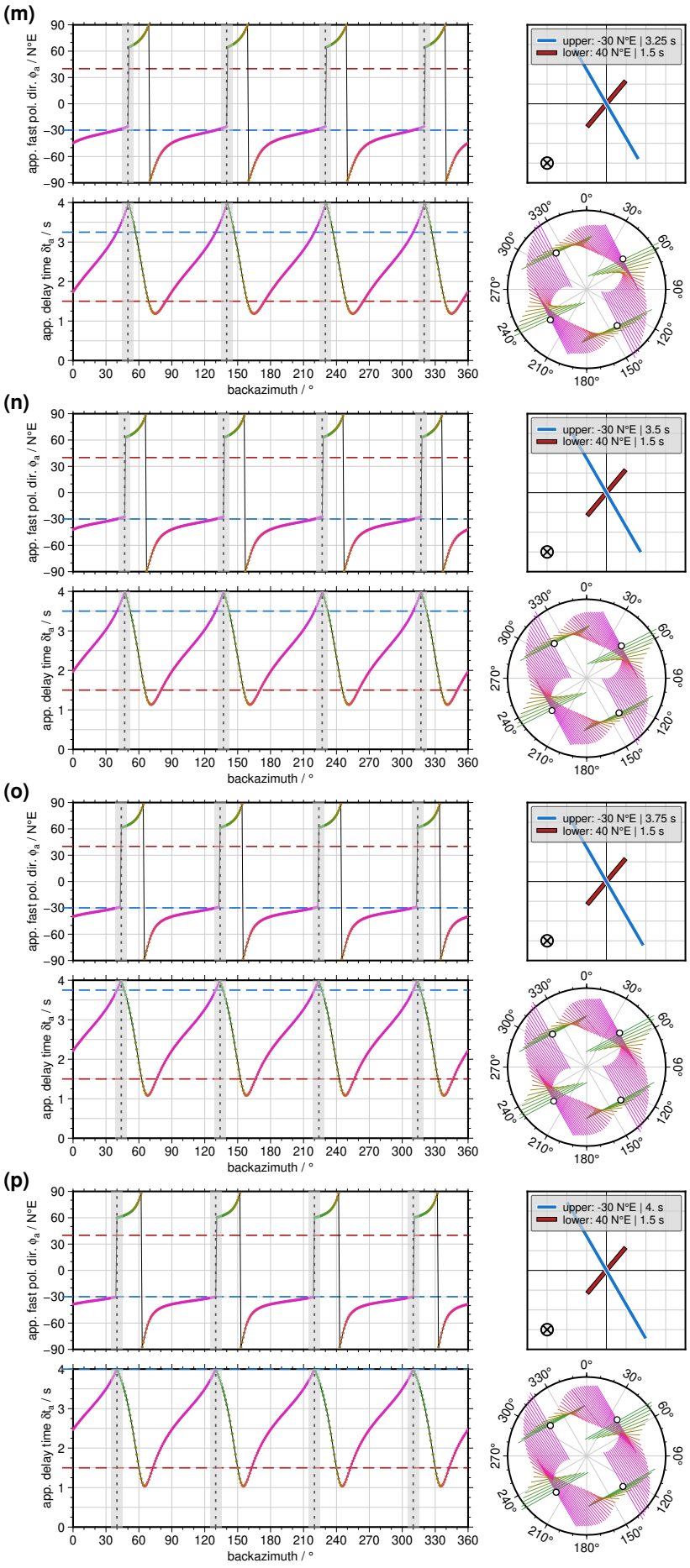

C.4 Concepts for *AxiSEM3D*

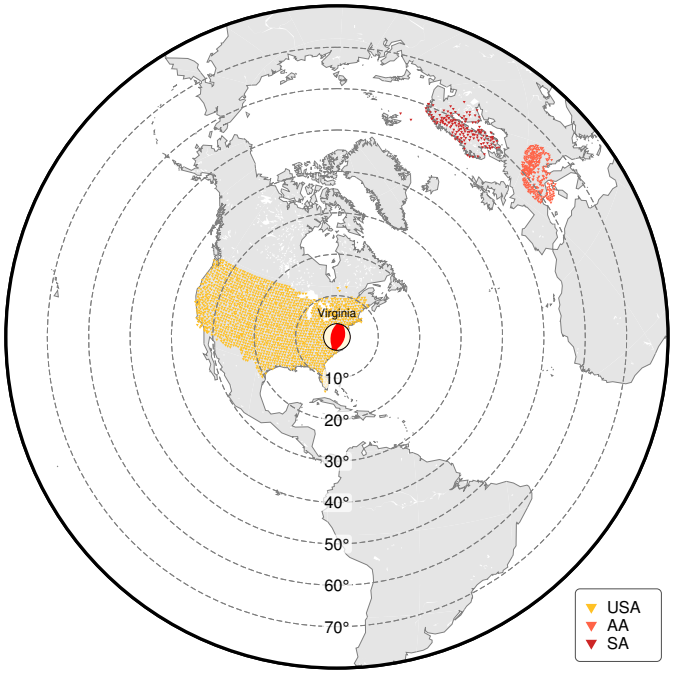

Figure C.9: Simulations with *AxiSEM3D*: source-receiver constellation of run A. The source or earthquake is located in Virginia (red beachball in the center of the epicentral distance plot) and the dashed circles give the epicentral distance in steps of 10°. The recording stations (inverse triangles) belong to the networks *USArray* (USA, yellow), *AlpArray* (AA, orange), and *ScanArray* (SA, red).

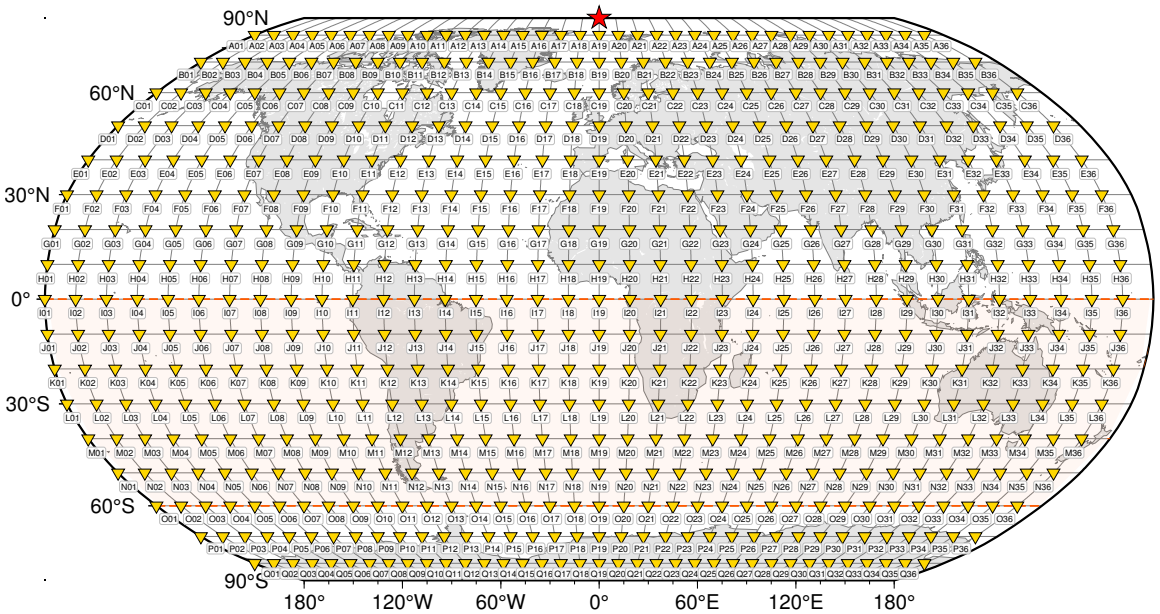

Figure C.10: Simulations with *AxiSEM3D*: source-receiver constellation of run B. Network of theoretical recording stations equally space by 10° in both longitude and latitude directions.

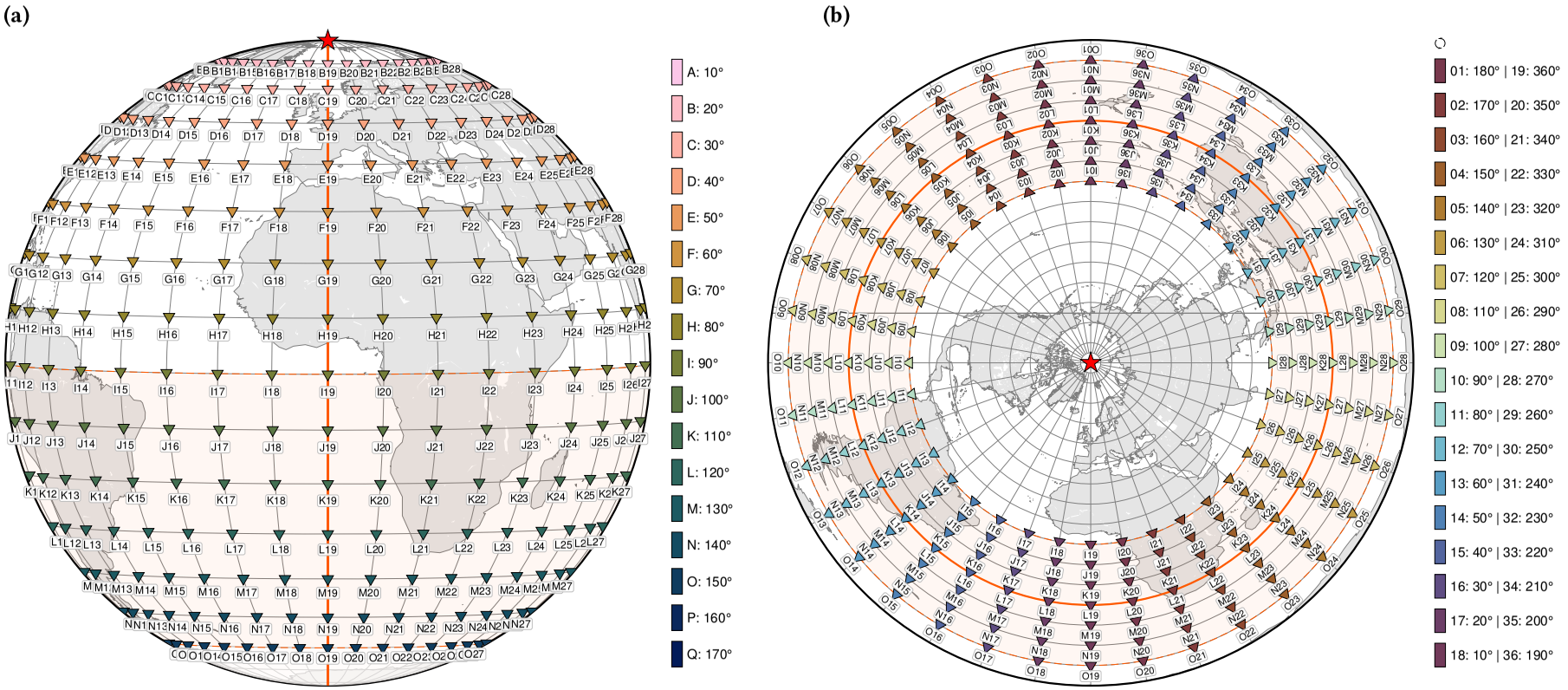

Figure C.11: Simulations with *AxiSEM3D*: usage of run B. Color-coding based on **(a)** the latitude representing the epicentral distance, and **(b)** the longitude representing the backazimuth.

D Data and Codes

D.1 Bug fix in *SplitLab*

Along with *Fröhlich et al.* (2022a; Ch. 6) corrected scripts of the MATLAB function `getFileAndEQseconds.m` for the publicity available *SplitLab* versions 1.0.5 (*Wüstefeld et al.*, 2008), 1.2.1 (*Porritt*, 2014), and 1.3.0 (*Creasy*, 2020), as well as test examples for users are available from the GitHub repository **SplitLab-TemporalAlignment** (*Fröhlich*, 2024; *Fröhlich and Grund*, 2021). For details, see the included README file. Additionally, this fix is included in *StackSplit* (*Grund*, 2017) up on version v3.0 (*Grund and Fröhlich*, 2021).

D.2 Datasets with SWSMs on *RADAR4KIT*

Datasets with the SWSMs related to *Ritter et al.* (2022; Ch. 7) and *Fröhlich et al.* (2024b; Ch. 8) are available from *RADAR4KIT* in CSV and PDF formats (Tab. D.1). For each recording stations, the *good* and *fair* qualities are provided separated by *nulls* and *splits*. For the URG dataset, the SWSMs at BFO are extended from *Ritter et al.* (2022), and additional to the splitting parameters the splitting intensity is reported. More details on these data can be found in the included README files (*Fröhlich et al.*, 2022b; *Fröhlich et al.*, 2024c). Scripts to load the CSV files into MATLAB, Python, and R are available from GitHub, see Sec. D.3 and Tab. D.2.

Table D.1: Datasets with SWSMs on *RADAR4KIT*.

Dataset	Recording station(s)	DOI	Related publication
BFO	BFO	10.35097/684	*Ritter et al.* (2022)
URG	BFO, WLS, STU, ECH, TMO44, TMO05	10.35097/685	*Fröhlich et al.* (2024b)

D.3 Codes for the visualization and modeling of SWSMs

Codes for the visualization and modeling of SWSMs used in *Ritter et al.* (2022; Ch. 7) and *Fröhlich et al.* (2024b; Ch. 8) are available from the GitHub repository **sws-visualization-and-modeling** (*Fröhlich*, 2025b; *Fröhlich and Grund*, 2022). These functions are written in MATLAB and Python (Tab. D.2), and optimized for the output files generated by *SplitLab* (*Wüstefeld et al.*, 2008; *Porritt*, 2014) and *StackSplit* (*Grund*, 2017; *Grund and Fröhlich*, 2021). For the forward calculation of synthetic splitting parameters within the modeling routine, the *MATLAB Seismic Anisotropy Toolbox* (MSAT; *Walker and Wookey*, 2012) is required. Details on the modeling procedure are given in the modeling-specific README file. Furthermore, the supporting information of *Grund and Ritter* (2020; pages 7-15) contains helpful introductions, especially carefully composed details on the model type T1.

Table D.2: Codes for visualization and modeling of SWSMs available from the GitHub repository **sws-visualization-and-modeling**.

Folder	Content	Language(s), packages
`001_stereoplot`	stereoplot representation	MATLAB
`002_visualization`	loading the *RADAR4KIT* datasets (Sec. D.2, Tab. D.1)	MATLAB, Python, R
	exploring synthetic splitting parameters	Python, *PyGMT*
`003_modeling`	forward calculating synthetic splitting parameters	MATLAB, MSAT
	fitting structural anisotropy models	MATLAB

D.4 Collection of *PyGMT* visualizations

A collection of Python codes to generate various visualizations (mainly maps) on geophysics and seismology focusing on seismic anisotropy and SWS is available from the GitHub repository **gmt-pygmt-plotting** (*Fröhlich*, 2025a). Overview images can be found in the Content section of the README file. As these materials are continuously updated, as well as extended based on new analysis, projects, posters, talks, and publications, Tab. D.3 reflects the status at the time of writing this doctoral thesis.

Table D.3: Collection of *PyGMT* visualizations (mainly maps) available from the GitHub repository **gmt-pygmt-plotting**.

Folder	Content
`000_general_stuff`	custom symbols, colorwheel, colorbar font scaling
`001_paper_RFSG_2022`	maps related to anisotropy and SWS underneath the BFO
`002_paper_FGR_2024`	maps related to anisotropy and SWS underneath the URG area
`003_taup`	travel paths and travel time curves of seismological phases
`004_earthquakes_eruptions`	maps of selected earthquakes and eruptions between 2021 and present
`005_global_seismicity`	analysis regarding global seismicity
`006_tomographies_databases`	maps of databases and tomographies
`007_dissertation_F_2025`	*up coming*
`008_urg_vs_norsa`	*up coming*
`009_deepdyn`	maps related to the *DeepDyn* project
`010_axisem`	maps related to *AxiSEM3D*
`011_agu_FTLJG_2024`	plots related to *PyGMT* = *GMT* + Python & SPE

D.5 Collection of geophysical visualizations and animations

Collections of different visualizations (reserved DOI `https://doi.org/10.5281/zenodo.15836683`) and animations (reserved DOI `https://doi.org/10.5281/zenodo.15641349`) on geophysics and seismology focusing on seismic anisotropy and SWS are in preparation. The animations refer to figures or maps shown in this doctoral thesis or listed in Tab. D.3. Tabs D.4 and D.5 reflect the planned content at the time of writing this thesis.

Table D.4: Collection of planned geophysical visualizations.

Folder	Content
`000_general`	
`001_seismology_basics`	
`002_seismic_anisotropy`	Figs of Ch. 3
`003_measuring_shear_wave_splitting`	Figs of Ch. 4
`004_modeling_shear_wave_splitting`	Figs of Ch. 5
`005_seismological_phases`	Figs 4.1, 4.2, C.1, C.2, 4.7

Table D.5: Collection of planned geophysical animations.

Folder	Content
`000_general`	
`001_global_seismicity`	rotating globe, over time
`002_travel_paths`	travel paths (and time curves) with epicentral distance
`003_shear_wave_splitting_measurements`	long-term measurements over time
`004_splitting_parameters`	forward calculated splitting parameters
`005_tomography_eu60`	with depth
`006_splitting_database`	over time

D.6 Involvement and contribution to the *PyGMT* project

The *PyGMT* project aims to implement a Python interface for the *Generic Mapping Tools* (*GMT*) and integrate it in the *Python scientific ecosystem* (Fig. D.1). I started contributing to this open source project in 2022/06. Currently, I am an active maintainer of *PyGMT* (`https://www.pygmt.org/dev/team.html#active-maintainers`) and a moderator on the related *GMT* forum (`https://forum.generic-mapping-tools.org/about`). At the moment, the team is discussing the second version of the alias system (`https://github.com/GenericMappingTools/pygmt/issues/3239`), the design of a separate *PyGMT* logo (`https://github.com/GenericMappingTools/pygmt/issues/1404`, `https://github.com/GenericMappingTools/pygmt/pull/3849`), and working on the visualizations for a *PyGMT* paper (`https://github.com/GenericMappingTools/pygmt-paper-figures`).

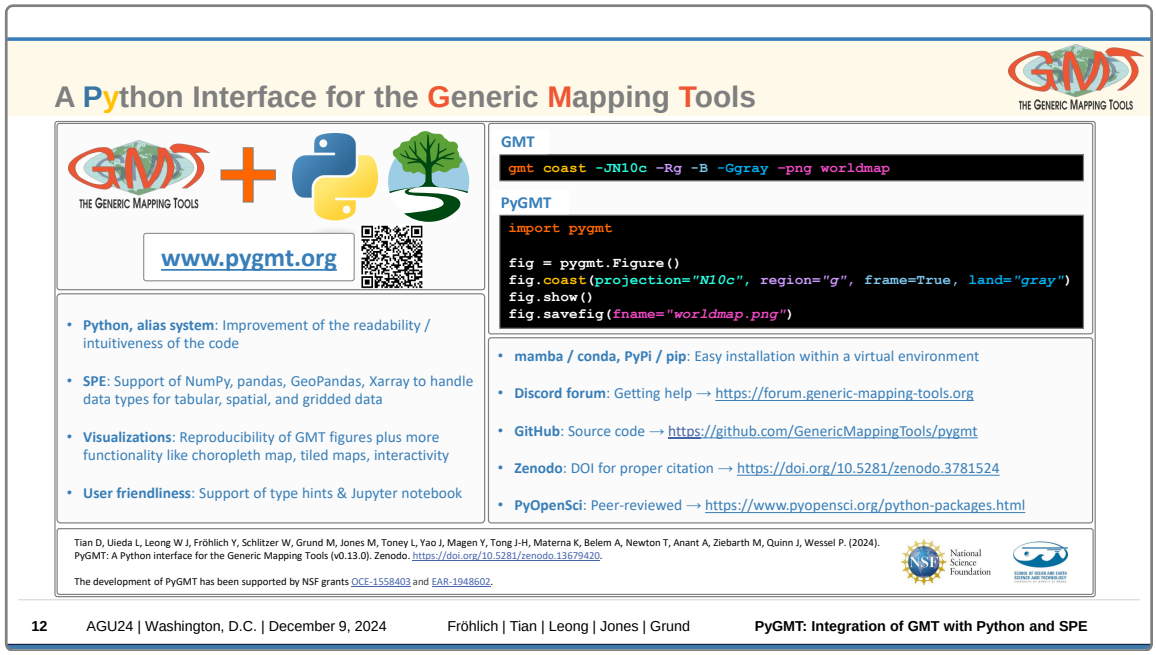

Figure D.1: *PyGMT* talk at the annual meeting of the American Geophysical Union (AGU) in Washington D.C. on December 9 2024: summary slide *Fröhlich et al.* (2024d). The talk was given within a union-wide session, set up as memorial session for Pål Wessel (1959/08/31 – 2024/03/26). Additional to this session, a pre-workshop on *GMT* and *PyGMT* was organized by the team (*Leong et al.*, 2024). At the point of writing this doctoral thesis the latest *PyGMT* release is v0.15.0 (*Tian et al.*, 2025b) and v0.16.0 (*Tian et al.*, 2025a) is planned to be released at the end of June 2025.

References

AlpArray Seismic Network (2015). AlpArray Seismic Network (AASN) temporary component. *AlpArray Working Group*. https://doi.org/10.12686/alparray/z3_2015.

Alsina, D. and Snieder, R. (1995). Small-scale sublithospheric continental mantle deformation: constraints fromSKSsplitting observations. *Geophysical Journal International*, 123(2):431–448. https://doi.org/10.1111/j.1365-246X.1995.tb06864.x.

Aragon, J. C., Long, M. D., and Benoit, M. H. (2017). Lateral Variations in SKS Splitting Across the MAGIC Array, Central Appalachians. *Geochemistry, Geophysics, Geosystems*, 18(11):4136–4155. https://doi.org/10.1002/2017GC007169.

Artemieva, I. M. (2019). Lithosphere structure in Europe from thermal isostasy. *Earth-Science Reviews*, 188:454–468. https://doi.org/10.1016/j.earscirev.2018.11.004.

Asch, K. (2005). IGME 5000 : 1 : 5 Million International Geological Map of Europe and Adjacent Areas - final version for the internet. *BGR, Hannover*. https://www.bgr.bund.de/EN/Themen/Sammlungen-Grundlagen/GG_geol_Info/Karten/Europa/IGME5000/IGME_Project/IGME_Downloads.html?nn=1556388.

Asplet, J., Wookey, J., and Kendall, M. (2020). A potential post-perovskite province in D'' beneath the Eastern Pacific: evidence from new analysis of discrepant SKS–SKKS shear-wave splitting. *Geophysical Journal International*, 221(3):2075–2090. https://doi.org/10.1093/gji/ggaa114.

Audet, P. and Schaeffer, A. J. (2019). SplitPy: Software for teleseismic shear-wave splitting analysis. *Zenodo*. https://doi.org/10.5281/zenodo.3564780.

Babuška, V. and Cara, M. (1991). Seismic anisotropy in the Earth. *Kluwer AcademicPublishers, Dordrecht*. ISBN 0-7923-1321-6.

Babuška, V. and Plomerová, J. (2001). Subcrustal lithosphere around the Saxothuringian–Moldanubian Suture Zone — a model derived from anisotropy of seismic wave velocities. *Tectonophysics*, 332(1–2):185–199. https://doi.org/10.1016/S0040-1951(00)00255-9.

Babuška, V., Plomerová, J., Vecsey, L., Granet, M., and Achauer, U. (2002). Seismic anisotropy of the French Massif Central and predisposition of Cenozoic rifting and volcanism by Variscan suture hidden in the mantle lithosphere. *Tectonics*, 21(4). https://doi.org/10.1029/2001TC901035.

Bamford, D. (1977). Pnvelocity anisotropy in a continental upper mantle. *Geophysical Journal International*, 49(1):29–48. https://doi.org/10.1111/j.1365-246X.1977.tb03699.x.

Barruol, G., Wüstefeld, A., and Bokelmann, G. (2009). SKS-Splitting-database. *SplitLab website*. https://doi.org/10.18715/sks_splitting_database.

Bastow, I. D., Owens, T. J., Helffrich, G., and Knapp, J. H. (2007). Spatial and temporal constraints on sources of seismic anisotropy: Evidence from the Scottish highlands. *Geophysical Research Letters*, 34(5). https://doi.org/10.1029/2006GL028911.

Berger, J., Davis, P., and Ekström, G. (2004). Ambient Earth noise: A survey of the Global Seismographic Network. *Journal of Geophysical Research: Solid Earth*, 109(B11). https://doi.org/10.1029/2004JB003408.

Bernard, R. E., Behr, W. M., Becker, T. W., and Young, D. J. (2019). Relationships Between Olivine CPO and Deformation Parameters in Naturally Deformed Rocks and Implications for Mantle Seismic Anisotropy. *Geochemistry, Geophysics, Geosystems*, 20(7):3469–3494. https://doi.org/10.1029/2019GC008289.

Beyreuther, M., Barsch, R., Krischer, L., Megies, T., Behr, Y., and Wassermann, J. (2010). ObsPy: A Python Toolbox for Seismology. *Seismological Research Letters*, 81(3):530–533. https://doi.org/10.1785/gssrl.81.3.530, https://docs.obspy.org, https://github.com/obspy/obspy.

Bird, P. (2003). An updated digital model of plate boundaries. *Geochemistry, Geophysics, Geosystems*, 4(3). https://doi.org/10.1029/2001GC000252.

Black Forest Observatory (1971). Black Forest Observatory Data. *GFZ Data Services*. https://doi.org/10.5880/BFO.

Bokelmann, G. H. R. and Silver, P. G. (2002). Shear stress at the base of shield lithosphere. *Geophysical Research Letters*, 29(23). https://doi.org/10.1029/2002GL015925.

Bowman, J. R. and Ando, M. (1987). Shear-wave splitting in the upper-mantle wedge above the Tonga subduction zone. *Geophysical Journal International*, 88(1):25–41. https://doi.org/10.1111/j.1365-246X.1987.tb01367.x.

Braunger, S., Marks, M. A. W., Walter, B. F., Neubauer, R., Reich, R., Wenzel, T., Parsapoor, A., and Markl, G. (2018). The Petrology of the Kaiserstuhl Volcanic Complex, SW Germany: The Importance of Metasomatized and Oxidized Lithospheric Mantle for Carbonatite Generation. *Journal of Petrology*, 59(9):1731–1762. https://doi.org/10.1093/petrology/egy078.

Brechner, S., Klinge, K., Krüger, F., and Plenefisch, T. (1998). Backazimuthal Variations of Splitting Parameters of Teleseismic SKS Phases Observed at the Broadband Stations in Germany. *Pure and Applied Geophysics*, 151(4):305. https://doi.org/10.1007/s000240050116.

Brett, H., Tromp, J., and Deuss, A. (2024). Tilted transverse isotropy in Earth's inner core. *Nature Geoscience*, 17(10):1059–1064. https://doi.org/10.1038/s41561-024-01539-6.

Bullen, K. E. (1940). The problem of the earth's density variation. *Bulletin of the Seismological Society of America*, 30(3):235–250. https://doi.org/10.1785/BSSA0300030235.

Bullen, K. E. (1949). Compressibility-Pressure Hypothesis and the Earth's Interior. *Geophysical Journal International or Geophysical Supplements to the Monthly Notices of the Royal Astronomical Society*, 5:335–368. https://doi.org/10.1111/j.1365-246X.1949.tb02952.x.

Cao, L., He, X., Yuan, H., Zhao, M., Qiu, X., and Savage, M. K. (2024). Upper-mantle seismic anisotropy in the southwestern North Island, New Zealand: Implications for regional upper-mantle and slab deformation. *Tectonophysics*, 887:230455. https://doi.org/10.1016/j.tecto.2024.230455.

Caswell, T. A., Droettboom, M., Lee, A., de Andrade, E. S., Hoffmann, T., Hunter, J., Klymak, J., Firing, E., Stansby, D., Varoquaux, N., Nielsen, J. H., Root, B., May, R., Elson, P., Seppänen, J. K., Dale, D., Lee, J.-J., McDougall, D., Straw, A., Hobson, P., hannah, Gohlke, C., Yu, T. S., Ma, E., Vincent, A. F., Silvester, S., Moad, C., Kniazev, N., Ernest, E., and Ivanov, P. (2021). Matplotlib (3.4.3). *Zenodo*. https://doi.org/10.5281/zenodo.5194481.

Chakraborty, M., Rümpker, G., Li, W., Faber, J., Srivastava, N., and Link, F. (2024). Feasibility of Deep Learning in Shear Wave Splitting analysis using Synthetic-Data Training and Waveform Deconvolution. *Seismica*, 3(1). https://doi.org/10.26443/seismica.v3i1.1124.

Chevrot, S. (2000). Multichannel analysis of shear wave splitting. *Journal of Geophysical Research: Solid Earth*, 105(B9):21579–21590. https://doi.org/10.1029/2000JB900199.

Chevrot, S., Favier, N., and Komatitsch, D. (2004). Shear wave splitting in three-dimensional anisotropic media. *Geophysical Journal International*, 159(2):711–720. https://doi.org/10.1111/j.1365-246X.2004.02432.x.

Christoffel, E. B. (1877). Über die Fortpflanzung von Stössen durch elastische feste Körper. *Annali di MatematicaPura ed Applicata (1867-1897)*, 8:193–243.

Crameri, F. (2021). Scientific colour maps (7.0.0). *Zenodo*. https://zenodo.org/records/4491293, https://www.fabiocrameri.ch/colourmaps/.

Crameri, F. (2023). Scientific colour maps (8.0.1). *Zenodo*. https://doi.org/10.5281/zenodo.8409685, https://www.fabiocrameri.ch/colourmaps/.

Crampin, S. (1984a). Effective anisotropic elastic constants for wave propagation through cracked solids. *Geophysical Journal International*, 76(1):135–145. https://doi.org/10.1111/j.1365-246X.1984.tb05029.x.

Crampin, S. (1984b). An introduction to wave propagation in anisotropic media. *Geophysical Journal International*, 76(1):17–28. https://doi.org/10.1111/j.1365-246X.1984.tb05018.x.

Crampin, S. and Chastin, S. (2003). A review of shear wave splitting in the crack-critical crust. *Geophysical Journal International*, 155(1):221–240. https://doi.org/10.1046/j.1365-246X.2003.02037.x.

Crampin, S. and Lovell, J. H. (1991). A decade of shear-wave splitting in the Earth's crust: what does it mean? what use can we make of it? and what should we do next? *Geophysical Journal International*, 107(3):387–407. https://doi.org/10.1111/j.1365-246X.1991.tb01401.x.

Creasy, N. (2020). SplitLab (v1.3.0). *GitHub*. https://github.com/nmcreasy/SplitLab1.3.0.

Creasy, N., Long, M. D., and Ford, H. A. (2017). Deformation in the lowermost mantle beneath Australia from observations and models of seismic anisotropy. *Journal of Geophysical Research: Solid Earth*, 122(7):5243–5267. https://doi.org/10.1002/2016JB013901.

Creasy, N., Miyagi, L., and Long, M. D. (2020). A Library of Elastic Tensors for Lowermost Mantle Seismic Anisotropy Studies and Comparison With Seismic Observations. *Geochemistry, Geophysics, Geosystems*, 21(4). https://doi.org/10.1029/2019GC008883.

Crotwell, H. P., Owens, T. J., and Ritsema, J. (1999). The TauP Toolkit: Flexible Seismic Travel-time and Ray-path Utilities. *Seismological Research Letters*, 70(2):154–160. https://doi.org/10.1785/gssrl.70.2.154.

Currie, C. A., Cassidy, J. F., Hyndman, R. D., and Bostock, M. G. (2004). Shear wave anisotropy beneath the Cascadia subduction zone and western North American craton. *Geophysical Journal International*, 157(1):341–353. https://doi.org/10.1111/j.1365-246X.2004.02175.x.

DeMets, C., Gordon, R. G., and Argus, D. F. (2010). Geologically current plate motions. *Geophysical Journal International*, 181(1):1–80. https://doi.org/10.1111/j.1365-246X.2009.04491.x. See also Erratum, 2011. Geophysical Journal International, volume 187, issue 1, page 538, https://doi.org/10.1111/j.1365-246X.2011.05186.x.

Deng, J., Long, M. D., Creasy, N., Wagner, L., Beck, S., Zandt, G., Tavera, H., and Minaya, E. (2017). Lowermost mantle anisotropy near the eastern edge of the Pacific LLSVP: constraints from SKS–SKKS splitting intensity measurements. *Geophysical Journal International*, 210(2):774–786. https://doi.org/10.1093/gji/ggx190.

Dziewonski, A. M. and Anderson, D. L. (1981). Preliminary reference Earth model. *Physics of the Earth and Planetary Interiors*, 25(4):297–356. https://doi.org/10.1016/0031-9201(81)90046-7.

Eakin, C. M., Wirth, E. A., Wallace, A., Ulberg, C. W., Creager, K. C., and Abers, G. A. (2019). SKS Splitting Beneath Mount St. Helens: Constraints on Subslab Mantle Entrainment. *Geochemistry, Geophysics, Geosystems*, 20(8):4202–4217. https://doi.org/10.1029/2019GC008433.

Eckhardt, C. and Rabbel, W. (2011). P-receiver functions of anisotropic continental crust: a hierarchic catalogue of crustal models and azimuthal waveform patterns: Azimuthal P-receiver function patterns. *Geophysical Journal International*, 187(1):439–479. https://doi.org/10.1111/j.1365-246X.2011.05159.x.

Einstein, A. (1916). Die Grundlage der allgemeinen Relativitätstheorie. *Annalen der Physik*, 354(7):769–822. https://doi.org/10.1002/andp.19163540702.

Eisbacher, G. H. and Fielitz, W. (2010). Karlsruhe und seine Region. *Sammlung Geologischer Führer*, 103. Gebrüder Bornträger, Stuttgart.

Ekström, G., Nettles, M., and Dziewoński, A. M. (2012). The global CMT project 2004–2010: Centroid-moment tensors for 13,017 earthquakes. *Physics of the Earth and Planetary Interiors*, 200–201:1–9. https://doi.org/10.1016/j.pepi.2012.04.002.

Enderle, U., Mechie, J., Sobolev, S., and Fuchs, K. (1996). Seismic anisotropy within the uppermost mantle of southern Germany. *Geophysical Journal International*, 125(3):747–767. https://doi.org/10.1111/j.1365-246X.1996.tb06021.x.

Evans, M. S., Kendall, J.-M., and Willemann, R. J. (2006). Automated SKS splitting and upper-mantle anisotropy beneath Canadian seismic stations. *Geophysical Journal International*, 165(3):931–942. https://doi.org/10.1111/j.1365-246X.2006.02973.x.

Favier, N. and Chevrot, S. (2003). Sensitivity kernels for shear wave splitting in transverse isotropic media. *Geophysical Journal International*, 153(1):213–228. https://doi.org/10.1046/j.1365-246X.2003.01894.x.

Federal Institute for Geosciences and Natural Resources (1976). German Regional Seismic Network (GRSN). *Bundesanstalt für Geowissenschaften und Rohstoffe*. https://doi.org/10.25928/mbx6-hr74.

Fernando, B., Wolf, J., Leng, K., Nissen-Meyer, T., Eaton, W., Styczinski, M., Walker, A., Craig, T., Muir, J., Nunn, C., and Long, M. (2024). AxiSEM3D - an introduction to using the code and its applications. *Earth ArXiv*. https://doi.org/10.31223/X5TH7P.

Forsyth, D. W. (1975). The Early Structural Evolution and Anisotropy of the Oceanic Upper Mantle. *Geophysical Journal International*, 43(1):103–162. https://doi.org/10.1111/j.1365-246X.1975.tb00630.x.

Fouch, M. J., Fischer, K. M., Parmentier, E. M., Wysession, M. E., and Clarke, T. J. (2000). Shear wave splitting, continental keels, and patterns of mantle flow. *Journal of Geophysical Research: Solid Earth*, 105(B3):6255–6275. https://doi.org/10.1029/1999JB900372.

Fouch, M. J. and Rondenay, S. (2006). Seismic anisotropy beneath stable continental interiors. *Physics of the Earth and Planetary Interiors*, 158(2–4):292–320. https://doi.org/10.1016/j.pepi.2006.03.024.

Frost, D. A., Lasbleis, M., Chandler, B., and Romanowicz, B. (2021). Dynamic history of the inner core constrained by seismic anisotropy. *Nature Geoscience*, 14(7):531–535. https://doi.org/10.1038/s41561-021-00761-w.

Fröhlich, Y. (2020). Scherwellen-Doppelbrechung von SK(K)S-Phasen und lateral variierende Anisotropie im Gebiet des Oberrheingrabens. *Master thesis, Geophysical Institute (GPI), Karlsruhe Institute of Technology (KIT).* KITopen, https://doi.org/10.5445/IR/1000165525.

Fröhlich, Y. (2024). Temporal Alignment of Seismic Traces in SplitLab (v2.0). *Zenodo.* https://doi.org/10.5281/zenodo.13760807. Maintenance on GitHub at https://github.com/yvonnefroehlich/SplitLab-TemporalAlignment.

Fröhlich, Y. (2025a). Python Scripts and Jupyter Notebooks using PyGMT. *GitHub.* https://github.com/yvonnefroehlich/gmt-pygmt-plotting.

Fröhlich, Y. (2025b). Visualization and Modeling of Shear Wave Splitting (v2.0). *in preparation. Zenodo.* https://doi.org/10.5281/zenodo.13799086. Development on GitHub at https://github.com/yvonnefroehlich/sws-visualization-and-modeling.

Fröhlich, Y., Dillah, M. I. F., Dorn, F., and Ritter, J. R. R. (2024a). Investigation of seismic anisotropy in the D'' layer and at the CMB regarding intense magnetic flux regions. *18th Symposium of Study of the Earth's Deep Interior.* Poster available from Zenodo at https://doi.org/10.5281/zenodo.12658821.

Fröhlich, Y. and Grund, M. (2021). Temporal Alignment of Seismic Traces in SplitLab (v1.0). *Zenodo.* https://doi.org/10.5281/zenodo.5805030.

Fröhlich, Y. and Grund, M. (2022). Visualization and Modeling of Shear Wave Splitting (v1.0). *Zenodo.* https://doi.org/10.5281/zenodo.7213157.

Fröhlich, Y., Grund, M., and Ritter, J. R. R. (2022a). On the effects of wrongly aligned seismogram components for shear wave splitting analysis. *Annals of Geophysics*, 65(2). https://doi.org/10.4401/ag-8781. Source code available from GitHub at https://github.com/yvonnefroehlich/SplitLab-TemporalAlignment.

Fröhlich, Y., Grund, M., and Ritter, J. R. R. (2024b). Lateral and vertical variations of seismic anisotropy in the lithosphere–asthenosphere system underneath Central Europe from long-term splitting measurements. *Geophysical Journal International*, 239(1):112–135. https://doi.org/10.1093/gji/ggae245.

Fröhlich, Y., Grund, M., and Ritter, J. R. R. (2024c). Longterm Shear Wave Splitting Measurements in the Upper Rhine Graben Area. *RADAR4KIT.* https://dx.doi.org/10.35097/685.

Fröhlich, Y. and Ritter, J. (2024). Vertical and Small-scale Lateral Varying Seismic Anisotropy in the Upper Mantle Underneath the Upper Rhine Graben, Central Europe. *Annual Meeting of the American Geophysical Union.* Abstract ID 1578275 https://agu.confex.com/agu/agu24/meetingapp.cgi/Paper/1578275. Sides available from Zenodo at https://doi.org/10.5281/zenodo.14510993.

Fröhlich, Y., Ritter, J. R. R., Sanz Alonso, Y., and Grund, M. (2022b). Longterm Shear Wave Splitting Measurements at the Black Forest Observatory. *RADAR4KIT.* https://dx.doi.org/10.35097/684.

Fröhlich, Y., Tian, D., Leong, W. J., Jones, M., and Grund, M. (2024d). PyGMT – Accessing and Integrating GMT with Python and the Scientific Python Ecosystem (AGU24, U12B-05). *Annual Meeting of the American Geophysical Union.* Abstract ID 1578856 https://agu.confex.com/agu/agu24/meetingapp.cgi/Paper/1578856. Sides available from figshare at https://doi.org/10.6084/m9.figshare.28049495.

Fuchs, K. (1983). Recently formed elastic anisotropy and petrological models for the continental subcrustal lithosphere in southern Germany. *Physics of the Earth and Planetary Interiors*, 31(2):93–118. https://doi.org/10.1016/0031-9201(83)90103-6.

Fuchs, K., Bonjer, K.-P., Gajewski, D., Lüschen, E., Prodehl, C., Sandmeier, K.-J., Wenzel, F., and Wilhelm, H. (1987). Crustal evolution of the Rhinegraben area. 1. Exploring the lower crust in the Rhinegraben rift by unified geophysical experiments. *Tectonophysics*, 141(1–3):261–275. 10.1016/0040-1951(87)90190-9.

GEOFON Data Centre (1993). GEOFON (GeoForschungsNetz) Seismic Network. *Deutsches GeoForschungsZentrum (GFZ)*. https://doi.org/10.14470/TR560404.

GEOSCOPE (1982). French Global Network of broad band seismic stations. *Institut de physique du globe de Paris (IPGP) & Ecole et Observatoire des Sciences de la Terre de Strasbourg (EOST)*. https://doi.org/10.18715/GEOSCOPE.G.

Glahn, A. and Granet, M. (1992). 3-D structure of the lithosphere beneath the southern Rhine Graben area. *Tectonophysics*, 208(1–3):149–158. https://doi.org/10.1016/0040-1951(92)90341-3.

Glahn, A., Granet, M., and Rhine Graben Teleseismic Group (1993). Southern Rhine Graben: small-wavelength tomographic study and implications for the dynamic evolution of the graben. *Geophysical Journal International*, 113(2):399–418. https://doi.org/10.1111/j.1365-246X.1993.tb00896.x.

Granet, M., Glahn, A., and Achauer, U. (1998). Anisotropic Measurements in the Rhinegraben Area and the French Massif Central: Geodynamic Implications. *Pure and Applied Geophysics*, 151(2–4):333–364. https://doi.org/10.1007/s000240050117.

Grimmer, J. C., Ritter, J. R. R., Eisbacher, G. H., and Fielitz, W. (2017). The Late Variscan control on the location and asymmetry of the Upper Rhine Graben. *International Journal of Earth Sciences*, 106(3):827–853. https://doi.org/10.1007/s00531-016-1336-x.

Gripp, A. E. and Gordon, R. G. (2002). Young tracks of hotspots and current plate velocities. *Geophysical Journal International*, 150(2):321–361. https://doi.org/10.1046/j.1365-246X.2002.01627.x.

Grund, M. (2017). StackSplit - a plugin for multi-event shear wave splitting analyses in SplitLab. *Computers & Geosciences*, 105:43–50. https://doi.org/10.1016/j.cageo.2017.04.015. Source code available from GitHub at https://github.com/michaelgrund/stacksplit.

Grund, M. and Fröhlich, Y. (2021). StackSplit (v3.0). *Zenodo*. https://doi.org/10.5281/zenodo.5802051.

Grund, M., Mauerberger, A., Ritter, J. R. R., and Tilmann, F. (2017). Broadband Recordings for LITHOS-CAPP: LITHOspheric Structure of Caledonian, Archaean and Proterozoic Provinces, Sep. 2014 - Oct. 2016, Sweden and Finland. Scientific Technical Report STR - Data; 17/02. GIPP Experiment and Data Archive. *Potsdam : GFZ German Research Centre for Geosciences*. https://doi.org/10.2312/GFZ.b103-17029.

Grund, M. and Ritter, J. R. R. (2019). Widespread seismic anisotropy in Earth's lowermost mantle beneath the Atlantic and Siberia. *Geology*, 47(2):123–126. https://doi.org/10.1130/G45514.1.

Grund, M. and Ritter, J. R. R. (2020). Shear-wave splitting beneath Fennoscandia — evidence for dipping structures and laterally varying multilayer anisotropy. *Geophysical Journal International*, 223(3):1525–1547. https://doi.org/10.1093/gji/ggaa388.

Heimann, S., Kriegerowski, M., Isken, M., Cesca, S., Daout, S., Grigoli, F., Juretzek, C., Megies, T., Nooshiri, N., Steinberg, A., Sudhaus, H., Vasyura-Bathke, H., Willey, T., and Dahm, T. (2017). Pyrocko - An open-source seismology toolbox and library. *GFZ Data Services*. https://doi.org/10.5880/GFZ.2.1.2017.001.

Hein, G., Kolínsky, P., Bianchi, I., Bokelmann, G., and the AlpArray Working Group (2021). Shear wave splitting in the Alpine region. *Geophysical Journal International*, 227(3):1996–2015. https://doi.org/10.1093/gji/ggab305.

Helffrich, G. (1995). Lithospheric deformation inferred from teleseismic shear wave splitting observations in the United Kingdom. *Journal of Geophysical Research: Solid Earth*, 100(B9):18195–18204. https://doi.org/10.1029/95JB01572.

Hess, H. H. (1964). Seismic Anisotropy of the Uppermost Mantle under Oceans. *Nature*, 203(4945):629–631. https://doi.org/10.1038/203629a0.

Hetényi, G., Molinari, I., Clinton, J., Bokelmann, G., Bondár, I., Crawford, W. C., Dessa, J.-X., Doubre, C., Friederich, W., Fuchs, F., Giardini, D., Gráczer, Z., Handy, M. R., Herak, M., Jia, Y., Kissling, E., Kopp, H., Korn, M., Margheriti, L., Meier, T., Mucciarelli, M., Paul, A., Pesaresi, D., Piromallo, C., Plenefisch, T., Plomerová, J., Ritter, J., Rümpker, G., Šipka, V., Spallarossa, D., Thomas, C., Tilmann, F., Wassermann, J., Weber, M., Wéber, Z., Wesztergom, V., and Živčić, M. (2018). The AlpArray Seismic Network: A Large-Scale European Experiment to Image the Alpine Orogen. *Surveys in Geophysics*, 39(5):1009–1033. https://doi.org/10.1007/s10712-018-9472-4.

Hudson, J. (1980). The Excitation and Propagation of Elastic Waves. *Cambridge UniversityPress, Cambridge, U.K.*

Hudson, T. S., Asplet, J., and Walker, A. M. (2023). Automated shear-wave splitting analysis for single- and multi-layer anisotropic media. *Seismica*, 2(2). https://doi.org/10.26443/seismica.v2i2.1031.

Hunter, J. D. (2007). Matplotlib: A 2D Graphics Environment. *Computing in Science & Engineering*, 9(3):90–95. https://doi.org/10.1109/MCSE.2007.55.

Immoor, J., Marquardt, H., Miyagi, L., Lin, F., Speziale, S., Merkel, S., Buchen, J., Kurnosov, A., and Liermann, H.-P. (2018). Evidence for 100<011> slip in ferropericlase in Earth's lower mantle from high-pressure/high-temperature experiments. *Earth and Planetary Science Letters*, 489:251–257. https://doi.org/10.1016/j.epsl.2018.02.045.

Jung, H., Katayama, I., Jiang, Z., Hiraga, T., and Karato, S. (2006). Effect of water and stress on the lattice-preferred orientation of olivine. *Tectonophysics*, 421(1–2):1–22. https://doi.org/10.1016/j.tecto.2006.02.011.

Juretzek, C. and Hadziioannou, C. (2016). Where do ocean microseisms come from? A study of Love-to-Rayleigh wave ratios. *Journal of Geophysical Research: Solid Earth*, 121(9):6741–6756. https://doi.org/10.1002/2016JB013017.

Kaminski, E. (2006). Interpretation of seismic anisotropy in terms of mantle flow when melt is present. *Geophysical Research Letters*, 33(2). https://doi.org/10.1029/2005GL024454.

Kaminski, E., Ribe, N. M., and Browaeys, J. T. (2004). D-Rex, a program for calculation of seismic anisotropy due to crystal lattice preferred orientation in the convective upper mantle. *Geophysical Journal International*, 158(2):744–752. https://doi.org/10.1111/j.1365-246X.2004.02308.x.

Karato, S.-i., Jung, H., Katayama, I., and Skemer, P. (2008). Geodynamic Significance of Seismic Anisotropy of the Upper Mantle: New Insights from Laboratory Studies. *Annual Review of Earth and Planetary Sciences*, 36(1):59–95. https://doi.org/10.1146/annurev.earth.36.031207.124120.

Karato, S.-i. and Wu, P. (1993). Rheology of the Upper Mantle: A Synthesis. *Science*, 260(5109):771–778. https://doi.org/10.1126/science.260.5109.771.

Kennett, B. L. N. and Engdahl, E. R. (1991). Traveltimes for global earthquake location and phase identification. *Geophysical Journal International*, 105(2):429–465. https://doi.org/10.1111/j.1365-246X.1991.tb06724.x.

Kennett, B. L. N. . E. E. R. (1991). IASPEI 1991 seismological tables. *Terra Nova*, 3(2):122–122. https://doi.org/10.1111/j.1365-3121.1991.tb00863.x.

Kenyon, L. M. and Wada, I. (2025). Freezing of Crystal Preferred Orientation in the Mantle Wedge Corner and Shear Wave Splitting. *Journal of Geophysical Research: Solid Earth*, 130(4). https://doi.org/10.1029/2024JB030062.

Kirschner, S., Ritter, J., and Wawerzinek, B. (2011). Teleseismic wave front anomalies at a Continental Rift: no mantle anomaly below the central Upper Rhine Graben: Teleseismic Wave front Anomalies at URG. *Geophysical Journal International*, 186(2):447–462. https://doi.org/10.1111/j.1365-246X.2011.05071.x.

Komatitsch, D. and Tromp, J. (2002a). Spectral-element simulations of global seismic wave propagation-I. Validation. *Geophysical Journal International*, 149(2):390–412. https://doi.org/10.1046/j.1365-246X.2002.01653.x.

Komatitsch, D. and Tromp, J. (2002b). Spectral-element simulations of global seismic wave propagation-II. Three-dimensional models, oceans, rotation and self-gravitation. *Geophysical Journal International*, 150(1):303–318. https://doi.org/10.1046/j.1365-246X.2002.01716.x.

Kong, F., Wu, J., Liu, K. H., and Gao, S. S. (2016). Crustal anisotropy and ductile flow beneath the eastern Tibetan Plateau and adjacent areas. *Earth and Planetary Science Letters*, 442:72–79. https://doi.org/10.1016/j.epsl.2016.03.003.

Kreemer, C., Blewitt, G., and Klein, E. C. (2014). A geodetic plate motion and Global Strain Rate Model. *Geochemistry, Geophysics, Geosystems*, 15(10):3849–3889. https://doi.org/10.1002/2014GC005407.

Krischer, L., Megies, T., Barsch, R., Beyreuther, M., Lecocq, T., Caudron, C., and Wassermann, J. (2015). ObsPy: a bridge for seismology into the scientific Python ecosystem. *Computational Science & Discovery*, 8(1):014003. https://iopscience.iop.org/article/10.1088/1749-4699/8/1/014003.

Legendre, C. P., Meier, T., Lebedev, S., Friederich, W., and Viereck-Götte, L. (2012). A shear wave velocity model of the European upper mantle from automated inversion of seismic shear and surface waveforms: S-velocity model of the European upper mantle. *Geophysical Journal International*, 191(1):282–304. https://doi.org/10.1111/j.1365-246X.2012.05613.x.

Lehmann, I. (1936). P'. *Bureau Central Séismologique International Strasbourg: Publications du Bureau Central Scientifiques*, 14:87–115.

Leng, K., Korenaga, J., and Nissen-Meyer, T. (2020). 3-D scattering of elastic waves by small-scale heterogeneities in the Earth's mantle. *Geophysical Journal International*, 223(1):502–525. https://doi.org/10.1093/gji/ggaa331.

Leng, K., Nissen-Meyer, T., and van Driel, M. (2016). Efficient global wave propagation adapted to 3-D structural complexity: a pseudospectral/spectral-element approach. *Geophysical Journal International*, 207(3):1700–1721. https://doi.org/10.1093/gji/ggw363.

Leng, K., Nissen-Meyer, T., van Driel, M., Hosseini, K., and Al-Attar, D. (2019). AxiSEM3D: broad-band seismic wavefields in 3-D global earth models with undulating discontinuities. *Geophysical Journal International*, 217(3):2125–2146. https://doi.org/10.1093/gji/ggz092.

Leong, W. J., Fröhlich, Y., Tong, J.-H., Esteban, F., Jones, M., and Belem, A. L. (2024). Mastering Geospatial Visualizations with GMT/PyGMT. *Zenodo*. https://doi.org/10.5281/zenodo.15809716.

Liddell, M. V., Bastow, I., Darbyshire, F., Gilligan, A., and Pugh, S. (2017). The formation of Laurentia: Evidence from shear wave splitting. *Earth and Planetary Science Letters*, 479:170–178. https://doi.org/10.1016/j.epsl.2017.09.030.

Lin, Y., Zhao, L., and Hung, S. (2014). Full-wave effects on shear wave splitting. *Geophysical Research Letters*, 41(3):799–804. https://doi.org/10.1002/2013GL058742.

Link, F., Reiss, M. C., and Rümpker, G. (2022). An automatized XKS-splitting procedure for large data sets: Extension package for SplitRacer and application to the USArray. *Computers & Geosciences*, 158:104961. 10.1016/j.cageo.2021.104961.

Link, F. and Rümpker, G. (2021). Resolving Seismic Anisotropy of the Lithosphere–Asthenosphere in the Central/Eastern Alps Beneath the SWATH-D Network. *Frontiers in Earth Science*, 9. https://doi.org/10.3389/feart.2021.679887.

Link, F. and Rümpker, G. (2023). Shear-Wave Splitting Reveals Layered-Anisotropy Beneath the European Alps in Response to Mediterranean Subduction. *Journal of Geophysical Research: Solid Earth*, 128(9). https://doi.org/10.1029/2023JB027192.

Liu, K. H. and Gao, S. S. (2013). Making Reliable Shear-Wave Splitting Measurements. *Bulletin of the Seismological Society of America*, 103(5):2680–2693. https://doi.org/10.1785/0120120355.

Long, M. D. (2009). Complex anisotropy in D'' beneath the eastern Pacific from SKS–SKKS splitting discrepancies. *Earth and Planetary Science Letters*, 283(1–4):181–189. https://doi.org/10.1016/j.epsl.2009.04.019.

Long, M. D. and Becker, T. W. (2010). Mantle dynamics and seismic anisotropy. *Earth and Planetary Science Letters*, 297(3–4):341–354. https://doi.org/10.1016/j.epsl.2010.06.036.

Long, M. D. and Lynner, C. (2015). Seismic anisotropy in the lowermost mantle near the Perm Anomaly. *Geophysical Research Letters*, 42(17):7073–7080. https://doi.org/10.1002/2015gl065506.

Long, M. D. and Silver, P. G. (2009). Shear Wave Splitting and Mantle Anisotropy: Measurements, Interpretations, and New Directions. *Surveys in Geophysics*, 30(4–5):407–461. https://doi.org/10.1007/s10712-009-9075-1.

Long, M. D. and van der Hilst, R. D. (2005). Estimating Shear-Wave Splitting Parameters from Broadband Recordings in Japan: A Comparison of Three Methods. *Bulletin of the Seismological Society of America*, 95(4):1346–1358. https://doi.org/10.1785/0120040107.

Lynner, C. and Long, M. D. (2012). Evaluating Contributions to SK(K)S Splitting from Lower Mantle Anisotropy: A Case Study from Station DBIC, Cote D'Ivoire. *Bulletin of the Seismological Society of America*, 102(3):1030–1040. https://doi.org/10.1785/0120110255.

Lüschen, E., Nolte, B., and Fuchs, K. (1990). Shear-wave evidence for an anisotropic lower crust beneath the Black Forest, southwest Germany. *Tectonophysics*, 173(1–4):483–493. https://doi.org/10.1016/0040-1951(90)90240-9.

Mainprice, D. (2007). Seismic Anisotropy of the Deep Earth from a Mineral and Rock Physics Perspective. *Treatise on Geophysics, Elsevier*, pages 437–491. https://doi.org/10.1016/B978-044452748-6.00045-6.

Mainprice, D. and Silver, P. G. (1993). Interpretation of SKS-waves using samples from the subcontinental lithosphere. *Physics of the Earth and Planetary Interiors*, 78(3–4):257–280. https://doi.org/10.1016/0031-9201(93)90160-B.

Mainprice, D., Tommasi, A., Couvy, H., Cordier, P., and Frost, D. J. (2005). Pressure sensitivity of olivine slip systems and seismic anisotropy of Earth's upper mantle. *Nature*, 433(7027):731–733. https://doi.org/10.1038/nature03266.

Margheriti, L., Baccheschi, P., and Park, J. (2021). Seismic Anisotropy. *Encyclopedia of Geology (Second Edition)*, pages 622–635. https://doi.org/10.1016/B978-0-08-102908-4.00156-9.

Margheriti, L., Lucente, F. P., and Pondrelli, S. (2003). SKS splitting measurements in the Apenninic-Tyrrhenian domain (Italy) and their relation with lithospheric subduction and mantle convection. *Journal of Geophysical Research: Solid Earth*, 108(B4). https://doi.org/10.1029/2002JB001793.

Matte, P. (2001). The Variscan collage and orogeny (480–290 Ma) and the tectonic definition of the Armorica microplate: a review. *Terra Nova*, 13(2):122–128. https://doi.org/10.1046/j.1365-3121.2001.00327.x.

Maupin, V. and Park, J. (2007). Theory and Observations – Wave Propagation in Anisotropic Media. *Treatise on Geophysics*, 1:289–321. https://doi.org/10.1016/B978-044452748-6.00007-9.

McNamara, A. K. (2019). A review of large low shear velocity provinces and ultra low velocity zones. *Tectonophysics*, 760:199–220. https://doi.org/10.1016/j.tecto.2018.04.015.

Megies, T., Beyreuther, M., Barsch, R., Krischer, L., and Wassermann, J. (2011). ObsPy – What can it do for data centers and observatories? *Annals of Geophysics*, 54(1). https://doi.org/10.4401/ag-4838.

Meier, L. and Eisbacher, G. H. (1991). Crustal kinematics and deep structureof the northern Rhine graben, Germany. *Tectonics*, 10:621–630.

Meier, T., Soomro, R. A., Viereck, L., Lebedev, S., Behrmann, J. H., Weidle, C., Cristiano, L., and Hanemann, R. (2016). Mesozoic and Cenozoic evolution of the Central European lithosphere. *Tectonophysics*, 692:58–73. https://doi.org/10.1016/j.tecto.2016.09.016.

Merle, O. (2011). A simple continental rift classification. *Tectonophysics*, 513(1–4):88–95. https://doi.org/10.1016/j.tecto.2011.10.004.

Meschede, M. and Warr, L. N. (2019). The Geology of Germany: A Process-Oriented Approach. *Regional Geology Reviews*. https://doi.org/10.1007/978-3-319-76102-2.

Moore, M. M., Garnero, E. J., Lay, T., and Williams, Q. (2004). Shear wave splitting and waveform complexity for lowermost mantle structures with low-velocity lamellae and transverse isotropy. *Journal of Geophysical Research: Solid Earth*, 109(B2). https://doi.org/10.1029/2003JB002546.

Mousavi, S. M., Ellsworth, W. L., Zhu, W., Chuang, L. Y., and Beroza, G. C. (2020). Earthquake transformer—an attentive deep-learning model for simultaneous earthquake detection and phase picking. *Nature Communications*, 11(1). https://doi.org/10.1038/s41467-020-17591-w.

Nissen-Meyer, T., van Driel, M., Stähler, S. C., Hosseini, K., Hempel, S., Auer, L., Colombi, A., and Fournier, A. (2014). AxiSEM: broadband 3-D seismic wavefields in axisymmetric media. *Solid Earth*, 5(1):425–445. https://doi.org/10.5194/se-5-425-2014.

Nowacki, A. (2019). SeisSplit. *GitHub*. https://github.com/anowacki/SeisSplit.jl.

Nowacki, A. and Cottaar, S. (2021). Toward Imaging Flow at the Base of the Mantle with Seismic, Mineral Physics, and Geodynamic Constraints. *Mantle Convection and Surface Expressions*, pages 329–352. https://doi.org/10.1002/9781119528609.ch13.

Nowacki, A., Wookey, J., and Kendall, J.-M. (2011). New advances in using seismic anisotropy, mineral physics and geodynamics to understand deformation in the lowermost mantle. *Journal of Geodynamics*, 52(3–4):205–228. https://doi.org/10.1016/j.jog.2011.04.003.

Oldham, R. D. (1906). The Constitution of the Interior of the Earth, as Revealed by Earthquakes. *Quarterly Journal of the Geological Society of London*, 62(1–4):456–475. https://doi.org/10.1144/GSL.JGS.1906.062.01-04.21.

Panning, M. and Romanowicz, B. (2006). A three-dimensional radially anisotropic model of shear velocity in the whole mantle. *Geophysical Journal International*, 167(1):361–379. https://doi.org/10.1111/j.1365-246X.2006.03100.x.

Panton, J., Davies, J. H., Koelemeijer, P., Myhill, R., and Ritsema, J. (2025). Unique composition and evolutionary histories of large low velocity provinces. *Scientific Reports*, 15(1). https://doi.org/10.1038/s41598-025-88931-3.

Pearce, J. and Mittleman, D. (2002). Defining the Fresnel zone for broadband radiation. *Physical Review E*, 66(5). https://doi.org/10.1103/PhysRevE.66.056602.

Petrescu, L., Pondrelli, S., Salimbeni, S., and Faccenda, M. (2020). Mantle flow below the central and greater Alpine region: insights from SKS anisotropy analysis at AlpArray and permanent stations. *Solid Earth*, 11(4):1275–1290. https://doi.org/10.5194/se-11-1275-2020.

Pisconti, A., Creasy, N., Wookey, J., Long, M. D., and Thomas, C. (2022). Mineralogy, fabric and deformation domains in D" across the southwestern border of the African LLSVP. *Geophysical Journal International*, 232(1):705–724. https://doi.org/10.1093/gji/ggac359.

Plesinger, A., Hellweg, M., and Seidl, D. (1986). Interactive high-resolutionpolarization analysis of broad-band seismograms. *Journal of Geophysics*, 59(1):129–139.

Porritt, R. W. (2014). SplitLab (1.2.1). *Wordpress*. https://robporritt.wordpress.com/software/.

Prodehl, C., Mueller, S., Glahn, A., Gutscher, M., and Haak, V. (1992). Lithospheric cross sections of the European Cenozoic rift system. *Tectonophysics*, 208(1–3):113–138. https://doi.org/10.1016/0040-1951(92)90339-8.

Qiang, Z., Wu, Q., Li, Y., and Zhang, F. (2022). Varying Shear Wave Splitting Parameters Suggest Interaction Between Lithosphere and Asthenosphere in Arxan-Chaihe Volcanic Field, NE China. *Geophysical Research Letters*, 49(14). https://doi.org/10.1029/2022GL099129.

Reiss, M. C., Long, M. D., and Creasy, N. (2019). Lowermost Mantle Anisotropy Beneath Africa From Differential SKS-SKKS Shear-Wave Splitting. *Journal of Geophysical Research: Solid Earth*, 124(8):8540–8564. https://doi.org/10.1029/2018JB017160.

Reiss, M. C. and Rümpker, G. (2017). SplitRacer: MATLAB Code and GUI for Semiautomated Analysis and Interpretation of Teleseismic Shear-Wave Splitting. *Seismological Research Letters*, 88(2A):392–409. https://doi.org/10.1785/0220160191.

RESIF (1995). Epos-France Broad-band network (RLBP). *Epos-France Seismological Data Centre*. https://doi.org/10.15778/RESIF.FR.

Restivo, A. and Helffrich, G. (1999). Teleseismic shear wave splitting measurements in noisyenvironments. *Geophysical Journal International*, 137(3):821–830. https://doi.org/10.1046/j.1365-246x.1999.00845.x.

Ring, U. and Bolhar, R. (2020). Tilting, uplift, volcanism and disintegration of the South German block. *Tectonophysics*, 795:228611. https://doi.org/10.1016/j.tecto.2020.228611.

Ritter, J. R. R., Fröhlich, Y., Sanz Alonso, Y., and Grund, M. (2022). Short-scale laterally varying SK(K)S shear wave splitting at BFO, Germany — implications for the determination of anisotropic structures. *Journal of Seismology*, 26(6):1137–1156. https://doi.org/10.1007/s10950-022-10112-w. Correction regarding the initially missing supplementary information https://doi.org/10.1007/s10950-023-10136-w.

Ritter, J. R. R., Grund, M., and Sanz Alonso, Y. (2018). Laterally varying deep seismic anisotropy around the Black Forest Observatory, Germany. *Geophysical Research Abstracts*, 20(EGU2018-3403). https://meetingorganizer.copernicus.org/EGU2018/EGU2018-3403.pdf.

Romanowicz, B. and Wenk, H.-R. (2017). Anisotropy in the deep Earth. *Physics of the Earth and Planetary Interiors*, 269:58–90. https://doi.org/10.1016/j.pepi.2017.05.005.

Romanowicz, B. and Yuan, H. (2012). On the interpretation of SKS splitting measurements in the presence of several layers of anisotropy: Interpretation of SKS splitting measurements. *Geophysical Journal International*, 188(3):1129–1140. https://doi.org/10.1111/j.1365-246X.2011.05301.x.

Rost, S. and Thomas, C. (2002). ARRAY SEISMOLOGY: METHODS AND APPLICATIONS. *Reviews of Geophysics*, 40(3). https://doi.org/10.1029/2000RG000100.

Roy, C., Winter, A., Ritter, J. R. R., and Schweitzer, J. (2017). On the improvement of SKS splitting measurements by the Simultaneous Inversion of Multiple Waveforms (SIMW). *Geophysical Journal International*, 208(3):1508–1523. https://doi.org/10.1093/gji/ggw470.

Sanz Alonso, Y. (2017). Bestimmung von SKS-Splitting-Parametern und Anisotropiemodellenim Bereich des Oberrheingrabens. *Master thesis, Geophysical Institute (GPI), Karlsruhe Institute of Technology (KIT)*.

Savage, M. K. (1999). Seismic anisotropy and mantle deformation: What have we learned from shear wave splitting? *Reviews of Geophysics*, 37(1):65–106. https://doi.org/10.1029/98RG02075.

Schwarz, M. and Henk, A. (2005). Evolution and structure of the Upper Rhine Graben: insights from three-dimensional thermomechanical modelling. *International Journal of Earth Sciences*, 94(4):732–750. https://doi.org/10.1007/s00531-004-0451-2.

Seiberlich, C. K. A., Ritter, J. R. R., and Wawerzinek, B. (2013). Topography of the lithosphere–asthenosphere boundary below the Upper Rhine Graben Rift and the volcanic Eifel region, Central Europe. *Tectonophysics*, 603:222–236. https://doi.org/10.1016/j.tecto.2013.05.034.

Shearer, P. M. (2009). Introduction to Seismology, SECOND EDITION. *Cambrigde University Press*. ISBN-13: 978-0-521-88210-1 (Hardback), 978-0-521-70842-5 (Paperback), 978-0-511-58010-9 (eBook EBL).

Sieminski, A., Paulssen, H., Trampert, J., and Tromp, J. (2008). Finite-Frequency SKS Splitting: Measurement and Sensitivity Kernels. *Bulletin of the Seismological Society of America*, 98(4):1797–1810. https://doi.org/10.1785/0120070297.

Silver, P. G. (1996). SEISMIC ANISOTROPY BENEATH THE CONTINENTS: Probing the Depths of Geology. *Annual Review of Earth and Planetary Sciences*, 24(1):385–432. https://doi.org/10.1146/annurev.earth.24.1.385.

Silver, P. G. and Chan, W. W. (1988). Implications for continental structure and evolution from seismic anisotropy. *Nature*, 335(6185):34–39. https://doi.org/10.1038/335034a0.

Silver, P. G. and Chan, W. W. (1991). Shear wave splitting and subcontinental mantle deformation. *Journal of Geophysical Research: Solid Earth*, 96(B10):16429–16454. https://doi.org/10.1029/91JB00899.

Silver, P. G. and Savage, M. K. (1994). The Interpretation of Shear-Wave Splitting Parameters In the Presence of Two Anisotropic Layers. *Geophysical Journal International*, 119(3):949–963. https://doi.org/10.1111/j.1365-246X.1994.tb04027.x.

Simmons, N. A., Forte, A. M., Boschi, L., and Grand, S. P. (2010). GyPSuM: A joint tomographic model of mantle density and seismic wave speeds. *Journal of Geophysical Research: Solid Earth*, 115(B12). https://doi.org/10.1029/2010JB007631.

Skemer, P. and Hansen, L. N. (2016). Inferring upper-mantle flow from seismic anisotropy: An experimental perspective. *Tectonophysics*, 668–669:1–14. https://doi.org/10.1016/j.tecto.2015.12.003.

Song, L.-P., Koch, M., Koch, K., and Schlittenhardt, J. (2004). 2-D anisotropicPn-velocity tomography underneath Germany using regional traveltimes. *Geophysical Journal International*, 157(2):645–663. https://doi.org/10.1111/j.1365-246X.2004.02171.x.

Tait, J. A., Bachtadse, V., Franke, W., and Soffel, H. C. (1997). Geodynamic evolution of the European Variscan fold belt: palaeomagnetic and geological constraints. *Geologische Rundschau*, 86(3):585. https://doi.org/10.1007/s005310050165.

Tesoniero, A., Leng, K., D. Long, M., and Nissen-Meyer, T. (2020). Full wave sensitivity of SK(K)S phases to arbitrary anisotropy in the upper and lower mantle. *Geophysical Journal International*, 222(1):412–435. https://doi.org/10.1093/gji/ggaa171.

The ObsPy Development Team (2020). ObsPy (1.2.2). *Zenodo*. https://doi.org/10.5281/zenodo.3921997.

Thissen, C. (2015). Drex-MATLAB. *GitHub*. available at https://github.com/cthissen/Drex-MATLAB.

Thyng, K., Greene, C., Hetland, R., Zimmerle, H., and DiMarco, S. (2016). True Colors of Oceanography: Guidelines for Effective and Accurate Colormap Selection. *Oceanography*, 29(3):9–13. https://doi.org/10.5670/oceanog.2016.66.

Tian, D., Uieda, L., Leong, W. J., Fröhlich, Y., Grund, M., Schlitzer, W., Jones, M., Toney, L., Yao, J., Tong, J.-H., Magen, Y., Materna, K., Belem, A., Newton, T., Anant, A., Ziebarth, M., Quinn, J., and Wessel, P. (2025a). PyGMT: A Python interface for the Generic Mapping Tools (v0.16.0). *Zenodo*. https://doi.org/10.5281/zenodo.15628725.

Tian, D., Uieda, L., Leong, W. J., Fröhlich, Y., Schlitzer, W., Grund, M., Jones, M., Toney, L., Yao, J., Magen, Y., Tong, J.-H., Materna, K., Belem, A., Newton, T., Anant, A., Ziebarth, M., Quinn, J., and Wessel, P. (2024). PyGMT: A Python interface for the Generic Mapping Tools (v0.12.0). *Zenodo*. https://doi.org/10.5281/zenodo.11062720.

Tian, D., Uieda, L., Leong, W. J., Fröhlich, Y., Schlitzer, W., Grund, M., Jones, M., Toney, L., Yao, J., Tong, J.-H., Magen, Y., Materna, K., Belem, A., Newton, T., Anant, A., Ziebarth, M., Quinn, J., and Wessel, P. (2025b). PyGMT: A Python interface for the Generic Mapping Tools (v0.15.0). *Zenodo*. https://doi.org/10.5281/zenodo.15071586.

Uieda, L., Tian, D., Leong, W. J., Jones, M., Schlitzer, W., Grund, M., Toney, L., Yao, J., Magen, Y., Materna, K., Fröhlich, Y., Belem, A., Newton, T., Anant, A., Ziebarth, M., Quinn, J., and Wessel, P. (2022). PyGMT: A Python interface for the Generic Mapping Tools (v0.7.0). *Zenodo*. https://doi.org/10.5281/zenodo.6702566.

Uieda, L., Tian, D., Leong, W. J., Toney, L., Schlitzer, W., Grund, M., Newton, T., Ziebarth, M., Jones, M., and Wessel, P. (2021). PyGMT: A Python interface for the Generic Mapping Tool (v0.3.0). *Zenodo*. https://doi.org/10.5281/zenodo.4522136.

Vecsey, L., Plomerová, J., and Babuška, V. (2008). Shear-wave splitting measurements — Problems and solutions. *Tectonophysics*, 462(1–4):178–196. https://doi.org/10.1016/j.tecto.2008.01.021.

Vinnik, L. P., Krishna, V. G., Kind, R., Bormann, P., and Stammler, K. (1994). Shear wave splitting in the records of the German Regional Seismic Network. *Geophysical Research Letters*, 21(6):457–460. https://doi.org/10.1029/94GL00396.

Vinnik, L. P., Makeyeva, L. I., Milev, A., and Usenko, A. Y. (1992). Global patterns of azimuthal anisotropy and deformations in the con tinen t a1 mantle. *Geophysical Journal International*, 111:433–447.

Voigt, W. (1928). Lehrbuch der kristallphysik (mit ausschluss der kristalloptik). *Teubner, Leipzig, Germany*. ISBN-10: 3663153169, ISBN-13: 978-3663153160.

Wagner, M. (2007). Anisotropie-Untersuchungen am Mittleren Oberrheingraben. *Diplomarbeit, Geophysical Institute (GPI), University Karlsruhe (TH)*.

Walker, A. M. and Wookey, J. (2012). MSAT—A new toolkit for the analysis of elastic and seismic anisotropy. *Computers & Geosciences*, 49:81–90. http://dx.doi.org/10.1016/j.cageo.2012.05.031. Available at https://www1.gly.bris.ac.uk/MSAT/, https://github.com/andreww/MSAT.

Walker, K. T., Bokelmann, G. H. R., Klemperer, S. L., and Bock, G. (2005a). Shear-wave splitting around the Eifel hotspot: evidence for a mantle upwelling. *Geophysical Journal International*, 163(3):962–980. https://doi.org/10.1111/j.1365-246X.2005.02636.x.

Walker, K. T., Bokelmann, G. H. R., Klemperer, S. L., and Nyblade, A. (2005b). Shear wave splitting around hotspots: Evidence for upwelling-related mantle flow? *Geological Society of America*. https://doi.org/10.1130/0-8137-2388-4.171.

Walsh, E., Arnold, R., and Savage, M. K. (2013). Silver and Chan revisited. *Journal of Geophysical Research: Solid Earth*, 118(10):5500–5515. https://doi.org/10.1002/jgrb.50386.

Walther, M., Plenefisch, T., and Rümpker, G. (2014). Automated analysis of SKS splitting to infer upper mantle anisotropy beneath Germany using more than 20 yr of GRSN and GRF data. *Geophysical Journal International*, 196(2):1207–1236. https://doi.org/10.1093/gji/ggt456.

Waszek, L. (2024). Seismic methodologies key to unlocking Earth's lowermost mantle. *Nature Geoscience*, 17(4):272–274. https://doi.org/10.1038/s41561-024-01416-2.

Wenzel, F. and Brun, J.-P. (1991). A deep reflection seismic line across the Northern Rhine Graben. *Earth and Planetary Science Letters*, 104(2–4):140–150. https://doi.org/10.1016/0012-821X(91)90200-2.

Wessel, P., Luis, J. F., Uieda, L., Scharroo, R., Wobbe, F., Smith, W. H. F., and Tian, D. (2019). The Generic Mapping Tools Version 6. *Geochemistry, Geophysics, Geosystems*, 20(11):5556–5564. https://doi.org/10.1029/2019GC008515.

Wessel, P., Luis, J. F., Uieda, L., Scharroo, R., Wobbe, F., Smith, W. H. F., and Tian, D. (2020). The Generic Mapping Tools (6.1.1). *Zenodo*. https://doi.org/10.5281/zenodo.4010996.

Wessel, P., Luis, J. F., Uieda, L., Scharroo, R., Wobbe, F., Smith, W. H. F., Tian, D., Jones, M., and Esteban, F. (2022). The Generic Mapping Tools (6.4.0). *Zenodo*. https://doi.org/10.5281/zenodo.6623271.

Wessel, P., Luis, J. F., Uieda, L., Scharroo, R., Wobbe, F., Smith, W. H. F., Tian, D., Jones, M., and Esteban, F. (2024). The Generic Mapping Tools (6.5.0). *Zenodo*. https://doi.org/10.5281/zenodo.10119499.

White, S. M., Crisp, J. A., and Spera, F. J. (2006). Long-term volumetric eruption rates and magma budgets. *Geochemistry, Geophysics, Geosystems*, 7(3). https://doi.org/10.1029/2005GC001002.

Wolf, J., Becker, T. W., Garnero, E., Liu, K. H., and West, J. D. (2025). Comprehensive global data set of uniformly processed shear-wave splitting measurements. *Geophysical Journal International*, 241(2):863–875. https://doi.org/10.1093/gji/ggaf076.

Wolf, J., Creasy, N., Pisconti, A., Long, M. D., and Thomas, C. (2019). An investigation of seismic anisotropy in the lowermost mantle beneath Iceland. *Geophysical Journal International*, 219. https://doi.org/10.1093/gji/ggz312.

Wolf, J., Frost, D. A., Brewster, A., Long, M. D., Garnero, E., and West, J. D. (2024a). Widespread D'' Anisotropy Beneath North America and the Northeastern Pacific and Implications for Upper Mantle Anisotropy Measurements. *Journal of Geophysical Research: Solid Earth*, 129(10). https://doi.org/10.1029/2024JB029516.

Wolf, J., Li, M., Haws, A. A., and Long, M. D. (2024b). Strong seismic anisotropy due to upwelling flow at the root of the Yellowstone mantle plume. *Geology*, 52(5):379–382. https://doi.org/10.1130/G51919.1.

Wolf, J., Li, M., Long, M. D., and Garnero, E. (2024c). Advances in Mapping Lowermost Mantle Convective Flow With Seismic Anisotropy Observations. *Reviews of Geophysics*, 62(2). https://doi.org/10.1029/2023RG000833.

Wolf, J., Long, Maureen, D., Leng, K., and Nissen-Meyer, T. (2021). Sensitivity of SK(K)S and ScS phases to heterogeneous anisotropy in the lowermost mantle from global wavefield simulations. *Geophysical Journal International*, 228(1):366–386. https://doi.org/10.1093/gji/ggab347.

Wolf, J. and Long, M. D. (2023). Lowermost Mantle Structure Beneath the Central Pacific Ocean: Ultralow Velocity Zones and Seismic Anisotropy. *Geochemistry, Geophysics, Geosystems*, 24(6). https://doi.org/10.1029/2022GC010853.

Wolf, J. and Long, M. D. (2024a). ScS shear-wave splitting in the lowermost mantle: Practical challenges and new global measurements. *Seismica*, 3(1). https://doi.org/10.26443/seismica.v3i1.1128.

Wolf, J. and Long, M. D. (2024b). ScS shear-wave splitting in the lowermost mantle: Practical challenges and new global measurements. *Seismica*, 3(1). doi:10.26443/seismica.v3i1.1128.

Wolf, J., Long, M. D., and Frost, D. A. (2024d). Ultralow velocity zone and deep mantle flow beneath the Himalayas linked to subducted slab. *Nature Geoscience*, 17(4):302–308. https://doi.org/10.1038/s41561-024-01386-5.

Wolf, J., Long, M. D., Leng, K., and Nissen-Meyer, T. (2022). Constraining deep mantle anisotropy with shear wave splitting measurements: challenges and new measurement strategies. *Geophysical Journal International*, 230(1):507–527. https://doi.org/10.1093/gji/ggac055.

Wolf, J., Long, M. D., Li, M., and Garnero, E. (2023). Global Compilation of Deep Mantle Anisotropy Observations and Possible Correlation With Low Velocity Provinces. *Geochemistry, Geophysics, Geosystems*, 24(10). https://doi.org/10.1029/2023GC011070.

Wolfe, C. J. and Silver, P. G. (1998). Seismic anisotropy of oceanic upper mantle: Shear wave splitting methodologies and observations. *Journal of Geophysical Research: Solid Earth*, 103(B1):749–771. https://doi.org/10.1029/97JB02023.

Wookey, J. and Kendall, J.-M. (2007). Seismic anisotropy of post-perovskite and the lowermost mantle. *In Post-Perovskite: The Last Mantle Phase Transition*, pages 171–189. https://doi.org/10.1029/174gm13.

Woollam, J., Münchmeyer, J., Tilmann, F., Rietbrock, A., Lange, D., Bornstein, T., Diehl, T., Giunchi, C., Haslinger, F., Jozinović, D., Michelini, A., Saul, J., and Soto, H. (2022). SeisBench—A Toolbox for Machine Learning in Seismology. *Seismological Research Letters*, 93(3):1695–1709. https://doi.org/10.1785/0220210324.

Wüstefeld, A. (2007). Methods and applications of shear wave splitting: The East European Craton. *PhD thesis, Univ. de Montpellier, France*. http://splitting.gm.univ-montp2.fr/, last accessed 2025/05/05.

Wüstefeld, A., Al-Harrasi, O., Verdon, J. P., Wookey, J., and Kendall, J. M. (2010). A strategy for automated analysis of passive microseismic data to image seismic anisotropy and fracture characteristics. *Geophysical Prospecting*, 58(5):755–773. 10.1111/j.1365-2478.2010.00891.x.

Wüstefeld, A. and Bokelmann, G. (2007). Null Detection in Shear-Wave Splitting Measurements. *Bulletin of the Seismological Society of America*, 97(4):1204–1211. https://doi.org/10.1785/0120060190.

Wüstefeld, A., Bokelmann, G., Barruol, G., and Montagner, J.-P. (2009). Identifying global seismic anisotropy patterns by correlating shear-wave splitting and surface-wave data. *Physics of the Earth and Planetary Interiors*, 176(3–4):198–212. https://doi.org/10.1016/j.pepi.2009.05.006.

Wüstefeld, A., Bokelmann, G., Zaroli, C., and Barruol, G. (2008). SplitLab: A shear-wave splitting environment in Matlab. *Computers &; Geosciences*, 34(5):515–528. https://doi.org/10.1016/j.cageo.2007.08.002. Version 1.0.5 available at http://splitting.gm.univ-montp2.fr/ and version 1.9.0 available at https://github.com/IPGP/splitlab.

Yuan, H. and Levin, V. (2014). Stratified seismic anisotropy and the lithosphere-asthenosphere boundary beneath eastern North America. *Journal of Geophysical Research: Solid Earth*, 119(4):3096–3114. https://doi.org/10.1002/2013JB010785.

Yuan, H. and Romanowicz, B. (2010). Lithospheric layering in the North American craton. *Nature*, 466(7310):1063–1068. https://doi.org/10.1038/nature09332.

Yuan, K. and Beghein, C. (2014). Three dimensional variations in Love and Rayleigh wave azimuthal anisotropy for the upper 800 km of the mantle. *Journal of Geophysical Research: Solid Earth*, 119(4):3232–3255. https://doi.org/10.1002/2013JB010853.

Zhang, Y. and Gao, S. S. (2022). Classification of Teleseismic Shear Wave Splitting Measurements: A Convolutional Neural Network Approach. *Geophysical Research Letters*, 49(12). https://doi.org/10.1029/2021GL097101.

Zhu, H., Bozdağ, E., and Tromp, J. (2015). Seismic structure of the European upper mantle based on adjoint tomography. *Geophysical Journal International*, 201(1):18–52. https://doi.org/10.1093/gji/ggu492.

Zhu, W. and Beroza, G. C. (2018). PhaseNet: A Deep-Neural-Network-Based Seismic Arrival Time Picking Method. *Geophysical Journal International*. https://doi.org/10.1093/gji/ggy423.

Ziegler, P. A., Schumacher, M. E., Dèzes, P., Van Wees, J.-D., and Cloetingh, S. (2004). Post-Variscan evolution of the lithosphere in the Rhine Graben area: constraints from subsidence modelling. *Geological Society, London, Special Publications*, 223(1):289–317. https://doi.org/10.1144/GSL.SP.2004.223.01.13.

Index